

DISS. ETH NO. 27671

CONSTITUTIVE EQUATIONS FOR SIMULATION OF
METAL CUTTING WITH MESHLESS METHODS ON GPU

A dissertation submitted to
ETH ZÜRICH

for the degree of
DOCTOR OF SCIENCES

presented by
HAGEN KLIPPEL
Diplom-Ingenieur Maschinenbau (TU Dresden)
born 26. September 1980
citizen of Neubrandenburg, Germany

accepted on the recommendation of
Prof. Dr. Konrad Wegener, examiner
Prof. Dr. Pavel Hora, co-examiner

2021

ABSTRACT

Machining continues to be one of the most important industrial manufacturing processes and many advances in the understanding of the process have been made since Taylor began his systematic investigation in 1890. However, due to the complex physics involved in machining, there are still problems in process prediction today, which require not only complex material models but also powerful numerical methods. If this symbiosis of different disciplines (manufacturing science, materials science, continuum mechanics, numerics, computer science) succeeds, cutting tools can be developed in a resource-saving way and production can be optimized in a timely manner through extended tool life with increased material removal rates.

The currently prevailing method in the simulation of machining is based on the finite element method (FEM), which, however, requires constant adaptation of the computational grid to the continuously changing geometry in view of the deformations and material separations that occur. This is accompanied by a sharp increase in computational time requirements.

Alternatives to this are the mesh-free methods, which discretise the continuum with particles and approximate the field quantities including their derivatives in the current neighbourhood of each particle. This neighbourhood is inherently updated and therefore does not require any explicit remeshing in case of geometrical changes. Applied to problems that are subject to only minor deformations and no geometric changes, the method has no meaningful application in engineering practice due to large computational time requirements. However, when applied to machining simulation, the method shows drastic advantages over classical methods, especially when using massive parallelization on the GPU.

This work serves as a link between the doctoral theses of M. Röthlin and M. Afrasiabi, which have already been completed at the IWF, and extends the simulation tool with additional material models in the GPU-accelerated program `MFREE_IWF` for massive parallelization. The question of what requirements exist for a material model for machining simulation and how the chip segmentation of Ti6Al4V, which is difficult to machine, can be captured in the simulation is investigated. For this purpose, the implementation of different material models including damage modelling is described. The different material models are primarily applied to 2D problems (orthogonal cutting) and comparisons to FEM analyses and experimental results from the literature are shown. In addition, three-dimensional recalculations of high strain rate material tests (SHTB tests) are performed and the results are compared against FEM simulations and experiments. Furthermore, an application case to a micro milling simulation of pure copper (OFHC) with a diamond tool is shown, where the change from a standard material model to a physically motivated model allows much better process predictions.

In the last part, material tests and microstructure analyses are performed for Ck45 and Ti6Al4V, as well as an extensive machining test program for the same material batches to

obtain measurement data as input for parameter identification of material properties under the extreme conditions of machining. Thanks to GPU acceleration, process predictions can be made within a few minutes using the SPH simulation model, which is why this model serves as the basis for parameter identification of material parameters using inverse methods. Specially conducted orthogonal cutting experiments, in which the process forces were recorded, serve as input for the parameter identification. The material parameters are then modified in the SPH simulation model by means of optimization algorithms so that the errors in the numerically determined process forces become minimal compared to the process forces measured in the experiment. Different optimization methods are used and the advantages and disadvantages of each are shown. The obtained material parameters are then used to recalculate cutting experiments at other process conditions and the quality of the results is compared against experiments in terms of process force predictions as well as chip thicknesses. It is shown that chip segmentation of Ti6Al4V can also be represented by a standard material model with sufficiently fine discretization. Finally, the material parameters for the material model obtained with the different methods are compared. The material parameters determined inversely with the simulation program then represent the best possible state for the simulation of machining processes.

ZUSAMMENFASSUNG

Die Zerspanung stellt einen der wichtigsten industriellen Fertigungsprozesse dar und es wurden seit Beginn der systematischen Untersuchung durch Taylor ab 1890 viele Fortschritte im Verständnis des Prozesses erzielt. Auf Grund der komplexen physikalischen Vorgänge beim Zerspanungsvorgang gibt es dennoch bis heute Probleme in der Prozeßvorhersage, die neben komplexen Werkstoffmodellen auch leistungsfähige numerische Methoden erfordern. Gelingt diese Symbiose aus verschiedenen Disziplinen (Fertigungstechnik, Werkstoffkunde, Kontinuumsmechanik, Numerik, Informatik), lassen sich Zerspanungswerkzeuge ressourcenschonend entwickeln und zeitnah die Produktion durch verlängerte Standzeiten bei gesteigertem Abtragsvolumen optimieren.

Die derzeit vorherrschende Methode in der Simulation der Zerspanung beruht auf der finiten Elemente Methode (FEM), die jedoch bei den auftretenden Deformationen und Materialseparationen eine ständige Adaption des Diskretisierungsgitters auf die sich kontinuierlich ändernde Geometrie erfordert. Damit einher geht ein stark ansteigender Rechenzeitbedarf.

Alternativen hierzu stellen die netzfreien Methoden dar, welche das Kontinuum mit Partikeln diskretisieren und die Feldgrößen samt ihren Ableitungen in der aktuellen Nachbarschaft approximieren. Diese Nachbarschaft wird inhärent aktualisiert und erfordert daher bei geometrischen Änderungen keinerlei explizite Neuvernetzung. Angewendet auf Probleme die nur geringen Deformationen und keinerlei Geometrieänderungen unterliegen, besitzt die Methode auf Grund großen Rechenzeitbedarfs keinerlei sinnvolle Einsatzmöglichkeiten in der Ingenieurpraxis. Wendet man die Methode allerdings auf die Zerspanungssimulation an, zeigen sich hier drastische Vorteile gegenüber klassischen Verfahren, insbesondere unter Verwendung massiver Parallelisierung auf der GPU.

Diese Arbeit dient als Bindeglied zwischen den bereits am IWF fertiggestellten Doktorarbeiten von M. Röthlin und M. Afrasiabi und erweitert das Simulationswerkzeug um weitere Werkstoffmodelle im GPU-beschleunigten Programmwerk `MFREE_IWF` zur massiven Parallelisierung. Es wird der Frage nachgegangen, welche Anforderungen an ein Werkstoffmodell für die Zerspanungssimulation bestehen und wie die Spansegmentierung des schwierig zu bearbeitenden Ti6Al4V in der Simulation erfaßt werden kann. Hierzu wird die Implementierung verschiedener Werkstoffmodelle inklusive Schädigungsmodellierung beschrieben. Die verschiedenen Werkstoffmodelle werden vorrangig auf 2D-Probleme (Orthogonalschnitt) angewandt und Vergleiche zu FEM-Analysen und experimentellen Ergebnissen aus der Literatur werden gezeigt. Zusätzlich erfolgen dreidimensionale Nachrechnungen von Werkstoffversuchen mit hohen Dehnraten (SHTB-Versuche), deren Ergebnisse gegen FEM-Simulationen und Experimente verglichen werden. Darüber hinaus wird auch ein Anwendungsfall in der Mikrofräsimulation von Reinkupfer (OFHC) mit einem Diamantwerkzeug gezeigt, in der der Wechsel von einem Standardwerkstoffmodell zu einem physikalisch motivierten Modell wesentlich bessere Prozeßvorhersagen erlaubt.

Im letzten Teil werden Werkstoffversuche und Mikrostrukturanalysen für Ck45 und Ti6Al4V, sowie für die gleichen Werkstoffchargen ein umfangreiches Zerspanungstestprogramm zur Gewinnung von Meßdaten als Eingang zur Parameteridentifikation von Werkstoffkennwerten bei den extremen Beanspruchungen der Zerspanung durchgeführt. Dank der GPU-Beschleunigung lassen sich mit dem SPH-Simulationsmodell innerhalb weniger Minuten Prozeßvorhersagen durchführen, weshalb dieses Modell als Basis für die Parameteridentifikation von Werkstoffkennwerten mit inversen Methoden dient. Als Eingang für die Parameteridentifikation dienen eigens durchgeführte orthogonale Schnittversuche, bei denen die Prozeßkräfte aufgezeichnet wurden. Daraufhin werden im SPH-Simulationsmodell mittels Optimierungsalgorithmen die Werkstoffkennwerte dahingehend verändert, daß die Fehler aus den im Experiment gemessenen Prozeßkräften im Vergleich zu den numerisch ermittelten Kräften minimal werden. Verschiedene Optimierungsverfahren werden verwendet und die Vor- und Nachteile jeweils aufgezeigt. Die so gewonnenen Werkstoffkennwerte werden dann verwendet, um Zerspanungsexperimente bei anderen Prozeßbedingungen nachzurechnen und die Qualität der Ergebnisse wird durch Vergleich zwischen Experimenten und numerischen Vorhersagen der Prozeßkraft und Spandicke nachgewiesen. Es wird gezeigt, daß die Spansegmentierung von Ti6Al4V auch mit einem Standardwerkstoffmodell bei genügend feiner Diskretisierung dargestellt werden kann. Abschließend erfolgt ein Vergleich der mit den verschiedenen Verfahren gewonnenen Kennwerte für das Werkstoffmodell. Die mit dem Simulationsprogramm invers ermittelten Werkstoffkennwerte bilden dann den bestmöglichen Stand zur Simulation von Zerspanungsvorgängen ab.

ACKNOWLEDGEMENTS

This thesis concludes my work as a research assistant during the past years at the Institute of Machine Tools and Manufacturing (IWF) at ETH Zürich.

First of all, I would like to thank my supervisor Prof. Dr.-Ing. Konrad Wegener, director of the IWF for the guidance, fruitful discussions, support and the freedom required to conduct this research.

I also would like to thank Prof. Dr. Pavel Hora for co-examination and review of the thesis.

Special thanks to Dr. Matthias Röthlin, who initiated and pushed forward the whole meshfree simulation project and gave me lots of support not just in the beginning of my research. Further thanks are directed to my workmate Dr. Mohamadreza Afrasiabi for his contribution in this project. Hereby I'd like to thank as well my colleagues Andreas Zschippang and Marcel "GG" Gerstgrasser for numerous and long discussions even until sunrise.

Many thanks also to my group leaders Dr. Fredy Kuster and Dr. Michal Kuffa as well as to my colleagues Stefan Süßmaier, Moritz Wiessner, Knut Krieger, Thomas Tancogne-Dejean, Christoph Baumgart, Linus Meier, Fabian Kneubühler, Mikhail Klyuev, Sandro Wigger, Albert Weber and Lukas Seeholzer which not just helped me but also enabled the experimental part of this work with their huge experiences and valuable inputs. Thanks are directed also to the students Adrian Fuhrer and Igor Podjanin for their help.

Finally, I want to express my sincere gratitude to my family and friends for guiding me and making me what I became, giving support throughout easy and difficult times.

CONTENTS

Nomenclature	1
1 INTRODUCTION	7
2 STATE OF THE ART	11
2.1 Meshless Methods	11
2.2 GPGPU Acceleration	12
2.3 Metal Cutting (Simulation)	13
2.3.1 Meshfree Metal Cutting Simulations	14
2.4 Constitutive Modelling for Metal Cutting Simulations	14
2.4.1 Material Testing	15
2.4.2 Inverse Parameter Identification from Cutting Tests	16
2.5 Research Gap and Objectives	17
3 CONTINUUM MECHANICS	19
3.1 Eulerian and Lagrangian Description	19
3.2 Kinematics	19
3.2.1 Deformation Gradient	20
3.2.2 Additive Strain Rate Decomposition - Hypoelasticity	22
3.3 Kinetics	24
3.3.1 Stress Measures	24
3.3.2 Invariants of the Stress Tensor	25
3.4 Balance Equations	25
3.4.1 Mass Conservation	25
3.4.2 Momentum Equation	26
3.4.3 Angular Momentum Equation	27
3.4.4 Energy Equation	28
3.4.4.1 Frictional Dissipation	28
3.4.4.2 Plastic Dissipation	29
3.4.4.3 Modified Energy Equation	29
3.5 Material Behaviour and Constitutive Modelling	29
3.5.1 Linear Elastic Material Behaviour	30
3.5.1.1 Rate Form	30
3.5.1.2 Equation of State	32
3.5.1.3 Thermal Expansion	32
3.5.2 Nonlinear Material Behaviour - Plasticity	33
3.5.2.1 Monotonic Tensile Loading	33
3.5.2.2 Load Reversal	34
3.5.2.3 Behaviour at Elevated Temperatures	35
3.5.2.4 Recovery	36
3.5.3 Multiaxial Generalization of Plasticity	36
3.5.4 Integration of Plasticity Models - Radial Return Projection	42
3.6 Damage Modelling	45

Contents

3.6.1	Damage Initiation	45
3.6.2	Damage Evolution	47
4	MESHLESS METHODS	49
4.1	Derivation of the SPH	49
4.2	Issues and Improvements to the SPH	51
4.2.1	Conservation Properties	52
4.2.2	Tensile Instability	52
4.2.3	Zero Energy Modes	53
4.2.4	Boundary Condition Application	53
4.2.5	Interpolation Normalization and Consistency	54
4.2.6	Artificial Viscosity	56
4.2.7	Artificial Stresses	57
4.2.8	XSPH	58
4.3	Discretization of the Continuum Equations	59
4.3.1	Velocity Gradient Computation	59
4.3.1.1	Strain Rate	59
4.3.1.2	Stress Rate	60
4.3.2	Continuity Equation	60
4.3.3	Momentum Equation	60
4.3.4	XSPH	60
4.3.5	Heat Equation	61
4.3.6	Contact Algorithm	62
4.3.6.1	Contact Force	62
4.3.6.2	Friction Force	63
4.3.7	Time Integration	64
5	OXLEY'S PROCESS FORCE MODEL	65
5.1	Oxley Force Model	67
5.1.1	Solution Algorithm	70
5.1.2	Modified Algorithm	73
5.2	Extension to Other Flow Stress Models	75
5.3	Example Calculations	76
6	INVESTIGATION OF STRESS STATES IN ORTHOGONAL CUTTING	79
6.1	Numerical Model	79
6.1.1	Geometry and Mesh	79
6.1.2	Constitutive Model	80
6.1.2.1	Workpiece	80
6.1.2.2	Cutter	81
6.1.3	Boundary Conditions	81
6.1.4	Contact and Friction	83
6.2	Convergence Study	83
6.3	Results	84
6.3.1	Process Forces	86
6.3.2	Temperatures and Temperature Rates	88
6.3.3	Plastic Strains and Plastic Strain Rates	92
6.3.4	Stress State Investigation	95
6.3.4.1	Hydrostatic Stresses	95

6.3.4.2	Equivalent Stresses	95
6.3.4.3	Detailed Investigation of a Single Particle	98
6.3.4.4	Display in the Principal Axis System	99
6.3.4.5	Sorting Principal Stresses by Quaternions	101
6.3.5	Runtimes	103
6.4	Effect of Material Anisotropy	103
6.5	Discussion	105
7	SPH TEST SIMULATIONS	107
7.1	Improved SPH - Application Example	107
7.2	Artificial Stresses	109
7.3	Johnson-Cook Model Implementation and Validation	113
7.3.1	Accuracy of Radial Return Projection	113
7.3.1.1	Newton Method	113
7.3.1.2	Secant Method	115
7.3.2	Performance Newton and Secant Method	117
7.3.3	Integration of the Plasticity Model with Implicit and Explicit Method	121
7.4	Damage modelling	125
7.4.1	Johnson Cook Fracture Strain	125
7.4.2	Implementation Aspects of Damage Initiation and Evolution	126
7.4.2.1	Results	128
7.4.2.2	Results with Modified Particle Interactions	129
7.4.3	Modified Johnson Cook Fracture Strain Equation for 50SiB8	133
8	MACHINING SIMULATIONS	139
8.1	Johnson Cook Flow Stress Model Extensions	139
8.1.1	Johnson Cook Tanh Extension: Calamaz 2008	139
8.1.1.1	Derivative of JC-tanh2008 Model for Newton Iterations	140
8.1.2	Johnson Cook Tanh Extension - Calamaz 2010	142
8.1.3	Johnson-Cook Tanh Extension - Calamaz 2011	143
8.1.4	Johnson-Cook Tanh Extensions - Sima / Özel	143
8.1.5	Comparison of Johnson-Cook-Type Flow Stress Models	144
8.2	Orthogonal Cutting Simulations with Original and Modified JC-models	147
8.2.1	Results without Damage Modelling	149
8.2.2	Results with Damage Modelling	154
8.2.3	Discussion	159
8.3	Micro Milling of OFHC copper	160
8.3.1	Experiments	160
8.3.2	Numerical Model	160
8.3.3	SCGL Model	162
8.3.3.1	SCG Shear Modulus Model	162
8.3.3.2	SCG Melt Temperature Model	163
8.3.3.3	SCGL Flow Stress Model	163
8.3.3.4	Numerical Integration of the SCGL Flow Stress Model	165
8.3.4	Material Parameters	165
8.3.5	Results	166
8.3.6	Discussion	168
9	MATERIAL PARAMETER DETERMINATION	169

Contents

9.1	Raw Material	169
9.1.1	Chemical Analysis	171
9.1.1.1	Ti6Al4V	171
9.1.1.2	Ck45	171
9.1.2	Hardness	172
9.1.3	Microstructure	173
9.1.3.1	Etching	173
9.1.3.2	EBSD	177
9.2	Material Parameter Determination from Material Testing	184
9.2.1	Tensile Tests	184
9.2.2	Parameter A, B and n from Quasi-Static Tests at Room Temperature . .	186
9.2.3	Parameter C from Low Strain Rate Tests at Room Temperature	186
9.2.3.1	Ti6Al4V	187
9.2.3.2	Ck45	189
9.3	Cutting Experiments	193
9.3.1	Cut Tool	193
9.3.1.1	Optical Measurement of Cutter	195
9.3.2	Cutting Experiments	197
9.3.2.1	Force Measurement	197
9.3.2.2	Test Plan	198
9.3.2.3	Experimental Results	199
9.3.3	Chip Shapes	200
9.3.3.1	Ti6Al4V	202
9.3.3.2	Ck45	207
9.4	Inverse Material Parameter Identification	212
9.4.1	Optimization Algorithms	212
9.4.1.1	Simplex (Nelder-Mead)	212
9.4.1.2	Bayes	212
9.4.1.3	Differential Evolution	213
9.4.2	Test Simulations	213
9.5	Identification of Material Parameters with Oxley's Process Force Model	218
9.5.1	Ti6Al4V Results	220
9.5.2	Ck45 Results	222
9.5.3	Identification with Several Experiments Simultaneously	224
9.5.3.1	Ti6Al4V	224
9.5.3.2	Ck45	226
9.5.4	Results Discussion and Conclusion	227
9.6	Identification of Material Parameters using a SPH Cutting Simulation	228
9.6.1	Inverse Parameter Identification for Ti6Al4V	230
9.6.1.1	Inverse Parameter Identification with DE-method	230
9.6.1.2	Inverse Parameter Identification with BAYES-method	234
9.6.1.3	Inverse Parameter Identification with SIMPLEX-method	237
9.6.2	Inverse Parameter Identification for Ck45	239
9.6.2.1	Inverse Parameter Identification with DE-method	239
9.6.2.2	Inverse Parameter Identification with SIMPLEX-method	242
9.7	Identification of Material Parameters Including the Friction Coefficient	243

9.7.1	Identification of the Friction Coefficient Constant	243
9.7.1.1	Ti6Al4V	243
9.7.1.2	Ck45	243
9.7.2	Identification of a Friction Coefficient Using Shear Stress Limit	245
9.7.2.1	Ti6Al4V	245
9.7.2.2	Ck45	246
9.8	Recalculation of Cutting Experiments	247
9.8.1	Ti6Al4V	247
9.8.2	Ck45	253
9.8.3	Comparison of Parameter Identification Results	257
9.8.3.1	Static Flow Curve	257
9.8.3.2	Strain Rate Sensitivity	258
9.8.3.3	Flow Stress Curves at Different Strain Rates and Temperatures	260
9.8.4	Results Discussion	263
10	CONCLUSIONS AND OUTLOOK	265
11	APPENDIX	269
11.1	Stress States in Orthogonal Cutting	269
11.1.1	Load Path Visualization Particle A	269
11.1.2	Load Path Visualization Particle D	270
11.1.3	Load Path Visualization Particle E	271
11.1.4	Load Path Visualization Particle K	272
11.2	JC Flow Stress and Fracture Strain Material User Subroutine VUMAT	273
11.2.1	Abaqus VUMAT User Subroutine	273
11.2.2	Abaqus Input File Template	283
11.3	Orthogonal Cutting Experiments	286
	Curriculum Vitae	319
	Publications	321

NOMENCLATURE

NOTATION AND OPERATORS

Symbol	Meaning
x	scalar quantity
\underline{X}	1st order tensor (vector)
$\underline{\underline{X}}$	2nd order tensor
$\underline{\underline{\underline{X}}}$	3rd order tensor
$\underline{\underline{\underline{\underline{X}}}}$	4th order tensor
$\underline{\underline{Z}} = \underline{\underline{\underline{X}}} : \underline{\underline{Y}}$	contraction of a 4th order tensor with a 2nd order tensor
$\det(\underline{\underline{\underline{X}}})$	determinant of a tensor
∇	Vector with partial derivatives wrt coordinates
$\nabla_{\underline{\underline{\sigma}}}$	Vector with partial derivatives wrt to stress components $\nabla_{\underline{\underline{\sigma}}}F = [\partial F / \partial \sigma_{xx}, \dots]^T$
∇_0	Vector with partial derivatives wrt to reference configuration
$tr(\underline{\underline{X}})$	trace of a tensor $tr(\underline{\underline{X}}) = X_{ii}$
$\langle \cdot \cdot \rangle$	approximated quantity
$ X $	absolute value of X
$ \underline{\underline{X}} $	tensor norm

SPECIFIC SYMBOLS

Symbol	Meaning
α	clearance angle of the cutter
α_{av}	artificial viscosity parameter
α_{th}	thermal expansion coefficient
A	area in the current configuration
A, B, C, m, n	Johnson-Cook flow stress model constants
$A_{contact}$	contact surface area
\underline{b}	volume force
β_{av}	artificial viscosity parameter
c_p	specific heat
c	speed of sound
C	material parameter (Oxley model)
$\underline{\underline{C}}$	right Cauchy-Green tensor
\underline{D}	damage variable for damage evolution
D_{RT1}, D_{RT2}	Rice & Tracey damage parameter

Contents

$D_1 - D_5$	Johnson-Cook fracture strain equation constants
$D_1 - D_8$	modified Johnson-Cook fracture strain equation constants
$\underline{\underline{D}}$	rate of deformation tensor
δ	thickness ratio, material parameter (Oxley model)
$\underline{\underline{\varepsilon}}$	strain tensor
$\underline{\underline{\varepsilon}}_{el}$	elastic strain tensor
$\underline{\underline{\varepsilon}}_{pl}$	plastic strain tensor
$\bar{\varepsilon}_{pl}$	equivalent plastic strain
$\bar{\varepsilon}_f$	fracture strain
$\dot{\bar{\varepsilon}}_{pl}$	equivalent plastic strain rate
$\dot{\varepsilon}_{pl}^0$	reference plastic strain rate
$\bar{\varepsilon}_{th}$	thermal strain
ϵ_{ijk}	Levi-Civita symbol
ϵ_{as}	artificial stress parameter
ϵ_{RR}	control parameter for radial return algorithm in Secant B method
ϵ_{XSPH}	parameter for XSPH
η_{av}	artificial viscosity parameter
η_{fric}	fraction of frictional work dissipated into heat
η_{TQ}	fraction of plastic work converted into heat (Taylor-Quinney coefficient)
E	Young's modulus
$\underline{\underline{E}}$	Green-Lagrange strain tensor
$\underline{\underline{E}}_{lin}$	linearised Green-Lagrange strain tensor (engineering strain)
$\underline{\underline{E}}$	elasticity tensor
$\underline{\underline{E}}_{ijkl}$	elasticity tensor
f	feed per revolution
\underline{f}	surface force
$\bar{F}(\cdot)$	plastic potential
\underline{F}	force vector
F_c	cut force
F_c^{exp}	experimentally measured cut force
F_c^{sim}	simulated cut force
ΔF_c	cut force error
F_f	feed force
F_f^{exp}	experimentally measured feed force
F_f^{sim}	simulated feed force
ΔF_f	feed force error
ΔF_{total}^2	summed square error of cut and feed force
F_F	friction force $F_F = \underline{E}_{fric} $
\tilde{F}_{drift}	drift of the measurement signal
\tilde{F}_{meas}	measured force signal including drift \tilde{F}_{drift}
\tilde{F}_{proc}	measured force signal drift corrected
\underline{E}_{fric}	friction force vector
\underline{E}_{cont}	contact force vector
$\underline{\underline{F}}$	deformation gradient

$\underline{\underline{F}}_{el}$	elastic part of the deformation gradient
$\underline{\underline{F}}_{pl}$	plastic part of the deformation gradient
$G(\cdot)$	plastic potential non-associative flow rule
G	shear modulus
G_f	critical energy release rate
γ	rake angle of the cutter
γ_{AB}	shear strain in the shear plane
$\dot{\gamma}_{AB}$	shear strain rate in the shear plane
Γ_0	domain boundary of a body Ω_0 in the reference (initial) configuration
Γ_c	domain boundary of a body Ω_c in the current configuration
h	tool-chip contact length (Oxley model)
h_{avg}	average chip thickness
h_{SPH}	smoothing length (SPH)
\underline{H}	displacement gradient
\underline{I}	identity matrix
\underline{I}	total momentum
$\dot{\underline{I}}$	rate of total momentum
IC	Inscribed Circle
I_1, I_2, I_3	stress tensor invariants
J_2, J_3	deviatoric stress tensor invariants
k_{AB}	shear flow stress in the shear plane
k_{chip}	shear flow stress in the tool-chip interface
k_{int}	shear flow stress in the tool-chip interface
K	bulk modulus
K_{1C}	critical stress intensity factor for mode I fracture
LE	Cutting edge length
\underline{L}	velocity gradient
$\underline{\underline{L}}_{el}$	elastic part of the velocity gradient
$\underline{\underline{L}}_{pl}$	plastic part of the velocity gradient
L	characteristic element length
$\Delta\lambda$	plastic multiplier $\Delta\lambda = \dot{\lambda} \cdot \Delta t$
λ	friction angle (Oxley's force model)
λ	heat conductivity
$\dot{\lambda}$	time derivative of plastic multiplier
m_i	mass of particle i
m_p	mass of particle
μ	shear modulus
\underline{n}	surface normal
n_{calls}	maximum number of optimizer function calls
n_{Stress}	stress exponent artificial stresses
n_x	number of particles in x direction
n_y	number of particles in y direction
ν	Poisson's ratio
Ω_0	domain of a body in the reference (initial) configuration
Ω_c	domain of a body in the current configuration

Contents

ω	damage variable for damage initiation
ω_{CL}	damage variable according to Cockcroft-Latham
p	hydrostatic pressure
ϕ	shear angle
$\varphi(\cdot)$	mapping between current and reference configuration
\dot{Q}	heat rate
r_c	cutting edge radius
r_{chip}	chip curling radius
r_n	optically measured cutting edge radius
ρ	density
R	resultant force on the tool
RE	Radius of cutter Edge
R_T	thermal number (Oxley model)
\underline{R}	rotation matrix
S	Cutting edge height
\underline{S}	deviatoric part of the Cauchy stress tensor
\underline{S}^{trial}	deviatoric trial stress tensor
σ_N	normal stress acting on the rake face
$\underline{\sigma}_H$	Volumetric part of the Cauchy stress tensor
$\underline{\sigma}$	Cauchy stress tensor
$\dot{\underline{\sigma}}$	time derivative of Cauchy stress tensor
$\underline{\sigma}^{cor}$	corotated Cauchy stress tensor
$\underline{\sigma}^{PK1}$	First Piola-Kirchhoff stress tensor
$\underline{\sigma}^{PK2}$	Second Piola-Kirchhoff stress tensor
$\sigma_I, \sigma_{II}, \sigma_{III}$	principal stresses
σ^*	stress triaxiality
σ_{eq}	equivalent stress according to von Mises
σ_y	yield stress
θ	angle between resultant force R and the shear plane
t	time
Δt	time increment
t_1	uncut chip thickness
t_2	chip thickness
\underline{t}	traction vector
T	temperature
\dot{T}	temperature rate
T^*	homologous temperature
T_{AB}	shear plane temperature
T_C	chip temperature (Oxley model)
T_f	melt temperature
T_{int}	tool-chip interface temperature
T_{mod}	velocity modified temperature (Oxley model)
T_{ref}	reference temperature
T_W	initial workpiece temperature
τ_y	shear yield limit

\underline{u}	displacement vector
$v_{T_{mod}}$	dimensionless material parameter for velocity modified temperature T_{mod}
\underline{u}	displacement vector
$\underline{\underline{U}}$	right stretch tensor
v_c	cut speed
$\underline{\underline{V}}$	left stretch tensor
$\underline{\underline{V}}_{el}$	elastic part of the left stretch tensor
$\underline{\underline{V}}_{pl}$	plastic part of the left stretch tensor
V	volume in the current configuration
V_0	volume in the reference (initial) configuration
W	Kernel function
$\underline{\underline{W}}$	spin tensor
ω_c	weighting factor cut force
ω_f	weighting factor feed force
\underline{x}	position vector in current configuration
$\underline{\underline{X}}$	position vector in reference configuration

ACRONYMYS

Acronym	Meaning
ALE	Arbitrary Lagrangian Eulerian
ANOVA	ANalysis Of VAriance
BCC	Body-Centered Cubic lattice
BEM	Boundary Element Method
CFD	Computational Fluid Dynamics
CPFE	Crystal Plasticity Finite Element
CFL	Courant-Friedrichs-Lewy number
CPU	Central Processing Unit
CSPM	Corrected Smoothed Particle Method
CUDA	Compute Unified Device Architecture
DE	Differential Evolution algorithm
DIN	Deutsches Institut für Normung
DOE	Design Of Experiments
EFG	Element Free Galerkin Method
FE	Finite Element
FDM	Finite Difference Method
FEM	Finite Element Method
FLIP	Fluid Implicit Particle
FPM	Finite Point set Method
GPGPU	General Purpose Computing on the GPU
GPU	Graphics Processing Unit
HCP	Hexagonal Close-Packed lattice
ISO	International Organization for Standardization
JC	Johnson-Cook
MPM	Material Point Method

Contents

OFHC	Oxygen-Free High thermal Conductivity copper
PDE	Partial Differential Equation
PIC	Particle In Cell
PFEM	Particle Finite Element Method
PSE	Particle Strength Exchange
RKPM	Reproducing Kernel Particle Method
RSM	Response Surface Method
SCG	Steinberg-Cochran-Guinan
SCGL	Steinberg-Cochran-Guinan-Lund
SHB	Split Hopkinson Bar
SHPB	Split Hopkinson Pressure Bar
SHTB	Split Hopkinson Tension Bar
SSL	Shear Stress Limit
SPH	Smoothed Particle Hydrodynamics
TL	Total Lagrangian
UL	Updated Lagrangian

INTRODUCTION

Cutting operations are within the most important manufacturing processes worldwide. According to Merchant [154], machining operations contribute to 15% of the total product value in the industrialized countries. The cutting process is applicable to various materials but needs to be optimized for each one individually. The main questions are which cutter geometry and which process parameters (cut speed, feed) are required to minimize tool wear, maximize the material removal rate and optimize surface finish and chip shapes. The classic approach is based on cut tests in order to develop a new cutter or to adapt it to new process conditions. An example for resulting chip shape and tool wear during a cut test is provided with figure 1.1. These tests are time consuming and it is desirable to shorten the development time of new cutters for reduced times to market.

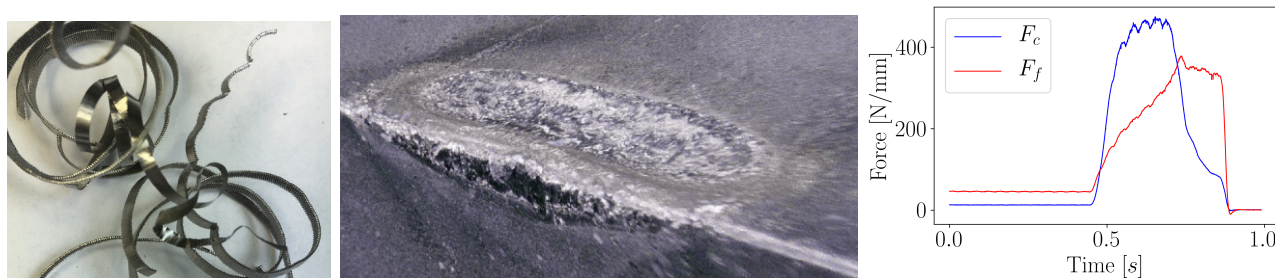


Figure 1.1: Orthogonal cutting test without coolant and lubrication of Ti6Al4V with $v_c = 300 \frac{m}{min}$ and $f = 0.4mm$, cut width 2.05mm, average cut diameter $d_{avg} = 64.45mm$, $n=6$ revolutions resulting in a removal of $V_{mr} = 996.2mm^3$ material. The pictures show the chip shape (left), tool wear (middle) and measured process forces (right). The process forces, specifically the feed force, do not reach a steady state possibly due to high wear.

Research is focussed on this task for more than 100 years [154] and went through three main development steps for the prediction of metal cutting processes. Initially empirical models were used to predict process forces and tool wear. In the 1940s science based modelling evolved where force models were used to resolve the physics in the shear zone. Lately, computer based modelling approaches came up to simulate cutting processes with numerical methods. This was made possible by the development of computers and their strongly increased computer power in the recent past. These simulations allow to predict chip forming and breaking, the resulting process forces as well as the thermal and mechanical loads on the cutting edge and its wear behaviour. Thus, tool and process optimization becomes possible before the first in-situ tests are conducted. With the help of numerical simulations the early cutter and process development are supported and can help to reduce the experimental effort. On top, simulation results will deliver a better understanding of the processes occurring in the micro-scale in and around the cutter and the cut surfaces.

Numerical modelling approaches for structural simulations can be classified into four main types:

- Finite Difference Method (FDM), listed for the sake of completeness but outdated in structural mechanics.
- Boundary Element Method (BEM), some research has been done on metal cutting simulation with BEM in the past.
- Finite Element Method (FEM)
- Meshless Methods (Particle Methods)

Nowadays, the FEM is dominating in numerical simulations of the cutting process. The FEM is a very powerful and mature tool with several vendors on the market. It is based on a mesh discretization of the continuum which leads in cutting simulation to its biggest drawback: when higher deformations occur the mesh is prone to severe distortions leading to numerical instabilities with a solution subsequently spoiled. This can be avoided by regular remeshing of the domain but requires considerable computation time and may even need manual user input. In order to avoid these drawbacks particle methods come into play: In particle methods a mesh is not required. The continuum is resolved into particles only, with each particle carrying the local field information. Fields and it's gradients are assessed by so called kernel functions which are defined in the vicinity of each particle. These kernel functions have a limited diameter of influence around each particle and use field values from neighbouring particles inside this diameter to approximate field values. In each time-step of the analysis new neighbour constellations are possible due to particle movement induced by stresses. By the help of these kernel functions, new particle compositions with changing neighbours are inherently included in the assessment. Thus, any distortion of the domain / continuum can be tracked automatically with arbitrary new particle arrangements.

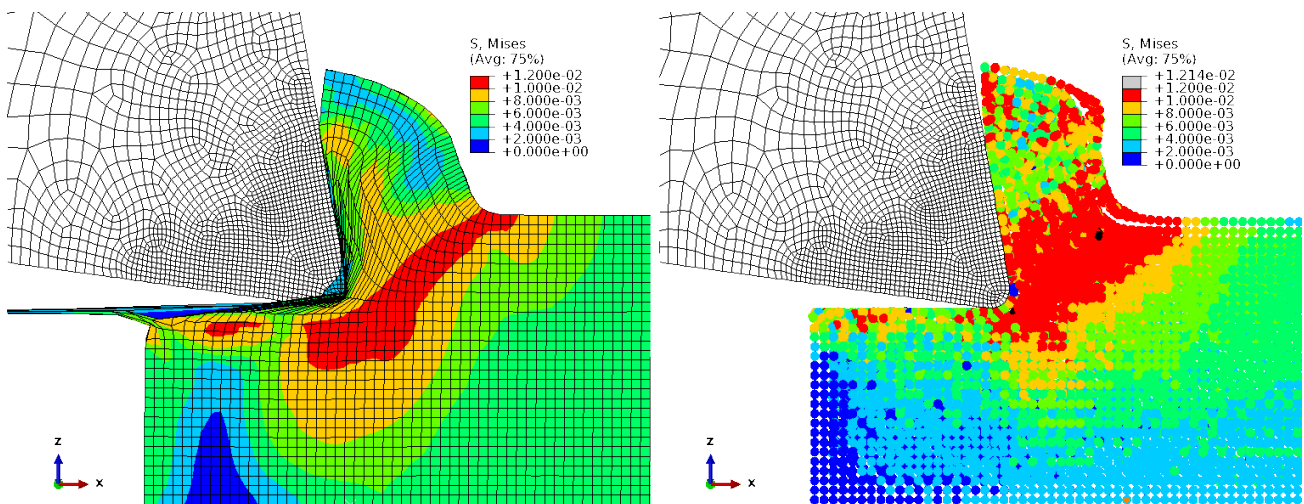


Figure 1.2: Orthogonal cutting simulation of Ti6Al4V with FEM (left) shows severe mesh distortion without domain remeshing while the SPH (right) resolves the material separation without issues. The displayed result is the equivalent stress (von Mises) in the bomb unit system [$10^{-2}GPa$].

Even though particle methods are efficient in handling large deformations and material separations the computational effort is still high resulting in large runtimes. With the advent

of parallel computing, in particular general purpose computations on the graphics processing unit (GPGPU), these can be reduced significantly to reasonable levels making the solver use in optimization problems feasible.

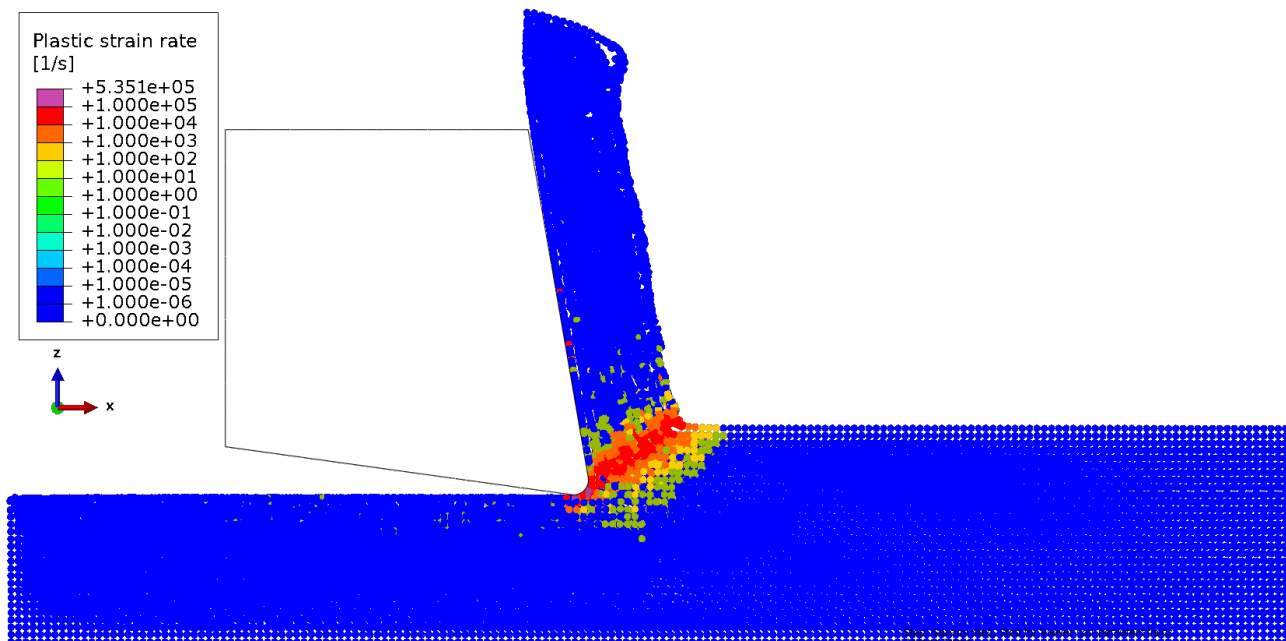


Figure 1.3: Orthogonal cutting simulation of Ti6Al4V ($v_c = 70 \frac{m}{min}$ and $f = 0.1mm$) with SPH in Abaqus/Explicit. Displayed are the plastic strain rates [1/s] which are in the peak location at the cutting edge up to $\dot{\epsilon}_{pl} \approx 500'000/s$ and in the primary shear zone $\dot{\epsilon}_{pl} \approx 100'000/s$.

Besides the numerical method for discretizing the continuum another important aspect is the selection of an appropriate constitutive model for the simulation. This is not an easy task since in metal cutting the most severe imaginable conditions occur [13]:

- large deformations with strains up to 700% and strain rates reaching $10^6 s^{-1}$,
- temperatures in the range of $500^\circ C$ to $1400^\circ C$,
- temperature rates up to $10^6 K/s$, temperature gradients up to $60K/\mu m$ and
- compressive pressures up to 3 GPa.

Since these conditions cannot be reproduced in classic material testing, e.g. tensile tests, it is required to use the "machining as a high-strain-rate property test" [182] to inversely identify constitutive model constants from cutting experiments itself. Hence, this thesis focuses on the constitutive modelling for numerical cutting simulations and the main contributions are as follows:

- An in-depth investigation of the occurring stress states in metal cutting is performed and requirements for constitutive models are derived.

INTRODUCTION

- Different constitutive models are implemented into a GPGPU-accelerated meshfree solver. They are applied within 2D and 3D cutting cases and compared to experimental results.
- For two materials, Ck45 & Ti6Al4V, material tests and orthogonal cutting experiments are conducted.
- The results of the orthogonal cutting experiments will be used to inversely identify constitutive model constants within optimization loops. The resulting constitutive model constants are compared to the results of the material tests and will be used to validate numerically predicted process forces at different process conditions with the experimental results.

An overview of relevant work related to the fields broached in this thesis are provided. Starting with an overview of meshless methods, GPGPU computations are introduced followed by metal cutting simulations in general with a special focus set on meshfree computations. Finally, constitutive modelling for cutting simulations and material parameter identification conclude the state of the art, followed by a deduction of the research gap and the objectives for this thesis.

2.1 MESHLESS METHODS

Solutions for partial differential equations (PDE) can be derived in analytical form for special cases only. Where this is impossible, approximations of the solution have to be computed on discrete spatial points. When these spatial points are located on a grid with fixed connectivity one recovers well known meshbound methods like the Finite-Difference-Method (FDM), Finite-Element-Method (FEM) or Boundary-Element-Method (BEM). An alternative to meshbound methods are meshless methods which discretize the continuum with loosely connected points. From these methods only those relevant to this work are listed in short. Most prominent example of such meshless methods is today the smoothed particle hydrodynamics (SPH) which works on the strong form. Its beginnings were in the 1970s where it was developed by [140] and Gingold and Monaghan [196] to solve astrophysical problems. Since then the method found applications not only in astrophysics but various other disciplines, e.g. fluid dynamics [109, 136], highly dynamic events like explosions [135], solid mechanics [8, 188], geophysics [124], in engineering problems [253] or virtual surgery for medicine applications [169]. A large summary of SPH applications is compiled in [68].

Even though the SPH found intense use in various disciplines, it has some deficiencies which require special attention. For various problems correctors have been introduced in order to tackle the boundary deficiency [103, 106, 195, 259]. Under shock loading spurious oscillations can occur in the velocity and pressure field leading to divergent simulations which is usually attenuated by artificial viscosity terms [165]. Other issues are the tensile instability, which can be improved with [103, 163]. A comprehensive overview can be found in [219].

Another meshfree method is the Material Point Method (MPM) which is based on the Particle In Cell (PIC) method for fluid dynamics applications [85] and was improved by the FLuid Implicit Particle method (FLIP) [30]. Based on PIC and FLIP the MPM has developed for solid mechanics [235, 236]. In contrast to the SPH which works on the strong form, the MPM is based on the weak form. Particles (material points) are used to carry mass, density, velocity, stresses and other internal variables in a Lagrangian description, while a fixed background

grid is used to solve the balance of momentum in an Eulerian description. This is the main difference to other particle methods, where all equations are solved on the particles. The weak form used in the MPM gives an advantage over the SPH as stress free boundaries are fulfilled automatically. Further, the MPM is first order complete and therefore rigid body modes are correctly treated without any additional needs. A disadvantage of the method is the higher computational cost which it shares with meshfree methods in general.

The last meshless method of interest in this work is the Particle Finite Element Method (PFEM) which uses features of meshless and meshbound methods [178]. The continuum is resolved by particles which are then used to mesh the domain. On this mesh the Lagrangian equations are solved and the state variables are updated. The nodes of the mesh then move accordingly and create the new particle positions of the next step. The method was initially developed for fluid mechanics [178] and found application in various fields [176, 206].

From the aforementioned particle methods only the SPH (ABAQUS, LS-DYNA) and the MPM (MPMSIM) are available in commercial software.

2.2 GPGPU ACCELERATION

Numerical simulations often require large amounts of compute time. In an attempt to keep runtimes reasonable developers strive to divide the work load of such simulations and process in parallel on multiple CPU cores. The amount of CPU cores in workstations is limited and further speedups would require swapping to compute cluster which is not accessible to everyone and usually expensive. An alternative and rather recent development are graphics processing units (GPUs) which were initially developed for computer games to perform shader computations for visualizations purposes. These computations require fast internal data transfer and multiple compute cores for performance reasons. Since shader operations are in general nothing else then large scale vector operations, researchers started to exploit these capabilities for solving a linear heat equation [212]. While this was a rather clumsy approach things have changed since then with the introduction of CUDA by Nvidia, which offers programming in a higher programming language like C or Fortran and makes developments attractive for the research community.

Numerical simulations have since then utilized the advantages of GPGPU-computations for example in FEM for solving the Poisson equation [70, 71], for surgical simulations [241] or a mechanical cutting simulation of rock chipping and fragmentation in [161]. Already in 2011 it found adoption to the commercially available FEM-software ABAQUS offering at least partial GPU-support. Recently, the simulation of 50 million atoms in molecular dynamics on a single GPU was reported by [263]. Related to SPH, in 2003 the first trials on GPU-accelerated SPH were performed in [10] but a breakthrough was achieved with [75] which lead to various SPH implementations for fluid dynamics, for example GPUSPH and DUALSPHYSICS.

2.3 METAL CUTTING (SIMULATION)

In the early stage of metal cutting, valuable information about the cutting process could be gained by experiments only. Groundbreaking work has been performed in 1907 by Taylor [238] whose investigations over 26 years lead to productivity increases between 200 – 300%. According to Merchant [154], the development continued with some empiric relations, of which the Kienzle-Victor model [110] is probably the most renowned and still in use today. The empirical models do not consider real physical behaviour due to the very complex process during the cutting. A science-based modeling was initiated with the work of Ernst [64] and Merchant [155, 156] where the first force model of the cutting process was developed. With several further steps these developments culminated in Oxley's predictive machining theory [182] which was extended in the mean time by some more recent material models in [1, 120] and enhanced temperature prediction in [44].

With the development of computers two branches developed for the simulation of cutting according to [50]: kinematic and numeric simulation. The kinematic simulation is an overall simulation on the "macro-scale" of the cutting process and can deliver information on forces and energies based on empirical relations but does not resolve detailed thermo-mechanical aspects, unlike the numerical simulation.

As summarized in [13] the numerical simulation enables the prediction of process forces, tool wear, chip formation and breaking, burr formation, surface finish and formation of residual stresses. Due to the severe conditions of the cutting process this is however complicated, since not only the material modelling is challenging but also the treatment of the large deformations and material separations require special attention with regards to the domain discretization.

In general, numerical simulations can be roughly classified into Eulerian approaches, with a mesh fixed in space and the material flowing through; Lagrangian approaches, where the mesh is fixed to the material and a mixture of both, the Arbitrary Eulerian-Lagrangian (ALE) approach. Early work in metal cutting simulations [220, 234] utilized an Eulerian approach, which has the advantage that the material can flow around the cutter. In order to model the same with an Lagrangian approach (FEM) the material separation at the cutting edge needs special treatment for which different approaches were developed. The separation itself is modelled either by regular remeshing [174], element deletion [277] or a predefined separation path [269]. All these approaches have drawbacks as the computational cost is either high or inaccuracies are introduced into the solution due to remeshing or when a predefined separation path or element deletion is used. Therefore, most often orthogonal cutting processes are simulated because they allow for computationally efficient idealization in 2D. Nevertheless, the FE-method can be seen as a standard approach for numerical cutting simulations and can be used for 3D simulations as well [6, 35, 133].

A different attempt is the ALE which tries to overcome disadvantages of Eulerian and Lagrangian approaches by calculating in parallel on Eulerian and Lagrangian meshes. Quantities between the configurations are remapped. By that, the body behaves like a fluid in zones of material separation and large deformations. In the recent past, the method became quite popular in metal cutting simulations [12, 14, 138].

2.3.1 Meshfree Metal Cutting Simulations

A completely different attempt are meshfree techniques. They easily represent large deformations and material separation and offer an elegant way to model the plastic flow around the cutter without the need of any remeshing of the continuum which is in contrast to meshbound methods like the FEM. The utilization of meshless techniques for structural simulations started in the early 1990s with the SPH[188] and are a rather new approach in numerical cutting simulations initiated with [88]. Some more recent work was conducted by [145, 177, 214] and the latest developments were performed at the IWF of ETH including GPU-accelerated machining simulations [4, 5, 210, 211].

Besides SPH, other meshfree methods used for metal cutting simulations are mainly the PFEM [205, 206, 215] and very rare use is found for MPM [11, 172] (only 2D) and the finite point set method (FPM) [246, 247]. A comparison of the two main meshfree methods SPH and FPEM versus FEM and ALE in metal cutting simulations is performed in [229].

2.4 CONSTITUTIVE MODELLING FOR METAL CUTTING SIMULATIONS

While the discretization of the continuum for numerical simulations can be solved with different methods, each with advantages and drawbacks, another issue common to all numerical (cutting) simulations is the constitutive model which describes the stress-strain relationship. The requirements for the constitutive model in metal cutting are severe and manifold, its validity has to be for large temperature ranges up to melting temperature, as well as huge ranges for strain and strain rates [182].

In general, constitutive models can be classified into empiric, semi-empiric and physical models [21, 217]. Empiric models describe the material behaviour with a few parameters based on observations without real physical motivation, meaning that there is not necessarily a physical meaning of the constants. The most prominent example for such an empirical model in metal cutting simulations is the Johnson-Cook (JC) flow stress model [105]. In contrast are physical models which aim to consider microstructural processes where each material model constant has a physical meaning, for example the models of Preston, Tonks & Wallace [191], Zerilli & Armstrong [266, 267, 268] or Babu & Lindgren [16, 17]. A combination of both models are semi-empiric models with a partial physical meaning, e.g. the Steinberg-Cochran-Guinan-Lind (SCGL) model [230, 231] or the Mechanical Threshold Model (MTS) model [67, 74, 114]

In state of the art metal cutting simulations the empirical JC flow stress model is a de facto standard used in the majority of research, for example in [100, 174, 277]. It found wide use since its 5 model constants can be fitted comparably easy from experiments. However, some deficiencies exist. For example Sievert [223] highlight that the temperature during chip formation is overpredicted. Other important issues are the large variation in predicted cutting and thrust forces as well as the prediction of residual stresses [102, 166] or the underestimation of passive forces in both, FEM and SPH models [213]. Another problem

are the large variations of available material parameters even for the same material [61]. The JC-model was modified by several researchers to improve the results prediction, most notably are the extensions for Ti6Al4V material comprising a tanh-term [38, 39, 40, 224] to model thermal softening at higher temperatures. With this model the prediction of chip segmentation has improved significantly for Ti6Al4V[62].

Besides the JC flow stress model some other constitutive models are applied in machining simulations, but to a lesser extent. For example good results were achieved with kinematic hardening models according to Chaboche [43] in [99, 149] or according to the BCJ-model [20] in [81]. Other approaches use a dislocation density model [16, 17] for machining simulations in [202, 203, 204, 205, 206] or crystal plasticity finite element (CPFE) models for the cutting simulation of copper [254] and for orthogonal micro-cutting of Ti-17 in [15].

The stress-strain relation cannot characterize the material desintegration upon accumulated plastic straining and misses subsequent reduction of the load carrying capacity until rupture. This gap can be closed by the utilization of fracture strain models which usually depend on stress state, strain rate and temperature. Fracture strain models according to Johnson-Cook [73] or Cockcroft-Latham [45] are often applied in metal cutting. Recently, the Johnson-Cook fracture strain model found extensions to Lode-angle dependency [18] and inclusion of blue-brittleness effects [69]. The predicted fracture strains are compared to the current plastic strain increments and damage increments are computed. These damage increments are linearly accumulated until a damage criterion is met which is often followed by a cohesive crack model approach based on [93].

The damage modelling allows to model ductile failure upon which the chip forms and separates. It is also possible to simulate the chip formation indirectly without damage modelling but continuous remeshing such that the material flows around the cutter. Modelling the damage with a fracture strain equation in combination with JC flow stress model or derivatives of it results in reduced cutting forces but more realistic chip morphologies [58, 62].

2.4.1 *Material Testing*

Constitutive models require for their application material dependent coefficients which have to be determined within experiments. These experiments can be divided into direct and indirect methods. Direct methods utilize rather basic experiments and usually comprise tensile and compression tests where at a constant temperature and very low loading rates at quasi-static conditions the load is increased until rupture of the specimen. These tests are performed on servo-hydraulic test machines and can be performed at low loading rates up to $\dot{\epsilon}_{pl} \approx 100s^{-1}$ [91]. The tests are repeated at several temperature levels and allow the determination of the strain hardening coefficients for static yield curves and its sensitivity to temperature and low strain rates [171]. These kind of tests are far below the strain rates of machining operations and therefore more involved testing at higher loading rates is required for which different testing devices are needed. A commonly used device is a refinement of the Hopkinson bar [97] which is called Split Hopkinson Bar (SHB) or Kolsky-bar [115]

test and can be used in tension (SHTB) and compression (SHPB). It allows to determine the strain rate dependencies up to $\dot{\epsilon}_{pl} \approx 5'000s^{-1}$. Similar to servo-hydraulic testing, the tests are repeated at different temperature levels and can then be used to derive flow stress model coefficients [157]. Still, conditions occurring at machining are not achieved with these direct methods and indirect methods have to be favoured where impact tests, e.g. Taylor tests [239], allow loading rates up to $\dot{\epsilon}_{pl} \approx 100'000s^{-1}$ [217] but still stay one order of magnitude below cutting conditions which leads to the need for inverse identification of constitutive model constants directly out of the cutting experiments.

2.4.2 *Inverse Parameter Identification from Cutting Tests*

The determination is indirect, because the occurring effects (temperatures, strains, strain rates, temperature gradients) are overlaid and cannot be separated into single causes anymore and therefore they are not accessible by basic experiments. Instead, the determination of the constitutive model constants is performed with a numerical model of the process itself where process observables, such as process forces, chip shapes and temperatures are compared to model predictions and the constitutive model constants are accordingly adjusted in an attempt to reduce the differences between measured and predicted process observables. This approach is however costly as the constants are not found ad-hoc but need to be iterated within an optimization loop. For this reason some attempts use a design-of-experiment (DOE) plan to compute numerical results at selected sampling points which are used to drive a response surface method (RSM) [111] or analysis of variance (ANOVA) [190], offering an analytical model (metamodel) which is then used for optimization to replace the costly numerical evaluations [147, 179]. Various optimization algorithms are used in the literature for the determination of constitutive model parameter by optimization of the metamodel, for example gradient-based methods [243] or particle swarm optimization [127, 132]. While being more efficient, the accuracy of the prediction, even at the sampling points, can be questionable especially if the "true" shape of the response cannot be approximated well by the response surface. An alternative is then to work directly on a numerically inexpensive analytical force model [47, 147]. Another option is to work directly on the numerical solution as for example in [25, 84] where a Simplex-algorithm is used. This approach requires a good guess for the initial simplex otherwise the optimization can result in long computing times.

Problematic to all optimization algorithms, especially to gradient based and Simplex-type algorithms, is how to ensure the minimum - if found at all - is global and not local. Additionally, different sets of constitutive model parameter can lead to very similar cutting forces [221, 222] which does not necessarily guarantee physically meaningful constitutive model constants.

Left out so far from the provided overview is the determination of the friction coefficient to be used in the cutting simulations. A standard approach used very often in cutting simulations is the Coulomb model where the friction force is proportional to the normal force with the proportionality factor being the friction coefficient. A modification to the Coulomb model was introduced by Zorev [276] who divided the contact condition into a sliding zone (external friction) and a sticking zone (internal friction). In the internal friction case the material slides

inside the chip due to plastic shear which is under consideration of the required energy more favourable than external friction. The assumption of a constant coefficient of friction is however not justified since experimental results indicate dependencies e.g. on the interface temperature [167] or the sliding speed [193, 265]. The friction coefficient can be measured with an in-process tribometer [152] during cutting experiments. An alternative solution is the identification within a numerical simulation of the cutting process, where the constitutive model constants remain unchanged, for example in [5]. Inverse parameter identification of constitutive model constants and the friction law coefficients within the same optimization is not reported so far.

2.5 RESEARCH GAP AND OBJECTIVES

The following research gaps are identified from the literature review presented before:

- A GPU accelerated meshfree simulation software with advanced material models is not available.
- A framework for fast numerical simulations of the cutting process for the inverse parameter identification of material constitutive constants directly from orthogonal cutting experiments does not exist.
- The inverse parameter identification of constitutive model constants together with the friction law parameter has not been performed yet.
- Orthogonal cutting experiments at high cutting speeds as input for the inverse parameter identification are not available.
- A thorough analysis of the requirements for a constitutive model for the harsh conditions of metal cutting is missing in the literature.
- Damage modelling with meshfree methods including material separation without deletion is only sparsely investigated in the literature.
- Simulations of 3D cutting processes on a macro scale cannot be solved efficiently with available numerical methods.

From the listed research gaps the objectives of this thesis have been defined as follows. First the required continuum mechanics and numerics of meshless methods are introduced. It is followed by a thorough analysis of the requirements for a constitutive model for the harsh conditions of metal cutting and a review of available constitutive models will be conducted and suitable models for the metal cutting simulation will be implemented into the `MFREE_IWF` meshfree solver suite. Applications to 2D problems with validation against analytical and commercial code solutions will ensure the correctness of the extensions. Then, the solver for GPU computation will be enhanced by these constitutive models and massively reduce the computational cost by utilization of high-performance parallel processing capabilities of the GPGPU. The extended solver will then be applied to 2D prototype simulation of orthogonal

cutting with material data available from literature and compared against existing cutting test results. In the main part two materials, Ck45 and Ti6Al4V will undergo material tests, e.g. tensile tests, and a microstructural investigation. From the same batch of material orthogonal cutting experiments are performed such that a unified description of the material can be generated. The results from the cutting experiments will serve as input to the determination of constitutive model constants with inverse parameter identification methods for which the GPU-accelerated meshfree cutting simulation will be used. The constitutive model constants determined from material testing and those acquired from the inverse parameter identification are compared. Finally, 3D simulations of micro milling with a diamond tool will be performed. Overall, a significant increase in the quality of the numerical prediction of cutting simulations is expected which will leverage new insights to the cutting process such as process forces, chip generation and potentially burr formation and tool loading, wear and even built-up edges.

The continuum mechanics is introduced in this chapter with the equations relevant to this work. It starts with the kinematic description of the deformation, followed by kinetics and material behaviour. The denominations and equations follow mainly [9, 23, 184].

3.1 EULERIAN AND LAGRANGIAN DESCRIPTION

The motion of a body can be treated from two perspectives, where in the Eulerian description the continuum flows through a fixed spatial grid. In contrast, in the Lagrangian description material points of the body are followed through the motion of the continuum, see figure 3.1.

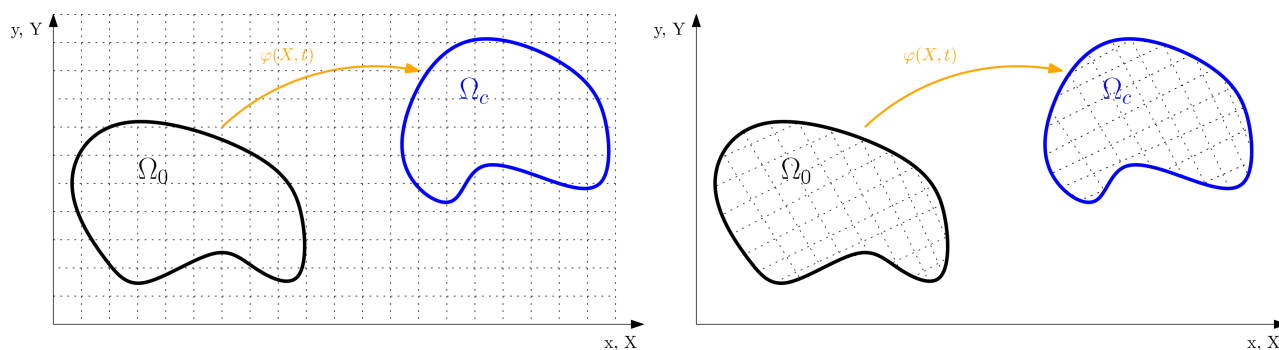


Figure 3.1: Eulerian (left) and Lagrangian (right) description of a deformable continuum in the initial configuration Ω_0 and current configuration Ω_c .

In this work the Lagrangian description is chosen to describe the motion.

3.2 KINEMATICS

In figure 3.2 a deformable body is shown in the initial configuration Γ_0 and in the deformed (current) configuration Γ_c .

The motion of the material points can be described by a function $\varphi(\underline{X}, t)$ depending on the initial configuration position \underline{X} and maps at time t to a deformed position \underline{x} :

$$\underline{x} = \varphi(\underline{X}, t) \quad (3.1)$$

The distance vector $\underline{u} = \underline{X} - \underline{x}$ is the displacement of a material point and its derivative is the velocity \underline{v} :

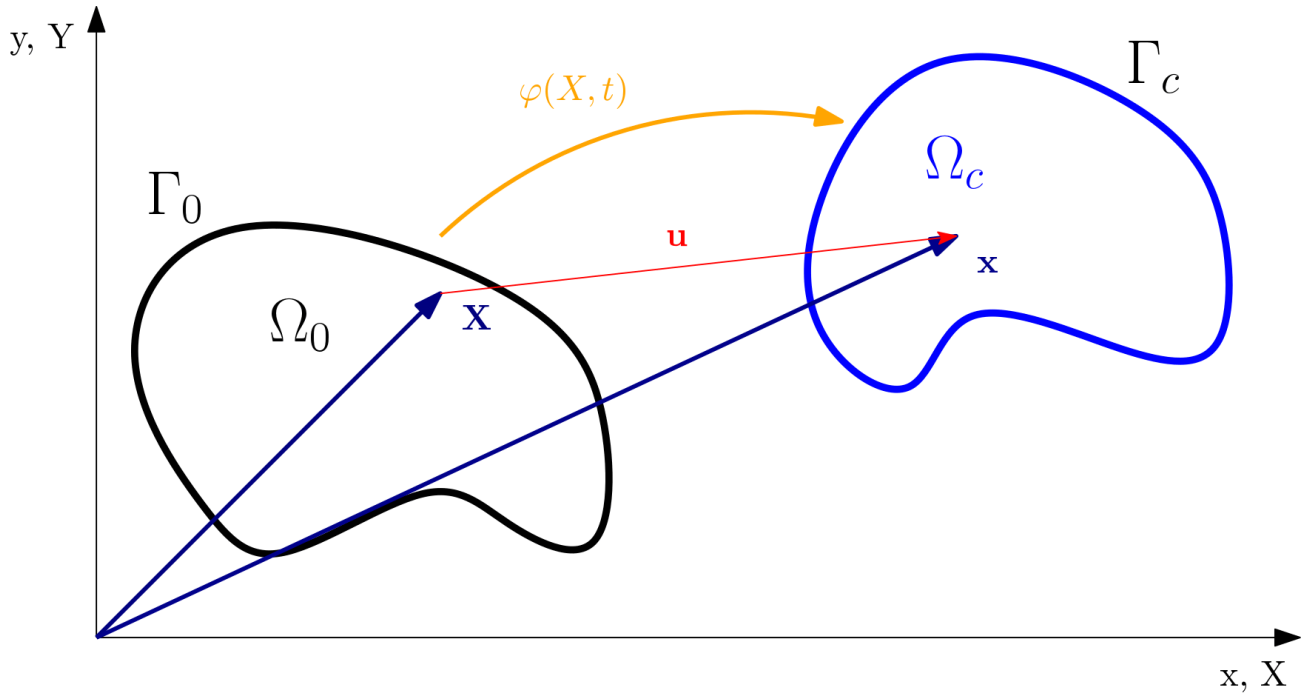


Figure 3.2: Deformable body with a material point in the initial configuration (left) and after some deformation in the current configuration (right).

$$\underline{v} = \dot{\underline{x}} = \frac{d}{dt}\underline{x} = \frac{d}{dt}(\underline{X} + \underline{u}) = \dot{\underline{u}} \quad (3.2)$$

The spatial derivative of $\varphi(\underline{X}, t)$ with regards to the initial configuration is:

$$\frac{\partial \varphi(\underline{X}, t)}{\partial \underline{X}} = \frac{\partial \underline{x}}{\partial \underline{X}} = \nabla_0 \underline{u} \quad (3.3)$$

and is called deformation gradient $\underline{\underline{F}}$.

3.2.1 Deformation Gradient

The deformation gradient $\underline{\underline{F}}$ maps the displacement of a material line element from the reference frame \underline{X} to the current frame \underline{x} and is defined as:

$$\underline{\underline{F}} = \frac{\partial \underline{x}}{\partial \underline{X}} \quad (3.4)$$

\underline{x} and \underline{X} are connected via the displacement vector \underline{u} :

$$\underline{u} = \underline{x} - \underline{X} \quad (3.5)$$

The determinant of the deformation gradient, labelled J , is always:

$$J = \det(\underline{\underline{F}}) > 0 \quad (3.6)$$

and relates the volumetric change of a material element from the reference to the current configuration:

$$dV = \det(\underline{\underline{F}})dV_0 \quad (3.7)$$

Because the deformation gradient is non singular, equation (3.6), it can be decomposed by a polar decomposition into a stretch and a rotation:

$$\underline{\underline{F}} = \underline{\underline{R}} \cdot \underline{\underline{U}} = \underline{\underline{V}} \cdot \underline{\underline{R}} \quad (3.8)$$

with $\underline{\underline{R}}$ being a proper orthogonal tensor which describes the rotation of the material element and the right $\underline{\underline{U}}$ and left $\underline{\underline{V}}$ stretch tensors, both symmetric and positive-definite, contain the stretch of the material element.

Because the polar decomposition is quite some effort for retrieving the stretch one usually prefers to use another rotation-free stretch measure which is the right Cauchy-Green tensor $\underline{\underline{C}}$:

$$\underline{\underline{C}} = \underline{\underline{F}}^T \cdot \underline{\underline{F}} \quad (3.9)$$

its rotation-freeness can be easily shown by combining equations (3.8) and (3.9) and utilization of $(\underline{\underline{A}} \cdot \underline{\underline{B}})^T = \underline{\underline{B}}^T \cdot \underline{\underline{A}}^T$:

$$\underline{\underline{C}} = \underline{\underline{F}}^T \cdot \underline{\underline{F}} = (\underline{\underline{R}} \cdot \underline{\underline{U}})^T \cdot \underline{\underline{R}} \cdot \underline{\underline{U}} = \underline{\underline{U}}^T \cdot \underbrace{\underline{\underline{R}}^T \cdot \underline{\underline{R}}}_{=\underline{\underline{I}}} \cdot \underline{\underline{U}} = \underline{\underline{U}}^2 \quad (3.10)$$

This measure is in unstretched condition $\underline{\underline{C}} = \underline{\underline{I}}$ which is undesired behaviour and it is preferred to have a 0-measure for unstretched mappings for which the Green-Lagrange strain tensor is introduced:

$$\underline{\underline{E}} = \frac{1}{2}[\underline{\underline{F}}^T \cdot \underline{\underline{F}} - \underline{\underline{I}}] \quad (3.11)$$

This can be rewritten with the displacement gradient $\underline{\underline{H}}$:

$$\underline{\underline{H}} = \underline{\underline{F}} - \underline{\underline{I}} = \nabla_0 \underline{\underline{u}} - \underline{\underline{I}} \quad (3.12)$$

$$\underline{\underline{E}} = \frac{1}{2}[(\underline{\underline{H}} + \underline{\underline{I}})^T \cdot (\underline{\underline{H}} + \underline{\underline{I}}) - \underline{\underline{I}}] = \frac{1}{2}[\underline{\underline{H}} + \underline{\underline{H}}^T + \underline{\underline{H}}^T \cdot \underline{\underline{H}}] \quad (3.13)$$

For small deformations $\underline{\underline{H}}^T \cdot \underline{\underline{H}}$ vanishes and (3.13) reduces to the linearised Green-Lagrange strain tensor (engineering strain):

$$\underline{\underline{E}}_{lin} = \frac{1}{2}[\underline{\underline{F}} + \underline{\underline{F}}^T] \quad (3.14)$$

Another measure for the deformation is the velocity gradient $\underline{\underline{L}}$:

$$\underline{\underline{L}} = [\nabla \underline{\underline{v}}]^T = \dot{\underline{\underline{F}}} \cdot \underline{\underline{F}}^{-1} \quad (3.15)$$

which can be split into symmetric $\underline{\underline{D}}$ and asymmetric $\underline{\underline{W}}$ components:

$$\underline{\underline{L}} = \underline{\underline{L}}_{symm} + \underline{\underline{L}}_{asymm} = \underline{\underline{D}} + \underline{\underline{W}} \quad (3.16)$$

with

$$\underline{\underline{D}} = \frac{1}{2}(\underline{\underline{L}} + \underline{\underline{L}}^T) \quad (3.17)$$

$$\underline{\underline{W}} = \frac{1}{2}(\underline{\underline{L}} - \underline{\underline{L}}^T) \quad (3.18)$$

$$(3.19)$$

where the symmetric part $\underline{\underline{D}}$ is the rate of deformation and the asymmetric part $\underline{\underline{W}}$ is the spin tensor. $\underline{\underline{D}}$ relates to the time derivative of the linearised Green-Lagrange strain tensor (3.11) simply as:

$$\dot{\underline{\underline{E}}}_{lin} = \underline{\underline{D}} \quad (3.20)$$

3.2.2 Additive Strain Rate Decomposition - Hypoelasticity

Basis for the derivation of the additive strain rate decomposition is the multiplicative split of the deformation gradient $\underline{\underline{F}}$ into elastic and plastic parts [119, 122]:

$$\underline{\underline{F}} = \underline{\underline{F}}_{el} \cdot \underline{\underline{F}}_{pl} \quad (3.21)$$

Following the derivations in [90], inserting (3.21) into the equation for the velocity gradient (3.15) and using $(\underline{\underline{A}} \cdot \underline{\underline{B}})^{-1} = \underline{\underline{B}}^{-1} \cdot \underline{\underline{A}}^{-1}$ one can write:

$$\underline{\underline{L}} = \underline{\underline{\dot{F}}} \cdot \underline{\underline{F}}^{-1} \quad (3.22)$$

$$= (\underline{\underline{F}}_{el} \cdot \underline{\underline{F}}_{pl}) \cdot (\underline{\underline{F}}_{el} \cdot \underline{\underline{F}}_{pl})^{-1} \quad (3.23)$$

$$= (\underline{\underline{\dot{F}}}_{el} \cdot \underline{\underline{F}}_{pl} + \underline{\underline{F}}_{el} \cdot \underline{\underline{\dot{F}}}_{pl}) \cdot (\underline{\underline{F}}_{pl}^{-1} \cdot \underline{\underline{F}}_{el}^{-1}) \quad (3.24)$$

$$= \underbrace{\underline{\underline{\dot{F}}}_{el} \cdot \underline{\underline{F}}_{pl} \cdot \underline{\underline{F}}_{pl}^{-1}}_{=\underline{\underline{L}}_{el}} \cdot \underline{\underline{F}}_{el}^{-1} + \underline{\underline{F}}_{el} \cdot \underbrace{\underline{\underline{\dot{F}}}_{pl} \cdot \underline{\underline{F}}_{pl}^{-1}}_{=\underline{\underline{L}}_{pl}} \cdot \underline{\underline{F}}_{el}^{-1} \quad (3.25)$$

$$= \underbrace{\underline{\underline{\dot{F}}}_{el} \cdot \underline{\underline{F}}_{el}^{-1}}_{=\underline{\underline{L}}_{el}} + \underline{\underline{F}}_{el} \cdot \underline{\underline{L}}_{pl} \cdot \underline{\underline{F}}_{el}^{-1} \quad (3.26)$$

$$= \underline{\underline{L}}_{el} + \underline{\underline{F}}_{el} \cdot \underline{\underline{L}}_{pl} \cdot \underline{\underline{F}}_{el}^{-1} \quad (3.27)$$

$$(3.28)$$

Since $\underline{\underline{F}}$ consists of rigid body motion and deformation and postulating that the rotation is neither associated partially to inelastic and elastic deformation one can write:

$$\underline{\underline{F}} = \underline{\underline{V}}_{el} \cdot \underline{\underline{V}}_{pl} \cdot \underline{\underline{R}} \quad (3.29)$$

with

$$\underline{\underline{V}}_{el} = \underline{\underline{I}} + \underline{\underline{\varepsilon}}_{el} \quad (3.30)$$

and assuming that the principal values of the nominal elastic strain ε are closely to unity then:

$$\underline{\underline{F}}_{el} = \underline{\underline{V}}_{el} \quad (3.31)$$

and inserting into (3.27):

$$\underline{\underline{L}} = \underline{\underline{L}}_{el} + \underbrace{(\underline{\underline{I}}_{el} + \underline{\underline{\varepsilon}}_{el})}_{\approx \underline{\underline{I}}} \cdot \underline{\underline{L}}_{pl} \cdot \underbrace{(\underline{\underline{I}}_{el} + \underline{\underline{\varepsilon}}_{el})^{-1}}_{\approx \underline{\underline{I}}} \quad (3.32)$$

$$\approx \underline{\underline{L}}_{el} + \underline{\underline{L}}_{pl} \quad (3.33)$$

results for the symmetric part of $\underline{\underline{L}}$ in the additive strain rate decomposition:

$$\underline{\dot{\underline{\epsilon}}} \approx \underline{\dot{\underline{\epsilon}}}_{el} + \underline{\dot{\underline{\epsilon}}}_{pl} \quad (3.34)$$

which is shown to yield under small elastic strains the same solution in a metal forming simulation [255] as with the correct treatment (Hyperelasticity [227]). For this reason the additive strain rate decomposition (Hypoelasticity) is used throughout this work.

3.3 KINETICS

As of yet only geometric relations for the continuum were introduced which do not associate any external forces exerted to the deformable body. These external forces result in deformations and internal forces. The latter are subject of kinetics.

3.3.1 Stress Measures

An internal force $\Delta \underline{F}$ acting on a cross section ΔA results in an averaged loading in this element which is for the limit:

$$\underline{t} = \lim_{\Delta A \rightarrow 0} \frac{\Delta \underline{F}}{\Delta A} = \frac{d\underline{F}}{dA} \quad (3.35)$$

is the traction vector in the cross section. Its component towards the normal \underline{n} of the cross section dA is:

$$\sigma = \underline{t} \cdot \underline{n} \quad (3.36)$$

and is named normal stress. The normal stress depends on the orientation of the cross section dA . Orienting the cross section normal to each of the coordinate axes \underline{e}_i results in three traction vectors \underline{t}_j which can be expressed as:

$$\underline{t}_j = \sigma_{ji} \underline{e}_i \quad (3.37)$$

The nine entries of σ_{ij} are the cartesian components of the Cauchy stress tensor $\underline{\underline{\sigma}}$. It relates the force over the area in the deformed (current) configuration. The stress tensor can be split into a deviatoric and a volumetric part:

$$\underline{\underline{\sigma}} = \underline{\underline{S}} + \underline{\underline{\sigma}}_H \quad (3.38)$$

where $\underline{\underline{S}}$ is the deviatoric part and the volumetric part $\underline{\underline{\sigma}}_H$ is a diagonal tensor related to the hydrostatic pressure p :

$$\underline{\underline{\sigma}}_H = -p\underline{\underline{I}} \quad (3.39)$$

Other stress tensors exist which are related to other configurations, for example the first Piola-Kirchhoff stress tensor relates a force element in the current configuration to a cross section in the reference configuration which is defined as:

$$\underline{\underline{\sigma}}^{PK1} = J\underline{\underline{F}}^{-T} \cdot \underline{\underline{\sigma}} \quad (3.40)$$

In general, the first Piola-Kirchhoff stress tensor is not symmetric and therefore the second Piola-Kirchhoff stress tensor was constructed such that the symmetry property is recovered:

$$\underline{\underline{\sigma}}^{PK2} = J\underline{\underline{F}}^{-1} \cdot \underline{\underline{\sigma}} \cdot \underline{\underline{F}}^{-T} \quad (3.41)$$

3.3.2 Invariants of the Stress Tensor

A stress tensor exhibits three invariants which are independent from the spatial framework. They are defined as [199]:

$$I_1 = \sigma_{xx} + \sigma_{yy} + \sigma_{zz} = tr(\underline{\underline{\sigma}}) \quad (3.42)$$

$$I_2 = -(\sigma_{xx}\sigma_{yy} + \sigma_{yy}\sigma_{zz} + \sigma_{xx}\sigma_{zz}) + \sigma_{xy}^2 + \sigma_{xz}^2 + \sigma_{yz}^2 \quad (3.43)$$

$$I_3 = det(\underline{\underline{\sigma}}) \quad (3.44)$$

for the stress deviator $\underline{\underline{S}}$ invariants can be computed as well:

$$J_1 = S_{xx} + S_{yy} + S_{zz} = tr(\underline{\underline{S}}) = 0 \quad (3.45)$$

$$J_2 = \frac{1}{2}(S_{xx}^2 + S_{yy}^2 + S_{zz}^2) + S_{xy}^2 + S_{xz}^2 + S_{yz}^2 \quad (3.46)$$

$$J_3 = det(\underline{\underline{S}}) \quad (3.47)$$

3.4 BALANCE EQUATIONS

3.4.1 Mass Conservation

The mass of a material volume is constant throughout the loading history:

$$M = \int_m dm = \underbrace{\int_V \varrho(\underline{x}, t) dV}_{\text{current configuration}} = \underbrace{\int_{V_0} \varrho_0(\underline{X}) dV_0}_{\text{initial configuration}} = \text{const} \quad (3.48)$$

or formulated for a material volume dV :

$$dm = \varrho_0(\underline{X}) dV_0 = \varrho(\underline{x}, t) dV \quad (3.49)$$

3.4.2 Momentum Equation

The change rate of the total momentum $\dot{\underline{I}}$ equals the sum of forces \underline{F} exerted to the body:

$$\dot{\underline{I}} = \frac{d}{dt} \int \underline{v} \varrho dV = \underline{F} \quad (3.50)$$

The forces \underline{F} consist of surface forces $\underline{f}(\underline{x}, t)$ and volume forces $\varrho \underline{b}(\underline{x}, t)$:

$$\frac{d}{dt} \int \underline{v} \varrho dV = \int \underline{f}(\underline{x}, t) dA + \int \varrho \underline{b}(\underline{x}, t) dV \quad (3.51)$$

Rearranging (3.51) such that all terms are brought under one integral by using:

$$\frac{d}{dt} \int \underline{v} \varrho dV = \frac{d}{dt} \int \underline{v} \varrho_0 dV_0 = \int \dot{\underline{v}} \varrho_0 dV_0 = \int \dot{\underline{v}} \varrho dV \quad (3.52)$$

and using the divergence theorem (Gauß's-theorem):

$$\int \underline{t}(\underline{x}, t) dA = \int \underline{\underline{\sigma}} \cdot \underline{n} dA = \int \text{div} \underline{\underline{\sigma}} dV \quad (3.53)$$

leads to

$$\int \underbrace{(\text{div} \underline{\underline{\sigma}} + \varrho \underline{b} - \varrho \dot{\underline{v}})}_{\stackrel{!}{=} \underline{0}} dV = \underline{0} \quad (3.54)$$

Because the integral in (3.54) must be valid for arbitrary volumes, the term in brackets must be zero which finally yields the momentum equation in local form:

$$\text{div} \underline{\underline{\sigma}} + \varrho \underline{b} - \varrho \dot{\underline{v}} = \underline{0} \quad (3.55)$$

3.4.3 Angular Momentum Equation

The angular momentum balance requires that the time derivative of the angular momentum equals the externally applied torque:

$$\int (\underline{\bar{x}} \times \underline{\dot{v}}) \rho dV = \int (\underline{\bar{x}} \times \underline{f}(\underline{x}, t)) dA + \int (\underline{\bar{x}} \times \underline{b}(\underline{x}, t)) \rho dV \quad (3.56)$$

with $\underline{\bar{x}}$ being a position vector. This equation is basically (3.50) multiplied with $\underline{\bar{x}}$ and therefore not a new conditional equation. Equation (3.56) can be reorganized with some tedious math (details in [184]) written in coordinate form with the Levi-Civita-Symbol:

$$\varepsilon_{ijk} = \begin{cases} + 1 & \text{if } (i,j,k) \text{ is } (1,2,3), (2,3,1), \text{ or } (3,1,2) \\ - 1 & \text{if } (i,j,k) \text{ is } (3,2,1), (1,3,2), \text{ or } (2,1,3) \\ 0 & \text{if } i=j, \text{ or } j=k, \text{ or } k=i \end{cases} \quad (3.57)$$

to:

$$\int \underbrace{\varepsilon_{ijk}(\sigma_{jk} - \sigma_{kj})}_{\stackrel{\perp}{=}0} dV = \underline{0} \quad (3.58)$$

Equation (3.58) must be valid for arbitrary volumes similar to (3.55) and therefore it follows:

$$\varepsilon_{123}(\sigma_{23} - \sigma_{32}) = 0 \quad (3.59)$$

$$\varepsilon_{231}(\sigma_{31} - \sigma_{13}) = 0 \quad (3.60)$$

$$\varepsilon_{312}(\sigma_{12} - \sigma_{21}) = 0 \quad (3.61)$$

$$(3.62)$$

Which means that the Cauchy stress tensor $\underline{\underline{\sigma}}$ must be symmetric:

$$\underline{\underline{\sigma}} = \underline{\underline{\sigma}}^T \quad (3.63)$$

The application of the angular momentum balance to the second Piola-Kirchhoff stress tensor reveals its symmetry as well:

$$\underline{\underline{\sigma}}^{PK2} = \left(\underline{\underline{\sigma}}^{PK2} \right)^T \quad (3.64)$$

3.4.4 Energy Equation

The energy equation is defined as:

$$\dot{T} = \underbrace{\frac{\lambda}{\rho \cdot c_p} \nabla^2 T}_{\text{Fourier's law}} + \underbrace{\frac{\dot{q}}{\rho \cdot c_p}}_{\text{source term}} \quad (3.65)$$

with the material parameters density ρ , specific heat c_p and heat conductivity λ . Since thermally isotropic media are considered λ is a scalar. The source term accounts for introduced heat fluxes, e.g. from plastic or frictional dissipation.

3.4.4.1 Frictional Dissipation

A Coulomb friction model is used in the simulations. The friction force $|\underline{E}_{fric}|$ depends linearly on the contact force $|\underline{E}_{cont}|$ in the contact surface:

$$|\underline{E}_{fric}| = \mu_{fric} \cdot |\underline{E}_{cont}| \quad (3.66)$$

where μ_{fric} is the friction coefficient. The frictional power is related to the relative (sliding) velocity v_{rel} of the mating contact surfaces:

$$P_{fric} = |\underline{E}_{fric}| \cdot |v_{rel}| \quad (3.67)$$

This power is dissipated with a certain fraction η_{fric} into heat:

$$\dot{Q}_{fric} = \eta_{fric} \cdot P_{fric} = \eta_{fric} \cdot |\underline{E}_{fric}| \cdot |v_{rel}| \quad (3.68)$$

with \dot{Q}_{fric} being distributed into the mating surfaces A and B:

$$\dot{Q}_{fric} = \dot{Q}_A + \dot{Q}_B = \underbrace{f_{\mu}^{AB} \cdot \dot{Q}_{fric}}_{=\dot{Q}_A} + \underbrace{(1 - f_{\mu}^{AB}) \cdot \dot{Q}_{fric}}_{=\dot{Q}_B} \quad (3.69)$$

where f_{μ}^{AB} is a heat partition factor and describes how much of the generated frictional heat power is received by the two contacting surfaces A and B. If the heat power is transmitted into one of both surfaces, it becomes written in terms of the heat flux density:

$$\dot{q}_{fric} = \frac{\eta_{fric} \cdot |\underline{E}_{fric}| \cdot |v_{rel}| \cdot \rho}{m} \quad (3.70)$$

where it is assumed that m is the mass of the body to which the frictional dissipation is released to. It is usually assumed that the frictional energy is fully dissipated into heat and therefore $\eta_{fric} = 1.0$.

3.4.4.2 Plastic Dissipation

Another source of heat is due to plastic deformation of metallic materials which lead to energy release in the form of heat. The ratio of the mechanical work w_{mech} converted into heat energy w_{heat} is described with the Taylor-Quinney coefficient η_{TQ} [240]:

$$w_{heat} = \eta_{TQ} \cdot w_{mech} = \eta_{TQ} \cdot \int \sigma_y \cdot \varepsilon_{pl} d\varepsilon_{pl} \quad (3.71)$$

and gives the heat energy introduced per volume V . Deriving (3.71) with respect to time yields the heat flux:

$$\dot{q}_{pl} = \eta_{TQ} \cdot \sigma_y \cdot \dot{\varepsilon}_{pl} \quad (3.72)$$

The Taylor-Quinney coefficient is usually assumed to be in the order of $\eta_{TQ} = 90\%$. This is however a subject for debate as some research [87, 95, 218, 274] discovered larger variation during loading history where values can be as low as $\eta_{TQ} \approx 10\%$ in cycling loading [24] and even higher than $\eta_{TQ} = 100\%$ if phase transformations occur [264].

3.4.4.3 Modified Energy Equation

With the plastic dissipation (3.72) and the friction heat (3.70) the energy equation (3.65) updates to:

$$\dot{T} = \frac{\lambda}{\rho \cdot c_p} \nabla^2 T + \frac{\dot{q}_{fric} + \dot{q}_{pl}}{\rho \cdot c_p} \quad (3.73)$$

3.5 MATERIAL BEHAVIOUR AND CONSTITUTIVE MODELLING

The constitutive model describes the material response due to mechanical loading. In its simplest representation a linear relationship (Hooke's law) describes the stress-strain behaviour of the loaded material. This holds true only for quasi-static and small loads below the yield limit and temperatures below absolute temperatures of $T < 0,4 \cdot T_{melt}$. Violating the aforementioned boundaries, the material will respond in a nonlinear fashion. If, for example, the material is loaded beyond the yield limit, irreversible deformations will remain after completely unloading the structure.

In general, the material behaviour can be characterized according to [82] with the following two classifications:

- rate independent (scleronomic) and

- rate dependent (rheonomic), such as viscoelasticity and viscoplasticity

Rate independence is characterized by deformations immediately following the applied loads, whereas in rate dependence the deformations still change after load application. A rate independent behaviour can be treated as a valid simplification to steady state problems (disregarding creep effects which will occur at absolute temperatures above $0,4 \cdot T_{melt}$).

In the following sections a brief introduction to the requirements on a material model will be given.

3.5.1 Linear Elastic Material Behaviour

Linear elastic material behaviour is characterised by reversible deformations which are described in the simplest case with a linear relationship, known as Hooke's law. It reads as:

$$\underline{\underline{\sigma}} = \underline{\underline{E}} : \underline{\underline{\varepsilon}} \quad (3.74)$$

$$\sigma_{ij} = E_{ijkl} \varepsilon_{kl}, \quad \text{component form} \quad (3.75)$$

where the elasticity tensor E_{ijkl} is a fourth order tensor and contains in its general form 81 free components which have to be determined by experiments. These 81 components are not independent and can be reduced due to the symmetry of the stress and strain tensor to 36 components (Cauchy elasticity). Further steps, see detailed steps in [9], lead under consideration of isotropy and small strains to:

$$\sigma_{ij} = 2\mu\varepsilon_{ij} + \lambda\varepsilon_{ii}\delta_{ij} \quad (3.76)$$

with Lamé parameters of elasticity μ (shear modulus G) and λ . The two parameters can be expressed with the Young's modulus E and the Poisson's ratio ν as:

$$\lambda = \frac{\nu}{1-2\nu} \cdot \frac{1}{1+\nu} \cdot E \quad (3.77)$$

$$\mu = G = \frac{1}{2 \cdot (1+\nu)} \cdot E \quad (3.78)$$

3.5.1.1 Rate Form

The time integration in numerical simulations leads to incremental solutions based on time derivatives of field values, e.g. the strain rate tensor. A straight forward approach is the time derivative of (3.74):

$$\underline{\underline{\dot{\sigma}}} = \underline{\underline{E}} \cdot \underline{\underline{\dot{\varepsilon}}} \quad (3.79)$$

This however bears difficulties under rigid body rotations. While the Cauchy stress tensor transforms from the initial to the current configuration as:

$$\underline{\underline{\sigma}}^{cor} = \underline{\underline{R}} \cdot \underline{\underline{\sigma}} \cdot \underline{\underline{R}}^T \quad (3.80)$$

its time derivative does not:

$$\underline{\underline{\dot{\sigma}}}^{cor} = \underline{\underline{\dot{R}}} \cdot \underline{\underline{\sigma}} \cdot \underline{\underline{R}}^T + \underline{\underline{R}} \cdot \underline{\underline{\dot{\sigma}}} \cdot \underline{\underline{R}}^T + \underline{\underline{R}} \cdot \underline{\underline{\sigma}} \cdot \underline{\underline{\dot{R}}}^T \neq \underline{\underline{R}} \cdot \underline{\underline{\dot{\sigma}}} \cdot \underline{\underline{R}}^T \quad (3.81)$$

A correct treatment of the stress derivative with regard to time can be deduced [251] by using the relation of the time derivative of an arbitrary vector a_i in a spatially fixed cartesian coordinate system to the same vector in a rotating cartesian coordinate system with angular velocity $\underline{\underline{\omega}}$:

$$\frac{da_i}{dt} = \frac{d'a_i}{dt} + \omega_{ki}a_k \quad (3.82)$$

replacing the vector a_i with the stress vector $\sigma_{ji}n_j$ yields:

$$n_j \frac{d\sigma_{ji}}{dt} + \sigma_{ji} \frac{dn_j}{dt} = n_j \frac{d'\sigma_{ji}}{dt} + \omega_{ki}\sigma_{jk}n_j \quad (3.83)$$

It follows from (3.82):

$$\frac{dn_j}{dt} = \omega_{kj}n_k \quad (3.84)$$

and combining (3.83) and (3.84) with relabelling of indices:

$$\underline{\underline{\dot{\sigma}}}^J = \frac{d'\sigma_{ji}}{dt} = \frac{d\sigma_{ji}}{dt} + \sigma_{ki}\omega_{jk} - \sigma_{jk}\omega_{ki} \quad (3.85)$$

one arrives at the Jaumann rate $\underline{\underline{\dot{\sigma}}}^J$ of the Cauchy stress tensor.

3.5.1.2 *Equation of State*

The simplest equation of state (EOS) can be derived from Hooke's law (3.74) where the volumetric change e is the trace of the strain tensor ε :

$$e = \underbrace{\varepsilon_{xx} + \varepsilon_{yy} + \varepsilon_{zz}}_{=\frac{V-V_0}{V_0}} = \frac{1-2\nu}{E} \underbrace{(\sigma_{xx} + \sigma_{yy} + \sigma_{zz})}_{=3\cdot p} \quad (3.86)$$

$$e = \frac{V - V_0}{V_0} = \underbrace{\frac{1-2\nu}{E}}_{=1/K} \cdot 3 \cdot p = \frac{p}{K} \quad (3.87)$$

reshaping and inserting the continuity equation (3.49) results in:

$$p = K \cdot \frac{V - V_0}{V_0} = K \cdot \left(\frac{V}{V_0} - 1 \right) = K \cdot \left(\frac{\varrho_0}{\varrho} - 1 \right) \quad (3.88)$$

and finally inserting the bulk modulus for longitudinal waves $K = \varrho \cdot c^2$ one arrives at:

$$p = K \cdot \left(\frac{\varrho_0}{\varrho} - 1 \right) = \varrho \cdot c^2 \cdot \left(\frac{\varrho_0}{\varrho} - 1 \right) = c^2 \cdot (\varrho_0 - \varrho) \quad (3.89)$$

It has to be noted that in this derivation compressive hydrostatic pressures lead to negative signs of p , while often a convention is used where compressive hydrostatic pressures have positive signs and (3.89) becomes:

$$p = c^2 \cdot (\varrho - \varrho_0) \quad (3.90)$$

The latter convention (3.90) is used in this work.

Other EOS exist, where probably the EOS of the Mie-Grüneisen-type [77, 159] for highly compressed matter is popular but usually not used for metal cutting simulations.

3.5.1.3 *Thermal Expansion*

Thermal expansion occur when the temperature changes. The amount of length change due to temperature change is proportional to the thermal expansion coefficient α_{th} . It leads, similar to hydrostatic pressures, to volume changes and reads in rate form as:

$$\dot{\underline{\underline{\varepsilon}}}_{th} = \alpha_{th}(T) \cdot \dot{T} \cdot \underline{\underline{I}} \quad (3.91)$$

$$\dot{\underline{\underline{\sigma}}}_{th} = K \cdot \dot{\underline{\underline{\varepsilon}}}_{th} \quad (3.92)$$

or in total form:

$$\Delta \underline{\underline{\varepsilon}}_{th} = \alpha_{th}(T) \cdot \Delta T \cdot \underline{\underline{I}} \quad (3.93)$$

$$\Delta \underline{\underline{\sigma}}_{th} = K \cdot \Delta \underline{\underline{\varepsilon}}_{th} \quad (3.94)$$

3.5.2 Nonlinear Material Behaviour - Plasticity

Within the elastic range deformations are reversible. Upon reaching the yield limit, irreversible deformations (plasticity) will occur and the constitutive models need modifications to accurately predict the material behaviour. On an atomistic scale, plasticity is mainly due to movement of dislocations through the grid.

3.5.2.1 Monotonic Tensile Loading

Figure 3.3 shows various uniaxial stress-strain relations for which the simplest representation is the linear elastic curve with constant slope (purple line). Real materials behave like this in an approximate fashion only up to the yield limit. If for a material the stress cannot increase beyond the yield limit, a description for this is the linear elastic - perfectly plastic behaviour (green dotted line). Linear elastic - perfectly plastic behaviour does not describe any hardening. A material that exhibits hardening behaviour is schematically shown with the "elastic plastic with hardening" curve (blue dash-dotted curve). The elastic plastic behaviour with hardening (blue dash-dotted line) is valid for steady state conditions only. When it comes to high loading rates (rate dependence) the material will respond dependent to the applied strain rate, such characteristics are shown with the red curves. At higher strain rates, the stress response increases in comparison to loadings at lower strain rates.

An often used flow stress model in the modeling of metal machining is the Johnson-Cook [105] model which actually plays in a theory of plasticity the role of an isotropic hardening law:

$$\sigma_y = \underbrace{(A + B \cdot (\varepsilon_{pl})^n)}_{\text{work hardening}} \underbrace{\left(1 + C \cdot \ln \left(\frac{\dot{\varepsilon}_{pl}}{\dot{\varepsilon}_{pl}^0}\right)\right)}_{\text{strain rate sensitivity}} \underbrace{\left(1 - \left(\frac{T - T_{ref}}{T_f - T_{ref}}\right)^m\right)}_{\text{thermal softening}} \quad (3.95)$$

with the five material parameters: A, B, C, m and n . The model describes the current flow stress depending on the current plastic strain ε_{pl} , plastic strain rate $\dot{\varepsilon}_{pl}$ and current

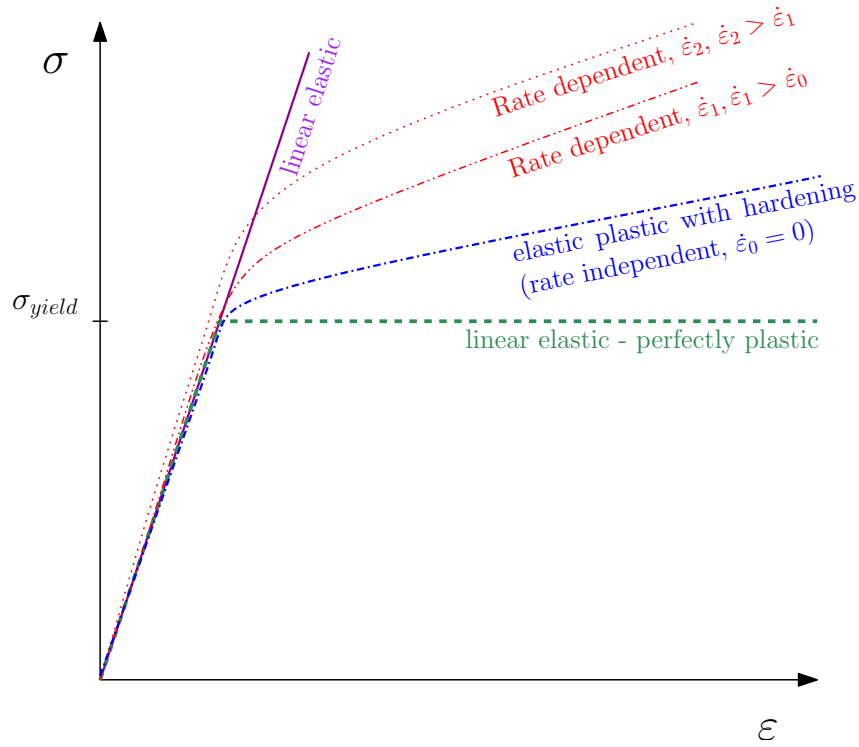


Figure 3.3: Classes of stress strain relationships: elastic (purple), linear elastic - perfectly plastic (green dotted), plastic with hardening (blue dash-dotted) and time dependent plasticity (red dotted / dash-dotted)

temperature T . The model consists of three multiplicative terms of which the first describes work hardening, the second the strain rate sensitivity and the last one the thermal softening. The melting temperature of the material is T_f and the reference temperature of the material tests is at T_{ref} . The reference strain rate of the material test is $\dot{\epsilon}_0$.

The thermal softening term is often expressed with the homologous temperature T^* :

$$T^* = \frac{T - T_{ref}}{T_f - T_{ref}} \quad (3.96)$$

and the dimensionless plastic strain rate $\dot{\epsilon}_{pl}^*$ is:

$$\dot{\epsilon}_{pl}^* = \frac{\dot{\epsilon}_{pl}}{\dot{\epsilon}_{pl}^0} \quad (3.97)$$

3.5.2.2 Load Reversal

So far, only uniaxial monotonic tensile loading was considered. When it comes to unloading different characteristics can be observed for different materials.

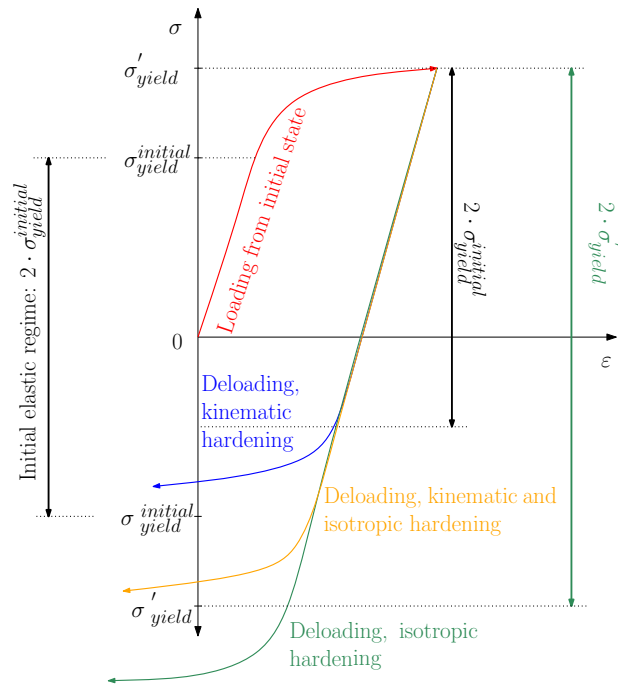


Figure 3.4: Schematic representation of isotropic (green line), kinematic (blue line) and a combination of isotropic and kinematic (yellow) hardening behaviour

In figure 3.4, a loading beyond the initial yield limit $\sigma_{yield}^{initial}$ up to the new yield limit σ'_{yield} is shown (red curve). Upon unloading, materials can behave differently:

1. Yielding in reverse direction starts when the negative new yield limit $-\sigma'_{yield}$ is reached. This case is well known as "isotropic hardening", the elastic regime has increased from initial $2 \cdot \sigma_{yield}^{initial}$ to $2 \cdot \sigma'_{yield}$.
2. Experiments, first conducted by Bauschinger [22], show that reverse yielding will start even before the negative initial yield limit $-\sigma_{yield}^{initial}$ is reached, this effect is called Bauschinger effect. That leads to the assumption that the elastic regime stays at $2 \cdot \sigma_{yield}^{initial}$ but shifts in the stress-strain space (blue curve) and is therefore called "kinematic hardening".
3. Some materials combine both, kinematic and isotropic hardening. Its characteristic is depicted with the yellow curve.
4. Another material behaviour is the formative hardening. Its characteristic cannot be shown by means of uniaxial tests - it requires a multiaxial generalization which is introduced in the next section 3.5.3.

3.5.2.3 Behaviour at Elevated Temperatures

At elevated temperature creep occurs which also introduces rate dependence into the constitutive equations. For metals the phenomenon is observed usually at absolute temperatures

$T > 0,4 \cdot T_{melt}$. Under constant external force (constant stress) a specimen would elongate over time whereas under constant external displacement (constant total strain) the stresses in the specimen would decrease over time. With increasing temperature and/or stress, the effect of creep becomes more pronounced. The characteristics of creep under constant stress and under constant external displacement are shown in figure 3.5.

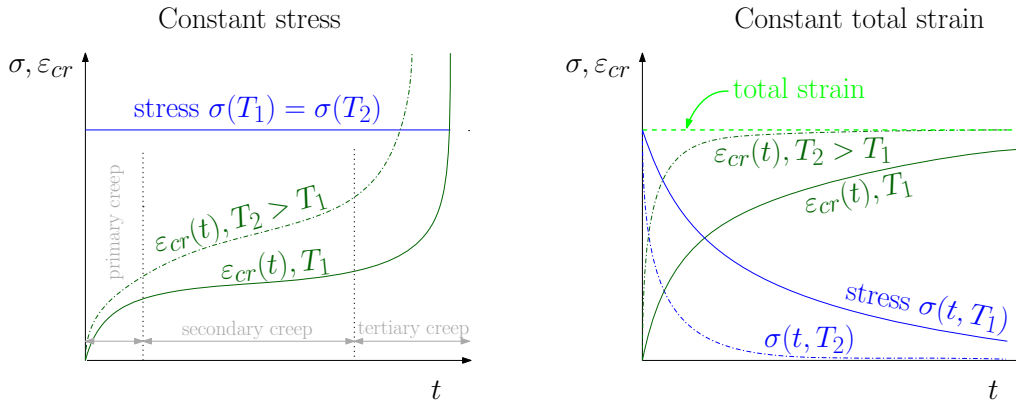


Figure 3.5: Schematic representation of creep under constant stress (left) / strain (right)

The creep under constant stress can be divided into three stages: primary creep with initially high creep strain rates, secondary creep with approximately constant creep rates and tertiary creep with again increasing creep strain rates until fracture.

The simplest mathematical description of the creep under constant stress is due to Norton [175] and Bailey [19] for the secondary stage of creep:

$$\dot{\epsilon}_{cr} = B\sigma^n \tag{3.98}$$

where B and n are material parameters. There are more sophisticated models available, for example the characteristic strain model [27] which comprises primary, secondary and tertiary creep. An overview of various other creep models can be found [63].

3.5.2.4 Recovery

Recovery describes a process of defect removal or rearrangement in the crystal structure of deformed grains. The defects mainly consist of dislocations and were induced by plastic deformations. The recovery process reduces the dislocation density and by that the ductility increases (decrease of hardening), see also [56].

3.5.3 Multiaxial Generalization of Plasticity

So far, only uniaxial material behaviour was discussed. In this section the extension to three dimensions is introduced. In 1D, there is only one stress and one strain but in 3D, the stress and strain tensor consist of 6 independent components each. The question is now, how to

define a measure in order to mathematically describe plastic yielding of the material in three dimensions. For that purpose the so called yield surface is introduced:

$$F(\underline{\underline{\sigma}}) \leq 0 \quad (3.99)$$

For stress states inside the yield surface $F(\underline{\underline{\sigma}}) < 0$ the material behaves elastic and plastic deformations occur for stress states on the outer boundary of the yield surface $F(\underline{\underline{\sigma}}) = 0$.

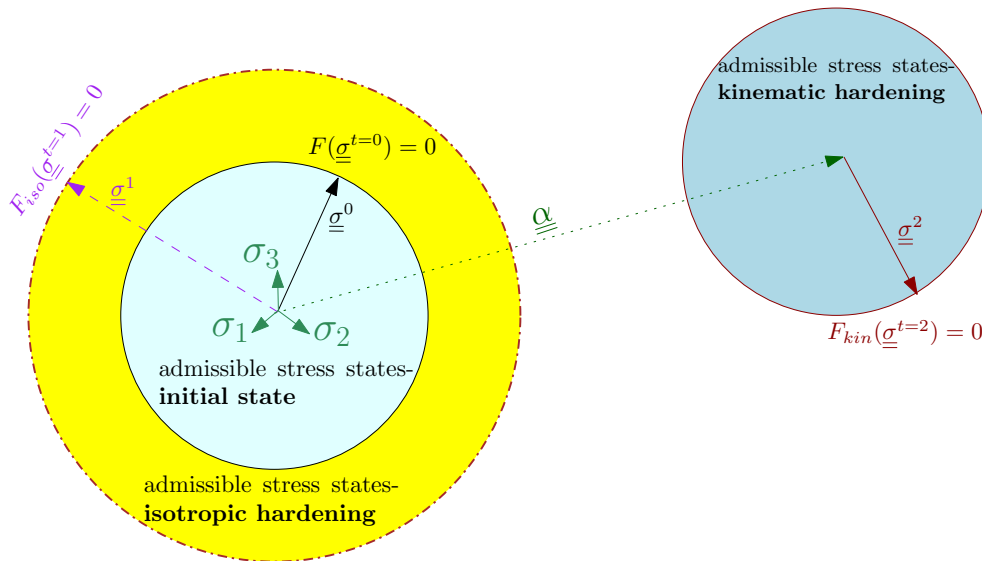


Figure 3.6: Yield surfaces: schematic representation of initial yield surface (light cyan circle), kinematic hardening yield surface (light blue surface) and isotropic hardening yield surface (yellow circle)

Figure 3.6 shows three different yield surfaces in the principal axes system in a diagonal view. In the diagonal view, the yield surfaces appear as circles. Depending on the material, the initial yield surface can behave upon loading to the yield limit in different ways:

- linear elastic - perfectly plastic material behaviour (light cyan circle) is characterized by the yield surface not changing place nor size
- isotropic hardening (yellow circle): the yield surface increases its size self-similar due to hardening/softening of the material but stays at the initial center, e.g. the material model according to Johnson-Cook [105]
- kinematic hardening (light blue circle): the yield surface does not change size but the center moves to another place in space
- kinematic + isotropic hardening (not shown in the figure): the yield surface changes center and changes its size self-similarly
- formative hardening (not shown in the figure): the yield surface changes its shape

According to [76], the yield surface depends for an isotropic material only on the three invariants (I_1, I_2, I_3) of the Cauchy stress tensor $\underline{\underline{\sigma}}$:

$$F(I_1, I_2, I_3) \leq 0 \tag{3.100}$$

Equation (3.100) can be expressed also in terms of the second and third invariant (J_2 and J_3) of the stress deviator:

$$F(I_1, J_2, J_3) \leq 0 \tag{3.101}$$

For many materials it was found that yielding is not influenced by the hydrostatic pressure. The hydrostatic pressure p is linked to the first invariant of the stress tensor with $p = I_1/3$. Therefore, the yield condition can be rewritten as:

$$F(J_2, J_3) \leq 0 \tag{3.102}$$

For the discussion of the treatment of the third invariant the Haigh-Westergard coordinate system [180] is introduced. It allows to display the stress tensor without performing an eigenvalue decomposition to retrieve the principal stresses σ_1, σ_2 and σ_3 of a stress tensor. A stress point in the Haigh-Westergard coordinate system is described by three values ρ, ζ and the Lode-angle θ , see figure 3.7. The parameter ζ depicts the position on the hydrostatic axis and scales with the hydrostatic stress, ρ is the radius in the deviatoric plane and the Lode-angle θ is the angular position on the radius ρ .

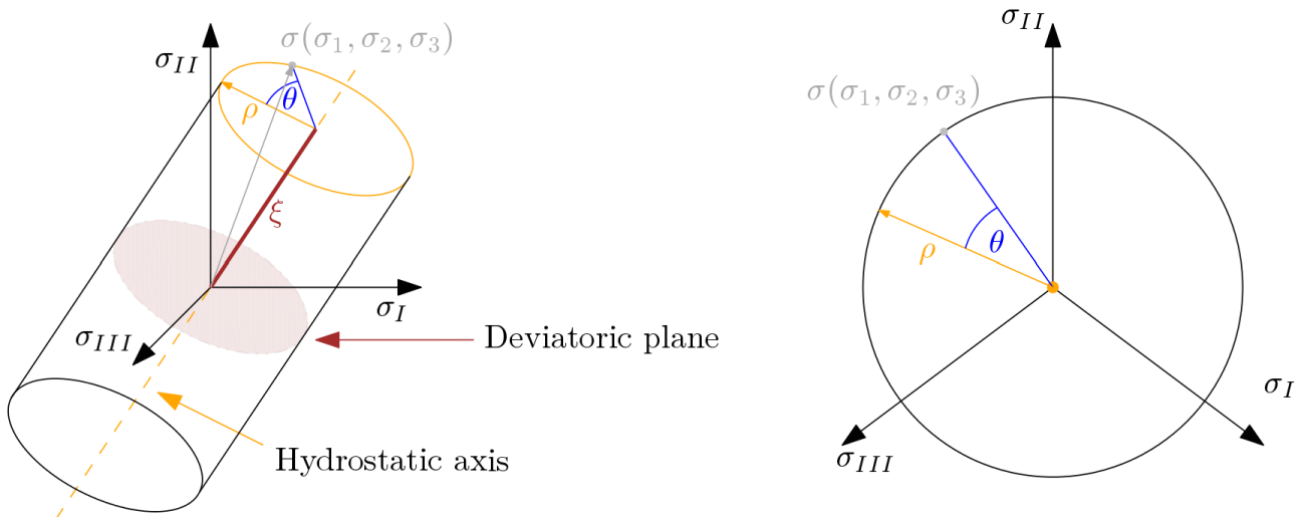


Figure 3.7: Haigh-Westergard coordinate in the principal axis system: isometric view with flow cylinder (left), view in direction of hydrostatic axis (right) where the flow cylinder coincides with a circle.

Following the denominations in [180], the three parameters ρ, ζ and θ can be computed from the stress tensor invariants I_1, J_2 and J_3 :

$$\rho = \sqrt{2J_2} \quad (3.103)$$

$$\xi = \frac{I_1}{\sqrt{3}} \quad (3.104)$$

$$\cos 3\theta = \frac{3\sqrt{3}J_3}{2J_2^{3/2}} \quad (3.105)$$

From this definition it can be seen that J_3 is related to the Lode[139]-angle θ and therefore describes the angular position along the circle with radius ρ . Assuming that the angular position described by the angle θ does not influence the yield limit one arrives at the isotropic von Mises yield surface which is defined as:

$$F(J_2) = 0 \quad (3.106)$$

Yielding occurs when the stress state described with the equivalent stress according to von Mises equals the yield limit:

$$\sigma_{eq} - \sigma_y = 0 \quad (3.107)$$

where σ_y is the yield limit. The second invariant J_2 of the stress deviator is linked to the equivalent stress σ_{eq} :

$$\sigma_{eq} = \sqrt{3J_2} \quad (3.108)$$

with the equivalent stress according to von Mises being defined as:

$$\sigma_{eq} = \sqrt{3J_2} = \sqrt{\sigma_{xx}^2 + \sigma_{yy}^2 + \sigma_{zz}^2 - \sigma_{xx}\sigma_{yy} - \sigma_{xx}\sigma_{zz} - \sigma_{yy}\sigma_{zz} + 3(\sigma_{xy}^2 + \sigma_{xz}^2 + \sigma_{yz}^2)} \quad (3.109)$$

$$= \sqrt{3J_2} = \sqrt{3} \cdot \sqrt{\underbrace{\frac{1}{2} (S_{xx}^2 + S_{yy}^2 + S_{zz}^2) + S_{xy}^2 + S_{xz}^2 + S_{yz}^2}_{=J_2}} \quad (3.110)$$

Analogous to the equivalent stress an equivalent plastic strain can be defined [199]:

$$\bar{\varepsilon}^{pl} = \frac{2}{\sqrt{3}} \sqrt{\frac{(\varepsilon_{xx}^{pl} - \varepsilon_{yy}^{pl})^2 + (\varepsilon_{xx}^{pl} - \varepsilon_{zz}^{pl})^2 + (\varepsilon_{yy}^{pl} - \varepsilon_{zz}^{pl})^2}{6} + (\varepsilon_{xy}^{pl})^2 + (\varepsilon_{xz}^{pl})^2 + (\varepsilon_{yz}^{pl})^2} \quad (3.111)$$

$$= \frac{2}{\sqrt{3}} \sqrt{\frac{1}{2} [(\varepsilon_{xx}^{pl})^2 + (\varepsilon_{yy}^{pl})^2 + (\varepsilon_{zz}^{pl})^2] + (\varepsilon_{xy}^{pl})^2 + (\varepsilon_{xz}^{pl})^2 + (\varepsilon_{yz}^{pl})^2} \quad (3.112)$$

Combining (3.107) and (3.108) gives the isotropic von Mises yield criterion:

$$F(J_2) = \sqrt{3J_2} - \sigma_y = 0 \quad (3.113)$$

If however the yield is not isotropic but depends on the direction an extension to Mises' model was proposed by Hill [92] in the so called Hill 48 model:

$$F(\sigma_{ij}) = \sqrt{F(\sigma_{yy} - \sigma_{zz})^2 + G(\sigma_{zz} - \sigma_{xx})^2 + H(\sigma_{xx} - \sigma_{yy})^2 + 2(L\sigma_{yz}^2 + M\sigma_{zx}^2 + N\sigma_{xy}^2)} - \sigma_y \quad (3.114)$$

with 6 parameters F, G, H, L, M and N describing the anisotropy of the yield and which can be computed by the yield stress ratios $R_{11}, R_{22}, R_{33}, R_{12}, R_{13}$ and R_{23} in the 6 directions by:

$$F = \frac{(\sigma^0)^2}{2} \left(\frac{1}{\sigma_{22}^2} + \frac{1}{\sigma_{33}^2} - \frac{1}{\sigma_{11}^2} \right) = \frac{1}{2} \left(\frac{1}{R_{22}^2} + \frac{1}{R_{33}^2} - \frac{1}{R_{11}^2} \right) \quad (3.115)$$

$$G = \frac{(\sigma^0)^2}{2} \left(\frac{1}{\sigma_{33}^2} + \frac{1}{\sigma_{11}^2} - \frac{1}{\sigma_{22}^2} \right) = \frac{1}{2} \left(\frac{1}{R_{33}^2} + \frac{1}{R_{11}^2} - \frac{1}{R_{22}^2} \right) \quad (3.116)$$

$$H = \frac{(\sigma^0)^2}{2} \left(\frac{1}{\sigma_{11}^2} + \frac{1}{\sigma_{22}^2} - \frac{1}{\sigma_{33}^2} \right) = \frac{1}{2} \left(\frac{1}{R_{11}^2} + \frac{1}{R_{22}^2} - \frac{1}{R_{33}^2} \right) \quad (3.117)$$

$$L = \frac{3}{2} \left(\frac{\tau^0}{\sigma_{23}} \right)^2 = \frac{3}{2R_{23}^2} \quad (3.118)$$

$$M = \frac{3}{2} \left(\frac{\tau^0}{\sigma_{13}} \right)^2 = \frac{3}{2R_{13}^2} \quad (3.119)$$

$$N = \frac{3}{2} \left(\frac{\tau^0}{\sigma_{12}} \right)^2 = \frac{3}{2R_{12}^2} \quad (3.120)$$

with σ^0 being the reference yield stress and $\tau^0 = \sigma^0 / \sqrt{3}$ the reference shear yield strength. For $F = G = H = 0.5$ ($R_{11} = R_{22} = R_{33} = 1$) and $L = M = N = 1.5$ ($R_{12} = R_{23} = R_{13} = 1$) the isotropic von Mises yield criterion (3.113) is recovered.

As long as $F(J_2) < 0$ there is no plastic strain. When $F(J_2) = 0$ plastic straining occurs and the total strain is the sum of elastic and plastic strain:

$$d\underline{\underline{\varepsilon}} = d\underline{\underline{\varepsilon}}_{el} + d\underline{\underline{\varepsilon}}_{pl} \quad (3.121)$$

It is assumed for the plastic strain that it can be derived from some plastic potential G :

$$d\underline{\underline{\varepsilon}}_{pl} = d\lambda \frac{\partial G}{\partial \underline{\underline{\sigma}}} = d\lambda \nabla_{\underline{\underline{\sigma}}} G \quad (3.122)$$

where $d\lambda$ is a proportionality factor. $\nabla_{\underline{\underline{\sigma}}}G$ is the normal vector to the surface G with a length scaled by $d\lambda$. As the determination of G is a difficult task it is often assumed that $G = F$, which is known as associative flow-rule, while the general case $G \neq F$ is a non-associative flow rule for example used in [168].

With $F = G$ (3.122) becomes:

$$d\underline{\underline{\varepsilon}}_{pl} = d\lambda \frac{\partial F}{\partial \underline{\underline{\sigma}}} = d\lambda \nabla_{\underline{\underline{\sigma}}}F \quad (3.123)$$

Figure 3.8 shows an example where the stress state leads to $F = 0$ and results in a plastic strain increment $d\underline{\underline{\varepsilon}}_{ij}^{pl}$ along the normal direction $\nabla_{\underline{\underline{\sigma}}}F$ scaled by $d\lambda$.

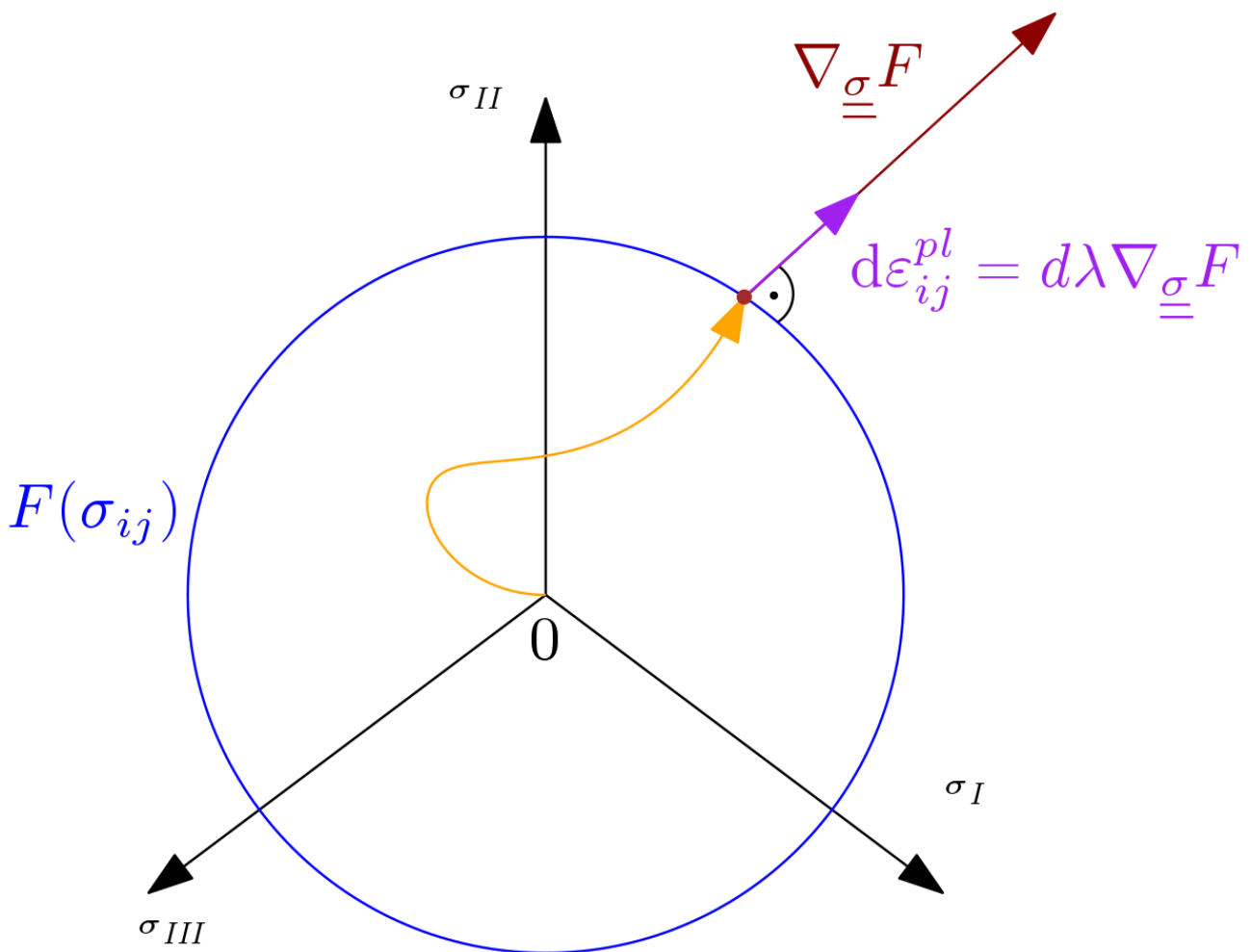


Figure 3.8: A loading state to $F = 0$ results in a plastic strain increment $d\underline{\underline{\varepsilon}}_{ij}^{pl}$ directed into the normal direction $\nabla_{\underline{\underline{\sigma}}}F$ scaled by $d\lambda$.

The associated flow rule (3.123) bears with the von Mises yield locus (3.113) an attractive feature since:

$$\nabla_{\underline{\underline{\sigma}}}F = \underline{\underline{S}} \quad (3.124)$$

with $\underline{\underline{S}}$ being the deviatoric part of the Cauchy stress tensor $\underline{\underline{\sigma}}$, see (3.38).

3.5.4 Integration of Plasticity Models - Radial Return Projection

During the loading, the stress state must not exceed the flow surface $F(\underline{\underline{\sigma}}) \leq 0$ (3.99). This can be ensured by a special integration technique named radial return projection which was introduced by [258]. It is used to determine the plastic multiplier in (3.123) and to compute the plastic strain increment. For simple plasticity models these equations can be solved analytically but more complex models require an iterative procedure for the computation of the plastic multiplier which is explained in the following based on [78, 208]. The yield limit σ_y in (3.113) is set to the Johnson-Cook flow stress model (3.95):

$$\begin{aligned} F(J_2) &= \sqrt{3J_2} - \sigma_y = \sqrt{3J_2} - \sigma_y(\bar{\varepsilon}_{pl}, \dot{\varepsilon}_{pl}, T) \\ &= \sqrt{3J_2} - (A + B \cdot (\varepsilon_{pl})^n) \left(1 + C \cdot \ln \left(\frac{\dot{\varepsilon}_{pl}}{\dot{\varepsilon}_{pl}^0} \right) \right) \left(1 - \left(\frac{T - T_{ref}}{T_f - T_{ref}} \right)^m \right) \end{aligned} \quad (3.125)$$

inserting into (3.123) and applying the chain rule yields with (3.124):

$$d\varepsilon_{pl} = d\lambda \frac{\partial F}{\partial \underline{\underline{\sigma}}} \quad (3.126)$$

$$= d\lambda \frac{\partial(\sqrt{3J_2} - \sigma_y)}{\partial \underline{\underline{\sigma}}} \quad (3.127)$$

$$= d\lambda \frac{1}{2\sqrt{3J_2}} \cdot 3 \cdot \frac{\partial J_2}{\partial \underline{\underline{\sigma}}} \quad (3.128)$$

$$= d\lambda \frac{\sqrt{3}}{2\sqrt{J_2}} \underline{\underline{S}} \quad (3.129)$$

$$= d\lambda \sqrt{\frac{3}{2}} \frac{\underline{\underline{S}}}{\|\underline{\underline{S}}\|} \quad (3.130)$$

where in equation (3.130) it was used that:

$$\|\underline{\underline{S}}\| = \sqrt{2J_2} \quad (3.131)$$

This result means that the plastic strain increment directs in the same direction as the stress deviator $\underline{\underline{S}}$. The deviatoric stress rate updates with the elastic strain rate (3.121) as:

$$\dot{\underline{\underline{S}}} = 2G \cdot dev(\dot{\underline{\underline{\varepsilon}}}_{el}) = 2G \cdot (dev(\dot{\underline{\underline{\varepsilon}}}) - dev(\dot{\underline{\underline{\varepsilon}}}_{pl})) = 2G \cdot (dev(\dot{\underline{\underline{\varepsilon}}}) - \dot{\underline{\underline{\varepsilon}}}_{pl}) \quad (3.132)$$

where the plastic strain is yet undetermined. The equations are integrated with an Euler implicit scheme such that the resulting stress state fulfils $F(J_2) = 0$ at the end of the increment $n + 1$. It is assumed that the plastic strain rate is constant within the increment and therefore $\dot{\underline{\underline{\varepsilon}}}_{pl} = \bar{\varepsilon}_{pl}/\Delta t$. The idea is to compute an elastic trial stress $\underline{\underline{S}}^{trial}$ and check whether it violates the yield criterion (3.113):

$$\underline{\underline{S}}^{trial} = \underline{\underline{S}}^n + 2G \cdot dev(\underline{\underline{\dot{\varepsilon}}})\Delta t \quad (3.133)$$

with $\underline{\underline{S}}^n$ being the deviatoric stress from the last increment and Δt the time step. For $F(\underline{\underline{S}}^{trial}) \leq 0$ the plastic strain and the plastic strain rate remain unchanged and the constitutive update is:

$$\underline{\underline{S}}^{n+1} = \underline{\underline{S}}^{trial} \quad (3.134)$$

$$\bar{\varepsilon}_{pl}^{n+1} = \bar{\varepsilon}_{pl}^n \quad (3.135)$$

$$\dot{\underline{\underline{\varepsilon}}}_{pl}^{n+1} = \dot{\underline{\underline{\varepsilon}}}_{pl}^n \quad (3.136)$$

$$\underline{\underline{\varepsilon}}_{el}^{n+1} = \underline{\underline{\varepsilon}}_{el}^n + \underline{\underline{\dot{\varepsilon}}}\Delta t \quad (3.137)$$

If $F(\underline{\underline{S}}^{trial}) > 0$ the plastic multiplier has to be determined such that $F(\underline{\underline{S}}^{n+1}) = 0$. It starts with combining (3.132), (3.133), (3.134) and inserting (3.123):

$$\underline{\underline{S}}^{n+1} = \underline{\underline{S}}^n + \underline{\underline{\dot{S}}}\Delta t \quad (3.138)$$

$$= \underline{\underline{S}}^{trial} - 2G \cdot dev(\underline{\underline{\dot{\varepsilon}}})\Delta t + \underline{\underline{\dot{S}}}\Delta t \quad (3.139)$$

$$= \underline{\underline{S}}^{trial} - 2G \cdot dev(\underline{\underline{\dot{\varepsilon}}})\Delta t + 2G \cdot (dev(\underline{\underline{\dot{\varepsilon}}}) - \dot{\underline{\underline{\varepsilon}}}_{pl})\Delta t \quad (3.140)$$

$$= \underline{\underline{S}}^{trial} - 2G \cdot \dot{\underline{\underline{\varepsilon}}}_{pl}\Delta t \quad (3.141)$$

$$= \underline{\underline{S}}^{trial} - 2G \cdot \left(\lambda \sqrt{\frac{3}{2}} \frac{\underline{\underline{S}}^{n+1}}{\|\underline{\underline{S}}^{n+1}\|} \right) \Delta t \quad (3.142)$$

Rearranging (3.142) leads to:

$$\underline{\underline{S}}^{n+1} = \underline{\underline{S}}^{trial} - \left(\sqrt{\frac{3}{2}} \frac{(2G \cdot \lambda \cdot \Delta t \cdot \underline{\underline{S}}^{n+1})}{\|\underline{\underline{S}}^{n+1}\|} \right) \quad (3.143)$$

$$\underline{\underline{S}}^{trial} = \underline{\underline{S}}^{n+1} + \left(\sqrt{\frac{3}{2}} \frac{(2G \cdot \lambda \cdot \Delta t \cdot \underline{\underline{S}}^{n+1})}{\|\underline{\underline{S}}^{n+1}\|} \right) \quad (3.144)$$

$$\underline{\underline{S}}^{trial} = \underline{\underline{S}}^{n+1} \cdot \left[1 + \left(\sqrt{\frac{3}{2}} \frac{(2G \cdot \lambda \cdot \Delta t)}{\|\underline{\underline{S}}^{n+1}\|} \right) \right] \quad (3.145)$$

In (3.145) the term in brackets is a scalar from which it can be concluded that $\underline{\underline{S}}^{trial}$ and $\underline{\underline{S}}^{n+1}$ have the same direction which allows to write:

$$\frac{\underline{\underline{S}}^{trial}}{\|\underline{\underline{S}}^{trial}\|} = \frac{\underline{\underline{S}}^{n+1}}{\|\underline{\underline{S}}^{n+1}\|} \quad (3.146)$$

which can be inserted into (3.145):

$$\left[\frac{\|\underline{\underline{S}}^{trial}\|}{\underline{\underline{S}}^{trial}} \right] \underline{\underline{S}}^{trial} = \underline{\underline{S}}^{n+1} \cdot \left[1 + \left(\sqrt{\frac{3}{2}} \frac{(2G \cdot \dot{\lambda} \cdot \Delta t)}{\|\underline{\underline{S}}^{n+1}\|} \right) \right] \left[\frac{\|\underline{\underline{S}}^{n+1}\|}{\underline{\underline{S}}^{n+1}} \right] \quad (3.147)$$

$$\|\underline{\underline{S}}^{trial}\| = \left[1 + \left(\sqrt{\frac{3}{2}} \frac{(2G \cdot \dot{\lambda} \cdot \Delta t)}{\|\underline{\underline{S}}^{n+1}\|} \right) \right] \|\underline{\underline{S}}^{n+1}\| \quad (3.148)$$

$$\|\underline{\underline{S}}^{trial}\| = \|\underline{\underline{S}}^{n+1}\| + \sqrt{\frac{3}{2}} (2G \cdot \dot{\lambda} \cdot \Delta t) \quad (3.149)$$

Since the stress state needs to fulfil $F(J_2) = 0$ the stress $\|\underline{\underline{S}}^{n+1}\|$ is:

$$\|\underline{\underline{S}}^{n+1}\| = \sqrt{\frac{2}{3}} \sigma_y(\bar{\epsilon}_{pl}^{n+1}, \dot{\epsilon}_{pl}^{n+1}, T) \quad (3.150)$$

which can be inserted into (3.149):

$$\|\underline{\underline{S}}^{trial}\| = \sqrt{\frac{2}{3}} \sigma_y(\bar{\epsilon}_{pl}^{n+1}, \dot{\epsilon}_{pl}^{n+1}, T) + \sqrt{\frac{3}{2}} (2G \cdot \dot{\lambda} \cdot \Delta t) \quad (3.151)$$

$$g(\dot{\lambda}) = 0 = \|\underline{\underline{S}}^{trial}\| - \sqrt{\frac{2}{3}} \sigma_y(\bar{\epsilon}_{pl}^{n+1}, \dot{\epsilon}_{pl}^{n+1}, T) - \sqrt{\frac{3}{2}} (2G \cdot \dot{\lambda} \cdot \Delta t) \quad (3.152)$$

and is a function that only depends on $\dot{\lambda}$. This equation is with the flow stress $\sigma_y(\bar{\epsilon}_{pl}, \dot{\epsilon}_{pl}, T)$ nonlinear and needs to be solved by some numerical method to find $G(\dot{\lambda}) = 0$. Only for the case that the flow stress is constant (ideal plasticity) a direct analytical solution for $\dot{\lambda}$ could be obtained:

$$\sqrt{\frac{3}{2}} 2G \cdot \dot{\lambda} \cdot \Delta t = \|\underline{\underline{S}}^{trial}\| - \sqrt{\frac{2}{3}} \sigma_y \quad (3.153)$$

$$\dot{\lambda} = \frac{1}{\sqrt{6G \cdot \Delta t}} \left(\|\underline{\underline{S}}^{trial}\| - \sqrt{\frac{2}{3}} \sigma_y \right) \quad (3.154)$$

$$(3.155)$$

The full constitutive update is then:

$$\Delta \underline{\underline{\varepsilon}}_{pl} = \dot{\lambda} \Delta t \sqrt{\frac{3}{2}} \frac{\underline{\underline{S}}^{trial}}{\|\underline{\underline{S}}^{trial}\|} \quad (3.156)$$

$$\underline{\underline{S}}^{n+1} = \underline{\underline{S}}^{trial} - 2G \Delta \underline{\underline{\varepsilon}}_{pl} \quad (3.157)$$

$$\bar{\underline{\underline{\varepsilon}}}_{pl}^{n+1} = \bar{\underline{\underline{\varepsilon}}}_{pl}^n + \dot{\lambda} \Delta t \quad (3.158)$$

$$\dot{\bar{\underline{\underline{\varepsilon}}}}_{pl}^{n+1} = \dot{\lambda} \quad (3.159)$$

$$\underline{\underline{\varepsilon}}_{pl}^{n+1} = \underline{\underline{\varepsilon}}_{pl}^n + \Delta \underline{\underline{\varepsilon}}_{pl} \quad (3.160)$$

$$\underline{\underline{\varepsilon}}_{el}^{n+1} = \underline{\underline{\varepsilon}}_{el}^n + \dot{\underline{\underline{\varepsilon}}}_{el} \Delta t - \Delta \underline{\underline{\varepsilon}}_{pl} \quad (3.161)$$

3.6 DAMAGE MODELLING

Besides the material behaviour at various strains, strain rates and temperatures another important aspect is the structural integrity after stressing the continuum beyond the yield limit. The generally observed behaviour for ductile material is depicted in the stress-strain-curve in figure 3.9 with different phases in the stress-strain curve.

While upon loading beyond the elastic limit (from (I) to (II)) irreversible deformation occurs and the material hardens with an increase in the yield stress. Exceeding a certain point (III), the material starts to lose its stiffness (IV) until complete loss and material separation occurs (V).

The stages (II)-(V) are subject of the damage mechanics, whose beginnings date back to 1958 when Kachanov [108] introduced a scalar variable D assuming isotropic damage. In recent works tensorial damage variables are used [51, 183] which is not the subject in this work. Rabotnov [197] developed the effective stress concept for isotropic damage where the stresses are scaled with increasing damage assuming a reduced cross section due to pore formation. A good overview into the topic is provided with [125, 126].

Other research [63] uses energy based approaches [185, 237] for the damage accumulation in creep fatigue interaction analyses. However, such interactions are not of interest in this work since machining processes are subject to much smaller time scales in the order of less than a second.

3.6.1 Damage Initiation

Usually the first phases (II-III) are modelled with a fracture strain model which gives the fracture strain as a function of stress state, plastic strain, plastic strain rate and temperature:

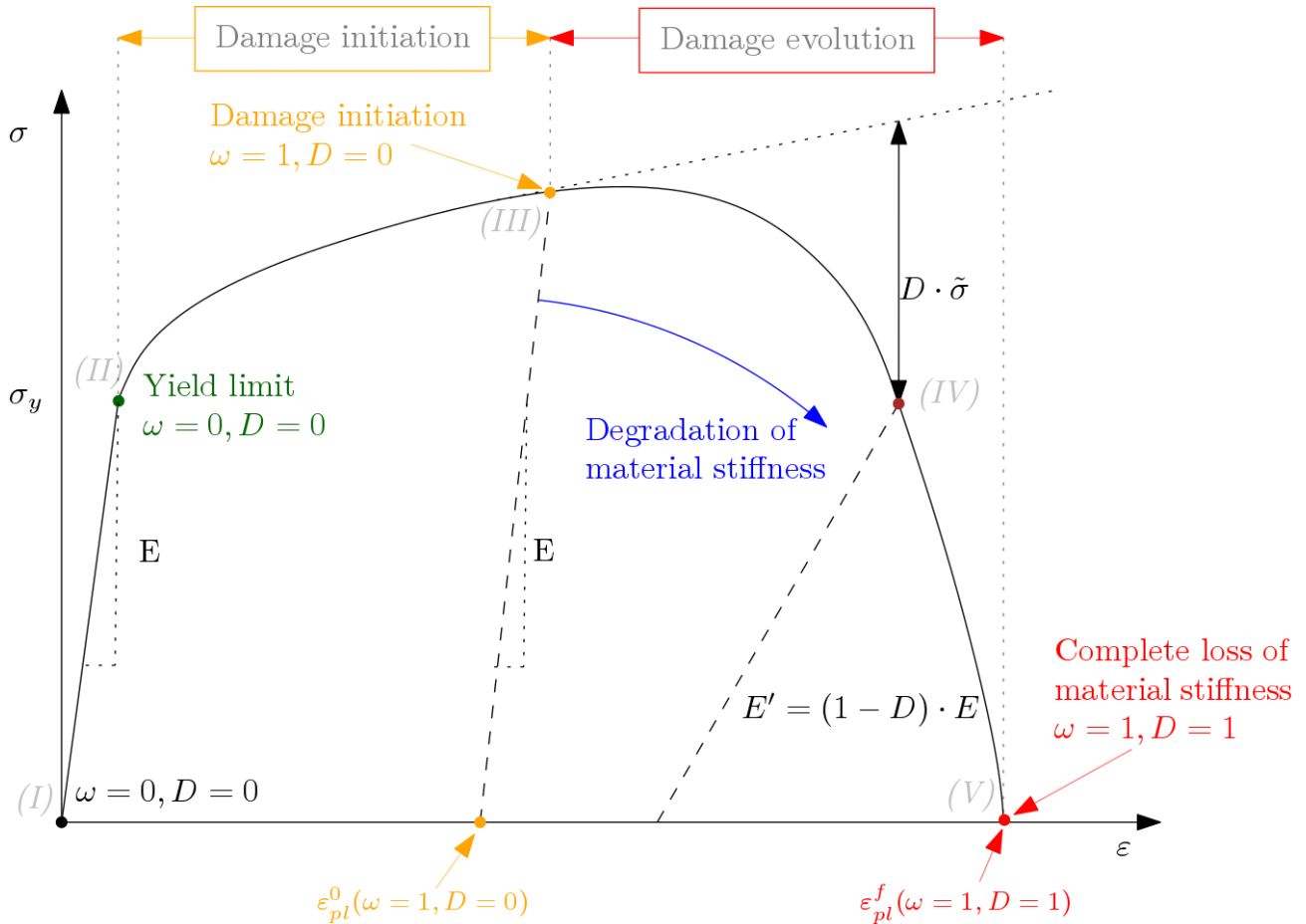


Figure 3.9: Damage initiation and evolution

$$\varepsilon^f = f(\underline{\sigma}, \dot{\varepsilon}_{pl}, T, \dots) \quad (3.162)$$

The effect of the pressure on tensile properties was investigated by [31] and later [150, 201] derived an expression for the effect of stress triaxiality on the fracture strain by analysis of void growth in ductile metals leading to an expression for the fracture strain $\bar{\varepsilon}^f$:

$$\bar{\varepsilon}_{RT}^f = D_{RT1} \cdot e^{D_{RT2} \cdot \sigma^*} \quad (3.163)$$

with D_{RT1} and D_{RT2} being material parameters and σ^* the stress triaxiality ratio defined as:

$$\sigma^* = \frac{\sigma_H}{\sigma_{eq}} = \frac{\sigma_{xx} + \sigma_{yy} + \sigma_{zz}}{3 \cdot \sigma_{equiv}} \quad (3.164)$$

with σ_H being the average of the trace of the stress tensor and σ_{eq} is the von Mises equivalent stress (3.110).

An extension of this early model (3.163) is the fracture model introduced by Johnson and Cook [73]. It considers strain sensitivity and temperature dependency of the fracture strain as:

$$\bar{\epsilon}^f = \underbrace{(D_1 + D_2 \cdot e^{D_3 \cdot \sigma^*})}_{\text{stress triaxiality dependency}} \underbrace{(1 + D_4 \cdot \ln(\dot{\bar{\epsilon}}^*))}_{\text{strain rate sensitivity}} \underbrace{(1 + D_5 T^*)}_{\text{temperature dependency}} \quad (3.165)$$

and D_1 to D_5 material parameters. The dimensionless plastic strain rate $\dot{\bar{\epsilon}}^*$ and the homologous temperature T^* are defined similar to the Johnson-Cook flow stress model in equation (3.95).

The Johnson-Cook fracture strain model found a recent extension by [18] where an asymmetric fracture locus is considered with Lode-angle dependency.

The fracture strain model is used in simulations to compute the ratio of current plastic strain increment $\Delta\epsilon$ versus current fracture strain $\bar{\epsilon}^f$ which is linearly summed up over all increments into a damage variable ω :

$$\omega = \sum \frac{\Delta\epsilon}{\bar{\epsilon}^f} \quad (3.166)$$

When the damage ω reaches a critical value ω_{crit} (usually $\omega_{crit} = 1$) the damage is fully initiated and it is either assumed that fracture/separation occurs and the particle or element is deleted.

In cutting simulations sometimes another damage initiation criterion than (3.166) is used according to Cockcroft and Latham [45]:

$$\omega_{CL} = \int_0^{\epsilon^f} \sigma_1 d\epsilon \quad (3.167)$$

where σ_1 is the maximum principal stress. Similar to the linear damage evolution fracture/separation is fully initiated when ω_{CL} reaches a critical value ω_{CLcrit} . The drawback of this model is that it does not account for stress triaxiality effects.

An alternative to particle or element deletion is a follow-up damage evolution using a fictitious crack model.

3.6.2 Damage Evolution

In the damage evolution phase a second damage variable D is used to model the fracture growth. A pragmatic way is described in [93] where a fictitious crack is modelled. Upon increased separation described by an effective plastic displacement the remaining load carrying capacity is successively reduced until the critical energy release rate G_f is reached:

$$G_f = \int_{\epsilon_{pl}^0}^{\epsilon_{pl}^f} L\sigma_y d\bar{\epsilon}_{pl} = \int_0^{\bar{u}_{pl}^f} \sigma_y d\bar{u}_{pl} \quad (3.168)$$

with L being a characteristic length which in finite element applications is the element length. σ_y is the current yield limit and ε_{pl}^0 is the plastic strain when damage evolution starts and ε_{pl}^f is the strain at fracture. Similar, an equivalent plastic displacement \bar{u}_{pl} can be defined which is $\bar{u}_{pl} = 0$ at the onset of damage evolution and at fracture $\bar{u}_{pl} = \bar{u}_{pl}^f$. G_f is the critical energy release rate and is related to the fracture toughness K_{1C} for plane strain conditions with [76]:

$$G_f = K_{1C}^2 \frac{1 - \nu^2}{E} \quad (3.169)$$

During the load increments the accumulated damage of the evolution phase is computed with an exponential rule [62, 271]:

$$D = 1 - \exp\left(-\int_0^{\bar{u}_{pl}} \frac{\sigma_y}{G_f}\right) \quad (3.170)$$

This would require infinite plastic strain to reach $D = 1$ therefore the damage is usually set to $D = 1$ when:

$$\int_0^{\bar{u}_{pl}} \sigma_y d\bar{u}_{pl} = 0.99 \cdot G_f \quad (3.171)$$

It is shown [250] that the value for G_f has an important influence on the fracture morphology.

During the damage evolution the shear stiffness degrades with softening of the deviatoric stress components. The bulk stiffness is retained in hydrostatic compression ($p > 0$), but degrades in hydrostatic tension. Usually, the deviatoric stress $\underline{\underline{S}}$ and the hydrostatic pressure \bar{p} are then modified according to [89]:

$$\underline{\underline{S}} = (1 - D_{dev})\bar{\underline{\underline{S}}} \quad (3.172)$$

$$p = (1 - D_{vol})\bar{p} \quad (3.173)$$

with the deviatoric and volumetric damage variables defined as:

$$D_{dev} = D \quad (3.174)$$

$$D_{vol} = \begin{cases} D, & \text{if } \bar{p} \leq 0 \\ 0, & \text{if } \bar{p} > 0 \end{cases} \quad (3.175)$$

When the maximum damage D_{max} is reached the respective element is deleted from the simulation.

An evaluation of various damage initiation and evolution models is provided with [134].

MESHLESS METHODS

Within the class of numerical methods for solving boundary value problems particle methods are an approach to solve problems undergoing large deformations without the need to remesh the domain - in contrast to FEM where adaptive remeshing is required upon increased element distortion invoked by large deformations.

In contrast, particle methods in general do not suffer from large deformations or material separations. Basic principle of the SPH is the field value approximation based on each particle's neighbourhood within a circle (2D) or cube (3D) with radius $2h$. This neighbourhood is updated not just continuously but automatically during the analysis. Particles moving out of the radius $2h$ leave this neighbourhood and stop contributing to the approximation of the center particle, while particles entering will start to contribute.

Particle methods originate from astrophysics (Gingold et al. [196]) where a smoothed density is calculated from a set of points. In their publication, Gingold et al. utilized statistical methods in order to recover analytical expressions for physical quantities from a given set of fluid elements.

4.1 DERIVATION OF THE SPH

However, the method can be developed from different perspectives and in the following a more convenient derivation will be shown, it is based on the partition of unity. The concept is based on the approximation of a field value f at a location \underline{x} :

$$\langle f(\underline{x}) \rangle = \int_{\mathbb{R}^d} \delta(\underline{x} - \underline{x}') f(\underline{x}') d\Omega_{x'}, \quad \forall \underline{x} \in \mathbb{R}^d \quad (4.1)$$

with $\delta(\underline{x})$ being the Dirac-delta function which has the following two important properties:

$$\begin{aligned} \int_{-\infty}^{+\infty} \delta(\underline{x}) d\underline{x} &= 1 \\ \int_{-\infty}^{+\infty} \delta(\underline{\zeta} - \underline{x}) \cdot f(\underline{\zeta}) d\underline{\zeta} &= f(\underline{x}) \end{aligned} \quad (4.2)$$

The Dirac-delta function in equation (4.1) lacks continuity and differentiability and is therefore replaced by a smooth kernel $W(\underline{x} - \underline{x}', h_{SPH})$ with h_{SPH} being a smoothing length. The smooth kernel mimics the behaviour of the Dirac-delta function for the limit:

$$\lim_{h \rightarrow 0} W(\underline{x} - \underline{x}', h_{SPH}) = \delta(\underline{x} - \underline{x}'). \quad (4.3)$$

With this replacement the value of a function at any spatial location can be approximated from values at discrete locations:

$$\langle f(x) \rangle = \int_{-\infty}^{+\infty} f(\underline{x}') \cdot W(\underline{x} - \underline{x}', h_{SPH}) d\underline{x}' \quad (4.4)$$

Since the smoothing length h (support length) of the smooth kernel is chosen to be small, only neighbouring points (particles) will contribute to the approximation. The expression in equation (4.4) can be integrated using a Riemann-sum:

$$\begin{aligned} \langle f_i \rangle &= \int_{-\infty}^{+\infty} f(\underline{x}') \cdot W(\underline{x} - \underline{x}', h_{SPH}) d\underline{x}' \\ &\approx \sum_j f_j \cdot W(\underline{x}_{ij}, h_{SPH}) \Delta V_j \end{aligned} \quad (4.5)$$

with the distance between particles i and j defined as $\underline{x}_{ij} = |\underline{x}_i - \underline{x}_j|$. Some standard smooth kernel which are commonly used are the Gauß- kernel:

$$W(\underline{x}_{ij}, h_{SPH}) = \frac{1}{(\pi h_{SPH}^2)^{n/2}} e^{-\underline{x}_{ij}^2 / h_{SPH}^2} \quad (4.6)$$

and the cubic spline kernel:

$$W(\underline{x}_{ij}, h_{SPH}) = \frac{C}{h_{SPH}^n} \begin{cases} 1 - \frac{3}{2}q^2 + \frac{3}{4}q^3, & 0 \leq q \leq 1 \\ \frac{1}{4}(2 - q)^3, & 1 \leq q \leq 2 \\ 0, & q > 2 \end{cases} \quad (4.7)$$

$$\text{with } C = \begin{cases} \frac{2}{3}, & \text{in 1D} \\ \frac{10}{7}\pi, & \text{in 2D} \\ 1/\pi, & \text{in 3D} \end{cases}$$

with $q = \underline{x}_{ij}/h$ and n the dimension of \underline{x} . An example picture of the cubic spline Kernel is provided with figure 4.1. Other kernels are based on higher order splines described e.g. in Price [192] or the Wendland kernel [256].

The approximation provided with equation (4.5) has some very interesting properties: By differentiating equation (4.5) and applying the product rule one finds (see more detailed derivation e.g. in Li & Liu [219]) that the interpolants can be used to approximate derivatives of the interpolated field(s) in a rather simple manner:

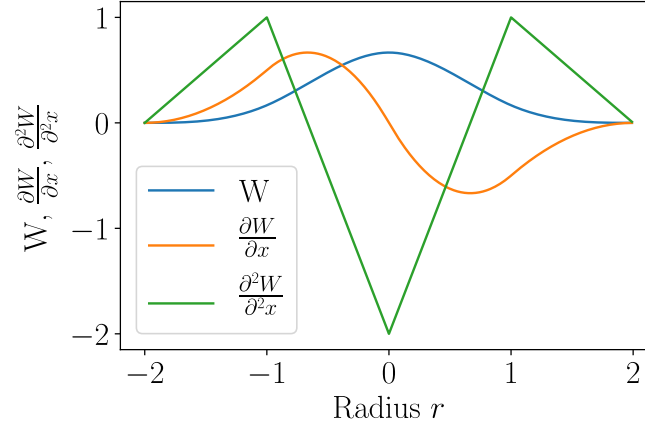


Figure 4.1: Function values of a cubic spline kernel with smoothing length $h_{SPH} = 1$ and its first and second derivative, based on [192].

$$\langle \nabla f_i \rangle = \sum_j f_j \cdot \nabla W(\underline{x}_{ij}, h_{SPH}) \Delta V_j \quad (4.8)$$

The big advantage here is that derivatives of point clouds can be assessed without any functional description or mesh-based relation between particles. By this relationship, a simple way was found to approximate field values and its derivatives which made the method attractive for applying it to the numerical solution of partial differential equations (PDE). While this appears like a straightforward approach, it was found during the application history of the method that some deficiencies exist. The encountered problems require solutions which are briefly explained in the next chapter.

4.2 ISSUES AND IMPROVEMENTS TO THE SPH

As mentioned above, the use of the approximation in equation (4.8) is not free of deficiencies. In practical applications the following problems can occur:

1. conservation of physical quantities not ensured, chapter 4.2.1
2. tensile instability, chapter 4.2.2
3. zero energy modes, chapter 4.2.3
4. difficult enforcement of boundary conditions, chapter 4.2.4 and
5. interpolation neither normalized nor consistent, chapter 4.2.5

The listed issues are addressed in the following.

4.2.1 Conservation Properties

Even though the approximation in equation (4.8) is rather simple, it has the drawback that it does not exhibit conservation properties [219] and therefore a simple correction, restoring the conservation properties, is made to equation (4.8), based on [164]. If a function $f(x)$ is constant its derivative should vanish. The approximation in equation (4.8) does not vanish for constant $f(\underline{x})$ and therefore a correction is made:

$$\frac{\partial f}{\partial \underline{x}} = \frac{1}{\Phi} \left(\frac{\partial(\Phi f)}{\partial \underline{x}} - f \frac{\partial \Phi}{\partial \underline{x}} \right) \quad (4.9)$$

Φ being an arbitrary differentiable function. Bringing the before into SPH form:

$$\left(\frac{\partial f}{\partial \underline{x}} \right)_i = \frac{1}{\Phi_i} \sum_j m_j \frac{\Phi_j}{\varrho_j} (f_j - f_i) \frac{\partial W_{ij}}{\partial \underline{x}_i} \quad (4.10)$$

and setting $\Phi = 1$ one finally receives:

$$\left(\frac{\partial f}{\partial \underline{x}} \right)_i = \sum_j \frac{m_j}{\varrho_j} (f_j - f_i) \frac{\partial W_{ij}}{\partial \underline{x}_i} \quad (4.11)$$

or with the approximation operator:

$$\langle \nabla f_i \rangle = \sum_j (f_j - f_i) \cdot \nabla W(\underline{x}_{ij}, h_{SPH}) \Delta V_j \quad (4.12)$$

4.2.2 Tensile Instability

An issue attracting attention since longer is the tensile instability: particles subjected to tensile stress will lump under certain conditions and subsequently spoil the solution. An analysis conducted by Swegle [54] revealed the cause not to lie within the numerical time integration algorithm but in the interaction between constitutive relation and the kernel function inducing imaginary sound speeds under special conditions. A partial solution is the use of artificial viscosity or a Total Lagrangian formulation, which is less prone to tensile instability, instead of the more common Updated Lagrangian approach. Another way to circumvent the tensile instability is the utilization of so called stress points which are briefly explained in the next paragraph.

4.2.3 *Zero Energy Modes*

Zero energy modes are characterized by stress- / strain-free deformation of the discretized continuum in numerical solutions. A common form of zero energy modes in FEM solutions is the so called "hour-glassing", for more details see [23].

In particle methods, zero energy modes arise due to all field values located on the same spatial location for each particle, shown by Vignjevic [130]. A solution is the introduction of so called "stress points", initially developed by Dyka & Ingel [48] for the treatment of the tensile instability in 1D by separating spatial locations carrying displacement and stress informations. Later, the stress point method was extended into two dimensions by Randles & Libersky [195]. The stress points not only solve the zero energy mode problem but also simplify the application of stress boundary conditions. So far, no extension of the stress point method exists for problems in three dimensions.

4.2.4 *Boundary Condition Application*

Due to the SPH being an interpolating method, the boundaries/edges of the domain are not captured well. Usually, displacement/velocity boundary conditions are imposed directly on the particles by overwriting these quantities in each time step. On free boundaries, the SPH method results in approximate zero pressure (fluid dynamics) or approximate stress free (structural dynamics) boundary conditions without explicit treatment. Randles & Libersky [194] explain the effect with the missing neighbour interpolation particles acting as if they are cancelling out in the momentum kernel sums due to zero stress/pressure components of the non-existent particles. Important to note here is that the approximately stress free boundaries work with the standard SPH only. For normalized and / or corrected SPH schemes (see next paragraph below) different measures for ensuring stress free boundary conditions have to be taken.

One way to improve boundary condition application is the use of the so called "ghost particle" approach. The idea is to place at least one additional layer of particles at the boundary outside of the domain. The number of layers depend on the chosen smoothing length h . The ghost particles carry the desired boundary condition. During the kernel interpolation of the main domain the ghost particles are incorporated automatically and by that imprinting the specified boundary conditions.

In case stress boundary conditions shall be applied, the stress point method, first introduced by Dyka & Ingel [48], is an elegant way to accomplish. A brief introduction of the stress point method is given in the paragraph above.

4.2.5 Interpolation Normalization and Consistency

The standard SPH approximation does not correctly approximate constant fields (zero order inconsistent) as well as constant fields resulting from the derivation of linear functions (first order inconsistent).

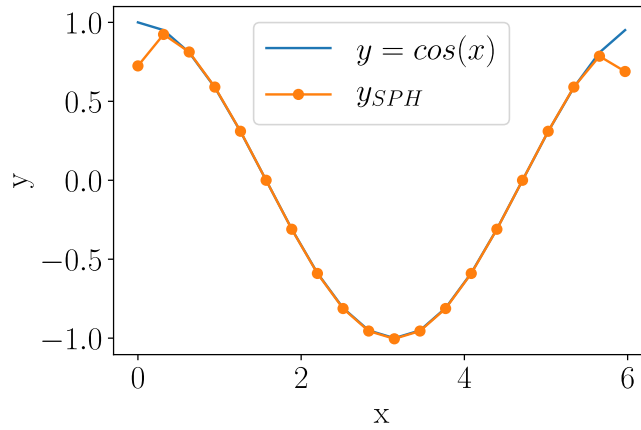


Figure 4.2: Cosine function in the interval $x = [0 : 2\pi]$ and its SPH approximation the showing boundary deficiency.

Another problems is the boundary deficiency where particles at the border of the domain approximate incorrect values. An example for this boundary deficiency is shown in figure 4.2 for cosine function and its SPH approximation with 20 particles in the domain. The requirement $\int_{\Omega} W(\underline{x} - \tilde{\underline{x}}, h_{SPH}) dV = 1$ (based on (4.2)) cannot be fulfilled at domain boundaries. This is illustrated with figure 4.3. Particle $P1$ is located at the domain boundary and has a neighbour to its right side (particle $P2$) only. When interpolating function values or its derivatives the missing interaction to the other side will lead to incorrect results since the kernel sum over neighbouring particles won't equal 1 and therefore does not mimic the Dirac delta property.

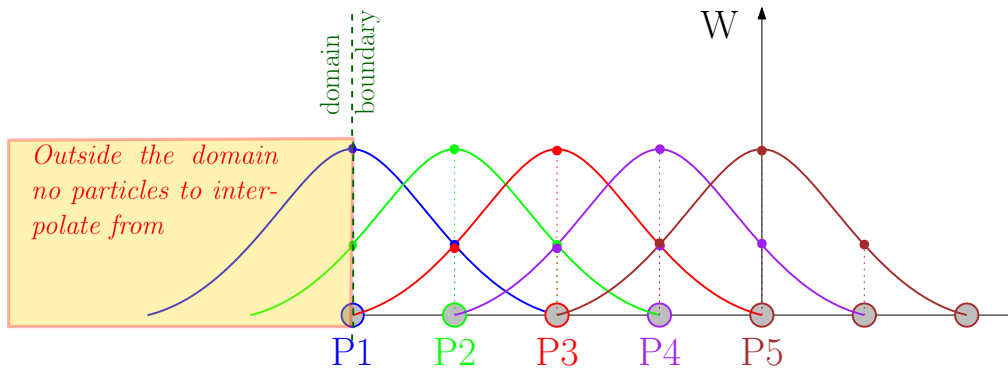


Figure 4.3: SPH boundary deficiency

Several approaches exist in order to resolve the boundary deficiency and to restore the zero and first order consistency. Two examples of them will be given below. In the following the convention of Vignjevic [41] is used, where normalization refers to improvements of the zero order consistency and correction to improvements of the first order consistency.

The first example is the Corrected Smoothed Particle Method (CSPM) developed by Chen [103]. Their modification is based on a Taylor series expansion of the SPH approximation of a function. The expansion is truncated with the first derivative terms and reads:

$$f_i \cong \frac{\sum_{j=1}^N f(\underline{x}_j) W(\underline{x}_{ij}, h_{SPH}) V_j}{\sum_{j=1}^N W(\underline{x}_{ij}) V_j} \quad (4.13)$$

The resulting expression is able to restore zero order consistency when interpolating a function, see the repeated approximation of the cosine function in figure 4.4.

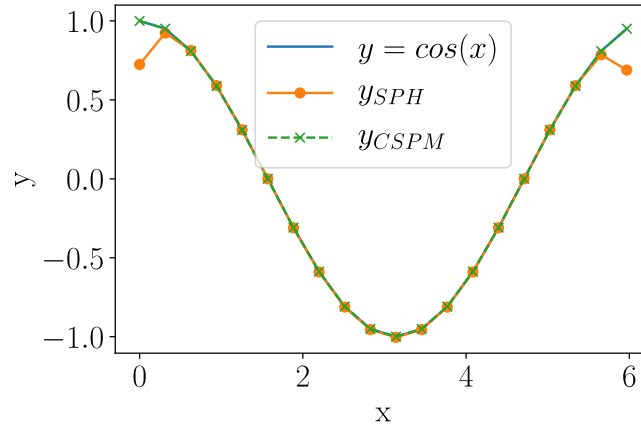


Figure 4.4: Cosine function in the interval $x = [0 : 2\pi]$ with SPH and CSPM approximation. The latter correctly approximates at the domain boundary.

Repeating the Taylor series expansion with the SPH approximation of the first derivative of a function gives a first order consistent approximation:

$$f_{xi} \cong \frac{\sum_{j=1}^N [f(\underline{x}_j) - f(\underline{x}_i)] W_{,x}(\underline{x}_{ij}, h_{SPH}) V_j \underline{x}}{\sum_{j=1}^N (\underline{x}_j - \underline{x}_i) W_{,x}(\underline{x}_{ij}, h_{SPH}) V_j} \quad (4.14)$$

The CSPM can be shown to be equivalent to the Randles-Libersky correction [129, 194] for which the reader is referred to [209].

The second example is the Reproducing Kernel Particle Method (RKPM) developed by Liu [259]. Starting from the finding that the basic reproduction requirements in standard SPH are violated:

$$\int_{\Omega} W(\underline{x} - \underline{\tilde{x}}) d\underline{\tilde{x}} = 1 \quad (4.15a)$$

$$\int_{\Omega} W(\underline{x} - \underline{\tilde{x}}) (\underline{x} - \underline{\tilde{x}}) d\underline{\tilde{x}} = 0 \quad (4.15b)$$

with Ω being the whole domain of the problem. Condition (4.15a) is based on equation (4.2) and is not fulfilled at the boundary for the standard SPH. A corrective kernel is deduced by

enforcing the conditions from equations (4.15) in each location. The corrective kernel then reads:

$$\begin{aligned} K(\underline{x}, \tilde{\underline{x}}) &= C(\underline{x}, \tilde{\underline{x}})W(\underline{x} - \tilde{\underline{x}}) \\ C(\underline{x}, \tilde{\underline{x}}) &= [C_0(\underline{x}) + C_1(\underline{x}) \cdot (\underline{x} - \tilde{\underline{x}})] \end{aligned} \quad (4.16)$$

with $K(\underline{x}, \tilde{\underline{x}})$ being the corrective kernel, $W(\underline{x} - \tilde{\underline{x}})$ the SPH kernel and $C(\underline{x}, \tilde{\underline{x}})$ a correction function. The corrective kernel $K(\underline{x}, \tilde{\underline{x}})$ is then used to substitute the kernel expression $W(\underline{x}_{ij}, h)$ in equations (4.5) and (4.8), respectively.

Other examples for kernel modifications are:

- Corotated SPH as described by Becker [148],
- Vignjevic [41] or
- Johnson and Beissel [106]

A detailed discussion about first order kernel derivatives and corrections, exemplarily for elastodynamics applications, is provided with [209] and for second order derivatives kernel corrections in [3].

4.2.6 Artificial Viscosity

Oscillations in the field value, e.g. induced by shock loading, can lead to instabilities and divergence of the solution. A remedy is the introduction of an artificial viscosity. Initially, it was developed for the simulation of compressible flows under presence of shocks [252].

Two different kinds of artificial viscosity [165] are used where the first is the viscous pressure (von Neumann - Richtmyer[252]) which is proportional to the square of the velocity gradient:

$$q = \begin{cases} \alpha_{av} \rho h_{SPH}^2 (\nabla \cdot \underline{v})^2, & \text{for } \underline{v}_{ij} \cdot \underline{x}_{ij} < 0 \\ 0, & \text{for } \underline{v}_{ij} \cdot \underline{x}_{ij} \geq 0 \end{cases} \quad (4.17)$$

and the second is the bulk viscosity being proportional to the linear velocity gradient:

$$q = \begin{cases} -\alpha_{av} \rho h_{SPH} c (\nabla \cdot \underline{v}), & \text{for } \underline{v}_{ij} \cdot \underline{x}_{ij} < 0 \\ 0, & \text{for } \underline{v}_{ij} \cdot \underline{x}_{ij} \geq 0 \end{cases} \quad (4.18)$$

SPH simulations use a combined form of (4.17) and (4.18) which results in[219]:

$$\Pi_{ij} = \begin{cases} \frac{-\alpha_{av}\bar{c}_{ij}\mu_{ij} + \beta_{av}\mu_{ij}^2}{\bar{q}_{ij}}, & \text{for } \underline{v}_{ij} \cdot \underline{x}_{ij} < 0 \\ 0, & \text{for } \underline{v}_{ij} \cdot \underline{x}_{ij} \geq 0 \end{cases} \quad (4.19)$$

and

$$\mu_{ij} = \frac{h_{SPH}\underline{v}_{ij} \cdot \underline{x}_{ij}}{\underline{x}_{ij}^2 + \eta_{av}^2} \quad (4.20)$$

with α_{av} , β_{av} are dimensionless parameters and η_{av} is a small parameter to prevent divergences. Some standard parameters for the artificial viscosity are $\alpha_{av} = \beta_{av} = 1$ and $\eta_{av} = 0.1$ [208].

4.2.7 Artificial Stresses

Artificial stresses were introduced by [107] to prevent the tensile instability. Attracting particles are assigned with repulsive stresses to prevent from clumping. For this purpose a new "artificial" stress tensor $\underline{\underline{R}}$ is introduced. In the first step an eigenvalue decomposition of the Cauchy stress tensor $\underline{\underline{\sigma}}$ is performed for each particle:

$$\underline{\underline{E}} = \underline{\underline{Q}} \cdot \underline{\underline{\sigma}} \cdot \underline{\underline{Q}}^T = \begin{bmatrix} E_1 & 0 & 0 \\ 0 & E_2 & 0 \\ 0 & 0 & E_3 \end{bmatrix} \quad (4.21)$$

The principal stresses E_i are then modified as:

$$\hat{E}_i = \begin{cases} \epsilon_{as} \frac{E_i}{\bar{q}^2}, & E_i > 0 \\ 0, & E_i \leq 0 \end{cases} \quad (4.22)$$

with ϵ_{as} being a parameter which determines the "strength" of the artificial stress. Grey [107] proposed a value of $\epsilon_{as} \approx 0,3$. After modification of the principal stresses they are rotated back into the initial system and form the artificial stress tensor $\underline{\underline{R}}$:

$$\underline{\underline{R}} = \underline{\underline{Q}}^T \cdot \hat{\underline{\underline{E}}} \cdot \underline{\underline{Q}} \quad (4.23)$$

The principal stress determination is in mathematical terms an eigenvalue decomposition which can be solved either analytically or numerically for example with the QR-algorithm.

The artificial stress tensor between two particles i and j is then defined as:

$$\underline{\underline{\Theta}}_{ij} = (\underline{\underline{R}}_i + \underline{\underline{R}}_j) \cdot f_{as}^{n_{Stress}} \quad (4.24)$$

where the factor f_{as} is computed with:

$$f_{as} = \frac{W(r_{ij})}{W(\Delta p)} \quad (4.25)$$

with Δp being the particle spacing (usually constant) and r_{ij} the current distance between particle i and j . This leads to a strong decay of f_{as} between h and $2h$ such that the artificial stresses are mainly effective when the particles are very close to each other. n_{Stress} is the stress exponent and controls the decay of f_{as} . Standard parameters are $\epsilon_{as} = 0.3$ and $n_{Stress} = 4$ [208]. Figure 4.5 shows an example of impacting rubber rings where in the top half no stabilization is performed and in the lower part the stabilization is switched on. Material parameters according to table 4.1 were used.

Young's modulus E [Pa]	Poisson ratio ν [-]	Density ρ [kg/m^3]	Initial velocity v_{init} [m/s]
10000	0.4	1	170

Table 4.1: Material parameters and initial conditions for rubber ring impact simulation.

The unstabilized rings are diverging while the stabilized rings behave as expected without instabilities.

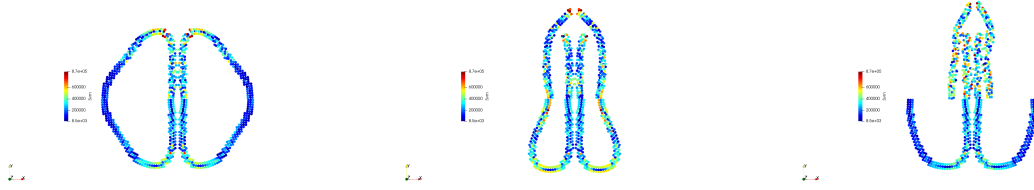


Figure 4.5: Impacting rubber rings at three different time points during / after collision. The von Mises equivalent stresses are displayed. Top halves of the pictures show SPH results without stabilization and numerical fracture of the rings while the lower halves show the SPH results with stabilization and without any indications of numerical fracture.

4.2.8 XSPH

For problems in tension the XSPH [162] can stabilize the solution since the particle velocities are averaged over the neighboring particles which is controlled by a parameter ϵ_{XSPH} where $\epsilon_{XSPH} = 0$ is no averaging and $\epsilon_{XSPH} = 1$ is maximum averaging. This computation does not necessarily require the same kernel W as in the other interactions [107]. The form of the XSPH given here is from [200]:

$$\frac{d\underline{u}_i}{dt} = \underline{v}_i + \epsilon_{XSPH} \cdot \sum_{j \in S} m_j \left(\frac{\underline{v}_j}{\varrho_{ji}} \right) W(\underline{x}_i - \underline{x}_j, h_{SPH}) \quad (4.26)$$

with

$$\varrho_{ji} = \frac{\varrho_j + \varrho_i}{2} \quad (4.27)$$

and a constant:

$$0 \leq \epsilon_{XSPH} \leq 1 \quad (4.28)$$

whose value defines how much is averaged in the particle neighbourhood where $\epsilon_{XSPH} = 0$ is no averaging at all.

4.3 DISCRETIZATION OF THE CONTINUUM EQUATIONS

In this chapter the discretised SPH-equations of the continuum equations are introduced. The approximation operator $\langle \cdot \rangle$ is left out from the left sides of the equations for brevity and $W(\underline{x}_i - \underline{x}_j, h_{SPH})$ is written as W_{ij} .

4.3.1 Velocity Gradient Computation

The velocity gradient $\underline{\underline{L}}$ is required for the determination of the strain and stress rates and is approximated with:

$$\underline{\underline{L}}_i = \sum_{j=1}^N (\underline{v}_j - \underline{v}_i) \otimes \nabla W_{ij} \cdot \frac{m_j}{\varrho_j} \quad (4.29)$$

4.3.1.1 Strain Rate

The strain rate tensor $\underline{\underline{\dot{\epsilon}}}$ is computed from the symmetric part of the velocity gradient:

$$\underline{\underline{\dot{\epsilon}}} = \underline{\underline{D}}_i = \frac{1}{2} (\underline{\underline{L}}_i + \underline{\underline{L}}_i^T) \quad (4.30)$$

4.3.1.2 Stress Rate

The deviatoric stress rate is computed with the Jaumann rate of the stress tensor $\underline{\underline{S}}^J$ (3.85):

$$\underline{\underline{W}}_i = \frac{1}{2}(\underline{\underline{L}}_i - \underline{\underline{L}}_i^T) \quad (4.31)$$

$$\underline{\underline{S}}_i^J = \dot{\underline{\underline{S}}}_i + \underline{\underline{W}}_i \underline{\underline{S}}_i - \underline{\underline{S}}_i \underline{\underline{W}}_i \quad (4.32)$$

and the hydrostatic pressure is:

$$p_i = c^2(\varrho^i - \varrho_0^i) \quad (4.33)$$

4.3.2 Continuity Equation

The continuity equation is discretised in this work as:

$$\dot{\varrho}_i = \varrho_i \cdot \sum_{j=1}^N (\underline{v}_j - \underline{v}_i) \cdot \nabla W_{ij} \frac{m_j}{\varrho_j} \quad (4.34)$$

4.3.3 Momentum Equation

The form of the discretised momentum equation is given as:

$$\dot{\underline{v}}_i = \sum_{j=1}^N \left(\frac{\underline{\underline{\sigma}}_i}{\varrho_i^2} + \frac{\underline{\underline{\sigma}}_j}{\varrho_j^2} + \Pi_{ij} \cdot \underline{\underline{I}} + \underline{\underline{\Theta}}_{ij} \right) \cdot \nabla W_{ij} \cdot m_i + \underline{b}_i \quad (4.35)$$

with \underline{b}_i the body forces which can be applied due to contact forces, see chapter 4.3.6. The artificial viscosity Π_{ij} is specified in (4.24) and the artificial stress $\underline{\underline{\Theta}}_{ij}$ in (4.23).

4.3.4 XSPH

The XSPH-stabilization is computed with:

$$\dot{\underline{x}}_i = \underline{v}_i + \epsilon^{XSPH} \cdot \sum_{j=1}^N \frac{m_j}{\varrho_i + \varrho_j} (\underline{v}_j - \underline{v}_i) \cdot W_{ij} \quad (4.36)$$

4.3.5 Heat Equation

Solving the heat equation (3.65) requires the computation of second order derivatives. As shown in [164] using straightforward second order kernel derivatives yields:

$$\nabla(\nabla f(\underline{x})) \approx \int_{\Omega} f(\underline{x}') \nabla(\nabla W_h(\underline{x} - \underline{x}')) d\underline{x}' \quad (4.37)$$

which is cumbersome and simply motivated by deriving (4.5) twice. It is very sensitive to particle disorder, the transfer of heat between two particles can be positive or negative thus violating the second law of thermodynamics. This is induced due to the nature of the second derivative of the kernel which changes its sign with increasing particle distance, see also figure 4.1. A more elaborated method is according to [65]:

$$\nabla(\nabla f(\underline{x})) \approx \int_{\Omega} (f(\underline{x}) - f(\underline{x}')) \nabla(\nabla W_h(\underline{x} - \underline{x}')) d\underline{x}' \quad (4.38)$$

which can have some issues with instabilities and a second derivative based on a finite difference scheme proposed by Brookshaw [34] is introduced:

$$\nabla(\nabla f(\underline{x})) \approx 2 \cdot \sum_{j=1}^N \left(\frac{f(\underline{x}) - f(\underline{x}_j)}{|\underline{x} - \underline{x}_j|} \right) \underline{e}_{ij} \nabla W_h(\underline{x} - \underline{x}_j) \omega_j \quad (4.39)$$

The advantage of (4.39) is that a second kernel derivative is required. More such schemes exist but are not part of this review. A completely different approach is the Particle Strength Exchange (PSE) which was introduced by [49]. PSE is motivated to design specific kernels for the derivatives required which means that between different derivatives completely different kernels will be created. The basic principal is shown in one dimension motivated by a Taylor series expansion:

$$f(\underline{x}') = f(\underline{x}) + (\underline{x}' - \underline{x}) \frac{\partial f(\underline{x}')}{\partial \underline{x}} \Big|_{\underline{x}} + \frac{1}{2} (\underline{x}' - \underline{x})^2 \frac{\partial^2 f(\underline{x}')}{\partial^2 \underline{x}} \Big|_{\underline{x}} + \dots \quad (4.40)$$

subtracting $f(\underline{x})$ and multiplication by a PSE kernel W_h^{PSE} not yet determined and integration over the complete domain:

$$\int_{\Omega} (f(\underline{x}') - f(\underline{x})) W_h^{PSE}(\underline{x}' - \underline{x}) = \int_{\Omega} (\underline{x}' - \underline{x}) \frac{\partial f(\underline{x}')}{\partial \underline{x}} \Big|_{\underline{x}} W_h^{PSE}(\underline{x}' - \underline{x}) + \frac{1}{2} (\underline{x}' - \underline{x})^2 \frac{\partial^2 f(\underline{x}')}{\partial^2 \underline{x}} \Big|_{\underline{x}} W_h^{PSE}(\underline{x}' - \underline{x}) + \dots \quad (4.41)$$

and W_h^{PSE} is now chosen that:

$$\frac{1}{2} \frac{\partial^2 f(\underline{x}')}{\partial^2 \underline{x}} \Big|_{\underline{x}} \underbrace{\int_{\Omega} (\underline{x}' - \underline{x})^2 W_h^{PSE}(\underline{x}' - \underline{x})}_{\stackrel{!}{=}2} \quad (4.42)$$

for which a kernel is selected that exhibits symmetry and terms containing $(x' - x)^p$ vanish for odd p . An intuitive choice in 1D is then:

$$W_h^{PSE}(\underline{x}' - \underline{x}) = \frac{1}{2h\sqrt{\pi}} e^{-\frac{|\underline{x}' - \underline{x}|^2}{4h^2}} \quad (4.43)$$

A detailed derivation can be found in [3]. The discretised heat equation without source terms becomes then for the PSE:

$$\dot{T}_i = \frac{\lambda}{\rho_i c_p} \sum_j (T_j - T_i) W_{ij}^{PSE} V_j \quad (4.44)$$

In this work the energy equation (3.73) is discretised with kernels of the type (4.39) and (4.43).

4.3.6 Contact Algorithm

4.3.6.1 Contact Force

Contact with tools are handled with a penalty contact algorithm in the SPH-simulations. The basic idea is to allow small penetration through the surface and apply repulsive forces based on the penetration depth multiplied by a contact stiffness. The repulsive force is then applied as body force \underline{b} in the momentum equation (4.35), see figure 4.6. The full algorithm is outlined in [208].

The contact force is then computed:

$$\underline{b} = \underline{F}_{cont} = F_{cont} \cdot \underline{n} = \frac{d \cdot \kappa \cdot m_p}{\Delta t^2} \underline{n} \quad (4.45)$$

with d being the penetration depth of the particle to the closes exterior boundary of the contacting tool, κ the contact stiffness, m_p the particle mass and \underline{n} the normal at the contact surface.

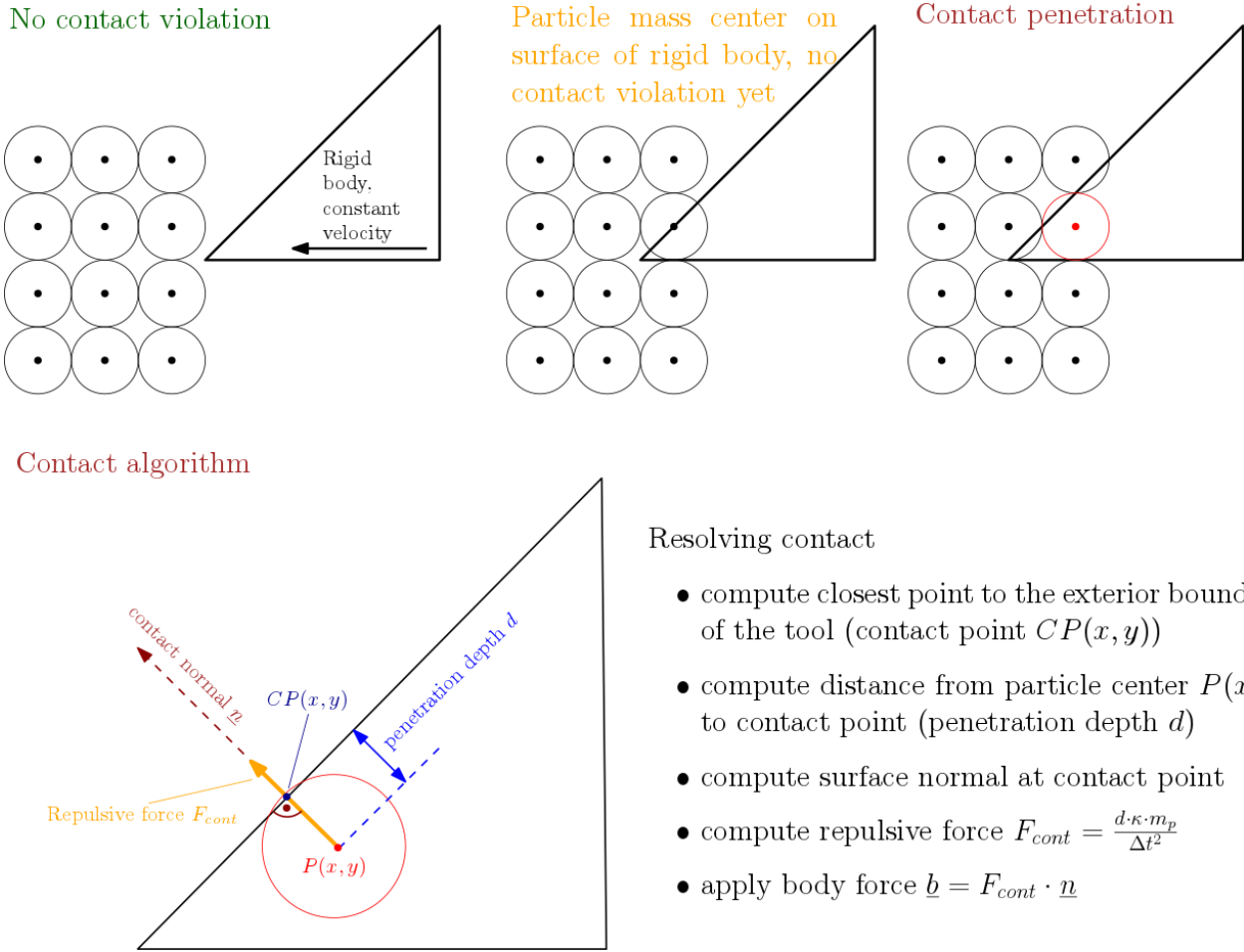


Figure 4.6: Penalty contact algorithm for SPH particles with rigid body.

4.3.6.2 Friction Force

Friction is computed with (3.66):

$$|\underline{F}_{fric}| = \mu_{fric} \cdot |\underline{F}_{cont}| \quad (4.46)$$

this equation does not yet define the direction vector of \underline{F}_{fric} . When it is related to the current sliding velocity between particle and contacting body oscillations can occur and therefore another more sophisticated approach needs to be chosen which penalizes directional changes of the friction force in successive increments. For this purpose the algorithm used in LS-DYNA [83] is implemented where first the friction \underline{F}_{fric}^n from the last increment n is used to compute \underline{F}^* :

$$\underline{F}^* = \underline{F}_{fric}^n - \underline{v}^{rel} \cdot m_p / \Delta t \quad (4.47)$$

The friction force $\underline{F}_{fric}^{n+1}$ in the current increment $n + 1$ is then:

$$\underline{F}_{fric}^{n+1} = \begin{cases} |\underline{F}_{fric}| \cdot \underline{E}^* / |\underline{E}^*|, & \text{if } |\underline{E}^*| > |\underline{F}_{fric}| \\ \underline{E}^* & \text{if } |\underline{E}^*| \leq |\underline{F}_{fric}| \end{cases} \quad (4.48)$$

4.3.7 Time Integration

The time derivatives occurring in equations for continuity (4.34), momentum (4.35), advection (4.36) stresses (4.32) and the energy equation (4.44) need to be integrated with respect to time. A second order leapfrog time integration is used in the SPH-simulations. The integration scheme requires first the computation of the solution variables at the half time step $t + \Delta t/2$:

$$\underline{x}_{n+1/2} = \underline{x}_n + \dot{\underline{x}}_n \cdot \frac{\Delta t}{2} \quad (4.49)$$

$$\underline{q}_{n+1/2} = \underline{q}_n + \dot{\underline{q}}_n \cdot \frac{\Delta t}{2} \quad (4.50)$$

$$\underline{v}_{n+1/2} = \underline{v}_n + \dot{\underline{v}}_n \cdot \frac{\Delta t}{2} \quad (4.51)$$

$$\underline{S}_{n+1/2} = \underline{S}_n + \dot{\underline{S}}_n^J \cdot \frac{\Delta t}{2} \quad (4.52)$$

$$\underline{T}_{n+1/2} = \underline{T}_n + \dot{\underline{T}}_n \cdot \frac{\Delta t}{2} \quad (4.53)$$

With the values at $t + \Delta t/2$ the continuity (4.34), momentum (4.35), advection (4.36) stresses (4.32) and the energy equation (4.44) are solved and the updated values are used to finally update:

$$\underline{x}_{n+1} = \underline{x}_n + \dot{\underline{x}}_{n+1/2} \cdot \Delta t \quad (4.54)$$

$$\underline{q}_{n+1} = \underline{q}_n + \dot{\underline{q}}_{n+1/2} \cdot \Delta t \quad (4.55)$$

$$\underline{v}_{n+1} = \underline{v}_n + \dot{\underline{v}}_{n+1/2} \cdot \Delta t \quad (4.56)$$

$$\underline{S}_{n+1} = \underline{S}_n + \dot{\underline{S}}_{n+1/2}^J \cdot \Delta t \quad (4.57)$$

$$\underline{T}_{n+1} = \underline{T}_n + \dot{\underline{T}}_{n+1/2} \cdot \Delta t \quad (4.58)$$

Deviatoric stresses \underline{S}_{n+1} not fulfilling $F(\underline{\sigma}) \leq 0$ (3.113) are corrected in the plasticity algorithm and the resulting deviatoric stresses and plastic strain increments are stored. Finally the boundary conditions are applied and the contact algorithm is invoked to resolve potential contact violations.

OXLEY'S PROCESS FORCE MODEL

In this chapter Oxley's [182] process force model is introduced. It is then applied to the prediction of process forces for an orthogonal cutting case and the computational results are compared to experimental results. The model will be used in chapter 9.5 for the prediction of process forces within an inverse identification of constitutive model parameters where by variation of these constitutive model constants the error between predicted and experimental process forces is minimized.

Oxley's force model is an analytical approach based on the slipline theory of plasticity to estimate the process forces in an orthogonal cutting setup. It was developed as a continuation of Ernst's [64] force model which considers, supported by observations, the chip formation in a narrow zone by plastic deformation. This zone is called shear plane and extends from the tool tip (point B) to the free surface of the workpiece at the outer root of the chip (point A), represented by the line AB in figure 5.1.

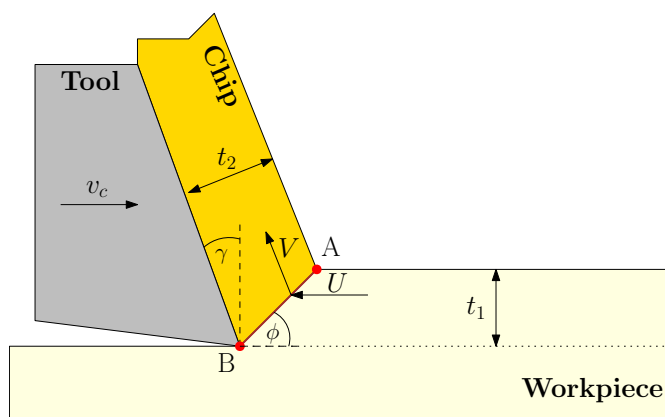


Figure 5.1: Oxley force model

The angle ϕ depicts the shear plane angle, the angle γ is the rake angle and t_1 and t_2 are the uncut chip thickness and the chip thickness, respectively. The clearance face and the clearance angle are not considered in this model.

In this model the tool is assumed stationary and the workpiece moves with the velocity U where the chip changes its velocity instantaneously to V in the shear plane. Therefore, it is limited to perfectly-plastic material behaviour. The consequences are an infinite shear strain rate in the shear plane which of course is not realistic. Further, this model cannot describe the strain rate sensitivity as well as the work hardening of a material. Some basic relations can be obtained by analysing the velocity diagram given in figure 5.2.

The velocity normal to the shear plane is:

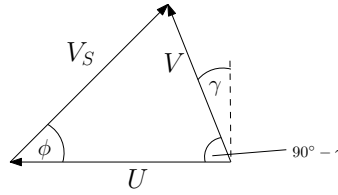


Figure 5.2: Oxley force model: velocity diagram

$$V_N = U \cdot \sin \gamma \quad (5.1)$$

The chip velocity V is related to the workpiece velocity U by:

$$V = \frac{U \cdot \sin \phi}{\cos(\phi - \gamma)} \quad (5.2)$$

and the tangential component V_S of the velocity in the shear plane (A-B):

$$V_S = \frac{U \cdot \cos \alpha}{\cos(\phi - \gamma)} \quad (5.3)$$

The total tool force R in figure 5.3 can be decomposed:

$$F_C = R \cdot \cos(\lambda - \gamma) \quad \text{cut force} \quad (5.4)$$

$$F_T = R \cdot \sin(\lambda - \gamma) \quad \text{normal force (feed force)} \quad (5.5)$$

$$F = R \cdot \sin(\lambda) \quad \text{friction force at tool-chip interface} \quad (5.6)$$

$$N = R \cdot \cos(\lambda) \quad \text{normal force at tool-chip interface} \quad (5.7)$$

$$R = \frac{F_S}{\cos \theta} = \frac{k_{AB} \cdot t_1 \cdot w}{\sin \phi \cdot \cos \theta} \quad \text{total tool force} \quad (5.8)$$

$$t_2 = \frac{t_1 \cos(\phi - \gamma)}{\sin \phi} \quad \text{chip thickness} \quad (5.9)$$

where k_{AB} is the shear flow stress in the shear plane between the points A and B, t_1 is the uncut (undeformed) chip thickness and w the width of cut.

The shear strain in the shear plane can be obtained from:

$$\gamma_{AB} = \frac{V_S}{V_N} = \frac{\cos \alpha}{\sin \phi \cdot \cos(\phi - \gamma)} \quad (5.10)$$

With the equation above the problem cannot be solved yet for a given rake angle γ and uncut chip thickness t_1 as the shear plane angle ϕ is not defined. For this problem different solutions were developed which are compiled in table 5.

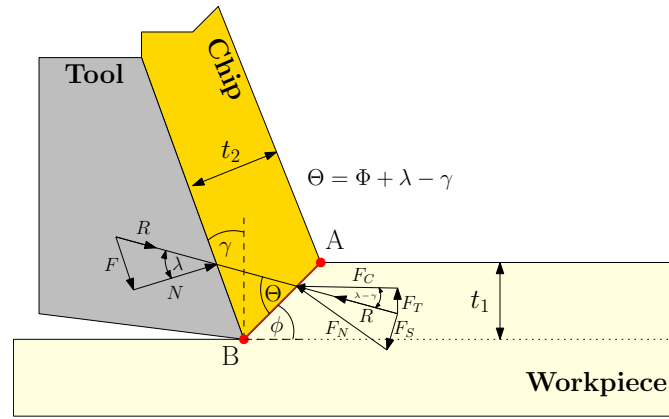


Figure 5.3: Oxley force model: force decomposition

Shear plane angle ϕ	Reference	Comments
$\phi = \frac{\pi}{4} + \frac{\gamma}{2} - \frac{\lambda}{2}$	Ernst and Merchant [153]	Φ such that AB is direction of max. shear stress
$2\phi = \cot^{-1}s + \gamma - \lambda$	Merchant [155]	γ_{AB} increases linear with normal stress along AB
$\phi = \frac{\pi}{4} + \gamma - \lambda$	Lee and Shaffer [121]	shear angle based on slipline field model

Following the discussion in Oxley [182], the shear plane model is valid for non-hardening materials only. This is a severe restriction and does not hold for a majority of materials. Further, materials not only show a strain-hardening but also a hardening tendency towards higher strain rates. For this reason the shear plane model was extended such that the shear deformation takes place in a small finite zone instead of a infinite zone as in figures 5.1 and 5.3.

5.1 OXLEY FORCE MODEL

In Oxley's force model a power law is used for the yield stress σ :

$$\sigma = \sigma_1 \cdot \varepsilon_{pl}^n \quad (5.11)$$

with σ_1 being a constant and n the strain-hardening exponent. To account for strain rate and temperature effects a velocity modified temperature T_{mod} , first introduced by [144], is calculated:

$$T_{mod} = T \cdot \left(1.0 - v_{T_{mod}} \cdot \ln \left(\frac{\dot{\varepsilon}_{pl}}{\dot{\varepsilon}_{pl}^0} \right) \right) \quad (5.12)$$

with $v_{T_{mod}}$ being a dimensionless material parameter, $\dot{\varepsilon}_{pl}^0$ the reference strain rate and the strain rate $\dot{\varepsilon}_{pl}$.

In addition to the equations (5.9) the shear strain rate in the shear zone is:

$$\dot{\gamma}_{AB} = C \frac{V_S}{l} \quad (5.13)$$

with C being a material dependent parameter. The angle θ is expressed similarly to the shear plane model as:

$$\theta = \phi + \lambda - \gamma \quad (5.14)$$

And the shear plane strain γ_{AB} is:

$$\gamma_{AB} = \frac{1}{2} \frac{\cos \gamma}{\sin \phi \cdot \cos(\phi - \gamma)} \quad (5.15)$$

The temperature in the shear plane T_{AB} is:

$$T_{AB} = T_W + \eta \Delta T_{SZ} \quad (5.16)$$

with T_W being the initial temperature of the workpiece, η_{TQ} the conversion factor of plastic work into heat (Taylor-Quinney coefficient) and ΔT_{SZ} is given by:

$$\Delta T_{SZ} = \frac{1 - \eta_{TQ}}{\rho \cdot c_p \cdot t_1 \cdot w} \frac{F_S \cdot \cos \gamma}{\cos(\phi - \gamma)} \quad (5.17)$$

with ρ the density and c_p the specific heat of the material, l the length between points A and B and F_S the shear force along AB.

The amount of heat conducted into the workpiece is described with $0 \leq \beta \leq 1$ and is given according to [2]:

$$\beta = \begin{cases} 0.5 - 0.35 \cdot \lg(R_T \cdot \tan \phi), & \text{for } 0.04 \leq R_T \cdot \tan \phi \leq 10.0 \\ 0.3 - 0.15 \cdot \lg(R_T \cdot \tan \phi), & \text{for } R_T \cdot \tan \phi > 10.0 \end{cases} \quad (5.18)$$

where R_T is the "thermal number" and defined as:

$$R_T = \frac{\rho \cdot c_p \cdot U \cdot t_1}{K} \quad (5.19)$$

with K being the thermal conductivity of the workpiece. The average tool-chip interface temperature is computed by:

$$T_{int} = T_W + \Delta T_{SZ} + \psi \Delta T_M \quad (5.20)$$

with ΔT_M being the temperature rise in the chip and $0 < \psi \leq 1$ being a factor for controlling temperature variations along the interface. Considering the thickness of the tool-chip interface as $\delta \cdot t_2$ and the tool-chip contact length as h , the chip temperature increase is assessed as:

$$\lg \left(\frac{\Delta T_M}{\Delta T_C} \right) = 0.06 - 0.195 \cdot \delta \left(\frac{R_T \cdot t_2}{h} \right)^{1/2} + 0.5 \cdot \lg \left(\frac{R_T \cdot t_2}{h} \right) \quad (5.21)$$

Here, ΔT_C is the average temperature rise in the chip:

$$\Delta T_C = F \sin \phi / \rho c_p t_1 w \cos(\phi - \gamma) \quad (5.22)$$

The tool-chip contact length h is derived from a moment equilibrium of the normal stresses on AB about point B and is:

$$h = \frac{t_1 \cdot \sin \theta}{\cos \lambda \cdot \sin \phi} \left(1 + \frac{C \cdot n}{3[1 + 2(1/4\pi - \phi) - C \cdot n]} \right) \quad (5.23)$$

The maximum tool-chip shear strain rate is:

$$\dot{\gamma}_{int} = \frac{v}{\delta t_2} \quad (5.24)$$

where it is assumed, supported by observations [244] that the chip material and the cutter are interlocked in their interface such that the shear flow stress of the chip limits the friction only. In the equation above δ is the ratio of the tool-chip plastic zone thickness to the chip thickness.

The shear stress in the shear plane AB is:

$$k_{AB} = \frac{\sigma_1 \varepsilon_{AB}^n}{\sqrt{3}} \quad (5.25)$$

and the shear stress at the tool-chip interface is for a given ϕ :

$$\tau_{int} = \frac{F}{hw} \quad (5.26)$$

On the other hand, the shear flow stress in the tool-chip interface is.

$$k_{chip} = \frac{\sigma_1}{\sqrt{3}} \quad (5.27)$$

Now, with equations (5.26) and (5.27) the intersection point of both lines can be found by varying ϕ . By the set of equations above the determination of process forces still requires the knowledge of the shear plane angle ϕ . Oxley [181] proposed to use the stress boundary condition in point B in an attempt to find the parameters C and $\dot{\gamma}_{AB}$. Therefore the normal stress on the tool face B is computed with:

$$\sigma'_N = k_{AB} \cdot (1 + \pi/2 - 2 \cdot \gamma - 2 \cdot C \cdot n) \quad (5.28)$$

on the other hand the normal stress at B is also given by:

$$\sigma_N = N / (h \cdot w) \quad (5.29)$$

With these equations for a given tool rake angle γ and cutting speed U , undeformed chip thickness t_1 , cut width w and initial temperature T_W the process forces can be computed iteratively with three nested loops over a range of δ , C and ϕ .

5.1.1 Solution Algorithm

The original solution scheme [182] for Oxley's algorithm is shown in figure 5.6. A short summary of the algorithm is provided in the following. First the boundaries and increment steps for δ , C and ϕ have to be defined, typical values in literature [120] are:

- $\delta_{min} = 0.005$, $\delta_{max} = 0.2$, $\Delta\delta = 0.005$
- $C_{min} = 2.0$, $C_{max} = 10.0$, $\Delta C = 0.1$
- $\phi_{min} = 5^\circ$, $\phi_{max} = 45^\circ$, $\Delta\phi = 0.1^\circ$

Next, the computation is performed within three nested loops:

- loop over $\delta = \delta_{min} \dots \delta_{max}$ with step size $\Delta\delta$
 - loop over $C = C_{min} \dots C_{max}$ with step size ΔC
 - * loop over $\phi = \phi_{min} \dots \phi_{max}$ with step size $\Delta\phi$, store $k_{chip}(\phi)$ and $\tau_{int}(\phi)$.
 - * the shear plane angle ϕ is then found for the condition $k_{chip}(\phi) = \tau_{int}(\phi)$. This is shown left in figure 5.4 where at $\delta = 0.16$ and $C = 2.5$ a shear plane angle $\phi \approx 31^\circ$ is found. Store corresponding $\sigma_N(C)$ and $\sigma'_N(C)$ at this ϕ .
 - C is found for the condition $\sigma'_N(C) = \sigma_N(C)$, see right chart in figure 5.4. The corresponding cut force $F_c(\delta)$ is stored

- At each δ the cut force $F_c(\delta)$ can be determined after C and ϕ are found. The cut force has a characteristics as shown in figure 5.5 and the final δ is taken from the point where the cut force is a minimum: $F_c(\delta) = \min$.

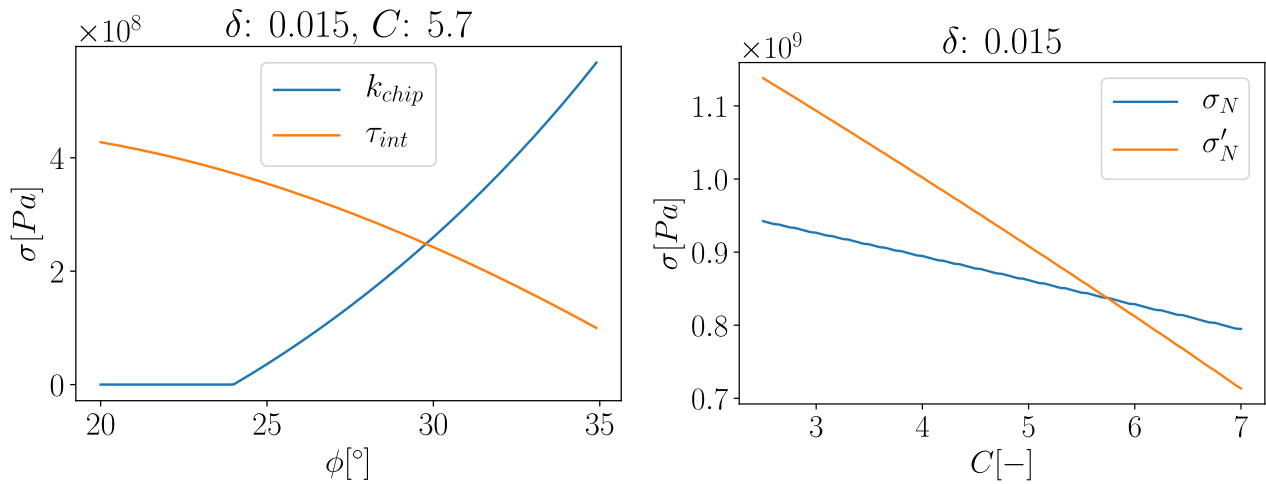


Figure 5.4: Left: example characteristics of $k_{chip}(\phi)$ and $\tau_{int}(\phi)$ depending on the shear plane angle ϕ and constant $\delta = 0.15$ and $C = 5.7$. Right: determination of the material constant C from the intersection point of $\sigma_N(C) = \sigma'_N(C)$

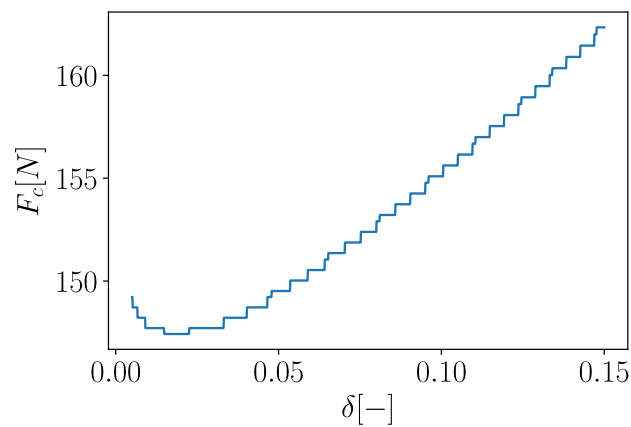


Figure 5.5: Cut force variation $F_c(\delta)$ - its minimum determines the final δ .

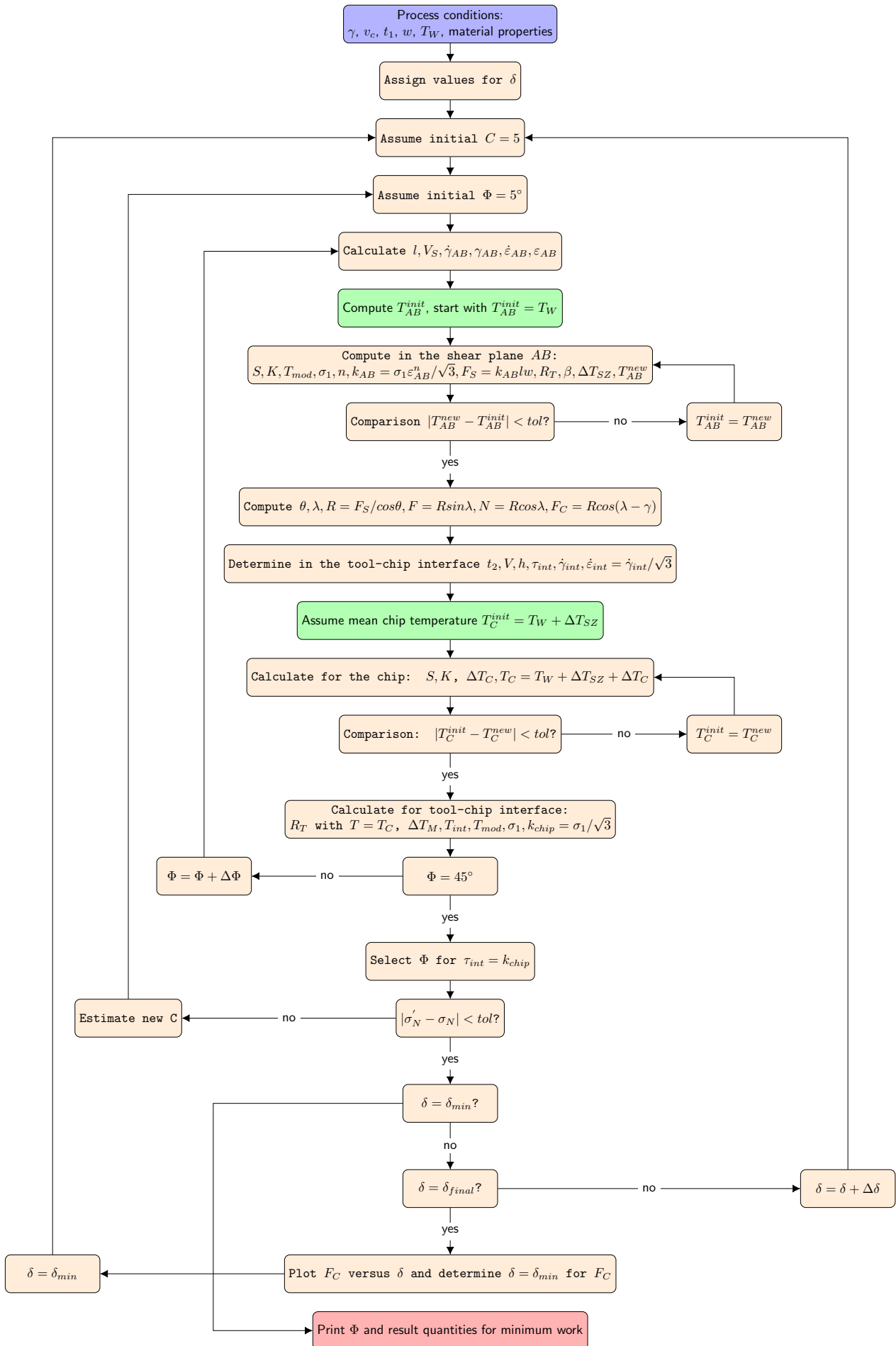


Figure 5.6: Oxley force model: structural chart of the algorithm.

The execution time of this algorithm is in the order of a few seconds. Which makes it attractive to be used for inverse identification of constitutive model parameters. However, the resolution, e.g. $F_c(\delta)$ in this example, is questionable and can be improved by reducing the increment sizes $\Delta\delta$, ΔC and $\Delta\phi$ at the expense of computation time. For this reason a modified algorithm is proposed in the next section 5.1.2.

5.1.2 Modified Algorithm

The original algorithm can be significantly improved by avoiding the three nested loops over ϕ , C and δ as in the original algorithm from section 5.1.1. Instead, the intersections of $k_{chip}(\phi) = \tau_{int}(\phi)$ and $\sigma_N(C) = \sigma'_N(C)$ as well as the minimum $F_c(\delta)$ are evaluated within three separate algorithms using numerical methods:

- ALGORITHM 1: determination of ϕ
 - approximation of the functions $k_{chip}(\phi)$ and $\tau_{int}(\phi)$ by a straight line each at a constant δ and C , therefore:
 - compute at two different ϕ_1^n and $\phi_2^n = \epsilon \cdot \phi_1^n$ the values of $k_{chip}(\phi_1^n)$, $k_{chip}(\phi_2^n)$, $\tau_{int}(\phi_1^n)$, $\tau_{int}(\phi_2^n)$, choose small ϵ for a good approximation of the gradient, e.g. $\epsilon = 1.0001$
 - compute the intersection point $\phi_{intersect}$ of the two approximated lines $\langle k_{chip}(\phi) \rangle$ and $\langle \tau_{int}(\phi) \rangle$
 - this intersection point $\phi_{intersect}$ forms the start point $\phi_1^{n+1} = \phi_{intersect}$ for the next loop until a termination criteria is met
 - the determination of ϕ_1^{n+1} within one iteration loop is shown in the left chart in figure 5.7
- ALGORITHM 2: determination of C
 - similar to ALGORITHM 1 the functions $\sigma_N(C)$ and $\sigma'_N(C)$ are linearly approximated with straight lines at a constant δ
 - the gradient of each function is determined with two different C_1 and $C_2 = \epsilon \cdot C_1$, ϵ is chosen small for a good approximation of the gradient, e.g. $\epsilon = 1.0001$
 - compute with ALGORITHM 1: for C_1 and C_2 the shear plane angles at which $k_{chip}(\phi) = \tau_{int}(\phi)$
 - compute the intersection point $C_{intersect}$ of the two approximated lines
 - this intersection point $C_{intersect}$ forms the start point $C_1^{n+1} = C_{intersect}$ for the next loop until a termination criteria is met

- the determination of C_1^{n+1} within one iteration loop is shown in the right chart in figure 5.7
- ALGORITHM 3: determination of δ
 - this algorithm uses a different strategy since the minimum of the function $F_c(\delta)$ is searched. A quadratic function is fitted with three points and the minimum point of this fitted function is determined analytically. The minimum point is then used as a new start point in the next iteration loop.
 - choose three different $\delta_1, \delta_2 = \epsilon \cdot \delta_1$ and $\delta_3 = (\epsilon - 1) \cdot \delta_1$, choose ϵ for a good approximation of the quadratic function, e.g $\epsilon = 1.1$
 - compute with ALGORITHM 2: $F_{c1}(\delta_1^n), F_{c2}(\delta_2^n)$ and $F_{c3}(\delta_3^n)$
 - fit quadratic function $\langle F_c(\delta) \rangle = a \cdot \delta^2 + b \cdot \delta + c$ through $F_{c1}(\delta_1^n), F_{c2}(\delta_2^n)$ and $F_{c3}(\delta_3^n)$ and determine its minimum point $\delta_{intersect} = -b/2a$
 - set $\delta_1 = \delta_{intersect}$ and repeat loop until a termination criteria is met.
 - the determination of δ_{min}^n within one iteration loop is shown in figure 5.8
- the shear plane temperature T_{AB} is determined with a secant method instead of a simple but computationally expensive loop

These improvements were implemented resulting in compute times of a fraction of a second.

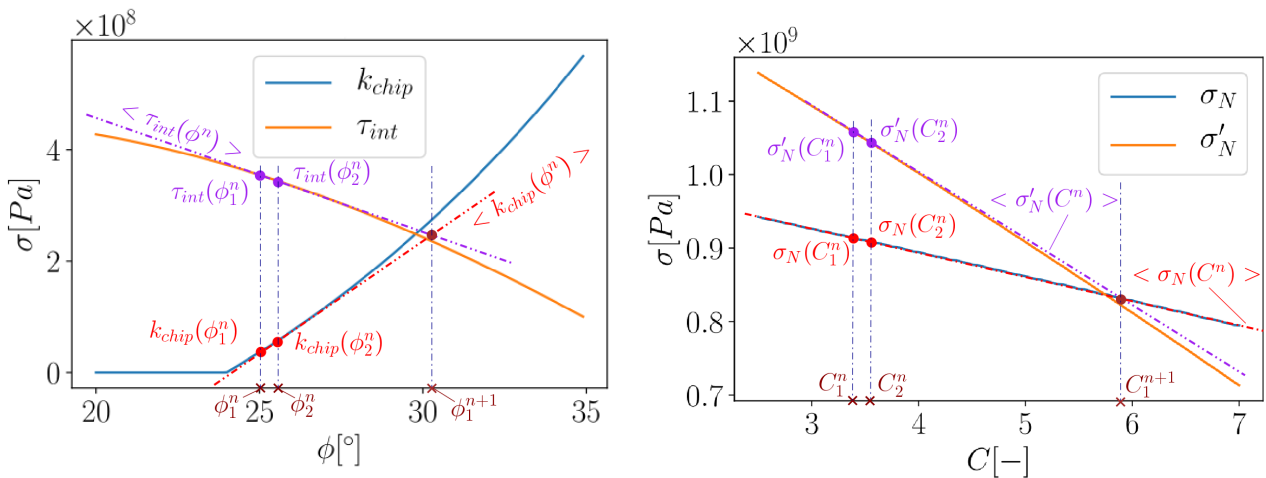


Figure 5.7: Determination of ϕ (left) with algorithm 1 and determination of C (right) with algorithm 2.

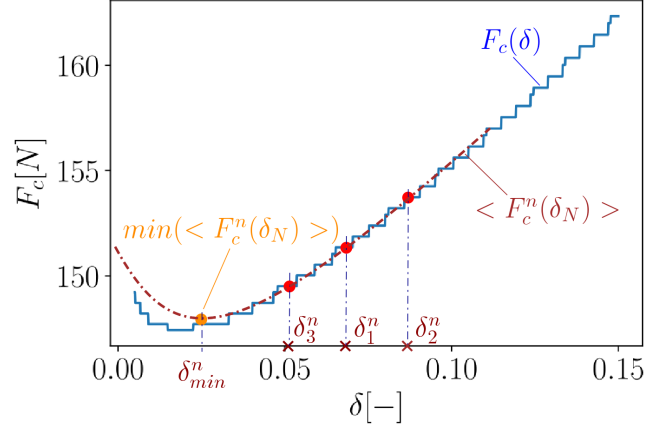


Figure 5.8: Determination of the minimum of $F_c(\delta)$ with algorithm 3.

5.2 EXTENSION TO OTHER FLOW STRESS MODELS

Adibi-Sedeh et al[1] extended Oxley's force model for the use with the Johnson-Cook [105] and mechanical threshold stress (MTS) flow stress models [67]. This extension was limited to the secondary deformation zone and Lalwani[120] extended this with a purely Johnson-Cook description by replacing the strain-hardening exponent n in Oxley's force model with an equivalent strain-hardening exponent n_{eq} . The shear flow stress in the shear plane AB (5.25) becomes then:

$$k_{AB} = \frac{\sigma_1 \varepsilon_{AB}^n}{\sqrt{3}} = \sqrt{\frac{1}{3}} (A + B \cdot (\varepsilon_{AB})^n) \left(1 + C \cdot \ln \left(\frac{\dot{\varepsilon}_{AB}}{\dot{\varepsilon}_{pl}^0} \right) \right) \left(1 - \left(\frac{T - T_{ref}}{T_f - T_{ref}} \right)^m \right) \quad (5.30)$$

The angle θ can be expressed with either (5.14) or:

$$\tan \theta = 1 + 2(\pi/4 - \phi) - C \cdot n = 1 + 2(\pi/4 - \phi) - C \cdot n_{eq} \quad (5.31)$$

where n is replaced with the equivalent strain hardening exponent n_{eq} :

$$n_{eq} \approx \frac{n \cdot B \cdot \varepsilon_{AB}^n}{A + B \varepsilon_{pl}^n} \quad (5.32)$$

and similarly n is replaced for n_{eq} in the expression for the tool contact length h (5.23):

$$h = \frac{t_1 \cdot \sin \theta}{\cos \lambda \cdot \sin \phi} \left(1 + \frac{C \cdot n_{eq}}{3[1 + 2(1/4\pi - \phi) - C \cdot n_{eq}]} \right) \quad (5.33)$$

The normal stress σ'_N on the tool face B (5.28) becomes:

$$\sigma'_N = k_{AB} \cdot (1 + \pi/2 - 2 \cdot \gamma - 2 \cdot C \cdot n_{eq}) \quad (5.34)$$

And the last equation modified is the computation of the shear flow stress in the tool-chip interface:

$$k_{chip} = \frac{1}{\sqrt{3}} = \sqrt{\frac{1}{3}} (A + B \cdot (\epsilon_{int})^n) \left(1 + C \cdot \ln \left(\frac{\dot{\epsilon}_{int}}{\dot{\epsilon}_{pl}^0} \right) \right) \left(1 - \left(\frac{T - T_{ref}}{T_f - T_{ref}} \right)^m \right) \quad (5.35)$$

5.3 EXAMPLE CALCULATIONS

An example calculation is performed for an orthogonal cutting experiment of Ti6Al4V from [260] with a cut speed of $v_c = 70m/min$, a feed of $f = 0.1mm$ and a tool rake angle $\gamma = 10^\circ$. The measured process forces are $F_c = 180N$ for the cut force and $F_f = 85N$ for the feed force. The Johnson-Cook flow stress model is used with two different material parameter set, see table 5.1.

Material	$A[MPa]$	$B[MPa]$	$C[-]$	$m[-]$	$n[-]$	$\epsilon_{pl}^0[s^{-1}]$	$T_{ref}[K]$
Ti6Al4V set 1 [213]	896	656	0.0128	0.8	0.5	1.0	300.0
Ti6Al4V set 2 [104]	862.5	331.2	0.012	0.8	0.34	1.0	300.0
	$T_{melt}[K]$	$\eta_{TQ}[-]$	$c_p[J/kgK]$	$\lambda[W/mK]$	$\frac{\partial \lambda}{\partial T} [\frac{W}{mK^2}]$	$q[kg/m^3]$	
	1678	0.9	526.0	4.7793	0.0206	4430.0	

Table 5.1: Material parameters used for Oxley's force model

The process force model predicts the following process quantities:

Oxley's process force model is a fast analytical approach for the determination of process forces in orthogonal cutting. However, the process forces are underpredicted compared to the experimental results for both material parameter sets. The cut force deviates by at least 20% and the feed force deviates by more than 60%. Given the fact that Oxley's force model does not consider cutting edge radii, clearance angle or friction coefficients and is limited to isotropic hardening its predictive quality is not too bad. It is noted that these results can differ for other material parameter sets as there are lots of different sets available for Ti6Al4V[61].

Quantity	Ti6Al4V set 1	Ti6Al4V set 2	Experimental
Shear plane angle ϕ	33.8°	34.9°	
δ	0.0942	0.0637	
Material constant C	1.923	3.964	
Chip thickness t_2	0.164mm	0.159mm	
Shear plane strain ε_{AB}	0.558	0.548	
Shear plane strain rate $\dot{\varepsilon}_{AB}$	7770s ⁻¹	16600s ⁻¹	
Tool-chip interface strain ε_{int}	4.03	5.34	
Tool-chip interface strain rate $\dot{\varepsilon}_{int}$	26500s ⁻¹	42000s ⁻¹	
Shear plane temperature T_{AB}	402.3°C	350.2°C	
Tool-chip interface temperature T_{int}	979.7°C	873.0°C	
Shear plane stress k_{AB}	576.8MPa	501.1MPa	
Normal stress on the tool face B σ'_N	889.3MPa	791.4MPa	
Tool-chip contact length h	0.1559mm	0.1486	
Cut force F_c	146.5N	123.7N	$F_c^{exp} = 180N$
Feed force F_f	32.58N	24.14N	$F_f^{exp} = 85N$

Table 5.2: Comparison of measured and simulated process forces

INVESTIGATION OF STRESS STATES IN ORTHOGONAL CUTTING

A numerical study of orthogonal cutting of Ti6Al4V material is presented. The assessments were carried out with the SPH method in Abaqus/Explicit to explore the capabilities of the SPH implementation in Abaqus and to benchmark the solver speed on the one hand. On the other hand, the main focus in this investigation is on the stress states occurring during metal cutting. For this purpose material points (particles) are tracked which allows the analysis of the evolution of physical quantities at material points, like stress and strain tensors. They are analysed in detail with a newly developed method for tracking of eigenvectors and eigenvalues and shall answer to which extent the assumption of isotropic hardening is justified for the stress states occurring in metal cutting. For this purpose the time-wise evolution of stress states at material points in and around the primary shear zone were analysed with the SPH for two different cutting speeds, two different friction coefficients as well as rigid and elastic cutter models.

6.1 NUMERICAL MODEL

For the analyses presented here the SPH was used within Abaqus 6.14-1/Explicit. Since Abaqus SPH does not support 2D SPH models, a 3D model was used for the orthogonal cutting simulation. In order to keep the computational effort as low as possible a small strip of metal was simulated only. The cutter was modelled as a rigid tool as well as an elastic tool. All simulations considered adiabatic heating due to plastic dissipation. Heat conduction is not considered as it is not supported in Abaqus SPH and the effect can be neglected in this case since the time to cut is lower than $1ms$ where the rather slow heat conduction is expected to play a minor role. The time stepping was used with Abaqus default settings resulting in increment times of $3 \cdot 10^{-3} \mu s$ (rigid tool model) to $4 \cdot 10^{-4} \mu s$ (elastic tool model). A convergence study is performed prior to the main analysis to ensure stable results at the chosen simulation resolution.

6.1.1 Geometry and Mesh

The numerical model consists of the cutter and the workpiece. It is based on the LS-Dyna model from [213]. The main dimensions of the workpiece are: length= $2mm$, height= $0.3mm$ and width= $0.1mm$. A schematic representation of the geometry is provided with figure 6.1. In the convergence study the particle resolution of the workpiece is varied from one particle per cut width up to 12 particles. Based on the results from this convergence study, in the main analysis the workpiece is discretised with 60'000 particles (200x30x10) with an

inter-particle distance of $\Delta x = 0.01\text{mm}$. The effective particle radius was set to $\frac{\Delta x}{2} = 0.005\text{mm}$ which is relevant for the computation of the particle volume, the contact algorithm and the outer surface definition of the particle domain. It has to be noted that the effective particle radius is not equivalent to the smoothing length!

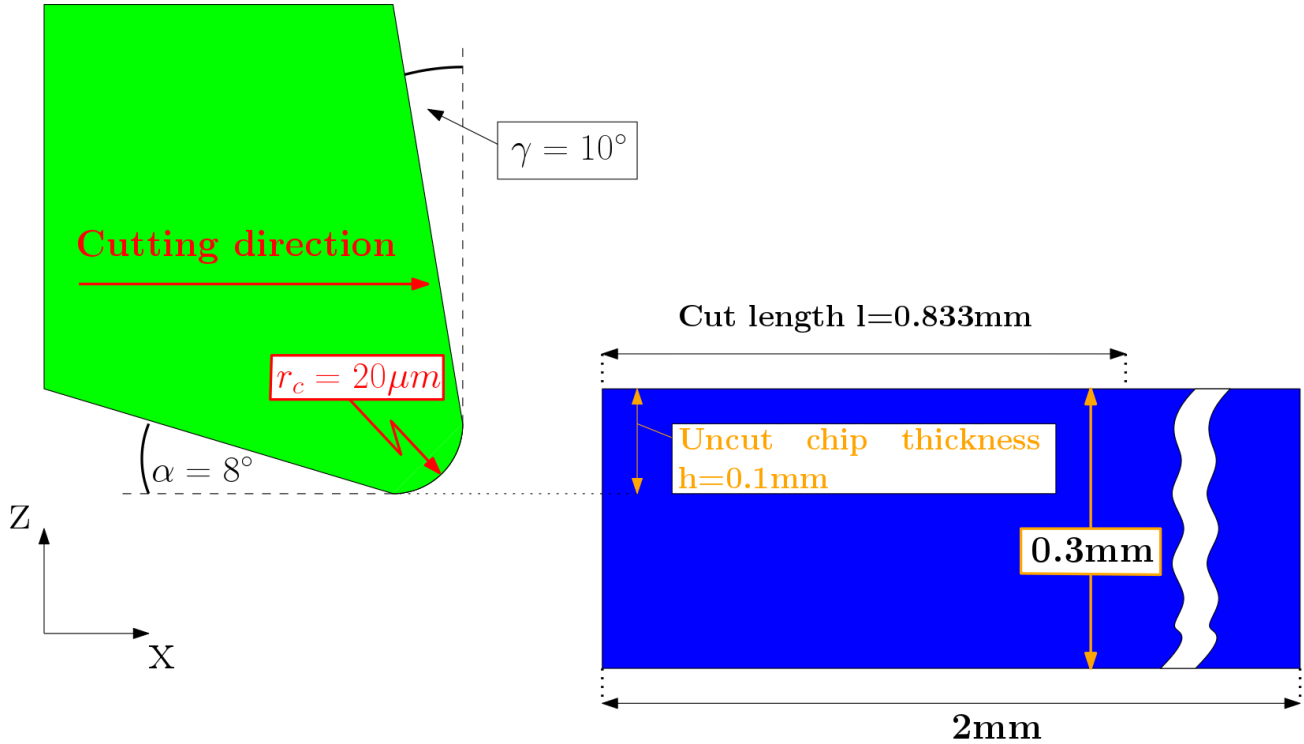


Figure 6.1: Schematic representation of cutter (green) and workpiece (blue) geometry

The cutter is modelled with 10865 elements based on elements of type C3D8. The clearance angle is $\alpha = 8^\circ$, the rake angle is $\gamma = 10^\circ$ and the cutting edge radius is $r_c = 20\mu\text{m}$. The meshed/discretised model of the cutter and the workpiece is shown in figure 6.2.

6.1.2 Constitutive Model

6.1.2.1 Workpiece

The workpiece material is the titanium alloy Ti6Al4V. A flow stress model according to Johnson-Cook (JC) came to application, see equation (3.95). All workpiece material parameters used throughout the analysis are provided in tables 6.1 and 6.2. Plastic dissipation into thermal energy (adiabatic heating) was considered with a Taylor-Quinney coefficient of $\eta_{TQ} = 0.90$:

$$\Delta T = \frac{\eta_{TQ} \cdot \sigma_y}{\rho \cdot c_p} \Delta \epsilon_{pl} \quad (6.1)$$

The temperature dependency of the elastic modulus, the density and the Poisson's ratio as well as the thermal expansion of the workpiece were not considered in the present work.

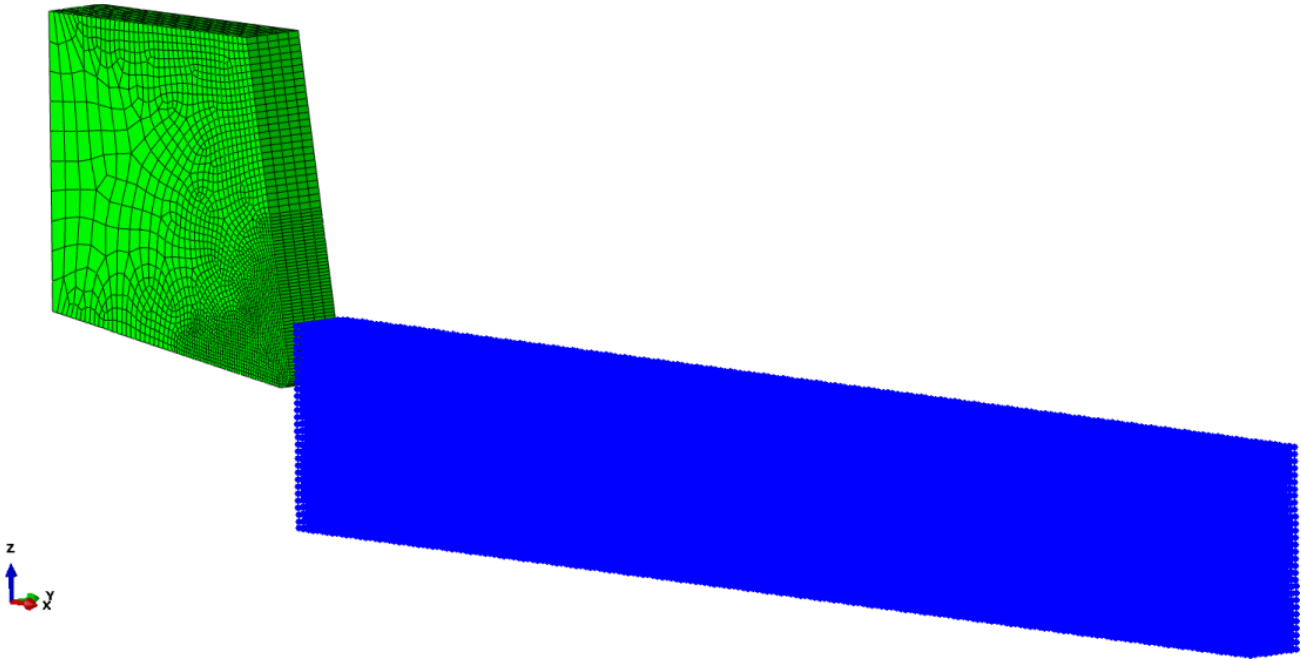


Figure 6.2: Meshed model of cutter(green) and workpiece(blue)

Material	E [GPa]	Poisson ν [-]	Density ρ [kg/m ³]	Specific heat capacity c_p [J/kgK]	Source
Ti6Al4V	110.0	0.35	4300	526.0	[213]

Table 6.1: Physical properties of Ti6Al4V.

6.1.2.2 Cutter

Simulations were carried with rigid as well as elastic cutter models. The rigid cutter model used a reference point for prescription of the cut velocity v_c . For the simulations with an elastic cutter the material properties for tungsten carbide from table 6.3 were used. Boundary conditions were applied according to figure 6.3, where the top and back side (marked in red) have fixed displacements in z -direction and the x -displacement is prescribed with the tool velocity. The displacements in y -direction were fixed for the whole cutter model throughout the analysis.

Material	E [GPa]	Poisson ν [-]	Density ρ [kg/m ³]	Source
WC	635.0	0.21	14700	[213]

Table 6.3: Physical properties of tungsten carbide cutter.

6.1.3 Boundary Conditions

The workpiece temperature was initialized with $T = 300K$. The workpiece displacements are restrained at the bottom and back side (red surfaces in figure 6.3). To the left and right side,

Material	A	B	C	m	n	$\dot{\epsilon}_{pl}^0$	T_{ref}	T_f	Source
	[MPa]	[MPa]	[-]	[-]	[-]	[s ⁻¹]	[K]	[K]	
Ti6Al4V	896	656	0.0128	0.8	0.5	1.0	300.0	1678	[158, 213]

Table 6.2: Johnson Cook flow stress model parameters for Ti6Al4V.

the particle movement is laterally blocked by frictionless contact to analytical rigid surfaces (grey surfaces in figure 6.3) which ensures that any particle is prevented from leaving the left or right side of the bounded space during the course of the analysis - which cannot be accomplished by simply restraining the displacement degree of freedom at the (initially) outer layer of particles.

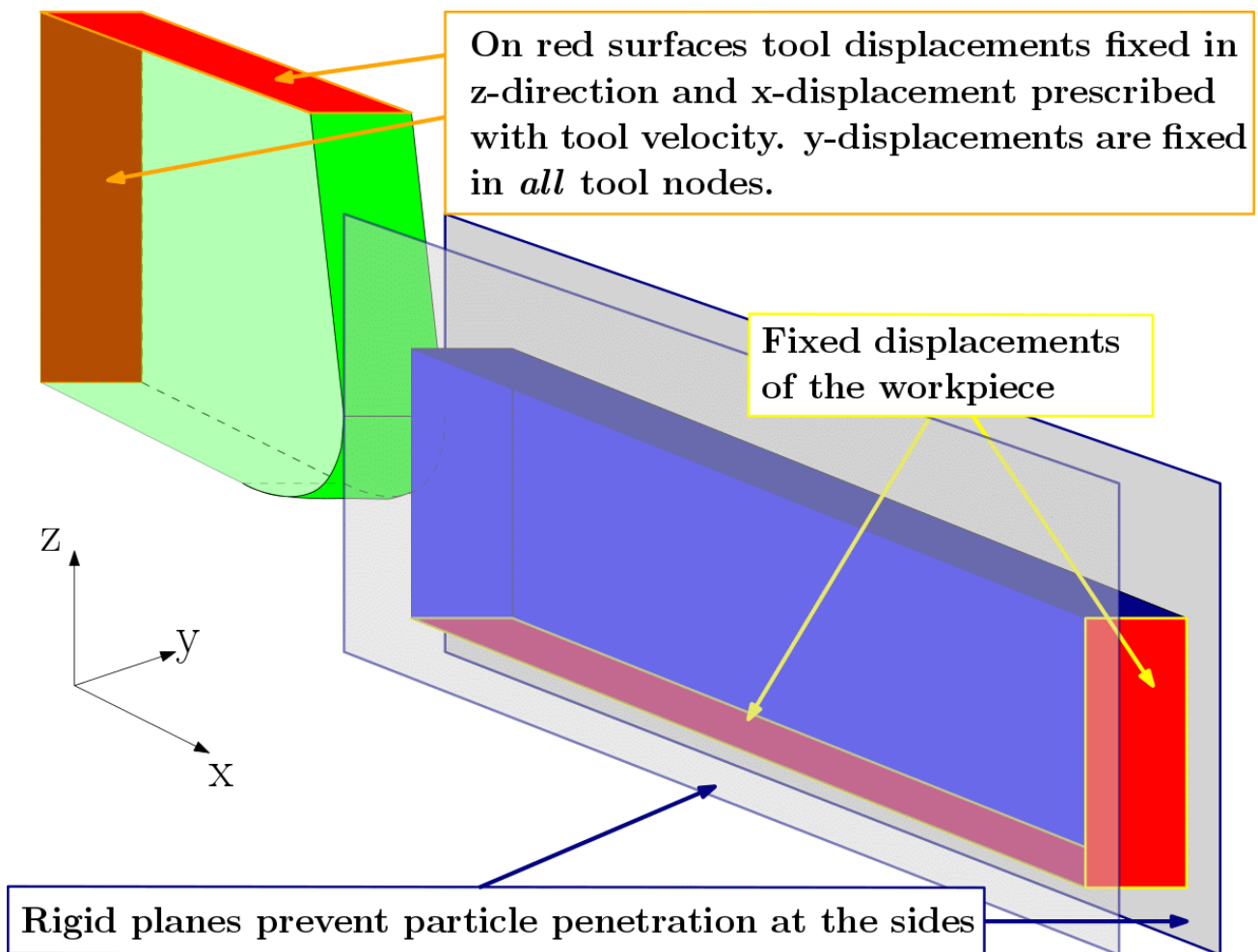


Figure 6.3: Faces to where displacement boundary conditions were applied for the model with elastic cutter

At the free workpiece boundaries stress-free boundary conditions are included since Abaqus uses an uncorrected SPH with cubic spline kernel by default. Therefore, stress free boundaries are inherently included in an averaged fashion, see for example the discussion in [209].

6.1.4 Contact and Friction

A general contact formulation with a kinematic contact algorithm has been used with default settings. Some of the analyses (see chapter 6.3) utilize Coulomb friction where the maximum frictional shear stress τ_{fric} is proportional to the (positive) normal stress σ_N by a friction coefficient μ :

$$\tau_{fric} = \begin{cases} \mu \cdot \sigma_N & \text{if } \sigma_N > 0 \\ 0 & \text{if } \sigma_N \leq 0 \end{cases} \quad (6.2)$$

Frictional heating was not considered in the simulations.

6.2 CONVERGENCE STUDY

In the convergence study it is investigated which resolution is required to achieve converged process forces in the simulation at a cut speed of $v_c = 500 \frac{m}{min}$, a feed $f = 0.1mm$, a friction coefficient of $\mu = 0.35$ and a rigid cutter model. The resolution per cut width is varied from 1 to 12 particles with the number of particles in the height and length direction as well as the total particle number is given in table 6.4 for the 12 simulation cases.

Simulation	Number of particles			
	width	height	length	total
1	1	3	20	60
2	2	6	40	480
3	3	9	60	1'620
4	4	12	80	3'840
5	5	15	100	7'500
6	6	18	120	12'960
7	7	21	140	20'580
8	8	24	160	30'720
9	9	27	180	43'740
10	10	30	200	60'000
11	11	33	220	79'860
12	12	36	240	103'680

Table 6.4: Overview of particle resolutions in the convergence study.

The predicted process forces versus the particle resolution is shown in figure 6.4. It can be seen that from resolutions above 9 particles per cut width the process forces are converged. At the lowest resolution (simulation 1) the runtime is about 15 seconds while for the highest resolution (simulation 12) the computational time is already 37 hours. In the following investigation a resolution of 10 particles per cut width is chosen since the runtimes of the

simulations are within 5...6 hours which is seen as an acceptable compromise between accuracy and computation time.

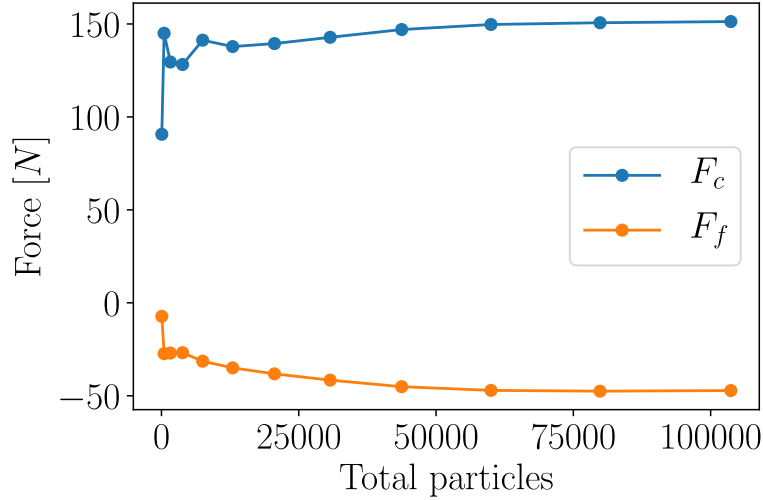


Figure 6.4: Convergence study of process forces versus particle resolution in the SPH simulation showing stable results for more than 50'000 particles.

6.3 RESULTS

The simulations were conducted as a parametric study with simulated cut speeds of $v_c = 70 \frac{m}{min}$ and $v_c = 500 \frac{m}{min}$. The cutter was modelled as rigid tool as well as an elastic tool. Contact with and without friction were simulated. The friction coefficient was used with a friction coefficient experimentally determined by Wyen [260] for a cutting edge radius of $r_c = 0.02mm$, feed $f = 0.1mm$, cut speed of $v_c = 70 \frac{m}{min}$, clearance angle of $\alpha = 8^\circ$ and rake angle of $\gamma = 10^\circ$. The cut length is $l = 0.833mm$. The uncut chip thickness is $h = 0.1mm$, which is equivalent to the feed f in orthogonal cutting. All conducted simulations are compiled with the main process parameters in table 6.5.

Simulation case	Cut speed $v_c [\frac{m}{min}]$	Feed $f [mm]$	Friction coefficient $\mu [-]$	Cutter model
1	70	0.1	0.00	rigid
2	70	0.1	0.35	rigid
3	70	0.1	0.35	elastic
4	500	0.1	0.00	rigid
5	500	0.1	0.35	rigid
6	500	0.1	0.35	elastic

Table 6.5: Overview of simulated orthogonal cutting cases

Results have been evaluated and interpreted for temperature and temperature rates, strains and strain rates and with a main emphasize the stress characteristics. These evaluations

were performed on a small selection of particles. They are located close to the middle plane of the workpiece such that the interference with the left and right contact surface is lowest. The selected particles are located in a line vertical to the cutting direction, see red particles labelled "A" to "O" in figure 6.5. In the initial configuration particles "A" to "J" are within the uncut chip thickness region and particles "K" to "O" are below the uncut chip thickness. The movement of the reviewed particles during the cutting up to time $t_{sim} = 31.5\mu s$ is shown in figure 6.6 and the location of the particles after the cut is provided with table 6.6. All particles that were initially below the uncut chip thickness were also there after the cut. For particles initially within the uncut chip thickness the picture is slightly different: particle "J" went, except from case 2, into the workpiece. Particles "A" to "I" went, except from case 3, into the chip. The results indicate that the stagnation point of the material flow around the cutter is influenced by the friction coefficient as well as the used tool model (elastic/rigid) and therefore the particle position after the cut slightly change.

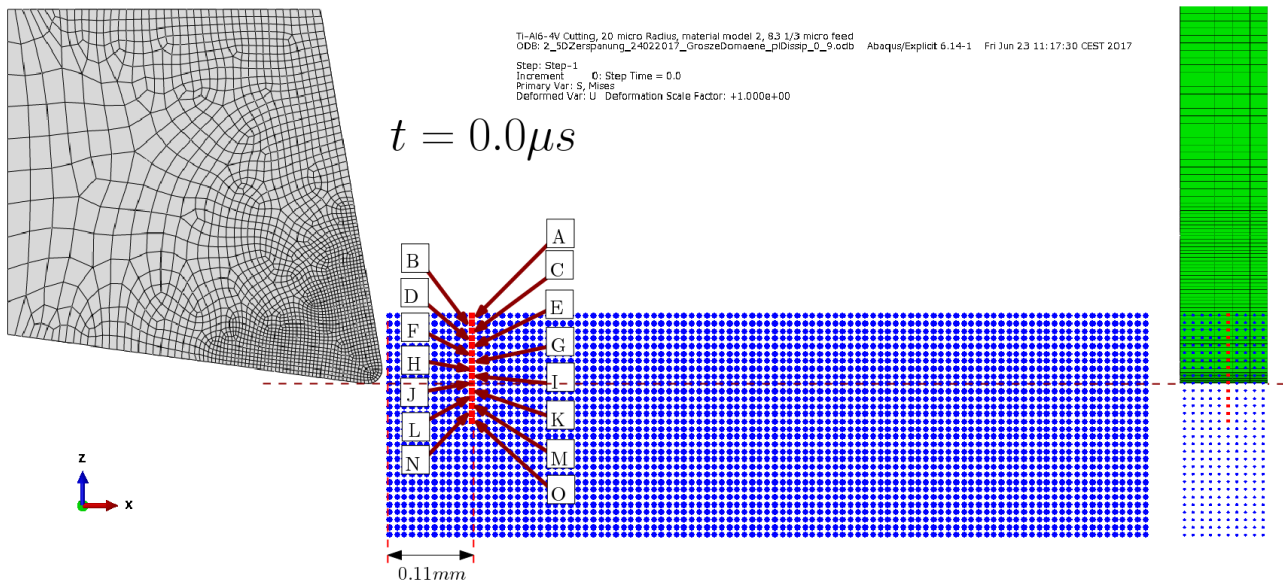


Figure 6.5: Initial positions of investigated particles, side view (left) and front view (right)

Case	v_c [$\frac{m}{min}$]	μ [-]	Tool	A	B	C	D	E	F	G	H	I	J	K	L	M	N	O
1	70	0	rigid	C	C	C	C	C	C	C	C	C	W	W	W	W	W	W
2	70	0.35	rigid	C	C	C	C	C	C	C	C	C	C	W	W	W	W	W
3	70	0.35	elastic	C	C	C	C	C	C	C	C	W	W	W	W	W	W	W
4	500	0	rigid	C	C	C	C	C	C	C	C	C	W	W	W	W	W	W
5	500	0.35	rigid	C	C	C	C	C	C	C	C	C	W	W	W	W	W	W
6	500	0.35	elastic	C	C	C	C	C	C	C	C	C	W	W	W	W	W	W

Table 6.6: Overview of particle locations after cut, W=workpiece, C=chip

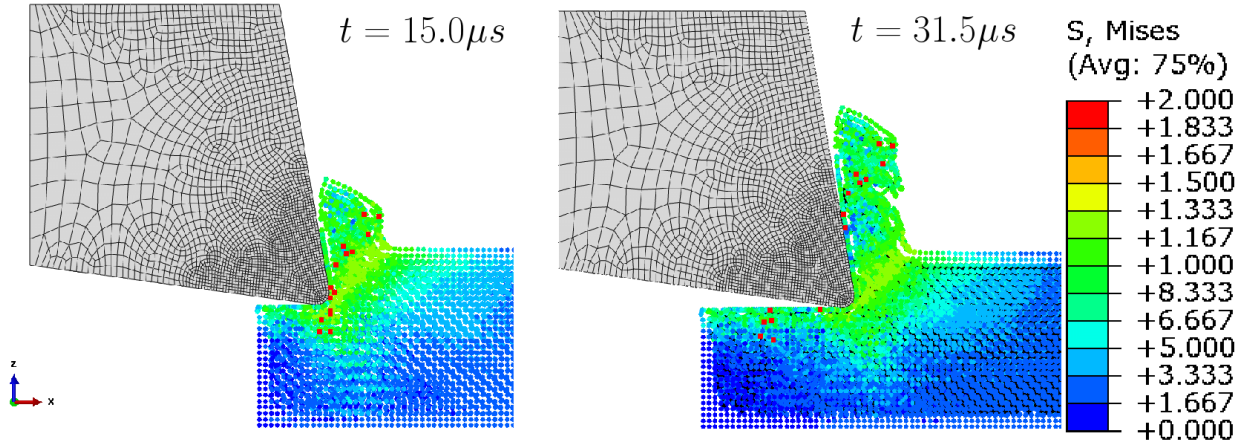


Figure 6.6: Equivalent stress (von Mises) [GPa] and redistribution of particles at two time points. Results without friction $\mu = 0.0$ at a cut speed of $v_c = 500 \frac{m}{min}$ (case 4). The analysed particles A-O are shown in red.

6.3.1 Process Forces

The process forces obtained from the simulations are compiled in table 6.7 together with experimental results from orthogonal cutting tests [260], where a cutting force of $F_c \approx 180N$ and a feed force of $F_f \approx -85N$ was measured for the process parameters of $\alpha = 8^\circ$, $\gamma = 10^\circ$, $r_c = 20\mu m$, $v_c = 70 \frac{m}{min}$ and $f = 0.1mm$. The numerical prediction of cutting and feed forces versus time are shown in figure 6.7 together with averaged process forces (dashed lines) which were determined in the range from 20% to 80% of the simulated time. All force values are standardized to a cut width of $b = 1mm$. It is observed that cutting and feed forces increase with an increasing coefficient of friction. The simulations with elastic cutter model (cases 4/6) show very small differences compared to the same simulation with rigid cutter (cases 2/4). In comparison to the experimental result, the simulation cases 2 and 3 underpredict the cut force (-23%) and the feed force (-50%) which is possibly due to the Johnson-Cook flow stress parameters used in this analysis. An indepth discussion of this issue on Ti6Al4V material can be found in [61]. Interestingly, the predicted cut and feed forces are similar to those obtained with OXLEY's process force model, see table 5.2.

Simulation case	Cut speed $v_c [\frac{m}{min}]$	Friction $\mu [-]$	Cut force $F_c [N]$	Feed force $F_f [N]$
1	70	0.00	91	-17
2	70	0.35	138	-42
3	70	0.35	138	-42
4	500	0.00	104	-22
5	500	0.35	150	-46
6	500	0.35	148	-46
Experiment [260]	70	-	180	-85

Table 6.7: Comparison of measured and simulated process forces

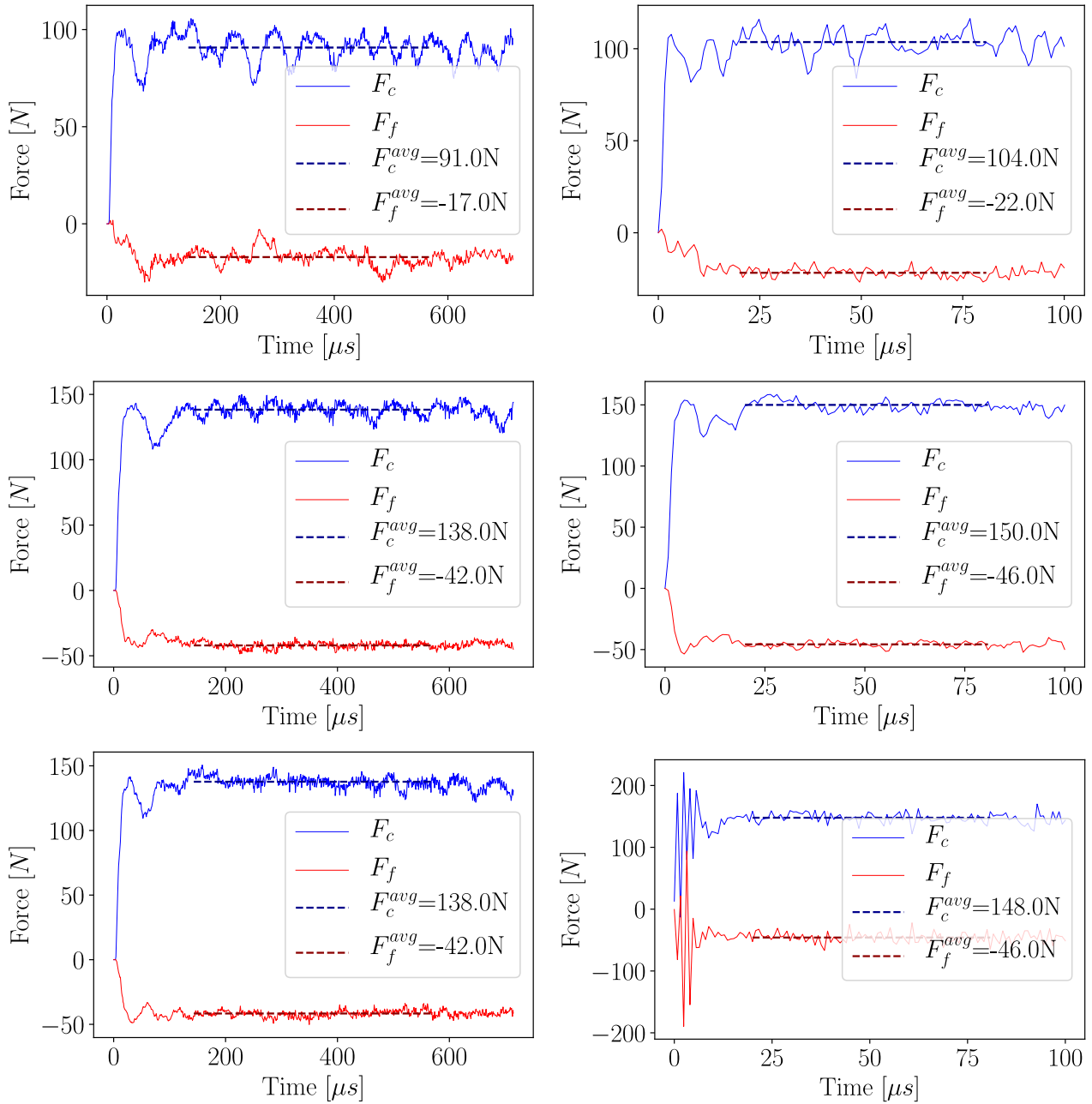


Figure 6.7: Tool forces: cutting and feed force exerted to the tool for the simulation cases from table 6.5. Top row case 1 (left) and case 4 (right), middle row case 2 (left) and case 5 (right), bottom row case 3 (left) and case 6 (right).

6.3.2 Temperatures and Temperature Rates

Due to plastic dissipation, there is a general temperature increase mainly in the area of the chip and in the freshly formed cut surface. The distribution of temperatures and temperature rates are shown in figures 6.8 and 6.9 for case 2 ($v_c = 70 \frac{m}{min}$, $\mu = 0.35$). Locally some particles reach almost the melting temperature of $T_{melt} = 1678K$ at the tool tip and the temperature rates are up to $\dot{T} = 230 \cdot 10^6 K/s$. It has to be emphasized, that peak temperatures would decrease to some extent when considering heat conduction in tool and workpiece. The majority of particles in the chip are within a temperature range of $T = 500K \dots 800K$. The temperature and temperature rate characteristics of particles A-O are given in figures 6.10 and 6.11 for all 6 simulation cases from table 6.7. It is observed that temperature levels rise for the cases with friction compared to the frictionless cases and a further increase is seen for the cases with elastic cutter model. In contrast, the temperature rates decrease when friction is considered. The temperature rates increase in the simulation models with rigid cutter models and an increase is seen also with increasing cut speed. The temperature rates in simulations with rigid and elastic cutter are similar. The whole plastic deformation takes place within roughly $200\mu s$ for the lower cutting speed of $v_c = 70m/min$ (cases 1-3) and within $25\mu s$ for the higher cutting speed of $v_c = 500m/min$ (cases 4-6).

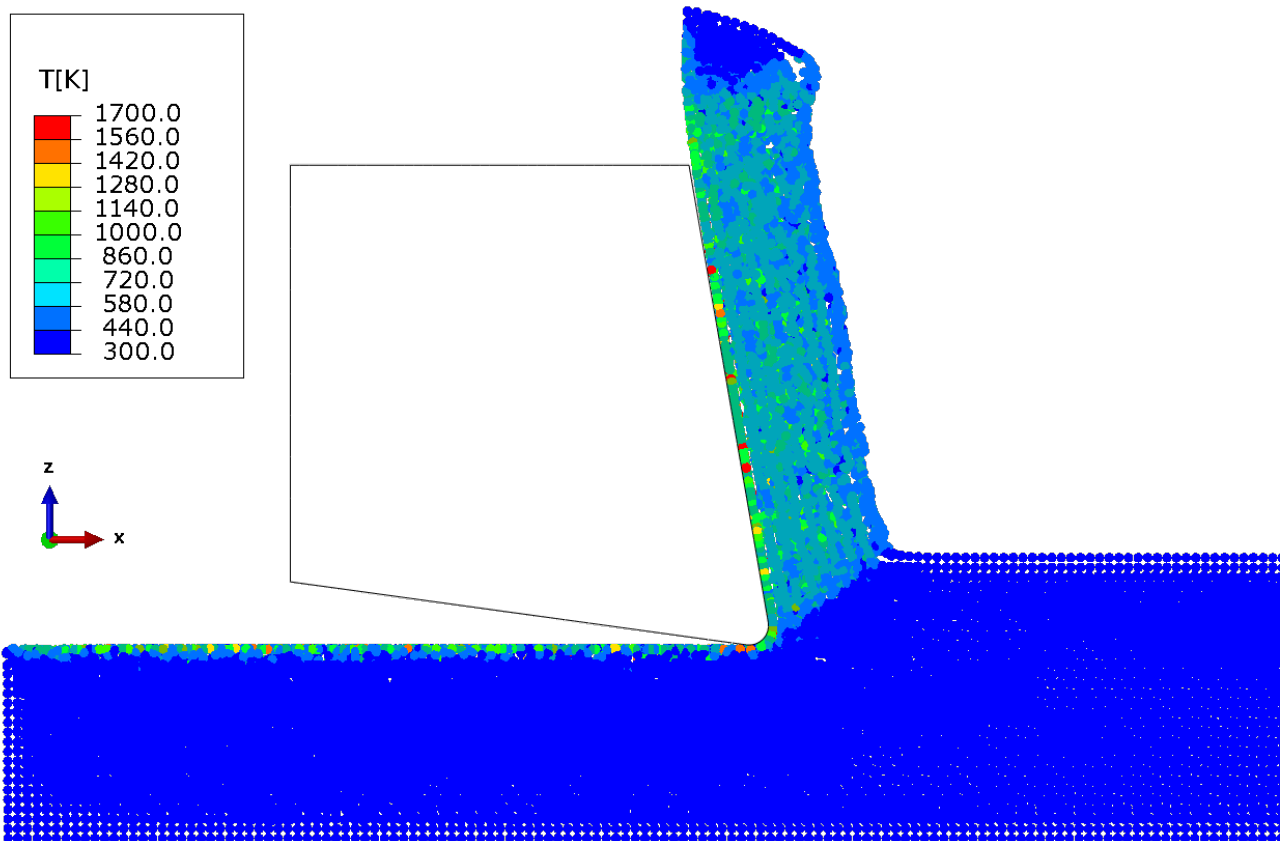


Figure 6.8: Workpiece temperature distribution [K], case 2 ($v_c = 70 \frac{m}{min}$, $\mu = 0.35$) at $t = 683.2\mu s$

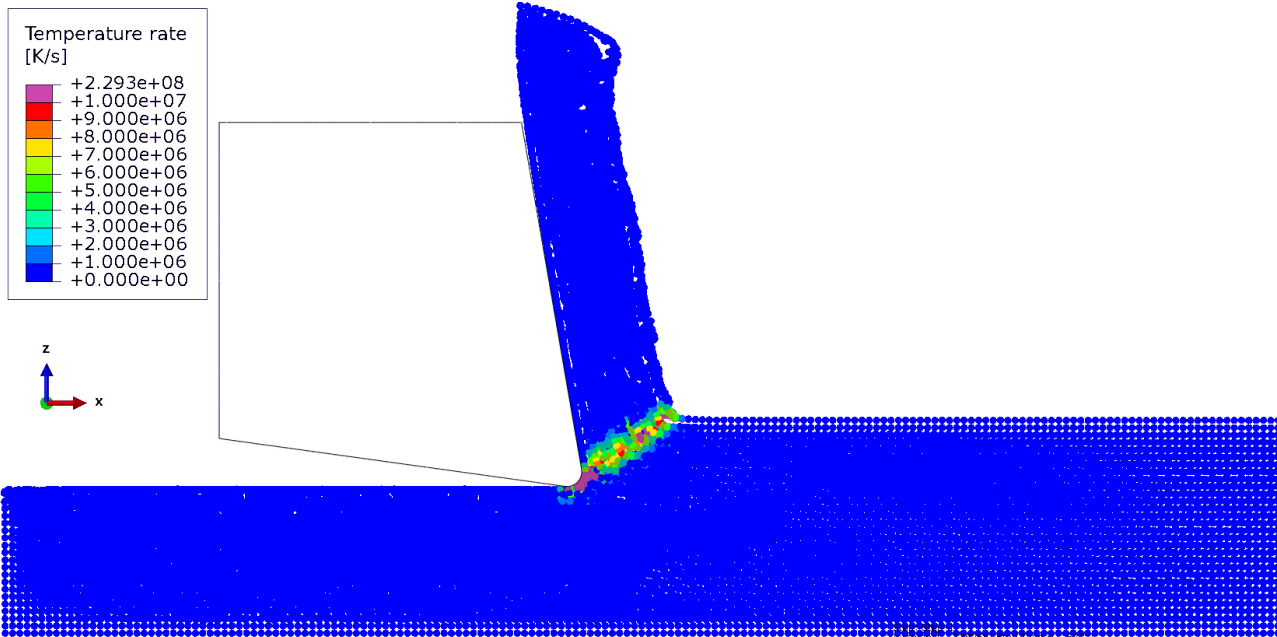


Figure 6.9: Workpiece temperature rates [K/s], $v_c = 70 \frac{m}{min}$, $\mu = 0.35$ at $t = 683.2 \mu s$

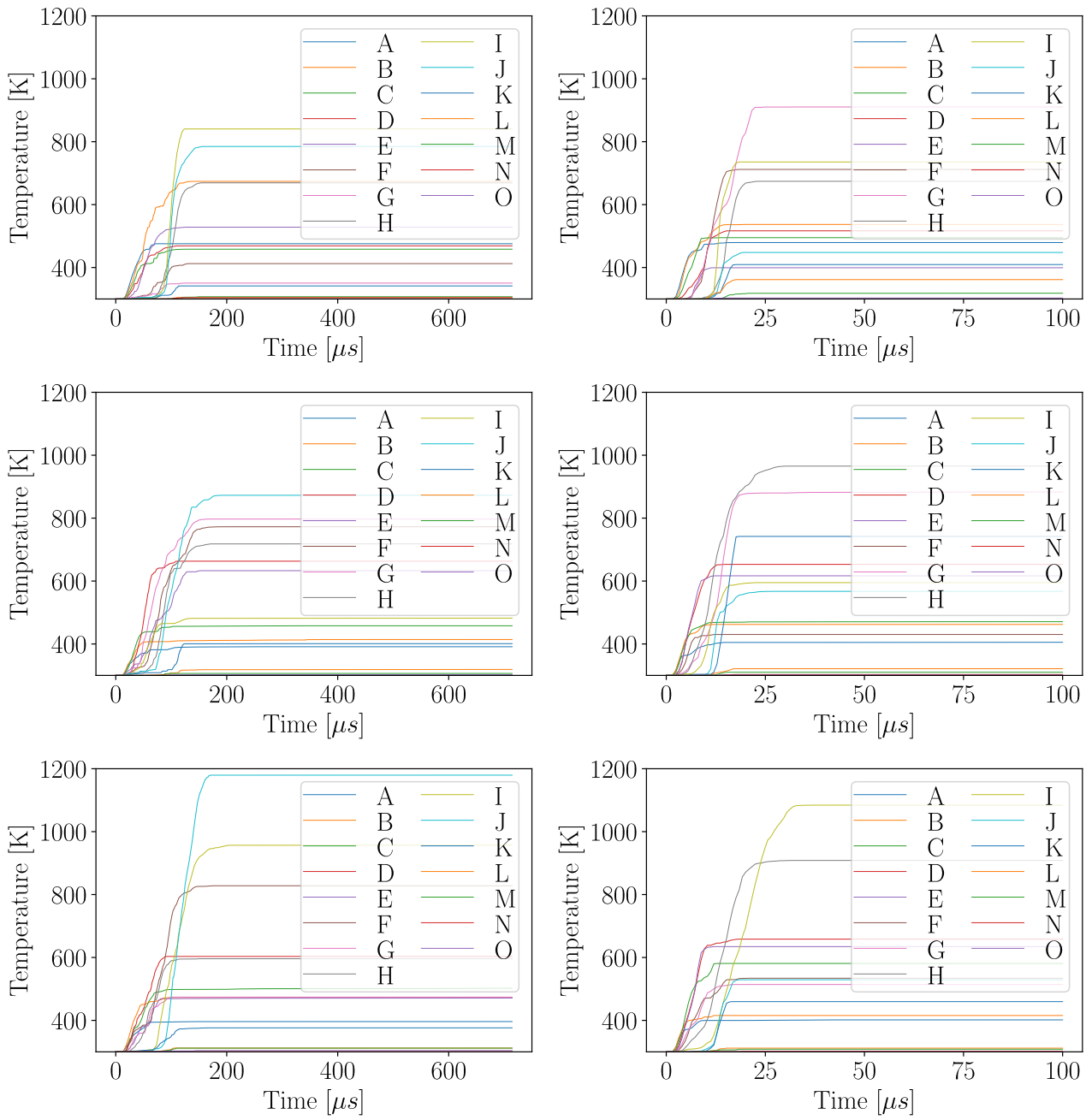


Figure 6.10: Temperature characteristics for particles A-O for the simulation cases from table 6.5. Top row case 1 (left) and case 4 (right), middle row case 2 (left) and case 5 (right), bottom row case 3 (left) and case 6 (right).

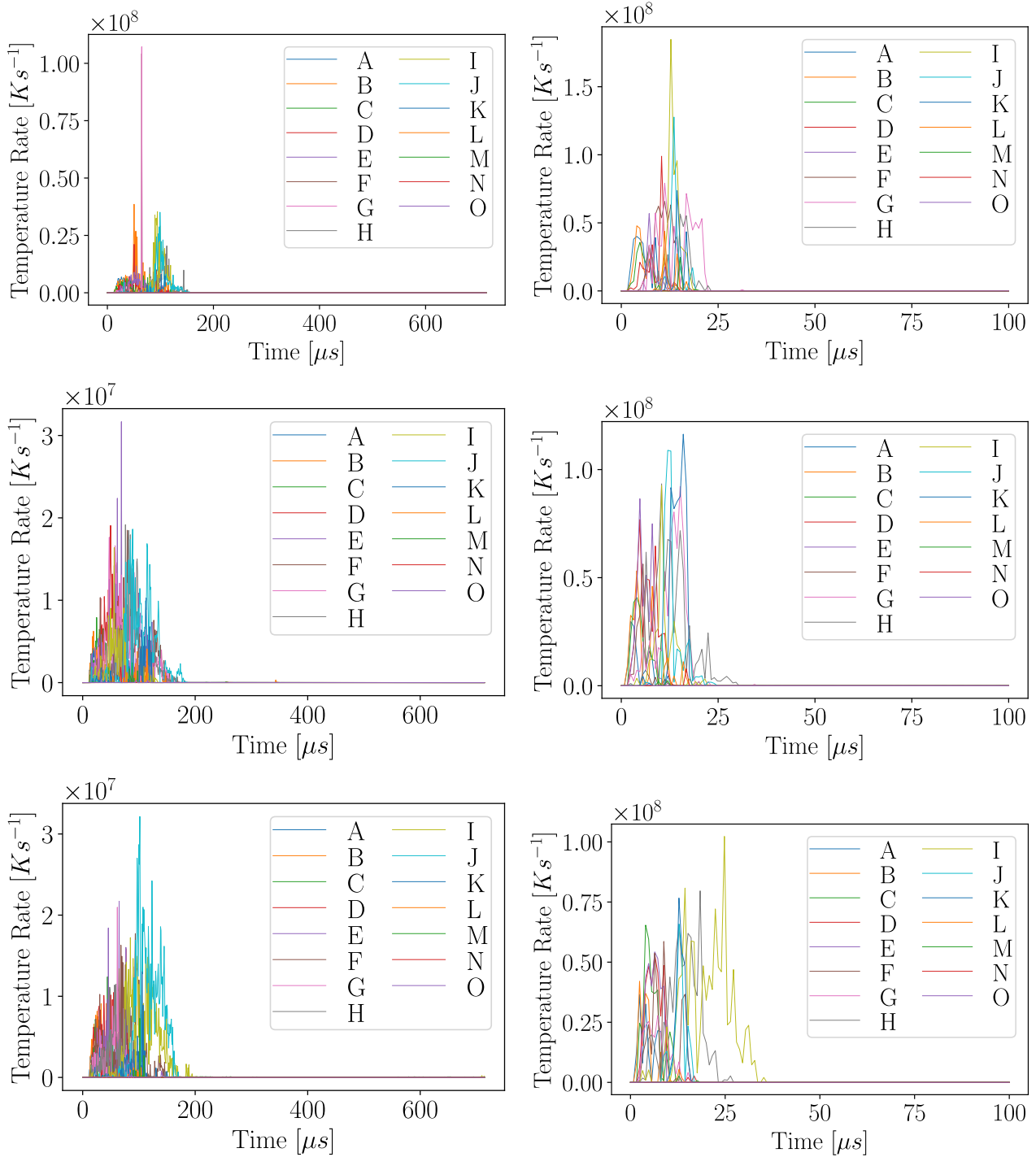


Figure 6.11: Temperature rates for particles A-O for the simulation cases from table 6.5. Top row case 1 (left) and case 4 (right), middle row case 2 (left) and case 5 (right), bottom row case 3 (left) and case 6 (right).

6.3.3 Plastic Strains and Plastic Strain Rates

The distribution of plastic strain rates is shown exemplarily in figure 6.12 for case 2 ($v_c = 70 \frac{m}{min}$, $\mu = 0.35$). A peak strain rate in the order of $\dot{\epsilon}_{pl} \approx 535'000/s$ is observed at the cutting edge radius. In the shear zone itself, strain rates reach levels in the order of $\dot{\epsilon}_{pl} \approx 10'000/s \dots 100'000/s$. Figures 6.13 and 6.14 show for particles A-O the characteristics of the numerically predicted plastic strains and plastic strain rates during the cutting simulation for all 6 simulation cases from table 6.7. Simulations including friction predict higher plastic strains which increase further when considering an elastic tool model. A strong influence of the friction coefficient on the plastic strain rates is seen where without friction, higher plastic strain rates are predicted compared to the simulations with friction. Simulations with elastic and rigid cutter show very similar plastic strain rates, which means that the type of cutter model has a minor influence on the plastic strain rates. Peak plastic strains and plastic strain rates are observed for the particles G, H, I and J which are located in the vicinity of the uncut chip thickness of $h = 0.1mm$ and can reach levels of even higher than 200%. Particles which remain in the workpiece after the cut, show rather small strains.

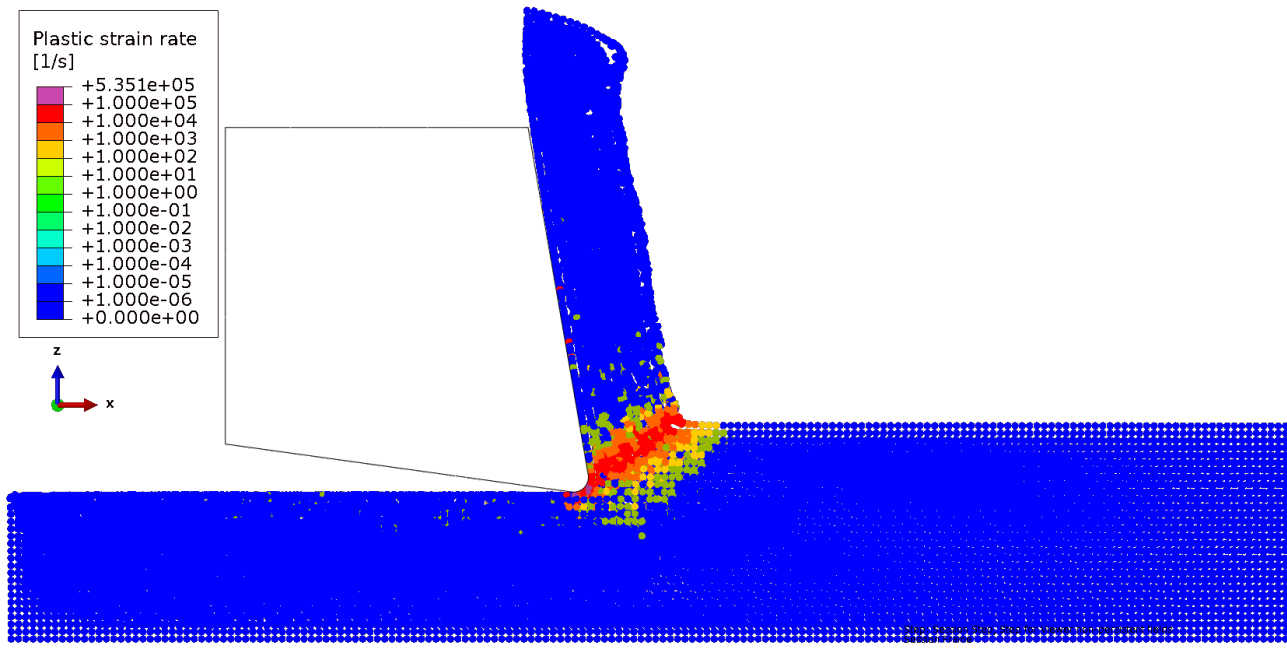


Figure 6.12: Plastic strain rate [1/s] distribution, case 2 ($v_c = 70 \frac{m}{min}$, $\mu = 0.35$) at $t = 683.2\mu s$

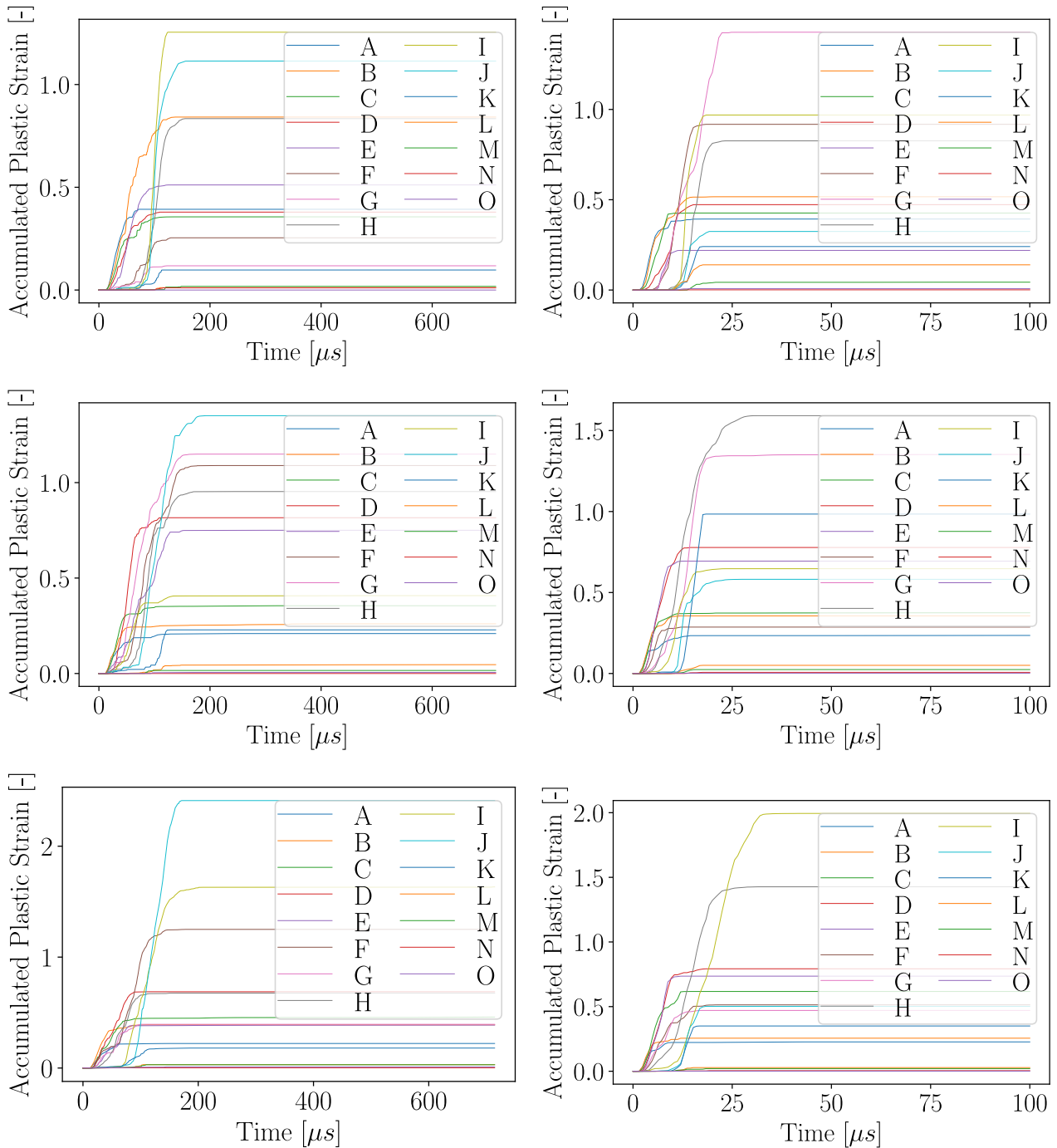


Figure 6.13: Accumulated plastic strain characteristics for particles A-O for the simulation cases from table 6.5. Top row case 1 (left) and case 4 (right), middle row case 2 (left) and case 5 (right), bottom row case 3 (left) and case 6 (right).

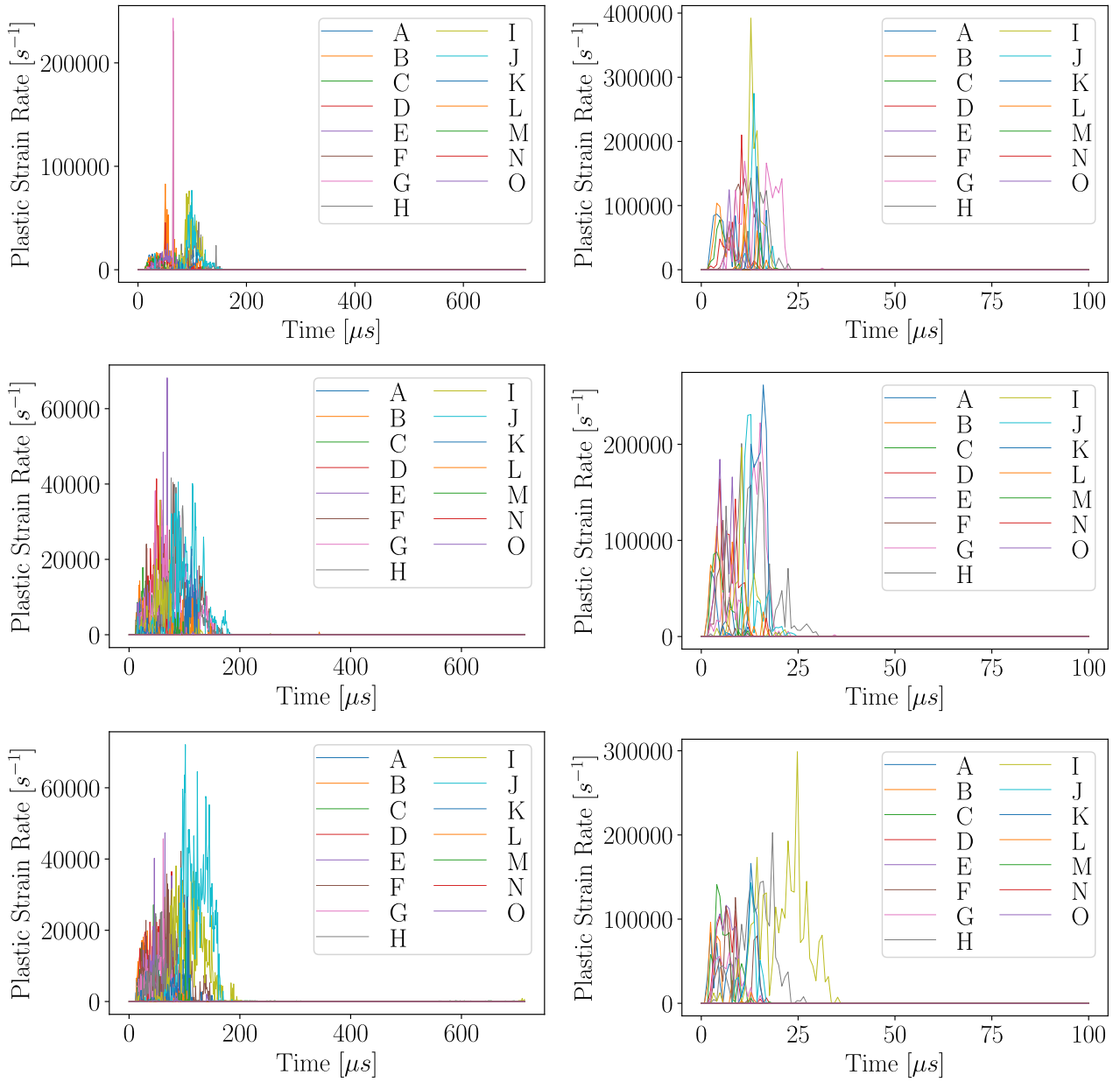


Figure 6.14: Plastic strain rates for particles A-O for the simulation cases from table 6.5. Top row case 1 (left) and case 4 (right), middle row case 2 (left) and case 5 (right), bottom row case 3 (left) and case 6 (right).

6.3.4 Stress State Investigation

In this chapter the stresses occurring during orthogonal cutting are investigated in detail. First, hydrostatic and equivalent stresses are analysed followed by some in depth analyses of the stress tensor including a display in the principal axis system which shall answer in how far the assumption of isotropic hardening is justified.

6.3.4.1 Hydrostatic Stresses

Hydrostatic stress characteristics for particles A-O are shown in Figure 6.15. Compressive stresses in this investigation have negative signs in contrast to Abaqus-terms. They are observed locally up to -4GPa which is slightly higher than reported in [13]. Hydrostatic pressures are mainly compressive before the cutter arrives in the reviewed particles A-O. After the cutter has passed a switch into tensile hydrostatic pressures is observed. The hydrostatic stress levels are in general higher for a cut speed of $v_c = 500 \frac{m}{min}$. The simulations with rigid cutter show about 50% lower hydrostatic stresses when friction is considered. On the other hand the simulations with elastic cutter showed higher hydrostatic stresses possibly due to tool vibrations exerted to the workpiece.

6.3.4.2 Equivalent Stresses

Equivalent stress characteristics for particles A-O are shown in Figure 6.16. The peak stresses during cutting are in the order of $\sigma_{eq} = 1200\text{MPa}$ and after cutting the residual stresses are at least 200MPa for cases 1-3 at $v_c = 70 \frac{m}{min}$ while for cases 4-6 at $v_c = 500 \frac{m}{min}$ these increase to a minimum of about 400MPa.

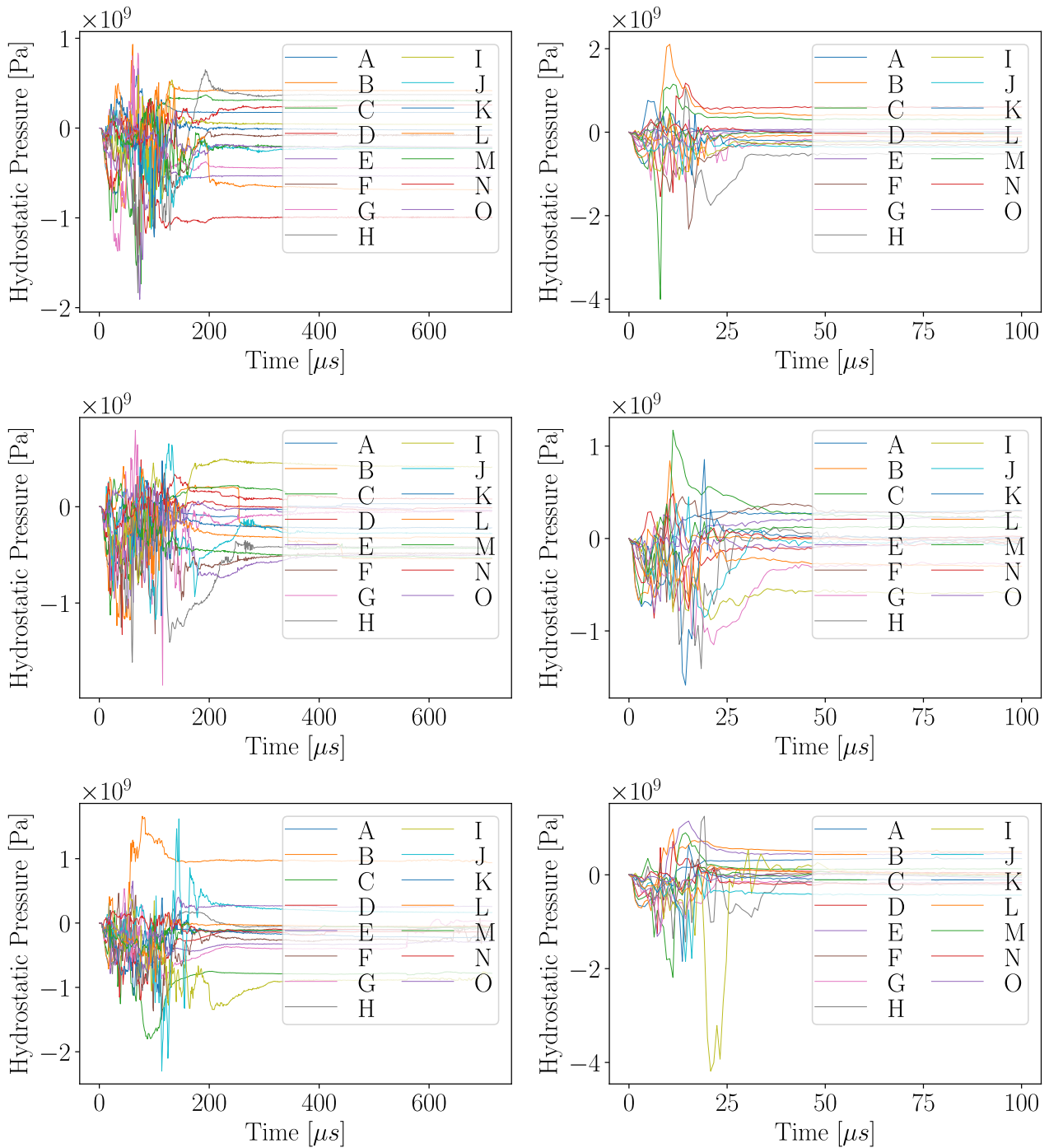


Figure 6.15: Hydrostatic stresses for particles A-O for the simulation cases from table 6.5. Top row case 1 (left) and case 4 (right), middle row case 2 (left) and case 5 (right), bottom row case 3 (left) and case 6 (right).

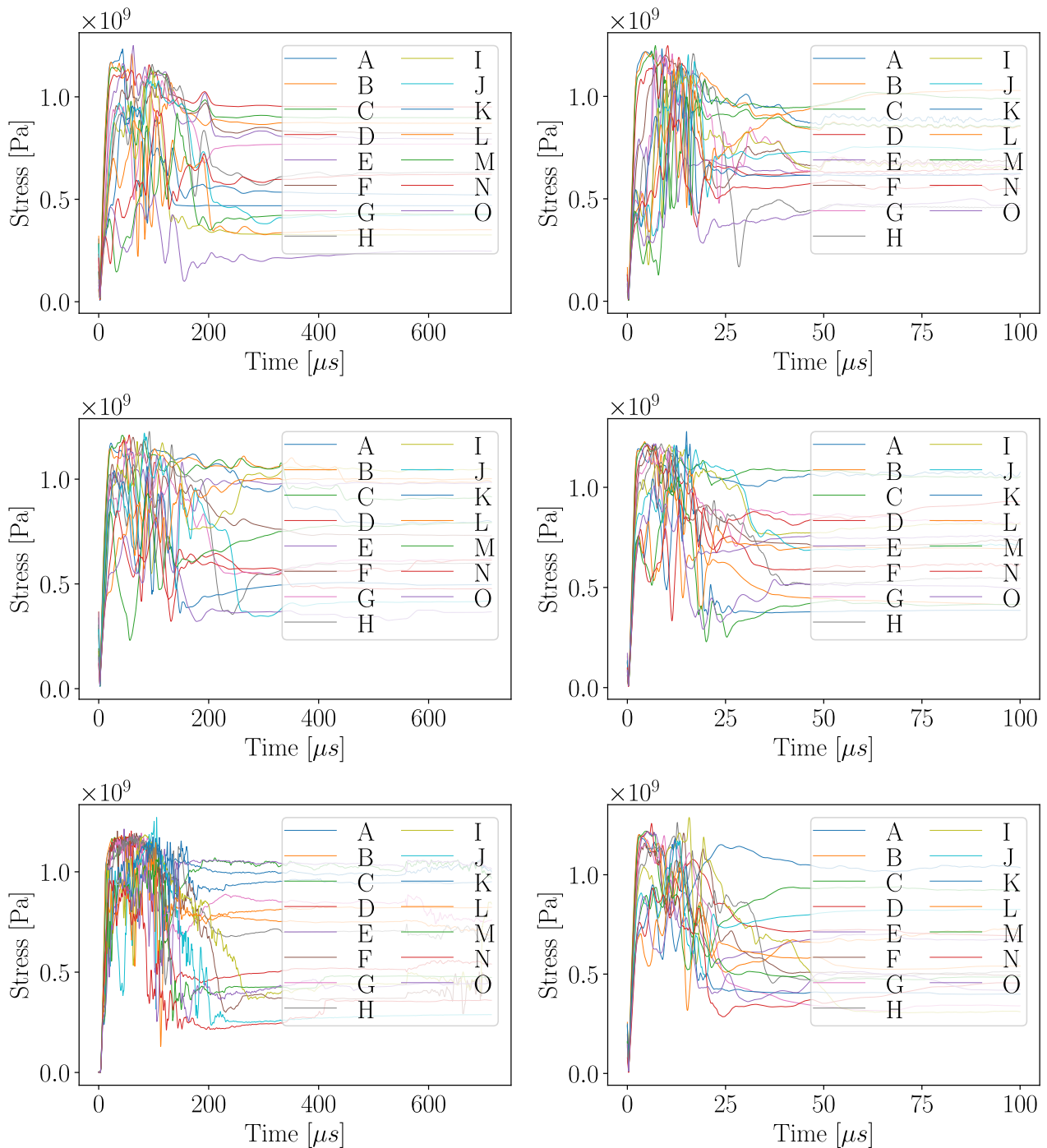


Figure 6.16: Equivalent stresses (von Mises) for particles A-O for the simulation cases from table 6.5. Top row case 1 (left) and case 4 (right), middle row case 2 (left) and case 5 (right), bottom row case 3 (left) and case 6 (right).

6.3.4.3 Detailed Investigation of a Single Particle

In figure 6.15 it is observed that hydrostatic pressures oscillate and change from compression into tension during the cut. This raises the questions if the load direction reverses during the cut and therefore a detailed analysis of the occurring stress states is conducted here. The analysis is performed exemplarily for particle I and case 2. The characteristics of hydrostatic stress and equivalent stress are shown in figure 6.17 with some smoothing using a Savitzky-Golay-filter in Python to remove oscillations.

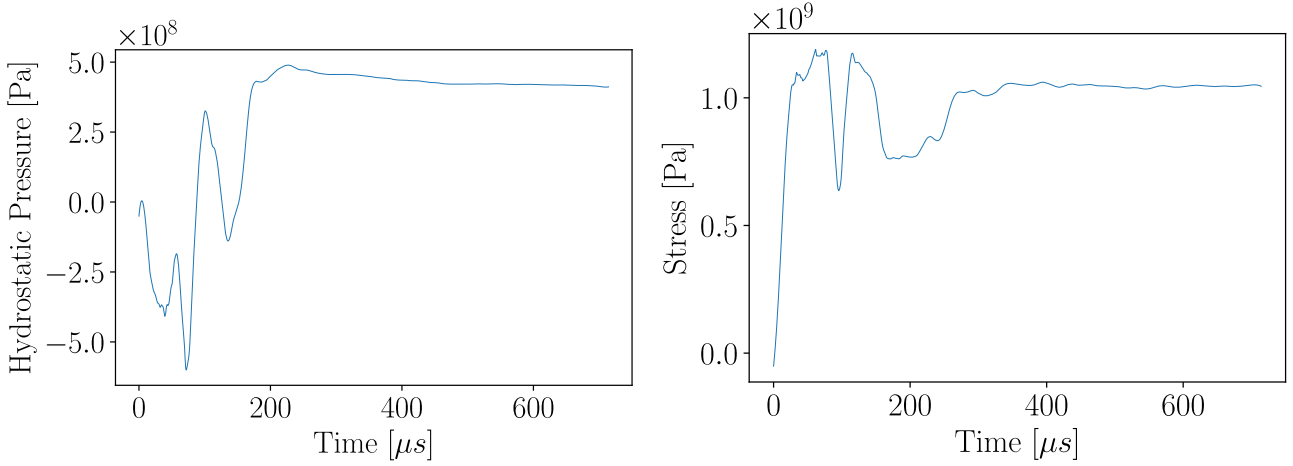


Figure 6.17: Hydrostatic stress in (left) and equivalent stress (right) in particle location I, case 2 ($v_c = 70 \frac{m}{min}$, $\mu = 0.35$)

The initial compressive hydrostatic pressure turns into tension ($t \approx 100\mu s$), shortly back to compression and then finally stays in tension. The equivalent stress fluctuates accordingly to the hydrostatic stress. In the stress tensor component display (figure 6.18 left) σ_{xx} , σ_{yy} & σ_{zz} are initially compressive and turn later into tension. Since the chip is rotated during cutting the stress tensor components are spilled due to rigid body rotations of the material points. In order to eliminate the rigid body rotation effect on the stress tensor components, the deformation gradients $\underline{\underline{F}}$ are extracted from the analysis and the material rotation is removed from the stress tensor $\underline{\underline{\sigma}}$ by using the corotated stress $\underline{\underline{\sigma}}^{cor}$:

$$\underline{\underline{\sigma}}^{cor} = \underline{\underline{R}}^T \cdot \underline{\underline{\sigma}} \cdot \underline{\underline{R}} \quad (6.3)$$

where $\underline{\underline{R}}$ is obtained from the polar decomposition of the deformation gradient $\underline{\underline{F}}$:

$$\underline{\underline{F}} = \underline{\underline{R}} \cdot \underline{\underline{U}} \quad (6.4)$$

Since Abaqus does not output the deformation gradient directly, a user material subroutine (VUMAT) was implemented for the Johnson-Cook flow stress model including adiabatic heating. Within this subroutine, access to the deformation gradient tensor $\underline{\underline{F}}$ is granted and

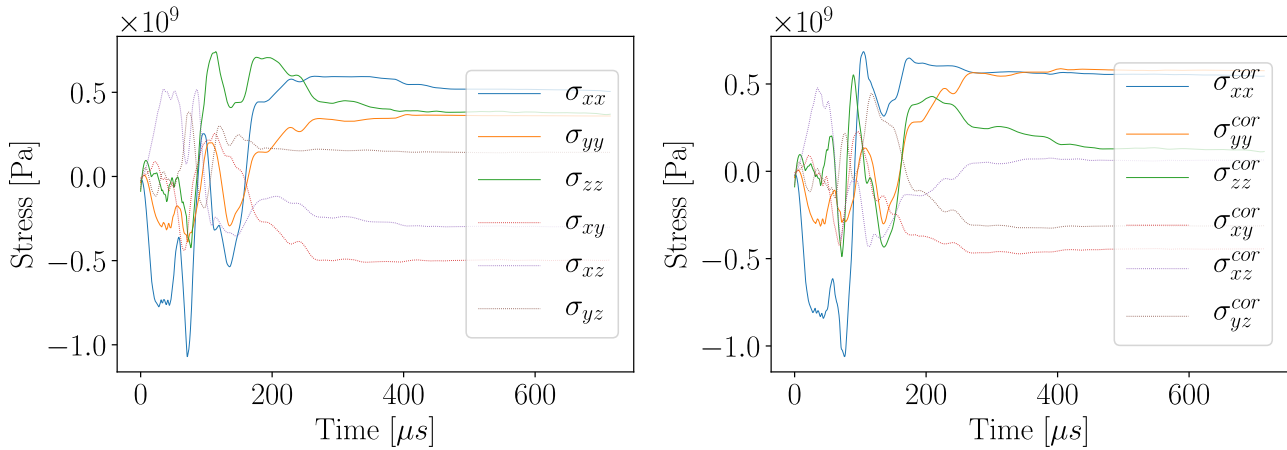


Figure 6.18: Cauchy stress tensor (left) and corotated stress components (right) in particle location I, case 2 ($v_c = 70 \frac{m}{min}$, $\mu = 0.35$)

was written to the output database in conjunction with the respective stress tensors $\underline{\underline{\sigma}}$. The components of the corotated stress tensor $\underline{\underline{\sigma}}^{cor}$ are shown for particle location I in Figure 6.18.

One can see a more pronounced change from compression to tension in the corotated stress tensor component σ_{xx}^{cor} , while σ_{zz}^{cor} shows a slightly reduced compression-tension change and σ_{yy}^{cor} is almost unaffected. The observed stress tensor characteristics may hint that monotonic loading is not the case and stress reversals or at least load path changes occur which would mean that the isotropic hardening assumption is possibly not sufficient to describe the phenomena accurately. Since for the Ti6Al4V alloy some Bauschinger effect was measured [29] this could have significance in the simulation and would require models considering combined (kinematic and isotropic) or formative (distortional) hardening for a more accurate description of the underlying physics. The problem is depicted graphically in figure 6.19 where a uniform loading towards the stress point \mathbf{S} can be described by pure isotropic (dark red circle) or combined hardening (yellow circle) equally. But if the load path reverses into opposite direction yielding occurs in the combined hardening model already when the yellow cylinder is crossed while yield in isotropic hardening starts later when crossing the dark red circle. This would result in less plastic work and lower forces. The maximum error occurs at 180° reverse loading and vanishes towards uniform loading. The stress tensor component analysis does not allow to draw a clear conclusion and therefore the load path is investigated in the principal axis system.

6.3.4.4 Display in the Principal Axis System

Bringing the problem into the space of principal stresses and showing the evolution during the loading sequence shall give a better impression of the loading path. For this purpose the time evolution of the stress tensor was analyzed with *Python/NumPy* [86]. Considering the principal stresses gives rise to the problem that there is no unique definition of how to sort the principal stresses, e.g. one could use the principal stresses [113]:

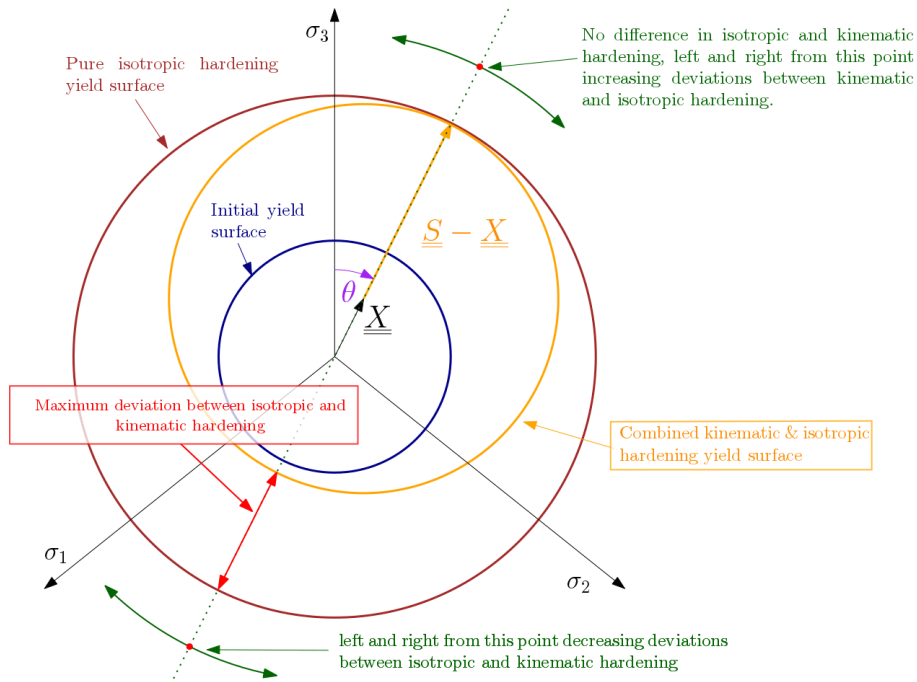


Figure 6.19: Schematic yield surfaces: initial (blue), pure isotropic hardening (brown) and combined kinematic and isotropic hardening(orange)

- METHOD 1: as is from the *Python/NumPy* Hermitean eigensolver *np.linalg.eigh*
- METHOD 2: as is from the *Python/NumPy* general eigensolver *np.linalg.eig*
- METHOD 3: sorted in descending order: $\sigma_I > \sigma_{II} > \sigma_{III}$
- METHOD 4: sorted in descending order of absolute values: $|\sigma_I| > |\sigma_{II}| > |\sigma_{III}|$
- METHOD 5: Haigh-Westergaard coordinate system

Table 6.8: Principle stress sorting methods

Visualized in the principal axis system, this results in the characteristics shown in figure 6.20. In the figure the diameter of the initial yield surface with the static yield limit of $\sigma_{y0} = 896MPa$ (JC-CLASSIC parameter A) is shown as well. All load paths start in the center with blue line color and end with red line color. In all path displays a zigzag movement is visible which is induced by the overlay of stress waves due to the explicit time stepping method of the solver. Each of the five methods gives a different load paths in the visualization. The path display with METHOD 2 and METHOD 4 show strong kinks and could be misinterpreted as load reversals. The paths in METHOD 1, METHOD 3 and METHOD 5 are very similar but rotated around the center to different angular positions. Given the 5 different visualizations the question is why they differ and which one should be selected finally. The differences in the principal stress display are caused by ambiguities in the eigenvalue determination which are discussed in [113] and a proposal is made how to sort eigenvalues such that eigenvector basis rotations within successive increments are minimized. This proposed sorting algorithm for principal stresses is applied to the orthogonal cutting simulation in the next chapter.

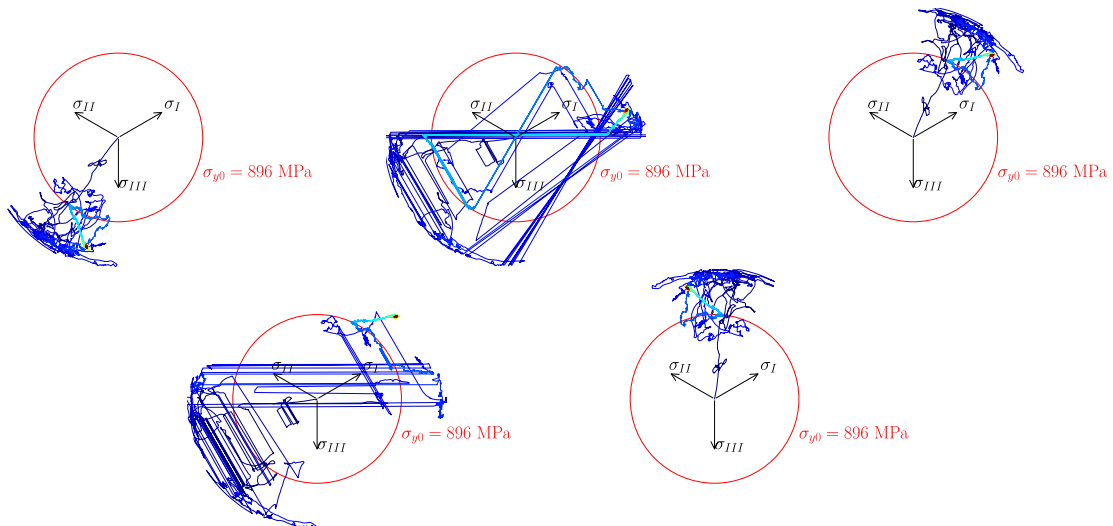


Figure 6.20: Principal stress evolution in the principal axis system displayed with different methods for principle stress extraction according to table 6.8. All load paths start in the center and the color indicates the normalized time where blue color is in the initial state and the final state is in red color. The top row shows the load path with METHOD 1 (left), METHOD 2 (middle) and METHOD 3 (right) and the bottom row shows them with METHOD 4 (left) and METHOD 5 (right).

6.3.4.5 *Sorting Principal Stresses by Quaternions*

The input to the principal stress sorting algorithm is the time trace of the stress tensor $\underline{\sigma}(t)$ of the material point of interest. The principal stresses of the stress tensor are computed and the eigenvector base is aligned such that the eigenvector base rotation from the old to the current increment is minimized by quaternion analysis. For this purpose the stress tensors of the particles A-O were written to the output database at every increment of the analysis. The result is the time trace of the three principal stresses which can then be displayed in the principal axis system. Applied to particle I (case 2) the load path in figure 6.21 results.

Accidentally, the load path in figure 6.21 equals METHOD 1 in figure 6.20. In general this is not necessarily the case as depicted in [113]. The quaternion sorting algorithm was applied to all simulation cases of particle I and the resulting loading paths are displayed in figure 6.22. Similar load path visualizations can be found in the appendix for particles A (11.1.1), D (11.1.2), E (11.1.3) and K (11.1.4). All visualizations show non uniform load paths but full load reversals of 180° do not occur.

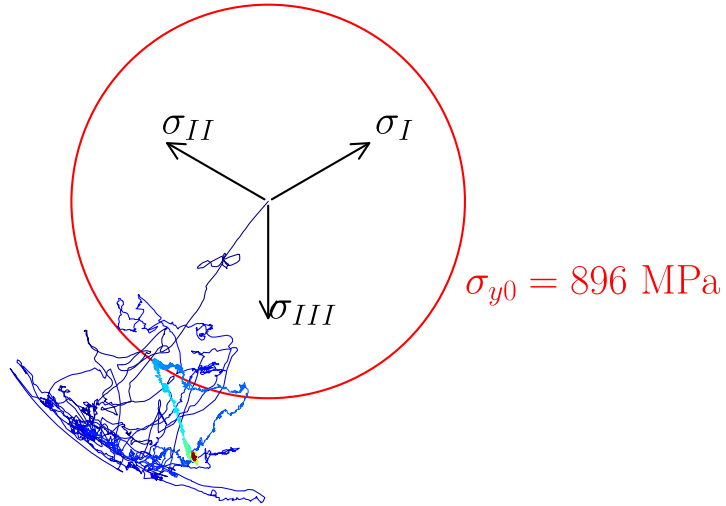


Figure 6.21: Load path display of particle I in the principal axis system for case 2, the principal stresses are sorted by quaternion analysis.

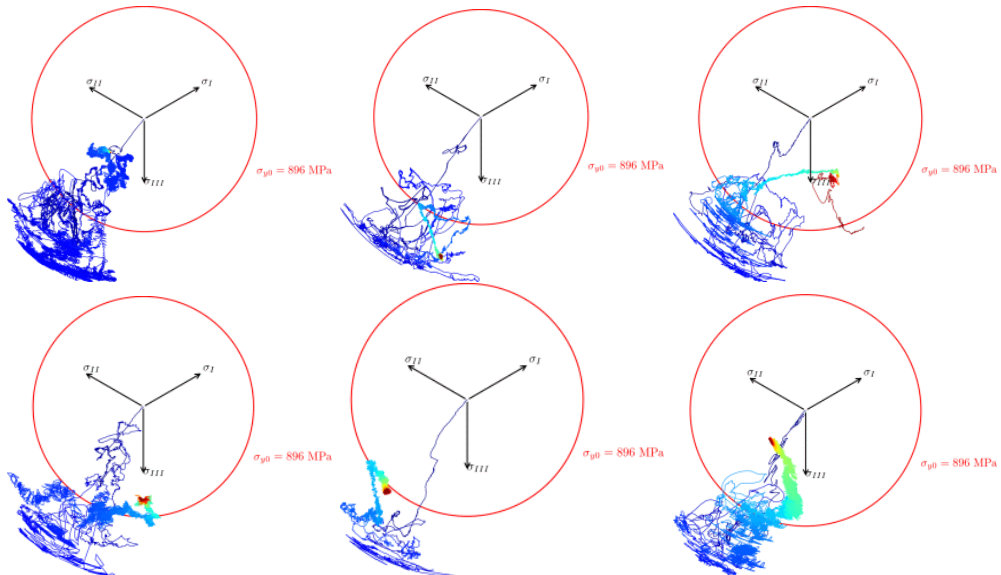


Figure 6.22: Load path visualization of particle I in the principal axis system for the simulation cases from table 6.5. Top row case 1 (left), case 2 (middle) and case 3 (right), bottom row case 4 (left), case 5 (middle) and case 6 (right).

6.3.5 Runtimes

The analysis runtimes heavily depend on the simulated cut-speed v_c and whether the cutter is modelled as a rigid or elastic body. The computations were carried out on a single core of a Intel(R) Xeon(R) CPU E5-2620 v4 @ 2.10GHz and the measured runtimes $t_{compute}$ are compiled in table 6.9. Computations with the elastic cutter model consumed significantly more compute time since the small elements of the cutter required smaller time increments due to the CFL-condition. Mass scaling could be a viable method to significantly reduce the compute times.

Simulation case	Cutter	Cut speed $v_c[\frac{m}{min}]$	Process time $t_{sim}[\mu s]$	Analysis runtime $t_{compute}[h]$
1	Rigid	70	714	42
2	Rigid	70	714	36
3	Elastic	70	714	231.5
4	Rigid	500	100	5.3
5	Rigid	500	100	5.5
6	Elastic	500	100	34

Table 6.9: Simulation Runtimes

6.4 EFFECT OF MATERIAL ANISOTROPY

Based on the results of the load path analysis in chapter 6.3.4.5 the Hill 48 model (3.114) is used here to predict the effect of the anisotropy on the process forces within the orthogonal cutting model. In contrast to the previous analysis, Abaqus 2021/Explicit is used here because it allows the Hill 48 model to be used with the SPH as well. However, it is not possible to consider adiabatic heating, that is why only isothermal simulations ($\eta_{TQ} = 0.0$) are used to determine the sensitivities with respect to anisotropy. The cutting speed is in all simulations $v_c = 500m/min$ and the feed is $f = 0.1mm$. In total 8 different cases were analysed with R_{11}, R_{22} and R_{33} being varied and its values are given in table 6.10 together with the resulting averaged process forces. The anisotropy coefficients in shear are set to constant $R_{12} = R_{13} = R_{23} = 1$ for all simulation cases.

Simulation case	R_{11}	R_{22}	R_{33}	$F_c[N]$	$F_f[N]$	Comment
1	1	1	1	199	-58	von Mises criterion, no anisotropy, baseline
2	1.1	1	1	214	-61	anisotropy in length direction
3	1.2	1	1	222	-64	anisotropy in length direction
4	1.5	1	1	263	-76	anisotropy in length direction
5	1.8	1	1	322	-94	anisotropy in length direction
6	2.0	1	1	366	-109	anisotropy in length direction
7	1	1.5	1	183	-50	anisotropy in width direction
8	1	1	1.5	250	-74	anisotropy in height direction

Table 6.10: Investigated cases for the anisotropy study with average process force results.

Figure 6.23 shows the predicted process forces for different anisotropies in the length direction. Even a slightly higher yield stress in length direction ($R_{11} = 1.1$) leads to $\approx +10\%$ increase in the cut force and $\approx +5\%$ in the feed force when compared to the baseline case. With increasing yield stress in length direction, the process forces are steadily increasing, see also table 6.10.

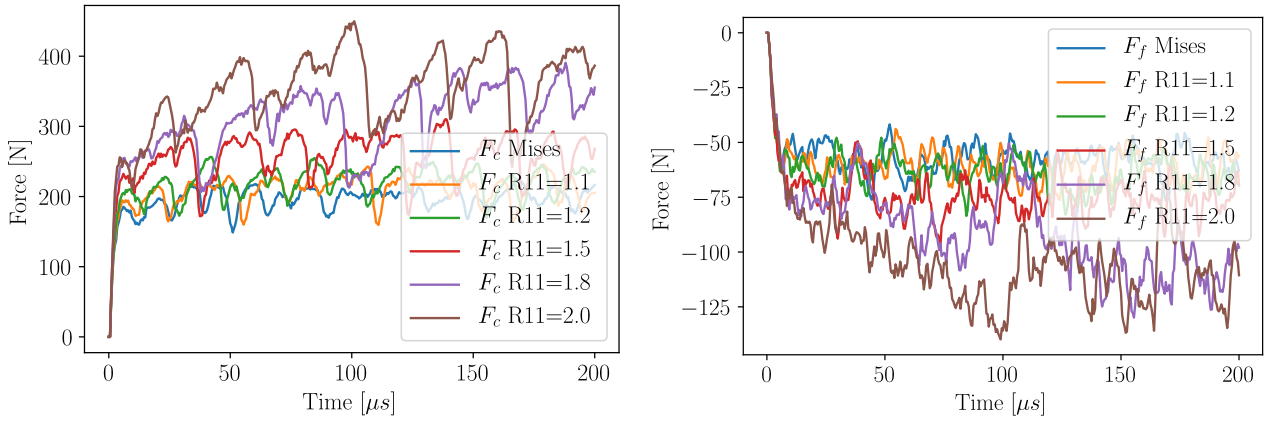


Figure 6.23: Cut (left) and feed (right) forces with different anisotropy coefficients in length direction (2-6) compared to the isotropic simulation case (1). In brackets the number of the respective simulation case from table 6.10 is given.

In figure 6.24 the influence of the anisotropy towards different directions with respect to process forces is shown. The baseline case is the isotropic von Mises criterion and it can be seen that an anisotropy in the width direction with $R_{22} = 1.5$ leads to slightly reduced process forces of about 10%. On the other hand, anisotropies towards length ($R_{11} = 1.5$) or height ($R_{33} = 1.5$) direction increase the cut and feed force by about 30% compared to the baseline case.

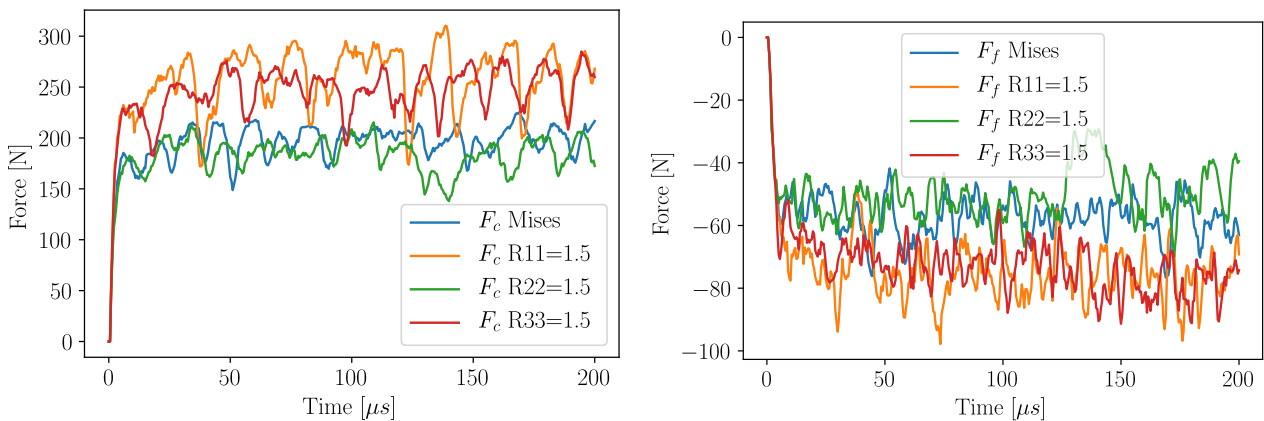


Figure 6.24: Cut (left) and feed (right) forces with anisotropy in length (4), width (7) or height (8) direction compared to the isotropic simulation case (1). In brackets the number of the respective simulation case from table 6.10 is given.

6.5 DISCUSSION

SPH simulations were performed at two cutting speeds with rigid and elastic cutter model as well as friction and frictionless contact. The main findings are:

- The friction model plays an important role in the process prediction, as the friction coefficient influences the plastic strain rates, temperature rates, process forces and hydrostatic pressures. It does not affect or only to a small extent the temperature and accumulated plastic strains.
- The predicted hydrostatic stresses were found inline with literature values. A mild dependence on the cutting speed is visible.
- Strain rates were found with up to $70'000s^{-1}$ at $v_c = 70\frac{m}{min}$ and up to $300'000s^{-1}$ at $v_c = 500\frac{m}{min}$. Even at the very high cutting speed the strain rates are below literature values which are reported up to $\dot{\epsilon}_{pl} = 10^6s^{-1}$ in [13].
- Temperatures can reach locally almost melting temperature (1678K) and the temperature rates are locally up to $230 \cdot 10^6K/s$ at the tool tip. Temperatures are most likely exaggerated as no heat conduction inside the workpiece nor into the tool was considered here.
- It is found by detailed analysis of stress states in specific material points (particle locations) that loading paths during the cutting process are in general not proportional but load reversals do not occur. Materials exhibiting anisotropic yield should be simulated with appropriate constitutive models to improve the quality of the numerical process prediction and further reduce the gap to experimental observations. The effect of potential anisotropies is shown within a parametric study to have an effect on the predicted process forces. It has to be noted, that capturing such material anisotropies requires extensive testing on the material, see for example [28]. By this the the uncertainties can be reduced in the constitutive modelling and will help to improve in other areas of the process prediction, for example when numerical models of the cutting experiments are used to identify the parameter of friction laws.
- The runtimes of the SPH are very large in Abaqus due to lack of (sufficient) parallelization

SPH TEST SIMULATIONS

In this chapter SPH test simulations are conducted with the `MFREE_IWF` code. Corrected and stabilized SPH schemes are investigated as well as the implementation and validation of the Johnson-Cook plasticity model. Challenges of damage modelling within the SPH are introduced and solutions to specific problems are derived and tested within a fracture mechanics CT test specimen. Finally, a SHTB-Test is computed with the SPH and the fracture strains and diameter are compared to experimental and FEM results.

7.1 IMPROVED SPH - APPLICATION EXAMPLE

The SPH corrections like CSPM and RKPM perform well in normalizing the kernels and restoring consistency but induce another problem: in contrast to standard SPH, corrected SPH schemes like the RKPM are not able to implicitly model stress-free boundaries. This is highlighted by an example of the interaction between the SPH scheme and the material model.

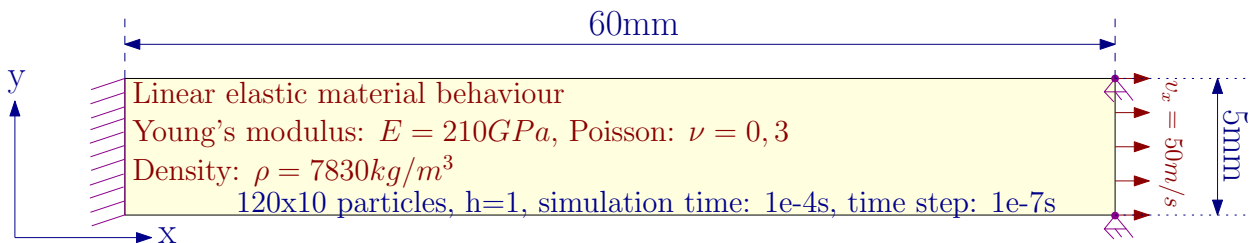


Figure 7.1: Simulation of a tensile test. Test setup, geometry, boundary conditions and material properties

A linear elastic plane stress (2D) tensile test of a plate is simulated. A total Lagrangian formulation on the strong form of the continuum equations is used. The plate dimensions are 60mm x 5mm, with a Young's modulus of $E = 210\text{GPa}$, a Poisson's ratio of $\nu = 0.3$ and a density of $\rho = 7830\text{kg/m}^3$. The left edge is constrained in x- and y- direction. On the right edge the y- displacement is restrained and a constant velocity in x-direction $v_x = 50\text{m/s}$ is applied. Test setup, geometry, boundary conditions and material properties are shown in figure 7.1. The tensile test is performed with particle methods and with the FEM in Abaqus/Explicit, the latter acting as a baseline solution. The simulated time is 10^{-4} seconds with a constant time step of 10^{-7} seconds for the particle methods, for the Abaqus solution automatic time stepping is chosen. Figure 7.2 shows the lateral contractions u_y due to tensile stretching in x-direction for the FEM result with Abaqus/Explicit and for the particle simulations with standard SPH and RKPM without and with enforced stressfree BC at free surfaces. The minimum and maximum y-displacements are for the:

FEM with Abaqus/Explicit:	$\pm 66,6\mu m$	(baseline)
Standard SPH:	$\pm 67,9\mu m$	(error: $\approx 2\%$)
RKPM without enforced stressfree BC:	$\pm 1,3\mu m$	(error: $\approx 98\%$)
RKPM with enforced stressfree BC:	$\pm 67,1\mu m$	(error: $\approx 1\%$)

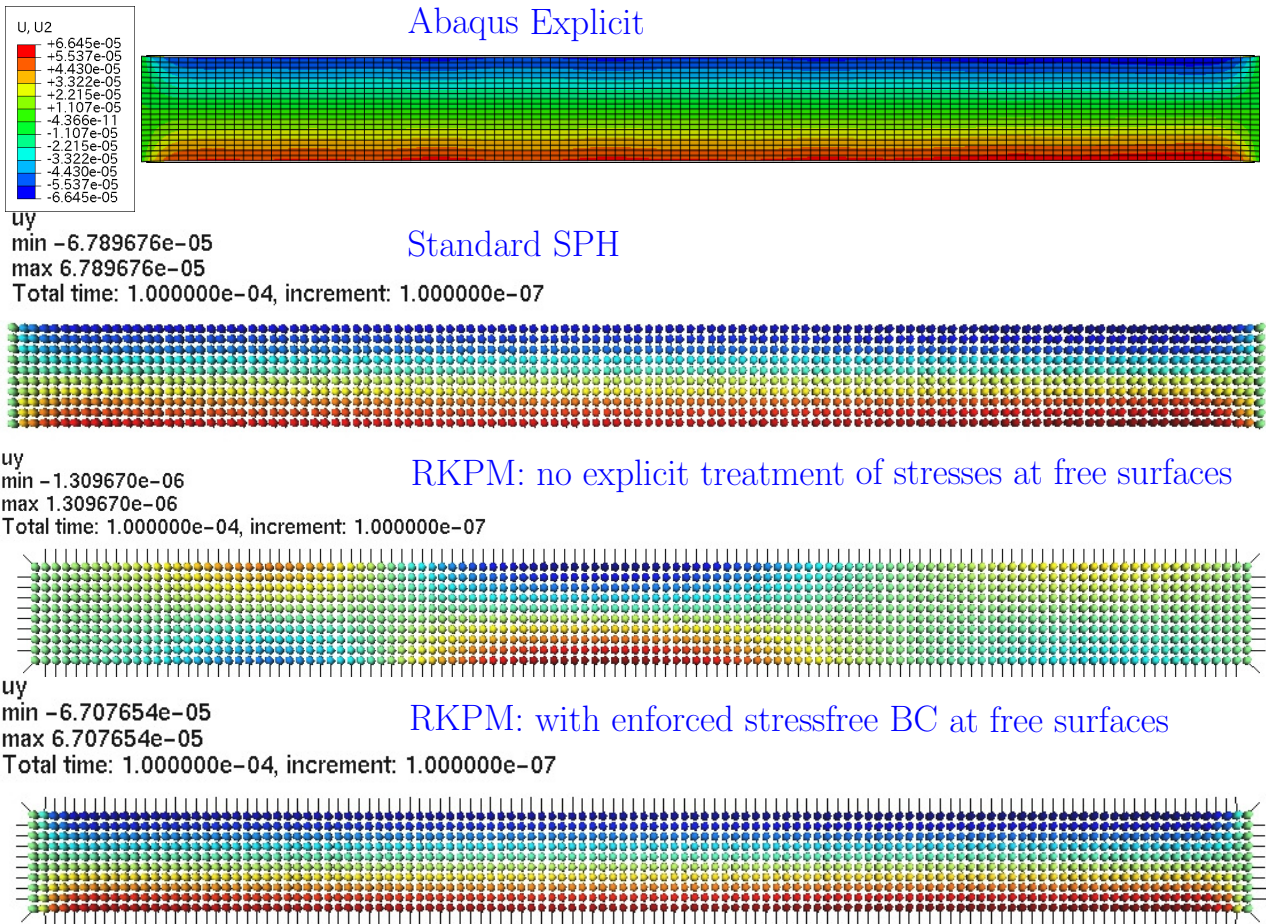


Figure 7.2: Simulation of a tensile test. From top to bottom: displacement results u_y obtained with Abaqus/Explicit and different SPH schemes: standard SPH / RKPM / RKPM with stressfree boundary conditions at free surfaces where the small lines show the computed surface normals.

According to the given results, it becomes obvious that the RKPM without enforced stressfree BC massively underpredicts the lateral contraction. The reason for this is that in SPH missing neighbour particles at boundaries result in approximate stressfree states. The RKPM-correction does not exhibit this behaviour and therefore the lateral contraction is blocked. A workaround is the explicit enforcement of a stressfree state on free surfaces in RKPM based on the surface normals. Doing so, the lateral contraction becomes very similar compared to that of the standard SPH, which is displayed in the bottom case of the figure. While in this simple example the determination of surface normals is rather simple, it becomes a problem when simulating cutting operations as the material separates and new surfaces are created. For this reason such SPH correctors are not used in the following.

7.2 ARTIFICIAL STRESSES

While in 2D updated Lagrangian SPH simulations artificial stresses are required for the rubber ring impact simulation to prevent instability modes, in the 3D simulation of a rubber ball impact these problems do not appear. Instead, the simulations are used to study the impact of artificial stress and viscosity terms as well as XSPH on the result. A comparison to a FE model is performed.

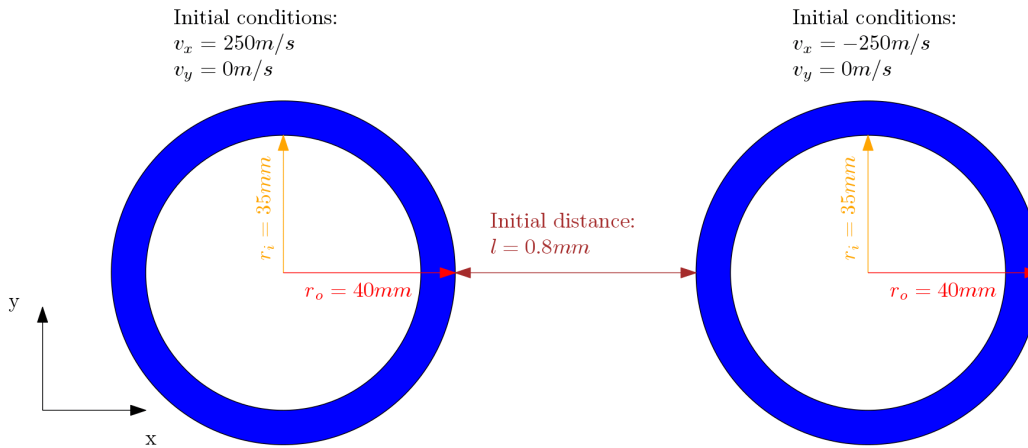


Figure 7.3: Geometry of the sphere impact simulation.

The spheres have an outer radius of $r_o = 40mm$ and an inner radius of $r_i = 35mm$ and the initial minimum distance between the two spheres is $l = 0.8mm$. The velocity is set for the left sphere to $v_x = 250m/s$ and for the right sphere to $v_x = -250m/s$. A sketch is provided with figure 7.3. Rubber like material parameters are chosen with $E = 10^7 Pa$, $\nu = 0.4$ and $\rho_0 = 1.0kg/m^3$ and the time step in the SPH simulations is set to $\Delta t = 10^{-7}s$. The FE mesh is discretised with higher element density resulting in a stable time increment of $\Delta t = 5.517 \cdot 10^{-8}s$. The total time simulated is $t_{total} = 4.5 \cdot 10^{-4}s$. The SPH model does not use a contact formulation since the collision is handled by particle interactions automatically. In the FE model a general contact formulation is used and the bulk viscosity is used with the linear parameter $b_1 = 0.06$ and the quadratic parameter $b_2 = 1.2$. Four different SPH cases were modelled where different stabilizers are switched on or off - see table 7.1. When switched on, artificial viscosity is used with $\alpha_{av} = 1$, $\beta_{av} = 1$, $\eta_{av} = 0.1$, artificial stresses with $n_{stress} = 4$ and the XSPH with $\epsilon_{XSPH} = 0.5$.

Case	Method	XSPH	Artificial stresses	Artificial viscosity	Particles / Elements	Runtime (single CPU core)
1	SPH	on	on	on	40208	40min
2	SPH	on	off	on	40208	38min
3	SPH	on	on	off	40208	34min
4	SPH	off	off	off	40208	29min
5	Abaqus/Explicit	-	-	*	161626 C3D10M 251330 nodes	20min

Table 7.1: Overview of impacting spheres simulations

Figure 7.4 shows the stress distribution at $t = 1.5 \cdot 10^{-4}s$ for SPH cases 1 (top half) and 2 (bottom half). The peak stresses are in the order of 2 MPa. The same is shown for the Abaqus simulation (case 5) in figure 7.6 but peak stresses reach 3.5 MPa. Compared to the SPH, the inward bulging of the rubber balls in the impact contact zone is less pronounced in the Abaqus simulation. SPH cases 3 and 4 are shown at $t = 2 \cdot 10^{-4}s$ in figure 7.5. The simulation without artificial viscosity (case 3) shows much larger inward bulging than the FEM and both SPH simulations with artificial viscosity (case 1 and 2). Without any stabilizers the SPH simulation shows even temporary openings of the rubber balls which close in a later stage of the simulation (not shown in the figures).

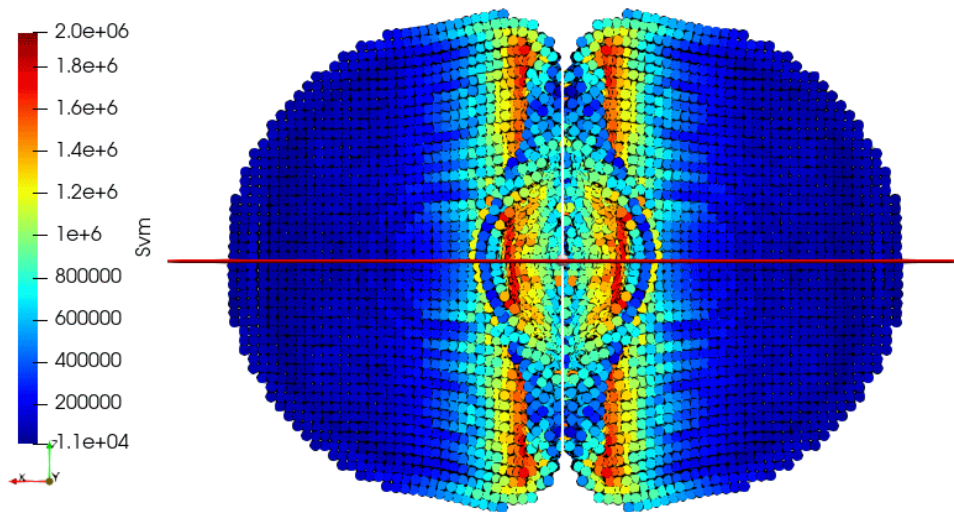


Figure 7.4: Equivalent stress distribution computed with SPH cases 1 (top half) and 2 (bottom half) at $t = 1.5 \cdot 10^{-4}s$.

The comparison of the kinetic, strain and total energy reveals, see figures 7.7, 7.8 and 7.9, that the total energy is almost constant in Abaqus - the bulk viscosity leads to small reductions only. In contrast are the SPH simulations which do not conserve the energy. For cases 1 and 2 the total energy constantly reduces over time, while for cases 3 and 4 it first reduces and then increases again. The increase is mainly attributed to the increase of kinetic energy after the impact while the strain energy remains at an almost constant high level. In case 4 the increase is even above the initial kinetic energy. The findings are as follows:

- all simulations with artificial viscosity show loss of total energy
- simulations without artificial viscosity show even increases in the total energy beyond the initial value which is not physical
- the XSPH averages linearly velocities in the particle neighbourhood therefore reducing the kinetic energy
- artificial stresses have a small effect on the energy losses, see results of cases 1 and 2
- the form of the discretised momentum equation is possibly not energy conserving

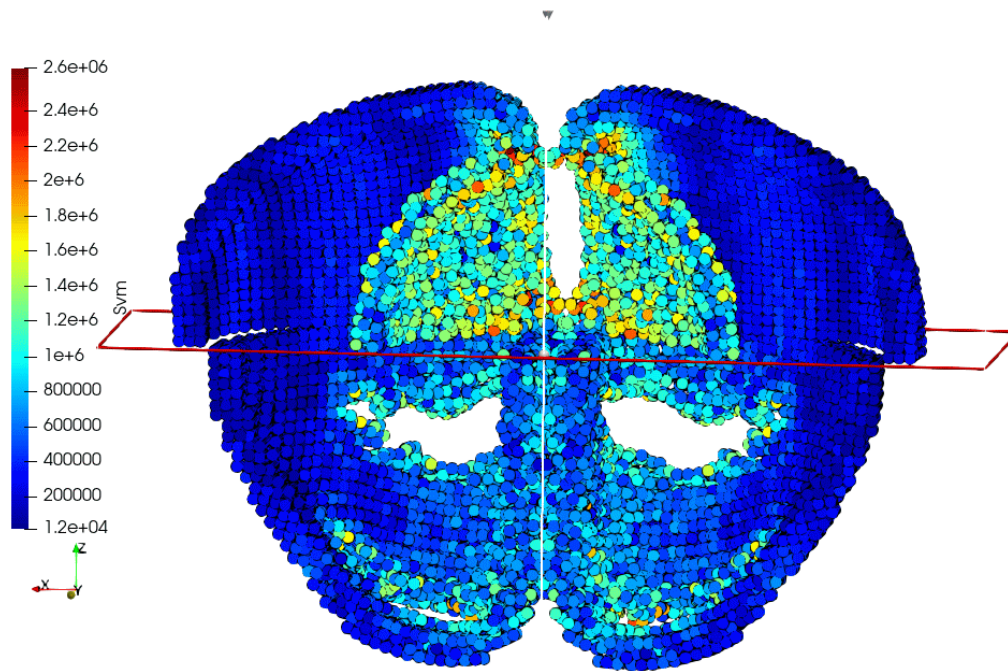


Figure 7.5: Equivalent stress distribution computed with SPH cases 3 (top half) and 4 (bottom half) at $t = 2 \cdot 10^{-4}s$.

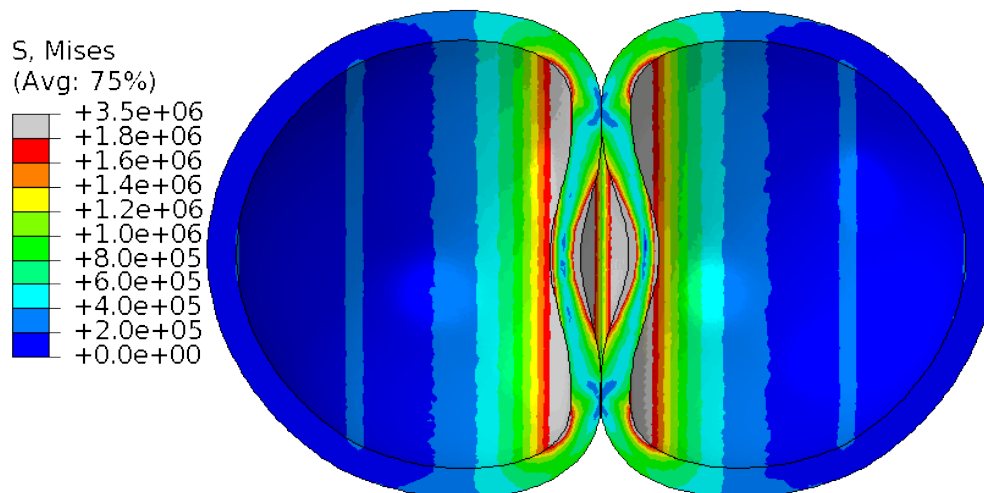


Figure 7.6: Equivalent stress distribution computed with Abaqus (case 5) at $t = 1.5 \cdot 10^{-4}s$.

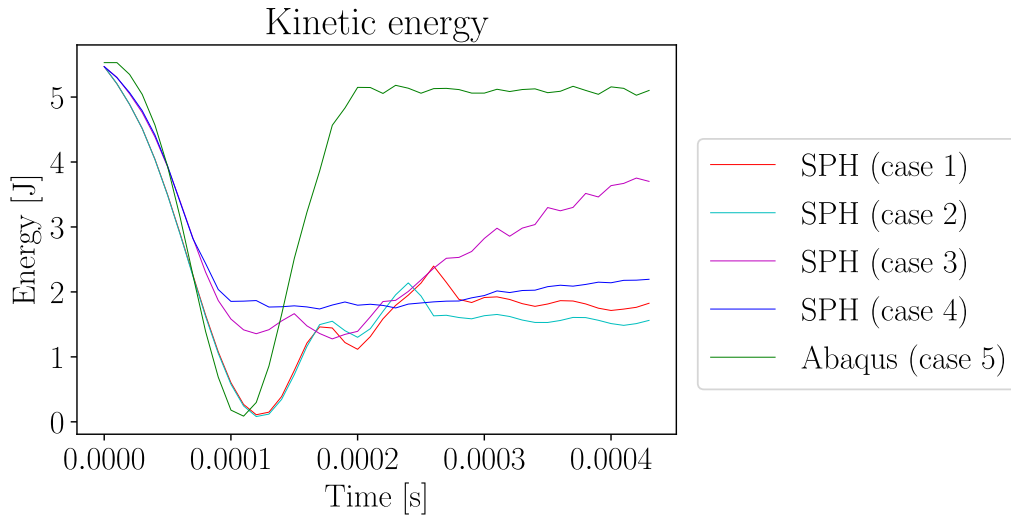


Figure 7.7: Kinetic energy evolution during rubber ball impact simulation.

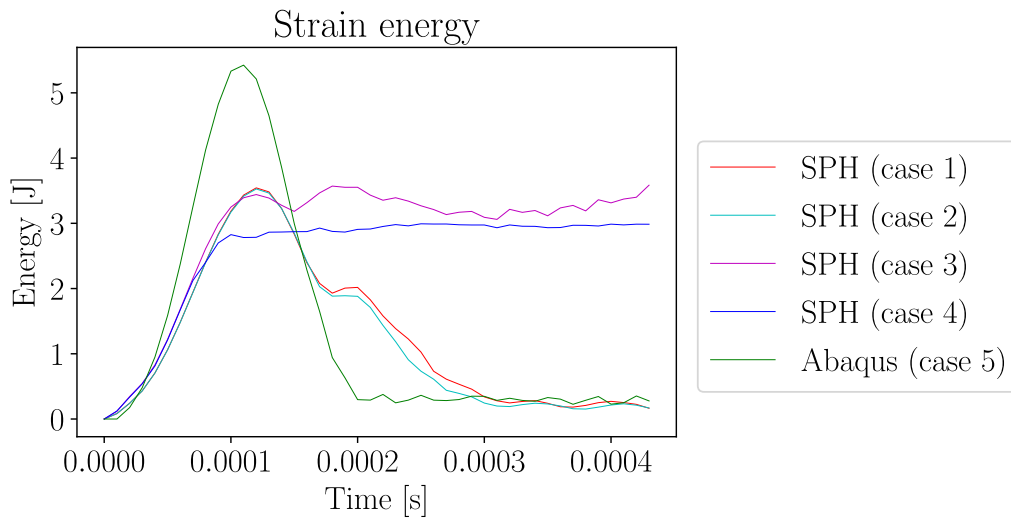


Figure 7.8: Strain energy evolution during rubber ball impact simulation.

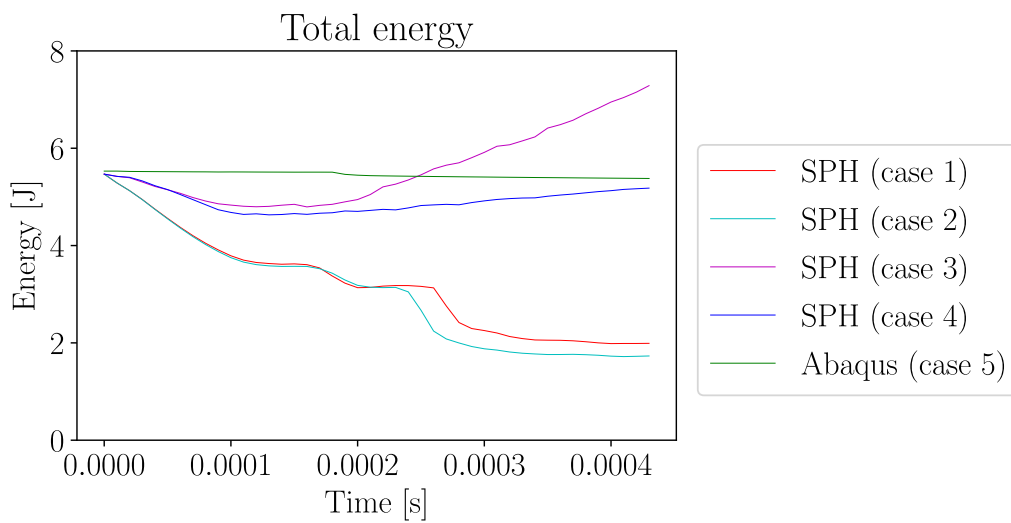


Figure 7.9: Total energy evolution during rubber ball impact simulation.

7.3 JOHNSON-COOK MODEL IMPLEMENTATION AND VALIDATION

In this section the integration of plasticity models with the radial return algorithm derived in chapter 3.5.4 is discussed. The implementation in `MFREE_IWF` is described and potential issues are outlined. A comparison to an explicit integration procedure based on an overstress-type law is performed. A 2D tensile test model with SPH is created and the results are compared to a FEM model solution of a commercial code, here Abaqus/Explicit.

7.3.1 Accuracy of Radial Return Projection

The implementation of the radial return projection algorithm is explained and three different methods for the determination of the required derivative are analysed.

7.3.1.1 Newton Method

A well known method for the iterative resolution is the Newton method which requires an analytical first derivative of the function $f(\Delta\lambda)$:

$$\Delta\lambda_{n+1} = \Delta\lambda_n - \frac{f(\Delta\lambda_n)}{f'(\Delta\lambda_n)} \quad (7.1)$$

Applied to (3.152) and changing $f()$ to $g()$ and using $\Delta\lambda$ instead of $\dot{\lambda}\Delta t$ the Newton method reads:

$$g(\Delta\lambda) = 0 = \|\underline{S}^{trial}\| - \sqrt{\frac{2}{3}}\sigma_y(\bar{\epsilon}_{pl}^{n+1}, \dot{\bar{\epsilon}}_{pl}^{n+1}, T) - \sqrt{\frac{3}{2}}(2G \cdot \Delta\lambda) \quad (7.2)$$

The equivalent plastic strain increment is derived from inserting (3.130) into (3.112) and using (3.131):

$$\Delta\bar{\epsilon}^{pl} = \frac{2}{\sqrt{3}}\sqrt{\frac{1}{2}\left((\Delta\epsilon_{xx}^{pl})^2 + (\Delta\epsilon_{yy}^{pl})^2 + (\Delta\epsilon_{zz}^{pl})^2\right) + (\Delta\epsilon_{xy}^{pl})^2 + (\Delta\epsilon_{xz}^{pl})^2 + (\Delta\epsilon_{yz}^{pl})^2} \quad (7.3)$$

$$= \frac{2}{\sqrt{3}}\sqrt{\Delta\lambda^2\frac{3}{2}\frac{1}{\|\underline{S}\|^2} \cdot \underbrace{\frac{1}{2}(S_{xx}^2 + S_{yy}^2 + S_{zz}^2) + S_{xy}^2 + S_{xz}^2 + S_{yz}^2}_{=J_2}} \quad (7.4)$$

$$= \frac{2}{\sqrt{3}}\sqrt{\Delta\lambda^2\frac{3}{2}\frac{1}{\|\underline{S}\|^2} \cdot J_2} = \frac{2}{\sqrt{3}}\sqrt{\Delta\lambda^2\frac{3}{2}\frac{1}{\sqrt{2}J_2^2} \cdot J_2} \quad (7.5)$$

$$= \frac{2}{\sqrt{3}}\sqrt{\Delta\lambda^2\frac{3}{2} \cdot \frac{1}{2}} = \frac{2}{\sqrt{3}}\sqrt{\Delta\lambda^2\frac{3}{4}} = \sqrt{\Delta\lambda^2\frac{4}{3} \cdot \frac{3}{4}} \quad (7.6)$$

$$= \Delta\lambda \quad (7.7)$$

The updated plastic strain and strain rate are then:

$$\varepsilon_{pl}^{n+1} = \varepsilon_{pl}^n + \Delta t \dot{\lambda} = \varepsilon_{pl}^n + \Delta \lambda_{n+1} \quad (7.8)$$

$$\dot{\varepsilon}_{pl}^{n+1} = \dot{\lambda} = \frac{\Delta \lambda^{n+1}}{\Delta t} \quad (7.9)$$

The first derivative of $g(\Delta \lambda)$ is computed with the chain rule:

$$\frac{\partial g(\Delta \lambda_n)}{\partial \Delta \lambda} = -\sqrt{\frac{3}{2}} 2G - \sqrt{\frac{2}{3}} \left[\frac{\partial \sigma_y}{\partial \varepsilon_{pl}^{n+1}} \frac{\partial \varepsilon_{pl}^{n+1}}{\partial \Delta \lambda} + \frac{\partial \sigma_y}{\partial \dot{\varepsilon}_{pl}^{n+1}} \frac{\partial \dot{\varepsilon}_{pl}^{n+1}}{\partial \Delta \lambda} \right] \quad (7.10)$$

The derivatives of the plastic strain and plastic strain rate are:

$$\frac{\partial \varepsilon_{pl}^{n+1}}{\partial \Delta \lambda} = 1 \quad (7.11)$$

and

$$\frac{\partial \dot{\varepsilon}_{pl}^{n+1}}{\partial \Delta \lambda} = \frac{1}{\Delta t} \quad (7.12)$$

The derivatives of the yield stress are:

$$\frac{\partial \sigma_y}{\partial \varepsilon_{pl}} = \left(n \cdot B \cdot (\varepsilon_{pl})^{(n-1)} \right) \left(1 + C \cdot \ln \left(\frac{\dot{\varepsilon}_{pl}}{\dot{\varepsilon}_{pl}^0} \right) \right) \left(1 - \left(\frac{T - T_{ref}}{T_f - T_{ref}} \right)^m \right) \quad (7.13)$$

and

$$\frac{\partial \sigma_y}{\partial \dot{\varepsilon}_{pl}} = \left(A + B \cdot (\varepsilon_{pl})^n \right) \left(\frac{C}{\dot{\varepsilon}_{pl}} \right) \left(1 - \left(\frac{T - T_{ref}}{T_f - T_{ref}} \right)^m \right) \quad (7.14)$$

combining the equation (7.10) with (7.11), (7.12), (7.13) and (7.14) one arrives at:

$$\begin{aligned} \frac{\partial g(\Delta \lambda_n)}{\partial \Delta \lambda} = & -\sqrt{\frac{3}{2}} 2G - \sqrt{\frac{2}{3}} \left[\left(n \cdot B \cdot (\varepsilon_{pl})^{(n-1)} \right) \left(1 + C \cdot \ln \left(\frac{\dot{\varepsilon}_{pl}}{\dot{\varepsilon}_{pl}^0} \right) \right) \left(1 - \left(\frac{T - T_{ref}}{T_f - T_{ref}} \right)^m \right) \right. \\ & \left. + \left(A + B \cdot (\varepsilon_{pl})^n \right) \left(\frac{C}{\dot{\varepsilon}_{pl}} \right) \left(1 - \left(\frac{T - T_{ref}}{T_f - T_{ref}} \right)^m \right) \cdot \frac{1}{\Delta t} \right] \end{aligned} \quad (7.15)$$

7.3.1.2 Secant Method

If the first derivative of $f(\Delta\lambda)$ cannot be composed analytically or is computationally inefficient a better alternative is the secant method, see also figure 7.10.

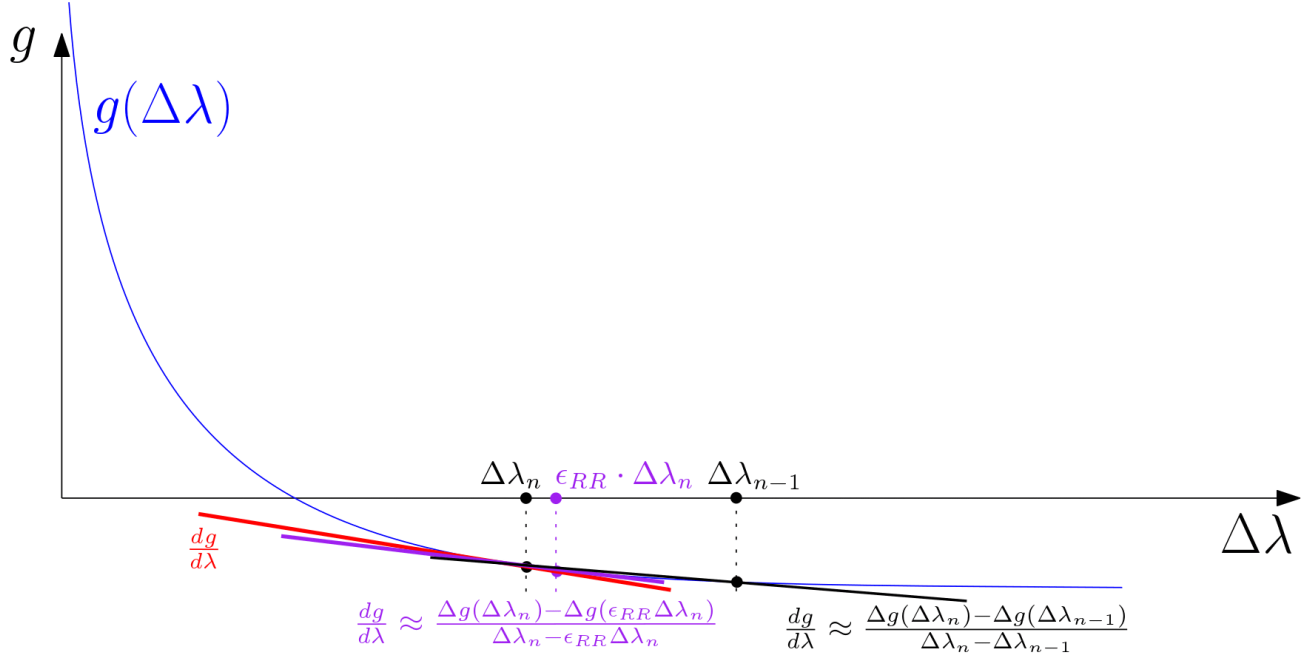


Figure 7.10: Radial return projection: exact tangent (red) $\frac{dg}{d\lambda}$ and approximations with secant method using $\Delta\lambda_{n-1}$ from former iteration (black) and secant method with support point in the close vicinity of $\Delta\lambda_n$ (purple).

The iterative procedure is the same as in the Newton method (7.1) but the derivative $f(\Delta\lambda)$ is replaced by a difference quotient computed with the function value from the last and the current increment:

$$f'(\Delta\lambda_n) \approx \frac{f(\Delta\lambda_n) - f(\Delta\lambda_{n-1})}{\Delta\lambda_n - \Delta\lambda_{n-1}} \quad (7.16)$$

inserting into (7.1) yields:

$$\Delta\lambda_{n+1} = \Delta\lambda_n - f(\Delta\lambda_n) \frac{\Delta\lambda_n - \Delta\lambda_{n-1}}{f(\Delta\lambda_n) - f(\Delta\lambda_{n-1})} \quad \text{Secant A} \quad (7.17)$$

This method is named *Secant A* in the following. The accuracy of the approximation of the first derivative in (7.16) can be poor for larger $\Delta\lambda_n - \Delta\lambda_{n-1}$ and therefore convergency of (7.17) can be increased by using:

$$f'(\Delta\lambda_n) \approx \frac{f(\Delta\lambda_n) - f(\epsilon_{RR} \cdot \Delta\lambda_n)}{\Delta\lambda_n - \epsilon_{RR} \cdot \Delta\lambda_n} \quad (7.18)$$

which gives a better approximation of the derivative for small ϵ_{RR} and results in the modified iterative procedure named *Secant B*:

$$\Delta\lambda_{n+1} = \Delta\lambda_n - f(\Delta\lambda_n) \frac{\Delta\lambda_n - \epsilon_{RR} \cdot \Delta\lambda_n}{f(\Delta\lambda_n) - f(\epsilon_{RR} \cdot \Delta\lambda_n)} \quad \text{Secant B} \quad (7.19)$$

The analytical derivative of $dg/d\lambda$ and its approximation with the secant method (7.19) with $\epsilon_{RR} = 1.01$ is shown in figure 7.11 and its obvious that both methods deliver the same results.

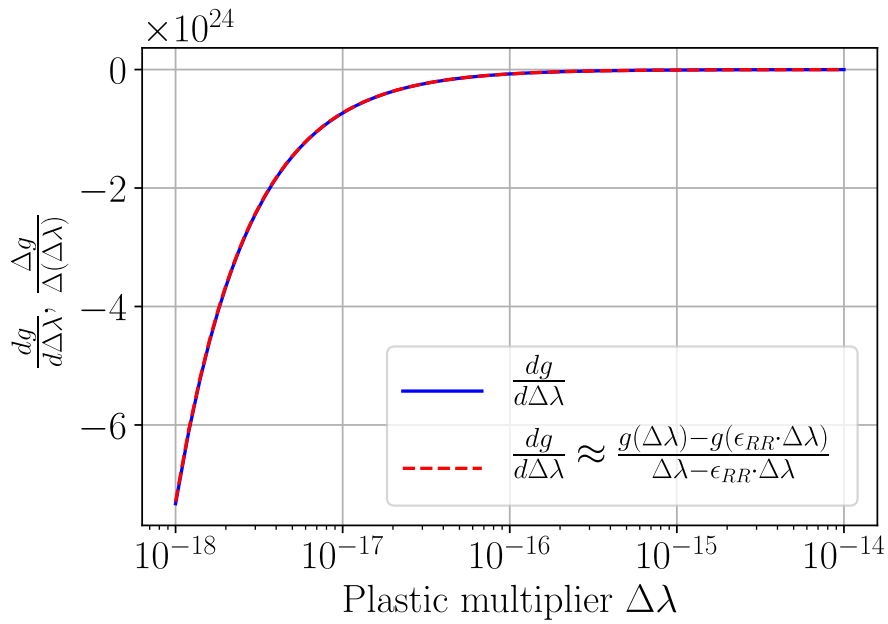


Figure 7.11: Analytical derivative of $dg/d\Delta\lambda$ and approximation with secant method.

7.3.2 Performance Newton and Secant Method

Here the performance of the iterative methods in equations (7.1), (7.17) and (7.19) is investigated. Different trials stresses $||S^{trial}||$ are given and different start values for the initial guess of $\Delta\lambda$ are tested. For the secant methods $\epsilon_{RR} = 1.01$ was used. The simulations were performed with PYTHON/NUMPY [86]. The radial return tests were conducted with the JC flow stress model with material parameters for Steel 4340 [73] which are given in table 7.3, other required constants are summarized in table 7.2.

Quantity	Symbol	Equation	Value
Homologous temperature	T^*	(3.96)	0.2
Young's modulus	E	-	200GPa
Poisson	ν	-	0.29
Shear modulus	G	$\frac{E}{2 \cdot (1+\nu)}$	77.5GPa
Time increment	Δt	-	$10^{-8}s$
Trial stress	$ \underline{S}^{trial} $	-	[638MPa...1274MPa], 30 steps
Initial plastic multiplier	$\Delta\lambda_{n=0}$	-	$[10^{-15}...10^{-3}]$, 30 steps
Tolerance plastic multiplier	λ_{tol}	$abs(\Delta\lambda_n - \Delta\lambda_{n-1})$	10^{-16}

Table 7.2: Quantities used in the radial return performance computations.

A	B	C	m	n	$\dot{\epsilon}_{pl}^0$	T_{ref}	T_f	Source
[MPa]	[MPa]	[-]	[-]	[-]	[s ⁻¹]	[K]	[K]	
792.0	510.0	0.014	1.03	0.26	1.0	273.0	1793.0	[73]

Table 7.3: Johnson Cook flow stress model parameters for Steel 4340.

Figure 7.12 shows the development of $\Delta\lambda$ during the iterations. A convergence criterion $|\Delta\lambda_n - \Delta\lambda_{n-1}| < \lambda_{tol}$ is used to terminate the iterative procedure. The Newton method performs best requiring 11 iterations until the convergence criterion is met while the two secant methods required 15 iterations each.

In another test the trial stress and the initial plastic multiplier are varied and the number of iterations required is recorded for the three methods. Figure (7.13) shows graphically the numbers of iteration until convergency for the Newton-method (7.1), the *Secant A* method (7.17) and the *Secant B* method (7.19). The color bar indicates the number of iterations until the coverage criterion is met. The *Newton*-method needs slightly less iterations than the two secant methods to the expense of much more arithmetics required to compute the gradient. The two secant methods perform very similar.

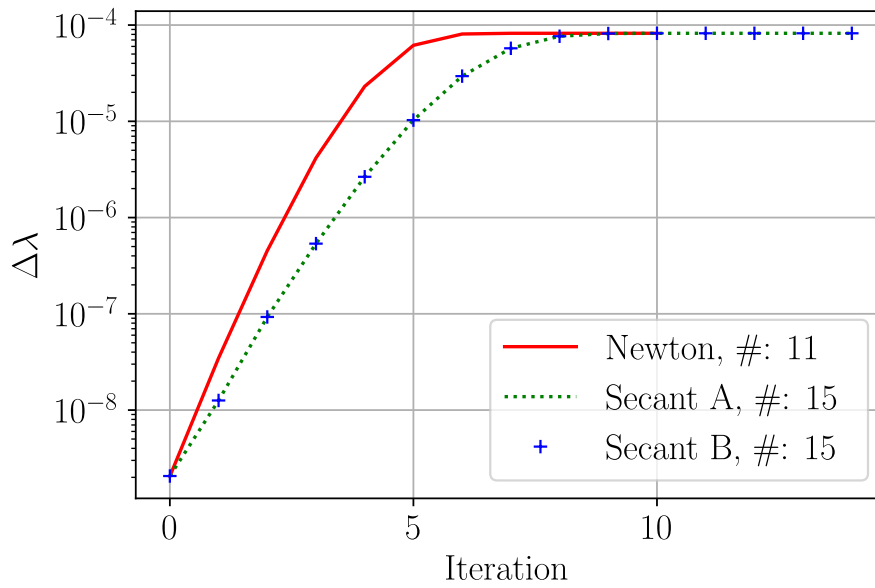


Figure 7.12: Radial return iteration: $\Delta\lambda$ versus number of iterations for the Newton method and the two secant methods.

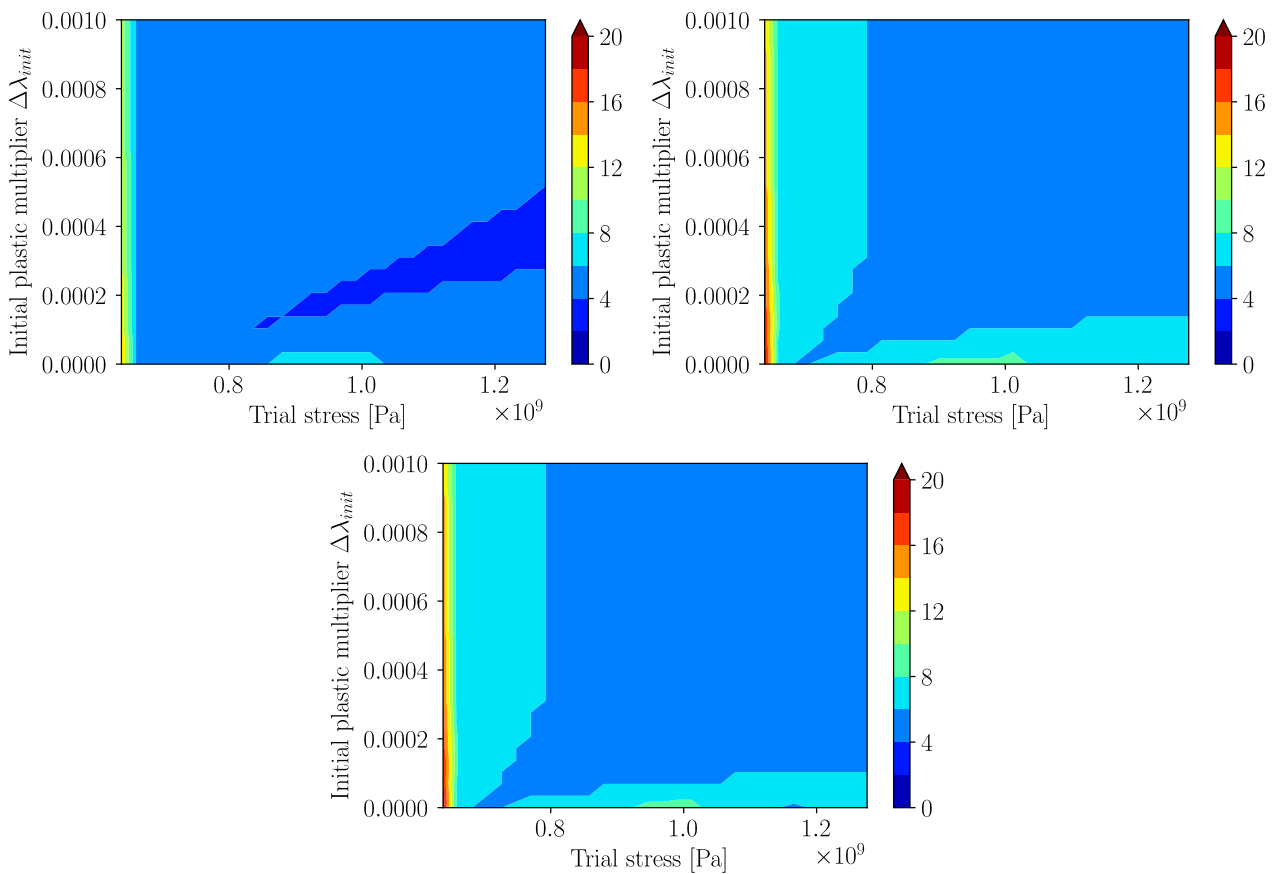


Figure 7.13: Radial return projection with *Newton* (top left), *Secant A* (top right) and *Secant B* (bottom) method: the color indicates the number of iterations required for the determination of the plastic multiplier depending on the trial stress and the initial plastic multiplier. The *Newton* method requires slightly fewer iterations to convergency than *Secant A* and *Secant B* which are very similar.

Sometimes the iterations predicted negative $\Delta\lambda_{n+1}$ which can happen for example for too large initial values of $\Delta\lambda_{n=0}$. A schematics of this issue is shown in figure 7.14. A useful workaround for this problem is to set $\Delta\lambda_{n+1} = 0.1 \cdot \Delta\lambda_n$ when a negative $\Delta\lambda_{n+1}$ is predicted.

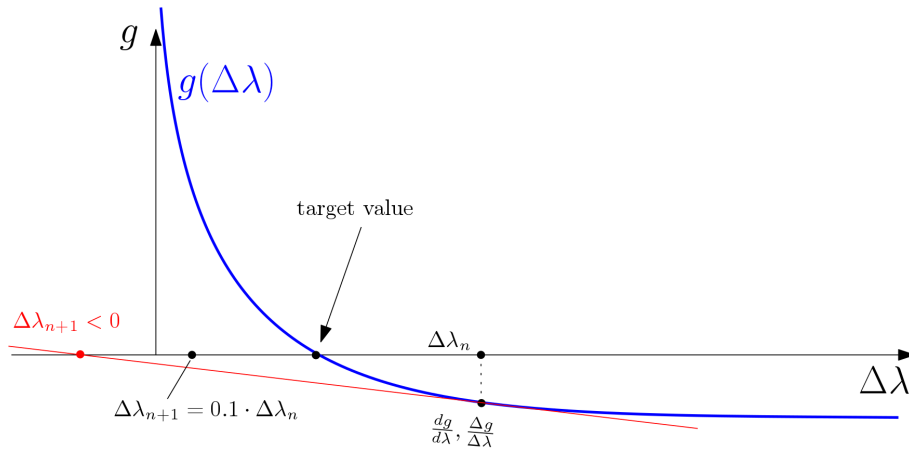


Figure 7.14: Radial return projection: treatment of negative lambda prediction

The following observations are made:

- $\Delta\lambda_n$ can be predicted even with negative sign during iteration with high initial guess for $\Delta\lambda_{n=0}$
- the Newton method needs usually less iterations from the initial guess $\Delta\lambda_{n=0}$ towards the region of the final $\Delta\lambda$
- the final $\Delta\lambda_n$ are predicted almost exactly the same for each of the iterative methods, there are only small differences in the very last digits after the comma - if at all
- the multiplication of very small and very large numbers in the analytical expression for the derivative of $g(\Delta\lambda)$ can introduce errors related to the computational accuracy of floating point numbers [72]
- when the trial stress $\underline{\underline{S}}^{trial}$ only slightly exceeds the yield stress, very small $\Delta\lambda$ are predicted. This can lead to accuracy problems since $\Delta\lambda$ can come close to the relative error in rounding of floating point numbers which is expressed by the machine epsilon [98]. For example single precision (32bit) numbers have a machine epsilon of $5.96 \cdot 10^{-8}$ and double precision numbers have a machine epsilon of $1.11 \cdot 10^{-16}$. Especially for small time steps the use of double precision numbers should be envisaged in the radial return algorithm which is especially important for the use on the GPU.

Another problem that can occur is when the plastic strain rate becomes small that $\dot{\epsilon}_{pl} \leq \epsilon_{pl}^0$ which troubles the strain rate dependent term f_{rate} of the JC flow stress leading to softening of the flow stress. A remedy is described in UINTAH [78] where a modification for the strain rate dependent term f_{rate} is introduced:

$$f_{rate} = \begin{cases} 1.0 + \left(\frac{\dot{\epsilon}_{pl}}{\dot{\epsilon}_{pl}^0}\right)^C, & \text{for } \frac{\dot{\epsilon}_{pl}}{\dot{\epsilon}_{pl}^0} < 1 & \text{UINTAH modification} \\ 1.0 + C \cdot \ln\left(\frac{\dot{\epsilon}_{pl}}{\dot{\epsilon}_{pl}^0}\right), & \text{for } \frac{\dot{\epsilon}_{pl}}{\dot{\epsilon}_{pl}^0} \geq 1 & \text{JC classic} \end{cases} \quad (7.20)$$

The difference between original and modified strain rate term is shown in figure 7.15 where the inadmissible reduction of the original strain rate term is visible.

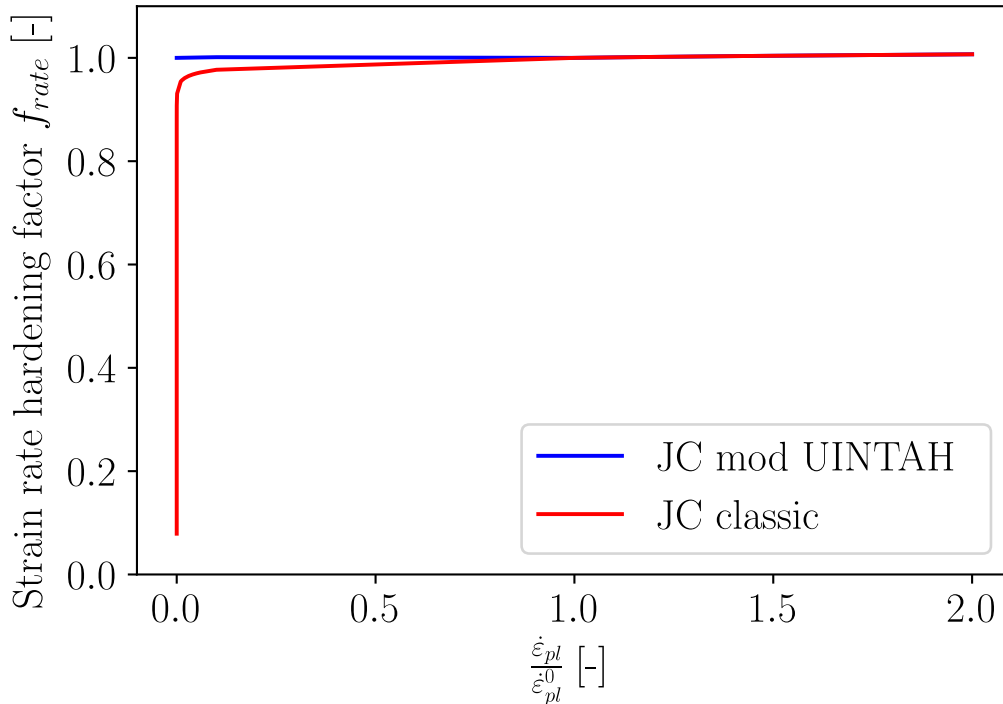


Figure 7.15: Original and modified JC strain rate term

From these tests no clear winner is evaluated. While the Newton method requires slightly fewer iterations the two secant methods require less computational effort. This can be of importance for more complex material models and therefore the secant method is used in all simulations unless stated differently.

7.3.3 Integration of the Plasticity Model with Implicit and Explicit Method

In explicit dynamic simulations small time steps occur and an Euler explicit integration of the equations can be sufficient [273]. For this reason a test case is constructed to investigate the performance of both methods, implicit with radial return and explicit, and a comparison is shown to a FEM solution of the same problem. For the Euler explicit integration the JC flow stress model is casted into the overstress type [187] of flow stress by reshaping (3.95) for the plastic strain rate:

$$\dot{\varepsilon}_{pl}(\sigma_{eq}, \varepsilon_{pl}, T) = \exp \left(\frac{1}{C} \left(\underbrace{\frac{\sigma_{eq}}{(A + B \cdot \varepsilon_{pl}^n) \left(1 - \frac{T - T_{ref}}{T_f - T_{ref}}\right)^m}}_{\text{Overstress ratio } R} - 1 \right) \right) \cdot \dot{\varepsilon}_{pl}^0 \quad (7.21)$$

where σ_{eq} is the current equivalent stress according to von Mises (3.110). With an Euler explicit scheme the plastic increment becomes for $R > 1.0$ with (7.21):

$$\varepsilon_{pl}^{t_{n+1}} = \dot{\varepsilon}_{pl}^{t_n}(\sigma_{eq}, \varepsilon_{pl}^{t_n}, (T^*)^{t_n}) \cdot \Delta t \quad (7.22)$$

First, a comparison of the implicit and explicit Euler method is performed with a variation of the overstress ratio R and resulting plastic strain increments for a single increment with a time step of $\Delta t = 1 \cdot 10^{-9}s$. The implicit methods give the same results and the explicit integration gives very similar results for small overstress ratios R .

A small 2D plane strain tension test case is constructed with 900 particles (30x30) using an Euler explicit integration as well as Euler implicit integration with the radial return algorithm. For validation purposes a similar FE model is constructed with Abaqus/Explicit with 900 (30x30) elements of the type CPE4R with 961 nodes. Material parameters for Steel 4340 are used, see tables 7.2 and 7.3. The initial temperatures were set to $T_{init} = 273.15K$ and a constant velocity of $v_x = 50m/s$ is applied to the right boundary of the model, see also figure 7.17. All models consider plastic dissipation into heat with a Taylor-Quinney coefficient of $f_{TQ} = 90\%$. The SPH models use XSPH ($\epsilon_{XSPH} = 0.5$), artificial stresses ($\epsilon_{as} = 0.3, n_{Stress} = 4$) and viscosity ($\alpha_{av} = 1, \beta_{av} = 1, \eta_{av} = 0.1$). In Abaqus default parameters for the bulk viscosity ($b_1 = 0.06, b_2 = 1.2$) are used. For overstress ratios $R \leq 1$ no plastic straining occurs. All simulations are run with a constant time step of $\Delta t = 2 \cdot 10^{-6}s$.

The main results summary is provided with table 7.4. Taking the Abaqus FEM results as a baseline one can see that the SPH simulation with explicit integration of the plasticity model slightly overpredicts the maximum temperature, while the SPH with implicit plasticity model integration predicts 15% lower plastic strains and 32K lower temperatures. The pattern of the plastic strain fields, equivalent stresses and temperatures are very similar between the three models (figures 7.17, 7.18, 7.19, 7.20 and 7.21). The explicit integration of the plasticity model reduces the total simulation runtime by about 30% since no iteration loops for the determination of the plastic multiplier are required.

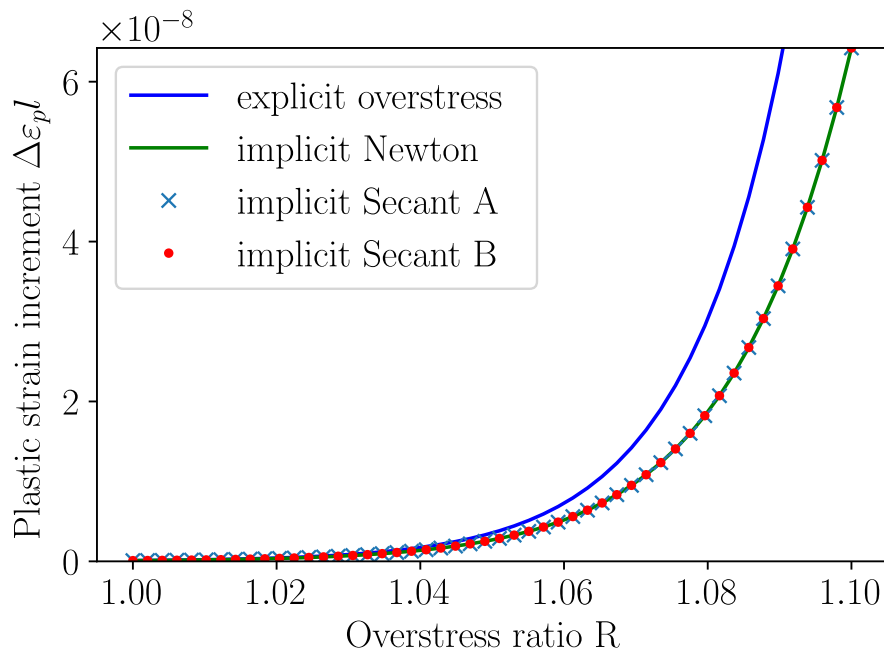


Figure 7.16: Comparison of explicit and implicit integration for a time increment of $\Delta t = 10^{-9}s$.

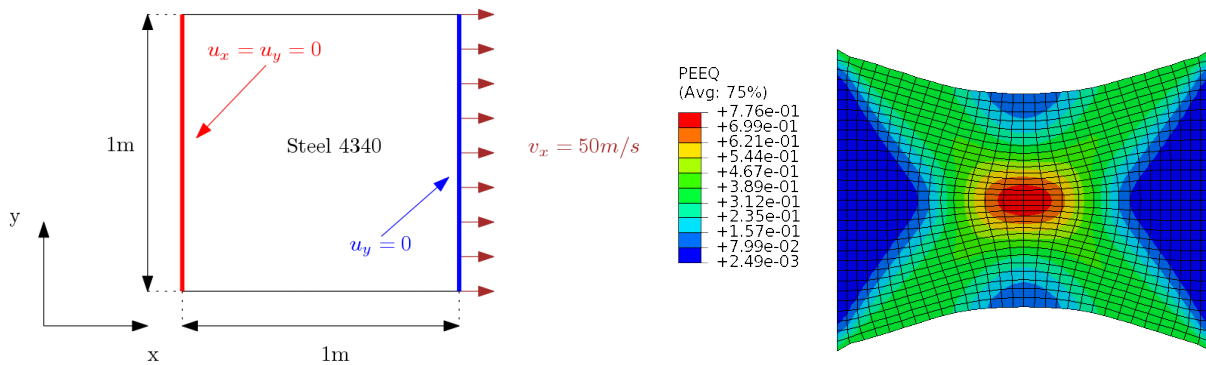


Figure 7.17: Tensile test geometry with boundary conditions (left) and Abaqus plastic strain field at time $t = 0.005s$ (right).

Case	Numerical model	Integration of plasticity model	$\bar{\epsilon}_{pl}^{max}$ [%]	σ_{eq}^{max} [GPa]	T_{max} [K]	Runtime [s]
1	SPH	Euler explicit	78	1.2	500	11
2	SPH	Euler implicit ($\lambda_{tol} = 10^{-6}$)	68	1.2	460	15
3	FEM	Euler implicit	78	1.2	492	4

Table 7.4: Main results of the three tensile test simulations.

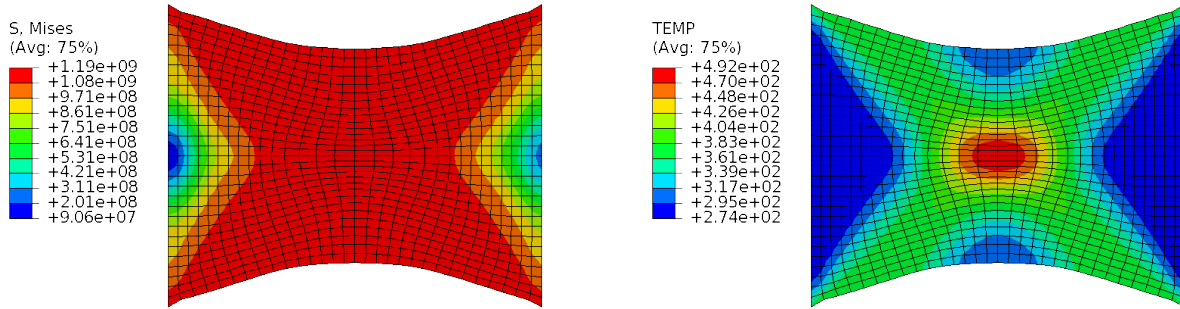


Figure 7.18: Abaqus von Mises equivalent stress field at time $t = 0.005s$ (left) and temperature field at time $t = 0.005s$ (right).

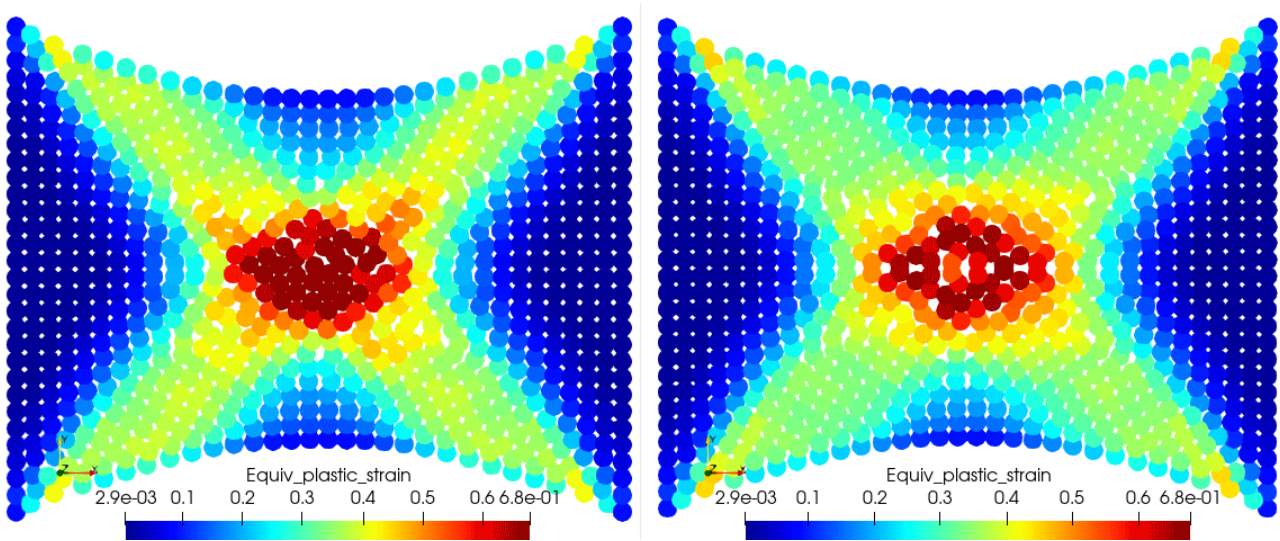


Figure 7.19: SPH plastic strain field at time $t = 0.005s$ for explicit (left) and implicit (right) integration of the plasticity model.

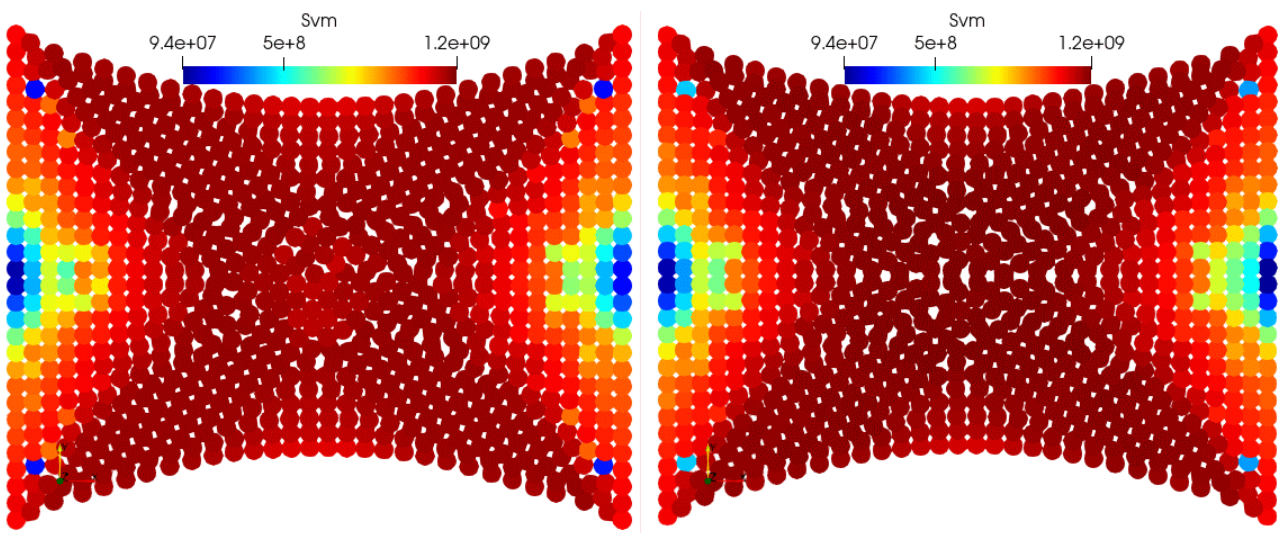


Figure 7.20: SPH von Mises equivalent stress field at time $t = 0.005s$ for explicit (left) and implicit (right) integration of the plasticity model.

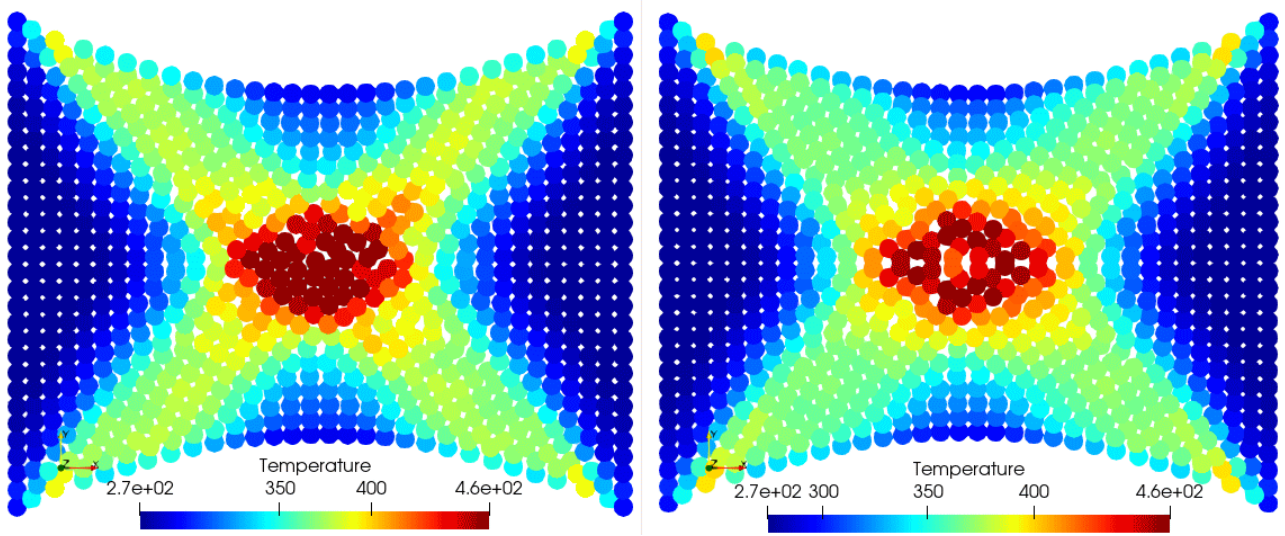


Figure 7.21: SPH temperature field at time $t = 0.005s$ for explicit (left) and implicit (right) integration of the plasticity model.

7.4 DAMAGE MODELLING

Damage modelling with damage initiation and evolution is implemented into the SPH-solver and test simulations are carried out which show some difficulties. These difficulties are analysed and solutions are proposed.

7.4.1 Johnson Cook Fracture Strain

A compact tension (CT) test specimen ASTM E647 [242] is simulated with the JC flow stress model, JC damage model and the Hillerborg [93] fictitious crack model. The geometry is shown left in figure 7.22. A JC flow stress model for Ti6Al4V is used with a JC fracture strain model with a linear accumulation of damage variable ω in the initiation phase until $\omega_{crit} = 1$ followed by an exponential rule for the damage variable D in the damage evolution phase. The damage is set to $D = 1$ when 99% of the critical energy release rate G_f is achieved, according to (3.171). The fracture toughness is $K_{1C} = 74.6 \text{MPa}\sqrt{\text{m}}$ [116, 189] which is converted with (3.169) into $G_f = 44501.7 \text{N/m}$. The initial crack length is $a_{init} = 0.2 \cdot W$ which is emulated by setting particle damage to $D = 1$ and $\omega = 1$ along the initial crack. This initial crack is shown on the right side of figure 7.22 with particles marked red. The load is transmitted through both lugs of the specimen using rigid circles with frictionless contact. The main dimension is chosen with $W = 50 \text{mm}$ and the initial crack length is $a = 0.2W$. Two test cases are simulated. In the first test case constant velocities are applied to the lugs with $v_{pull} = 20 \text{m/min}$ in the upper lug and $v_{pull} = -20 \text{m/min}$ in the lower lug. In the second load case load reversal is simulated, where the lugs are first pulled until $t_1 = 5 \cdot 10^{-5} \text{s}$ followed by $10 \cdot 10^{-5} \text{s}$ pushing into reverse direction until $t_2 = 15 \cdot 10^{-5} \text{s}$ and from then on reversing back to tension. Load charts for both cases are displayed in figure 7.23. In both simulations the specimen is pulled until rupture.

The model is discretised with 6144 particles. The dissipation heat into thermal energy is considered with a Taylor-Quinney coefficient of $\eta_{TQ} = 0.9$. Heat conduction is not modelled. The material parameter used for the JC flow stress model are provided in table 7.6, physical properties in table 7.5 and the damage model constants in table 7.7. A constant time step of $\Delta t = 3 \cdot 10^{-8} \text{s}$ is used.

E [GPa]	Poisson ν [-]	Density ρ [kg/m ³]	Specific heat capacity c_p [$\frac{\text{J}}{\text{kgK}}$]	Source
113.8	0.34	4430	580.0	[62]

Table 7.5: Physical properties of Ti6Al4V

A [MPa]	B [MPa]	C [-]	m [-]	n [-]	$\dot{\epsilon}_{pl}^0$ [s ⁻¹]	T_{ref} [K]	T_f [K]	Source
862.5	331.2	0.012	0.8	0.34	1.0	298.0	1878	[62]

Table 7.6: Johnson Cook flow stress model parameter Ti6Al4V

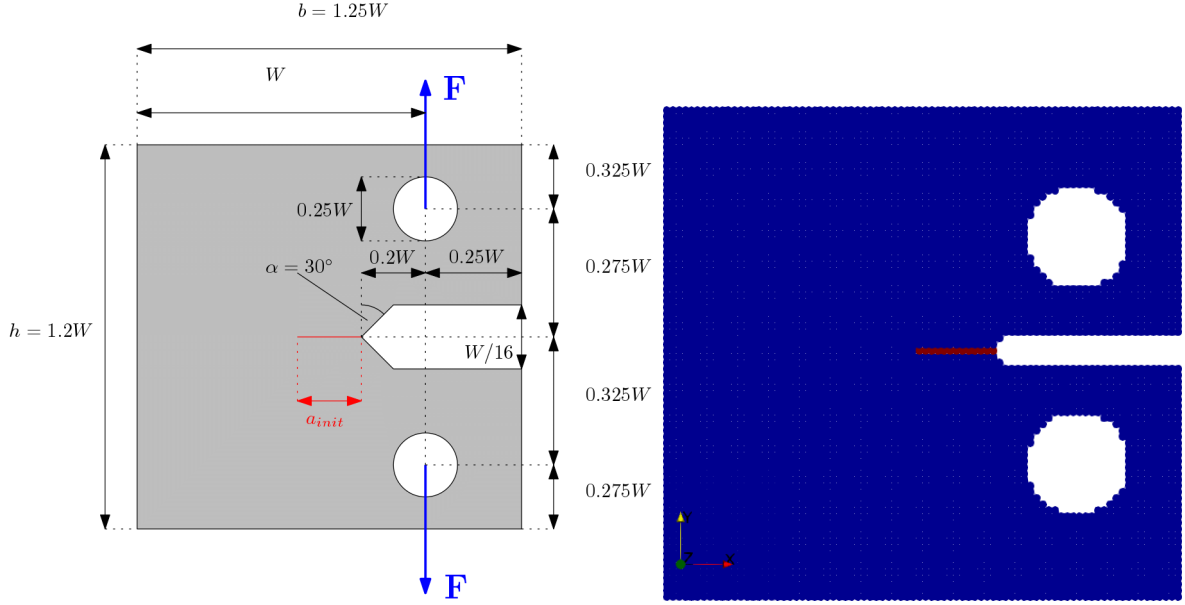


Figure 7.22: Dimensioned sketch of the ASTM E647 CT test specimen (left) and display of the particles (red) where the initial damage variables D and ω are set to full damage ($D = 1$ and $\omega = 1$) to simulate a pre-cracked specimen.

$D_1[-]$	$D_2[-]$	$D_3[-]$	$D_4[-]$	$D_5[-]$	$\dot{\epsilon}_{pl}^0[s^{-1}]$	$T_{ref}[K]$	$T_{melt}[K]$	Source
-0.09	0.27	0.48	0.014	3.87	1.0	273.0	1878.0	[73]

Table 7.7: Johnson Cook fracture strain equation parameter Ti6Al4V

7.4.2 Implementation Aspects of Damage Initiation and Evolution

The implementation of the damage evolution model is rather straightforward. A weak coupling of stress and damage update is used, where first the plasticity model is integrated and the damage variables are updated afterwards. A loop over all particles is conducted and in each time increment the damage increments computed with (3.165) are linearly accumulated with (3.166) until $\omega = \omega_{crit}$. For particles with initiated damage $\omega = \omega_{crit}$ the fictitious crack model is then applied to update the damage variable D . First the increment of D is computed for every particle with (3.168):

$$\Delta D^{n+1} = \frac{L_{char}^{n+1} \cdot \sigma_{eq}^{n+1} \cdot \Delta \bar{\epsilon}_{pl}^{n+1}}{G_{1C}} \quad (7.23)$$

with the characteristic "element" length L_{char}^{n+1} being the average "length" of a particle computed from the current particle volume as:

$$L_{char}^{n+1} = \sqrt{V_{particle}^{n+1}} \quad (7.24)$$

The damage increment is then linearly accumulated:

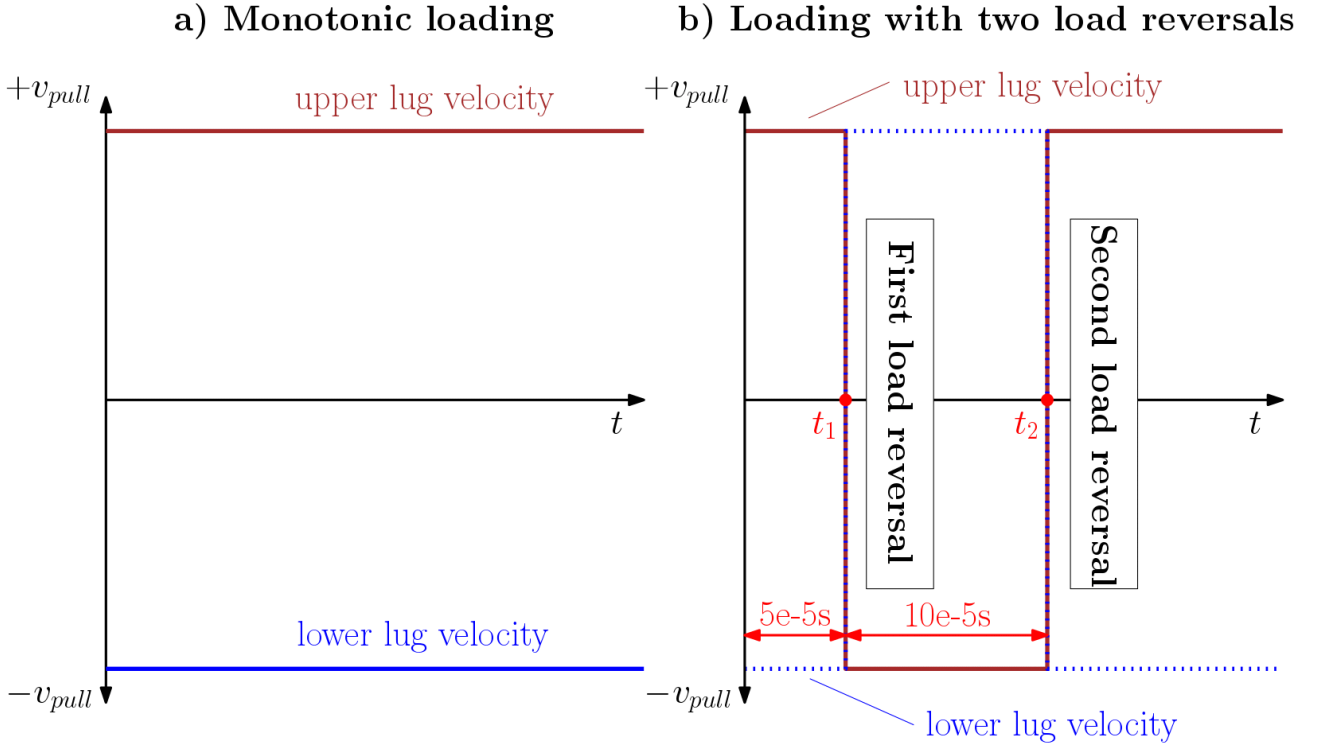


Figure 7.23: Boundary conditions applied to the lugs of the CT test specimen for the monotonic (left) and the load reversal simulation (right).

$$D^{n+1} = D^n + \Delta D^{n+1} \quad (7.25)$$

Second, the stress reduction factor is determined with:

$$D_{red}^{n+1} = \begin{cases} 1.0 - e^{-D^{n+1}} & , \text{ for } D^{n+1} < 0.99 \cdot G_{1C} \\ 0.0 & , \text{ for } D^{n+1} \geq 0.99 \cdot G_{1C} \end{cases} \quad (7.26)$$

The reduction factor D_{red} is then used to update the stress deviator:

$$\underline{\underline{S}}^{n+1} = \underline{\underline{S}}_{undamaged}^{n+1} \cdot D_{red}^{n+1} \quad (7.27)$$

and the hydrostatic stress:

$$p^{n+1} = \begin{cases} p_{undamaged}^{n+1} \cdot D_{red}^{n+1} & , \text{ for } p \leq 0 (\text{tension}) \\ p_{undamaged}^{n+1} & , \text{ for } p > 0 (\text{compression}) \end{cases} \quad (7.28)$$

Particles with $D^{n+1} > 0$ are treated specially in the plasticity model as it is assumed that ductile damage leads to pore / void formation which reduces the effective cross section in tension and therefore the deviatoric stress components are updated as:

$$\underline{\underline{S}}^{n+1} = \begin{cases} \underline{\underline{S}}_{undamaged}^{n+1} / D_{red}^{n+1} & , \text{ for } p^{n+1} < 0 \text{ (tension)} \\ \underline{\underline{S}}_{undamaged}^{n+1} & , \text{ for } p^{n+1} \geq 0, \text{ (compression)} \end{cases} \quad (7.29)$$

Fully damaged particles with $D_{red} = 0$ are not deleted but remain in the analysis which satisfies the continuity equation and still enables load transmission in compression.

7.4.2.1 Results

A results plot is shown at $t = 4.8 \cdot 10^{-5} \text{s}$ in figure 7.24. While particles with initial damage do not show a stress response a stress concentration is formed in the kerf as if there is no initial crack. This is unphysical as the stress concentration should be located at the tip of the initial crack. The distribution of the damage variable ω shows damage at the cracked edges due to the unphysical stress response.

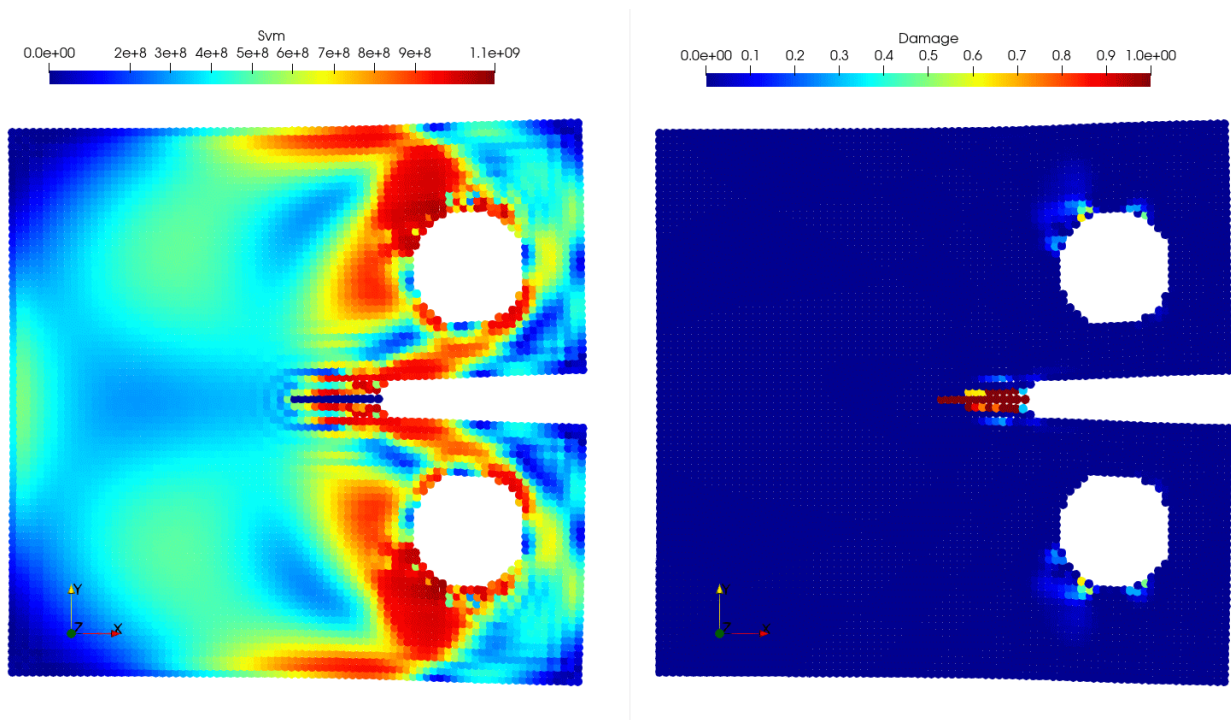


Figure 7.24: CT test specimen with equivalent stress field (left) and damage variable ω (right) at $t = 4.8 \cdot 10^{-5} \text{s}$. The crack remains closed upon loading which is incorrect. A correct opening requires modifications to the SPH particle interactions.

A deeper investigation revealed that the particle interactions performed for the continuum mechanics equations lead to the undesired behaviour with the initially fully damaged particles ($\omega = 1, D = 1$). Particle interactions are still active in:

- the computation of the velocity gradient $\underline{\underline{L}}$ (4.29) the velocities are considered from damaged particles - this prevents crack opening

- the computation of the stress derivative for the momentum equation (4.35) uses values from damaged particles
- the XSPH stabilizer (4.26) which averages velocities for all particles
- stabilization terms in the artificial viscosity (4.19) which act on interactions with damaged particles

For these reasons the four equations above are modified such that fully damaged particles participate only in compressive stress states when $p^{n+1} > 0$:

$$F_j = \begin{cases} 0, & \text{for } p_j < 0 \text{ and } D_{red,j} = 1.0 & \text{(no interaction)} \\ 1, & \text{for } p_j \geq 0 & \text{(full interaction)} \end{cases} \quad (7.30)$$

$$\underline{\underline{L}}_i = \sum_{j=1}^N (\underline{v}_j \cdot F_j - \underline{v}_i) \otimes \nabla W_{ij} \cdot \frac{m_j}{\varrho_j} \quad \text{(vel. gradient)} \quad (7.31)$$

$$\underline{\dot{v}}_i = \sum_{j=1}^N \left(\frac{\underline{\sigma}_j}{\varrho_j^2} + \frac{\underline{\sigma}_j \cdot F_j}{\varrho_j^2} + \Pi_{ij} \cdot \underline{\underline{I}} + \underline{\underline{\Theta}}_{ij} \right) \cdot \nabla W_{ij} \cdot m_i + \underline{b}_i \quad \text{(mom. equation)} \quad (7.32)$$

$$\frac{d\underline{u}_i}{dt} = \underline{v}_i + \epsilon^{XSPH} \cdot \sum_{j \in S} m_j \left(\frac{\underline{v}_j \cdot F_j}{\varrho_{ji}} \right) W_{ij} \quad \text{(XSPH)} \quad (7.33)$$

$$\mu_{ij} = \frac{h v_{ij} \cdot \underline{x}_{ij}}{\underline{x}_{ij}^2 + \eta_{av}^2} \cdot F_j \quad \text{(artif. viscosity)} \quad (7.34)$$

A sidemark: [249] came to similar conclusions for Total Lagrangian SPH but focused on the velocity difference \underline{v}_{ij} in the computation of the deformation gradient and its time derivative as well as the momentum equation. Stabilization terms like XSPH or artificial viscosity were not in their scope. The main difference to their work is that here particle interactions are deactivated only in tension but remain active in compression and modified particle interactions are limited here to the neighbourhood \underline{v}_j and do not concern \underline{v}_i as this approach did not prove success. Another problem is the visibility of particles due to the smoothing length - even if particles in the neighbourhood of particle i are fully damaged particles behind will still contribute to the kernel function and its derivative which is unphysical. A sketch of this problem is provided in figure 7.25.

A solution to this is the evaluation of a damage gradient which can be treated as the normal vector of a plane which is used to block interactions beyond. While this is possible for simple tension problems or fracture mode I crack openings, it becomes a tedious task when the crack surfaces shift laterally with respect to each other and then requires tracking of the newly forming surfaces upon separation.

7.4.2.2 Results with Modified Particle Interactions

With the modified particle interactions the equivalent stress and damage ω distribution behaves as expected - at the crack a typical stress field develops and the damage progresses at the crack tip only, see figure 7.26 for the same time $t = 4.8 \cdot 10^{-5}$ s. The crack runs through

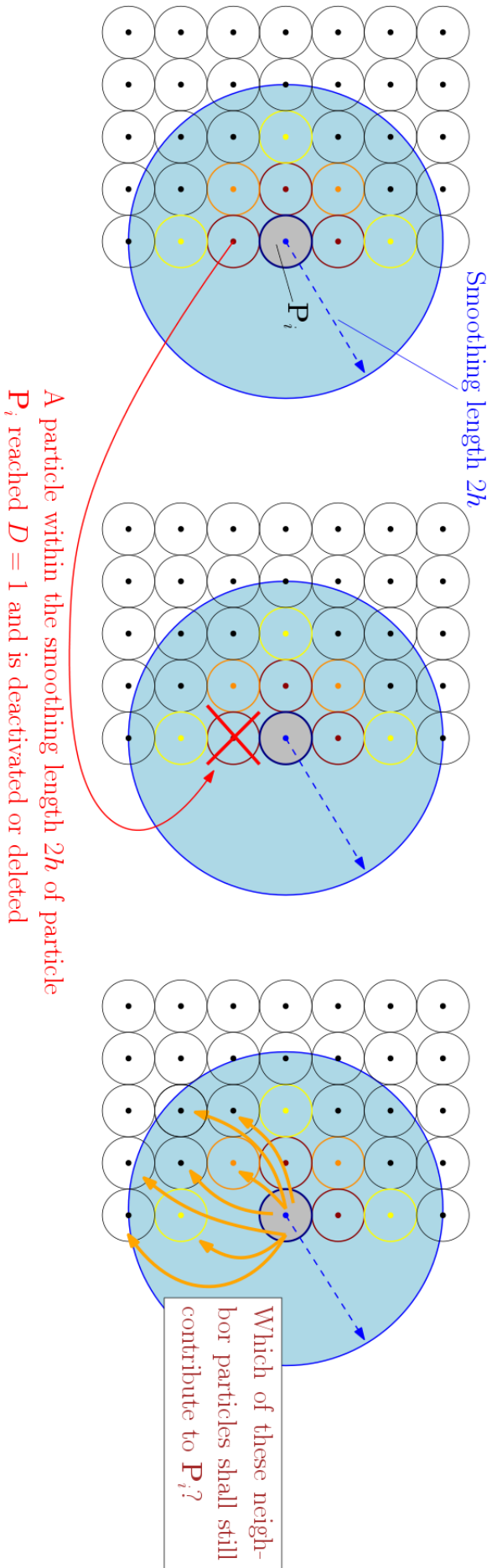


Figure 7.25: Visibility problem when particles are fully damaged.

the specimen and the stress concentration is always in front of the crack tip. The equivalent stress field and the distribution of the damage variable D are shown in figure 7.27. Motivated by the good results the simulation is now conducted with load reversals. The tensile load part in the beginning is not different to the purely tensile case. Upon load reversal the equivalent stress and hydrostatic pressure field as displayed in figure 7.28 is obtained during the compression phase at at $t = 1.32 \cdot 10^{-4}s$. While the damaged particles have equivalent stresses of $\sigma_{eq} = 0$, compressive hydrostatic pressures are still transmitted.

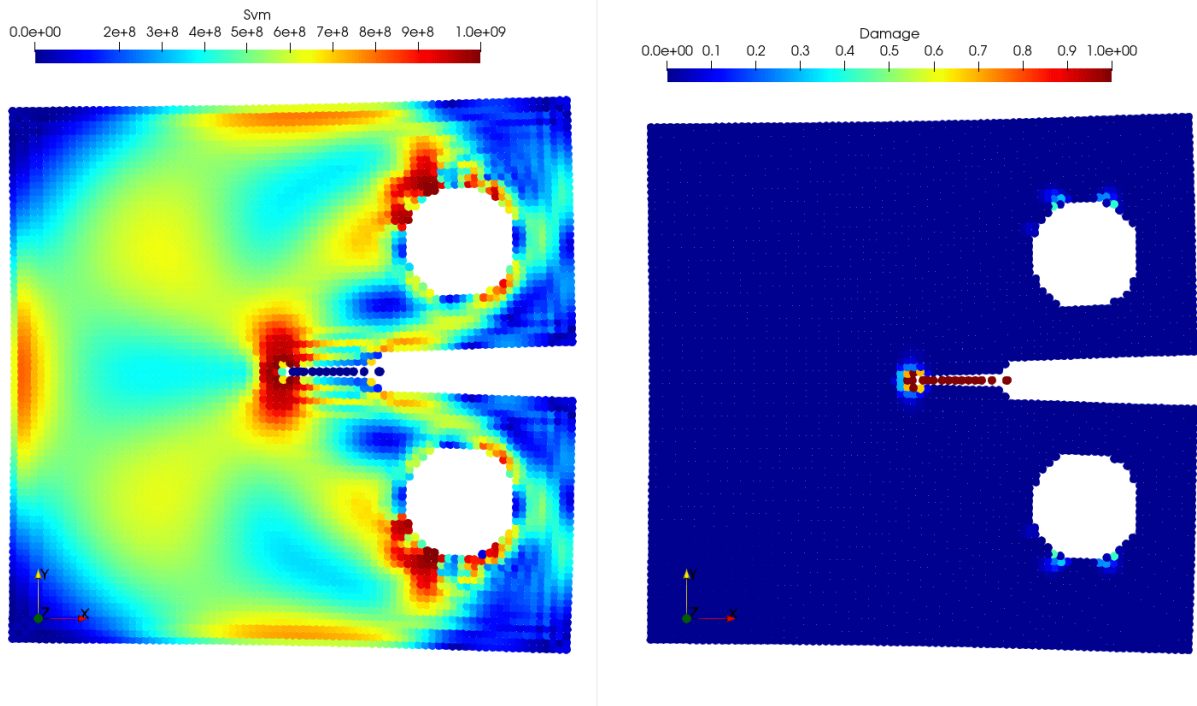


Figure 7.26: CT test specimen with equivalent stress field (left) and damage variable ω (right) at $t = 4.8 \cdot 10^{-5}s$.

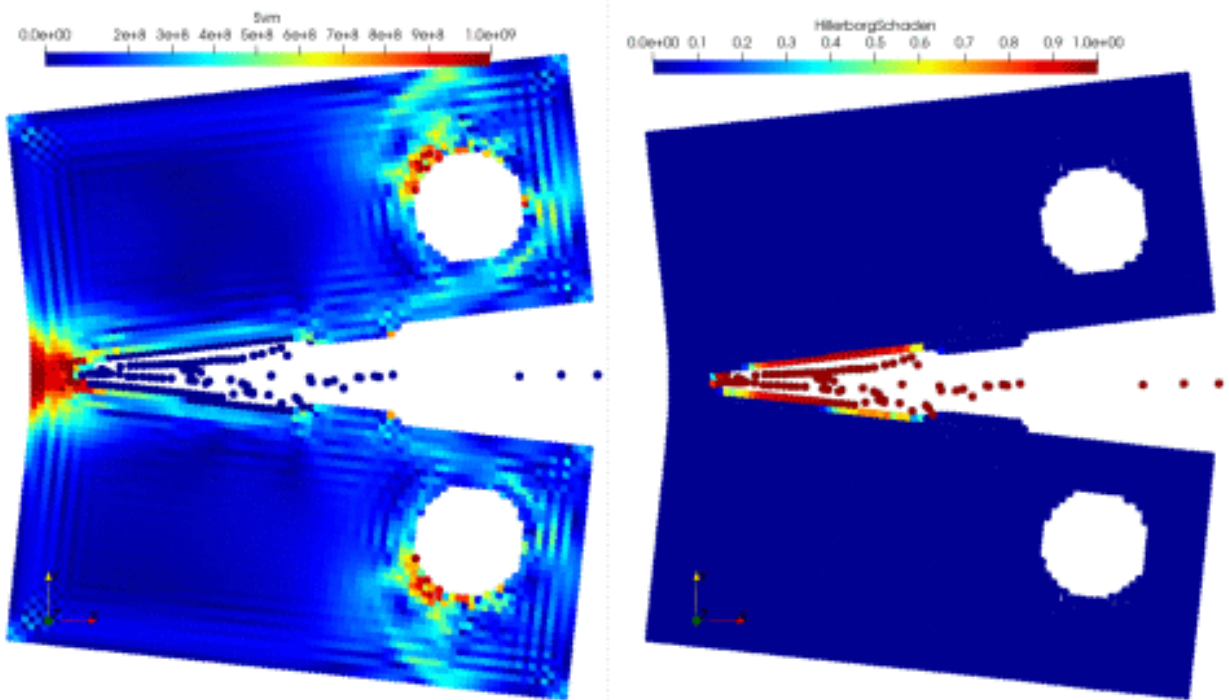


Figure 7.27: CT test specimen with equivalent stress field (left) and damage variable D (right) at $t = 2.52 \cdot 10^{-4}s$.

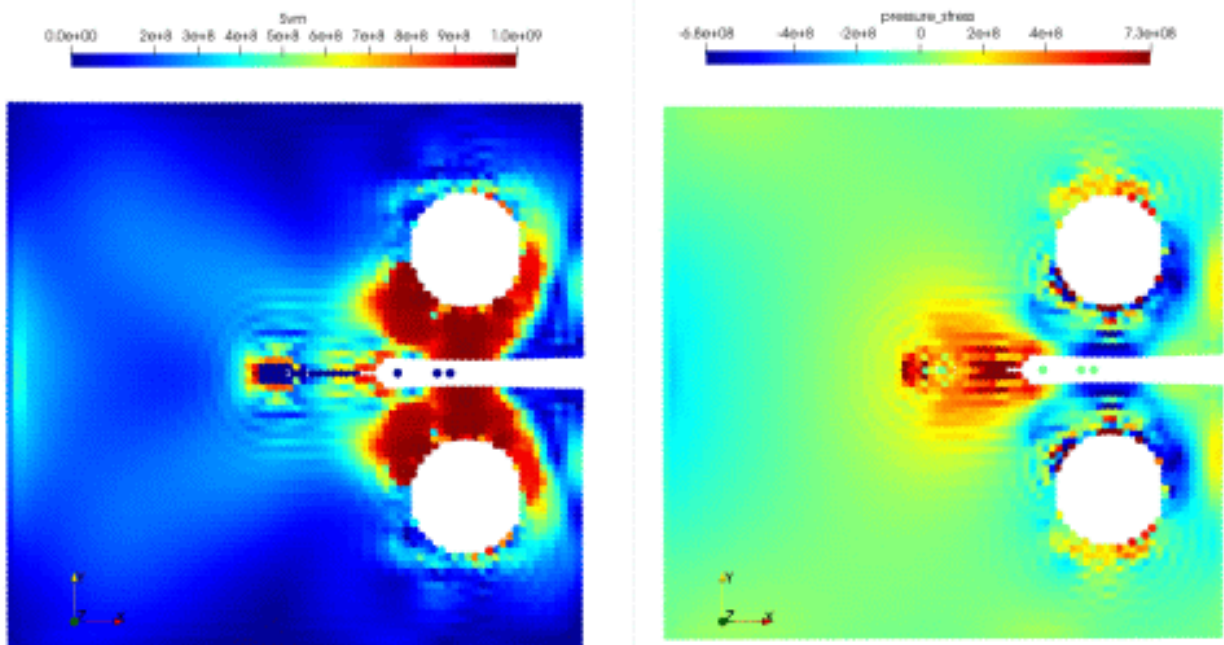


Figure 7.28: CT test specimen in the compression phase with equivalent stress field (left) and hydrostatic pressures p (right) at $t = 1.32 \cdot 10^{-4}s$. Note that compressive hydrostatic pressures are still transmitted with the fully damaged particles.

7.4.3 Modified Johnson Cook Fracture Strain Equation for 50SiB8

The relatively new material 50SiB8 [42, 207] was developed by Swiss Steel[©] as a lead free alternative for classical free cutting steels, e.g. 11SMnPb30 and 16MnCrS5Pb. The development became necessary as regulatory requirements have tightened and in future may ban vehicle components containing heavy metals, such as lead [53]. The idea is to exchange lead by graphite inclusions in order to keep the good machinability of free cuttings steels. Experiments [225] including quasi-static tension, SHTB and SHPB have been conducted to determine the material parameters [7, 69, 112] of this material for machining simulations. It was found that 50SiB8 shows a tendency to blue-brittleness at temperatures around 600°C where the fracture strains are reduced in comparison to smaller and higher temperatures. For this reason a modified fracture strain model based on the Johnson-Cook fracture strain (3.165) was proposed by [69] to consider the blue-brittleness. Instead of the original temperature term of the JC fracture strain equation this model uses a fourth order polynomial for the description of the fracture strain reduction:

$$\bar{\epsilon}^f = \left(D_1 + D_2 e^{D_3 \eta} \right) \left(1 + D_4 \cdot \ln \left(\frac{\dot{\epsilon}_{pl}}{\dot{\epsilon}_{pl}^0} \right) \right) \cdot T_{term} \quad (7.35)$$

$$T_{term} = \max \left(\left(1 + D_5 T^* + D_6 (T^*)^2 + D_7 (T^*)^3 + D_8 (T^*)^4 \right), 2.5 \right) \quad (7.36)$$

where $D_1 - D_4$ are the constants of the classic JC fracture strain equation and $D_5 - D_8$ are four new material parameters. The experimental temperature dependency of the fracture strain is shown in figure 7.29 together with the fourth order polynomial fit of the modified temperature term.

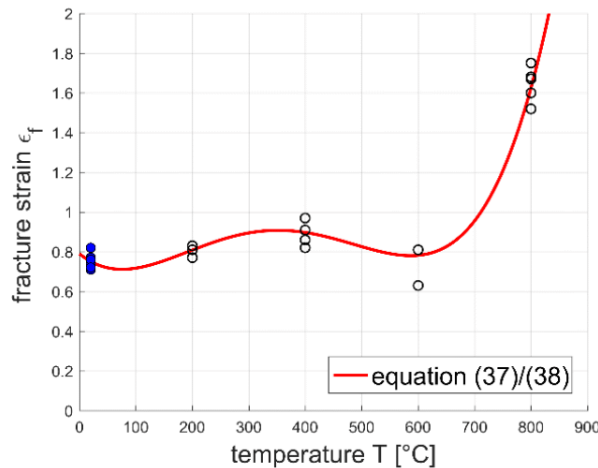


Figure 7.29: Experimental temperature dependency of the fracture strain and polynomial fit (red curve) of the temperature term in the modified JC fracture strain equation, from [69].

In [69, 112] JC flow stress and JC fracture strain model parameters were derived and successfully applied in numerical recalculations of the SHTB experiments at different strain

rates and temperatures. In the following one of these simulations ($T = 600^{\circ}\text{C}$, $\dot{\epsilon} = 900/\text{s}$) is repeated with an SPH model of the SHTB-test and compared to FEM and experimental results from [69]. The damage ω is linearly accumulated and upon reaching a damage of $\omega_{crit} = 1$ corresponding elements/particles are deleted from the analysis. The FEM model of the SHTB-test is based on [112] where the geometry of the SHTB-test specimen was created in ABAQUS/CAE according to the SHTB-test specimen drawing from figure 7.29. The FEM model is meshed with C3D8R elements and consists of 14032 elements with 16154 nodes. A picture of the mesh is provided with figure 7.31 together with the nodes where the boundary conditions are applied. The classic and modified fracture strain equations are implemented in an Abaqus user subroutine VUMAT for explicit analyses together with the JC flow stress model using the SECANT B method from (7.19) using $\epsilon = 0.01$. The source code is supplied in 11.2. The simulations are carried out with Abaqus 6-14.1 and the explicit solver.

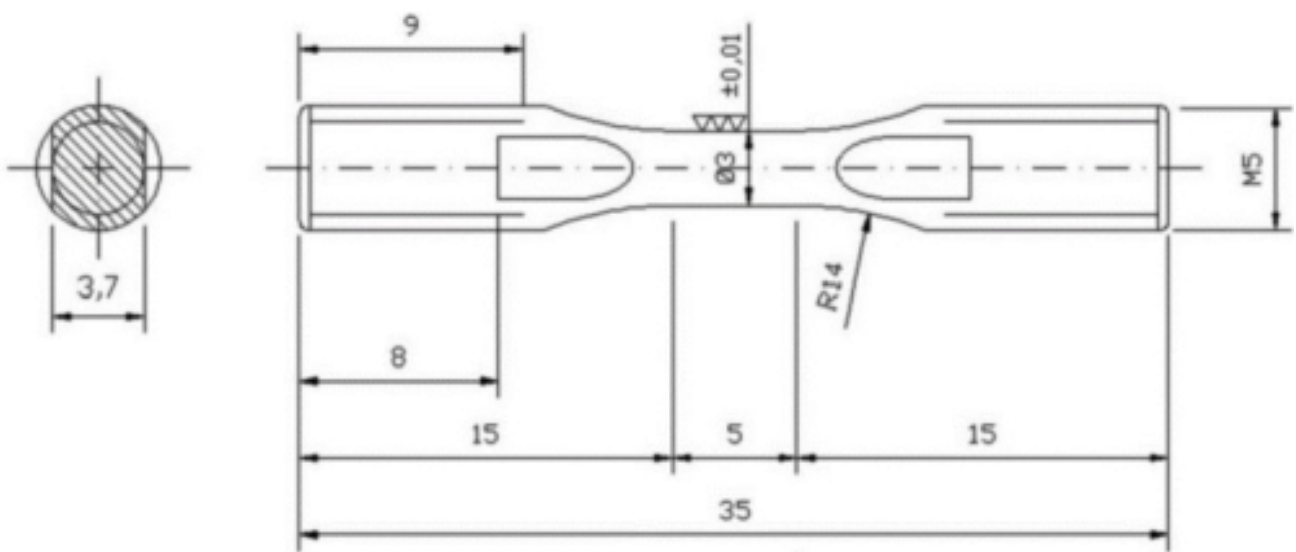


Figure 7.30: Drawing of the SHTB-test specimen, from [225].

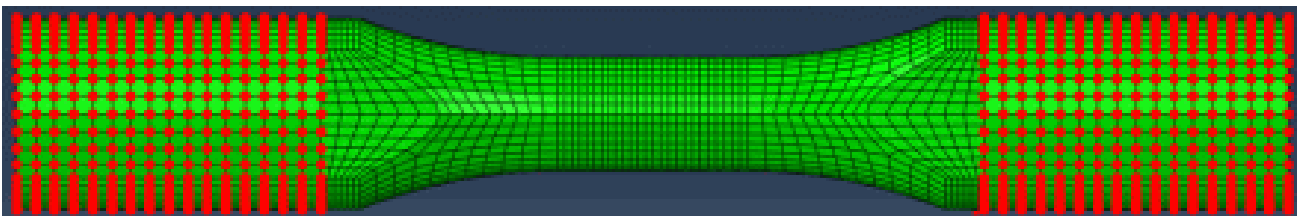


Figure 7.31: FEM model of the SHTB-test specimen and nodes where boundary conditions were applied (red), from [112].

The SPH model is based on the same geometry and is discretised with 65268 particles with a constant particle spacing of 0.2 mm. The model is displayed in figure 7.32.

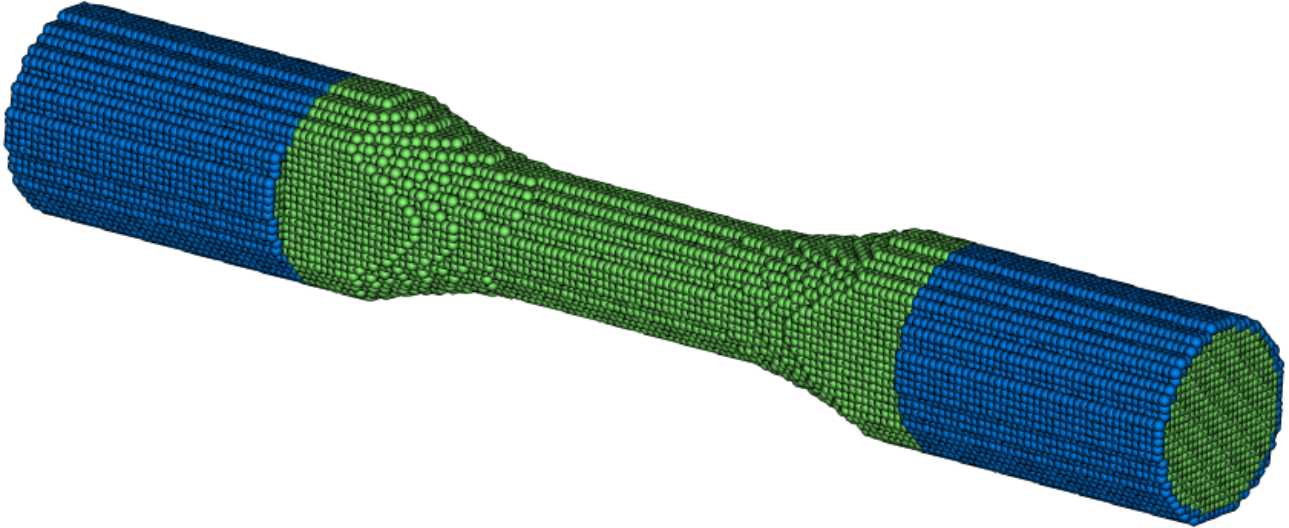


Figure 7.32: SPH model of the SHTB-test specimen with marked regions where boundary conditions were applied.

The physical properties of 50SiB8 are given in table 7.8, the JC-flow stress parameters in table 7.9 and the JC-fracture strain equations parameters for the original model in table 7.10 and for the modified model in table 7.11.

E	Poisson	Density	Specific heat capacity	Thermal conductivity	Thermal expansion	Source
[GPa]	$\nu[-]$	$\rho[\text{kg}/\text{m}^3]$	$c_p[\frac{\text{J}}{\text{kgK}}]$	$\lambda[\frac{\text{W}}{\text{mK}}]$	$\alpha_{th}[1/\text{K}]$	
214	0.334875	7850	466	-	-	[225]

Table 7.8: Physical properties of 50SiB8

A	B	C	m	n	$\dot{\epsilon}_{pl}^0$	T_{ref}	T_f	Source
[MPa]	[MPa]	$[-]$	$[-]$	$[-]$	$[\text{s}^{-1}]$	[K]	[K]	
430.9	908.7	0.0047	0.7361	0.3854	10^{-3}	293.15	2006	[112]

Table 7.9: Johnson Cook flow stress model parameters of 50SiB8

$D_1[-]$	$D_2[-]$	$D_3[-]$	$D_4[-]$	$D_5[-]$	$\dot{\epsilon}_{pl}^0[\text{s}^{-1}]$	$T_{ref}[\text{K}]$	$T_{melt}[\text{K}]$	Source
0.0733	0.7204	1.5643	0.0371	1.5583	$1\text{e-}3$	293.15	2006	[69]

Table 7.10: Johnson Cook fracture strain equation parameters of 50SiB8 (JC CLASSIC)

$D_1[-]$	$D_2[-]$	$D_3[-]$	$D_4[-]$	$D_5[-]$	$D_6[-]$
0.0733	0.7204	1.5643	0.0371	-3.5642	69.5723
$D_7[-]$	$D_8[-]$	$\dot{\epsilon}_{pl}^0[\text{s}^{-1}]$	$T_{ref}[\text{K}]$	$T_{melt}[\text{K}]$	Source
318.5630	428.9243	$1\text{e-}3$	293.15	2006	[69]

Table 7.11: Johnson Cook modified fracture strain equation parameters of 50SiB8 (JC GG)

Plastic dissipation into heat is considered in the FEM and SPH model with a Taylor-Quinney coefficient of $\eta_{TQ} = 0.90$ but heat conduction is not considered due to the very short test duration of 0.38 ms. All simulations are run on a single CPU core. The FEM model uses default bulk viscosity parameters ($b_1 = 0.06, b_2 = 1.2$). In the SPH model the stabilizers XSPH ($\epsilon_{XSPH} = 0.5$) and artificial viscosity ($\alpha_{av} = 1, \beta_{av} = 1, \eta_{av} = 0.1$) are used initially. This approach without artificial stresses was quickly dropped since the SPH suffered from the tensile instability mode leading to pair formation of particles and too early separation, see figure 7.33. Therefore the artificial stresses ($\epsilon_{as} = 0.3, n_{stress} = 4$) had to be used.

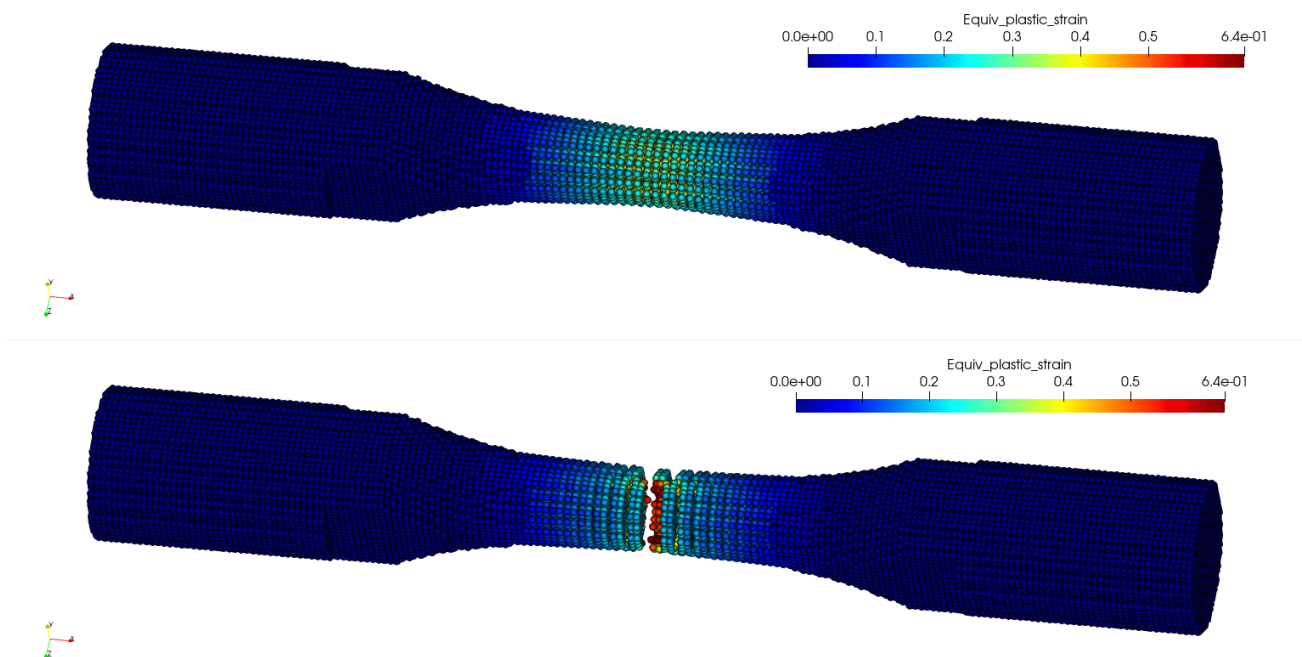


Figure 7.33: Plastic strain distribution in the SPH model with classic JC fracture strain and artificial stresses (top) and without artificial stresses (bottom). The simulation without artificial stresses is too early fully fractured and shows the typical pair formation hinting to the tensile instability issue.

The predicted plastic strain distribution in the SHTB-test specimen after separation are shown for the FEM simulations in figure 7.34 and for the SPH simulations in figure 7.35. The measurement result of the fracture diameter in the SPH models is given in figure 7.36.

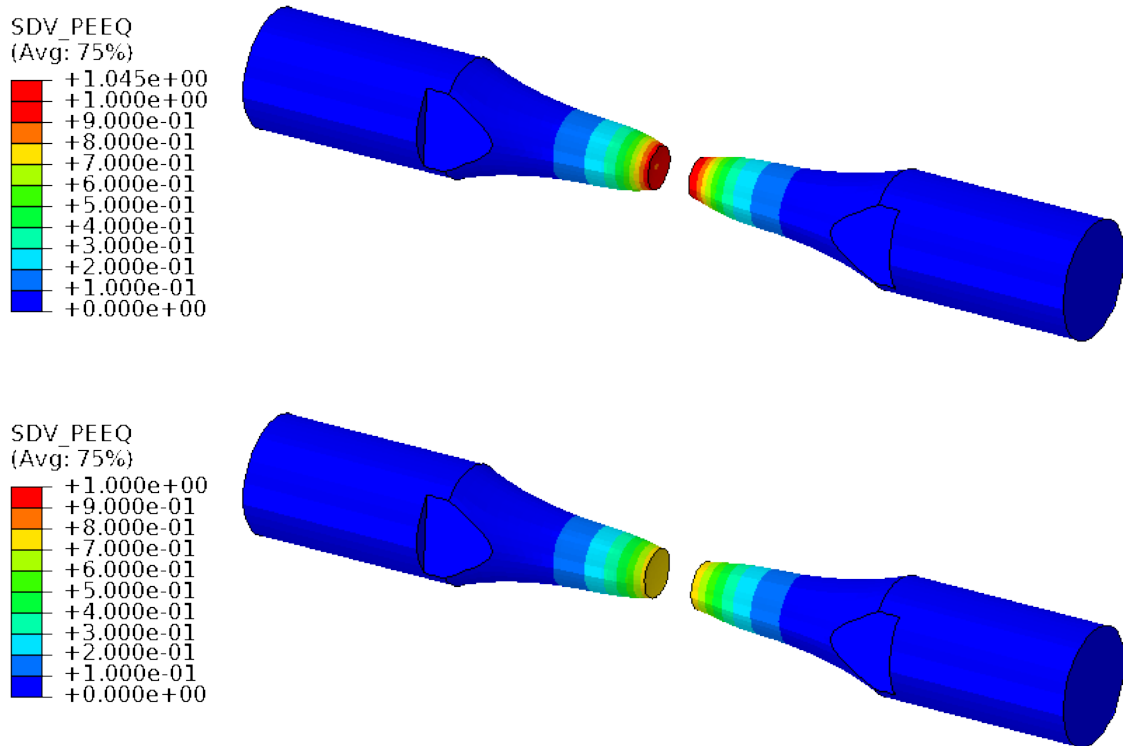


Figure 7.34: Plastic strains after fracture in the FEM model with classic JC fracture strain (top) and modified model (bottom). Deleted particles are not displayed.

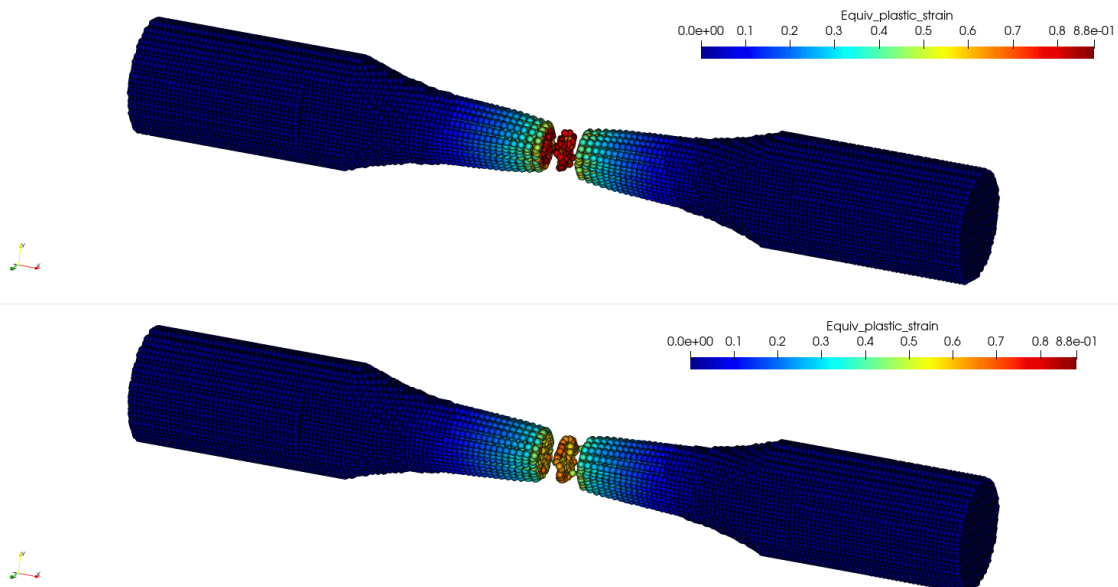


Figure 7.35: Plastic strains after fracture in the SPH model with classic JC fracture strain (top) and modified model (bottom). Note that particles between the fracture surfaces are deleted from the analysis but kept their last position without interfering with active particles.

SPH TEST SIMULATIONS

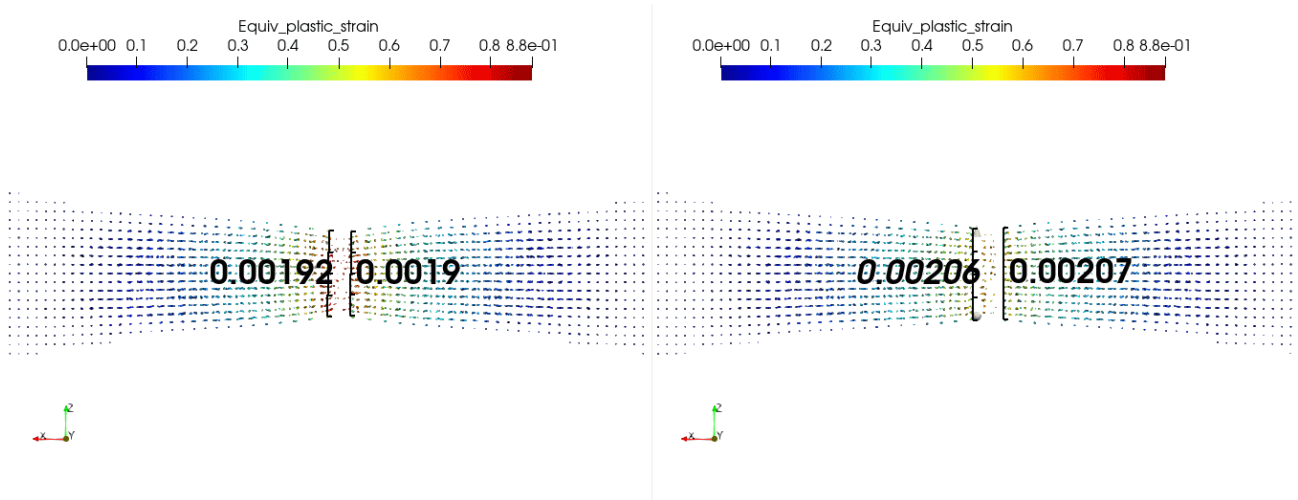


Figure 7.36: Fracture diameter of the STHB specimen. Classic Johnson-Cook fracture strain model (left) and modified model (right).

A results summary of the simulations is given in table 7.12 together with the experimental results. SPH and Abaqus results are very similar and with the modified JC fracture strain equation the experimental results can be reproduced which is not the case when using the original JC fracture strain equation. Obviously, the use of artificial stresses in the SPH does not negatively impact the physics of the model. Instead it enables a physical reasonable result which is not possible without this stabilization term. Note the large differences in the analysis times: while the SPH simulations took about 530 minutes, the FEM model required with 4 minutes only less than a percent of the SPH simulation. Without artificial stresses the runtimes of the SPH models are in the order of 372 minutes - which is a 30% reduction.

Case	Numerical model	Fracture strain model	Fracture strain $\bar{\epsilon}^f$	Fracture diameter	Runtime	Time step Δt
1	SPH	JC classic	88 %	1.90 mm to 1.92 mm	530 minutes	$10^{-8}s$
2	SPH	JC GG	68 %	2.06 mm to 2.07 mm	530 minutes	$10^{-8}s$
3	FEM	JC classic	100.6 %	1.76 mm	4 minutes	$1.1 \cdot 10^{-8}s$
4	FEM	JC GG	76.1 %	2.02 mm	4 minutes	$1.1 \cdot 10^{-8}s$
-	<i>Experiment</i>	-	62.7 % to 81.1 %	2.00 mm to 2.20 mm	0.38 ms	-

Table 7.12: Simulation and experimental results for the SHTB-test at $T = 600^\circ$ and a strain rate of $900s^{-1}$.

MACHINING SIMULATIONS

This chapter is dedicated to machining simulations with the GPU-accelerated `MFREE_IWF` code. In the beginning 2D simulations of orthogonal cutting are shown and later a 3D simulation of micro milling with a diamond tool is shown.

8.1 JOHNSON COOK FLOW STRESS MODEL EXTENSIONS

In metal cutting applications most often the Johnson-Cook flow stress model is used. Especially in the machining of the titanium alloy Ti6Al4V it often fails to correctly predict the chip shapes. For this reason several extensions were introduced.

8.1.1 Johnson Cook Tanh Extension: Calamaz 2008

The reason for the extension is a strain softening phenomenon observed for Ti6Al4V at higher temperatures [55]. An excerpt of these experimental observations is provided with figure 8.1.

The strain softening phenomenon is not completely understood and it is attributed to texture softening, dynamic recrystallisation and dynamic recovery effects. To account for this phenomenon Calamaz [38] extended the JC flow stress model with a special term using the TANGens Hyperbolicus (TANH). This extended JC-flow stress model is named JC-TANH2008 in the following and reads as:

$$\sigma_y = \left(A + B \cdot (\varepsilon_{pl})^n \right) \underbrace{\left(\frac{1}{e^{\varepsilon_{pl}^a}} \right)}_{\text{Modification}} \left(1 + C \cdot \ln \left(\frac{\dot{\varepsilon}_{pl}}{\dot{\varepsilon}_{pl}^0} \right) \right) \left(1 - \left(\frac{T - T_{ref}}{T_f - T_{ref}} \right)^m \right) \underbrace{\left(g + (1 - g) \cdot \tanh \left(\frac{1}{(\varepsilon_{pl} + S)^c} \right) \right)}_{\text{Modification}} \quad (8.1)$$

with

Werkstoff TiAl6V4 – Werkstoff-Nr. 3.7165

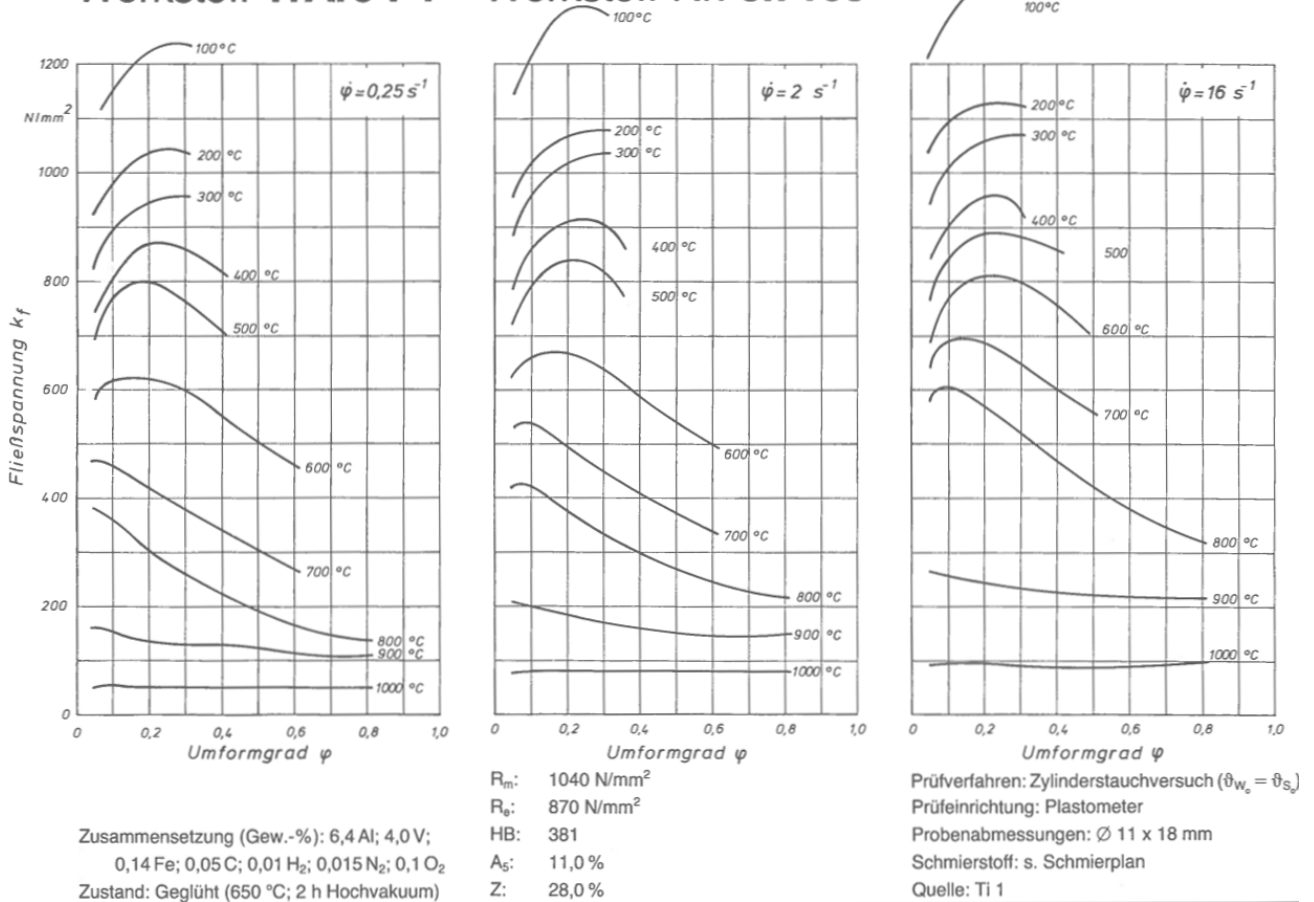


Figure 8.1: Measured flow stress curves of Ti6Al4V at different temperatures and plastic strain rates, from [55].

$$g = 1 - \left(\frac{T}{T_f}\right)^d \tag{8.2}$$

$$S = \left(\frac{T}{T_f}\right)^b \tag{8.3}$$

with a, b, c and d are material parameters in addition to the classic JC material parameters.

8.1.1.1 Derivative of JC-tanh2008 Model for Newton Iterations

Using this model requires for the radial return algorithm in the plasticity model integration the first derivative when using the Newton method (7.1). The derivatives are deduced in the following. First the model is split into four terms T_1, T_2, T_3 & T_4 :

$$\sigma_y = \underbrace{\left(A + B \cdot (\varepsilon_{pl})^n \cdot \left(\frac{1}{e^{\varepsilon_{pl}^a}} \right) \right)}_{\text{Term 1: } T_1} \underbrace{\left(1 + C \cdot \ln \left(\frac{\dot{\varepsilon}_{pl}}{\dot{\varepsilon}_{pl}^0} \right) \right)}_{\text{Term 2: } T_2} \underbrace{\left(1 - \left(\frac{T - T_{ref}}{T_f - T_{ref}} \right)^m \right)}_{\text{Term 3: } T_3} \underbrace{\left(g + (1 - g) \cdot \tanh \left(\frac{1}{(\varepsilon_{pl} + S)^c} \right) \right)}_{\text{Term 4: } T_4} \quad (8.4)$$

The derivative of the flow stress with regards to the plastic strain is then:

$$\frac{\partial \sigma_y}{\partial \varepsilon_{pl}} = \frac{\partial(T_1(\varepsilon_{pl}) \cdot T_2 \cdot T_3 \cdot T_4(\varepsilon_{pl}))}{\partial \varepsilon_{pl}} = \frac{\partial(T_1(\varepsilon_{pl}))}{\partial \varepsilon_{pl}} \cdot T_2 \cdot T_3 \cdot T_4 + T_1 \cdot T_2 \cdot T_3 \cdot \frac{\partial(T_4(\varepsilon_{pl}))}{\partial \varepsilon_{pl}} \quad (8.5)$$

with the derivative of the first term T_1 :

$$\frac{\partial T_1}{\partial \varepsilon_{pl}} = B \cdot e^{-\varepsilon_{pl}^a} \cdot \varepsilon_{pl}^{n-1} \cdot (n - a \cdot \varepsilon_{pl}^a) \quad (8.6)$$

and the derivative of the fourth term T_4 :

$$\frac{\partial T_4}{\partial \varepsilon_{pl}} = c \cdot (g - 1) (S + \varepsilon_{pl})^{-c-1} \cdot \text{sech}^2((S + \varepsilon_{pl})^{-c}) \quad (8.7)$$

The derivative of the flow stress with regards to the plastic strain rate is then:

$$\frac{\partial \sigma_y}{\partial \dot{\varepsilon}_{pl}} = \frac{\partial(T_1 \cdot T_2(\dot{\varepsilon}_{pl}) \cdot T_3 \cdot T_4)}{\partial \dot{\varepsilon}_{pl}} = T_1 \cdot \frac{\partial(T_2(\dot{\varepsilon}_{pl}))}{\partial \dot{\varepsilon}_{pl}} \cdot T_3 \cdot T_4 \quad (8.8)$$

with the derivative of the second term T_2 :

$$\frac{\partial T_2}{\partial \dot{\varepsilon}_{pl}} = \frac{C}{\dot{\varepsilon}_{pl}} \quad (8.9)$$

Inserting the derivatives (8.5) and (8.8) with (7.11) and (7.12) and (8.9) into the equation for the determination of the plastic multiplier (7.10) yields:

$$\begin{aligned} \frac{\partial g(\Delta\lambda_n)}{\partial \Delta\lambda} &= -\sqrt{\frac{3}{2}}2G - \sqrt{\frac{2}{3}} \left[\frac{\partial \sigma_y}{\partial \varepsilon_{pl}^{n+1}} \frac{\partial \varepsilon_{pl}^{n+1}}{\partial \Delta\lambda} + \frac{\partial \sigma_y}{\partial \dot{\varepsilon}_{pl}^{n+1}} \frac{\partial \dot{\varepsilon}_{pl}^{n+1}}{\partial \Delta\lambda} \right] \quad (8.10) \\ \frac{\partial g(\Delta\lambda_n)}{\partial \Delta\lambda} &= -\sqrt{\frac{3}{2}}2G - \sqrt{\frac{2}{3}}B \cdot e^{-\varepsilon_{pl}^a} \cdot \varepsilon_{pl}^{n-1} \cdot (n - a \cdot \varepsilon_{pl}^a) \cdot T_2 \cdot T_3 \cdot T_4 \\ &\quad - \sqrt{\frac{2}{3}}T_1 \cdot T_2 \cdot T_3 \cdot c \cdot (g - 1)(S + \varepsilon_{pl})^{-c-1} \cdot \operatorname{sech}^2((S + \varepsilon_{pl})^{-c}) \\ &\quad - \sqrt{\frac{2}{3}}T_1 \cdot \frac{C}{\dot{\varepsilon}_{pl}} \cdot T_3 \cdot T_4 \cdot \frac{1}{\Delta t} \end{aligned}$$

which is even without inserting the terms $T_1 - T_4$ an awkward expression to be used within a Newton method and obviously induce very high computational cost. For this reason only the SECANT B - method is used in the following.

8.1.2 Johnson Cook Tanh Extension - Calamaz 2010

Calamaz [39] later proposed an improved model of (8.1) because JC-TANH2008 shows strain softening at all temperatures which is unphysical for the lower temperature range. In their new model JC-TANH2010 the strain softening starts from $T \approx 0.3 \cdot T_f$ which is according to observations in [55].

$$\begin{aligned} \sigma_y &= (A + B \cdot (\varepsilon_{pl})^n) \left(1 + C \cdot \ln \left(\frac{\dot{\varepsilon}_{pl}}{\dot{\varepsilon}_{pl}^0} \right) \right) \left(1 - \left(\frac{T - T_{ref}}{T_f - T_{ref}} \right)^m \right) \quad (8.11) \\ &\quad \underbrace{\left(g_{2010} + (1 - g_{2010}) \cdot \tanh \left(\frac{1}{(\varepsilon_{pl} + \varepsilon_{pl}^0)} \right) \right)}_{\text{additional term } S_{2010}} \end{aligned}$$

where the term S_{2010} models the strain softening and ε_{pl}^0 shall modulate the strain corresponding to the peak stress. The parameter g_{2010} is defined as:

$$g_{2010} = 1 - \left(\frac{p \cdot \varepsilon_{pl}}{1 + p \cdot \varepsilon_{pl}} \cdot \tanh \left(\frac{T - T_r}{T_{rec} - T_r} \right)^q \right) \quad (8.12)$$

with p controlling the slope of the stress-strain curve after the peak stress, T_{rec} being the onset temperature of the strain softening phenomenon and q defines the temperature range over which the strain softening is developed. With a similar argumentation as for the JC-TANH2008-model the SECANT B - method is used exclusively for the determination of the plastic multiplier in the radial return algorithm.

8.1.3 Johnson-Cook Tanh Extension - Calamaz 2011

A further modification JC-CALAMAZ2011 of the original JC flow stress model was proposed [40] as:

$$\sigma_y = \left(A + B \cdot \left(\frac{1}{\dot{\varepsilon}_{pl}} \right)^a \cdot \varepsilon_{pl}^{(n-0,12 \cdot (\varepsilon_{pl} \dot{\varepsilon}_{pl})^a)} \right) \left(1 + C \cdot \ln \left(\frac{\dot{\varepsilon}_{pl}}{\dot{\varepsilon}_{pl}^0} \right) \right) \left(1 - \left(\frac{T - T_{ref}}{T_f - T_{ref}} \right)^m \right) \quad (8.13)$$

with only one additional parameter a affecting the first term of the JC flow stress and coupling it with a strain rate dependency.

8.1.4 Johnson-Cook Tanh Extensions - Sima / Özel

Sima and Özel [224] came up with another three extensions of the JC flow stress based on (8.1) and (8.11):

The first model JC-TANHSO1 is:

$$\sigma_y = (A + B \cdot (\varepsilon_{pl})^n) \left(1 + C \cdot \ln \left(\frac{\dot{\varepsilon}_{pl}}{\dot{\varepsilon}_{pl}^0} \right) \right) \left(1 - \left(\frac{T - T_{ref}}{T_f - T_{ref}} \right)^m \right) \left(M + (1 - M) \cdot \left(\tanh \left(\frac{1}{(\varepsilon_{pl} + p)^r} \right) \right)^S \right) \quad (8.14)$$

with M , p , r and S being constants.

Their second modification JC-TANHSO2 is:

$$\sigma_y = (A + B \cdot (\varepsilon_{pl})^n) \left(1 + C \cdot \ln \left(\frac{\dot{\varepsilon}_{pl}}{\dot{\varepsilon}_{pl}^0} \right) \right) \left(1 - \left(\frac{T - T_{ref}}{T_f - T_{ref}} \right)^m \right) \left(g + (1 - g) \cdot \left(\tanh \left(\frac{1}{(\varepsilon_{pl} + p)^r} \right) \right)^S \right) \quad (8.15)$$

with

$$g = 1 - \left(\frac{T}{T_f} \right)^d \quad (8.16)$$

$$p = \left(\frac{T}{T_f} \right)^b$$

which is a modified JC-TANH2008-model without the $\frac{1}{e^{\frac{a}{\epsilon_{pl}}}}$ -term but an additional exponent r in the *tanh*-term.

Their third modification JC-TANH303 reads:

$$\sigma_y = \left(A + B \cdot (\epsilon_{pl})^n \cdot \left(\frac{1}{e^{\frac{a}{\epsilon_{pl}}}} \right) \right) \left(1 + C \cdot \ln \left(\frac{\dot{\epsilon}_{pl}}{\dot{\epsilon}_{pl}^0} \right) \right) \left(1 - \left(\frac{T - T_{ref}}{T_f - T_{ref}} \right)^m \right) \left(g + (1 - g) \cdot \left(\tanh \left(\frac{1}{(\epsilon_{pl} + p)^r} \right) \right)^s \right) \quad (8.17)$$

with D and p using the same definition in (8.16). This model is a modified JC-TANH2008-model with an additional exponent r in the *tanh*-term. For $r = 1$ the model recovers the JC-TANH2008-model.

8.1.5 Comparison of Johnson-Cook-Type Flow Stress Models

All JC extensions shown before are compared against each other for the titanium alloy Ti6Al4V. For that purpose the five parameters A , B , C , m and n of the JC-CLASSIC are the same for each case and serve as a basis. Its values are given in table 8.1. The density and the specific heat are given in table 8.2. The models differ only in the additional constants of the respective parameters of the tanh-extensions which are given in table 8.3 together with the source of the additional constants. These additional constants are mainly identified from parametric simulations whose results are compared to experimental results. In the JC-TANH303-model SHPB-test data is used to modify the stress strain curve at very low strains while the final set is identified from parametric simulations and comparison to cutting experiments as well.

A	B	C	m	n	$\dot{\epsilon}_{pl}^0$	T_{ref}	T_f	Source
[MPa]	[MPa]	[-]	[-]	[-]	[s ⁻¹]	[K]	[K]	
968	380	0.0197	0.577	0.421	1.0	293.15	1903	[38, 128]

Table 8.1: Johnson Cook flow stress model parameters for Ti6Al4V.

Density ρ [kg/m ³]	Specific heat capacity c_p [$\frac{J}{kgK}$]	Source
4430	580.0	[62]

Table 8.2: Physical properties of Ti6Al4V .

Model	Used additional constants	Source
JC-CLASSIC	-	-
JC-TANH2008	$a = 1.6, a = 0.4, a=6.0, d = 1.0$	[38, 62]
JC-TANH2010	$\epsilon_0 = 0.7, p = 0.6, T_{rec} = 600.0, q = 5.0$	[39]
JC-CALAMAZ2011	$a = 0 / a = 0.11 / a = 0.22$	[40]
JC-TANHSO1	$p = 0, r = 1, S = 7.0, M = 0.7$	[224]
JC-TANHSO2	$b = 1.0, d = 0.5, r = 1.0, S = 5.0$	[224]
JC-TANHSO3	$a = 2.0, b = 1.0, d = 0.5, r = 1.0, S = 5.0$	[224]

Table 8.3: Extended JC flow stress model: additional material parameters used for comparison of these models.

First, the yield stress at a constant temperature of $T = 800K$ and a constant strain rate of $\dot{\epsilon}_{pl} = 10^4/s$ is shown in the range of $\epsilon_{pl} = 0...300\%$. Plastic dissipation is not considered and therefore the temperature remains constant.

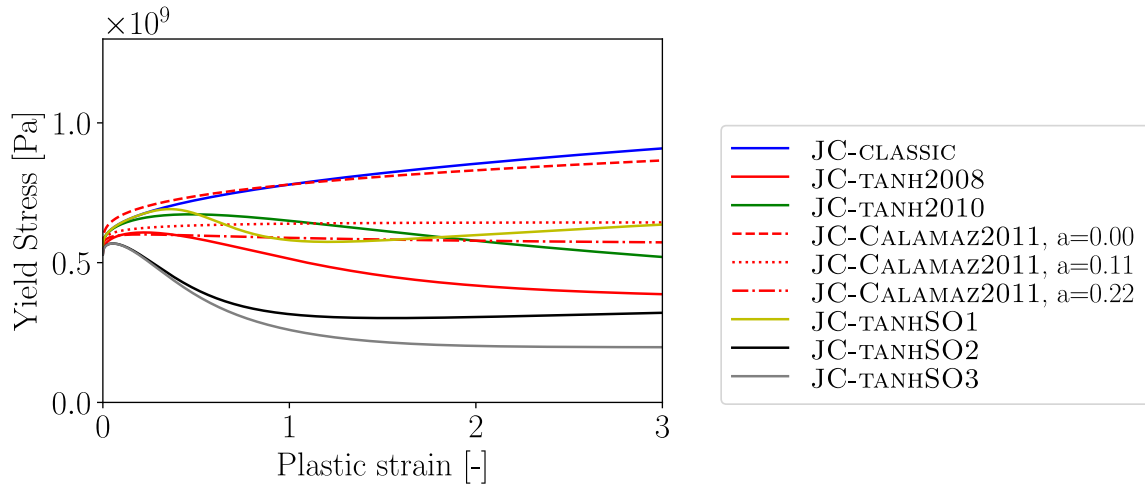


Figure 8.2: Computed stress-strain curves for various Johnson-Cook-type flow stress models, isothermal

At very low plastic strains all models predict the same yield stress and the evaluation shows that JC-CLASSIC and JC CALAMAZ2011 with $a = 0$ give very similar stress-strain curves. JC-CALAMAZ2011 with $a = 0.11$ and $a = 0.22$ show very flat yield curves and all TANH-modified models show more or less pronounced reductions of the yield stress where only JC-TANHSO1 shows first a decrease and beyond $\epsilon_{pl} = 1$ starts to rise again. JC-TANHSO2 and JC-TANHSO3 show the strongest yield stress decreases. It is difficult to judge which model and parameter

set is suited best to model the flow stress curve at high plastic strains since test data is available only up to $\varepsilon_{pl} = 80\%$, see figure 8.1. In a second test case the yield stress is adiabatic heating with a Taylor-Quinney coefficient of $\eta_{TQ} = 90\%$ is considered. The temperature increase is computed with an Euler explicit integration. The integration reads:

$$\Delta\bar{\varepsilon}_{pl} = 10^{-5} = const \quad (8.18)$$

$$\dot{\varepsilon}_{pl} = 10^{-5} s^{-1} = const \quad (8.19)$$

$$\Delta t = \Delta\bar{\varepsilon}_{pl} / \dot{\varepsilon}_{pl} \quad (8.20)$$

$$\bar{\varepsilon}_{pl}^{n=0} = 0 \quad (8.21)$$

$$T^{n=0} = T_{init} \quad (8.22)$$

$$\bar{\varepsilon}_{pl}^{n+1} = \bar{\varepsilon}_{pl}^n + \Delta\bar{\varepsilon}_{pl} \quad (8.23)$$

$$\sigma_y^{n+1} = \sigma(\bar{\varepsilon}_{pl}^{n+1}, \dot{\varepsilon}_{pl}, T^n) \quad (8.24)$$

$$T^{n+1} = T^n + \frac{\sigma_y^{n+1} \cdot \Delta\bar{\varepsilon}_{pl} \cdot \eta_{TQ}}{\rho \cdot c_p} \quad (8.25)$$

The equations (8.18)-(8.22) initialize the problem with an initial temperature of $T_{init} = 500K$, a constant strain rate of $\dot{\varepsilon}_{pl} = 10^5 s^{-1}$ and constant plastic strain increment of $\Delta\bar{\varepsilon}_{pl} = 10^{-5}$. The incrementation loop is performed with (8.23)-(8.25) until $\bar{\varepsilon}_{pl} = 0...300\%$. The resulting temperature characteristics for the flow stress models are given with figure 8.3.

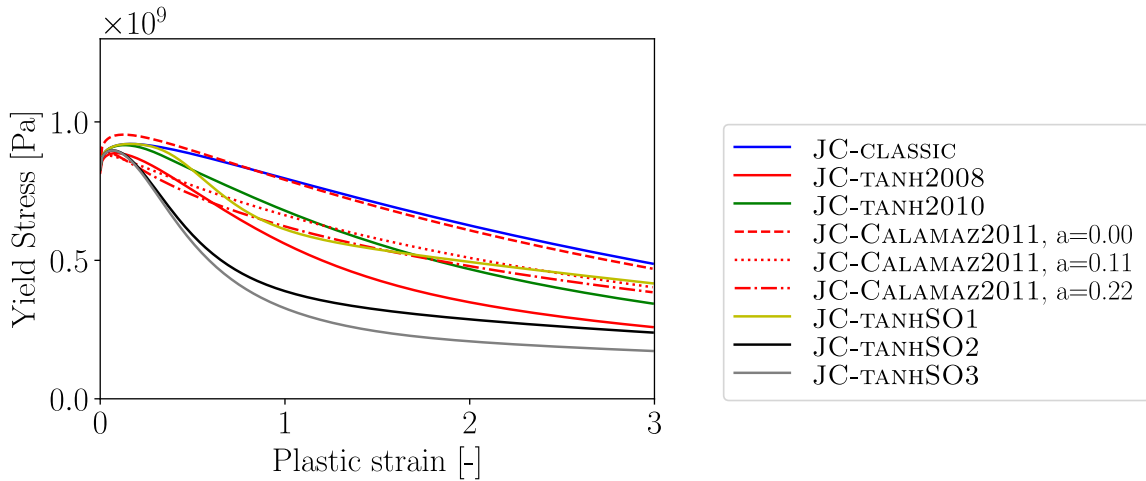


Figure 8.3: Computed stress-strain curves for various Johnson-Cook-type flow stress models, with adiabatic heating

A slightly different picture is seen when adiabatic heating is considered. JC-CLASSIC and JC-CALAMAZ2011 with $a = 0$ are still almost equal, while JC-TANHSO1 shows at strains higher than $\varepsilon_{pl} = 1$ shows a similar trend as JC CALAMAZ2011 with $a = 0.11$ and $a = 0.22$. JC-TANHSO2 and JC-TANHSO3 show again the strongest yield stress decreases with JC-TANH2008

catching up at larger plastic strains. Again, it is difficult to judge which model and parameter set is suited best to model the flow stress curve at high plastic strains since test data is available only up to $\varepsilon_{pl} = 80\%$, see figure 8.1.

8.2 ORTHOGONAL CUTTING SIMULATIONS WITH ORIGINAL AND MODIFIED JC-MODELS

The orthogonal cutting simulation allows a simplified simulation approach in 2D for plane strain conditions. In this part orthogonal cutting simulations of Ti6Al4V are performed with the JC-CLASSIC-, JC-TANH2008-, JC-TANH2010- and JC-TANH303-model. The results are compared against available FEM and experimental results from Ducobu [59, 62] whose results are chosen as they have been continuously working with extended JC-models on metal cutting simulations [57, 58, 60] and outlined the problem of suitable material parameters for Ti6Al4V[61] in machining simulations. The computations are performed for the process parameters given in table 8.4.

Cut speed	Uncut chip thickness	Rake angle	Clearance angle	Cutting edge radius
v_c	f	γ	α	r_c
30m/min	280 μ m	15°	2°	10 μ m

Table 8.4: Process parameter and cutter geometry of orthogonal cutting simulations, from [62].

Physical properties for the workpiece material Ti6Al4V and the tungsten-carbide cutter are given in table 8.5. In contrast to the work of [62], thermal expansion and elasticity of the tool are not considered in this work. Thermal expansion and heat conduction are considered for the workpiece where for the latter the Brookshaw-approximation of the Laplacian is used (4.39). The friction coefficient μ_{fric} is chosen very low in accordance with the reference [62]. Its value and the frictional and plastic dissipation coefficients are provided with table 8.6.

Material	E	Poisson	Density	Specific heat capacity	Conductivity	Thermal expansion	Source
	[GPa]	ν [-]	ρ [kg/m ³]	c_p [$\frac{J}{kgK}$]	λ [$\frac{W}{mK}$]	α_{th} [1/K]	
Ti6Al4V	113.8	0.34	4430	580.0	7.3	8.6e-6	[62]
WC	(800)	(-)	15000	203	46	(4.7e-6)	[62]

Table 8.5: Physical properties of Ti6Al4V and tungsten carbide.

Friction coefficient	Frictional energy converted into heat	Plastic dissipation into heat
μ_{fric}	η_{fric}	η_{TQ}
0.05	100%	90%

Table 8.6: Friction and dissipation coefficients, from [62].

The JC flow stress model parameters used for the four models as well as the parameters for the tanh terms are given in table 8.7. The parameters for the JC-CLASSIC model are taken from [158] who refer to [104]. Since the latter document is not accessible it is unknown how this material was treated and how the material parameters were determined. For the modified JC-models, material parameters from the respective publications were used in the simulations which are as well outlined in the table below. The material constitutive parameters for JC-CLASSIC are derived from SHPB-tests except for the JC-TANH2010-model, where the method for the parameter determination is not clear. The additional constants for the tanh-terms are mainly identified from parametric simulations whose results are compared to experimental results, see also chapter 8.1.5.

Parameter	Unit	JC-CLASSIC	JC-TANH2008	JC-TANH2010	JC-TANH2010	JC-TANH2010	JC-TANH2010	JC-TANH2010	JC-TANH2010
A	MPa	862.5	968.0	870.0	724.7				
B	MPa	331.2	380.0	990.0	683.1				
C	-	0.012	0.0197	0.011	0.035				
m	-	0.8	0.577	1.0	1.0				
n	-	0.34	0.421	0.25	0.47				
$\dot{\epsilon}_{pl}^0$	s ⁻¹	1.0	1.0	1.0	1.0				
T_{ref}	K	298.0	293.15	293.15	293.15				
T_f	K	1878	1903	1903	1903				
Source		SHPB [104, 158]	SHPB [38, 128]	[39, 62]	SHPB [62, 123, 224]				
<i>a</i>	—	-	1.6	-	2.0				
<i>b</i>	—	-	0.4	-	5.0				
<i>c</i>	—	-	6.0	-	-				
<i>d</i>	—	-	1.0	-	1.0				
<i>q</i>	—	-	-	5.0	-				
<i>p</i>	—	-	-	0.6	-				
T_{rec}	K	-	-	600	-				
ϵ_0	—	-	-	0.7	-				
<i>r</i>	—	-	-	-	1.0				
<i>S</i>	—	-	-	-	0.05				
Source		-	[62]	[62]	[62]				

Table 8.7: Material parameter used for Ti6Al4V in the analyses.

The workpiece geometry has a length $l = 1mm$ and a height of $h = 0.75mm$ and is discretised with 8586 particles. The right, bottom and half of the left particles are fixed. A picture is provided with figure 8.4. Tool heat transfer is considered only for the GPU-calculations due to the time demand, see cases 3-6 in table 8.8. For that purpose the tool is discretised with additional 3267 tool particles where the left side of the tool has a temperature boundary condition with $T = T_{room} = 298K$. The initial temperature for the workpiece and tool models is $T_{init} = T_{room} = 298K$.

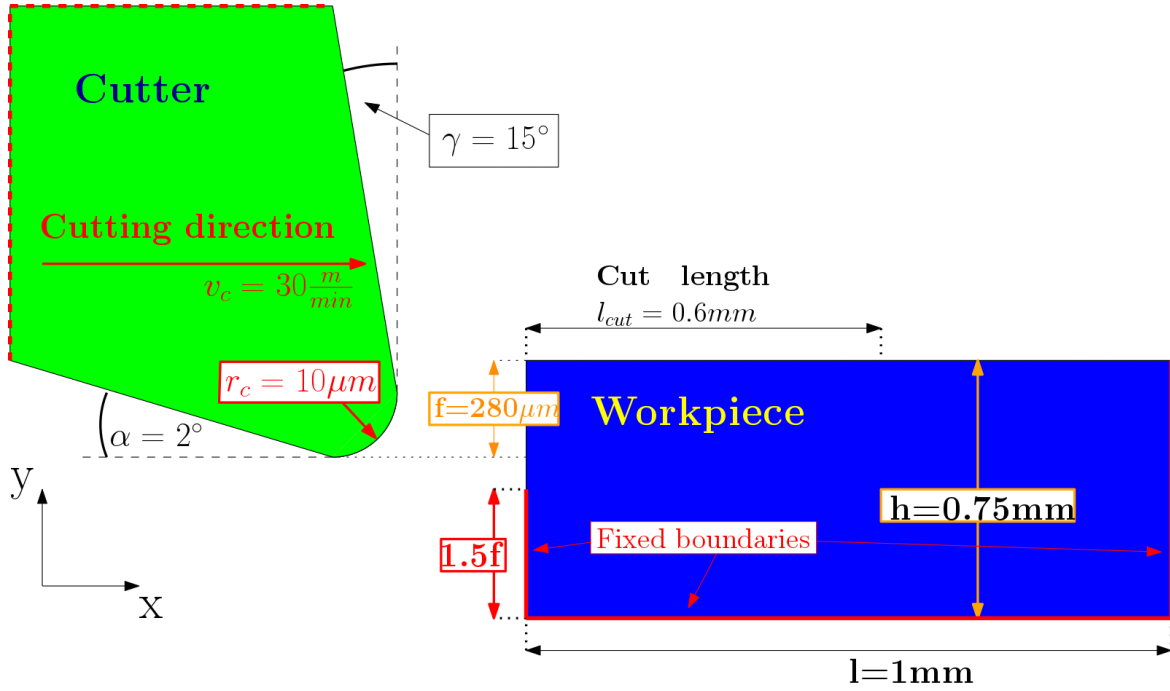


Figure 8.4: Geometry and boundary conditions of the SPH particle domain.

The simulated time is $t = 1.2\text{ms}$ which equals to a cut length of $l_{cut} = 0.6\text{mm}$.

8.2.1 Results without Damage Modelling

The computation for the JC-CLASSIC-model is conducted without tool heat transfer on a single core of the CPU (AMD®RYZEN 5 2600x) and serves as a performance comparison to all other simulations which are conducted on the GPU with a NVIDIA GeForce GTX 1650. An overview of the simulations is given in table 8.8.

Case	JC model	CPU / GPU	Runtime	Time step	Heat transfer
1	JC-CLASSIC	CPU	21.6 h	$\Delta t = 4.7 \cdot 10^{-10}\text{s}$	only workpiece
2	JC-CLASSIC	GPU	2.6 h	$\Delta t = 4.7 \cdot 10^{-10}\text{s}$	only workpiece
3	JC-CLASSIC	GPU	2.9 h ^a	$\Delta t = 4.7 \cdot 10^{-10}\text{s}$	tool and workpiece
4	JC-TANH2008	GPU	3 h	$\Delta t = 4.7 \cdot 10^{-10}\text{s}$	tool and workpiece
5	JC-TANH2010	GPU	3 h	$\Delta t = 4.7 \cdot 10^{-10}\text{s}$	tool and workpiece
6	JC-TANHSO3	GPU	3.3 h	$\Delta t = 4.7 \cdot 10^{-10}\text{s}$	tool and workpiece

Table 8.8: Computation times of the SPH models without damage modelling.

^a The same simulations require on high performance GPUs runtimes of only 0.6 h (NVIDIA TESLA P100) and 0.5 h (NVIDIA QUADRO GP100).

Comparing cases 1 and 2 in table 8.8 reveal a runtime reduction of about 88% when computing the same model on the GPU. When modelling tool heat transfer (case 2 vs. 3) the

computational expense increases and the compute time is about 10% higher. The extensions of the JC-classic-model (cases 4, 5, 6) show moderate runtime increases for JC-TANH2008 and JC-TANH2010 in the order of 3% and a slightly higher runtime increase of 13% for JC-TANHSO3.

The distribution of plastic strains is shown in figure 8.5 for the four simulations. Here, JC-TANH2008 shows clearly segmentation while JC-TANH2010 and JC-TANHSO3 show only smaller signs of segmentation while the JC-CLASSIC shows marginal traces of shear band formations.

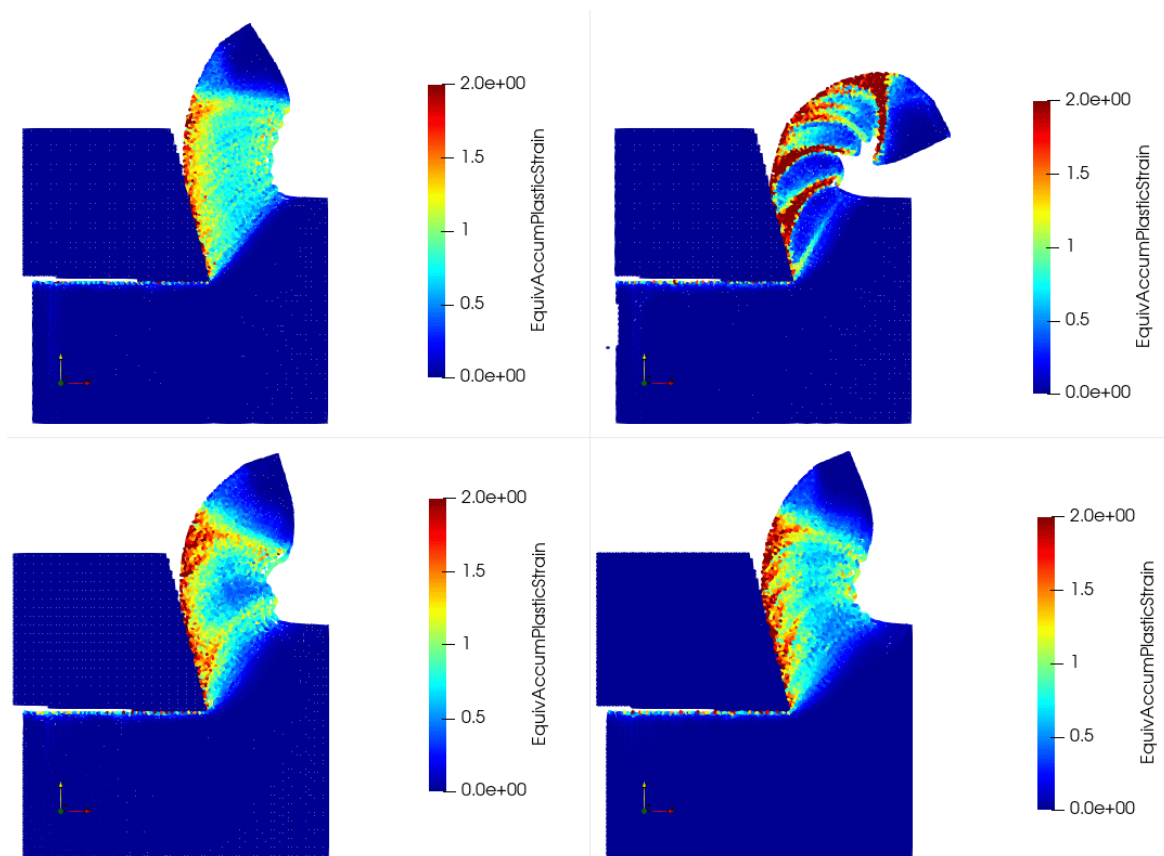


Figure 8.5: Plastic strain distribution for cases 3-6 from table 8.8 with tool and workpiece heat transfer: JC-CLASSIC (top left), JC-TANH2008 (top right), JC-TANH2010 (bottom left) and JC-TANHSO3 (bottom right).

The temperature distributions are given in figure 8.6 where the JC-TANH2010 shows significantly higher temperatures, mainly in the tool-chip interface, compared to the other flow stress models. This figure can be compared to FEM results from [62], their results are shown in figure 8.7 and show a similar pattern with the highest predicted temperatures for JC-TANH2010. This picture allows as well for a qualitative comparison of the predicted chip shapes which show similar segmentation results where JC-TANH2008 is most pronounced as well.

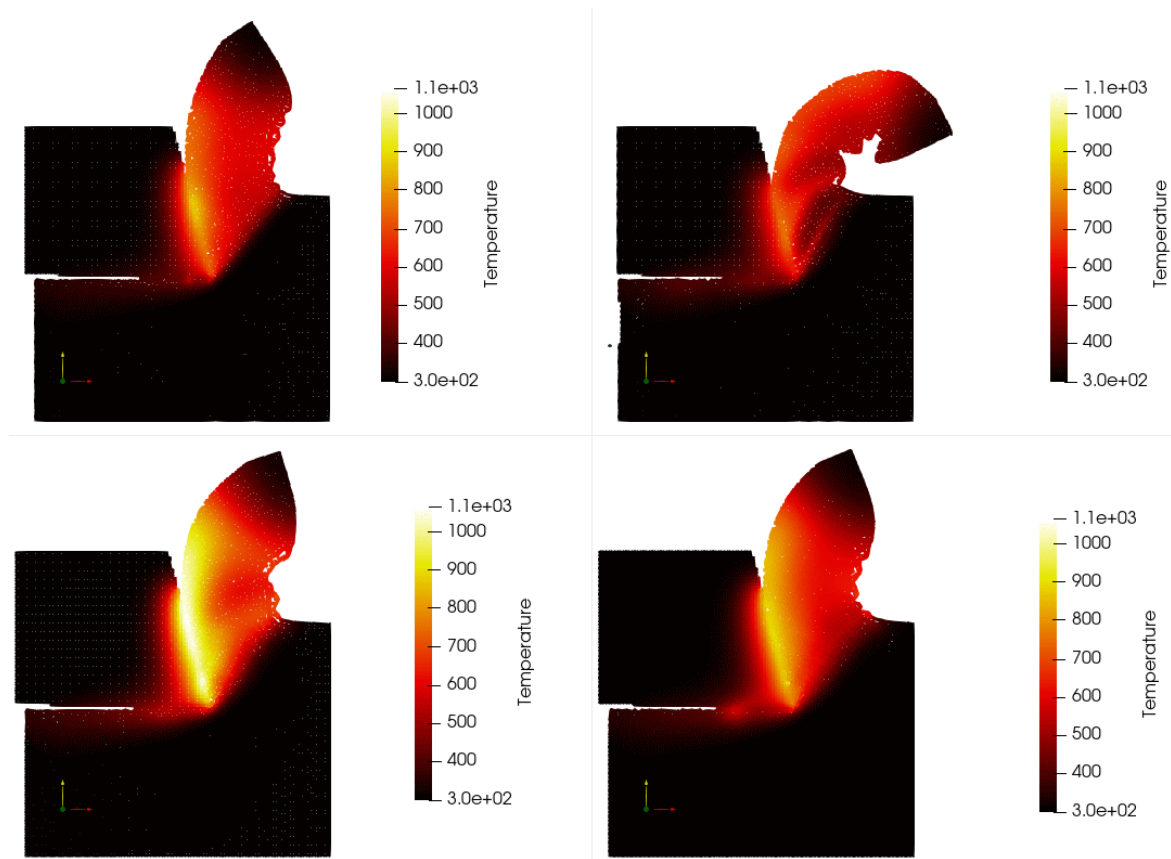


Figure 8.6: Temperature distribution for cases 3-6 from table 8.8 with tool and workpiece heat transfer: JC-CLASSIC (top left), JC-TANH2008 (top right), JC-TANH2010 (bottom left) and JC-TANH503 (bottom right). The temperature unit is in [K].

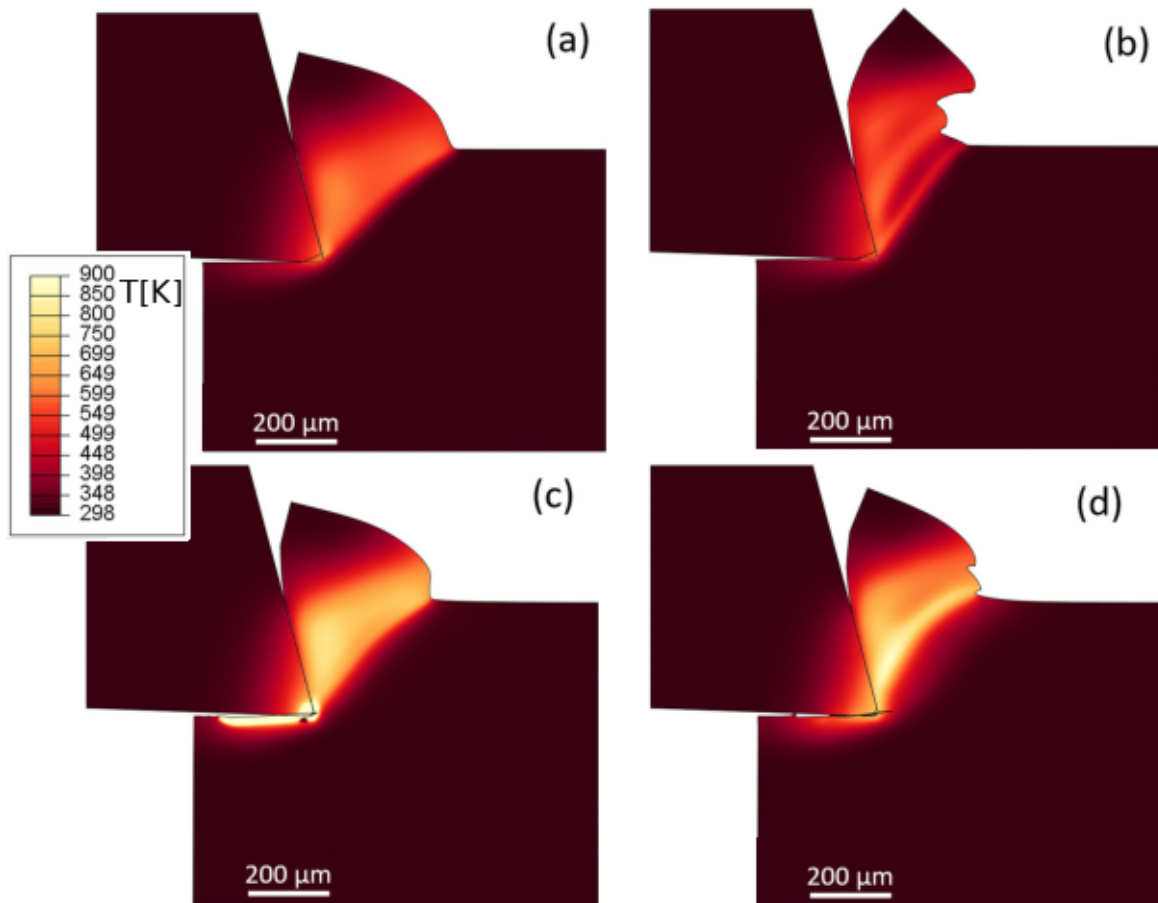


Figure 8.7: Temperature distribution of the FEM simulations conducted by [62] for JC-CLASSIC (top left), JC-TANH2008 (top right), JC-TANH2010 (bottom left) and JC-TANH303 (bottom right).

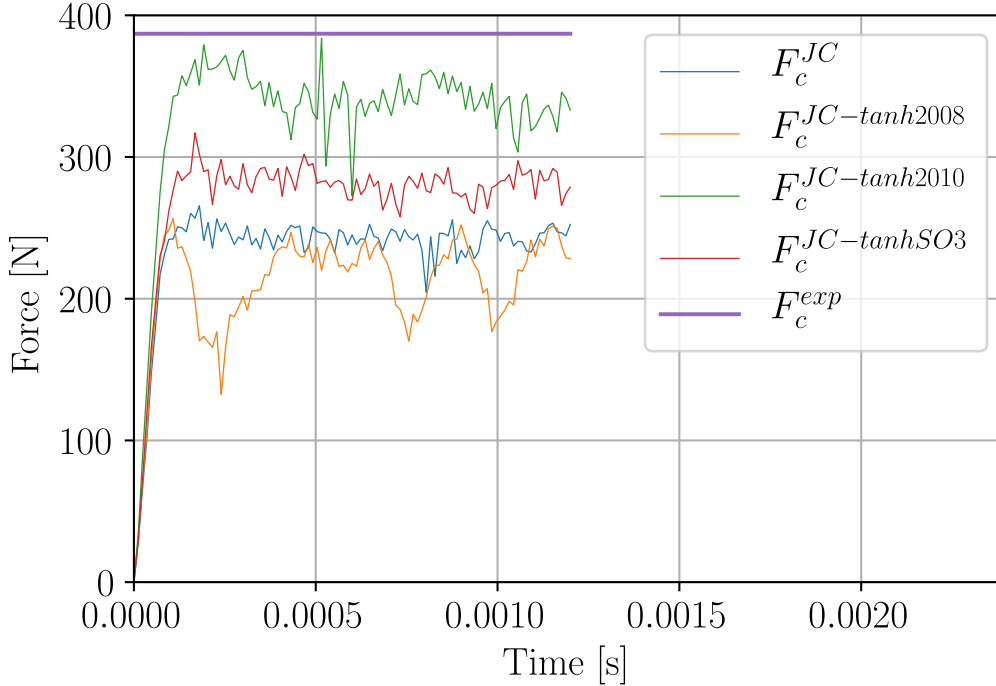


Figure 8.8: Cut force evolution with the SPH simulations for JC-CLASSIC (top left), JC-TANH2008 (top right), JC-TANH2010 (bottom left) and JC-TANHSO3 (bottom right). The cut forces are scaled to a cut width of 1mm.

The cut force evolution is shown in figure 8.8. A comparison of the averaged SPH cut forces to FEM and experimental results of [62] is displayed in table 8.9. The SPH prediction of cut forces are generally lower than the FEM results by about 20% – 30% where JC-TANH2010 comes closest to the experimentally determined cut force with a deviation of about 11%. The trend of the cut force is similar to the reported results in Ducobu [62]: cut force predictions obtained with JC-TANH2010 are closest to the experimental results while JC-TANH2008 gives the worst cut force prediction. Lower process force prediction of the SPH with commercial solvers like ABAQUS and LS-DYNA are reported in literature [229, 248]. but the issue is so far not understood and probably stems from the remeshing in FEM where due to remapping from the old to the new mesh internal variables are dispersed. Further, distorted elements appear to have higher stiffness than the continuum, which is the actual reason for remeshing.

JC model	SPH	FEM [62]	Experiment [62]
JC-CLASSIC	243 N	292 N	387 N
JC-TANH2008	215 N	255 N	387 N
JC-TANH2010	343 N	442 N	387 N
JC-TANHSO3	282 N	432 N	387 N

Table 8.9: Comparison of cut forces from the SPH with the FEM and experimental results from [62]. The cut forces are scaled to a cut width of 1mm.

8.2.2 Results with Damage Modelling

The use of a constitutive model in machining simulations without consideration of damage is often not satisfactory with respect to the predicted chip shapes. Therefore first attempts were made by [80, 141] using the JC fracture strain equation with linear damage accumulation and subsequent element deletion when reaching ω_{crit} . These approaches were refined [142, 272] and not just the damage initiation was considered but also the damage evolution phase where then the critical damage D_{crit} leads to element deletion in the simulations. In this investigation the deletion of particles (elements) is prevented such that fully damaged particles can still participate in the transmission of loads in compression. The damage initiation is computed with the Johnson Cook fracture strain model (3.165) and parameters according to table 8.10. In the damage evolution phase an exponential rule for the damage variable D is used. The damage is set to $D = 1$ when 99% of the critical energy release rate G_f is achieved, according to (3.171). The fracture toughness is $K_{1C} = 74.6 \text{MPa}\sqrt{m}$ [116, 189] which is converted with (3.169) into $G_f = 44501.7 \text{N}/m$. Material parameters according to table 8.10 are used and the SPH simulation cases 3-6 from table 8.8 are repeated this time including damage initiation and evolution.

Set	Material	$D_1[-]$	$D_2[-]$	$D_3[-]$	$D_4[-]$	$D_5[-]$	$\dot{\epsilon}_{pl}^0 [s^{-1}]$	$T_{ref} [K]$	$T_{melt} [K]$	Source
1	Ti6Al4V	-0.09	0.27	0.48	0.014	3.87	1.0	273.0	1878.0	[73]

Table 8.10: Johnson Cook fracture strain equation constants of Ti6Al4V.

The distribution of plastic strains is shown in figure 8.9 for the four simulations with the same model resolution as in chapter 8.2.1. The chip segmentation becomes visible for all 4 constitutive models but in between the segments material accumulates. For this reason the particle resolution is increased 4 times to a total of 48052 particles. The results are shown in figure 8.10. The predicted chip segmentation is improved and JC-CLASSIC, JC-TANH2008 and JC-TANH2010 show clearly segmentation while JC-TANH303 shows shear band formation but the chip segments are still interconnected. The distribution of the damage variable ω for damage initiation is shown in figure 8.11. Between each chip segment it reaches its maximum value of $\omega = 1$ which means that damage evolution has started in these regions. The distribution of the damage variable D (damage evolution) is shown in figure 8.12. In none of the simulations it ever reaches $D = 1$ which is conspicuous since [62] reports $D = 1$ with subsequent element deletion. The reason for this might be that they did not report their used value for the critical stress intensity K_{1C} . Possibly it is way lower than the one used here which could explain as well the different segmentation behaviour with less chip segments in the SPH than in the FEM. The temperature distributions are given in figure 8.13 where the JC-TANH2010 shows significantly higher temperatures, mainly in the tool-chip interface, compared to the other flow stress models. This figure can be compared to FEM results from [62], their results are shown in figure 8.14 and show a similar pattern with the highest predicted temperatures for JC-TANH2010. This picture allows as well for a qualitative comparison of the predicted chip shapes which show similar segmentation results where JC-TANH2008 is most pronounced as well.

The cut force evolution is shown in figure 8.15. A comparison of the averaged SPH cut forces to FEM and experimental results of [62] is displayed in table 8.11. The SPH cut force

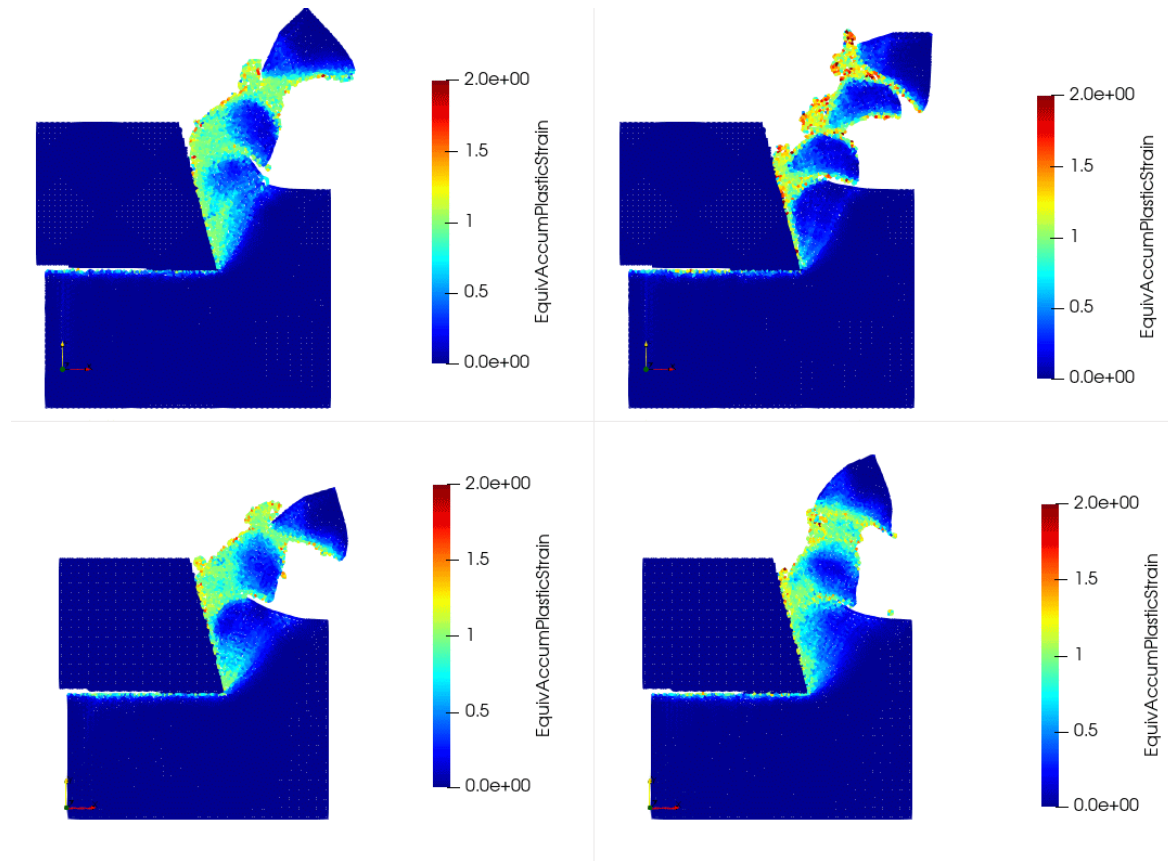


Figure 8.9: Plastic strain distribution for JC-CLASSIC (top left), JC-TANH2008 (top right), JC-TANH2010 (bottom left) and JC-TANH2003 (bottom right) with low particle resolution of 8586 workpiece and 3267 tool particles.

predictions are again generally lower than the FEM results by about 20% – 30%, except for JC-TANH2010 which gives "only" a 5% lower cut force compared to the respective FEM result. Compared to the SPH simulation without damage, the SPH cut forces dropped by about 20% when considering damage. Similar to the SPH simulations without damage, JC-TANH2010 gives the best match to the experimental result with still a large deviation of about 30%. The other three models deviate more, with JC-TANH2008 being the worst (> 50%). The trend of the cut force is different than for the FEM [62]: JC-TANH2010 still performs best in the SPH where JC-TANH2010 and JC-TANH2003 predict the same cut force in the FEM simulation.

JC model	SPH	FEM [62]	Experiment [62]
JC-CLASSIC	200 N	254 N	387 N
JC-TANH2008	169 N	220 N	387 N
JC-TANH2010	287 N	301 N	387 N
JC-TANH2003	241 N	301 N	387 N

Table 8.11: Comparison of cut forces from the SPH with the FEM and experimental results from [62]. The cut forces are scaled to a cut width of 1mm.

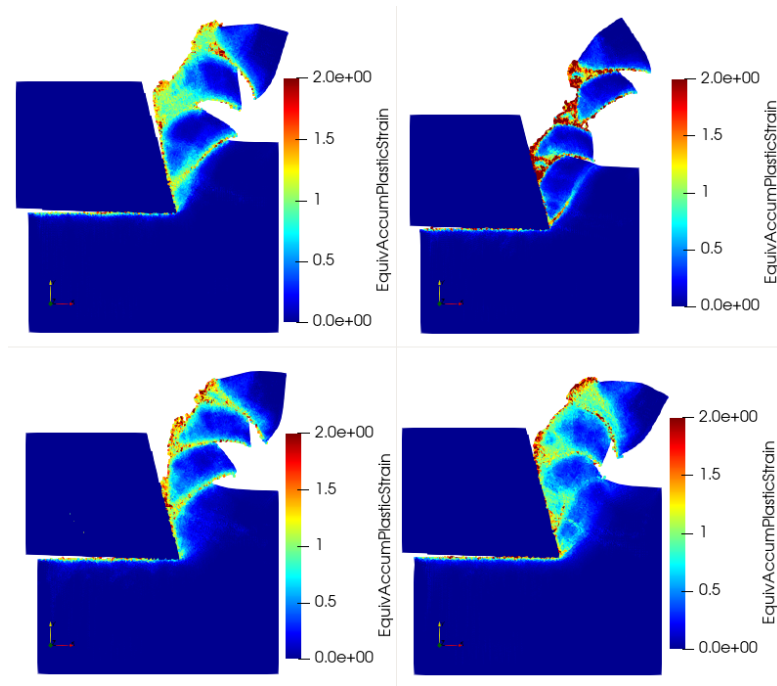


Figure 8.10: Plastic strain distribution for JC-CLASSIC (top left), JC-TANH2008 (top right), JC-TANH2010 (bottom left) and JC-TANH2003 (bottom right) with increased particle resolution of 34668 workpiece and 13384 tool particles.

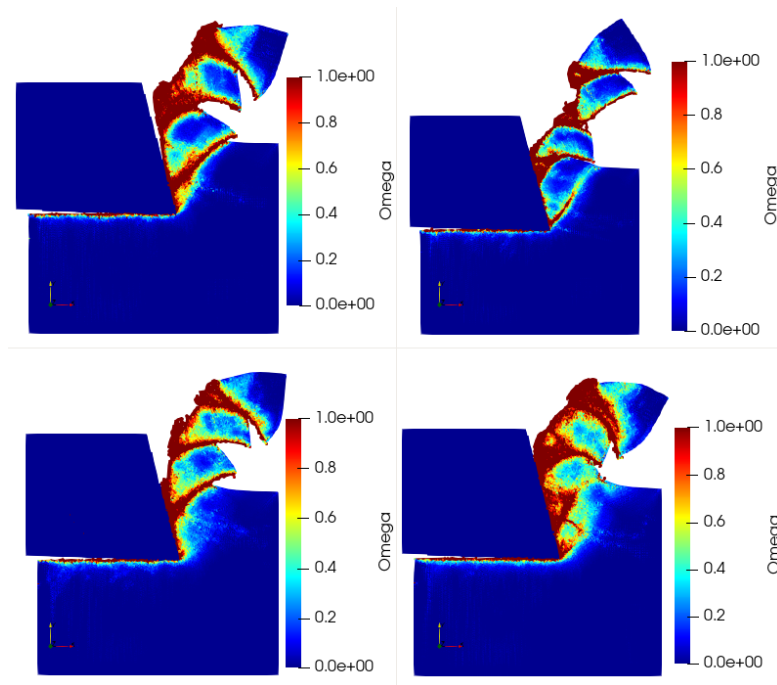


Figure 8.11: Damage variable ω (damage initiation) in the SPH simulations for JC-CLASSIC (top left), JC-TANH2008 (top right), JC-TANH2010 (bottom left) and JC-TANH2003 (bottom right) with increased particle resolution of 34668 workpiece and 13384 tool particles.

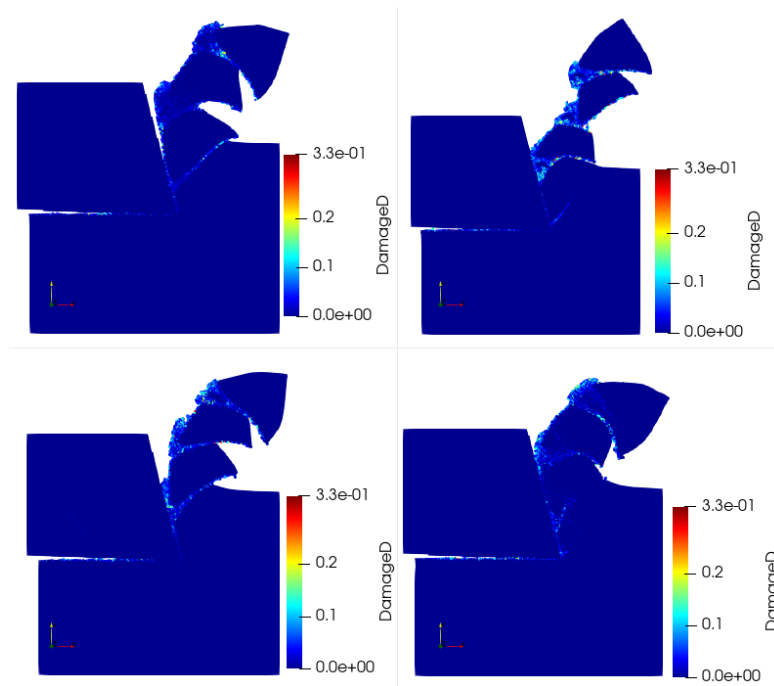


Figure 8.12: Damage variable D (damage evolution) in the SPH simulations for JC-CLASSIC (top left), JC-TANH2008 (top right), JC-TANH2010 (bottom left) and JC-TANH2010 (bottom right) with increased particle resolution of 34668 workpiece and 13384 tool particles.

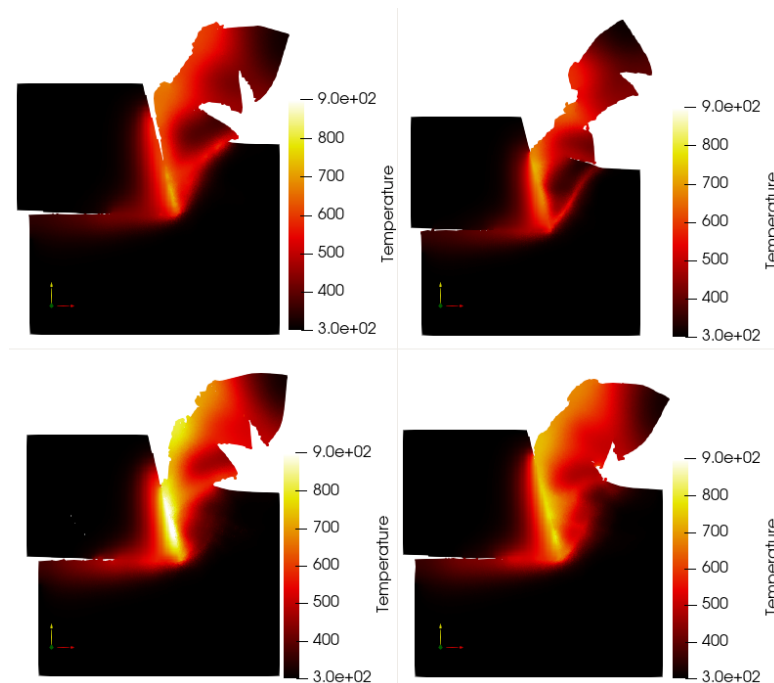


Figure 8.13: Temperature distribution for JC-CLASSIC (top left), JC-TANH2008 (top right), JC-TANH2010 (bottom left) and JC-TANH2010 (bottom right) with increased particle resolution of 34668 workpiece and 13384 tool particles. The temperature unit is in [K].

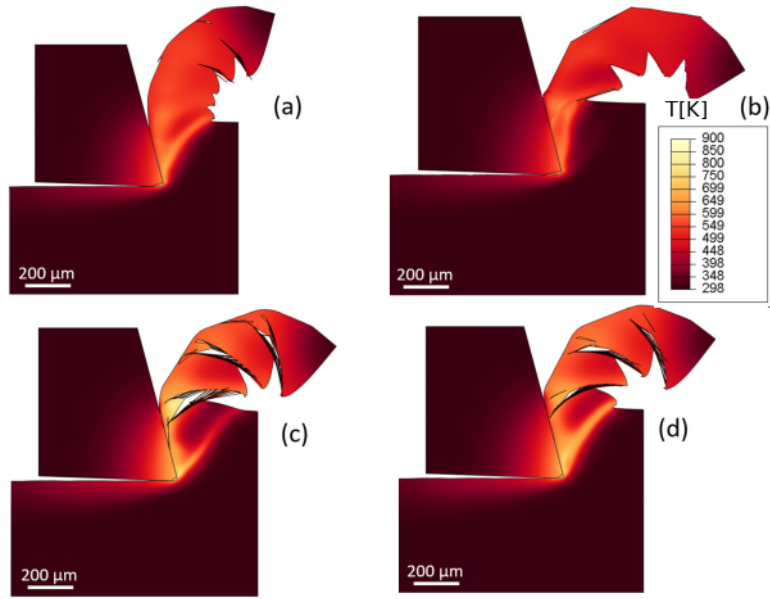


Figure 8.14: Temperature distribution of the FEM simulations conducted by [62] for JC-CLASSIC (top left), JC-TANH2008 (top right), JC-TANH2010 (bottom left) and JC-TANHSO3 (bottom right).

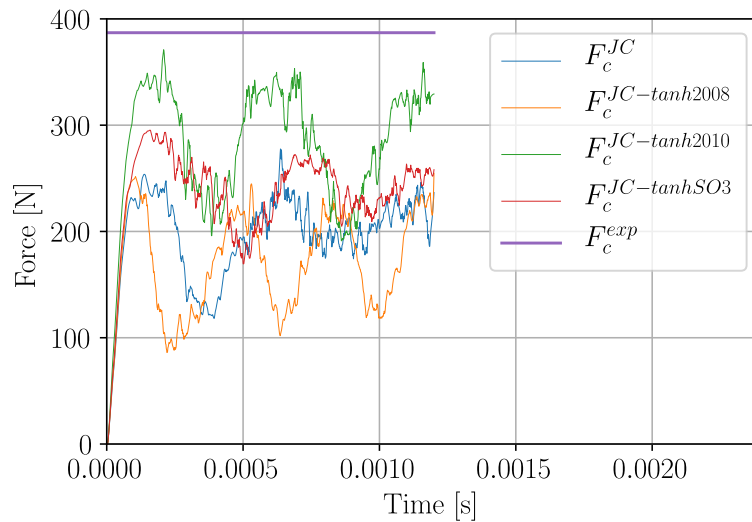


Figure 8.15: Cut forces evolution with the SPH simulations for JC-CLASSIC (top left), JC-TANH2008 (top right), JC-TANH2010 (bottom left) and JC-TANHSO3 (bottom right). The cut forces are scaled to a cut width of 1mm.

8.2.3 Discussion

Orthogonal cutting simulations of Ti6Al4V were performed with JC-classic and three extensions to it with and without damage modelling. The results are compared to the same analyses performed by [62] but with the FEM. The SPH simulations underpredict the cutting forces compared to the same simulations with FEM. The issue is known with commercial solvers like ABAQUS and LS-DYNA and is reported already in the literature [229, 248]. The reason for the lower process force predictions with the SPH are so far not understood and probably stems from the remeshing procedure in the FEM which introduces dispersion into the internal variables due to remapping. Another reason could be that distorted elements appear to have higher stiffness than the continuum, which is the actual reason for remeshing. Simulations without damage modelling gave similar chip segmentation pattern when compared to the FEM but when using damage modelling the chip segmentation does not match well with the FEM simulation in [62]. The reason might be that K_{1C} (G_f) used in the reference simulations in [62] is unknown and was therefore taken from other literature. It is rather obvious that FEM neither SPH predict well the cutting force when compared to experiments. One reason for the deviation is very likely the very low coefficient of friction used in these simulations. Another reason are the underlying constitutive models as well as their material parameters which are often fitted to experimental data at far less severe conditions than those of the cutting process, e.g. within SHPB experiments. A complicating factor here is that the cutting experiments and experiments for obtaining the material properties were carried out on different material batches, whereby their heat treatments as well as the processing prior to testing are unknown. As a consequence the conclusion is drawn that a numerical simulation model of the cutting experiment itself should serve for the inverse identification of material constitutive constants.

8.3 MICRO MILLING OF OFHC COPPER

Micro milling is a main application for the manufacturing of micro features in electrodes for die-sinking electrical discharge machining (EDM) [36, 37]. These electrode tools for the EDM process are commonly made of pure copper (OFHC) or tungsten reinforced copper. The shape and quality of the tool are crucial for the quality and reliability of the EDM process. In that light micro milling is an important part in the production of these electrodes. Key issues are the burr formation and surface roughness induced by the micro milling process. In the investigation conducted here a diamond two flute micro milling tool with a diameter of $d_{tool} = 200\mu m$ and a cutting edge radius of $r_c = 3\mu m$ is applied for a numerical analysis of the burr formation during micro milling of OFHC copper without lubricant and compared against experimental results. For the simulation two material models are used: the Johnson-Cook flow stress model and the Steinberg-Cochran-Guinan-Lund (SCGL) model. The latter, because in [21] it is shown that flow stress predictions are more accurate at higher temperatures with the SCGL-model compared to the JC-model.

8.3.1 Experiments

The experiments in [36, 37] were considered for OFHC and tungsten reinforced copper with and without lubricant. Relevant for this simulation are the experimental results for OFHC copper without lubricant for which unfortunately no force measurements are documented but the burr formation is given for a cut speed of $v_c = 125m/min$ ($n=200'000/min$ at $d_{tool} = 200\mu m$), width and depth of cut of $a_e = a_p = 40\mu m$ and a feed per tooth and revolution of $f_t = 15\mu m$ which gives a tool speed of $v_{tool} = 0.1m/s$ for two tool teeth.

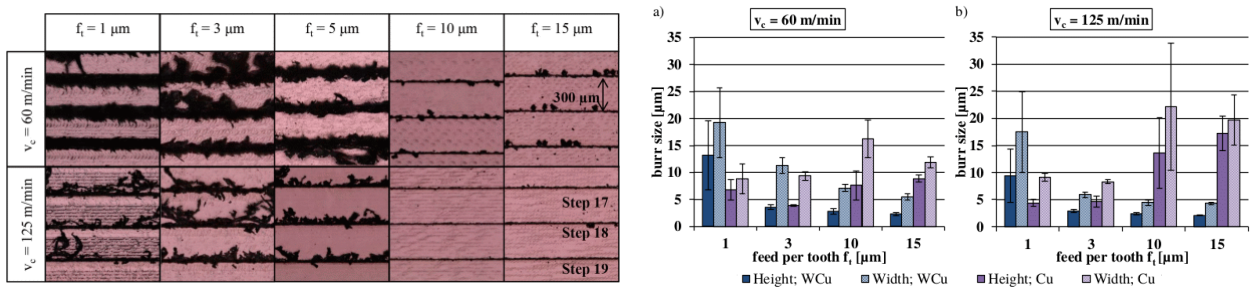


Figure 8.16: Experimental burr formation in micro milling [36, 37].

8.3.2 Numerical Model

The geometry and process parameter definition of the micro milling model are provided with figure 8.17 and the CAD-model of the diamond micro milling tool is displayed in figure 8.18. The following parameters are selected for the simulation:

Workpiece dimensions	Height H [μm]	Width W [μm]	Length L [μm]	
	100	100	100	
Tool geometry	d_{tool} [μm]	Edge radius r_c [μm]	Flutes / teeth	
	200	3	2	
Process parameter	a_p [μm]	a_e [μm]	ω [1/min]	v_{tool} [m/s]
	40	40	200'000	0.1

Table 8.12: Geometry and process parameter of the micro milling simulation.

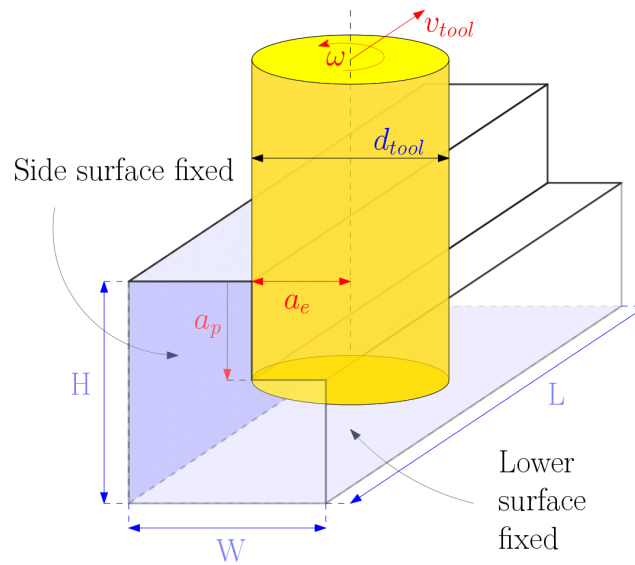


Figure 8.17: Workpiece dimension and process parameter definition of the micro cutting simulation.

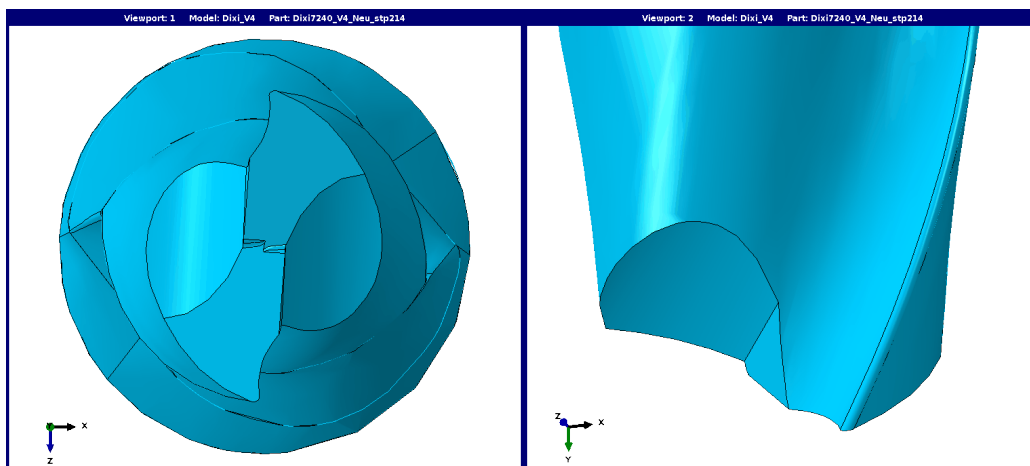


Figure 8.18: CAD model of the diamond tool DIXI v4 viewed from the bottom (left) and from the side (right).

The discretised tool and workpiece model are shown in figure 8.19. The tool is modelled as rigid with 1121 tetrahedrons and the workpiece is discretised with $30 \times 30 \times 30 = 27000$ particles.

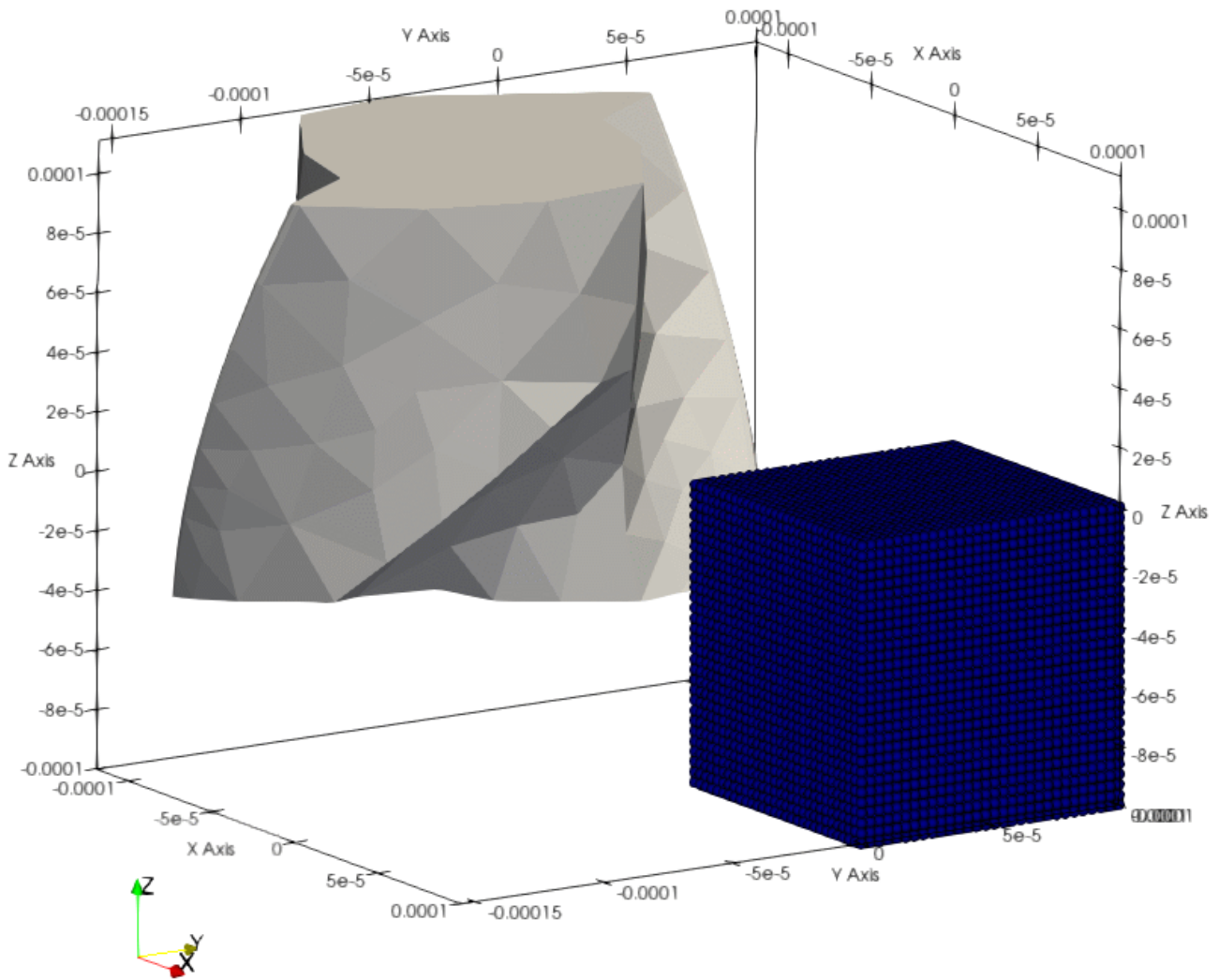


Figure 8.19: Discretised tool and workpiece model in the micro milling simulation.

8.3.3 SCGL Model

The Steinberg-Cochran-Guinan-Lund (SCGL) model is a semi-empirical model that was developed by Steinberg [231] for high strain-rate applications with an extension to low strain-rates by Steinberg and Lund [230]. This model incorporates a temperature and pressure dependent shear modulus as well as a melt temperature model based on the density which is affected by hydrostatic pressures.

8.3.3.1 SCG Shear Modulus Model

The Steinberg-Cochran-Guinan (SCG) shear modulus model [231, 275] is used in the simulation with the SCGL-flow stress model. It is pressure and temperature dependent and of the following form:

$$\mu(p, T) = \mu_0 + \frac{\partial\mu}{\partial p} \frac{p}{\eta^{1/3}} + \frac{\partial\mu}{\partial T} (T - 300.0), \text{ with } \eta = \frac{\rho}{\rho_0} \quad (8.26)$$

with μ_0 being the shear modulus at the reference state at $T = 300\text{K}$, $p = 0$ and $\eta = 1$. T is the temperature and p the hydrostatic pressure. With the temperature T approaching T_f the shear modulus is set to zero. The melting temperature T_f is computed with the SCG melt temperature model (8.27).

8.3.3.2 SCG Melt Temperature Model

The melting temperature T_f depends in this model on the hydrostatic pressure p which can be expressed also by the density ratio $\eta = \frac{\rho}{\rho_0}$:

$$T_f(\rho) = T_{m0} \cdot \exp\left(2 \cdot a \left(1 - \frac{1}{\eta}\right)\right) \cdot \eta^{2 \cdot (\Gamma_0 - a - 1/3)}, \text{ with } \eta = \frac{\rho}{\rho_0} \quad (8.27)$$

The melting temperature T_f is in hydrostatic tension constant $T_f = T_{m0}$ and increases for compressive hydrostatic pressure. Since in machining operations the hydrostatic pressures reach up to 3GPa this is expected to have some effect on the flow stress. The melt temperature characteristics is shown in figure 8.20 depending on the density.

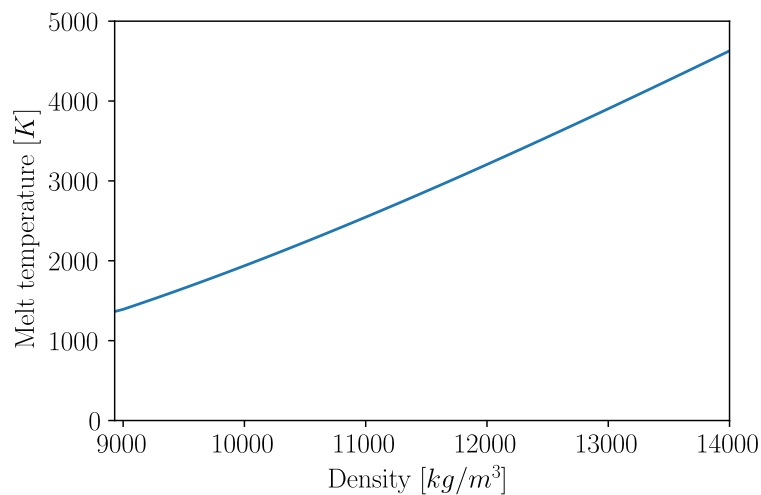


Figure 8.20: Melt temperature of OFHC copper predicted with the SCG-MELT-temperature model. The chart depends on the density which is related to the hydrostatic pressure.

8.3.3.3 SCGL Flow Stress Model

The flow stress model reads as:

$$\sigma_y(\varepsilon_{pl}, \dot{\varepsilon}_{pl}, T) = (\sigma_a \cdot f(\varepsilon_{pl}) + \sigma_{th}(\dot{\varepsilon}_{pl})) \cdot \frac{\mu(p, T)}{\mu_0} \quad \text{for } \sigma_a \leq \sigma_{max} \text{ and } \sigma_{th} \leq \sigma_p \quad (8.28)$$

with σ_a the athermal component of the flow stress, $f(\varepsilon_{pl})$ a function representing the hardening, σ_{th} is the thermally activated component of the flow stress, $\mu(p, T)$ is the pressure-dependent shear modulus and μ_0 is the shear modulus at standard temperature and pressure. The athermal stress component σ_a has a saturation at σ_{max} and the thermally activated stress has its saturation at the Peierls stress σ_p . The shear modulus $\mu(p, T)$ in this model is computed with the SCG shear modulus model (8.26).

The strain hardening function $f(\varepsilon_{pl})$ is:

$$f(\varepsilon_{pl}) = (1 + \beta \cdot (\varepsilon_{pl} + \varepsilon_{pi}))^n \quad (8.29)$$

with β and n being work hardening parameter and ε_{pi} is the initial equivalent plastic strain. The thermal component σ_{th} is given implicit:

$$\dot{\varepsilon}_{pl} = \left[\frac{1}{C_1} \cdot e^{\frac{2U_k}{k_b T} \left(1 - \frac{\sigma_{th}}{\sigma_p}\right)^2} + \frac{C_2}{\sigma_{th}} \right]^{-1} \quad (8.30)$$

with $2 \cdot U_k$ the energy to form a kink-pair in a dislocation segment of length L_d , k_b the Boltzmann constant and σ_p the Peierls stress. The constants C_1 and C_2 are given with:

$$C_1 = \frac{\rho_d \cdot L_d \cdot a \cdot b^2 \cdot \nu}{2 \cdot w^2} \quad (8.31)$$

$$C_2 = \frac{D}{\rho_d \cdot b^2} \quad (8.32)$$

and ρ_d is the dislocation density, a is the distance between Peierls valleys, b is the magnitude of the Burgers vector, ν the Debye frequency, w is the width of a kink loop and D the drag coefficient. In a 3D display the dependency of σ_{th} from temperature T and strain rate $\dot{\varepsilon}_{pl}$ displays as:

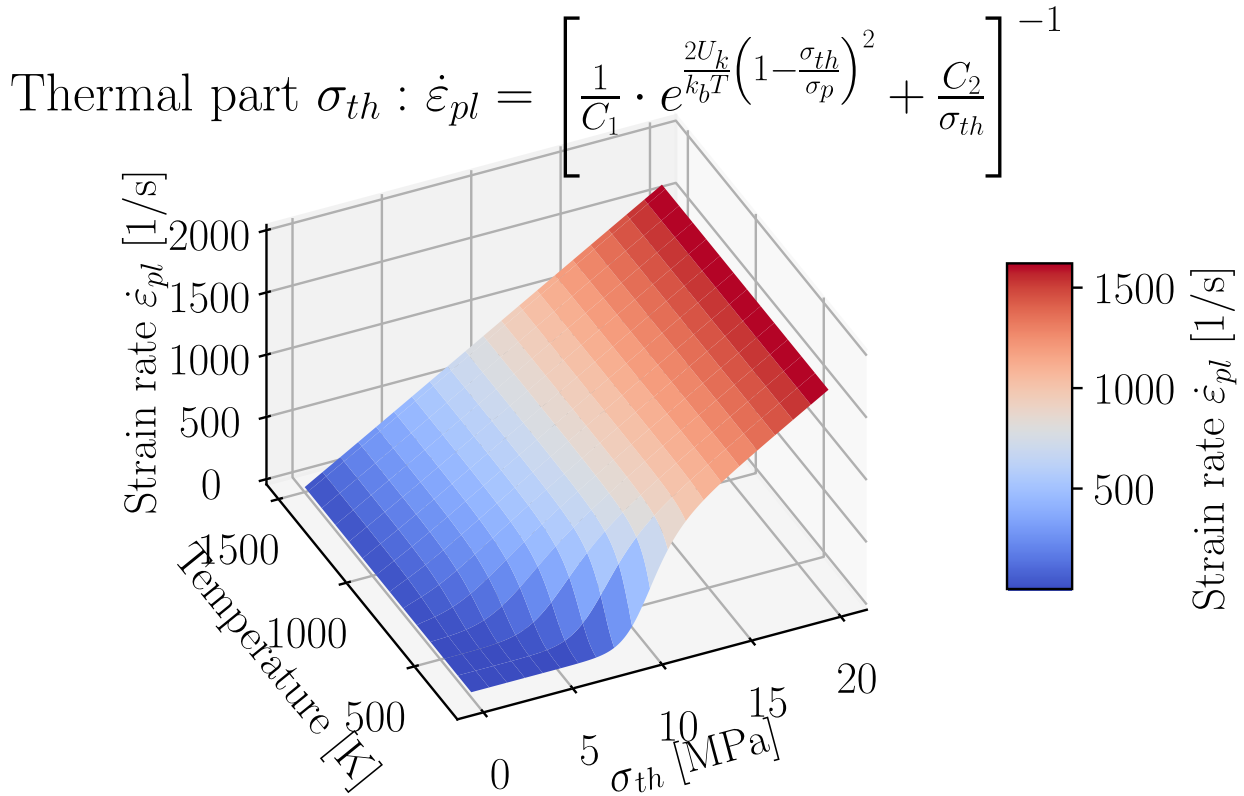


Figure 8.21: SCGL-model: thermal part $\sigma_{th}(T, \dot{\epsilon}_{pl})$ of the flow stress.

8.3.3.4 Numerical Integration of the SCGL Flow Stress Model

For similar reasons as in chapter 8.1.1.1 the SCGL-model is integrated with the SECANT B-method (7.19). Because the thermal part of the flow stress σ_{th} is given implicitly in (8.30), the equation is iteratively solved with a bisection algorithm to find $\sigma_{th}(\dot{\epsilon}_{pl}, T)$.

8.3.4 Material Parameters

The simulations are performed with the JC-CLASSIC and SCGL flow stress models with material parameters available from the literature. Physical properties are given in table 8.13. The JC-CLASSIC flow stress parameters are taken from [105] who conducted static tensile tests, torsion tests and dynamic SHB tests. The parameters are given in table 8.14. The SCGL flow stress model parameters are based on data from [231] for the athermal part, the Peierl's stress is from [94] and the other parameters from [21]. They are summarized in table 8.17. The material parameters for the SCG-MELT temperature model are given in table 8.15 and for the SCG-SHEAR modulus model in table 8.16. The simulations with both flow stress models consider heat transfer in the workpiece and plastic dissipation into heat was considered with a Taylor-Quinney coefficient of $\eta_{TQ} = 0.90$. Heating due to friction was assumed with

$\eta_{fric} = 0.5$ since no tool heat transfer is modelled. The friction coefficient is assumed as $\mu_{fric} = 0.35$. A time step of $\Delta t = 5 \cdot 10^{-11} s$ is used in both analyses.

E	Poisson	Density	Specific heat capacity	Conductivity	Thermal expansion	Source
[GPa]	$\nu[-]$	$\rho[kg/m^3]$	$c_p[\frac{J}{kgK}]$	$\lambda[\frac{W}{mK}]$	$\alpha_{th}[1/K]$	
110	0.34	8960	383	394	-	[105, 257]

Table 8.13: Physical properties of OFHC copper.

A	B	C	m	n	$\dot{\epsilon}_{pl}^0$	T_{ref}	T_f	Source
[MPa]	[MPa]	$[-]$	$[-]$	$[-]$	$[s^{-1}]$	[K]	[K]	
90	292	0.025	1.09	0.31	1.0	273	1356	[105]

Table 8.14: Johnson Cook flow stress model for OFHC copper.

$T_{m0}[K]$	$\Gamma_0[-]$	$a[-]$	Source
1356.5	1.99	1.5	[21, 79, 143]

Table 8.15: Material parameters for SCG melt temperature model used in the simulations.

$\mu_0[GPa]$	$\frac{\partial \mu}{\partial p}$	$\frac{\partial \mu}{\partial T}[GPa/K]$	Source
47.7	1.3356	0.018126	[21, 79]

Table 8.16: Material parameters for SCG shear modulus model used in the simulations.

$\sigma_a[MPa]$	$\sigma_{max}[MPa]$	$\beta[-]$	$\epsilon_{pi}[-]$	$n[-]$	$C_1[/math>/s]$	$U_k[eV]$	$\sigma_p[MPa]$	$C[MPa/s]$	Source
125	640	36	0	0.45	$0.71 \cdot 10^6$	0.31	20	0.012	[21, 231]

Table 8.17: Material parameters for SCGL flow stress model used in the simulations.

8.3.5 Results

The runtimes for the SPH simulations were in the order of 88h for 40'000'000 time steps on a NVIDIA QUADROGP 100 GPU. The raw process forces are shown in figure 8.22 for the simulation with the JC-classic- and the SCGL-flow stress model. Both show large force peaks for the time period when the cutting edge is engaged. These peaks are predicted with about 4 times higher magnitude by the SCGL-flow stress model in comparison to JC-CLASSIC. This is possibly due to the stronger thermal softening of JC-CLASSIC.

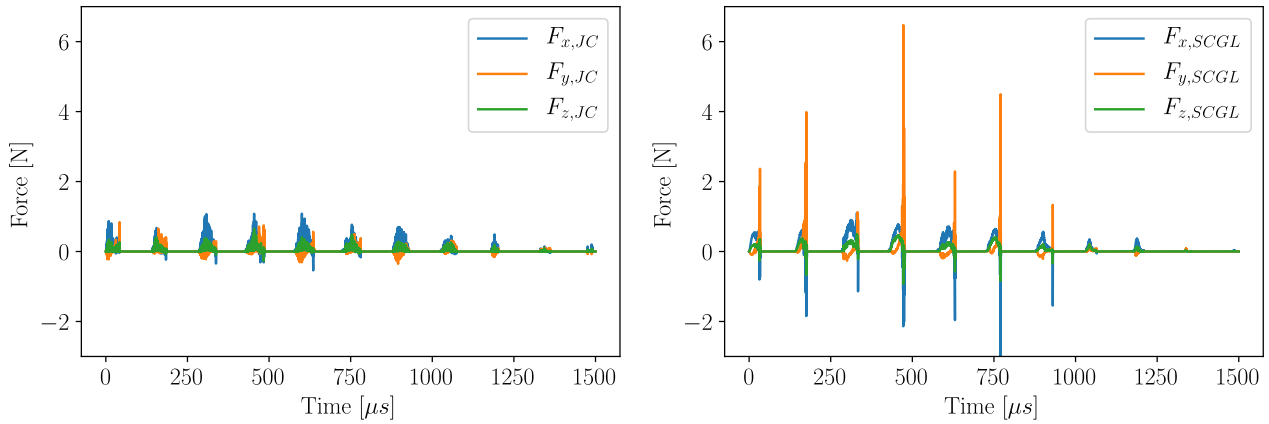


Figure 8.22: Resulting tool forces in the numerical micro milling simulation for JC-CLASSIC- (left) and SCGL (right)- flow stress model.

Figure 8.23 shows the residual stresses in the workpiece at the simulation end. The SCGL-model predicts higher residual stresses than the JC-CLASSIC-model. While with JC-CLASSIC almost no burr formation is predicted, with SCGL a large burr can be observed with a maximum height of $\approx 49\mu m$ and width of $\approx 65\mu m$, see figure 8.24. The burr is predicted roughly 2 – 3 times higher than in the experiment, where the burr height is between $15...20\mu m$ and the burr width is between $15...25\mu m$, see also figure 8.16.

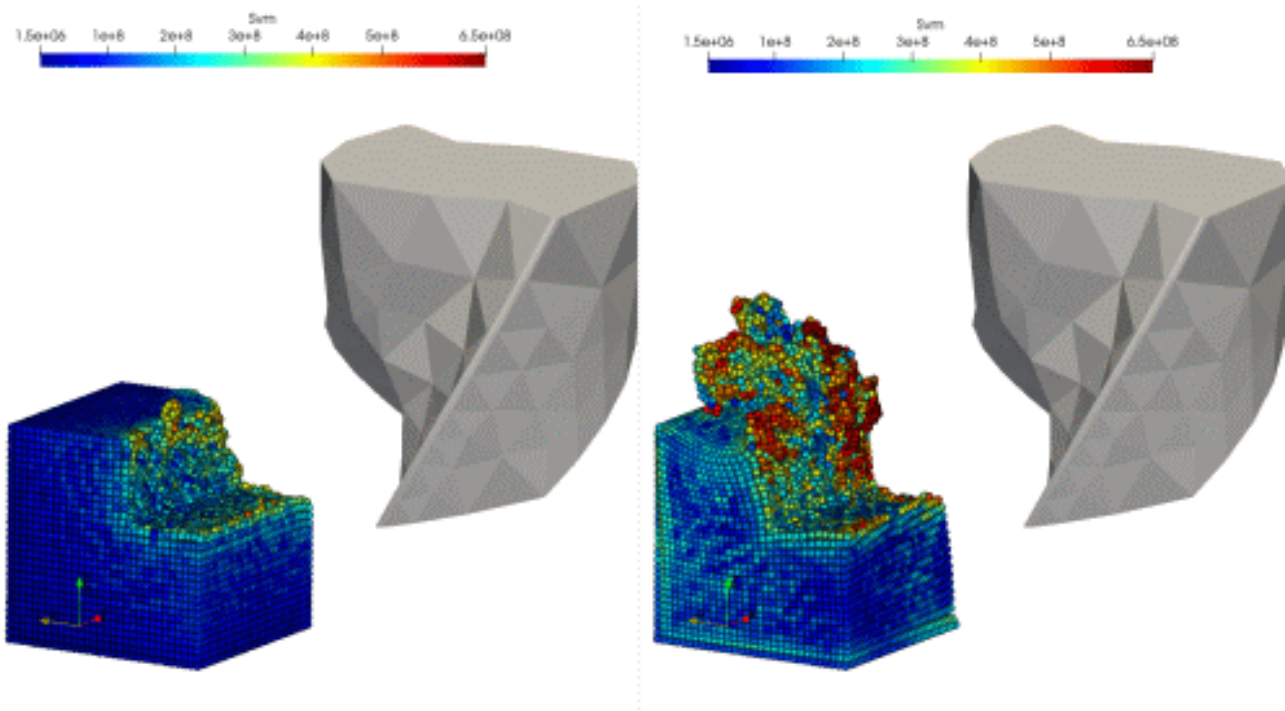


Figure 8.23: Stress distributions [Pa] after the simulation end in the numerical micro milling simulation for JC-CLASSIC- (left) and SCGL (right)- flow stress model.

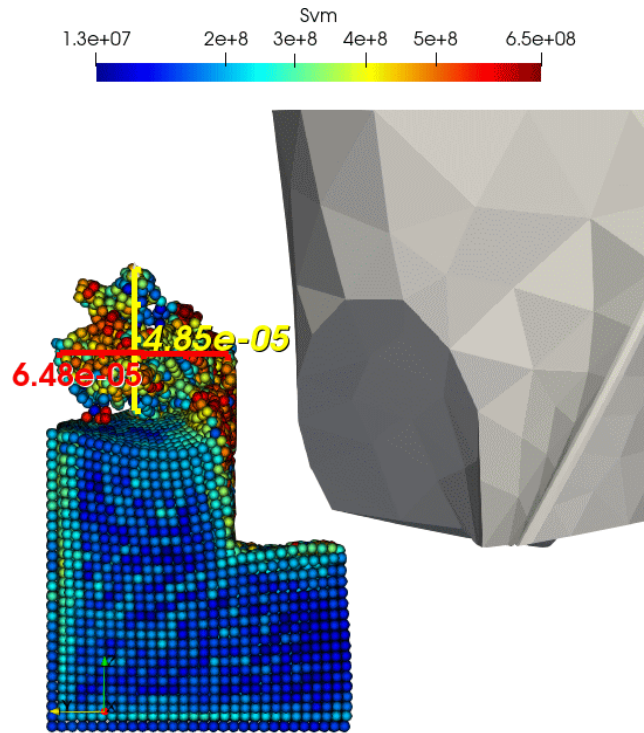


Figure 8.24: Maximum burr height (yellow line $48.5\mu m$) and width (red line $64.8\mu m$) predicted with the SCGL- flow stress model.

8.3.6 Discussion

Two different flow stress models, JC-CLASSIC and SCGL were applied to the simulation of micro milling. In comparison to experimental results SCGL outperforms JC-CLASSIC as it is able to predict the burr formation, even though to some higher extent than observed experimentally, but which cannot be seen with the JC-CLASSIC-model at all. Possibly JC-CLASSIC suffers due to the bad prediction of flow stresses towards higher temperatures due to thermal softening. This is probably also the reason for the prediction of lower process forces.

MATERIAL PARAMETER DETERMINATION

In the preceding chapter several orthogonal cutting simulations were performed with constitutive model constants taken from literature. These values show larger variations and so the results do. The 'same' material can have different 'initial conditions': slightly different chemical compositions within the tolerance bands as well as different heat treatments and processing methods of the raw material, e.g. rolling or forging. These are often not clear which makes it difficult to compare various constitutive model parameter sets from literature or to select the one suited best for simulations. In an attempt to circumvent this problem, a testing program is initiated where Ck45 (1.1191) and Ti6Al4V (3.7165, Grade 5) raw material in bar form has been purchased. Test specimen from this material are subjected to hardness tests to detect any irregularities that may be caused by the manufacturing process. The micro structure is then examined by means of etched samples and EBSD in order to investigate the microstructure as well as possible preferential orientations of the grains or anisotropies. Tensile tests are carried out on test specimen of this material and material parameter for quasi-stationary conditions are derived as well as the rate dependency at low strain rates. Further, the main part of this material is used for orthogonal cutting experiments. These cutting experiments are then used to drive inverse parameter identifications of constitutive model constants within numerical cutting simulations of these experiments. Since the inverse parameter identification requires many iteration loops it is crucial to use cutting experiments at high cut speeds as they scale inversely proportional to the required simulation time. The cutting simulations are performed with the 2D SPH orthogonal cutting model developed in the previous chapter 8.2 as it can provide fast and accurate results with low computing times. The inversely identified material parameters are used on the one hand to compare them to parameters derived from the tensile tests. On the other hand, the inversely identified material parameters are used for the numerical simulation of cutting at other process conditions and the results are compared versus experimental results.

9.1 RAW MATERIAL

Raw material was ordered in cylindrical form with a diameter of 80mm and a length of 90mm from the same badge/slab for each material. The inner parts of these cylinders were removed by the EDM process and then used for manufacturing of test specimens for tensile testing, see chapter 9.2.1. The outer cylinders were used for orthogonal cutting experiments. From each material a small disc with a height of $\approx 1\text{cm}$ was cut from the raw cylinder and used to perform hardness measurements on the top surface. After hardness measurements the same discs were cut to prepare etched samples from the top and side surface for microstructural investigations and EBSD analyses. A sketch of such a disc with denominations is shown together with the hardness measurement directions in figure 9.2.

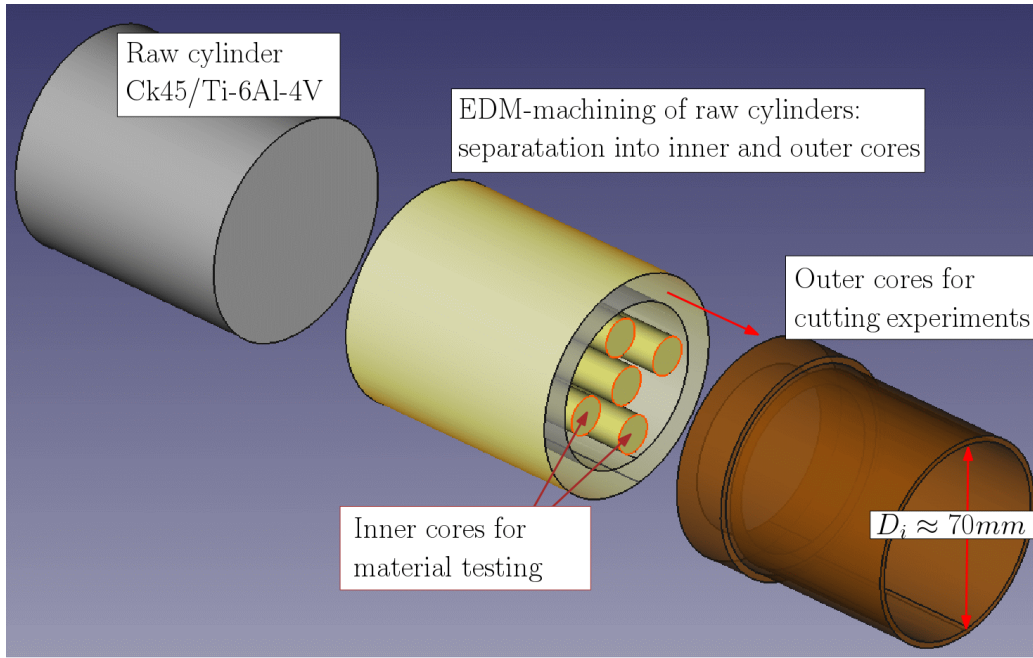


Figure 9.1: Raw material (left) usage for material tests (middle) and orthogonal cutting tests (right).

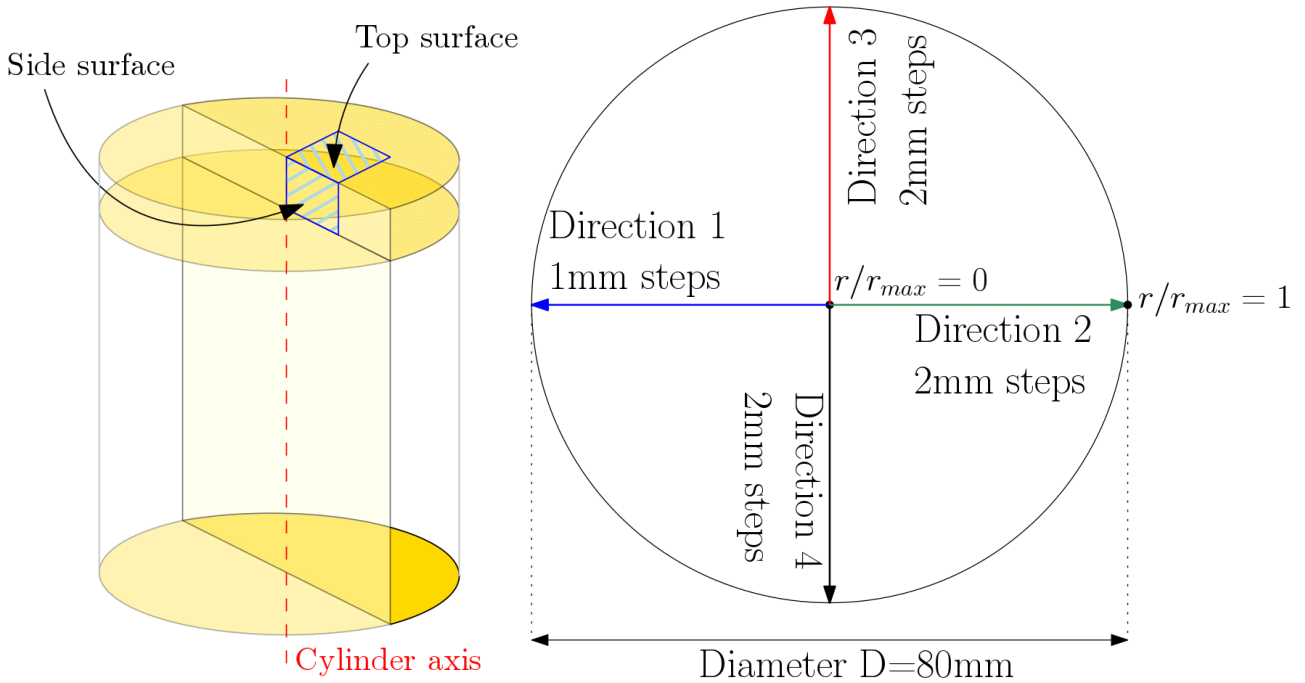


Figure 9.2: Sketch of a disc cut from raw cylinder with denominations (left) and top surface hardness measurement directions (right).

9.1.1 Chemical Analysis

9.1.1.1 Ti6Al4V

Ti6Al4V is an alloy containing 6% (weight) Aluminium and 4% (weight) of Vanadium. This alloy consists of two phases: α -phase and β -phase. The α -phase is stabilized by aluminium and has a hcp-structure, while the β -phase is stabilized by vanadium, consisting of a bcc-lattice [17]. This batch of material was produced using the triple Vacuum Arc Remelting (VAR) method. After production a heat treatment at 750°C for 90min was performed followed by air cooling. The chemical composition is given from the supplier in table 9.1 and the tensile properties (minimum values) in table 9.2.

Fe	C	N	H	O	Y	Al	V	Residuals each (Max)	Residuals total (max)	Ti
0.111	0.025	0.020	0.003	0.15	< 0.005	6.12	4.11	< 0.10	< 0.40	Balance

Table 9.1: Ti6Al4V: supplier information on the chemical composition from this material batch.

Tensile strength [MPa]	Yield strength (0,2% Offset) [MPa]	Elongation at break [%]	Reduction of Area [%]	Hardness test [HRC]
952	869	16.5	39	30.0

Table 9.2: Ti6Al4V: supplier information on tensile test results from this material batch.

9.1.1.2 Ck45

The material batch of Ck45 (C45E) was produced in an electric shaft furnace and afterwards rolled into cylindrical form. The chemical composition is given from the supplier in table 9.3 and the tensile properties are shown in table 9.4. A Jominy-test was performed by the supplier and the results are shown in table 9.5. The material exhibits a high hardenability at the outer surface where the hardness is up to 59 HRC which indicates a martensitic microstructure, while at higher depths the hardness drops to 19 HRC indicating a ferritic-perlitic microstructure.

C	Mn	Si	P	S	Cr	Ni	Mo	Cu
0,445	0,760	0,240	0,018	0,020	0,180	0,050	0,010	0,150
Sn	Al	Ti	V	Nb	B			
0,006	0,010	0,010	0,002	0,001	0,0000			

Table 9.3: Ck45: supplier information on the chemical composition from this material batch.

MATERIAL PARAMETER DETERMINATION

Tensile strength R_m [MPa]	Yield strength R_e (0,2% Offset) [MPa]	Elongation at break A5 [%]
671	420	22.2

Table 9.4: Ck45: supplier information on tensile test results from a normalized sample of this material batch.

[mm]	1	2	3	4	5	6	7	8	9	10	11	13	15	20	25	30
HRC	59	57	54	46	37	34	30	29	28	27	26	25	24	23	21	19

Table 9.5: Ck45: supplier information on Jominy test results from this material batch.

9.1.2 Hardness

Vickers hardness measurements HV10 were conducted for Ck45 and Ti6Al4V. The measurements were performed on the top faces along four directions of the samples where in one direction a 1mm stepping and in the others a 2mm stepping was used. Both discs are shown in figure 9.3. The results of the hardness measurement are shown in figure 9.4 where the Ck45 shows a hardness reduction at the disc center within a radius of around 6mm. Towards the outer radius the hardness is constant except for the very last measurement point in direction 2 which shows a slight drop in hardness. The hardness distribution of the Ti6Al4V sample is almost constant in all directions and radial positions with the exception of some spots.



Figure 9.3: Ck45 (left) and Ti6Al4V (right) discs from cylinders used for the hardness measurements. The Ck45 disc is shown here before grinding, polishing and hardness measurements while the Ti6Al4V is already cut in half for microstructural investigations with the right half showing imprints from the hardness measurements (2mm stepping) along the slightly visible red line.

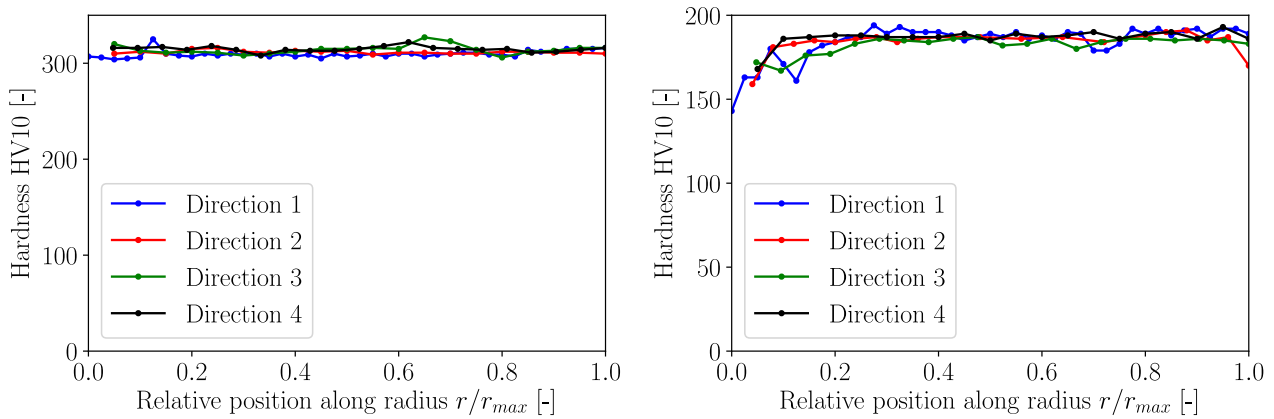


Figure 9.4: Hardness measurement Ti6Al4V(left) and Ck45 (right).

9.1.3 Microstructure

The microstructure of the two materials is investigated here by etching and EBSD-analysis. This investigation should indicate possible irregularities of the grain structure or anisotropies in the material which could influence the material modelling for numerical simulations.

9.1.3.1 Etching

Etched samples were prepared for microstructural analyses of the top and side surface. The Ti6Al4V samples were etched with Kroll. The microstructure of the top surface is shown in figure 9.5 and for the side surface in figure 9.6. Due to the heat treatment both show a uniform microstructure without any salience. The Ck45 was etched with Nital. A ferritic-perlitic microstructure is visible and towards the outer surface of the microstructure decarburations and mill scales are visible on the top surface, see figure 9.8. At the disc center the microstructure is uniform, see figure 9.8. The side surface microstructure revealed a columnar structure along the cylinder axis, see figure 9.9. This is likely to have been induced by rolling during the manufacturing process.

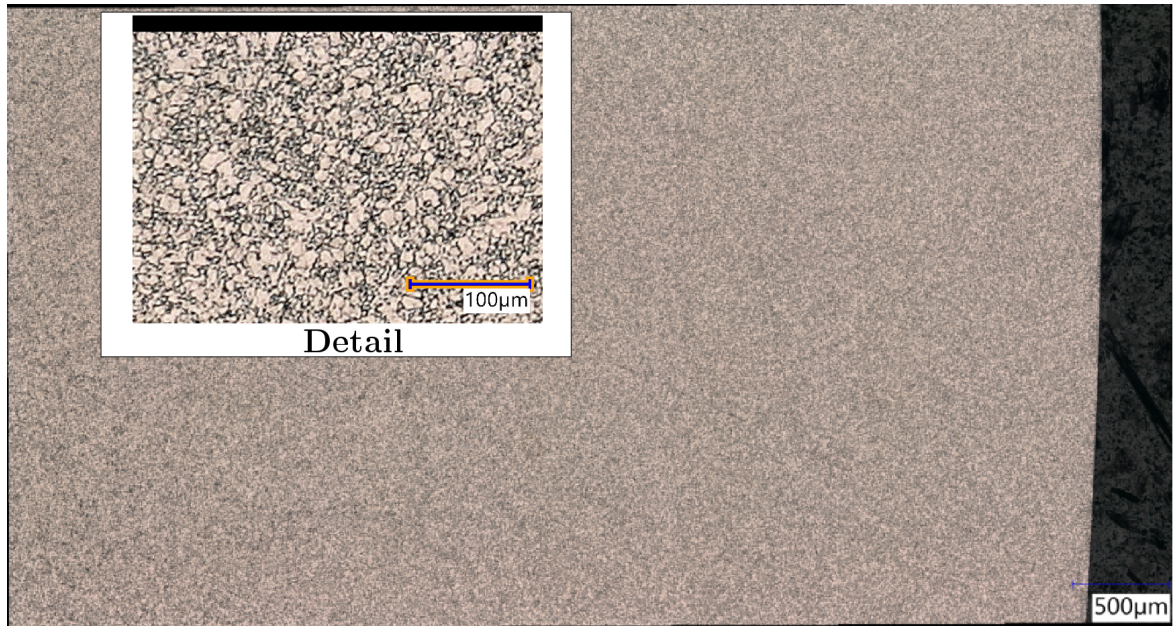


Figure 9.5: Microstructure of Ti6Al4V: the top surface shows a uniform grain structure.

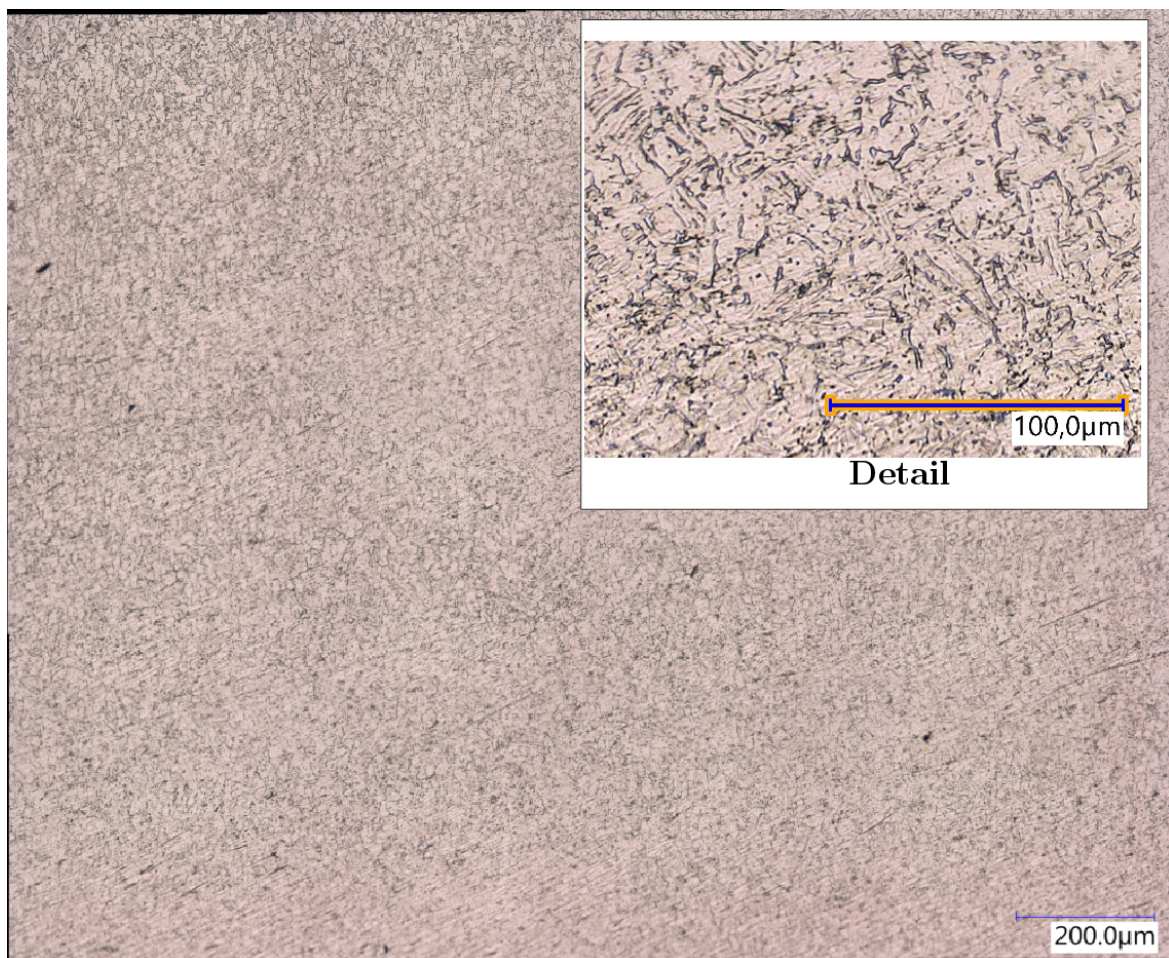


Figure 9.6: Microstructure of Ti6Al4V: the side surface shows a uniform grain structure.



Figure 9.7: Microstructure of Ck45 steel: top surface at the disc center showing a uniform grain structure.

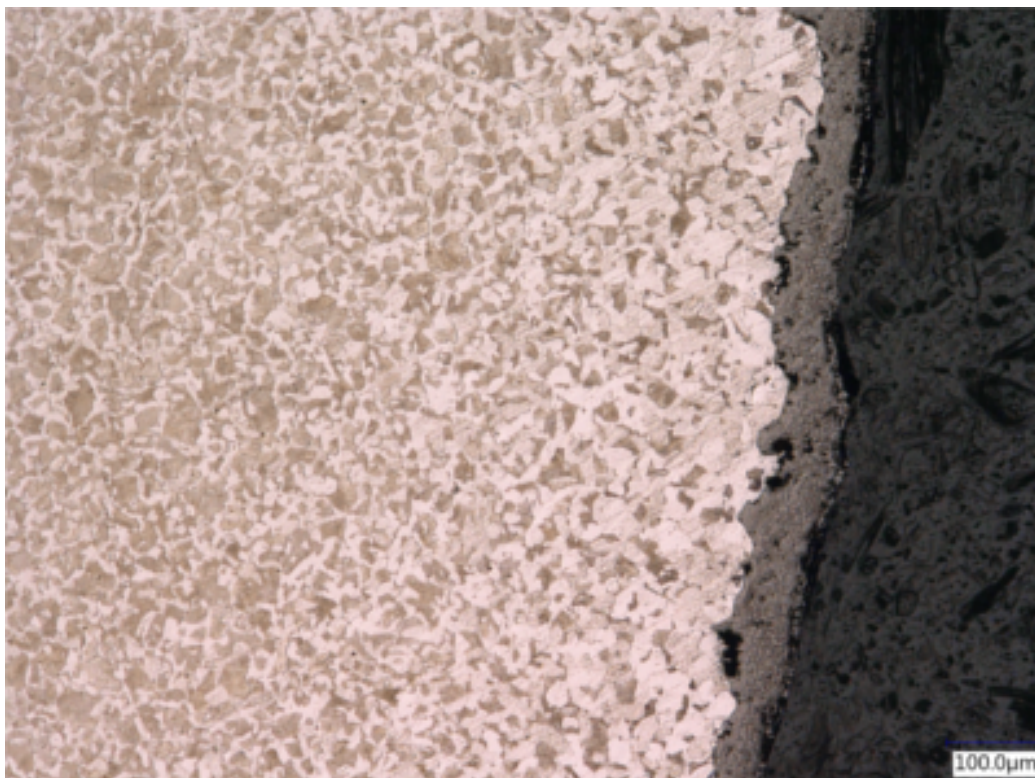


Figure 9.8: Microstructure of Ck45 steel: top surface at outer radius showing decarburation and mill scale.



Figure 9.9: Microstructure of Ck45 steel: side surface showing a columnar structure.

9.1.3.2 EBSD

The crystallographic orientations in the grains and the textures were measured by the Electron Back Scatter Diffraction-analysis (EBSD) for the top and side surfaces of the Ck45 and Ti6Al4V material. The measured areas of the samples are given in table 9.6. The EBSD-analysis of Ti6Al4V revealed a slightly different ratio of α - and β -phase for top and side surface. The average grain diameter and average aspect ratios of the grains are similar for the side and top surface. The results, together with grain sizes and aspect ratios, are given in table 9.7. Grain sizes and aspect ratios determined from the EBSD-analysis of the Ck45 material are shown with in table 9.8. The grain orientations of Ti6Al4V are shown for the side surface in figure 9.10 and for the top surface in figure 9.13, the distribution of α and β -phases for the side surface in figure 9.11 and for the top surface in figure 9.14. The pole figures of the α -phases are given with figures 9.12 and 9.15 for side and top surface, respectively. The pole figures reveal a slightly stronger texture in the side surface than in the top surface. The grain orientations of Ck45 are shown for the top surface in figure 9.16 and for the side surface in figure 9.18. Similar to Ti6Al4V, the side surface shows a stronger texture than the top surface which could have been induced from the rolling process during manufacturing.

Specimen	Surface	X-size [μm]	Y-size [μm]	Figures
Ti6Al4V	Side surface	443	347	9.10, 9.11, 9.12
Ti6Al4V	Top surface	331	428	9.13, 9.14, 9.15
Ck45	Side surface	545	428	9.16, 9.17
Ck45	Top surface	709	556	9.18, 9.19

Table 9.6: EBSD measurement sizes of the four specimen.

Surface	Avg. equiv. grain diameter D_g [μm]	Std.dev. μ_{D_g} [μm]	Avg. grain aspect ratio	Std.dev. grain aspect ratio	α -phase vol. %	β -phase vol.%
Side surface	9.862	4.198	1.79	0.621	96.69	3.31
Top surface	9.076	3.246	1.7	0.519	94.76	5.24

Table 9.7: Ti6Al4V: EBSD measurement results for side and top surface.

Surface	Average equiv. grain diameter D_g [μm]	Std. dev. μ_{D_g} [μm]	Avg. grain aspect ratio	Std. dev. grain aspect ratio	Comment
Side surface	17.75	13.47	1.75	0.5	noisy raw data
Top surface	14.30	9.25	1.81	0.6	

Table 9.8: Ck45: EBSD measurement results for side and top surface.

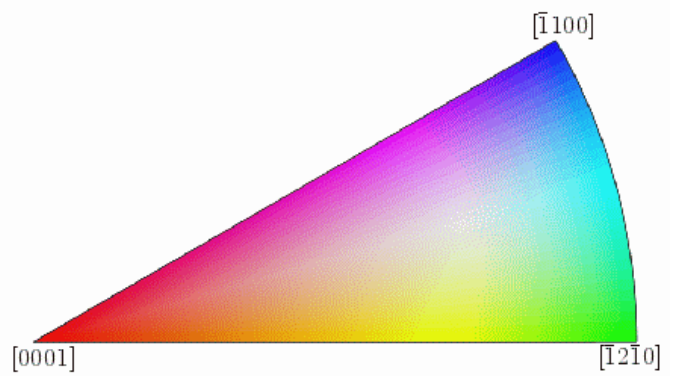
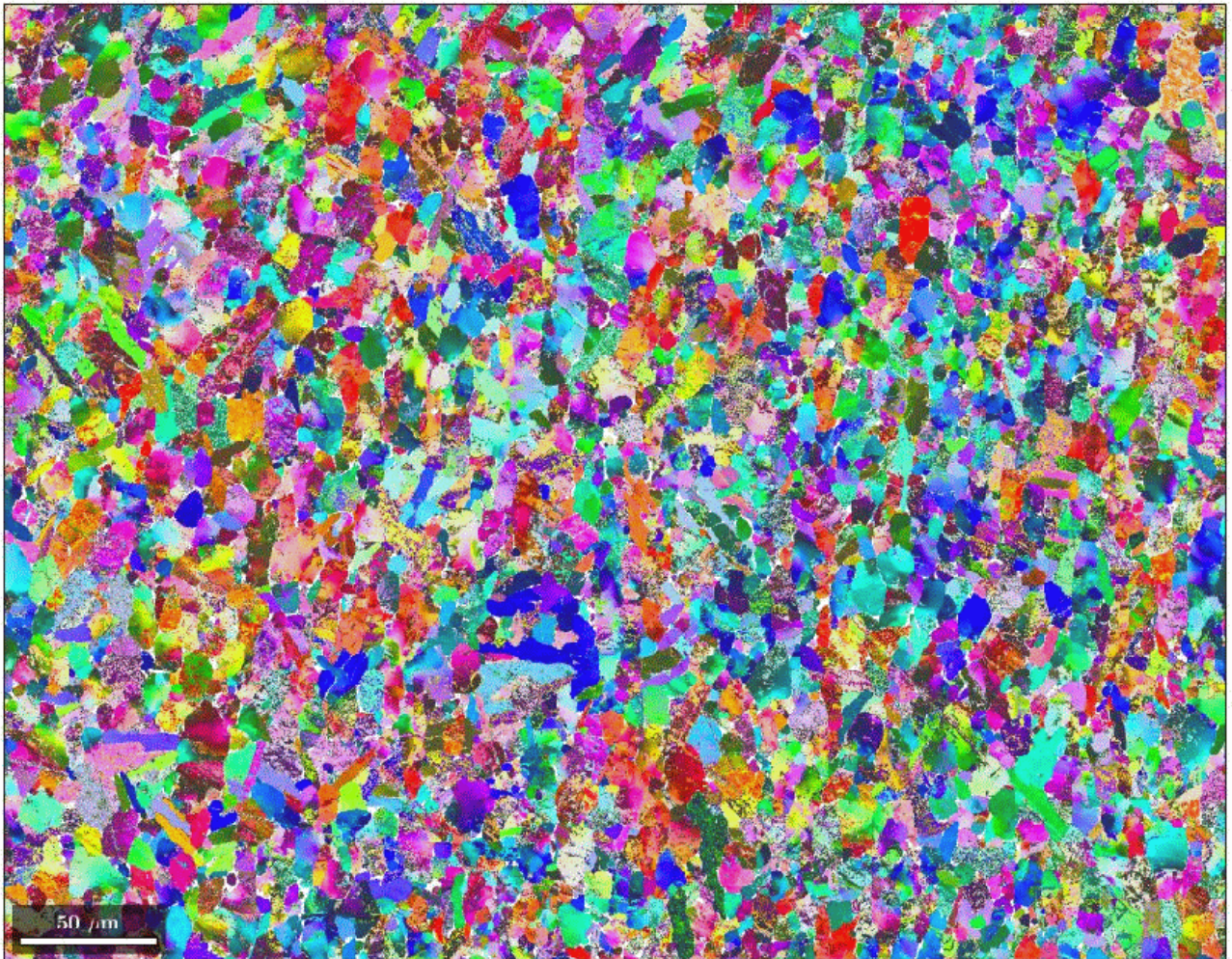


Figure 9.10: EBSD of Ti6Al4V: side surface with crystal orientations.

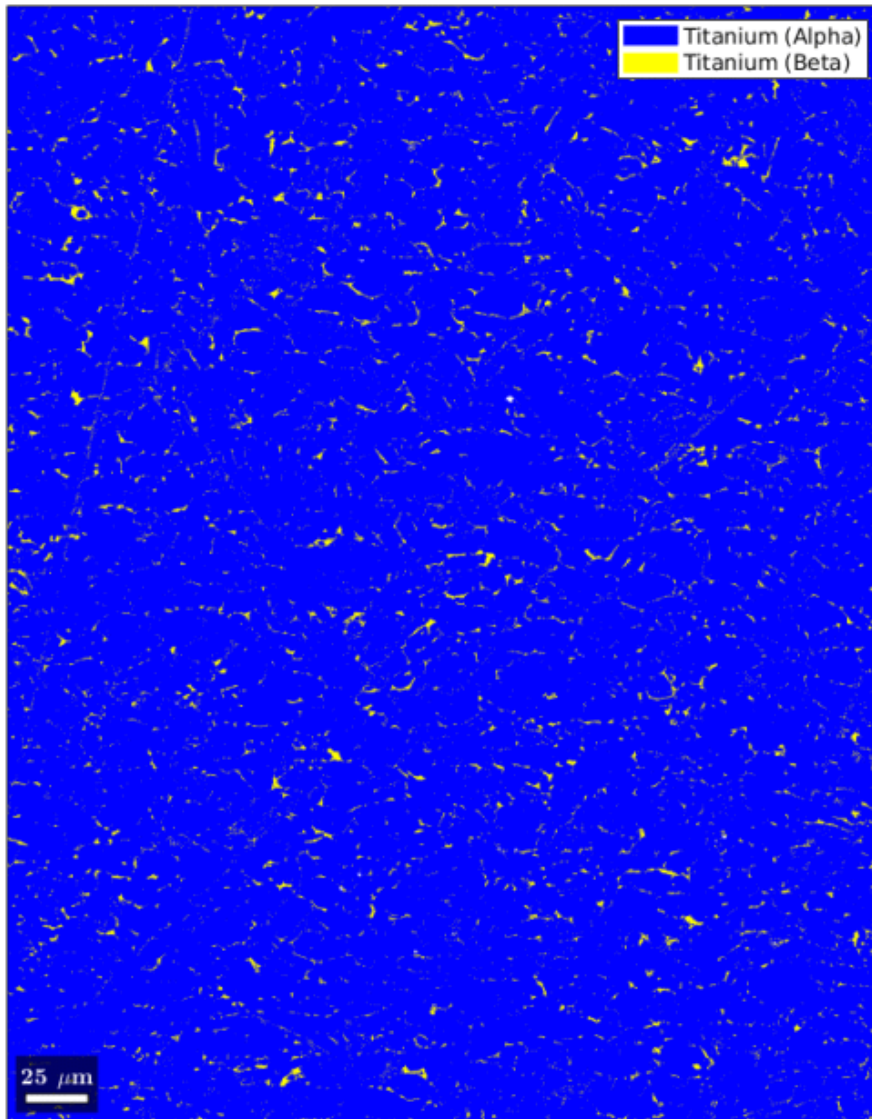


Figure 9.11: EBSD of Ti6Al4V: side surface with α / β - phase distribution.

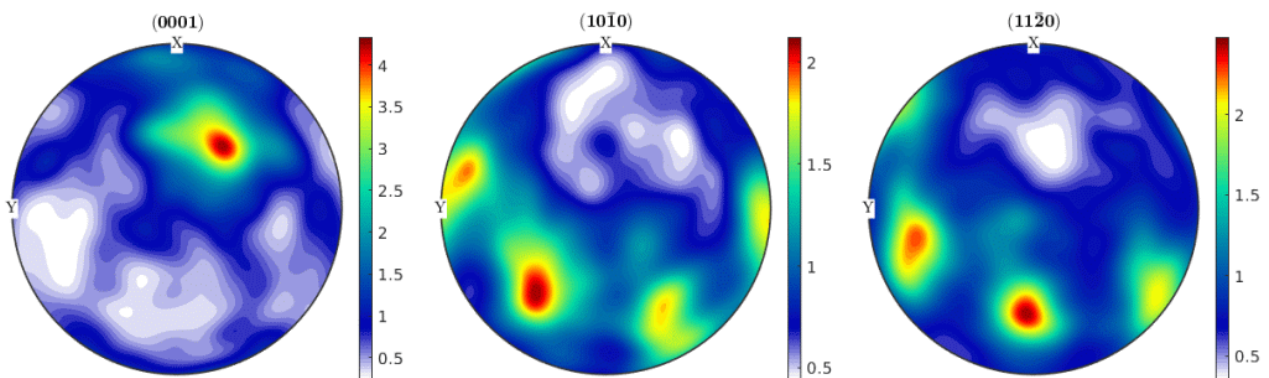


Figure 9.12: EBSD of Ti6Al4V: side surface pole figure of the α - phase.

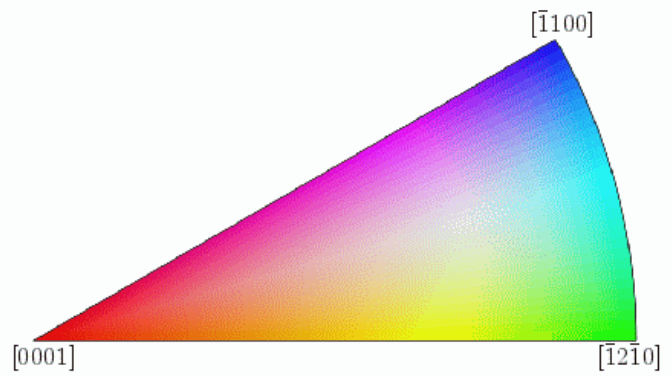
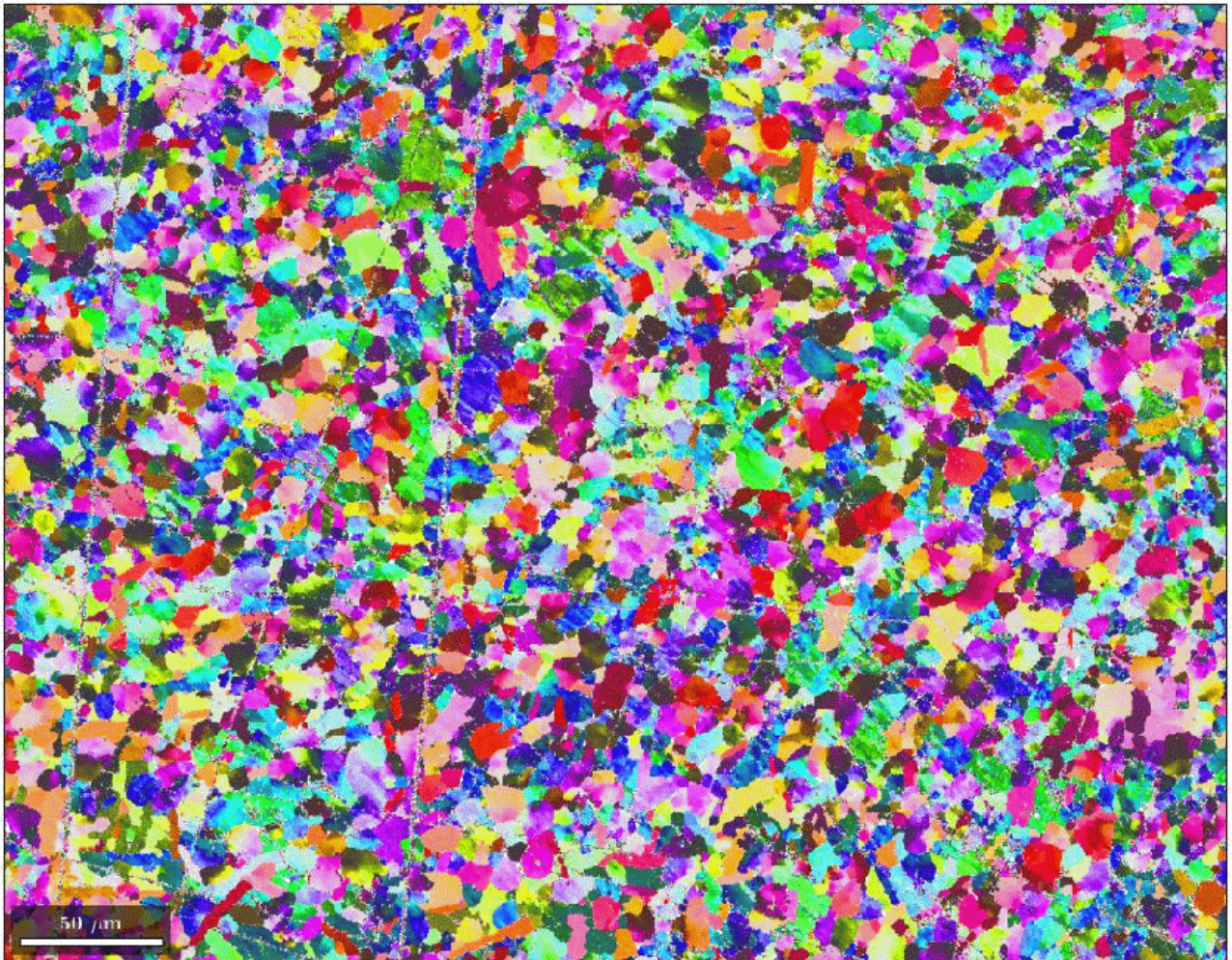


Figure 9.13: EBSD of Ti6Al4V: top surface with crystal orientations.

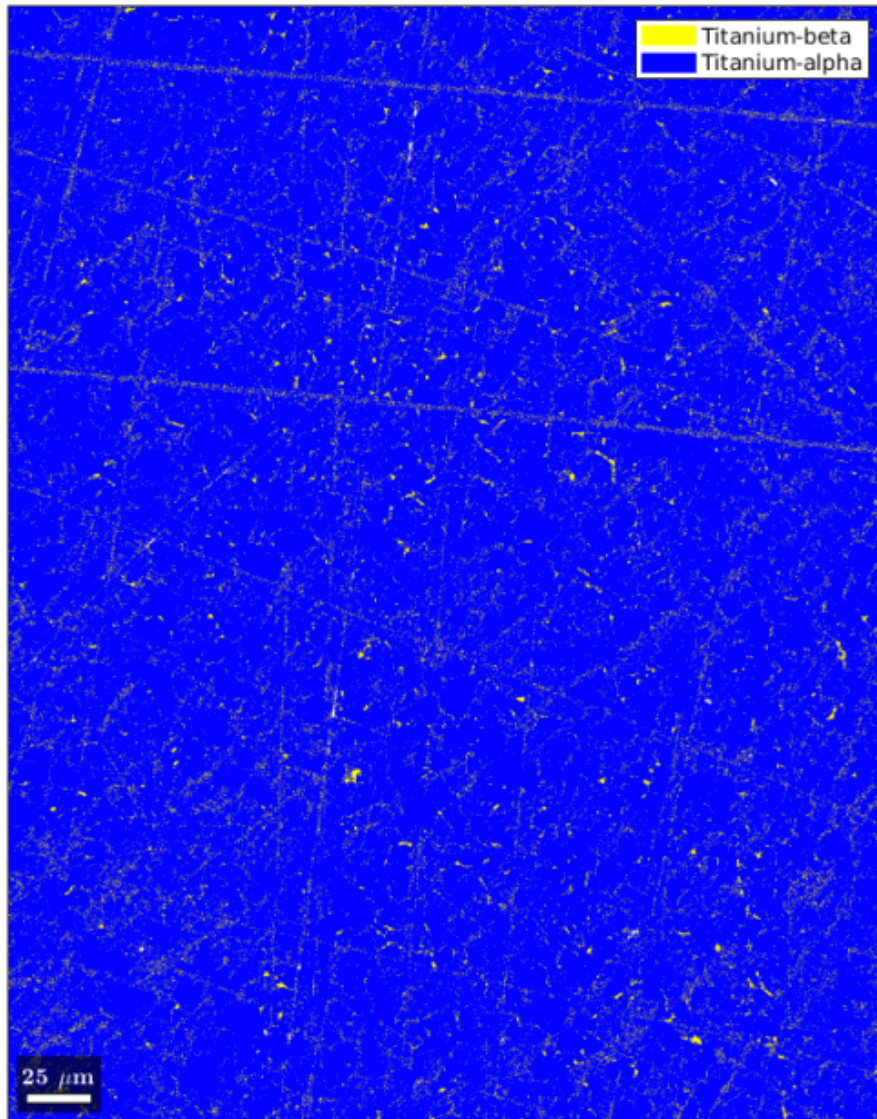


Figure 9.14: EBSD of Ti6Al4V: top surface with α / β - phase distribution.

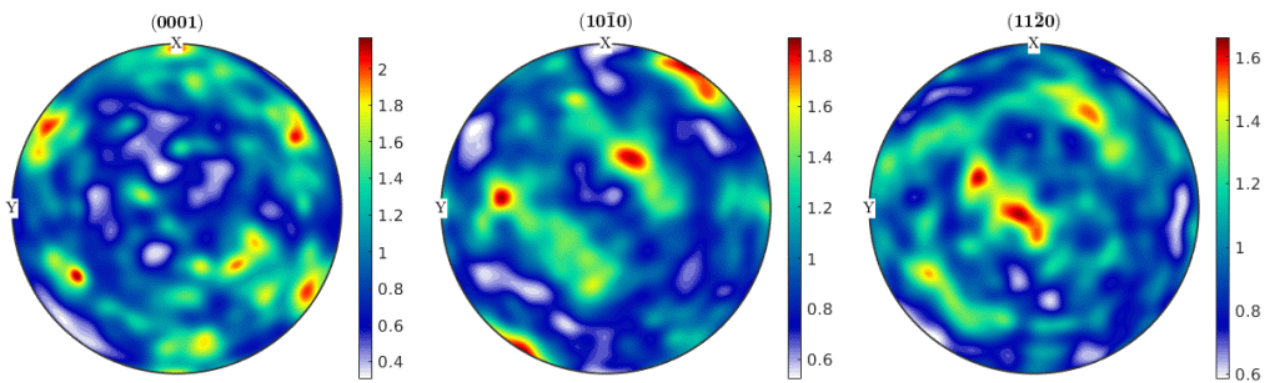


Figure 9.15: EBSD of Ti6Al4V: top surface pole figure of the α - phase.

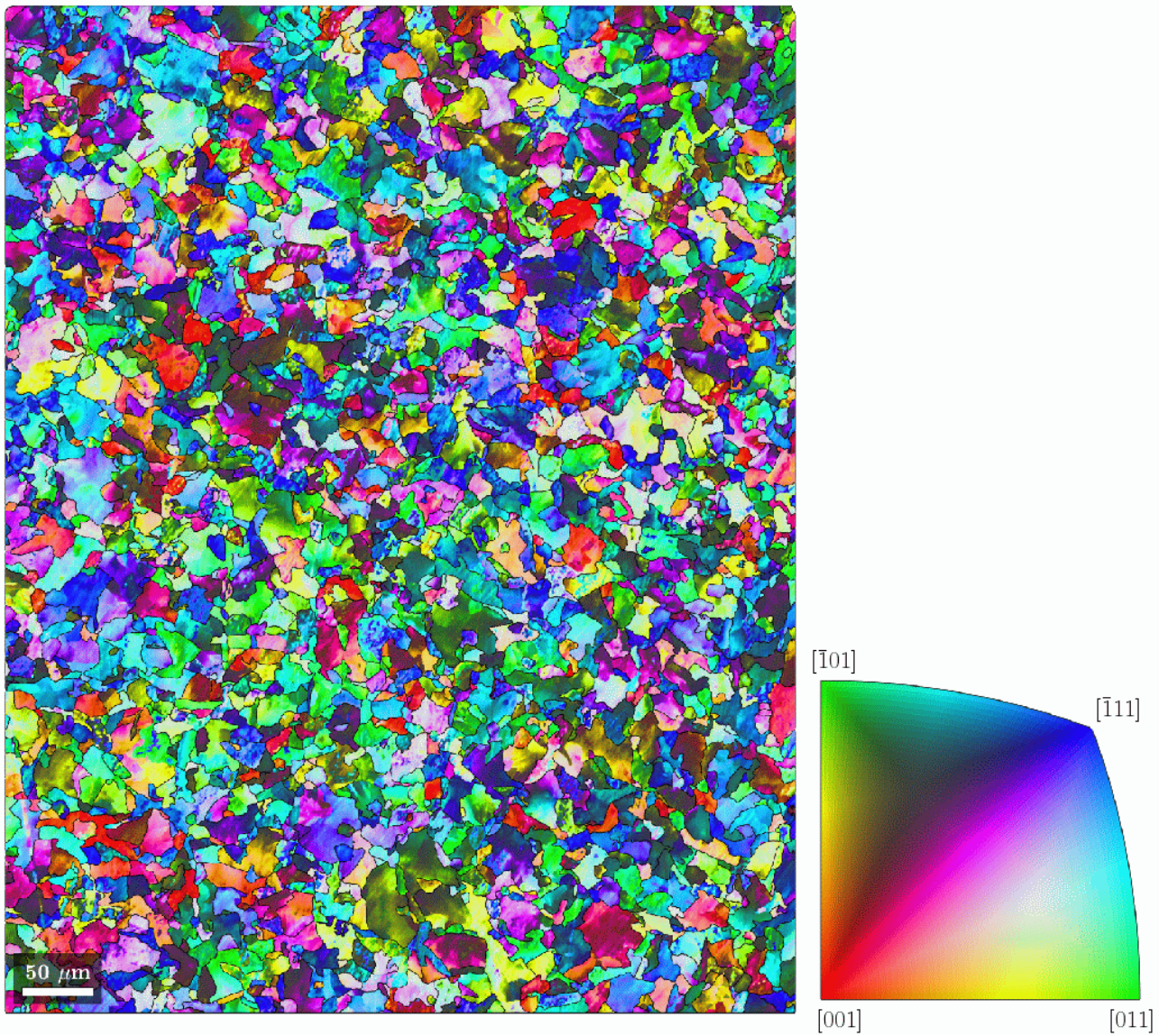


Figure 9.16: EBSD of Ck45: top surface with crystal orientations.

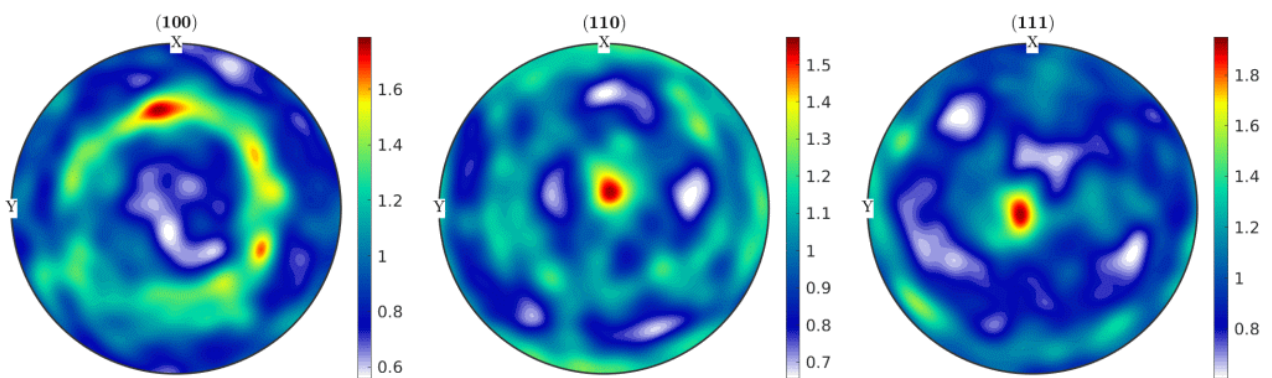


Figure 9.17: EBSD of Ck45: top surface pole figure.

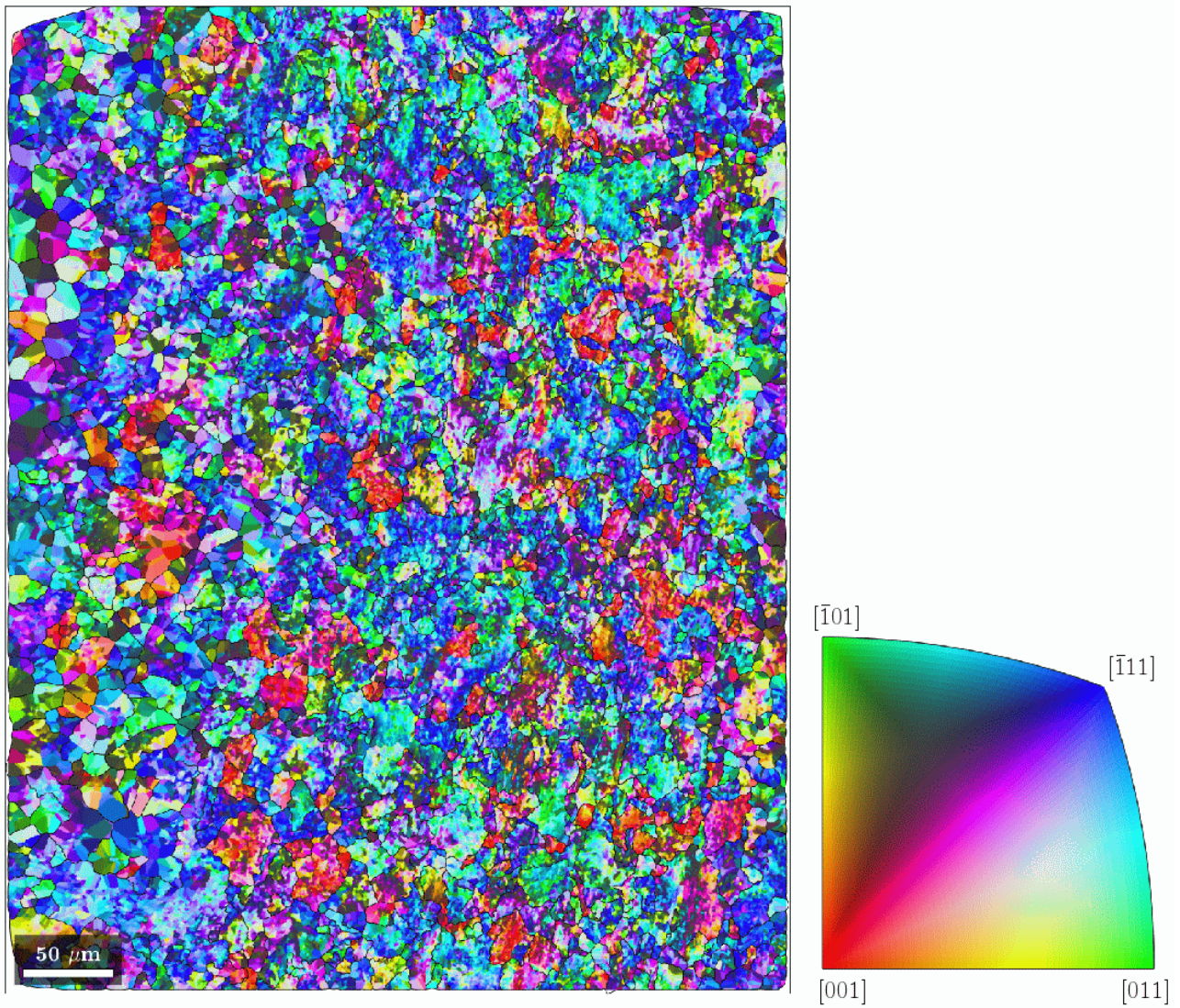


Figure 9.18: EBSD of Ck45: side surface with crystal orientations.

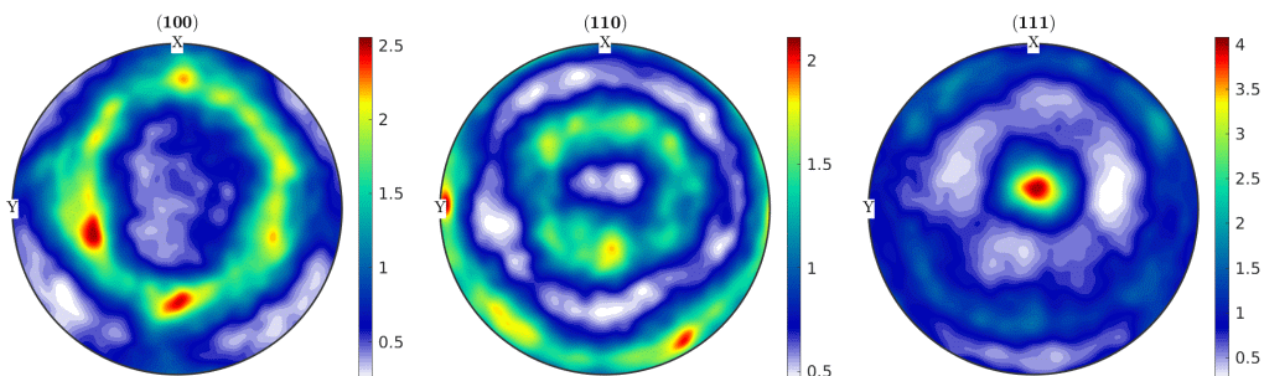


Figure 9.19: EBSD of Ck45: side surface pole figures.

9.2 MATERIAL PARAMETER DETERMINATION FROM MATERIAL TESTING

9.2.1 Tensile Tests

Tensile tests were performed for both materials, Ck45 and Ti6Al4V, at room temperature for three different strain rates and each repeated three times. The tensile test specimen were produced from the inner core of the cylinders according to DIN50125[52] with form B and the dimensions B8 x 40. A drawing of the tensile test specimen is shown in figure 9.20. Johnson-Cook parameters A, B, C and n were determined as in [112]. The strain rate sensitivity, parameter C, is valid at very low strain rates only, as the tests were conducted in the strain rate range from 0.002/s to 0.15/s. The Johnson-Cook parameter m was not determined as all tests were conducted at room temperature only. The test matrix is given in Table 9.9.

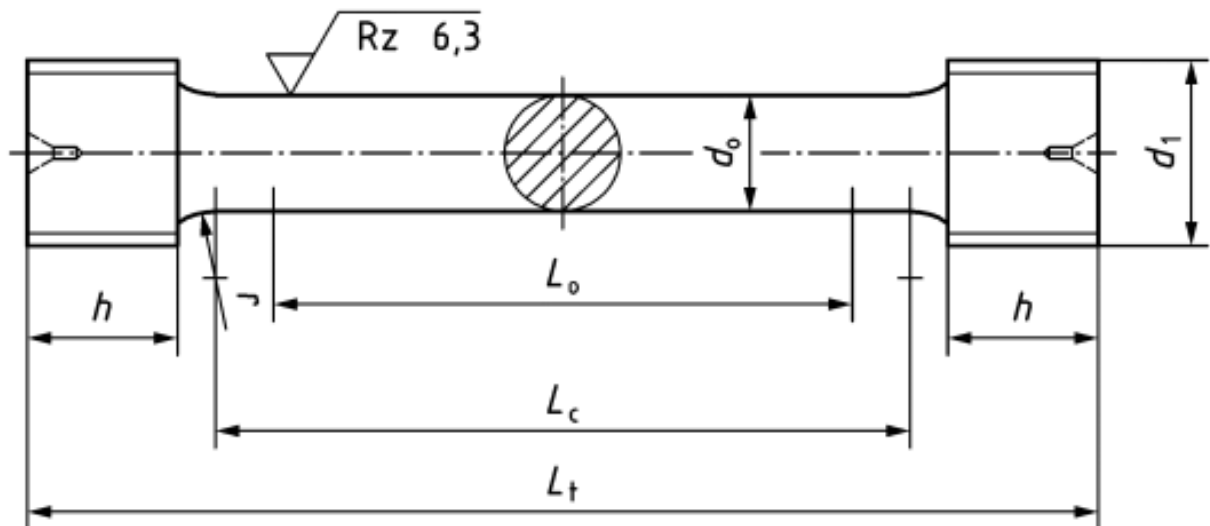


Figure 9.20: Drawing of tensile test specimen for Ck45 and Ti6Al4V according to DIN50125 form B[52].

Temperature [K]	Strain rate $\dot{\epsilon}_{pl}[s^{-1}]$	Repetitions
300	0.002	3
300	0.1	3
300	0.15	3

Table 9.9: Test matrix tensile tests

During the measurements engineering strain and stress values were recorded and later converted into true strains and stresses. Until uniform elongation A_G the conversion can be performed by the following equations given in [26]:

$$\varepsilon_{true} = \ln(1 + \varepsilon_{eng}) \quad (9.1)$$

and

$$\sigma_{true} = \sigma_{eng} \cdot (1 + \varepsilon_{eng}) \quad (9.2)$$

The true strain in equation (9.1) consists of elastic and plastic contributions. According to [26], assuming an additive split of both components, the true plastic strain can be computed by:

$$\varepsilon_{true}^{pl} = \varepsilon_{true} - \varepsilon_{true}^{el} = \varepsilon_{true} - \frac{\sigma_{true}}{E} \quad (9.3)$$

Beyond uniform elongation A_G the conversions (9.1) and (9.2) are invalid. The determination of true stresses and strains would require ad-hoc tracking of the progressively reducing diameter in the necking zone which is not performed in this investigation. Instead, the true strain at fracture ε_f can be computed from the measurement of initial D_i and fracture diameter D_f of the specimen according to [26]:

$$\varepsilon_f = \ln\left(\frac{A_i}{A_f}\right) = \ln\left(\frac{D_i^2}{D_f^2}\right) \quad (9.4)$$

The corresponding true stress σ_f at fracture is then computed from the force at fracture F_f and the fracture surface area A_f :

$$\sigma_f = \frac{F_f}{A_f} \cdot \zeta \quad (9.5)$$

with ζ being Bridgman's [32] stress correction factor for the three-dimensionality of the stress state after onset of necking. The stress correction factor is computed as:

$$\zeta = \frac{1}{\left(1 + \frac{2 \cdot R}{D_f/2}\right) \cdot \ln\left(1 + \frac{D_f/2}{2 \cdot R}\right)} \quad (9.6)$$

with D_f being the fracture diameter and R the necking radius of the specimen.

9.2.2 Parameter A, B and n from Quasi-Static Tests at Room Temperature

Quasi-static tensile test results at room temperature were used to derive the parameters A, B and n for the static part (first term) of the Johnson-Cook flow stress model (3.95):

$$\sigma_y^{static} = A + B \cdot \varepsilon_{pl}^n \quad (9.7)$$

The measured stresses and strains until uniform elongation A_G were converted into true plastic strains and true stresses by use of equations (9.1), (9.2) and (9.3). Additionally, the stresses and strains at fracture were incorporated to the true stress- true plastic strain data. They were computed by equations (9.4), (9.5) and (9.6) based on measured initial D_i and fracture diameter D_f of the specimen, the necking radius R of the specimen and the force at fracture F_f . The latter approach follows the proposal of [26] and is improved by consideration of Bridgman's stress correction factor which shall enhance predictions of the flow stress curve at higher strains towards fracture.

A least squares fit is used to fit the parameters A, B and n from equation (9.7) to the experimental data, by minimizing the sum of the squared error of the model prediction [33]:

$$\sum_i \left[\sigma_y^{static}(\varepsilon_{pl}^n) - \sigma_{y,i}^{measured}(\varepsilon_{pl}) \right]^2 = \sum_i \left[A + B \cdot \varepsilon_{pl}^n - \sigma_{y,i}^{measured}(\varepsilon_{pl}) \right]^2 = \min \quad (9.8)$$

9.2.3 Parameter C from Low Strain Rate Tests at Room Temperature

The strain rate sensitivity parameter C of the Johnson-Cook flow stress model is determined with tensile test data from the low strain rate range according to the test matrix in table 9.9. For this purpose, the yield stresses $\sigma_{y,i}$ are evaluated at a plastic strain of $\varepsilon_{pl} = 5\%$. Each yield stress $\sigma_{y,i}(\varepsilon_{pl} = 5\%)$ is then divided by the static yield stress $\sigma_y^{static}(\varepsilon_{pl} = 5\%)$ with (9.7) to compute the flow stress ratios $r_{\sigma,i}^{dyn}$:

$$r_{\sigma,i}^{dyn} = \frac{\sigma_{y,i}(\varepsilon_{pl} = 5\%)}{\sigma_y^{static}(\varepsilon_{pl} = 5\%)} \quad (9.9)$$

The reference strain rate is set to the strain rate of the tensile test with the lowest strain rate of $\dot{\varepsilon}_{pl}^{ref} = 0.002s^{-1}$. Finally, all flow stress ratios $r_{\sigma,i}^{dyn}$ are then used to find the parameter C by a least squares fit:

$$\sum_i \left(r_{\sigma,i}^{dyn} - \left[1 + C \cdot \ln \frac{\dot{\varepsilon}_{pl,i}}{\dot{\varepsilon}_{pl}^{ref}} \right] \right)^2 = \min \quad (9.10)$$

9.2.3.1 *Ti6Al4V*

The stress- strain curves for Ti6Al4V are given for $\dot{\epsilon}_{pl} = 0.002s^{-1}$ in figure 9.21, for $\dot{\epsilon}_{pl} = 0.1s^{-1}$ in figure 9.22 and for $\dot{\epsilon}_{pl} = 0.15s^{-1}$ in figure 9.23.

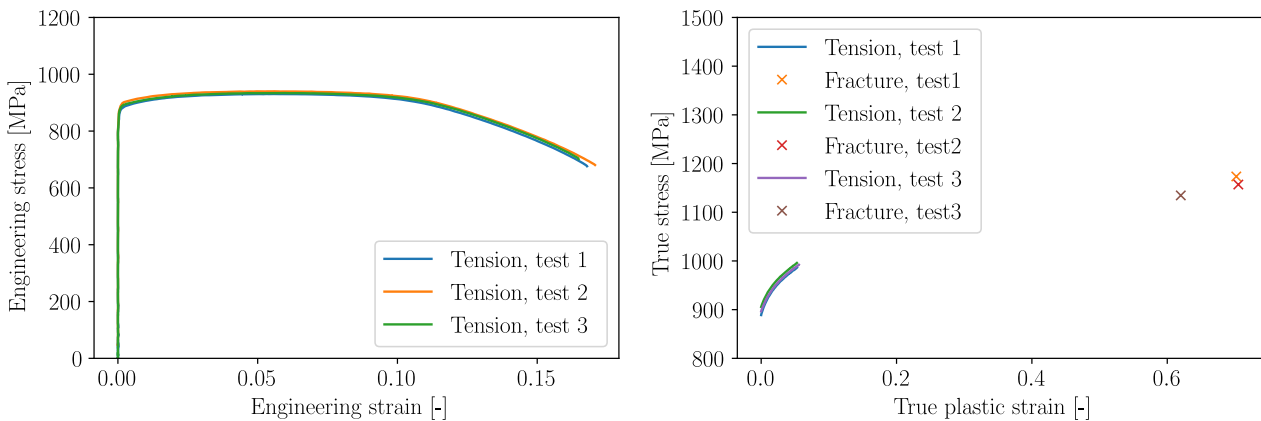


Figure 9.21: Engineering (left) and true stress strain (right) curves from Ti6Al4V tensile test at a strain rate of $\dot{\epsilon}_{pl} = 0.002/s$. Note that the true stress strain curve can be reconstructed until onset of necking only. The fracture stresses and strains are computed from the fracture surface measurement with (9.4) and (9.5).

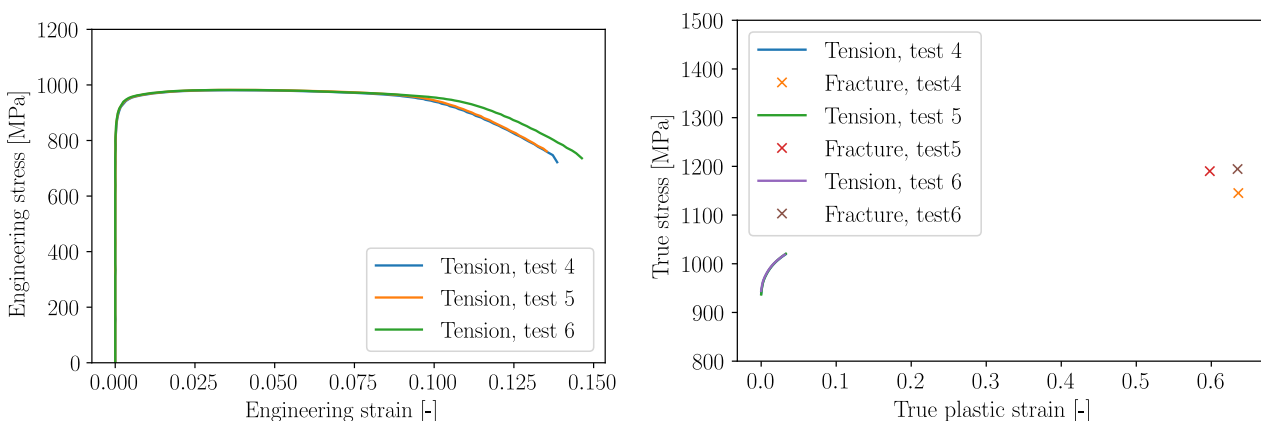


Figure 9.22: Engineering (left) and true stress strain (right) curves from Ti6Al4V tensile test at a strain rate of $\dot{\epsilon}_{pl} = 0.1/s$. Note that the true stress strain curve can be reconstructed until onset of necking only. The fracture stresses and strains are computed from the fracture surface measurement with (9.4) and (9.5).

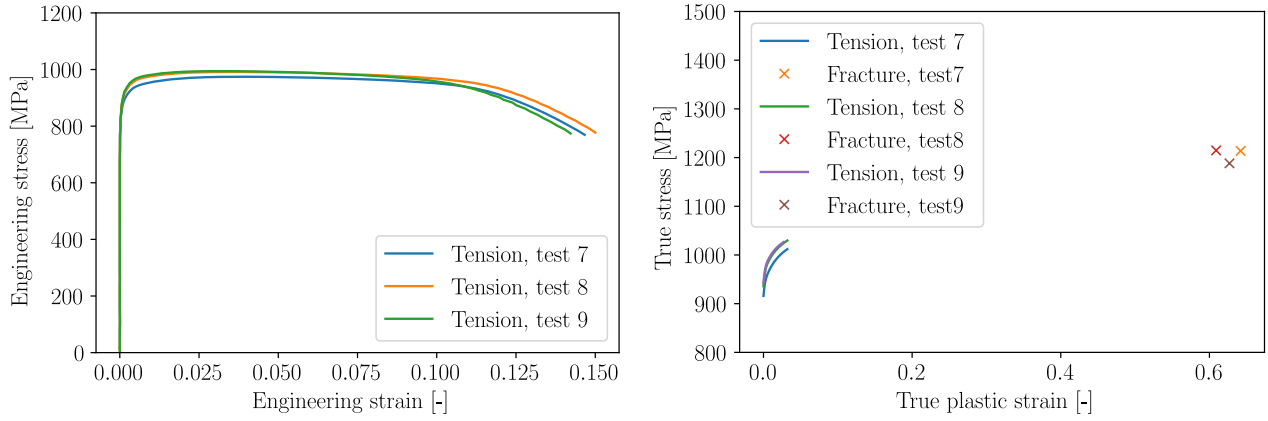


Figure 9.23: Engineering (left) and true stress strain (right) curves from Ti6Al4V tensile test at a strain rate of $\dot{\epsilon}_{pl} = 0.15/s$. Note that the true stress strain curve can be reconstructed until onset of necking only. The fracture stresses and strains are computed from the fracture surface measurement with (9.4) and (9.5).

Test	Strain rate $\dot{\epsilon}_{pl} [s^{-1}]$	Force at fracture $F_f [N]$	Fracture diameter [mm]	Fracture strain [-]	Stress at fracture [MPa]
T1	0.002	33991.6	5.63	0.702	1168.2
T2	0.002	34205.6	5.62	0.705	1159.5
T3	0.002	35263.3	5.87	0.62	1134.8
T4	0.1	36279.3	5.82	0.636	1146
T5	0.1	38254.4	5.93	0.598	1190.7
T6	0.1	36998.8	5.82	0.635	1197.5
T7	0.15	38678.2	5.8	0.642	1210
T8	0.15	39070.6	5.9	0.609	1210.1
T9	0.15	38908	5.85	0.627	1191

Table 9.10: Strains and stresses at fracture for Ti6Al4V.

The JC coefficients for the static part (9.7) are fitted for $\dot{\epsilon}_{pl} = 0.002s^{-1}$ under consideration of the fracture data provided in table 9.10 and resulted in the parameters A, B and n given in table 9.11. The fitted flow curve is given in figure 9.24. The fit of the strain rate sensitivity to the experimental data at 5% strain with (9.10) results in $C = 0.0145$ with the reference strain rate set to the lowest test speed $\dot{\epsilon}_{pl}^{ref} = 0.002/s$. The curve fit of the strain rate sensitivity is shown in figure 9.25 and its values are given in table 9.11.

A [MPa]	B [MPa]	n [-]	$\dot{\epsilon}_{pl}^{ref} [s]$	C [-]
867	344	0.361	0.002	0.0145

Table 9.11: Ti6Al4V: fit of the work hardening parameters A, B and n and the strain rate sensitivity C of the JC flow stress model (9.7).

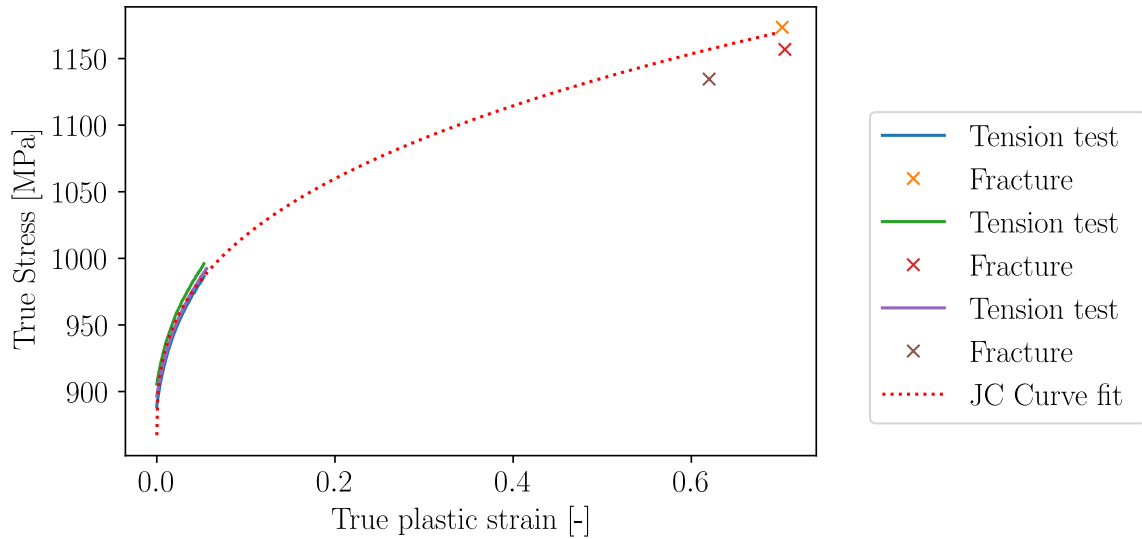


Figure 9.24: Ti6Al4V: fit of JC parameter A, B and n at a strain rate of $\dot{\epsilon}_{pl} = 0.002/s$.

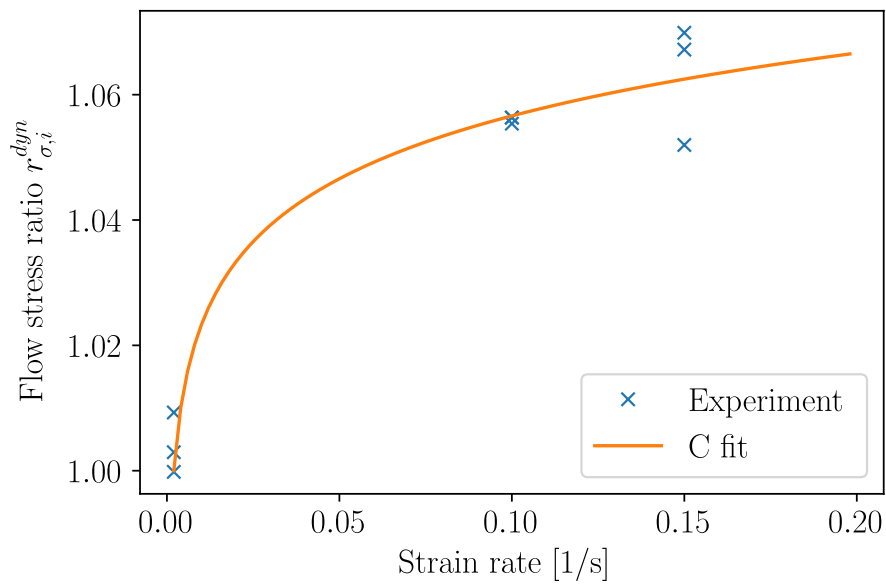


Figure 9.25: Ti6Al4V: fit of parameter C at a strain of $\epsilon_{pl} = 5\%$.

9.2.3.2 Ck45

The stress- strain curves for Ck45 are given for $\dot{\epsilon}_{pl} = 0.002s^{-1}$ in figure 9.26, for $\dot{\epsilon}_{pl} = 0.1s^{-1}$ in figure 9.27 and for $\dot{\epsilon}_{pl} = 0.15s^{-1}$ in figure 9.28. At all strain rates a Lüders-plateau is visible.

MATERIAL PARAMETER DETERMINATION

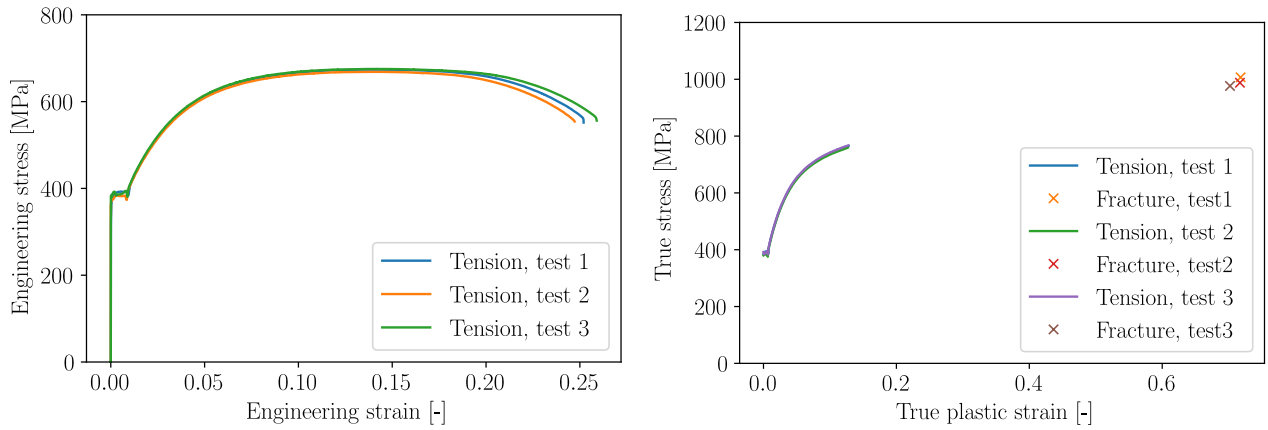


Figure 9.26: Engineering (left) and true stress strain (right) curves from Ck45 tensile test at a strain rate of $\dot{\epsilon}_{pl} = 0.002/s$. Note that the true stress strain curve can be reconstructed until onset of necking only. The fracture stresses and strains are computed from the fracture surface measurement with (9.4) and (9.5).

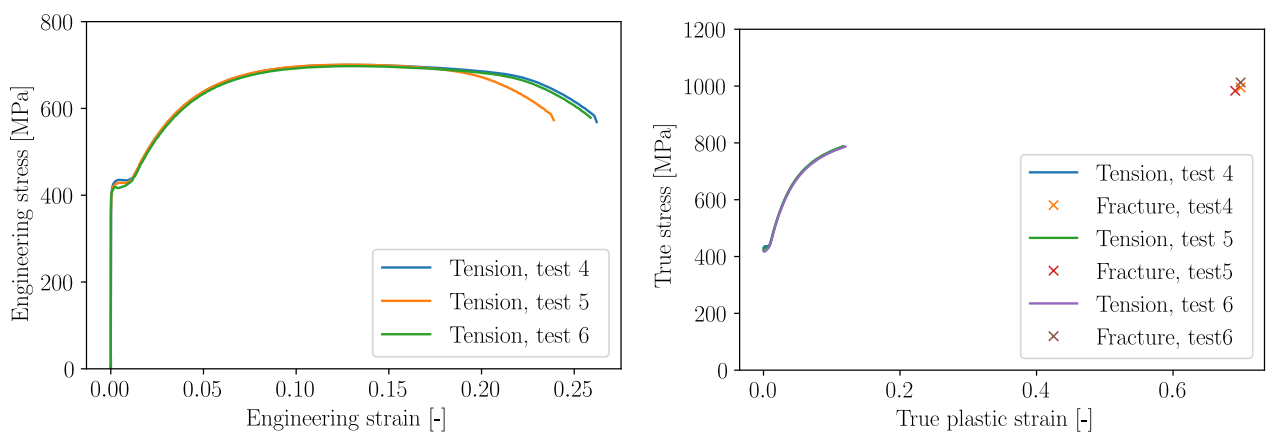


Figure 9.27: Engineering (left) and true stress strain (right) curves from Ck45 tensile test at a strain rate of $\dot{\epsilon}_{pl} = 0.1/s$. Note that the true stress strain curve can be reconstructed until onset of necking only. The fracture stresses and strains are computed from the fracture surface measurement with (9.4) and (9.5).

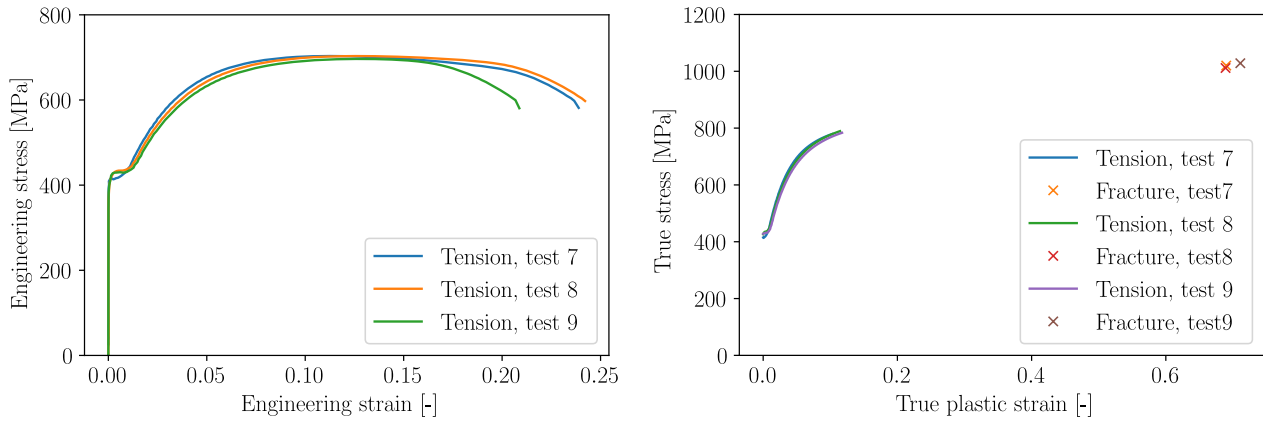


Figure 9.28: Engineering (left) and true stress strain (right) curves from Ck45 tensile test at a strain rate of $\dot{\epsilon}_{pl} = 0.15//s$. Note that the true stress strain curve can be reconstructed until onset of necking only. The fracture stresses and strains are computed from the fracture surface measurement with (9.4) and (9.5).

Test	Strain rate $\dot{\epsilon}_{pl}[s^{-1}]$	Force at fracture $F_f[N]$	Fracture diameter [mm]	Fracture strain [-]	Stress at fracture [MPa]
C1	0.002	27735.5	5.59	0.718	1001.7
C2	0.002	27862.7	5.59	0.717	988.5
C3	0.002	27960.6	5.63	0.702	978.8
C4	0.1	28577.7	5.64	0.699	997.9
C5	0.1	28800.1	5.66	0.691	981.7
C6	0.1	29090.2	5.64	0.699	1007.8
C7	0.15	29225.6	5.67	0.69	1022.3
C8	0.15	30036.1	5.67	0.689	1017.5
C9	0.15	29184.6	5.61	0.711	1034.1

Table 9.12: Strains and stresses at fracture for Ck45.

The JC coefficients for the static part (9.7) are fitted for $\dot{\epsilon}_{pl} = 0.002s^{-1}$ under consideration of the fracture data provided in table 9.12 and resulted in the parameters A , B and n given in table 9.13. The fitted flow curve is given in figure 9.29. The fit was improved by considering data above plastic strains of 2% only. This avoids bad fits with unphysical low static yield limits A which would be induced by the Lüders-plateau otherwise. The fit of the strain rate sensitivity to the experimental data at 5% strain with (9.10) results in $C = 0.0108$ with the reference strain rate set to the lowest test speed $\dot{\epsilon}_{pl}^{ref} = 0.002/s$. The curve fit of the strain rate sensitivity is shown in figure 9.30 and its values are given in table 9.13.

A [MPa]	B [MPa]	n [-]	$\dot{\epsilon}_{pl}^{ref}$ [s]	C [-]
392	735	0.304	0.002	0.0108

Table 9.13: Ck45: fit of the work hardening parameters A, B and n and the strain rate sensitivity C of the JC flow stress model (9.7).

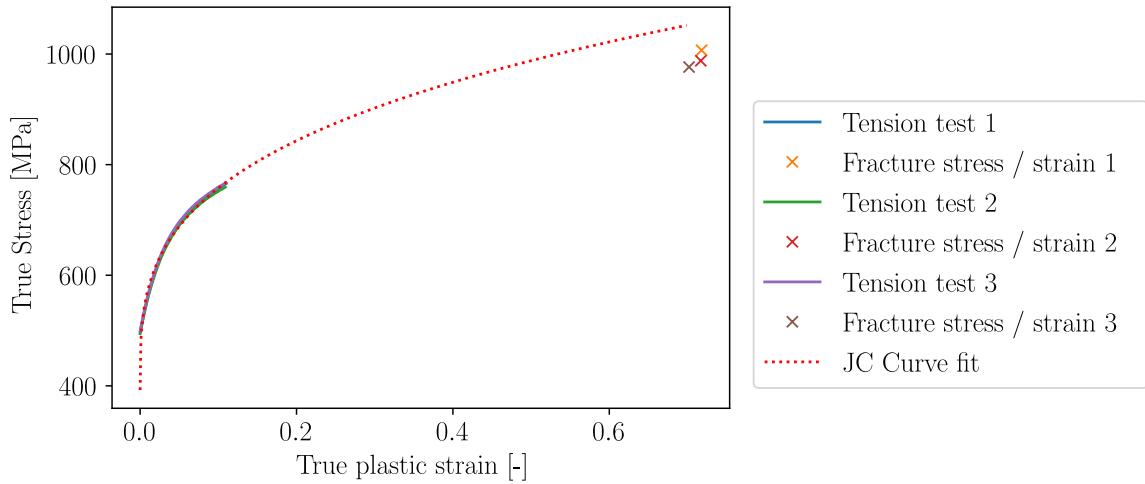


Figure 9.29: Ck45: fit of JC parameter A, B and n at a strain rate of $\dot{\epsilon}_{pl} = 0.002/s$.

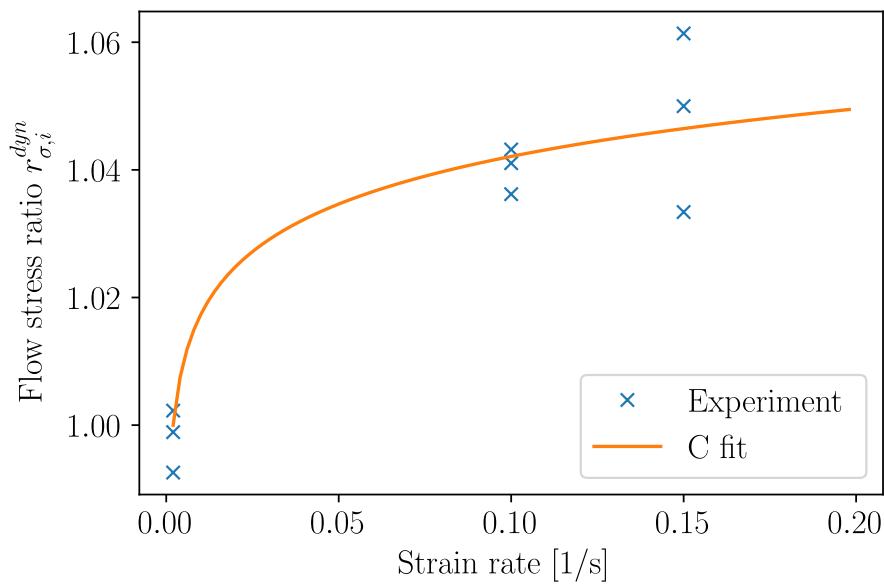


Figure 9.30: Ck45: fit of parameter C at a strain of $\epsilon_{pl} = 5\%$.

9.3 CUTTING EXPERIMENTS

The measurement of material parameters for constitutive models at high strains, strain rates and temperatures is not possible with standard material testing procedures as they are not able to reproduce such conditions, especially when overlaid. Instead, using process forces of cutting experiments as input for inverse identification of material parameters is a viable alternative. For this purpose orthogonal cutting experiments were conducted for Ti6Al4V (3.7165 Grade 5) and Ck45 (1.1191) as input for numerical parameter identification by inverse methods. The advantage of orthogonal cutting is that it can be modelled simplified in 2D. Resulting chip shapes of selected experiments as well as pre- measurements of the cutter geometries are provided. Orthogonal cuts were approximated by cutting cylinders with average diameters of $D \approx 72mm$ and a wall thickness of $d \approx 2mm$. Due to the rework of the outer surface the mill scale and the decarburated zone of the Ck45 cylinders were removed. In total 10 cylinders were prepared for cutting tests with 5 being of Ck45 and 5 out of Ti6Al4V material. Coolant and lubrication are not used in the test program so that numerical modelling of the cutting process is simplified since there is no viable approach to account for the effects of cooling and lubricant thus reducing unknowns in the numerical modelling of these cutting experiments. Test durations are kept short such that wear stays insignificant.

9.3.1 Cut Tool

150 uncoated turning inserts *CCMW 09 T3 04 H13A (ISO)* were acquired from Sandvik Coromant. Pictures of the turning insert geometry are provided in figure 9.31. The main geometrical data of the inserts are:

- Edge radius: $RE = 0,397mm$
- Cutting edge height: $S = 3,969mm$
- Inscribed circle : $IC = 9,525mm$
- Cutting edge length: $LE = 9,272mm$
- Clearance angle: $\alpha = 7^\circ$
- Rake angle: $\gamma = 0^\circ$

The cutting edge radii along the cutting edge length LE are not defined. Since these radii have a significant impact on the process forces they are optically measured, see chapter 9.3.1.1. The inserts are used with a tool holder Applitec SCACL-2020X-09 (ISO-2216). Each insert was used for four cutting experiments (2 cuts per side of the insert) where after every experiment another position A-D was used on the insert. The four cut positions are shown in figure 9.32.

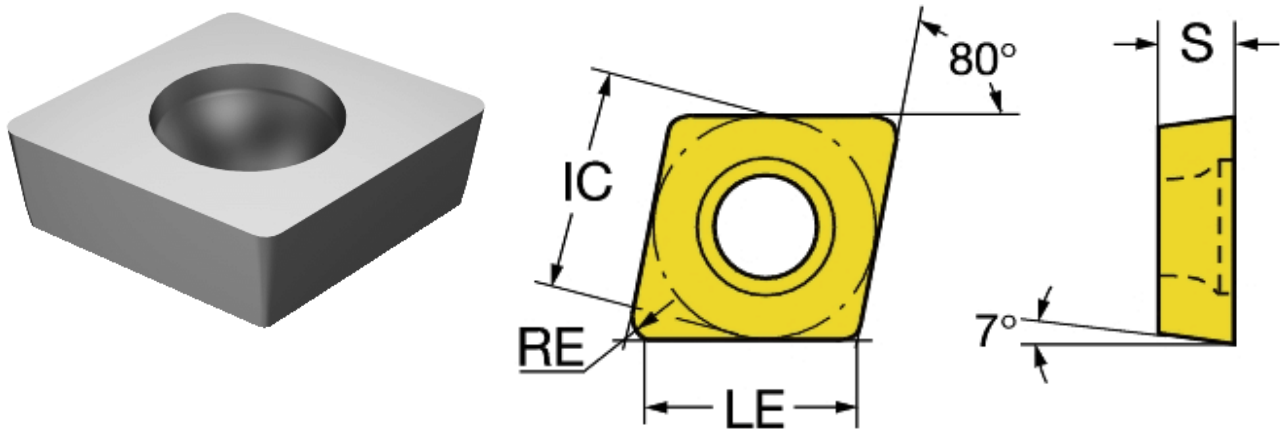


Figure 9.31: Cutting insert (left) and geometry (right) from [216].

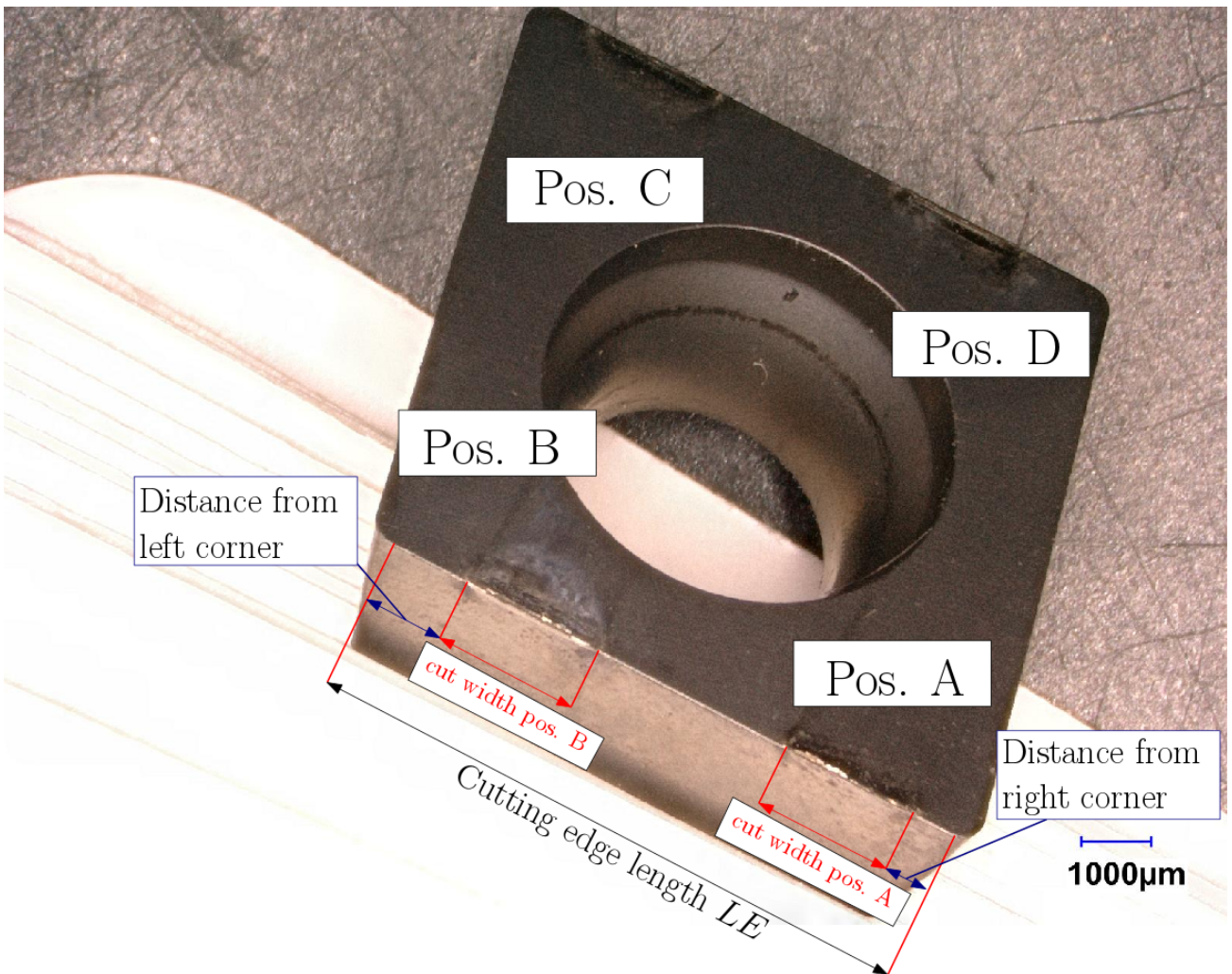


Figure 9.32: Cutting insert with the four cut positions A-D and corner reference points.

9.3.1.1 Optical Measurement of Cutter

The cutting edge radius of the insert has a major influence on the process forces of the turning operation. This dependency is shown in figure 9.33. With increasing cutting edge radius, the feed force F_f increases strongly, while there is a moderate increase in the cutting force F_c which becomes more pronounced towards higher feed. The effect of the cutting edge radius on the process forces is shown in figure 9.33.

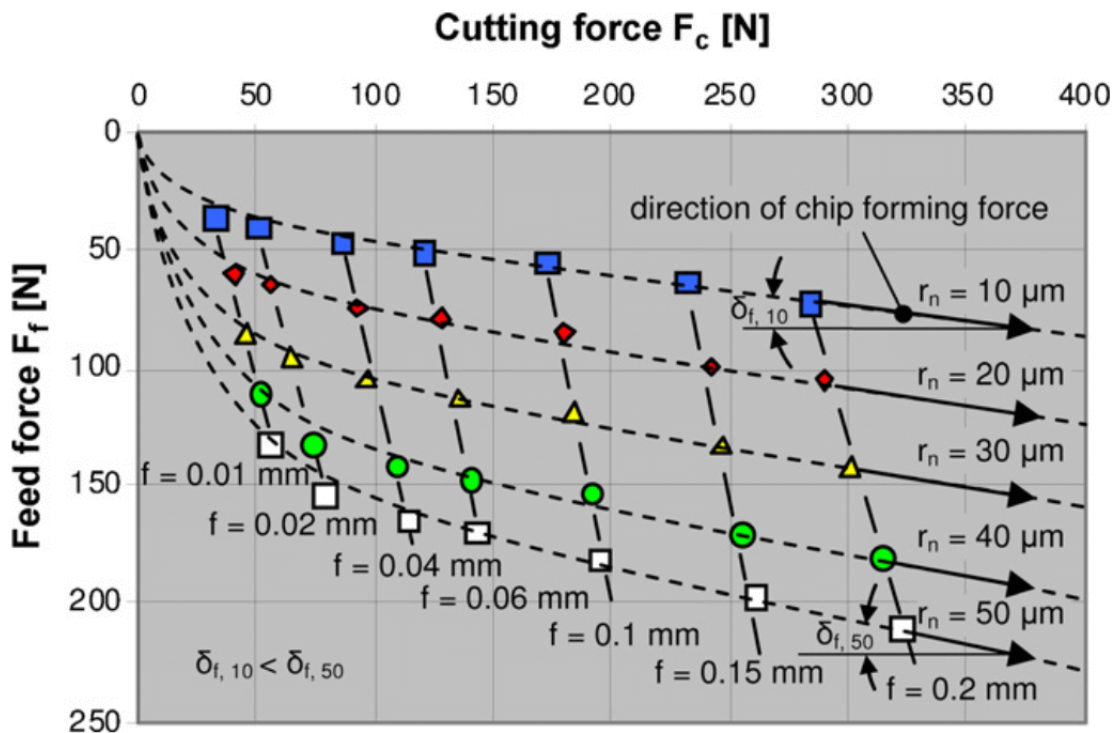


Figure 9.33: Influence of cutting edge radius r_n and feed f on the process forces for turning of Ti6Al4V. The forces are standardised to a cut width of $b = 1\text{mm}$, the cut speed was $v_c = 70\text{m/min}$, from [261]

The inserts in this investigation have an unspecified cutting edge radius and therefore all cutting edges (2×149 inserts) of the cutters were optically measured with an Alicona InfiniteFocusG4 microscope prior to the cut tests in unused condition. A $20\times$ magnification was used and the radii along the complete cutting edge length (LE) were scanned. The determination of the cutting edge radii follows the procedures outlined in [151, 262] in order to ensure reproducibility of the results. A total of almost 1'275'000 cutting edge radii were extracted from the scans. The cutting edge radius varies in the 149 cutters between $\approx 20\mu\text{m}$ and $\approx 50\mu\text{m}$. The mean cutting edge radius is $37.5\mu\text{m}$ with a standard deviation $4.9\mu\text{m}$. Since the length between the cutting edges is subject to tolerances the exact position of the cut was determined after the test for every insert and its four cut positions A-D. The insert's edge radii serve as reference points to determine the start point of the cut positions. From this start point the cutting edge radii were averaged along the cut width of $\approx 2\text{mm}$. Its averaged values along the cut width, including the standard deviation, are given for each cutting experiment in tables 11.2 and 11.1. Histogram plots of the cutting edge length LE

and the cutting edge radii are given in figure 9.34. The length of the cutting edge LE varies between $\approx 8.7...8.95mm$ which is due to the tolerance class of the selected inserts.

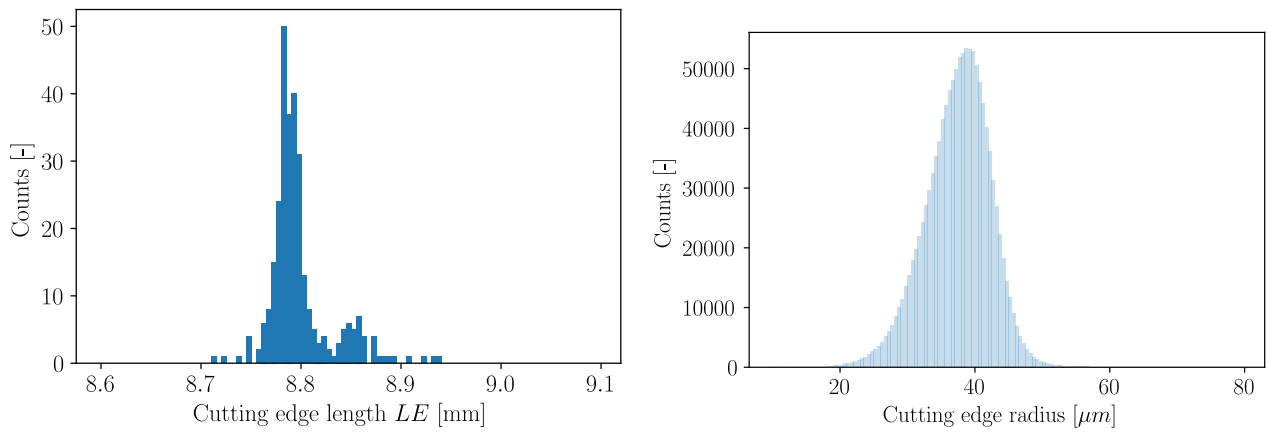


Figure 9.34: Histogramm of cutting edge lengths LE (left) and cutting edge radii (right).

The variation of the cutting edge radius along the cutting edge length LE can be significant see for example figure 9.35 where it varies between $\approx 25...50\mu m$.

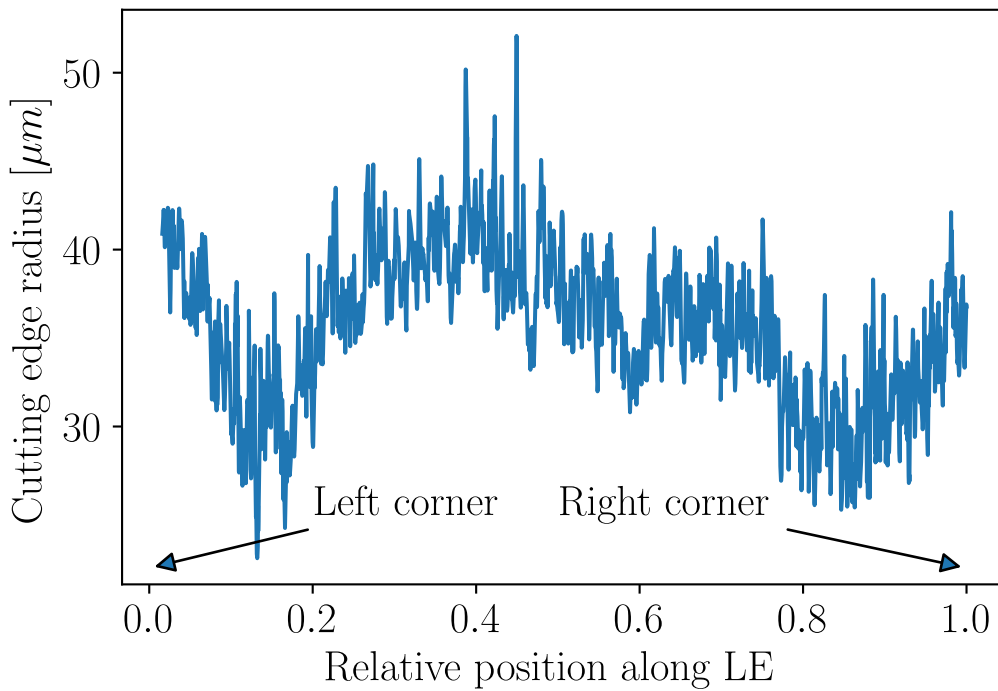


Figure 9.35: Example for cutting edge radii variation along a single cutting edge.

9.3.2 Cutting Experiments

A Schaublin 42L CNC turning machine is used for the orthogonal cutting experiments. From the procured raw material, see section 9.1, hollow cylinders from the outer cores according to figure 9.1 are manufactured and used for the cutting experiments. Such a cylinder is shown in figure 9.36 together with the experimental setup for the orthogonal cutting tests.

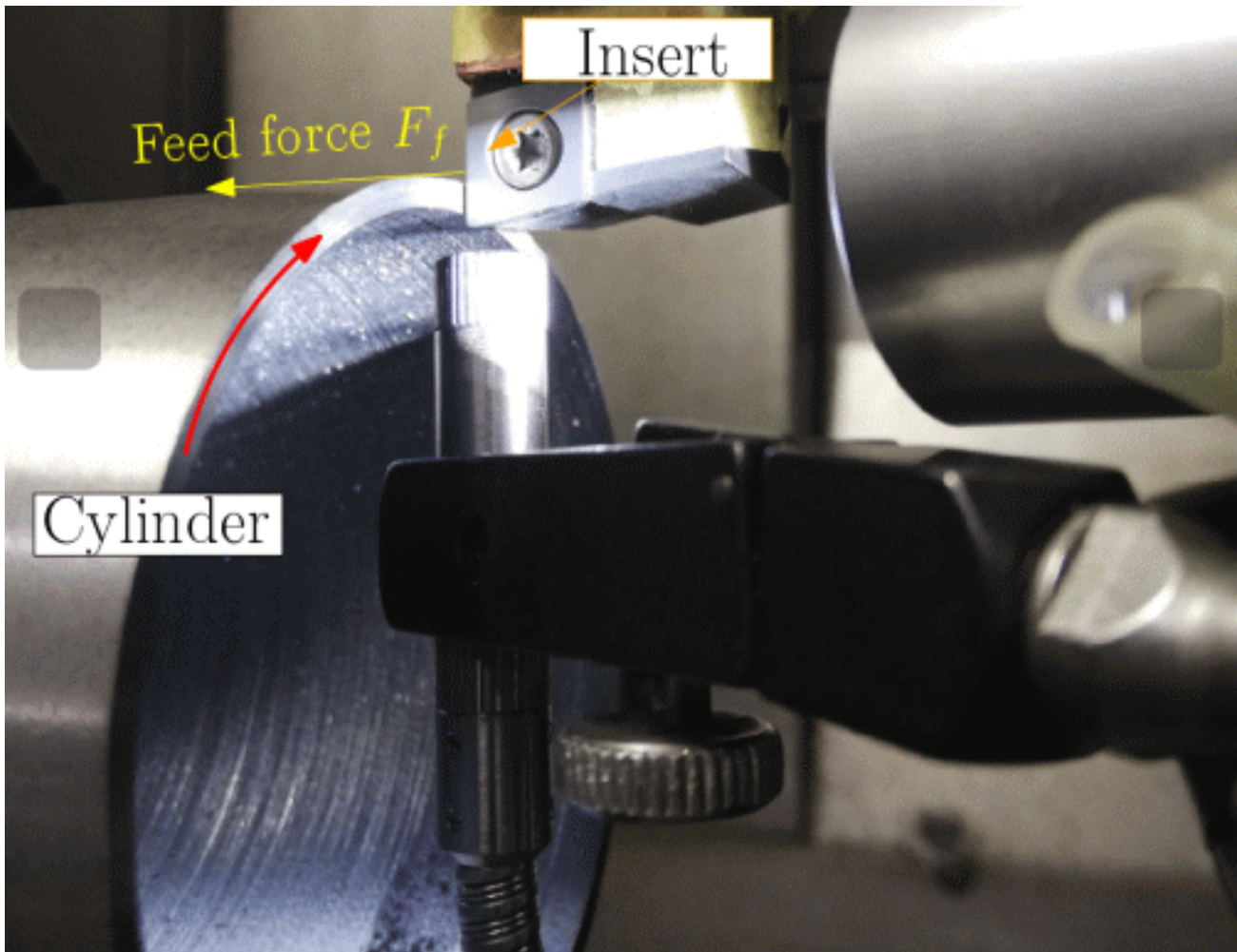


Figure 9.36: Orthogonal cutting setup: insert attached to the tool holder with cylinder to cut.

9.3.2.1 Force Measurement

The force measurements were conducted in three axes with a Kistler 9121A5 dynamometer. The dynamometer signals were amplified with a Kistler 5019A charge amplifier using a low pass filter with 30Hz. The measured force signals \tilde{F}_{meas} were corrected after the test since small drifts \tilde{F}_{drift} in the signal can occur and overlay the process forces \tilde{F}_{proc} :

$$\tilde{F}_{proc} = \tilde{F}_{meas} - \tilde{F}_{drift} \quad (9.11)$$

The drift \tilde{F}_{drift} was evaluated by positioning the cutter before the cut with a distance of one mm away from the cylinder to cut. With the desired feed of the experiment the cutter approached the workpiece and during this time the idle-forces $\tilde{F}_{drift} = \tilde{F}_{idle}$ were recorded and then used to correct to force signals with (9.11). A schematics is shown in figure 9.37.

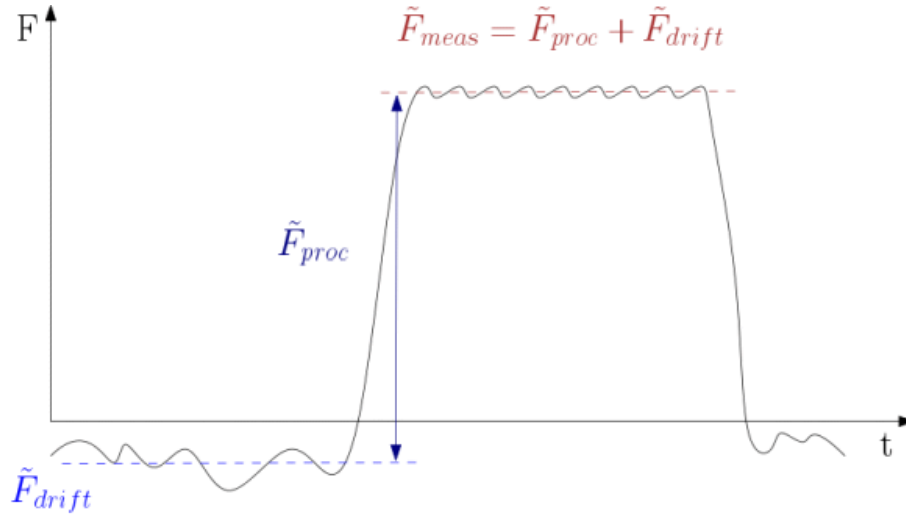


Figure 9.37: Force signal overlaid with a drift.

9.3.2.2 Test Plan

Orthogonal cutting tests were conducted for a large range of feeds and cut speeds. The parameter ranges are compiled in table 9.14 and all conducted cutting experiments of Ck45 and Ti6Al4V are provided with figure 9.38.

Material	Cutting speed v_c [m/min]	Feed f [mm]
Ti6Al4V	10...500	0.01...0.4
Ck45	10...500	0.01...0.4

Table 9.14: Test matrix of the cutting tests

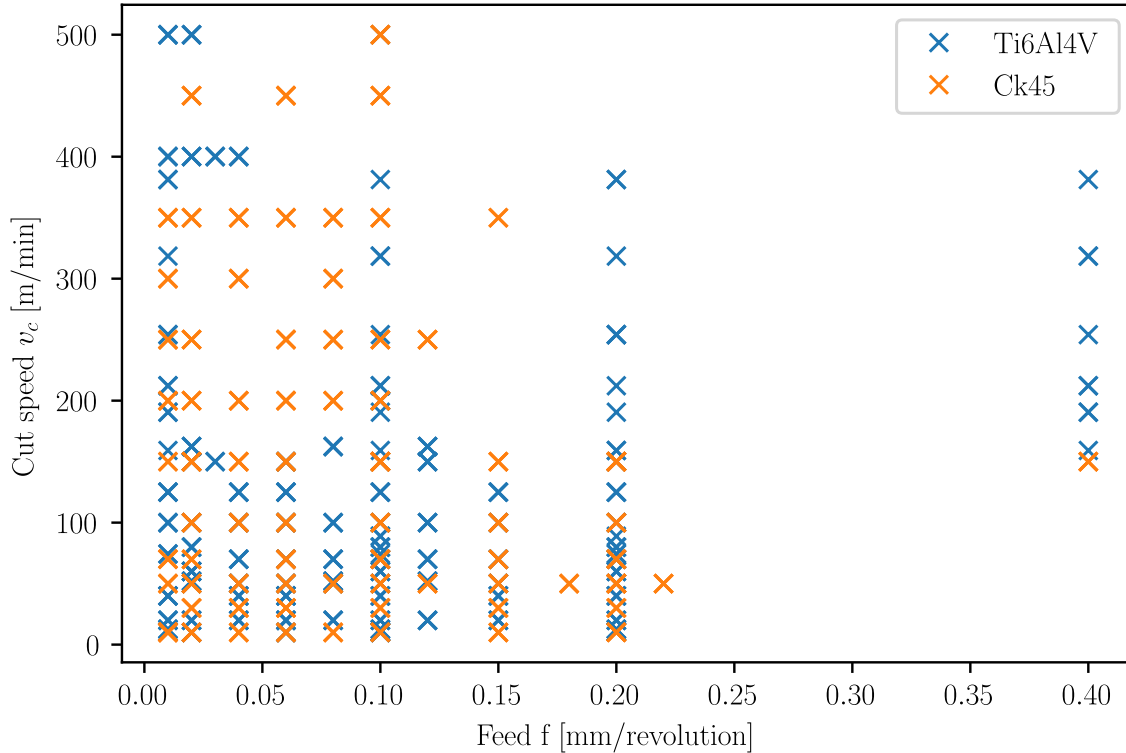


Figure 9.38: Process parameter combinations used in the cutting experiments

9.3.2.3 Experimental Results

The complete cutting test results are provided for Ti6Al4V (V0001-V0068, V0301-V0520) in table 11.1 and for Ck45 (V0069-V0300) in table 11.2 in the Appendix 11.3. The test results which are used in the inverse parameter identification (V0060, V0300) procedure and recomputations are given for Ti6Al4V in table 9.15 and for Ck45 in table 9.16. The process forces F_c and F_f were normalized to a cutting width of $w = 1\text{mm}$ and are given together with their respective standard deviations μ_{F_c} and μ_{F_f} . The second last two columns contain the averaged cutting edge radius r_n and its standard deviation μ_{r_n} . The last column STATUS gives a quality statement of the process forces. Tests labelled with **ok** are without any objections. Tests labelled **short** have to be treated with care as prolongations of such experiments is recommended. If however the standard deviations in the process forces of such tests are small, they still can be considered as valid. Results from tests labelled **questionable** or **initially stable** should not be used for parameter identifications while tests labelled with **saturation** ran into the amplifier limits and are therefore invalid for further use. Tests marked **instable** are most likely of insufficient quality and must not be used for parameter identifications.

Test	v_c [m/min]	f [mm]	F_c [N]	μ_{F_c} [N]	F_f [N]	μ_{F_f} [N]	r_n [μm]	μ_{r_n} [μm]	Status
V0060	381.3	0.1	157.5	3.3	115.5	2.8	33.0	2.4	short
V0320	19.9	0.01	55.9	3.1	84.5	5.2	40.5	2.8	ok
V0325	19.9	0.04	110.5	3.5	104.9	5.6	37.5	2.6	ok

Test	v_c [m/min]	f [mm]	F_c [N]	μ_{F_c} [N]	F_f [N]	μ_{F_f} [N]	r_n [μ m]	μ_{r_n} [μ m]	Status
V0348	125.0	0.01	42.7	0.9	77.5	2.6	38.3	2.4	ok
V0350	125.0	0.04	102.3	2.3	110.9	3.2	37.9	2.4	ok
V0461	400.1	0.01	41.2	0.2	74.3	0.4	35.5	4.5	ok
V0471	400.1	0.04	99.8	0.6	116.0	0.9	41.9	2.9	ok

Table 9.15: Experimental results Ti6Al4V orthogonal cutting tests

Test	v_c [m/min]	f [mm]	F_c [N]	μ_{F_c} [N]	F_f [N]	μ_{F_f} [N]	r_n [μ m]	μ_{r_n} [μ m]	Status
V0186	69.9	0.02	66.1	22.0	40.6	13.8	36.4	2.5	ok
V0189	69.9	0.06	167.0	16.7	109.4	11.7	39.9	2.8	ok
V0278	200.0	0.02	81.1	1.1	80.3	1.1	40.1	2.6	ok
V0280	200.0	0.06	213.6	1.9	220.6	3.3	38.8	2.6	short
V0286	450.0	0.02	86.5	1.2	91.1	0.6	40.0	2.7	short
V0289	450.0	0.06	193.1	2.6	167.8	1.9	38.0	2.4	short
V0300	500.0	0.1	260.3	1.5	174.6	2.3	42.0	2.4	ok

Table 9.16: Experimental results Ck45 orthogonal cutting tests

9.3.3 Chip Shapes

Chips from the experiments listed in tables 9.15 (Ti6Al4V) and 9.16 (Ck45) were embedded, ground and polished. After polishing, the chips were etched with Nital (Ck45) and Kroll (Ti6Al4V). The geometry and microstructure were then analysed with a Keyence VHX-5000 microscope. The main dimensions which were measured under the microscope are:

- the chip area A_{chip} ,
- the unrolled chip length l_{chip} ,
- the chip curling radius r_{chip} (if applicable),
- the segment distance l_{seg} (if applicable),
- the minimum chip thickness h_{min} (if applicable),
- the maximum chip thickness h_{max} (if applicable).

These dimensions are provided in figure 9.39. From the chip area A_{chip} and the unrolled chip length l_{chip} the average chip thickness h_{avg} was computed with:

$$h_{avg} = \frac{A_{chip}}{l_{chip}} \quad (9.12)$$

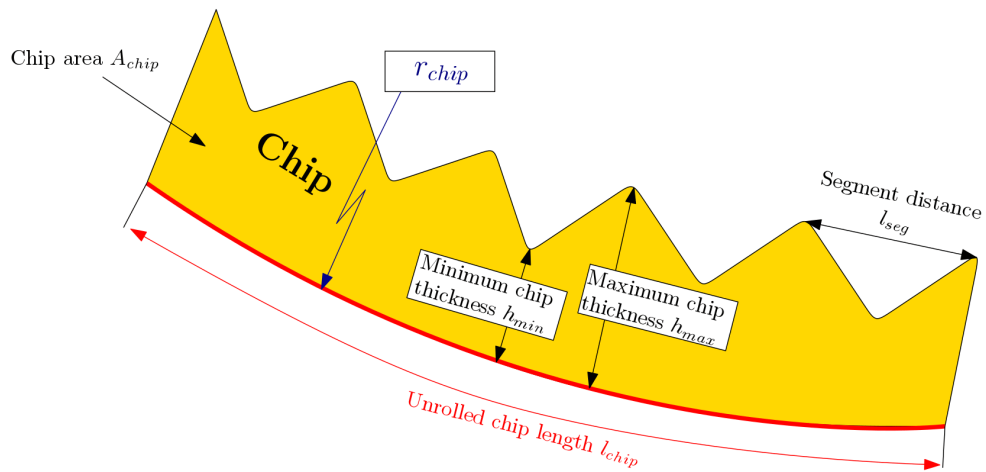


Figure 9.39: Measurement of main chip dimensions.

Further, the shear layer thicknesses in the primary shear zone t_{seg} and in the secondary shear zone t_{sl} were measured, if applicable, according to figure 9.40.

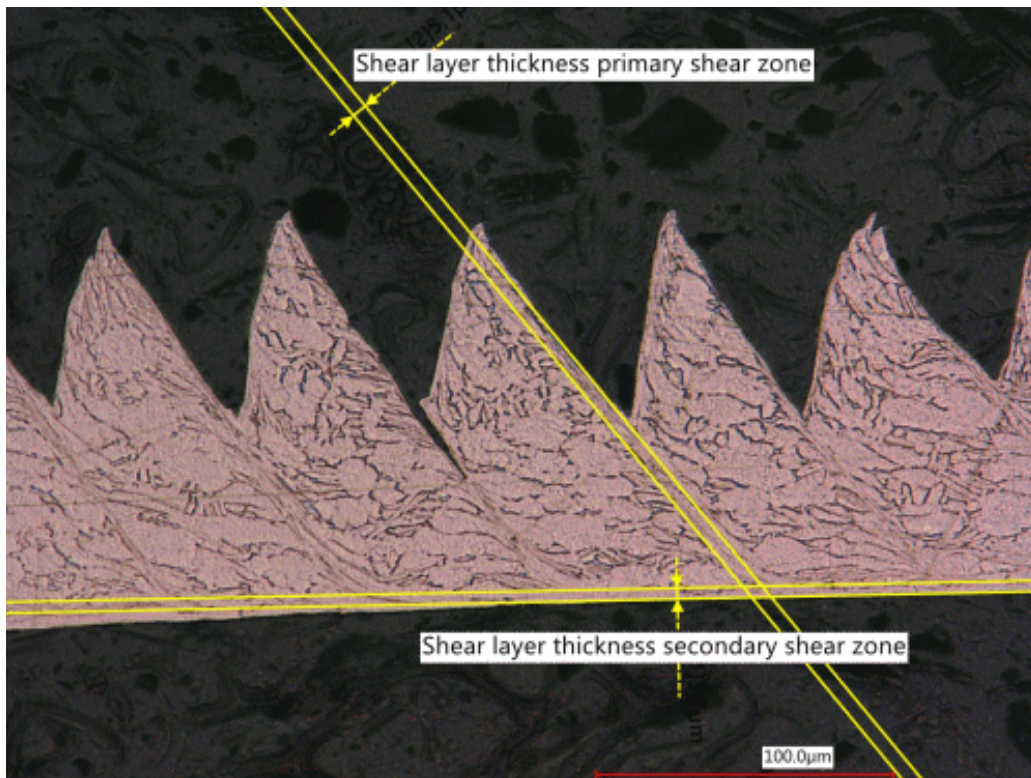


Figure 9.40: Measurement of shear layer thicknesses.

9.3.3.1 *Ti6Al4V*

Chips from experiments listed in table 9.15 were embedded, ground and polished. An overview of these chips is provided in table 9.17. The chips are analysed - where possible - with regards to chip thicknesses, chip shapes and the radius of chip curling - see table 9.19. Only the chip curling radius of the chip from experiment V0325 was determinable, all other chips were too soft or did not have a constant radii. All chips of these cutting experiments show chip segmentation.

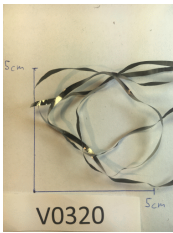




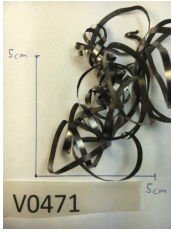

$v_c [\frac{m}{min}]$	20	125	381.3	400
$f [mm]$				
0.01				
0.04				
0.10				

Table 9.17: *Ti6Al4V*: chip overview of selected experiments.

Feed [mm]	$v_c = 20m/min$	$v_c = 125m/min$	$v_c = 381.3m/min$	$v_c = 400m/min$
0.01	V0320, figure 9.42	V0348, figure 9.44	-	V0461, figure 9.46
0.04	V0325, figure 9.43	V0350, figure 9.45	-	V0471, figure 9.47
0.1	-	-	V0060, figure 9.41	-

Table 9.18: *Ti6Al4V*: Investigated chip shapes.

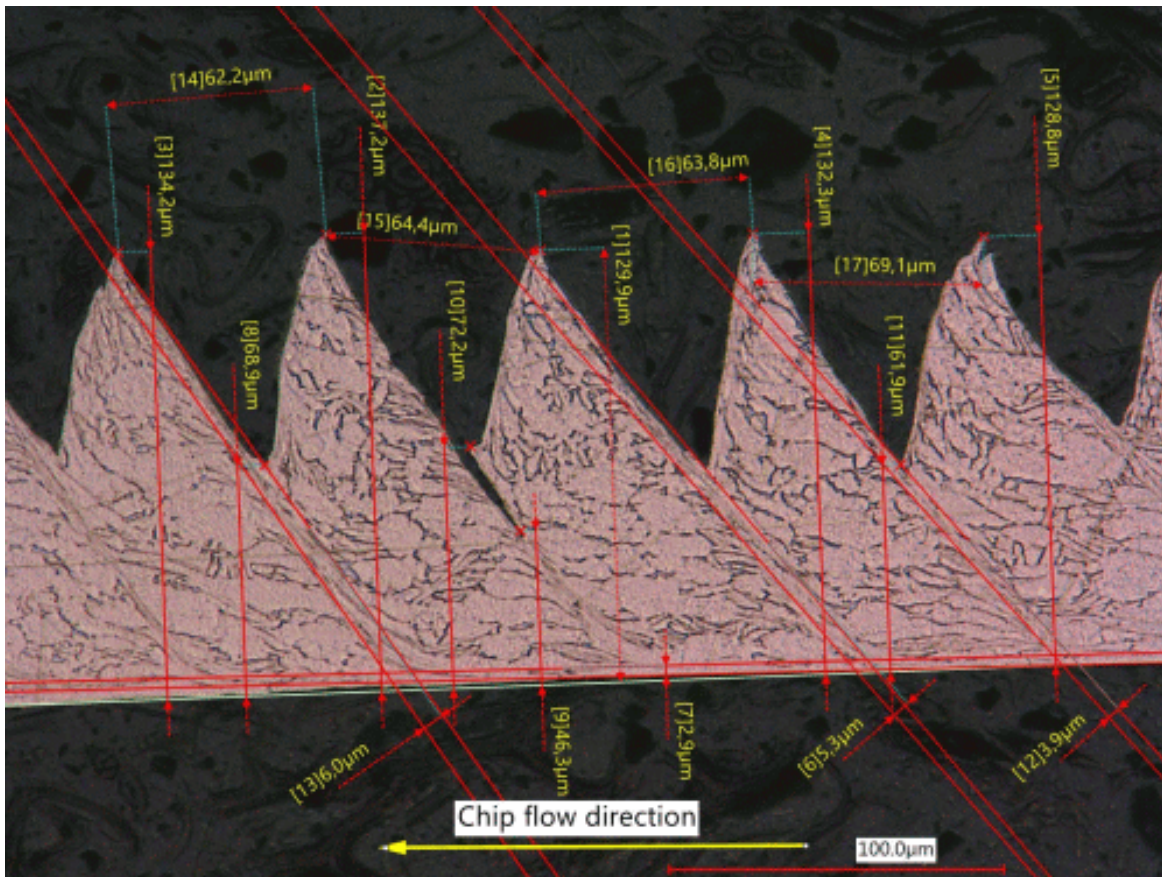


Figure 9.41: Chip from experiment V0060 $v_c = 381.3 \text{ m/min}$, $f = 0.10 \text{ mm}$.

Test	v_c [$\frac{m}{min}$]	f [mm]	h_{avg} [μm]	h_{min} [μm]	h_{max} [μm]	l_{seg} [μm]	r_{chip} [mm]	t_{seg} [μm]	t_{sl} [μm]	Segmentation?	BUE?
V0060	381.3	0.1	100	80	150	51-56	-	4-6	3	yes	no
V0320	20	0.01	28	24	35	13-23	-	-	-	yes	no
V0325	20	0.04	68	57	69	11-16	2.7-2.8	-	-	yes	no
V0348	125	0.01	16	12	23	6-15	-	-	-	yes	no
V0350	125	0.04	61	54	106	27-38	-	-	-	yes	no
V0461	400	0.01	16	7-12	23-25	15-24	-	-	-	yes	no
V0471	400	0.04	52	33-36	63-71	34-44	-	2-6	6	yes	no

Table 9.19: Ti6Al4V: measured chip thicknesses, chip shapes and chip curling radii from experiments

Chip pictures with measurement details can be found below with picture references according to table 9.18.

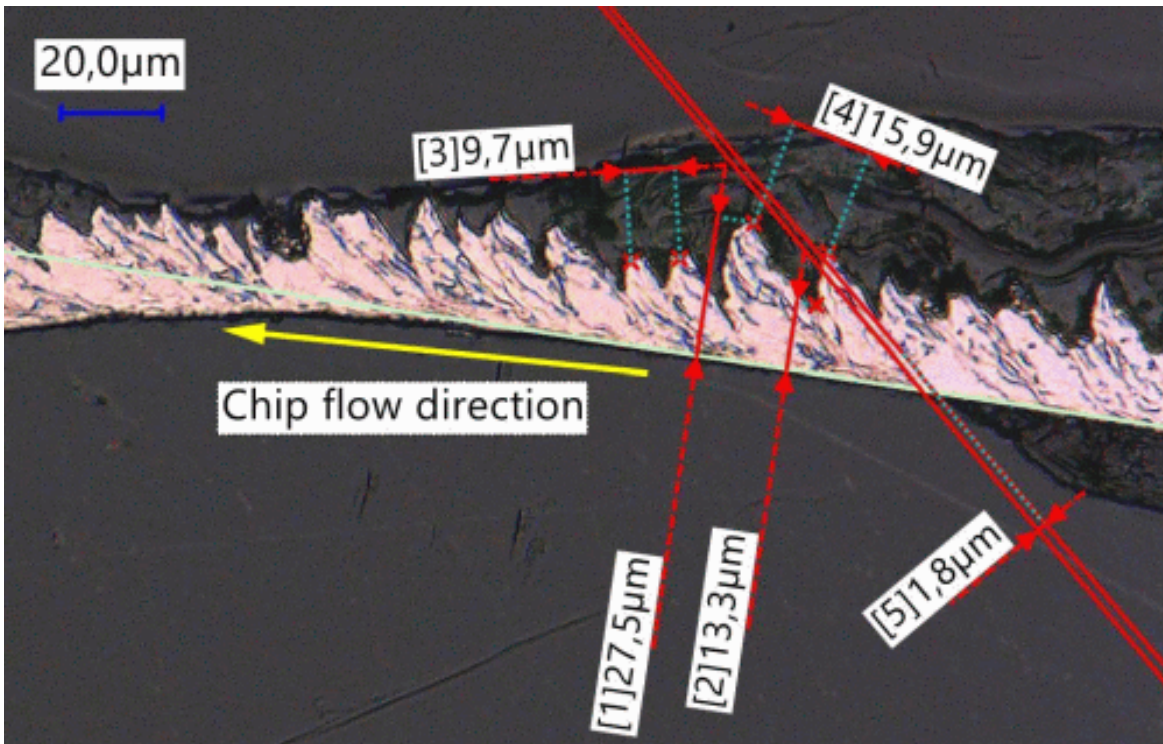


Figure 9.42: Chip from experiment V0320 $v_c = 20m/min$, $f = 0.01mm$.

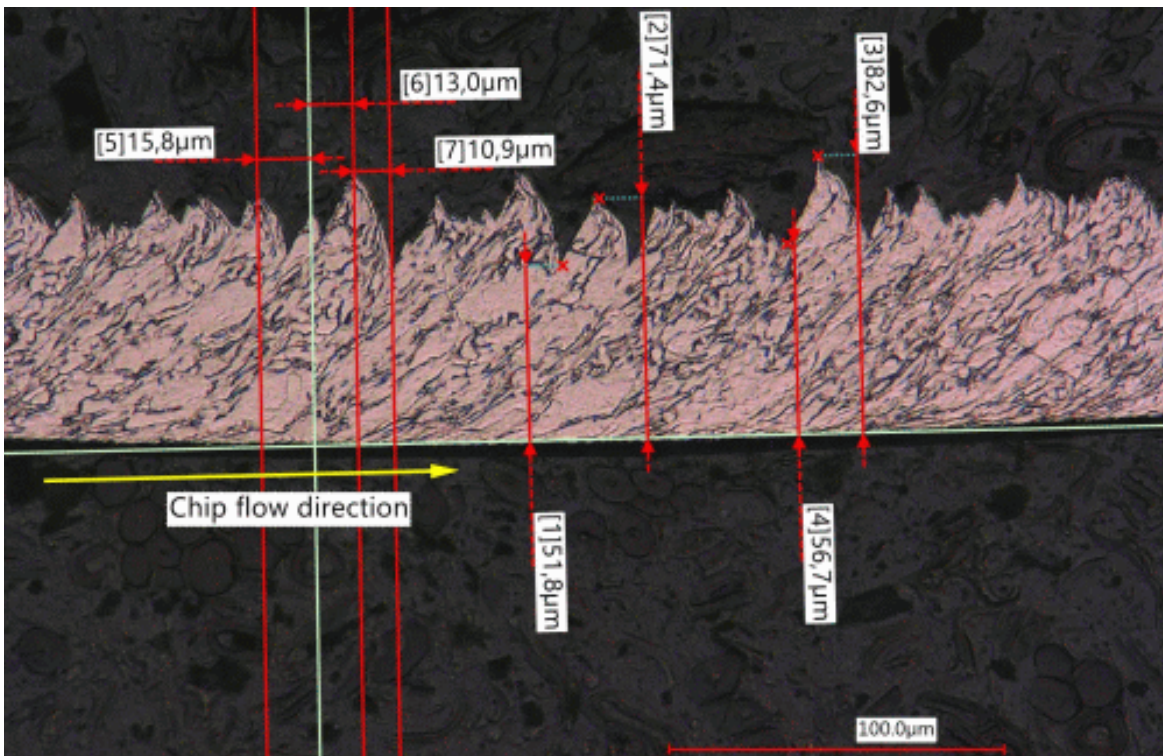


Figure 9.43: Chip from experiment V0325 $v_c = 20m/min$, $f = 0.04mm$.

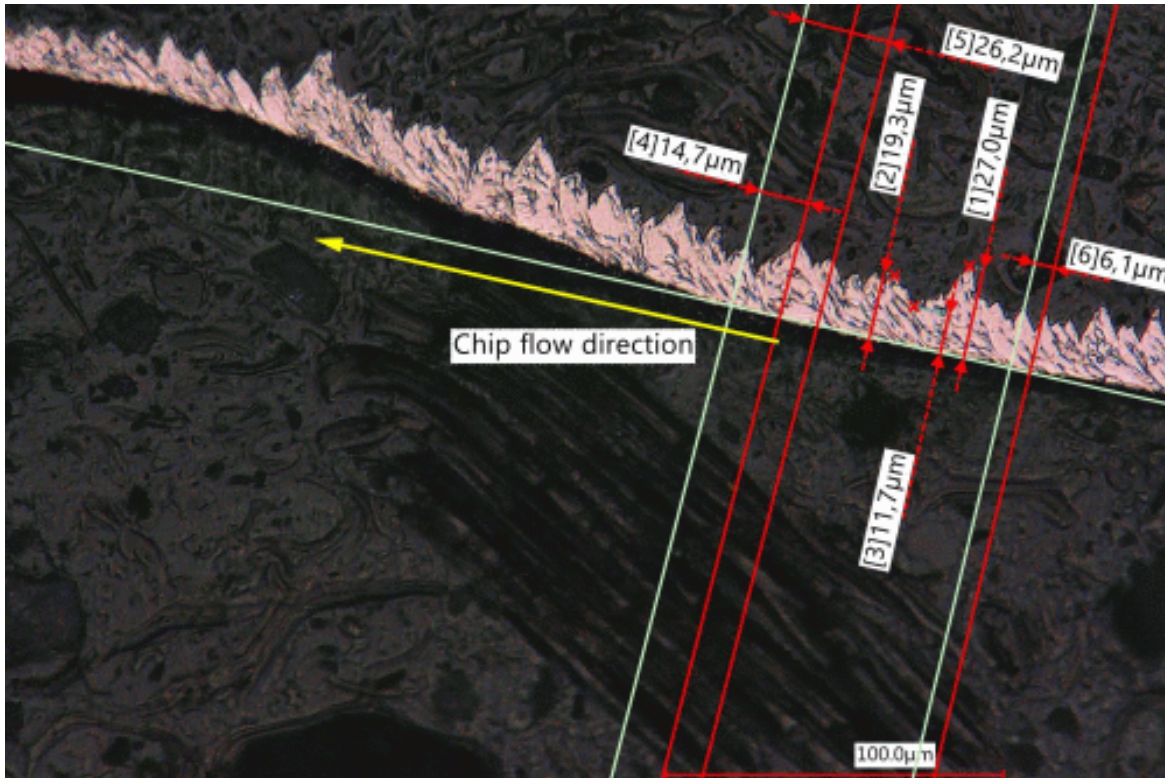


Figure 9.44: Chip from experiment V0348 $v_c = 125m/min, f = 0.01mm$.



Figure 9.45: Chip from experiment V0350 $v_c = 125m/min, f = 0.04mm$.

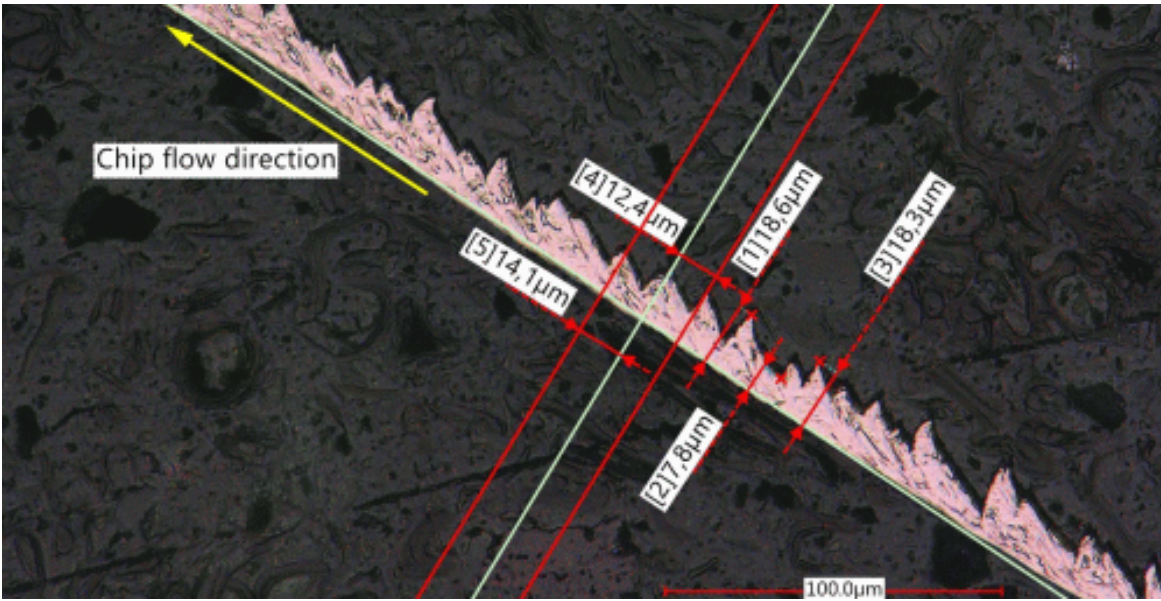


Figure 9.46: Chip from experiment V0461 $v_c = 400m/min, f = 0.01mm$.



Figure 9.47: Chip from experiment V0471 $v_c = 400m/min, f = 0.04mm$.

9.3.3.2 Ck45

Chips from experiments listed in table 9.16 were embedded, ground, polished and etched. An overview of these chips is provided in table 9.20. The chips are analysed - where possible - with regards to chip thicknesses, chip shapes and the radius of chip curling - see table 9.22. All investigated Ck45-chips show largely stretched grains with and the chip side sliding along the rake face sticking as the grains are stretched in sliding direction with the material above shearing over these grains in the contact zone which indicates very high friction coefficients. Only the chip from experiment V0300 shows chip segmentation, all other are continuous chips.


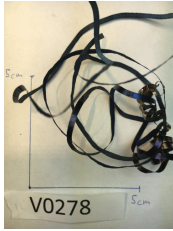



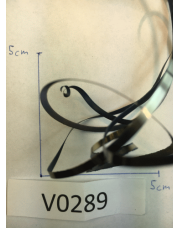
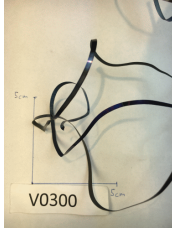
$v_c [\frac{m}{min}]$	70	200	450	500
$f [mm]$				
0.02				
0.06				
0.10				

Table 9.20: Ck45: chip overview of selected experiments.

Feed [mm]	$v_c = 70m/min$	$v_c = 200m/min$	$v_c = 450m/min$	$v_c = 500m/min$
0.02	V0186, figure 9.48	V0278, figure 9.50	V0286, figure 9.52	
0.06	V0189, figure 9.49	V0280, figure 9.51	V0289, figure 9.53	
0.10				V0300, figure 9.54

Table 9.21: Ck45: Investigated chip shapes.

MATERIAL PARAMETER DETERMINATION

Test	$v_c [\frac{m}{min}]$	$f [mm]$	$h_{avg} [\mu m]$	$h_{min} [\mu m]$	$h_{max} [\mu m]$	$l_{seg} [\mu m]$	$r_{chip} [mm]$	$t_{seg} [\mu m]$	$t_{sl} [\mu m]$	Segmentation?	BUE?
V0186	70	0.02	66	-	-	-	-	-	-	no	yes
V0189	70	0.06	166	109	235	-	3.2-3.4	-	8-10	no	yes
V0278	200	0.02	58	42	73	-	-	-	4	no	yes
V0280	200	0.06	201	177	212	-	-	-	6	no	no
V0286	450	0.02	69	67	81	-	5.02	-	4	no	no
V0289	450	0.06	146	133	162	-	26.2	-	7	no	no
V0300	500	0.1	217	194	238	85-95	-	19	6	yes	no

Table 9.22: Ck45: measured chip thicknesses, chip shapes and chip curling radii from experiments

Chip pictures with measurement details can be found below with picture references according to table 9.21.

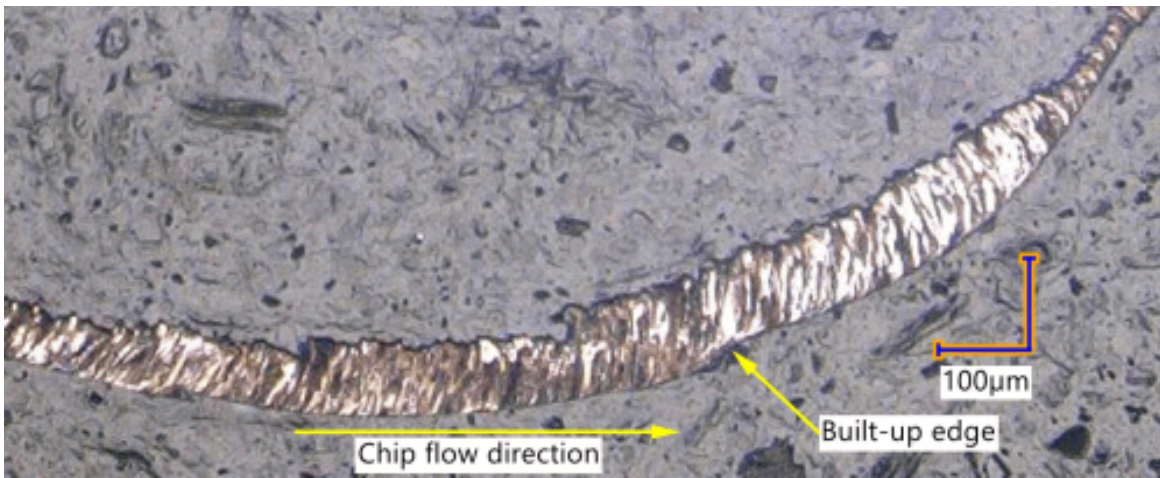


Figure 9.48: Chip from experiment V0186 $v_c = 70m/min, f = 0.02mm$.

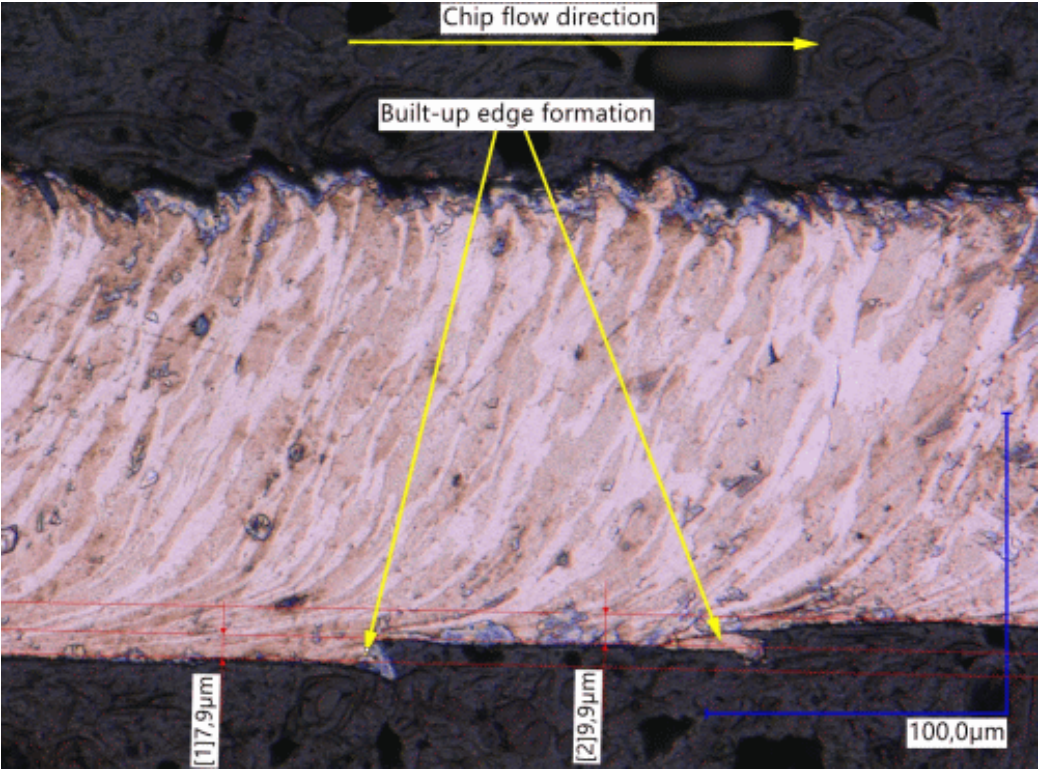


Figure 9.49: Chip from experiment V0189 $v_c = 70m/min, f = 0.06mm$.

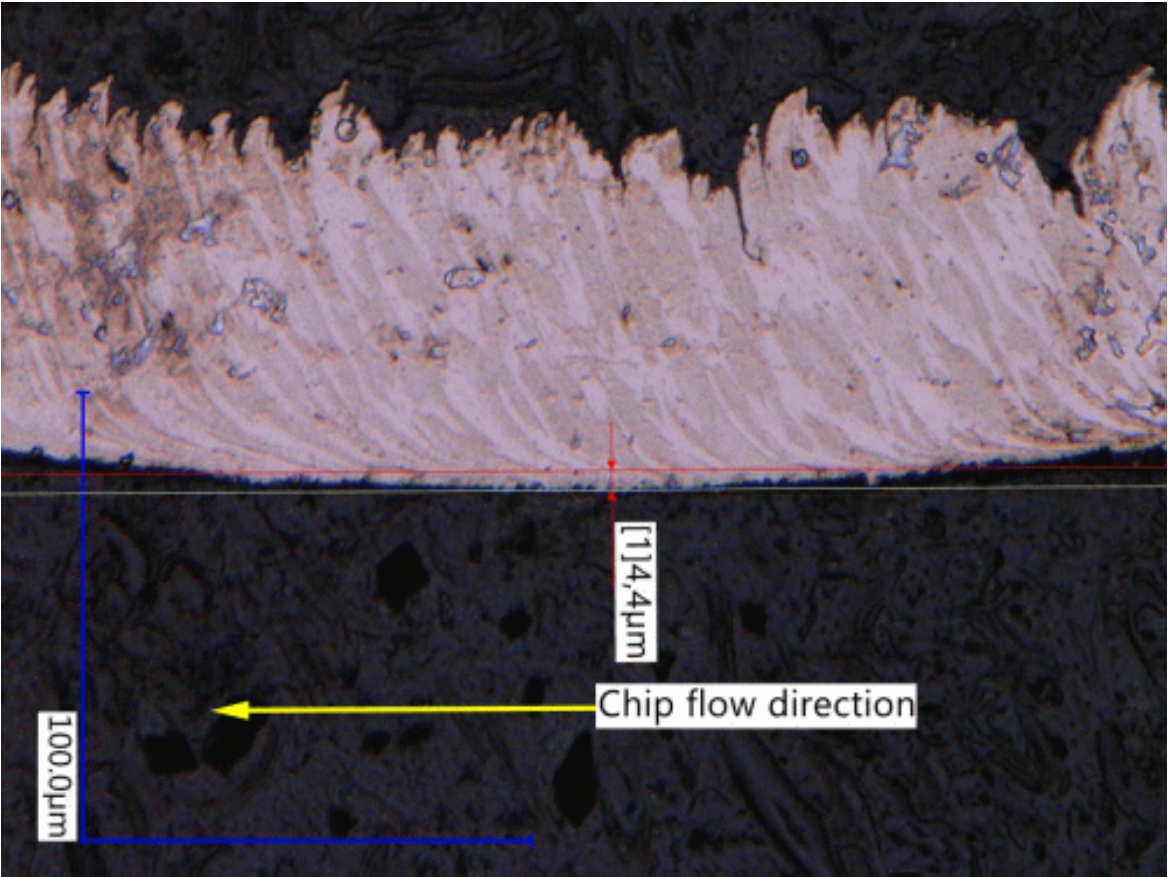


Figure 9.50: Chip from experiment V0278 $v_c = 200m/min, f = 0.02mm$.

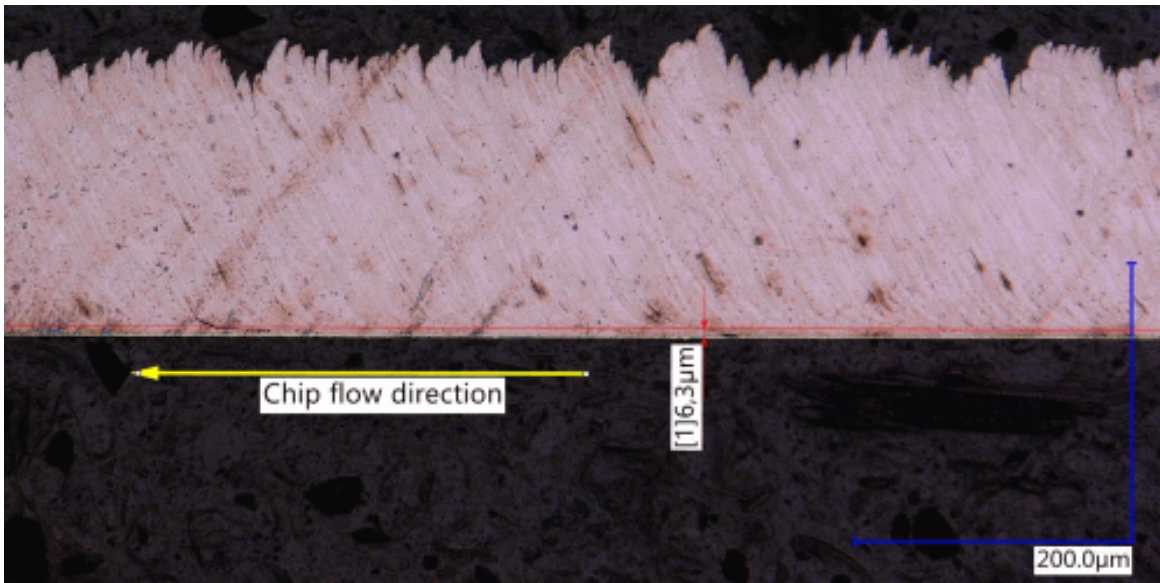


Figure 9.51: Chip from experiment V0280 $v_c = 200m/min, f = 0.06mm$.

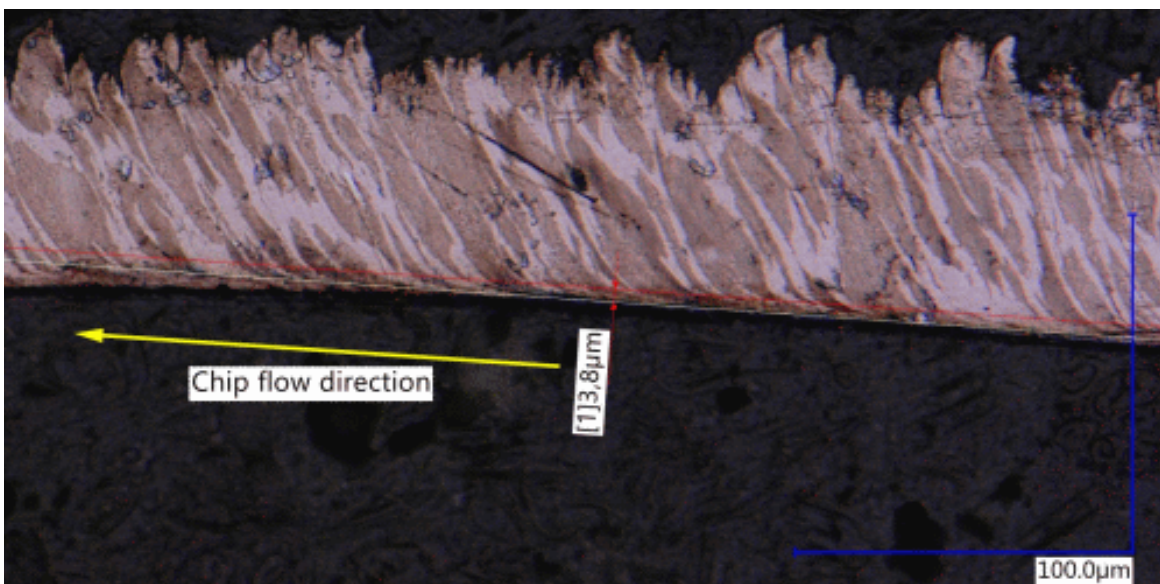


Figure 9.52: Chip from experiment V0286 $v_c = 450m/min, f = 0.02mm$.

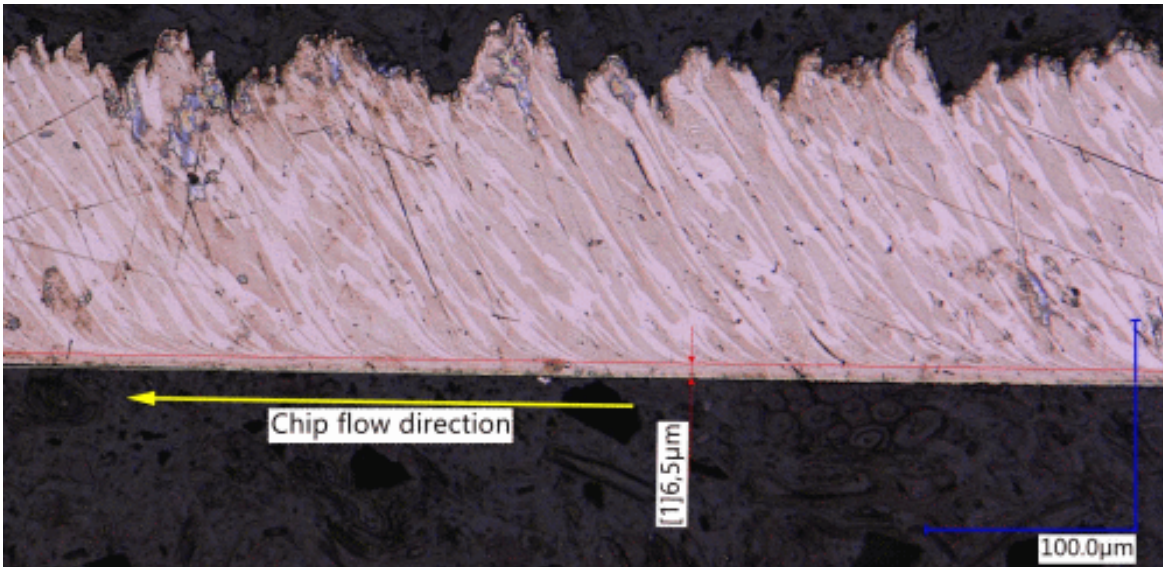


Figure 9.53: Chip from experiment V0289 $v_c = 450m/min, f = 0.06mm$.

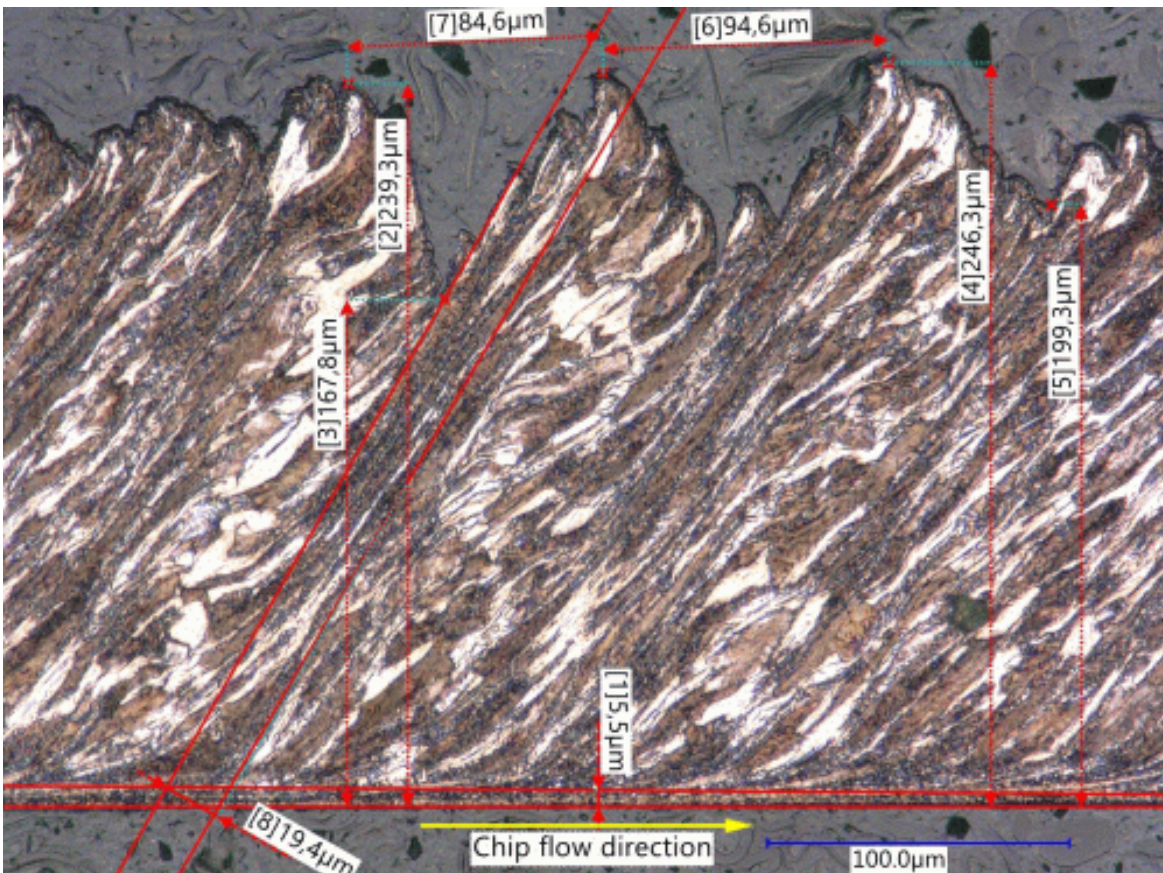


Figure 9.54: Chip from experiment V0300 $v_c = 500m/min, f = 0.1mm$.

9.4 INVERSE MATERIAL PARAMETER IDENTIFICATION

In this section the material constitutive parameters for the JC-CLASSIC-model are inversely identified based on cutting experiments from section 9.3.2. First an introduction is given into optimization including a test case using different optimization methods. In the next step OXLEY's force model is applied to derive material constitutive parameters for all conducted cutting experiments. This, in an attempt to down-select permissible constitutive model parameter ranges for the last part of this chapter where the SPH-solver MFREE_IWF is then used to inversely identify material constitutive model parameters directly within a numerical model of the cutting experiment. Experiments at very high cutting speeds are taken as basis for the inverse identification since the computation time linearly scales with the cut speed because an explicit time integration scheme used in the SPH solver: twice the cut speed results in half compute time. The identified constitutive model parameters are then used to recalculate cutting experiments at other process conditions and the experimental and numerical results are compared.

9.4.1 Optimization Algorithms

Optimization algorithms are iterative procedures which aim to reduce an objective/cost function depending on parameters x . Start point is an initial parameter set x_0 from which the design space is explored into various direction in an attempt to minimize the objective function [118]. The exploration of the design space depends on the optimization algorithm of which three are introduced in the following sections. The optimization finished when a convergence criterion is met. Optimization with only one objective are called single-objective optimization versus multi-objective optimizations with several objectives. A single-objective can be constructed from multi-objectives [232] where each objective has to be weighted versus the other objectives.

9.4.1.1 Simplex (Nelder-Mead)

The Nelder-Mead-Simplex[173, 228] method, also known as Downhill-Simplex, and in the following abbreviated with SIMPLEX is a robust method that does not require any derivatives of the objective function. The algorithm is based on the objective function evaluation at $n + 1$ corner points where n is the number of depending parameters of the objective function. In each iteration step the corner point with the worst objective function value is replaced by a new value. The optimization finishes when the $n + 1$ corner points are sufficiently close to each other which means they have centered in a minimum of the objective function. In this investigation the implementation of the SIMPLEX in PYTHON based on [186] is used.

9.4.1.2 Bayes

The Bayes optimization is a global optimization method introduced by [160]. The basic idea is the optimization of an a priori unknown objective function which can be difficult or expensive

to evaluate, e.g. by experiments or numerical simulations. Successful applications of the method can be found for example [137, 146, 226]. Commonly, the Bayesian optimization is coupled with a Gaussian process (GP) model which forms a surrogate model of the unknown objective and constraint function. The already available samples/function evaluations are used to estimate the cost function at other parameter sets. Based on the mean and uncertainty estimation of the GP model new parameters are selected to be evaluated next. The GP model is then continuously updated with the new data and derives the next parameter set to be evaluated. Here, the capabilities of NUMPY and SCIKIT-LEARN[186] are used for the application of the BAYES-optimization.

9.4.1.3 *Differential Evolution*

Evolutionary algorithms are based on biological principles such as reproduction, mutation, isolation, recombination and selection which are applied to individuals in a population [170]. The population members evolve over time with adaptation to their environment where in a every generation the individuals with the highest score / best fit are selected for recombination and mutation. The latter brings some stochastic into the development of the population which helps to explore the parameter space globally. As with SIMPLEX and BAYES no gradients are required for this kind of optimization. There are many different evolutionary algorithms, e.g. [66, 96, 117, 198, 233]. From these the DIFFERENTIAL EVOLUTION from [233] is selected to be used in the investigations presented here. The algorithm is available in NUMPY/SCIPY [86].

9.4.2 *Test Simulations*

A test case is created to analyse the three optimization algorithms presented before. The JC-model with parameters for 50SiB8 from table 7.9 is used to generate a flow stress curve including adiabatic heating with a Taylor-Quinney coefficient of $\eta_{TQ} = 0.90$. For this purpose the temperature is integrated with an Euler explicit integration scheme, see equations (8.19) - (8.25), thus introducing thermal softening with increasing strain. The simulation is conducted until a plastic strain of $\varepsilon_{pl} = 3.0$ is achieved. From this so generated flow curve a few flow stresses at different plastic strain levels are taken.

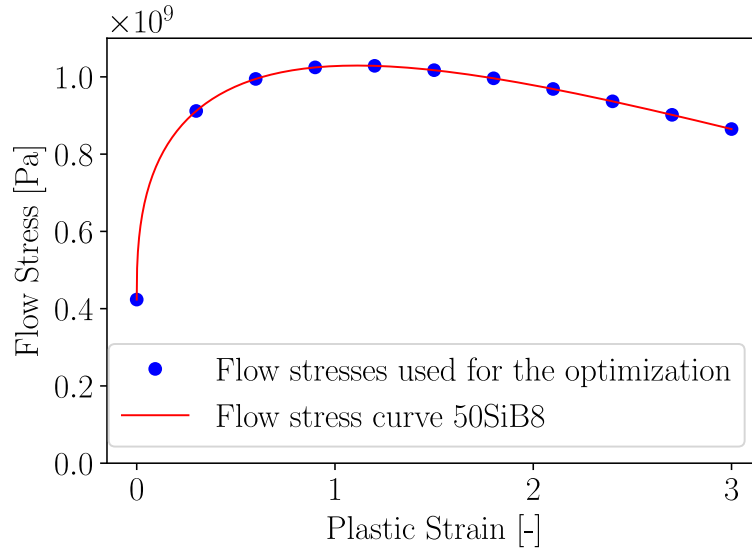


Figure 9.55: Flow stress curve of 50SiB8 computed with the JC-model including adiabatic heating. The blue points show the evaluation points of flow stresses used for the optimization.

The initial temperature is set $T_{init} = 300K$, the plastic strain rate is constant with $\dot{\epsilon}_{pl} = 1e - 3/s$ and from the resulting stress-strain curve 11 stress points were sampled to be taken as comparison values for the inverse parameter identification loop, see table 9.23.

ϵ_{pl}^j	0.0	0.3	0.6	0.9	1.2	1.5	1.8	2.1	2.4	2.7	3.0
$\sigma_{y,sample}^j$ [MPa]	423.5	911.7	994.6	1024.5	1028.5	1017.3	996.3	968.7	936.6	901.7	864.9

Table 9.23: Evaluation points for the cost function.

Since the second term of the JC-CLASSIC-model is a constant throughout the selected loading case it is scaling the other two terms with a constant which prevents the optimizer from finding a useful value and is therefore set to $\dot{\epsilon}_{pl} = \dot{\epsilon}_{pl}^0 = 1e - 3/s$. This makes the second term always 1 and the value found by the optimizer for parameter C is meaningless.

The objective (cost) function c for the optimization is the squared sums of the error in the 11 sampled stress points and shall be minimized:

$$c = \sum_j (\sigma_y^j - \sigma_{y,sample}^j)^2 = \min \tag{9.13}$$

The SIMPLEX-optimization was initialized with 6 simplexes in the parameter space for A, B, C, m and n:

Initial Simplex	A [MPa]	B [MPa]	C [-]	m [-]	[n]
1	100	7	0.001	0.2	0.6
2	100	60	0.05	0.1	0.5
3	200	5	0.02	0.9	0.4
4	500	4	0.1	0.4	0.3
5	800	3	0.001	0.7	0.2
6	1000	2	0.01	0.9	0.1

Table 9.24: Initial values for the SIMPLEX-optimization.

The optimization results are given in table 9.25. The SIMPLEX and DE-methods found both the correct values for A, B, m and n while the BAYES suffered but came close to the correct values. The SIMPLEX-method showed the shortest runtimes while the DE-method required around 40 times more function evaluations. The BAYES-method has an extreme runtime compared to the other methods. This is induced by the large overhead when evaluating the Gaussian process (GP) model - the function evaluations itself required in total 4 seconds while the remaining 2348s are attributed to the GP process model. A comparison of the yield curves from the optimized parameter sets is provided with figure 9.56. All methods match the sample points quite well even though BAYES did not end up at the correct values.

Result from	A [MPa]	B [MPa]	C [-]	m [-]	[n]	Iterations	Runtime
Simplex	430.9	908.7	(-1.4192)	0.7361	0.3854	912	8s
Bayes	424.6	764.2	(0.01)	1.0	0.302	400	2352s
DE	430.9	908.7	(0.0075)	0.7361	0.3854	39351	386s
Original data	430.9	908.7	0.0047	0.7361	0.3854	-	-

Table 9.25: Inversely identified parameter with different optimization methods.

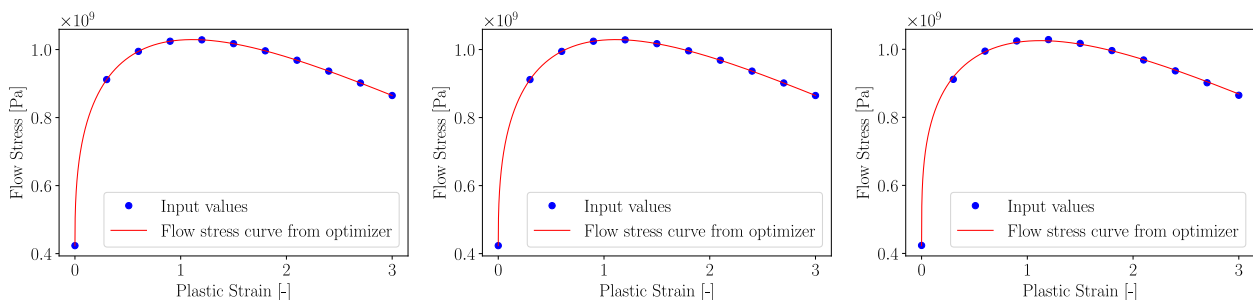


Figure 9.56: Comparison of the flow stress curves generated with inversely identified material parameters, SIMPLEX (left), DE (middle) and BAYES (right) algorithm.

The evolution of the material parameters A, B, C, m and n during the optimization is given in figure 9.57. Remind that C has no real meaning here, since its effect vanishes with $\dot{\epsilon}_{pl} = \dot{\epsilon}_{pl}^0$.

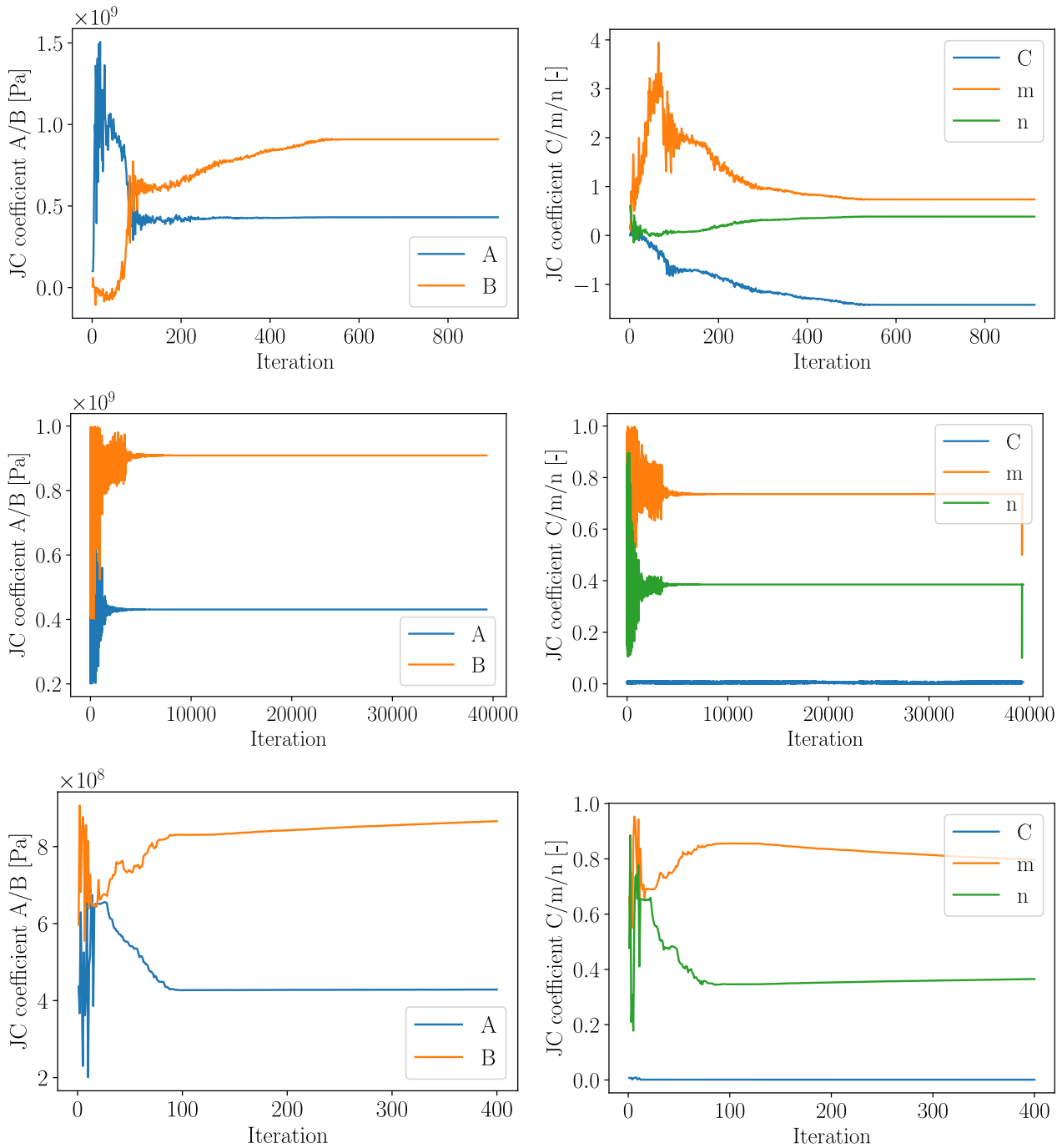


Figure 9.57: Evolutions of material parameter constants A, B, C, m and n during the optimization for the three optimization algorithms SIMPLEX (top), DE (middle), BAYES (bottom).

The most interesting comparison is however the development of the summed square error over the number of iterations in figure 9.58. BAYES performs best in the beginning phase (first 100 iterations) of the optimization but stagnates in the long run. As mentioned before, the problem of BAYES is the increasing overhead with increasing number of iterations which can be seen in figure 9.59 where the runtime per iteration is shown over the iterations. The

fast decay in the beginning phase makes BAYES still an interesting candidate for the inverse parameter identification from cutting experiments.

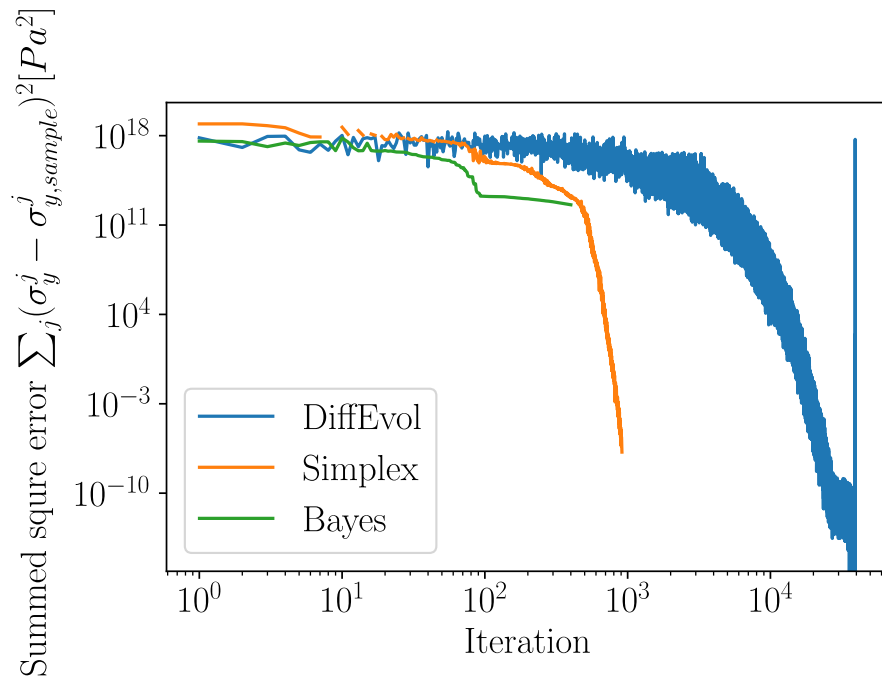


Figure 9.58: Evolution of the summed square error of the stresses with the three optimization methods.

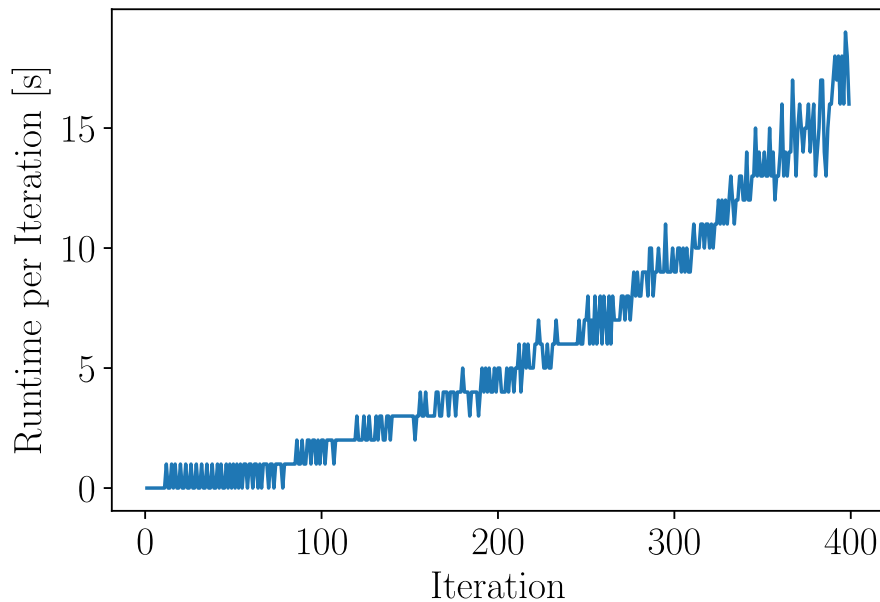


Figure 9.59: Evolution of the computation time per iteration with BAYES showing a steady increase due to the process model evaluation time.

9.5 IDENTIFICATION OF MATERIAL PARAMETERS WITH OXLEY'S PROCESS FORCE MODEL

Oxley's process force model is used to drive an inverse parameter identification of all cutting experiments with the SIMPLEX-method. The idea is to derive a possible constitutive model parameter range based on the experimental results. This parameter range would then serve as a guess for the input boundaries for the inverse identification using the meshfree simulation tool. Guess, because OXLEY's model uses some modelling simplifications, e.g. no clearance angle, no cutting edge radius and no friction coefficient is considered. The maximum number of iterations was restricted to a maximum of $n_{calls} = 500$ for the identification of parameters from each of the cutting experiments.

The optimization of a problem requires an objective function to be minimized. In this investigation a single-objective is constructed from the difference of experimental and simulated process forces, here cut and feed force. The passive force F_p is negligible in an orthogonal cutting setup which allows for a 2D plane strain numerical abstraction of the real cutting process. The experimental process forces stem from orthogonal cutting experiments whose results are given in tables 11.1 (Ti6Al4V) and 11.2 (Ck45). The cost function is the summed squared error of the predicted and experimental process force components:

$$\Delta F_c = F_c^{sim} - F_c^{exp} \quad (9.14)$$

$$\Delta F_f = F_f^{sim} - F_f^{exp} \quad (9.15)$$

$$\Delta F_{total}^2 = w_c \cdot \Delta F_c^2 + w_f \cdot \Delta F_f^2 \quad (9.16)$$

where the objectives are weighted with respective weights w_c and w_f for the force components. In all investigations conducted in this work these weights are $w_c = w_f = 1.0$ such that the minimization of cut and feed force errors are equally important. The structogram of the inverse parameter identification from cutting experiments is provided with figure 9.60.

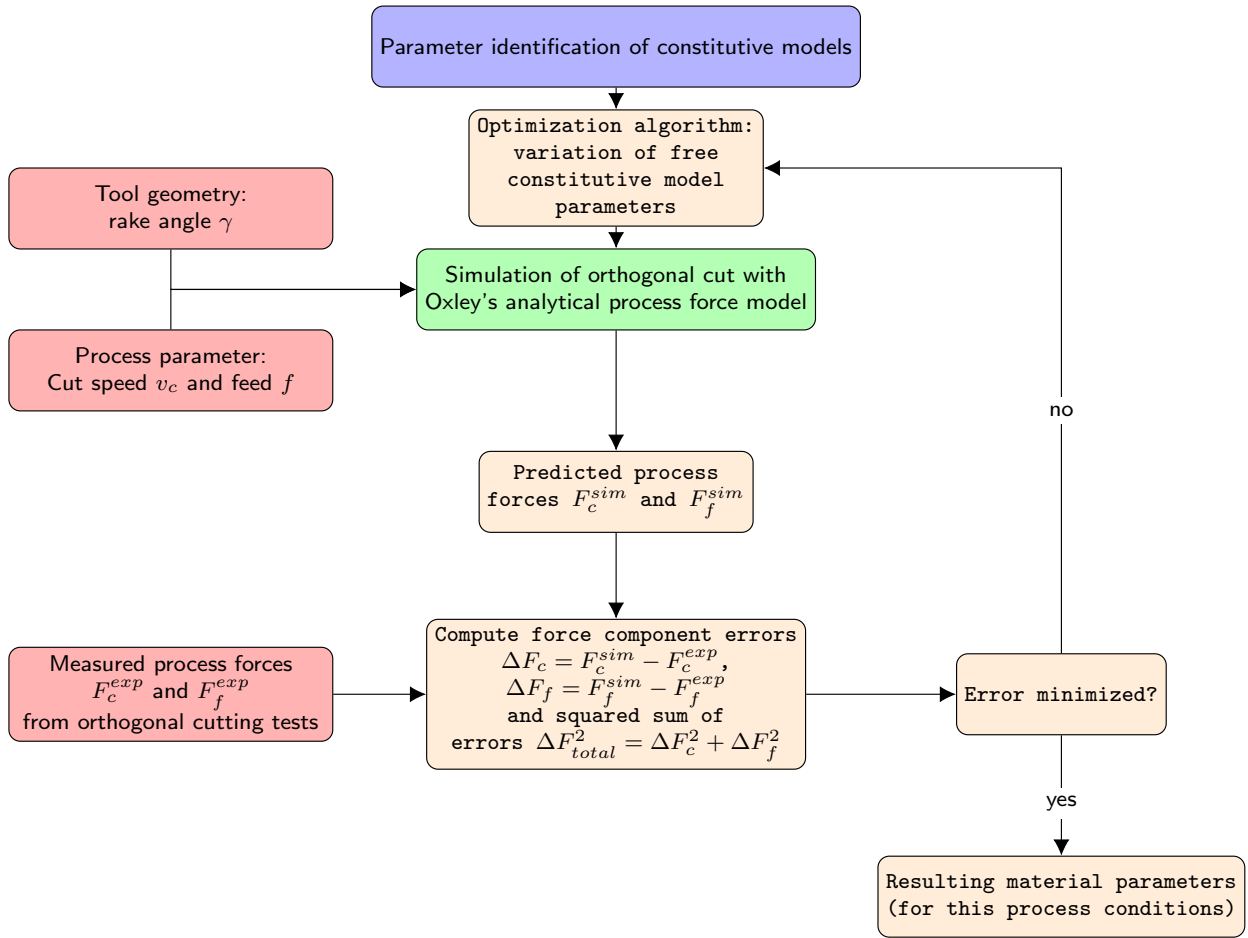


Figure 9.60: Structogram of the parameter identification with OXLEY'S process force model

The initial simplexes are computed with the equations given in table 9.26:

Simplex	$A^{i+1}[MPa]$	$B^{i+1}[MPa]$	$C^{i+1}[-]$	$m^{i+1} [-]$	$n^{i+1}[-]$
1	A^i	B^i	C^i	m^i	n^i
2	$A^i + (\Delta A)/20$	$B^i + (\Delta B)/20$	$C^i + (\Delta C)/20$	$m^i + (\Delta m)/20$	$n^i + (\Delta n)/20$
3	$(\Delta A)/2$	$(\Delta B)/2$	$C^i + (\Delta C)/20$	$m^i + (\Delta m)/20$	$n^i + (\Delta n)/20$
4	A^i	B^i	$(\Delta C)/2$	m^i	n^i
5	A^i	B^i	C^i	$(\Delta m)/2$	n^i
6	$(\Delta A)/2$	$(\Delta B)/2$	$(\Delta C)/2$	$(\Delta m)/2$	$(\Delta n)/2$

Table 9.26: Initial simplexes used in the SIMPLEX-optimization with OXLEY'S force model.

where ΔA , ΔB , ΔC , Δm and Δn are the differences between minimum and maximum permissible parameter ranges for Ck45 and Ti6Al4V as given in table 9.27.

Material	A [MPa]	B [MPa]	C [-]	m [-]	[n]
Ti6Al4V	[300...1200]	[50...1200]	[0.001...0.07]	[0.577...1.50]	[0.02...0.9]
Ck45	[100...800]	[50...1200]	[0.001...0.07]	[0.577...1.50]	[0.02...0.9]

Table 9.27: Permissible parameter ranges used in the SIMPLEX-optimization with OXLEY's force model.

The initial set at $i = 0$ for the JC-parameters is $A^{i=0} = 600MPa$, $B^{i=0} = 300MPa$, $C^{i=0} = 0.014$, $m^{i=0} = 0.9$ and $n^{i=0} = 0.1$ and is continuously updated with the parameters from the preceding inverse parameter identification: $A^{i+1} = A^i$, $B^{i+1} = B^i$, $C^{i+1} = C^i$, $m^{i+1} = m^i$, $n^{i+1} = n^i$.

The inverse parameter identification with OXLEY's model and the SIMPLEX-method took 3 weeks on a single CPU for a total of 510 cutting experiments. From these 510 results 229 are Ck45- and 281 Ti6Al4V cutting experiments. A summary of the optimizations is provided with table 9.28

Material	Number of experiments i	$\Delta F_{total}^2 = min$	$\Delta F_{total}^2 = 0$
Ti6Al4V	281	78	61
Ck45	229	106	71

Table 9.28: Overview of inverse parameter identifications with OXLEY's force model and SIMPLEX-method.

The comparison of the cases where a minimum is found ($\Delta F_{total}^2 = min$) and how much of them are $\Delta F_{total}^2 = 0$ reveals that the topology of the cost function ΔF_{total}^2 obviously has local minima. This means that in general gradient based methods or the SIMPLEX-method potentially can trap into one of these local minima subsequently excluding the chance to find a global minimum. In such cases the use of more costly optimization algorithms are required. On the other hand, this could be exploited to extend the optimization procedure for an additional parameter to be optimized, e.g. the chip thicknesses, shear angle and or the chip temperature.

9.5.1 Ti6Al4V Results

The resulting material constitutive parameters based on the inverse identification from each Ti6Al4V experiment shows a large range for each of the parameters. Even when considering successful optimizations ($\Delta F_{total}^2 = min$) only, a large scatter is visible. This is shown in histogram plots for parameters A and B in figure 9.61, C and m in figure 9.62 and for n in figure 9.63 together with the histogram of the runtimes for each experiment.

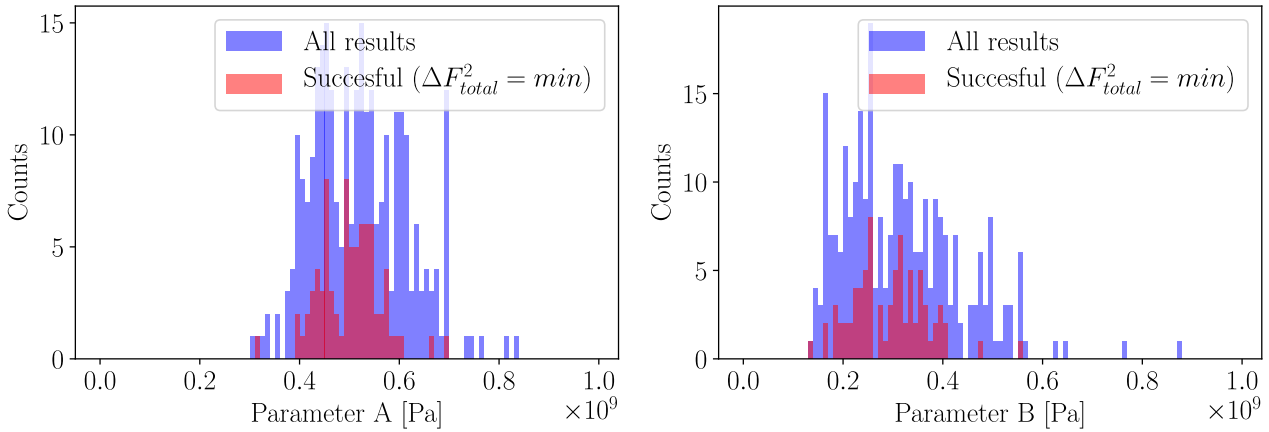


Figure 9.61: Histogram of parameters A (left) and B (right) resulting from the parameter identification of Ti6Al4V experiments with the SIMPLEX-method using OXLEY'S force model. Histograms in blue are the resulting coefficients from all identifications while histograms in red show the parameters for successful optimizations only.

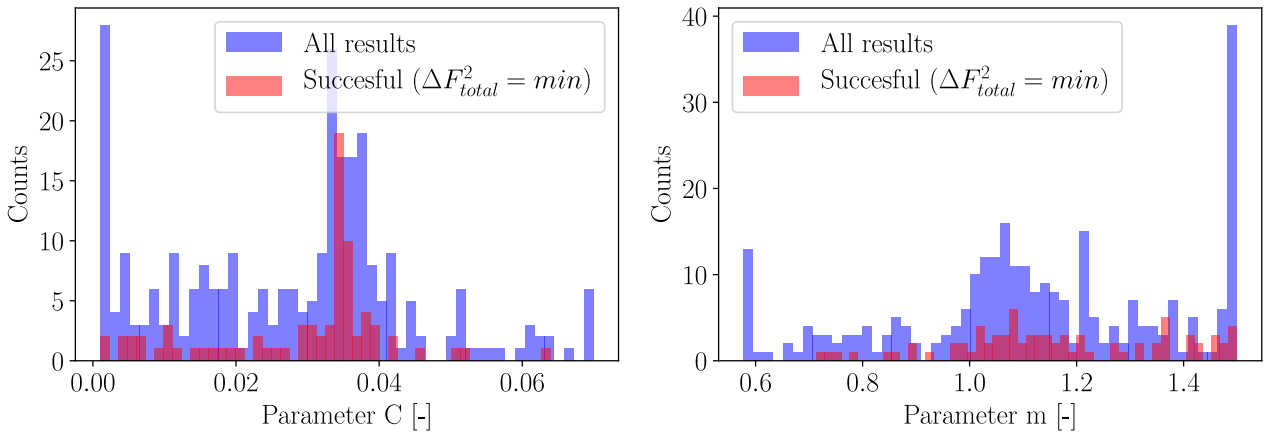


Figure 9.62: Histogram of parameters C (left) and m (right) resulting from the parameter identification of Ti6Al4V experiments with the SIMPLEX-method using OXLEY'S force model. Histograms in blue are the resulting coefficients from all identifications while histograms in red show the parameters for successful optimizations only.

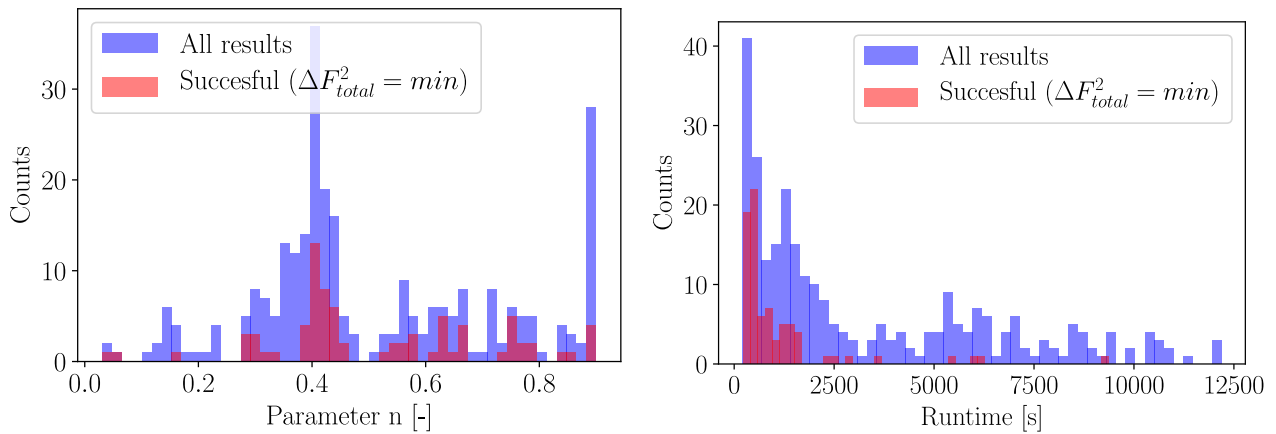


Figure 9.63: Histogram of parameters n (left) and runtimes (right) resulting from the parameter identification of Ti6Al4V experiments with the SIMPLEX-method using OXLEY's force model. Histograms in blue are the resulting coefficients from all identifications while histograms in red show the parameters from successful optimizations only.

9.5.2 Ck45 Results

Similar to the Ti6Al4V optimization the resulting material constitutive parameters based on the inverse identification from each Ck45 experiment show large ranges for each of the five parameters. Even when considering successful optimizations ($\Delta F_{total}^2 = min$) only, a large scatter is visible. This is shown in histogram plots for parameters A and B in figure 9.64, C and m in figure 9.65 and for n in figure 9.66 together with the histogram of the runtimes for each experiment.

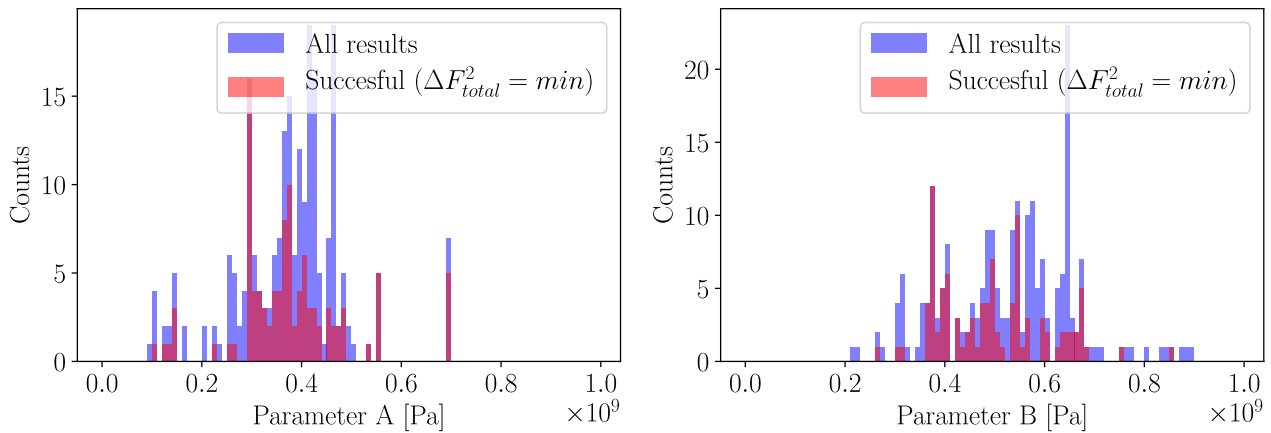


Figure 9.64: Histogram of parameters A (left) and B (right) resulting from the parameter identification of Ck45 experiments with the SIMPLEX-method using OXLEY's force model. Histograms in blue are the resulting coefficients from all identifications while histograms in red show the parameters for successful optimizations only.

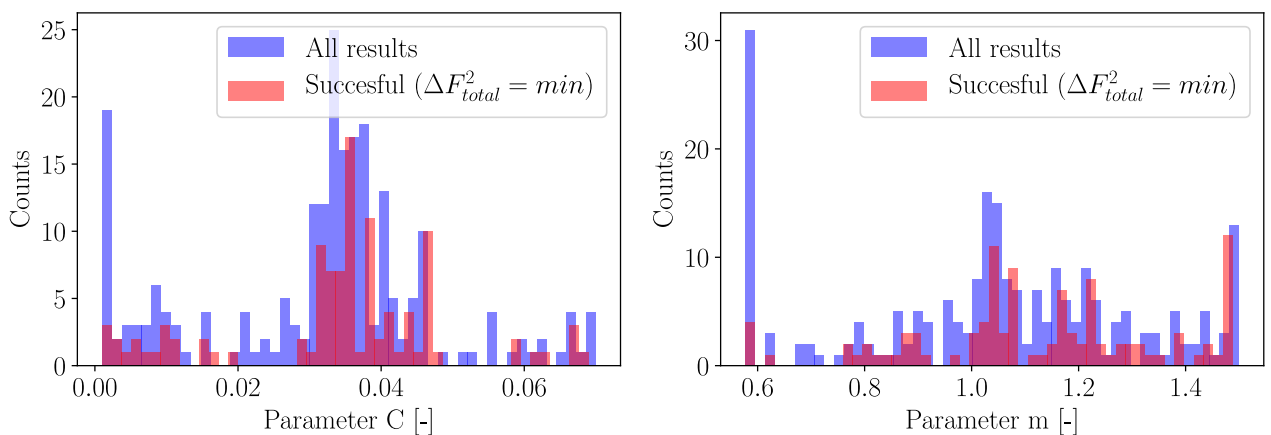


Figure 9.65: Histogram of parameters C (left) and m (right) resulting from the parameter identification of Ck45 experiments with the SIMPLEX-method using OXLEY's force model. Histograms in blue are the resulting coefficients from all identifications while histograms in red show the parameters for successful optimizations only.

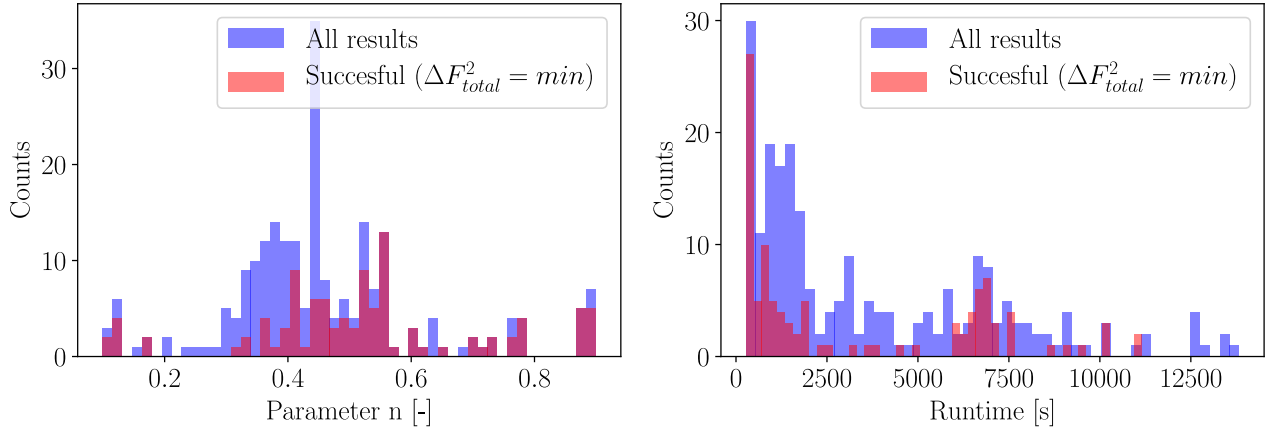


Figure 9.66: Histogram of parameters n (left) and runtimes (right) resulting from the parameter identification of Ck45 experiments with the SIMPLEX-method using OXLEY's force model. Histograms in blue are the resulting coefficients from all identifications while histograms in red show the parameters from successful optimizations only.

9.5.3 Identification with Several Experiments Simultaneously

Results for both materials, Ck45 and Ti6Al4V, show for each of the five constitutive model constants large possible parameter ranges. For this reason the parameter identification is repeated where instead of using a single cutting experiment, several cutting experiments are used simultaneously in an attempt to find a constitutive model parameter set that is optimal to all of the n selected experiments. This is realized by computing the total sum of the squared force errors:

$$F_{total}^2 = \sum_{i=1}^n \Delta F_{total,i}^2 = \sum_{i=1}^n \Delta F_{c,i}^2 + \Delta F_{f,i}^2 \quad (9.17)$$

which is the objective function to be minimized in the optimization procedure. The updated structogram of the inverse parameter identification is provided with figure 9.67. Again, the SIMPLEX-method is used here with a maximum number of iterations $n_{calls} = 500$.

9.5.3.1 Ti6Al4V

For the parameter identification $n = 8$ cutting experiments were selected with cut speeds between $v_c = 20 \dots 500 \text{ m/min}$ and feeds of $f = 0.03 \dots 0.15 \text{ mm}$. These are given in table 9.29.

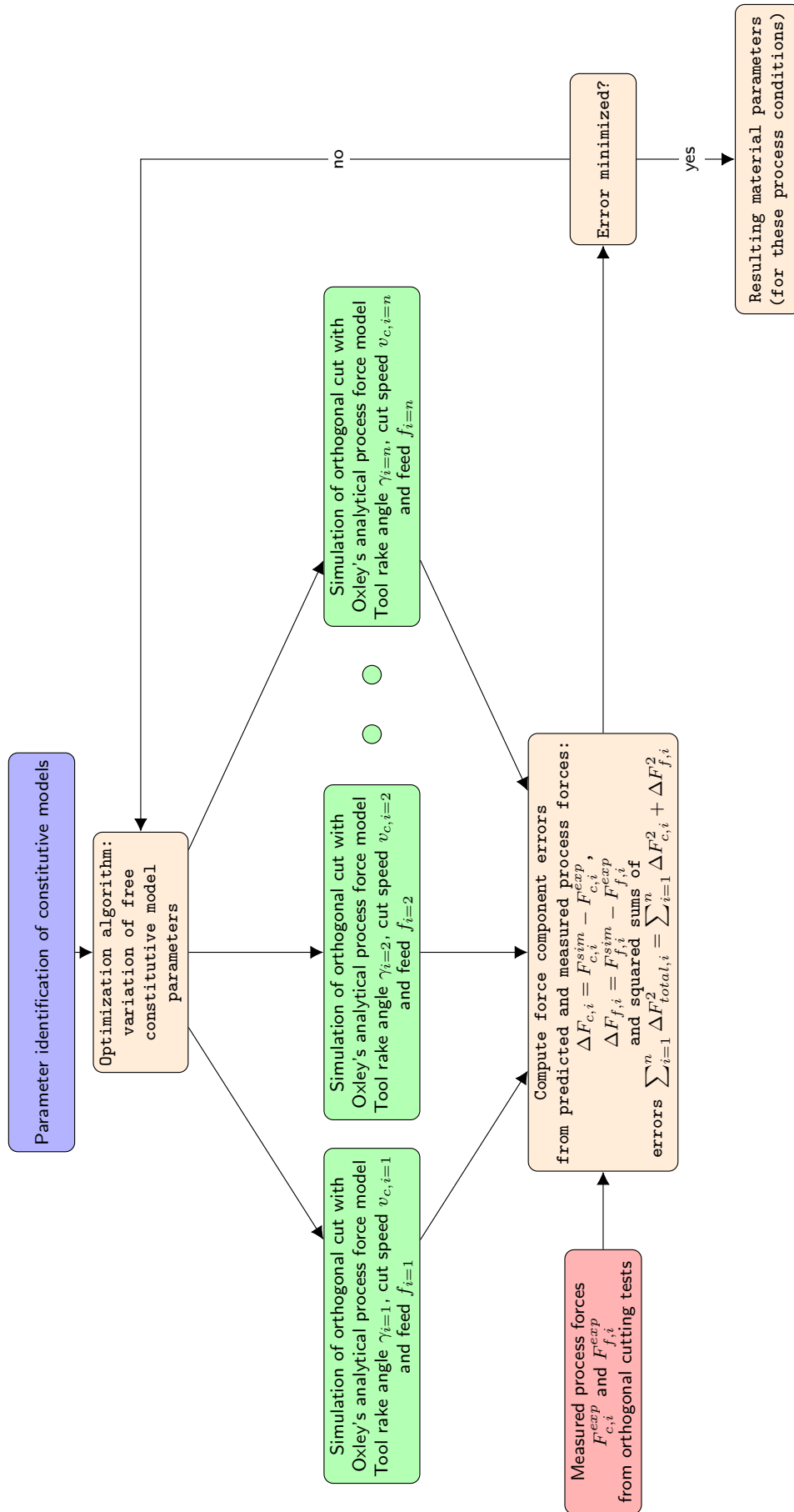


Figure 9.67: Structogram of the simultaneous parameter identification with Oxley's process force model

Experiment	V0375	V0429	V0433	V0448	V0478	V0484	V0508	V0519
$v_{c,i}$ [m/min]	19.9	162.4	162.4	79.9	500.0	40.0	150.0	150.0
f_i [mm]	0.06	0.08	0.12	0.10	0.02	0.15	0.06	0.03
$F_{c,i}$ [N]	150.9	171.5	222.6	213.0	65.6	286.8	139.8	85.4
$F_{f,i}$ [N]	134.9	137.6	150.6	148.4	98.7	173.3	130.6	105.7

Table 9.29: Ti6Al4V- cutting experiments used for simultaneous inverse parameter identification with OXLEY’s force model

The simulation of the parameter identification was 2 hours and resulted in a total squared error of $F_{total}^2 = 59932N^2$ and the 5 JC-parameters given in table 9.30. Compared to the JC-parameter fitted to tensile test results (table 9.11), the parameter A (static yield stress) is about 25% lower here, while parameter B is 40% lower and the strain hardening exponent n is similar.

A [MPa]	B [MPa]	C [-]	m [-]	[n]
671	558	0.0377	0.7429	0.3562

Table 9.30: Ti6Al4V: inversely identified JC-parameter with OXLEY’s force model using several cutting experiments simultaneously.

9.5.3.2 Ck45

For the parameter identification $n = 9$ cutting experiments were selected with cut speeds between $v_c = 10...250m/min$ and feeds of $f = 0.01...0.2mm$. These experiments are given in table 9.31.

Experiment	V0124	V0126	V0149	V0177	V0184	V0236	V0253	V0256	V0267
$v_{c,i}$ [m/min]	30.0	30.0	150.0	10.0	10.0	250.1	50.0	50.0	250.0
f_i [mm]	0.10	0.20	0.02	0.02	0.15	0.10	0.01	0.08	0.12
$F_{c,i}$ [N]	253.2	488.6	68.2	81.9	414.3	304.0	38.0	210.5	335.9
$F_{f,i}$ [N]	144.5	289.1	51.6	49.3	233.3	256.9	24.2	128.9	265.3

Table 9.31: Ck45- cutting experiments used for simultaneous inverse parameter identification with OXLEY’s force model

The simulation of the parameter identification was 2 hours and resulted in a total squared error of $F_{total}^2 = 167718N^2$ and the 5 JC-parameters given in table 9.32. Interestingly the parameters A (static yield stress) and B are similar to data from the tensile test fit of Ck45 in table 9.13. On the other hand parameter n is lower by almost one magnitude when compared to the JC-parameter fit to the tensile test, see table 9.13.

A [MPa]	B [MPa]	C [-]	m [-]	[n]
396	722	0.07	0.7467	0.0452

Table 9.32: Ck45: inversely identified JC-parameter with OXLEY’s force model using several cutting experiments simultaneously.

9.5.4 *Results Discussion and Conclusion*

Results for both materials, Ck45 and Ti6Al4V, show for each of the five constitutive model constants large possible parameter ranges when running the optimization for each cutting experiment separately. Using several cutting experiments simultaneously in the optimization loop results in JC-parameters that are partially similar to tensile test results for the static part. The results however do not allow for a down-selection / reduction of the possible parameter space for the inverse identification with the SPH. Possibly the inclusion of chip thicknesses from the experiments or chip temperatures into the objective function could help to improve the results.

9.6 IDENTIFICATION OF MATERIAL PARAMETERS USING A SPH CUTTING SIMULATION

From the cutting experiments conducted for each material an experiment with high cutting speed v_c was used to drive an inverse parameter identification to estimate material parameters for the JC flow stress model. The structogram of the inverse identification is a modification of figure 9.60, where now the full cutter geometry is considered with clearance angle and cutting edge radii. It is provided with figure 9.68.

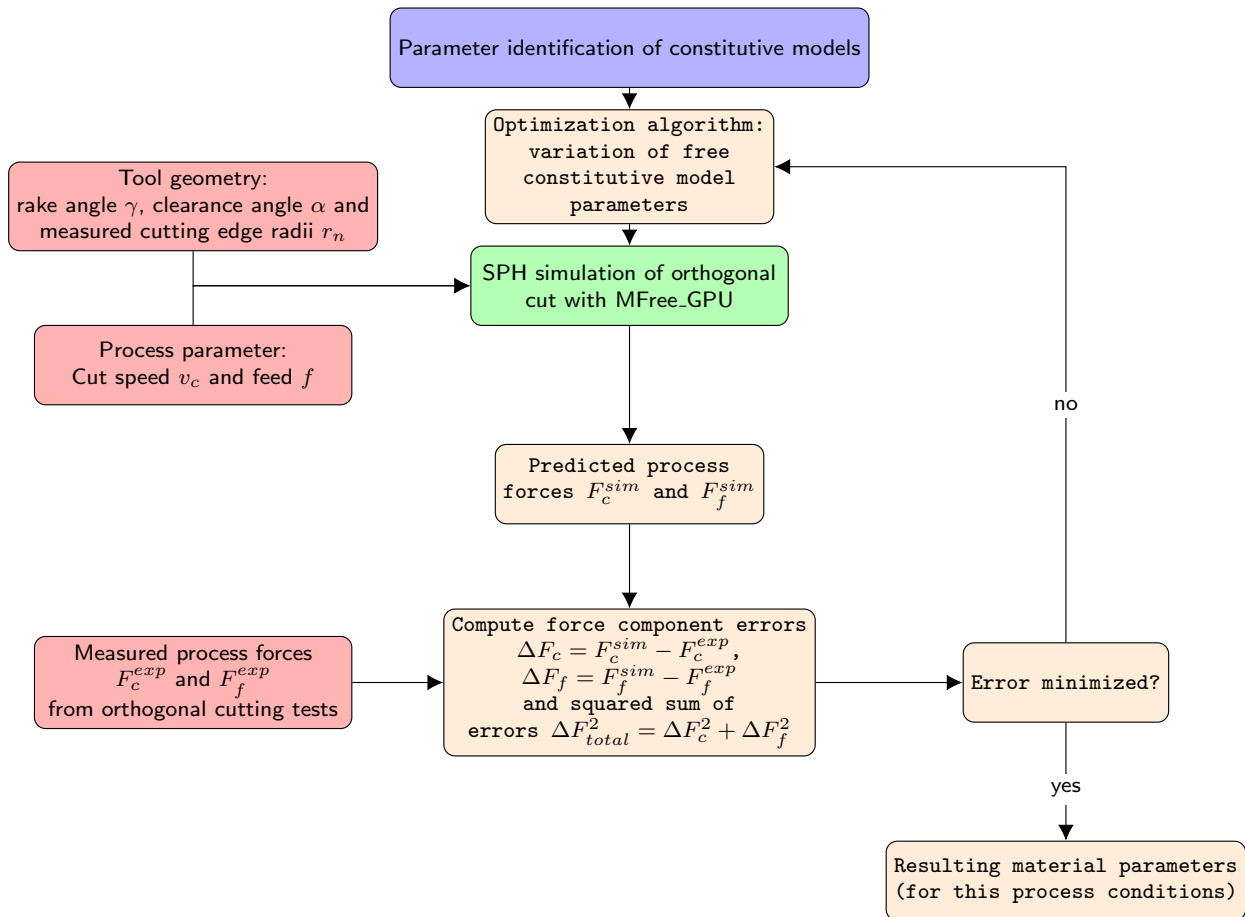


Figure 9.68: Structogram of the parameter identification with MFREE_IWF

The numerical model for the orthogonal cutting simulation is based on the 2D plane strain assumption which can be developed from the real 3D cutting experiment (figures 9.1 and 9.36) when the diameter of the cylinder to cut is becoming large. This is shown in figure 9.69 where on the left side a 3D visualization of the cutting experiment is shown together with the cutting plane (yellow color) in which approximately orthogonal cutting conditions prevail. On the right side the setup is displayed from the back side from which the numerical model used for the inverse parameter identification is constructed, see figure 9.70. The workpiece has fixed boundary conditions at the left, lower and right side. The model dimension in y-direction is automatically adopted with the feed and uses in this direction a discretization

with $n_y = 30$ particles, which guarantees always 10 particles in the uncut chip thickness. The number of particles in x-direction changes with the selected feed $n_x = \frac{l}{3f} \cdot n_y$. The cutter is modelled as a rigid with a rake angle of $\gamma = 0^\circ$ and a clearance angle of $\alpha = 7^\circ$, see chapter 9.3.1. The cutting edge radii r_n is adopted to the respective experiment from tables 11.1 and 11.2.

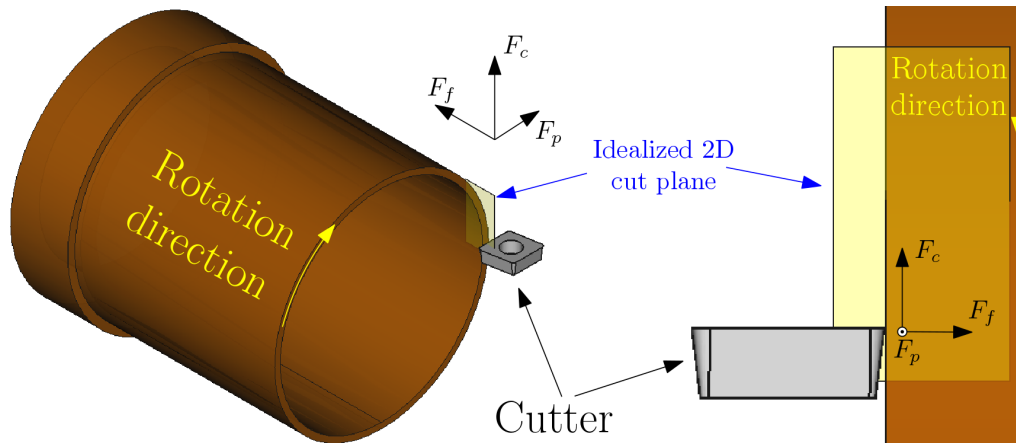


Figure 9.69: Development of a 2D plane strain orthogonal cutting model from a cylindric cutting test setup. On the left side a 3D visualization of the cutting experiment is shown together with the cutting plane (yellow color) where approximately orthogonal cutting conditions prevail. On the right side the same setup is displayed from the back side from which the numerical model used for the inverse parameter identification is constructed.

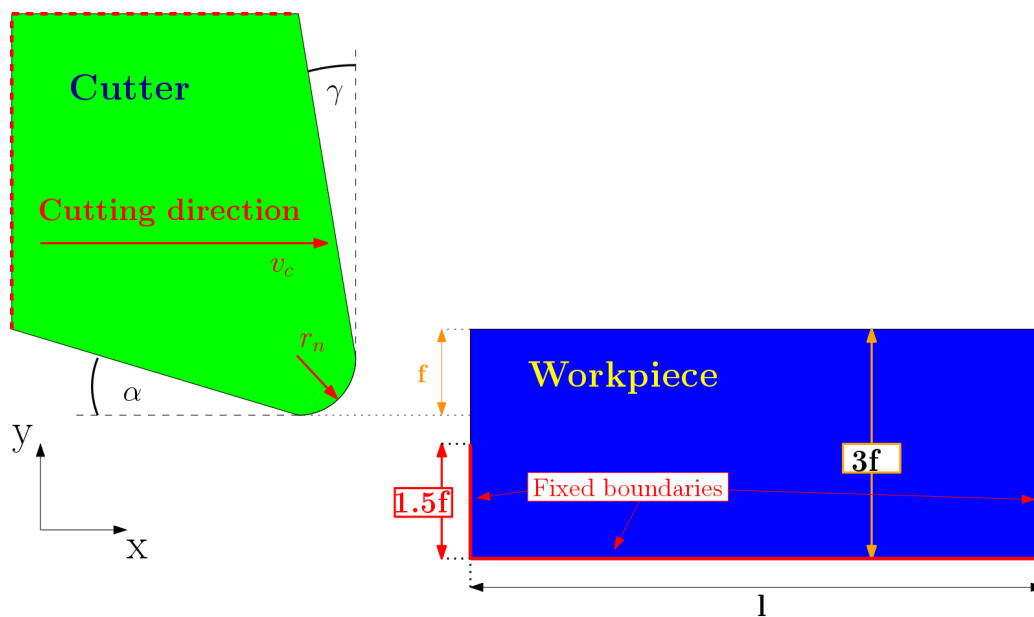


Figure 9.70: Numerical model of the orthogonal cut within MFREE_IWF for the inverse parameter identification.

9.6.1 Inverse Parameter Identification for Ti6Al4V

For the inverse identification of the constitutive model constants for the JC-CLASSIC-model the cutting test V0060 has been selected from table 11.1 with a feed of $f = 0.1\text{mm}$ and a very high cut speed of $v_c = 381.3\text{m/min}$. This experiment was chosen although it was short, but the standard deviations of the process forces indicate a stable signal. The high cut speed is attractive for the explicit `MFREE_IWF`-solver since the cut speed scales with the simulation time and enables very fast iteration loops - up to 400 per day. The cutting edge radii of this experiment was determined with $r_n = 33\mu\text{m}$ and the friction coefficient is assumed to be $\mu_{fric} = 0.35$ based on [213]. Adiabatic heating with a Taylor-Quinney coefficient of $\eta_{TQ} = 0.90$ is considered and the heat conduction is considered only in the workpiece. Frictional heating is not considered. The reference plastic strain rate was set to $\dot{\epsilon}_{pl}^0 = 1.0/\text{s}$. Physical constants according to table 9.33 were used.

Young's modulus E [GPa]	Density $\rho[\frac{\text{kg}}{\text{m}^3}]$	Poisson ratio [-]	Thermal conductivity $\lambda[\frac{\text{W}}{\text{mK}}]$	Specific heat $c_p[\frac{\text{J}}{\text{kgK}}]$
110	4430	0.35	6.8	526

Table 9.33: Physical constants used for Ti6Al4V in the parameter identifications.

9.6.1.1 Inverse Parameter Identification with DE-method

The permissible parameter ranges for the optimization are provided with table 9.34. They are based on the constitutive model parameter ranges provided in [61] under consideration of the results from the tensile tests in chapter 9.2.3.1 and the parameter identification with Oxley's force model in chapter 9.5.3.

	A [MPa]	B [MPa]	C [-]	m [-]	n [-]
min	400	300	0.008	0.577	0.12
max	1200	1200	0.05	1.51	1.01

Table 9.34: Permissible parameter range for the DE-optimization.

The cost function for the optimization is the summed square error of the predicted and experimentally measured process forces:

$$\Delta F_c = F_c^{sim} - F_c^{exp} \quad (9.18)$$

$$\Delta F_f = F_f^{sim} - F_f^{exp} \quad (9.19)$$

$$\Delta F_{total}^2 = w_c \cdot \Delta F_c^2 + w_f \cdot \Delta F_f^2 \quad (9.20)$$

with both force errors ΔF_c and ΔF_f in (9.20) being weighted equally with $w_c = w_f = 1.0$. The optimization was run for more than 37'000 iterations on a GPU NVIDIA QUADRO GP100

and the ten best results with lowest ΔF_{total}^2 are given in table 9.35 where positive force errors ΔF_c and ΔF_f indicate that the predicted force is higher than experimentally measured. The lowest summed square error of the process forces $\Delta F_{total}^2 = 56.2N^2$ results in a cut force error of about 3% and a feed force error of about 5%. The development of the process force errors and the summed square error during the optimization iterations is shown in figure 9.71. In the first few thousand iterations a slight decrease in the summed square error ΔF_{total}^2 is visible which is then stagnating and only a few parameter sets lead to $\Delta F_{total}^2 < 100N^2$. Histograms of the parameters evaluated by the DE-optimizer are given in figures 9.72, 9.73 and 9.74. The histograms show for each parameter a clustering around the values which give the lowest summed square errors ΔF_{total}^2 .

If however the focus is on a good prediction of the cutting force, very low errors in F_c of almost 0 are possible, see table 9.36 where the optimization results are sorted for lowest cutting force errors ΔF_c . It differs from the lowest summed square error results (table 9.35) with a lower static yield stress A , a slightly increased strain rate sensitivity C and significantly increased strain hardening exponent n . Contrary, if a low feed force error ΔF_f is targeted one can resort the optimization results for lowest feed force error, see table 9.37. The static yield stress A becomes even lower, the strain hardening factor B becomes drastically higher, the strain rate sensitivity C increases further and the strain hardening exponent n is in between the results for lowest error in ΔF_{total}^2 and ΔF_c .

Ranking	A [MPa]	B [MPa]	C [-]	m [-]	n [-]	ΔF_{total}^2 [N^2]	ΔF_c [N]	ΔF_f [N]
10	952.5	311.0	0.02015	0.5881	0.1835	104.40153	8.47227	5.71158
9	863.5	310.3	0.03492	0.5907	0.158	104.01427	7.73899	6.64247
8	887.5	313.7	0.02301	0.5913	0.1648	103.09502	4.90528	8.89006
7	952.7	347.8	0.01512	0.5847	0.1234	102.94207	3.65818	9.4636
6	971.2	312.4	0.02197	0.5823	0.1977	92.29864	6.30019	7.25302
5	949.1	345.3	0.01614	0.5834	0.1531	90.79748	3.57632	8.83218
4	816.5	304.0	0.02961	0.5847	0.1234	87.7417	0.0577	9.36688
3	778.2	351.5	0.03556	0.5872	0.1369	80.29325	4.08018	7.97781
2	906.1	323.8	0.0223	0.6048	0.1417	57.57823	4.06974	6.40433
1	852.1	338.9	0.02754	0.5961	0.1483	56.18071	5.31721	5.2828

Table 9.35: Inversely identified JC-parameter for Ti6Al4V with DE-method sorted for minimum ΔF_{total}^2 .

Ranking	A [MPa]	B [MPa]	C [-]	m [-]	n [-]	$\Delta F_{total}^2 [N^2]$	$\Delta F_c [N]$	$\Delta F_f [N]$
10	897.9	356.7	0.0193	0.5873	0.1677	1291.18376	-0.00532	35.93305
9	931.6	374.2	0.00915	0.5976	0.5021	827.48616	0.00376	28.76606
8	812.8	318.8	0.02633	0.583	0.133	850.3156	0.00291	29.16017
7	863.3	340.1	0.02831	0.5966	0.1545	1019.99345	0.00225	31.93734
6	830.9	340.2	0.02602	0.6007	0.1625	426.55488	-0.00172	20.6532
5	871.0	325.8	0.02663	0.5948	0.1602	1244.31108	-0.0015	35.27479
4	811.2	303.4	0.03202	0.5927	0.1612	348.04275	0.00075	18.6559
3	728.8	367.9	0.03331	0.6012	0.1477	908.36069	-0.00064	30.13902
2	802.9	367.1	0.02256	0.6017	0.1554	304.26632	-0.00025	17.44323
1	763.8	354.3	0.03056	0.5872	0.9036	973.74	8e-05	31.20481

Table 9.36: Inversely identified JC-parameter for Ti6Al4V with DE-method sorted for minimum cut force error ΔF_c .

Ranking	A [MPa]	B [MPa]	C [-]	m [-]	n [-]	$\Delta F_{total}^2 [N^2]$	$\Delta F_c [N]$	$\Delta F_f [N]$
10	886.7	300.6	0.03912	0.6049	0.1428	1024.77926	32.01217	0.02315
9	884.1	340.4	0.04244	0.6636	0.1701	831.41502	28.83426	0.02209
8	820.8	341.0	0.03304	0.8752	0.1253	1530.83821	39.12592	0.0214
7	965.5	300.6	0.0416	0.6046	0.1935	742.10836	27.24166	0.01854
6	853.4	334.8	0.03531	0.5917	0.1294	535.34367	23.13749	-0.01653
5	787.8	339.2	0.03602	1.2172	0.1436	4810.06216	69.35461	0.00758
4	968.9	471.7	0.03162	0.6482	0.2268	1611.34055	40.14151	-0.00542
3	774.6	343.1	0.0417	1.281	0.1316	5720.93779	75.63688	0.00507
2	800.4	375.4	0.04894	0.6151	0.1258	1195.7498	34.57961	0.00506
1	728.3	1156.9	0.04049	0.6095	0.4327	7042.96303	83.92236	-0.00356

Table 9.37: Inversely identified JC-parameter for Ti6Al4V with DE-method sorted for minimum feed force error ΔF_f .

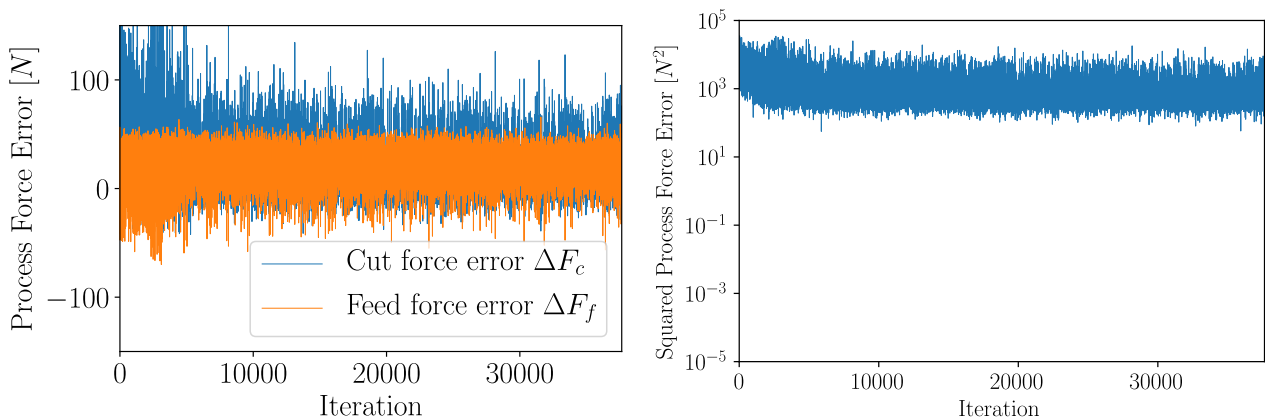


Figure 9.71: Evolution of process force errors (left) and summed square errors (right) during the optimization with the DE-method

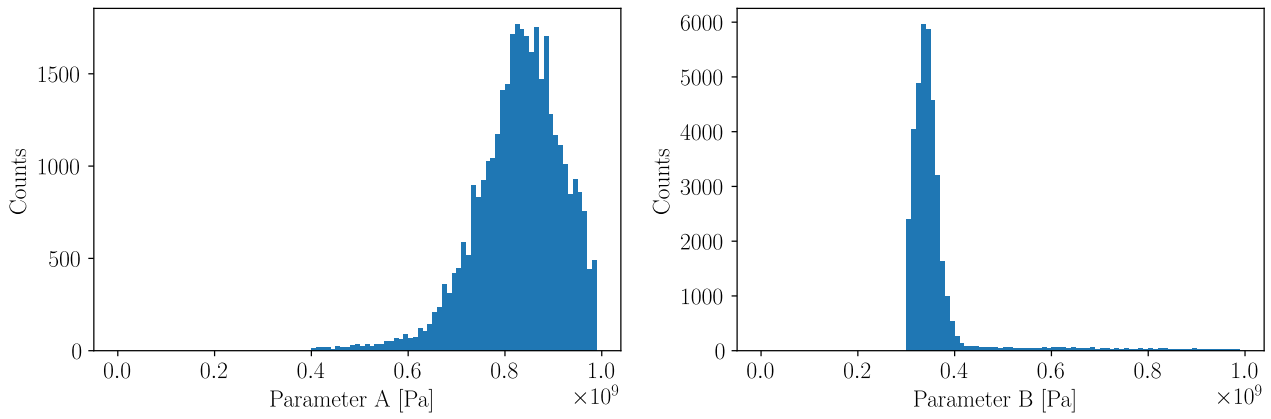


Figure 9.72: Histogram of parameters A (left) and B (right) considered during the optimization with the DE-method.

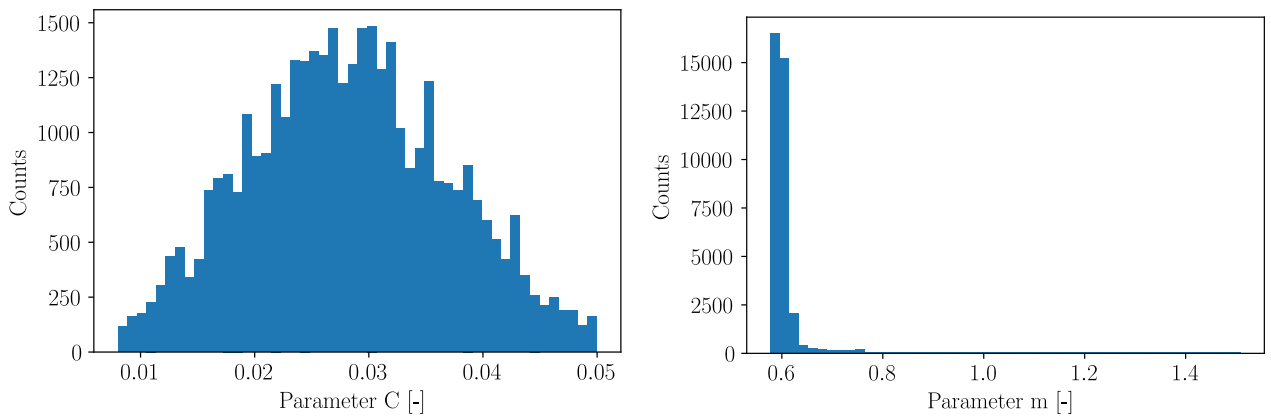


Figure 9.73: Histogram of parameters C (left) and m (right) considered during the optimization with the DE-method.

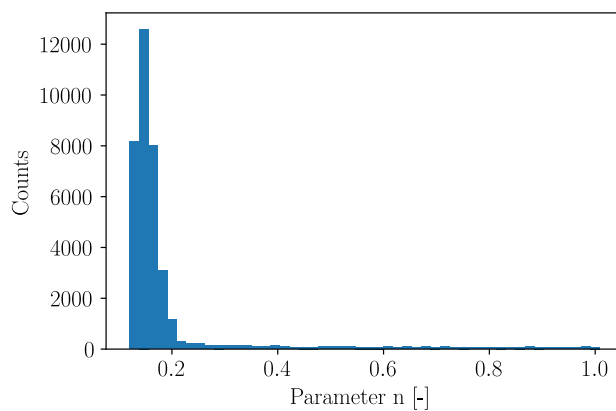


Figure 9.74: Histogram of parameter n considered during the optimization with the DE-method.

9.6.1.2 Inverse Parameter Identification with BAYES-method

The maximum number of iterations was set to $n_{calls} = 5000$ and noise was set to a small value of 10^{-5} since the numerical simulation gives the same results when repeated with the same set of parameters - in contradiction to experiments where a scatter can occur. The permissible parameter ranges in this optimization remained the same as before in the DE-method and are given in table 9.38.

	A [MPa]	B [MPa]	C [-]	m [-]	n [-]
min	400	300	0.008	0.577	0.12
max	1200	1200	0.05	1.51	1.01

Table 9.38: Permissible parameter range for the BAYES-optimization.

The cost function (9.20) is kept unchanged with both force errors ΔF_c and ΔF_f being weighted equally with $w_c = w_f = 1.0$. Again, the cutting test V0060 from table 11.1 has been selected for the inverse identification since it has a very high cut speed $v_c = 500m/min$. The optimization was run for 29 days with almost 3'000 iterations and the ten best results with lowest ΔF_{total}^2 are given in table 9.39 where positive force errors ΔF_c and ΔF_f indicate that the predicted force is higher than experimentally measured. The lowest summed square error of the process forces $\Delta F_{total}^2 = 351.8N^2$ results in a cut force error of about 8% and a feed force error of about 12%. Similar to the 1D-test case in chapter 9.4.2 the process overhead of the BAYES-method is increasing heavily. Since the computing time of one SPH simulation is almost constant in the order of 4-5 minutes, the runtime increase per iteration stems from the overhead of the BAYES-method which is towards the end after almost 3'000 iterations in the order of 20 minutes per iteration, see figure 9.75. The runtime spikes are because the SPH simulations were either run on a GPU NVIDIA TESLA P100 or a GPU NVIDIA QUADRO GP100 depending on the load of the server. It has to be noted that the DE-method performs almost 3 times more iterations (8'300) in the same time. The parameter identification with BAYES shows within the first 100 iterations a distinct reduction of ΔF_{total}^2 but almost no progress beyond which is similar to the inverse parameter identification in section 9.4.2 with BAYES. The development of the process force errors and the summed square error during the optimization iterations is shown in figure 9.76. In the first few thousand iterations a slight decrease in the summed square error ΔF_{total}^2 is visible which is then stagnating at around $\Delta F_{total}^2 \approx 1000N^2$ with only a few parameter sets leading to lower summed square errors. The bandwidth of the summed square errors is apparently lower compared to the DE-method from figure 9.76. Histograms of the parameters evaluated by the BAYES-optimization are given in figures 9.77, 9.78 and 9.79. Contrary to the histograms of the DE-method, no clustering of values is visible here except for parameter m.

Ranking	A [MPa]	B [MPa]	C [-]	m [-]	n [-]	ΔF_{total}^2 [N^2]	ΔF_c [N]	ΔF_f [N]
10	719.8	389.1	0.03796	0.6528	0.288	504.79653	16.51241	15.23603
9	477.6	434.4	0.02848	0.9523	0.143	504.13061	9.05484	20.54606
8	522.8	358.5	0.04906	0.7432	0.253	489.93979	7.93913	20.6618
7	550.2	606.8	0.03353	0.7162	0.1915	487.03043	16.35288	14.81937
6	802.6	367.2	0.01598	0.9184	0.1683	473.79723	16.09083	14.65887
5	630.5	369.3	0.04019	0.6278	0.3102	461.80828	3.82117	21.14727
4	407.8	529.2	0.0433	0.7297	0.168	449.22267	10.53	18.39407
3	772.9	409.0	0.04168	0.6078	0.3331	416.75913	15.03971	13.80457
2	407.8	529.3	0.0433	0.7297	0.1678	393.27756	8.61923	17.86019
1	799.9	400.1	0.01246	0.7585	0.217	351.82085	13.10105	13.42324

Table 9.39: Inversely identified JC-parameter for Ti6Al4V with BAYES-method sorted for minimum ΔF_{total}^2 .

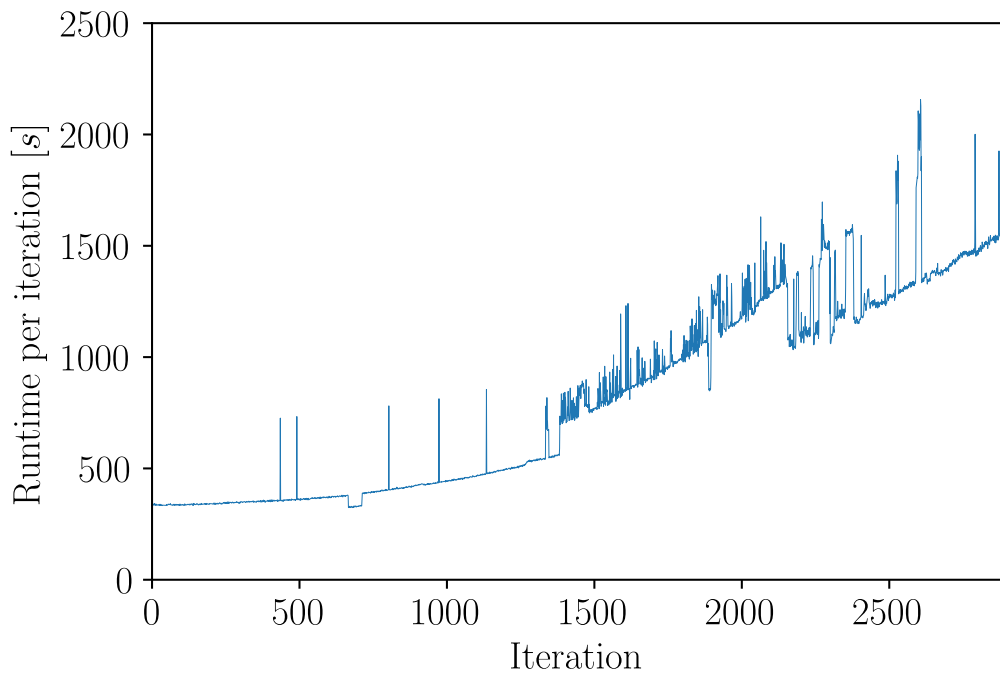


Figure 9.75: Runtime evolution during the optimization with the BAYES-method.

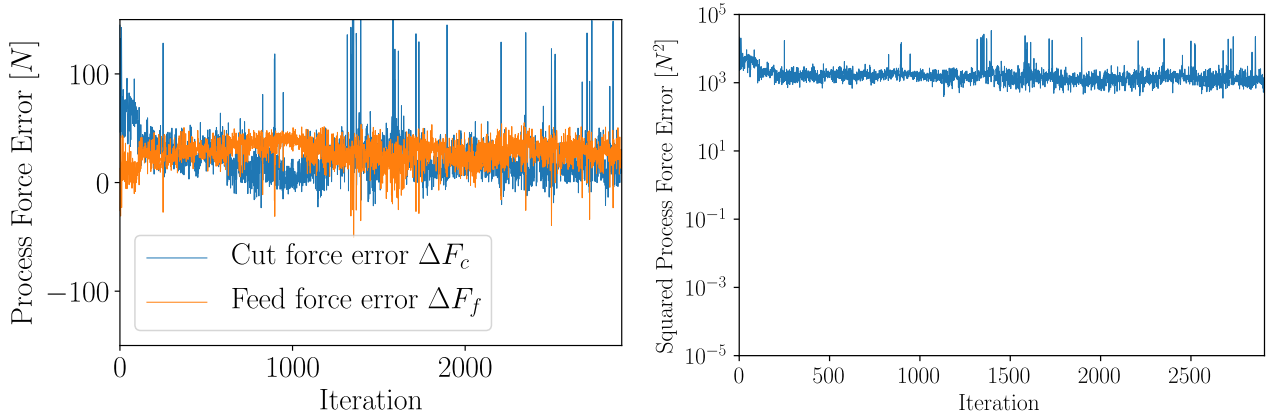


Figure 9.76: Evolution of process force errors (left) and summed square error (right) during the optimization with the BAYES-method

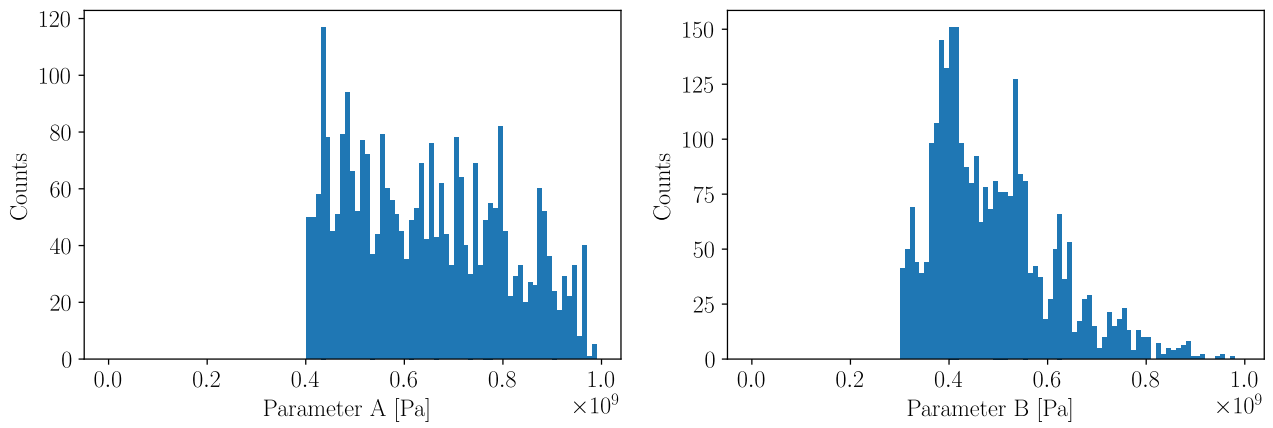


Figure 9.77: Histogram of parameters A (left) and B (right) considered during the optimization with the BAYES-method.

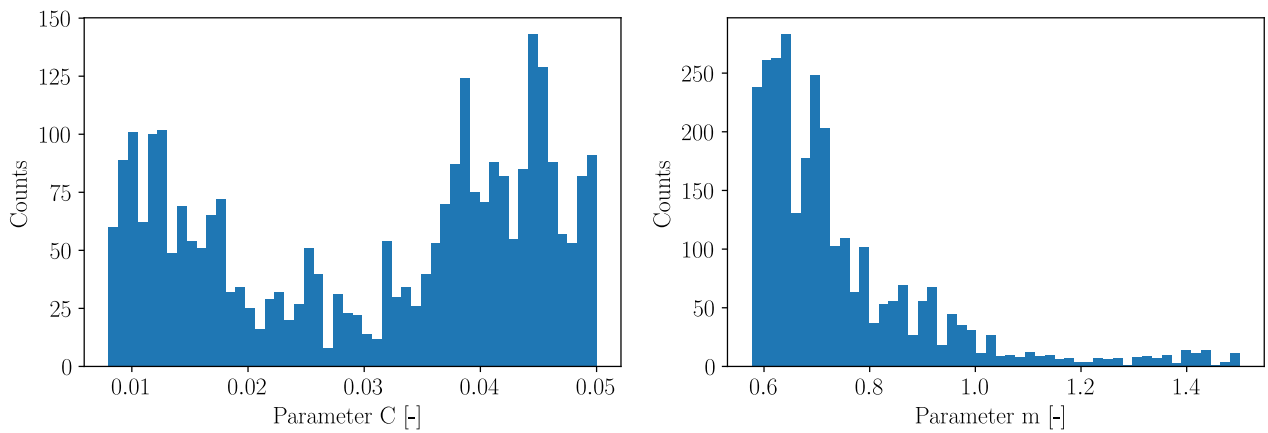


Figure 9.78: Histogram of parameters C (left) and m (right) considered during the optimization with the BAYES-method.

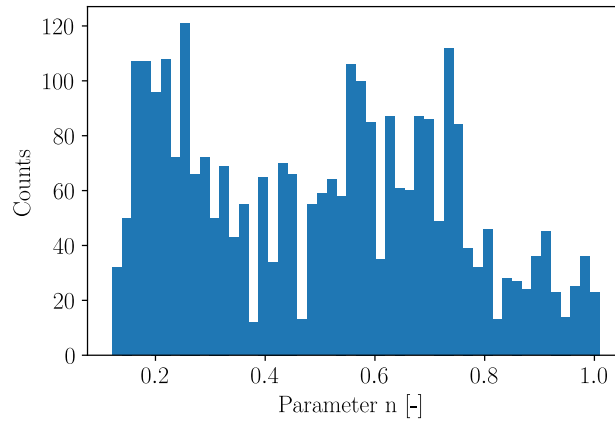


Figure 9.79: Histogram of parameter n considered during the optimization with the BAYES-method.

9.6.1.3 Inverse Parameter Identification with SIMPLEX-method

The optimization is here performed with the SIMPLEX-method. It is based on the same cutting experiment V0060 and uses start values for the initial simplexes based on the tensile test results in chapter 9.2.1. The 6 simplexes in the parameter space for A , B , C , m and n are given in table 9.40:

Initial Simplex	A [MPa]	B [MPa]	C [-]	m [-]	[n]
1	892	549	0.02754	0.6	0.58
2	942	599	0.03754	0.6	0.58
3	842	599	0.02754	0.7	0.58
4	892	499	0.02754	0.5	0.58
5	942	549	0.03754	0.6	0.68
6	892	549	0.04754	0.6	0.68

Table 9.40: Initial simplexes for the SIMPLEX-optimization.

The cost function for the optimization (9.20) is used with both force errors ΔF_c and ΔF_f being weighted equally with $w_c = w_f = 1.0$. A total of 549 iterations was run within 4 days and the 10 best results in terms of minimum squared force errors ΔF_{total}^2 are provided in table 9.41. The best results are all the same in terms of constitutive model parameters as well as force errors indicating that the SIMPLEX-method is trapped into a local minimum. The minimum error in ΔF_{total}^2 is more than four times higher than that achieved with the DE-method, but about 30% lower than with the BAYES-method.

MATERIAL PARAMETER DETERMINATION

Ranking	A [MPa]	B [MPa]	C [-]	m [-]	n [-]	ΔF_{total}^2 [N ²]	ΔF_c [N]	ΔF_f [N]
10	891.6	500.3	0.02769	0.5009	0.579	256.2671	8.40749	13.62282
9	891.6	500.3	0.02769	0.5009	0.579	256.2671	8.40749	13.62282
8	891.6	500.3	0.02769	0.5009	0.579	256.2671	8.40749	13.62282
7	891.6	500.3	0.02769	0.5009	0.579	256.2671	8.40749	13.62282
6	891.6	500.3	0.02769	0.5009	0.579	256.2671	8.40749	13.62282
5	891.6	500.3	0.02769	0.5009	0.579	256.2671	8.40749	13.62282
4	891.6	500.3	0.02769	0.5009	0.579	256.2671	8.40749	13.62282
3	891.6	500.3	0.02769	0.5009	0.579	256.2671	8.40749	13.62282
2	891.6	500.3	0.02769	0.5009	0.579	256.2671	8.40749	13.62282
1	891.6	500.3	0.02769	0.5009	0.579	256.2671	8.40749	13.62282

Table 9.41: Inversely identified JC-parameter for Ti6Al4V with SIMPLEX-method sorted for minimum ΔF_{total}^2 .

9.6.2 Inverse Parameter Identification for Ck45

For the inverse identification of the constitutive model constants for the JC-CLASSIC-model the cutting test V0300 from table 11.2 has been selected since it has a very high cut speed $v_c = 500m/min$. This is attractive for the explicit MFREE_IWF-solver since the cut speed scales with the simulation time and thus enables very fast iteration loops - up to 400 per day. The feed in this experiment is $f = 0.1mm$. The cutting edge radii of this experiment was determined with $r_n = 42\mu m$ and the friction coefficient is assumed with $\mu_{fric} = 0.35$. Adiabatic heating with a Taylor-Quinney coefficient of $\eta_{TQ} = 0.90$ is considered and the heat conduction is considered only in the workpiece. Frictional heating is not considered. The reference plastic strain rate was set to $\dot{\epsilon}_{pl}^0 = 1.0/s$. Physical constants according to table 9.42 were used.

Young's modulus E [GPa]	Density $\rho[\frac{kg}{m^3}]$	Poisson ratio [-]	Thermal conductivity $\lambda[\frac{W}{mK}]$	Specific heat $c_p[\frac{J}{kgK}]$
200	7870	0.29	42	470

Table 9.42: Physical constants used for Ck45 in the parameter identifications.

9.6.2.1 Inverse Parameter Identification with DE-method

The permissible parameter ranges for the optimization are provided with table 9.43. They are based on the constitutive model parameters provided in [101], results from the tensile tests in chapter 9.2.3.2 and the parameter identification with Oxley's force model in chapter 9.5.3.

	A [MPa]	B [MPa]	C [-]	m [-]	n [-]
min	200	300	0.008	0.577	0.02
max	700	800	0.07	1.0	0.3

Table 9.43: Permissible parameter range for the DE-method.

The cost function for the optimization is the summed square error from the difference of the predicted and experimentally measured process forces (9.20) with both force errors ΔF_c and ΔF_f being weighted equally with $w_c = w_f = 1.0$. The optimization was run for more than 40'000 iterations on a GPU NVIDIA TESLA P100 and the ten best results with lowest ΔF_{total}^2 are given in table 9.44 where positive force errors ΔF_c and ΔF_f indicate that the predicted force is higher than experimentally measured. The lowest summed square error of the process forces $\Delta F_{total}^2 = 0.006N^2$ results in a cut force error of about 0.02% and a feed force error of about 0.03%. The development of the process force errors and the summed square error during the optimization iterations is shown in figure 9.80. During the iterations the feed force tend to be overpredicted, while the cutting force is mainly underpredicted. In the first few thousand iterations a slight decrease in the summed square error ΔF_{total}^2 is visible which is then stagnating with a few parameter sets leading to $\Delta F_{total}^2 < 0.1N^2$. Histograms of the

parameters evaluated by the DE-optimizer are given in figures 9.81, 9.82 and 9.83. Similar to the DE-optimization for Ti6Al4V the histograms show for each parameter a clustering around the values which give the lowest summed square errors ΔF_{total}^2 .

Ranking	A [MPa]	B [MPa]	C [-]	m [-]	n [-]	ΔF_{total}^2 [N^2]	ΔF_c [N]	ΔF_f [N]
10	536.4	782.9	0.0571	0.6767	0.0521	0.05609	0.22255	0.08103
9	554.2	794.3	0.05826	0.6541	0.0451	0.05148	-0.20159	0.10412
8	636.4	679.6	0.06284	0.6675	0.0451	0.04808	-0.15828	0.15175
7	603.2	720.1	0.06017	0.697	0.0685	0.03959	0.19489	0.04012
6	533.6	749.2	0.05106	0.7643	0.021	0.03629	0.17667	0.07123
5	670.0	748.2	0.06076	0.612	0.1198	0.03324	0.05695	0.1732
4	596.8	728.4	0.06159	0.667	0.045	0.02186	0.13755	0.05422
3	602.8	684.7	0.06327	0.7164	0.0685	0.00979	0.02012	-0.0969
2	531.3	764.5	0.06051	0.7088	0.0501	0.00652	0.07832	0.0197
1	569.0	736.6	0.06005	0.7147	0.0685	0.00605	-0.05796	-0.05185

Table 9.44: Inversely identified JC-parameter for Ck45 with DE-method sorted for minimum ΔF_{total}^2 .

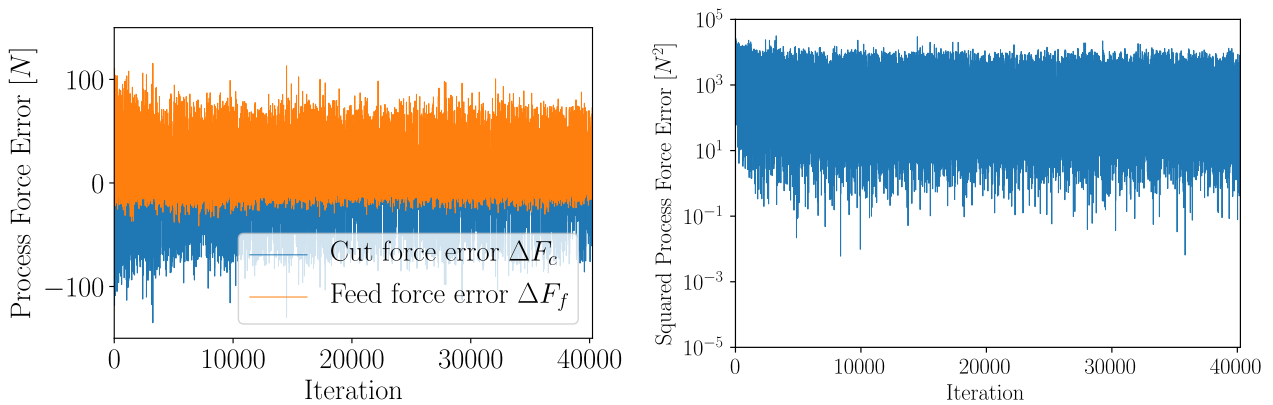


Figure 9.80: Evolution of process force errors (left) and summed square error (right) during the optimization with the DE-method.

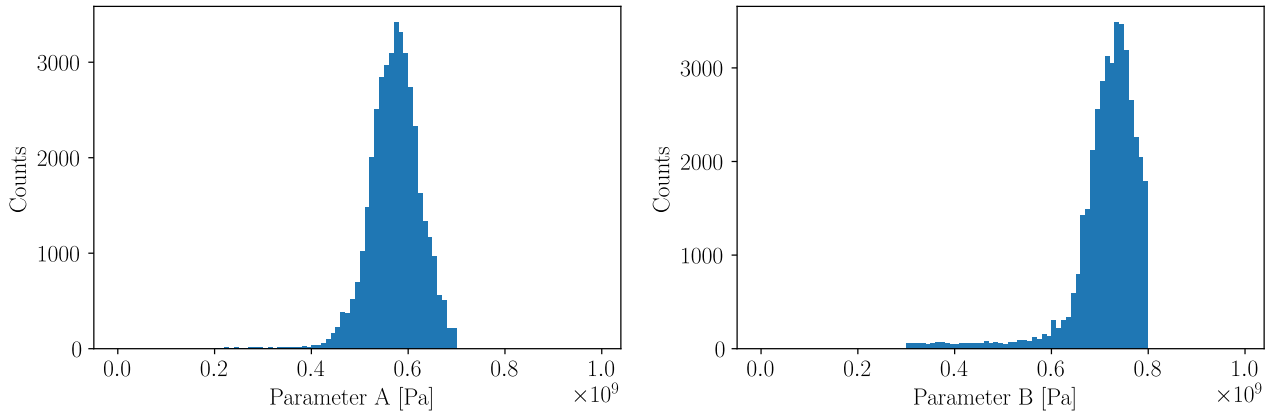


Figure 9.81: Histogram of parameters A (left) and B (right) considered during the optimization with the DE-method.

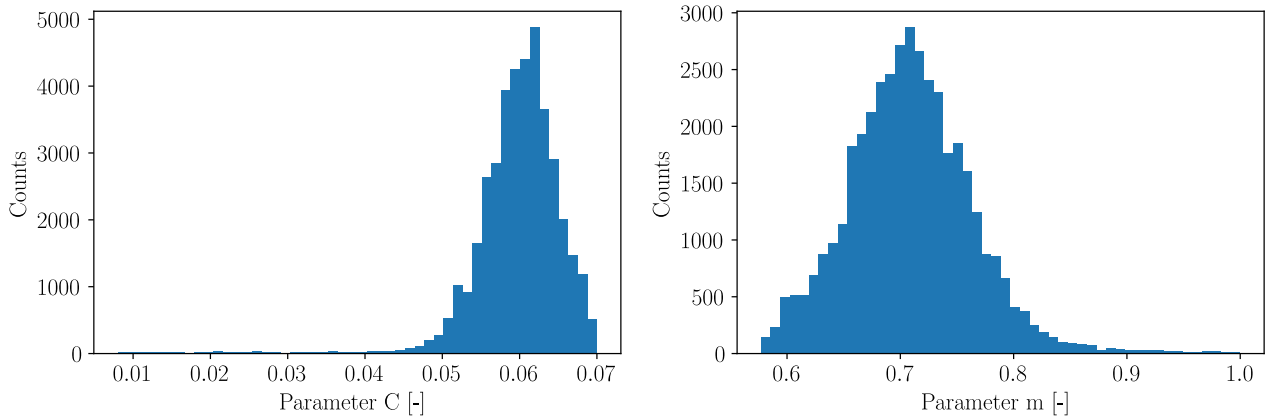


Figure 9.82: Histogram of parameters C (left) and m (right) considered during the optimization with the DE-method.

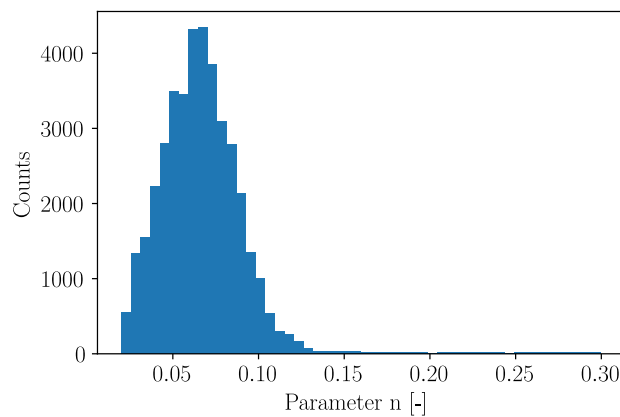


Figure 9.83: Histogram of parameter n considered during the optimization with the DE-method.

9.6.2.2 Inverse Parameter Identification with SIMPLEX-method

The optimization is here performed with the SIMPLEX-method. It is based on the same cutting experiment V0300 and uses start values for the initial simplexes based on the tensile test results in chapter 9.2.1. The 6 simplexes in the parameter space for A, B, C, m and n are given in table 9.45:

Initial Simplex	A [MPa]	B [MPa]	C [-]	m [-]	[n]
1	400	200	0.008	0.6	0.4
2	450	250	0.018	0.6	0.4
3	350	250	0.008	0.7	0.4
4	400	150	0.008	0.5	0.4
5	450	200	0.018	0.6	0.5
6	400	200	0.028	0.6	0.5

Table 9.45: Initial simplexes for the SIMPLEX-optimization.

A total of 1000 iterations was run within 6 days and the 10 best results in terms of minimum squared force errors ΔF_{total}^2 are provided in table 9.46.

Ranking	A [MPa]	B [MPa]	C [-]	m [-]	n [-]	ΔF_{total}^2 [N ²]	ΔF_c [N]	ΔF_f [N]
10	497.5074395093	457.7195338459	0.058569357741	0.943220289331	0.594913739302	1464.3971	18.86534	33.29408
9	497.507439247	457.7195281444	0.058569358678	0.943220287709	0.594913753808	1463.49908	18.76324	33.33827
8	497.5074395096	457.7195338489	0.058569357741	0.94322028933	0.594913739293	1463.13533	19.10258	33.1395
7	497.5074395096	457.7195338503	0.05856935774	0.943220289329	0.594913739289	1461.65111	19.04779	33.14864
6	497.5074395096	457.7195338503	0.05856935774	0.943220289329	0.594913739289	1459.44188	19.1956	33.02985
5	497.507439509	457.7195338439	0.058569357739	0.943220289331	0.5949137393	1458.64547	19.103	33.07145
4	497.5074395014	457.7195335443	0.058569357966	0.943220288723	0.59491374021	1458.2366	19.17168	33.02549
3	497.50743951	457.7195338472	0.058569357739	0.943220289332	0.594913739294	1457.84536	18.66255	33.30998
2	497.5074394947	457.7195338094	0.058569357744	0.943220289282	0.594913739323	1454.25568	18.80679	33.17469
1	497.5074395096	457.7195338503	0.05856935774	0.943220289329	0.594913739289	1453.7111	18.96408	33.0768

Table 9.46: Inversely identified JC-parameter for Ck45 with SIMPLEX-method sorted for minimum ΔF_{total}^2 .

The best results are already centred within a very small parameter range, they differ only in the last digits which are not displayed in the table. The minimum error is far higher than that achieved with the DE-method and the SIMPLEX seems to be trapped in a local minimum.

9.7 IDENTIFICATION OF MATERIAL PARAMETERS INCLUDING THE FRICTION COEFFICIENT

In the preceding section the friction coefficient was assumed to be constant with $\mu_{fric} = 0.35$ during the parameter identification of the constitutive model constants for Ti6Al4V and Ck45. This assumption is often made in machining simulations, but it is known from literature [260] that the magnitude of the friction coefficient can vary depending on the process parameters like the cutting speed and the cutting edge radius. The grain structure of the experimental chips reveal that there must be some sort of sticking condition on the rake face, see for example in figure 9.54. This indicates either very high friction coefficients, or very high contact pressures, or both. For this reason, in this part the friction coefficient is identified together with the constitutive model constants of the JC-CLASSIC-model which totals in 6 constants to be identified simultaneously.

9.7.1 Identification of the Friction Coefficient Constant

9.7.1.1 Ti6Al4V

Similar to the preceding parameter identification of Ti6Al4V the cutting test V0060 has been selected from table 11.1 with a feed of $f = 0.1mm$ and a very high cut speed of $v_c = 381.3m/min$. The cutting edge radii of this experiment was determined with $r_n = 33\mu m$. Adiabatic heating with a Taylor-Quinney coefficient of $\eta_{TQ} = 0.90$ is considered and the heat conduction is considered only in the workpiece. Frictional heating is not considered. The reference plastic strain rate was set to $\dot{\epsilon}_{pl}^0 = 1.0/s$. Physical constants according to table 9.33 were used. The permissible parameter ranges for the JC-model constants A, B, C, m and n remained unchanged and are provided with table 9.34, the permissible range for the friction coefficient is $\mu_{fric} = 0.1...1.0$. The cost function for the optimization is (9.20) with both force errors ΔF_c and ΔF_f being weighted equally with $w_c = w_f = 1.0$. The DE-method was used. Table 9.47 shows the lowest summed square errors ΔF_{total}^2 of the parameter identification. Interestingly, a more than 5 times lower ΔF_{total}^2 is found when identifying the friction coefficient together with the constitutive model constants for Ti6Al4V. On the other hand, the static yield stress (parameter A) lost its physical meaning and is now about 30% lower than in the tensile test result as well as in the identification without friction coefficient. Compared to the identification with a constant friction coefficient of $\mu_{fric} = 0.35$ the friction coefficient has increased to around $\mu_{fric} = 0.7$. Interestingly, this is in the order of the apparent friction coefficient of $\mu_{fric,app} = \frac{F_f}{F_c} = \frac{115.5N}{157.5N} = 0.73$ for this cutting test.

9.7.1.2 Ck45

The cutting test V0300 from table 11.2 served as a basis for the parameter identification as in the preceding parameter identification of Ck45. This experiment has a feed of $f = 0.1mm$ and a very high cut speed of $v_c = 500m/min$. The cutting edge radii of this experiment

Ranking	A [MPa]	B [MPa]	C [-]	m [-]	n [-]	μ_{fric} [-]	ΔF_{total}^2 [N ²]	ΔF_c [N]	ΔF_f [N]
10	651.3	373.9	0.01575	0.6436	0.1549	0.6101	39.46448	2.85532	5.59568
9	632.8	346.1	0.01437	0.6773	0.1593	0.7062	38.87475	5.46468	3.00201
8	633.5	405.4	0.01435	0.607	0.1496	0.5999	38.86439	1.30422	6.09618
7	621.8	371.7	0.01505	0.6023	0.138	0.6853	37.1847	-0.85824	6.03723
6	655.3	318.8	0.02073	0.6547	0.1755	0.6808	34.85521	5.90089	-0.1862
5	683.8	327.8	0.01667	0.6618	0.1417	0.5848	32.99311	5.3087	2.19335
4	711.6	318.3	0.0155	0.5848	0.1561	0.6762	31.14309	3.77397	4.11099
3	672.2	350.2	0.01602	0.6126	0.137	0.6335	24.70144	2.34395	4.38262
2	622.1	331.5	0.01631	0.6834	0.1415	0.7086	15.68025	1.62114	3.61277
1	611.9	357.7	0.01609	0.6239	0.1365	0.7009	10.1903	-1.83991	2.60865

 Table 9.47: Inversely identified JC-parameter and friction coefficient for Ti6Al4V with DE-method sorted for minimum ΔF_{total}^2 .

Ranking	A [MPa]	B [MPa]	C [-]	m [-]	n [-]	μ_{fric} [-]	ΔF_{total}^2 [N ²]	ΔF_c [N]	ΔF_f [N]
10	520.6	559.9	0.06652	0.6881	0.0625	0.5339	0.2402	-0.4743	-0.12346
9	690.6	521.9	0.05676	0.7348	0.1526	0.442	0.22906	0.26529	-0.39835
8	517.9	560.6	0.06179	0.7141	0.0457	0.6507	0.21295	0.39163	0.24408
7	502.0	516.4	0.06725	0.6609	0.079	0.6689	0.16651	-0.39411	0.10577
6	639.9	549.2	0.06287	0.7426	0.0963	0.437	0.15933	-0.39383	0.06499
5	517.5	553.3	0.05738	0.7031	0.0956	0.6716	0.15673	0.25911	-0.29932
4	549.0	687.8	0.06478	0.6565	0.0714	0.4346	0.10707	-0.31454	-0.0902
3	662.1	436.0	0.06101	0.6815	0.1159	0.594	0.10639	-0.28941	-0.15043
2	622.4	576.9	0.04954	0.7024	0.0714	0.559	0.09853	0.0095	-0.31376
1	567.5	592.6	0.06297	0.6742	0.0956	0.5107	0.0068	0.04805	-0.06705

 Table 9.48: Inversely identified JC-parameter and friction coefficient for Ck45 with DE-method sorted for minimum ΔF_{total}^2 .

was determined with $r_n = 42\mu m$. Adiabatic heating with a Taylor-Quinney coefficient of $\eta_{TQ} = 0.90$ is considered and the heat conduction is considered only in the workpiece. Frictional heating is not considered. The reference plastic strain rate was set to $\dot{\epsilon}_{pl}^0 = 1.0/s$. Physical constants according to table 9.42 were used. The permissible parameter ranges for the JC-model constants A, B, C, m and n remained unchanged and are provided with table 9.43, the permissible range for the friction coefficient is $\mu_{fric} = 0.1...1.0$. The cost function for the optimization is (9.20) with both force errors ΔF_c and ΔF_f being weighted equally with $w_c = w_f = 1.0$. The DE-method was used. Table 9.48 shows the lowest summed square errors ΔF_{total}^2 of the parameter identification. The minimum summed square error of the process forces ΔF_{total}^2 is at a comparable level to the inverse identification without friction coefficient. The identified friction coefficient is about 50% higher than in the preceding identification where the friction coefficient was constant $\mu_{fric} = 0.35$. Obviously, this high friction coefficient enforces a stick condition in the contact surface such that plastic flow is initiated in the chip close to the contact face (internal friction). It has to be noted that similar friction coefficients were reported in literature [270].

9.7.2 Identification of a Friction Coefficient Using Shear Stress Limit

It is convenient to limit the maximum friction force F_F^{max} [276] such that the yield limit in shear τ_Y of the mating materials are not exceeded in the contact surface $A_{contact}$:

$$F_F^{max} = m \cdot \tau_Y \cdot A_{contact} = m \cdot \frac{1}{\sqrt{3}} \cdot \sigma_Y \cdot A_{contact} \quad (9.21)$$

with a factor m which is in this investigation set to $m = 1$. Since tool materials are usually characterized with a huge yield limit because plastic deformations must not occur, the maximum flow stress, also shear stress limit (SSL), in (9.21) is that of the workpiece material at the current conditions $\sigma_Y = \sigma_Y(\bar{\epsilon}_{pl}, \dot{\epsilon}_{pl}, T)$:

$$F_F^{max} = m \cdot \frac{1}{\sqrt{3}} \cdot \sigma_Y(\bar{\epsilon}_{pl}, \dot{\epsilon}_{pl}, T) \cdot A_{contact} \quad (9.22)$$

In this formulation the shear stress has automatically a dependency on the strain, strain rate and temperature. Alternatively, other friction laws exist, e.g. in [5] with two parameters:

$$\mu(T) = \mu_0 \cdot \left(1 - \left(\frac{T - T_{ref}}{T_f - T_{red}} \right)^q \right) \quad (9.23)$$

where μ_0 is the friction coefficient and q controlling the temperature dependency. This is however not used here as the temperature dependency with (9.22) is already imposed by the current yield stress $\sigma_Y(\bar{\epsilon}_{pl}, \dot{\epsilon}_{pl}, T)$.

9.7.2.1 Ti6Al4V

The model from chapter 9.7.1.1 was reused without changes except that the frictional shear stress was limited to the shear strength of the material at current conditions (9.22). The minimum summed square error ΔF_{total}^2 is comparable to the identification without friction coefficient, but the static yield stress (parameter A) is about 10% lower than in the tensile test result as well as in the identification without friction coefficient. The identified friction coefficient μ_{fric} increases to almost 1, see table 9.49. This leads to a similar interpretation as in chapter 9.7.1.1 where a sticking condition is obviously imposed in the contact zone leading to more internal friction.

Ranking	A [MPa]	B [MPa]	C [-]	m [-]	n [-]	μ_{fric} [-]	ΔF_{total}^2 [N ²]	ΔF_c [N]	ΔF_f [N]
10	823.0	321.0	0.01379	0.5985	0.1824	0.9411	84.76589	6.13272	6.86699
9	830.2	317.6	0.01407	0.6356	0.1821	0.9353	83.67551	5.2079	7.52019
8	819.9	331.9	0.01164	0.5836	0.1605	0.9898	83.15855	6.38667	6.50915
7	833.4	345.7	0.01361	0.5791	0.1338	0.8656	81.1443	6.81223	5.89389
6	838.9	321.7	0.01337	0.6152	0.1409	0.9446	80.66476	5.63939	6.99014
5	903.9	323.7	0.01178	0.5999	0.1745	0.9467	77.07405	7.30751	4.86563
4	885.2	323.4	0.01157	0.5866	0.1628	0.959	74.45334	1.92273	8.41169
3	778.1	316.8	0.0138	0.5841	0.1426	0.9879	71.9409	3.35032	7.79206
2	808.2	313.4	0.01246	0.6042	0.1377	0.9979	59.11539	2.14979	7.38199
1	800.1	327.5	0.01292	0.5902	0.1833	0.9596	51.31082	1.85545	6.91868

Table 9.49: Inversely identified JC-parameter and friction coefficient with shear stress limit for Ti6Al4V with DE-method sorted for minimum ΔF_{total}^2 .

9.7.2.2 Ck45

A slight increase of the identified friction coefficient μ_{fric} can be seen, while the static yield limit A is in this identification below the tensile test yield limit for the fit with the lowest ΔF_{total}^2 . The summed square error of the process forces ΔF_{total}^2 is lower in this inverse identification compared to the identifications without friction coefficient and the identification with friction coefficient but without shear stress limit. An overview of the ten best parameter sets is given with table 9.50.

Ranking	A [MPa]	B [MPa]	C [-]	m [-]	n [-]	μ_{fric} [-]	ΔF_{total}^2 [N ²]	ΔF_c [N]	ΔF_f [N]
10	404.5	776.2	0.04336	0.8597	0.0419	0.5871	0.05618	0.13906	-0.19194
9	461.9	663.4	0.04798	0.8648	0.0503	0.6129	0.04911	0.14635	0.16641
8	414.0	730.2	0.04696	0.8749	0.0314	0.6633	0.04696	-0.18388	-0.11468
7	485.7	745.5	0.04708	0.8175	0.0251	0.5131	0.04636	0.15492	0.14953
6	284.1	762.8	0.05257	0.8578	0.0382	0.697	0.04165	-0.06025	0.19498
5	407.3	744.1	0.0367	0.952	0.022	0.6949	0.03272	-0.02055	-0.17971
4	504.9	730.0	0.0381	0.9158	0.0317	0.6329	0.03192	-0.04228	-0.17358
3	554.4	719.7	0.03094	0.9068	0.0351	0.6068	0.02884	0.10565	-0.13295
2	449.7	709.8	0.04263	0.8943	0.0221	0.6253	0.00824	0.01735	-0.08911
1	331.0	762.2	0.04534	0.9176	0.0215	0.6623	0.00237	0.04755	0.01025

Table 9.50: Inversely identified JC-parameter and friction coefficient with shear stress limit for Ck45 with DE-method sorted for minimum ΔF_{total}^2 .

9.8 RECALCULATION OF CUTTING EXPERIMENTS

9.8.1 *Ti6Al4V*

The material parameters determined from the parameter identifications:

- without friction coefficient, set 1 in table 9.35
- with friction coefficient and without SSL, set 1 in table 9.47
- with friction coefficient and SSL, set 1 in table 9.49

are used here to recompute a few cutting experiments at other process conditions and compare the experimental versus the computed process forces and chip thicknesses. The best parameter sets from the inverse identification of material constitutive constants for Ti6Al4V are displayed in table 9.52. The selection of experiments for the recomputation is compiled in table 9.51.

Feed [mm]	$v_c = 20m/min$	$v_c = 125m/min$	$v_c = 400m/min$
0.01	V0320 ($r_n = 40.5\mu m$)	V0348 ($r_n = 38.3\mu m$)	V0461 ($r_n = 35.5\mu m$)
0.04	V0325 ($r_n = 37.5\mu m$)	V0350 ($r_n = 37.9\mu m$)	V0471 ($r_n = 41.9\mu m$)

Table 9.51: Recomputation of cutting experiments with the identified material constitutive sets for Ti6Al4V.

A	B	C	m	n	μ_{fric}	Comment	SSL	Reference
[MPa]	[MPa]	[-]	[-]	[-]				
852.1	338.9	0.02754	0.5961	0.148	0.35		no	table 9.35
611.9	357.7	0.01609	0.6239	0.1365	0.7009	μ_{fric} identified	no	table 9.47
800.1	327.5	0.01292	0.5902	0.1833	0.9596	μ_{fric} identified	yes	table 9.49

Table 9.52: Best material constitutive sets for Ti6Al4V from the inverse parameter identifications.

A comparison of experimental and numerically predicted cut forces is provided in table 9.53 and for the feed force in table 9.54, a graphical comparison is provided in figure 9.84. The experimental and numerical chip thicknesses are given in table 9.55 and figure 9.85. Even though a very large range of cut speeds is used, the process force predictions are quite acceptable where the largest deviations is in the order of 20% at the lowest cut speed of $v_c = 20m/min$. The feed force error is higher with up to 47%. Simulations with parameter sets where the friction coefficient was identified together with the material constitutive parameters tend to higher process force errors where the results from the identification without shear stress limit is worse. A different picture is seen for the chip thickness prediction where the parameter identification without friction coefficient is closer to the experimental

values for the lower feed of $f = 0.01\text{mm}$ (V0320, V0348, V461) whereas at the higher feed of $f = 0.04\text{mm}$ (V0325, V0350, V0471) the parameter sets from both identifications including the friction coefficient show better predictions.

Experiment	$F_c^{exp} [N]$	$F_c^{\mu=0.35} [N]$	$\Delta[\%]$	$F_c^{\mu_{noSSL}} [N]$	$\Delta[\%]$	$F_c^{\mu_{SSL}} [N]$	$\Delta[\%]$
V0060	157.5	162.8	3.38	155.7	-1.17	159.4	1.2
V0320	55.9	47.7	-14.61	47.2	-15.63	51.4	-8.1
V0325	110.5	85.8	-22.33	76.9	-30.44	85.1	-23.0
V0348	42.7	44.3	3.75	45.6	6.9	49.6	16.1
V0350	102.3	84.8	-17.07	73.9	-27.74	81.0	-20.8
V0461	41.2	40.9	-0.73	45.3	9.86	48.2	17.0
V0471	99.8	92.6	-7.19	81.8	-18.01	85.9	-14.0

Table 9.53: Ti6Al4V: Experimental and simulated cut forces F_c with inversely identified material constitutive parameters.

Experiment	$F_f^{exp} [N]$	$F_f^{\mu=0.35} [N]$	$\Delta[\%]$	$F_f^{\mu_{noSSL}} [N]$	$\Delta[\%]$	$F_f^{\mu_{SSL}} [N]$	$\Delta[\%]$
V0060	115.5	120.8	4.57	118.1	2.26	122.4	6.0
V0320	84.5	63.0	-25.41	50.6	-40.12	58.6	-30.6
V0325	104.9	68.2	-35.01	54.9	-47.65	73.3	-30.1
V0348	77.5	69.7	-10.06	51.4	-33.71	57.2	-26.2
V0350	110.9	85.6	-22.85	66.7	-39.83	80.3	-27.6
V0461	74.3	76.4	2.81	51.8	-30.33	63.2	-15.0
V0471	116.0	108.5	-6.42	80.2	-30.89	102.9	-11.3

Table 9.54: Ti6Al4V: Experimental and simulated feed forces F_f with inversely identified material constitutive parameters.

Experiment	$h^{exp} [\mu m]$	$h^{\mu_{fric}=0.35} [\mu m]$	$\Delta[\%]$	$h^{\mu_{noSSL}} [\mu m]$	$\Delta[\%]$	$h^{\mu_{SSL}} [\mu m]$	$\Delta[\%]$
V0060	99.7	116.3	16.6	140.9	41.3	141.1	41.6
V0320	28.3	26.3	-7.1	24.9	-11.9	24.8	-12.3
V0325	67.7	51.7	-23.7	71.3	5.2	74.6	10.2
V0348	16	21.5	34.2	22.7	41.8	20.9	30.4
V0350	61.5	48.7	-20.7	54.5	-11.3	65.3	6.2
V0461	16	17.4	8.8	18.8	17.6	16.8	4.8
V0471	51.9	45	-13.3	52.1	0.5	54.6	5.3

Table 9.55: Ti6Al4V: Experimental and numerical predicted chip thicknesses h with inversely identified material constitutive parameters.

In figure 9.86 the experimental chip shape is shown together with numerical results for experiment V0060. In contrast to the chip from the experiment, none of the numerical simulations show chip segmentation. The explanation for this can be found when investigating the experimental chips. It can be seen for the experiment V0060 in figure 9.41 and from

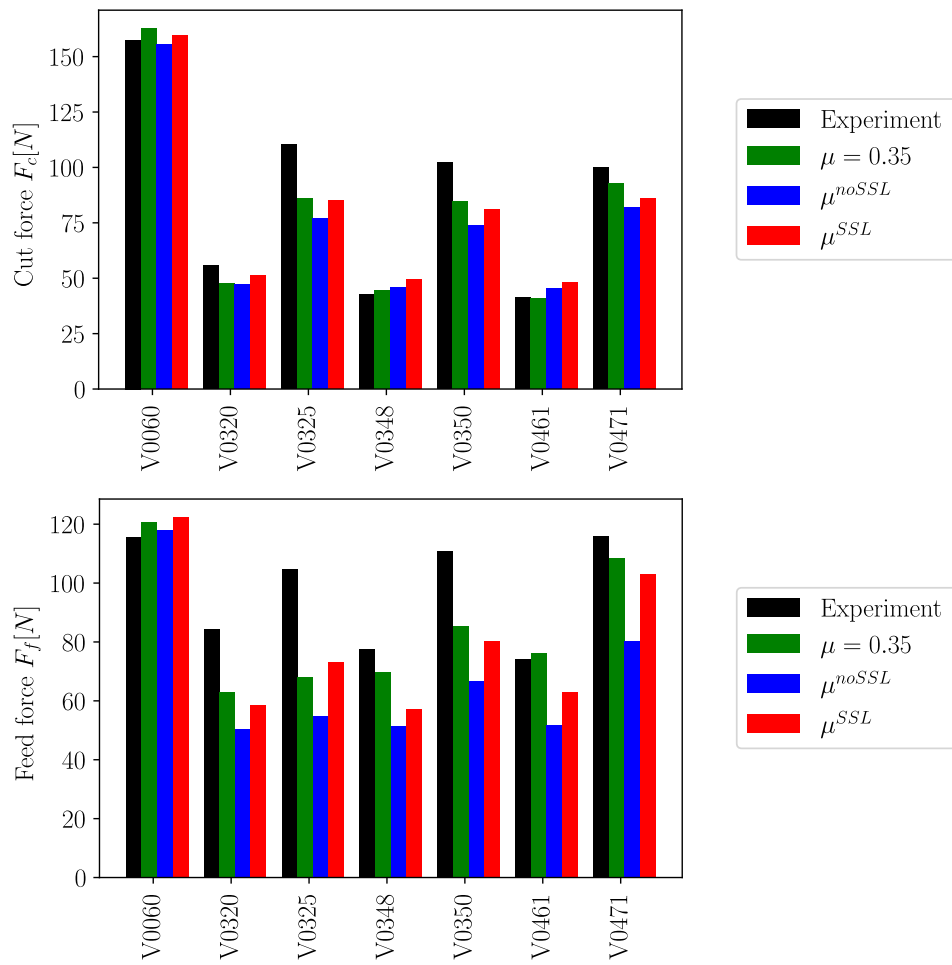


Figure 9.84: Ti6Al4V: Experimental and predicted cut (top) and feed force (bottom).

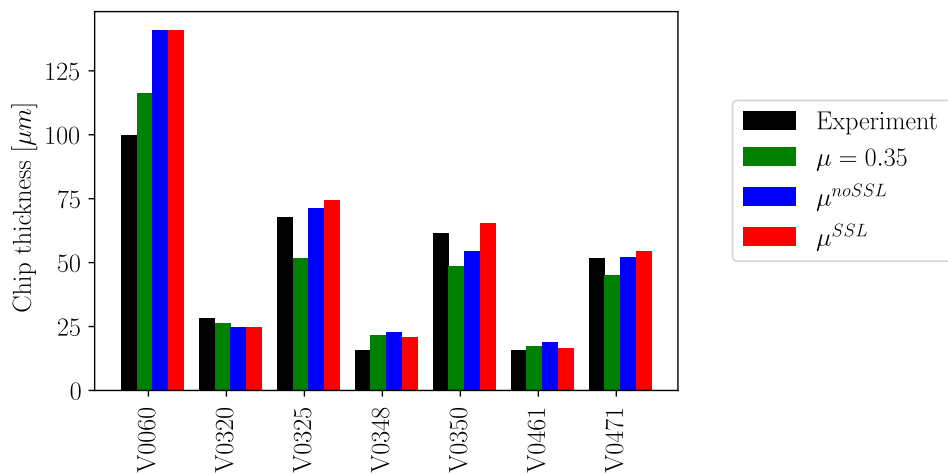


Figure 9.85: Ti6Al4V: Experimental and predicted chip thicknesses.

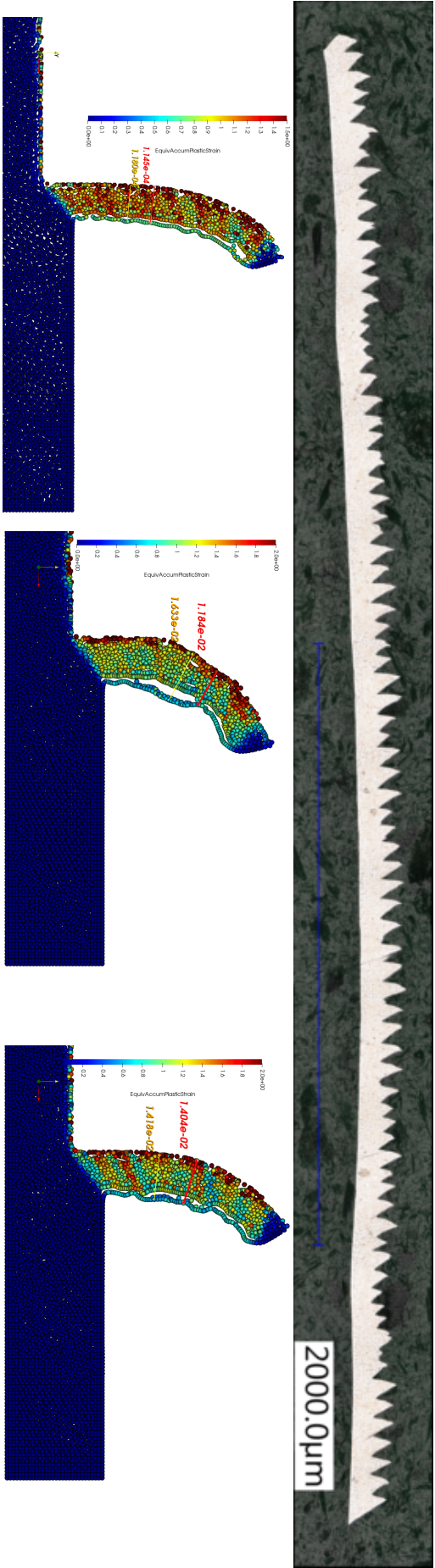


Figure 9.86: Ti6Al4V: Experimental chip from V0060 $v_c = 381.3m/min, f = 0.1mm$ (top) with numerical chip thicknesses: parameter identification without friction coefficient (bottom left), identification with friction coefficient and SSL (bottom middle) and with friction coefficient and SSL (bottom right).

table 9.19 that at an uncut chip thickness of $f = 0.1\text{mm}$ the thickness of the shear layer in the contact zone is about $3\mu\text{m}$ and in the shear layer of the primary shear zone is about $4 - 6\mu\text{m}$. Since for performance reasons the model resolution was chosen with 10 particles per uncut chip thickness, one particle covers a length scale of $10\mu\text{m}$ which is in comparison to the shear layer thickness too coarse to resolve the physics on this length scale. For this reason the heat released by plastic dissipation is averaged over a larger volume leading to a lesser thermal softening and thus preventing the chip to develop segmentation. To overcome this situation the resolution of the simulation is increased from the initial resolution with 5'640 particles over 64'300 particles up to 126'000 particles for the model with heat transfer in the workpiece only and without frictional heating using material parameters set 1 in table 9.35 from the parameter identification without friction coefficient. The effect on the chip segmentation is displayed in figure 9.87 where the simulation with 64'300 particles shows already some segmentation which becomes much more pronounced when simulating with 126'000 particles.

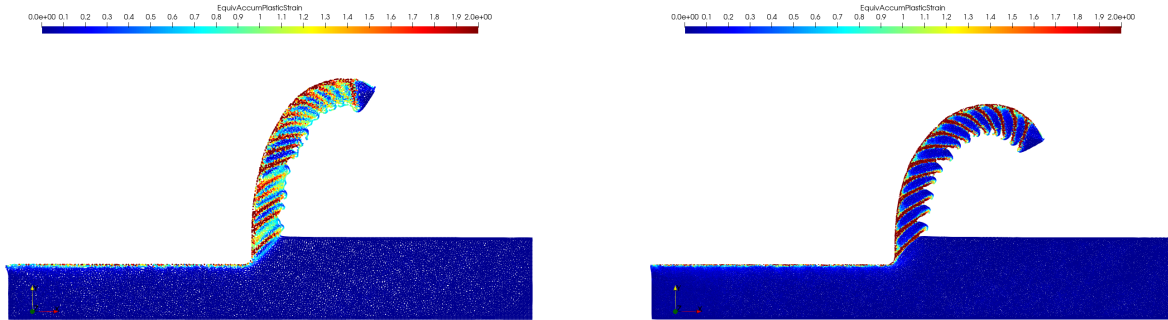


Figure 9.87: Ti6Al4V: Recomputation of experiment V0060 $v_c = 381.3\text{m/min}$, $f = 0.1\text{mm}$ with material parameters identified without friction coefficient (set 1 from table 9.35) and increased particle resolution: left (64'300 particles) and right (126'000 particles) show chip segmentation towards higher resolutions. The simulations are run with heat transfer in the workpiece but without tool heat transfer and without frictional heating.

If however a more realistic simulation of the cutting process is desired, the tool heat transfer and frictional heating need to be considered. In this case a further increase of the resolution to 208'732 particles is required to model the chip segmentation. The resulting segmented chip geometry is displayed in figure 9.88. A comparison of the numerically predicted and experimental chip geometry is provided in table 9.56. The predicted minimum chip thickness h_{min} is at a comparable level to the experiment while the maximum chip thickness h_{max} is roughly 20% lower predicted. The distance between segments l_{seg} is almost 50% lower, while the shear layer thicknesses in the primary and secondary shear zone, t_{seg} and t_{sl} , are overpredicted by about 100%. The process forces vary slightly with the different resolutions and the effect of tool heat transfer and frictional heating is small, see table 9.57.

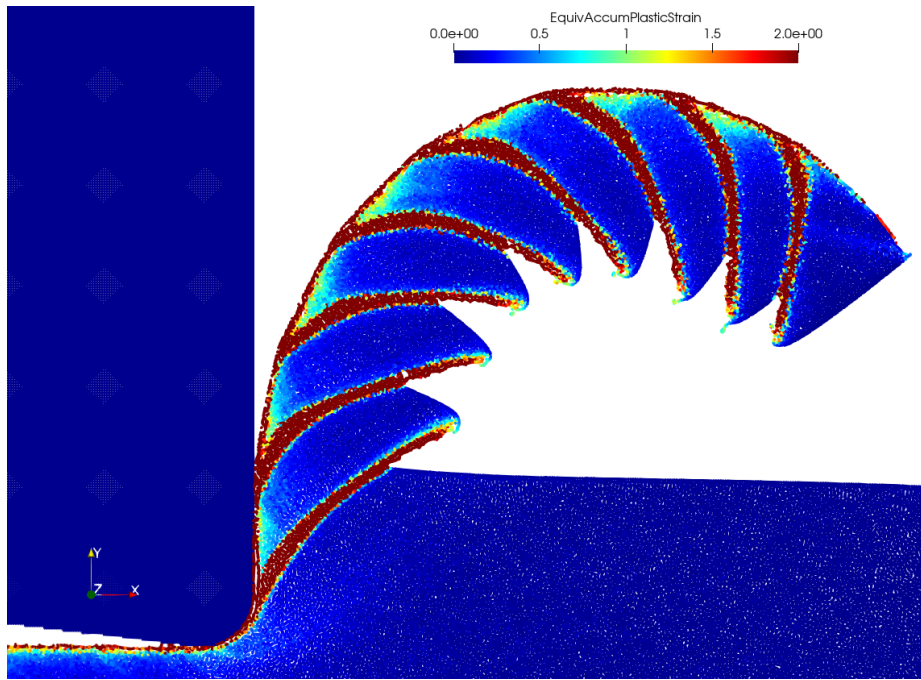


Figure 9.88: Ti6Al4V: Recomputation of experiment V0060 $v_c = 381.3m/min, f = 0.1mm$ with material parameters identified without friction coefficient (set 1 from table 9.35) shows chip segmentation when simulated with 208'732 particles. The simulations are run with heat transfer in the workpiece and tool including frictional heating.

Result	$h_{min}[\mu m]$	$h_{max}[\mu m]$	$l_{seg}[\mu m]$	$t_{seg}[\mu m]$	$t_{sl}[\mu m]$
Experiment	80	150	51-56	4-6	3
Simulation	73-82	120	33-39	6-11	5-6

Table 9.56: Ti6Al4V: Experimental and simulated chip shape for experiment V0060.

Result	$F_c[N]$	$F_f[N]$	Heat transfer workpiece	Heat transfer tool	Frictional heating	Particle number
Experiment	157.5	115.5	-	-	-	-
Simulation	162.8	120.8	yes	no	no	5'640
Simulation	170.0	113.3	yes	no	no	64'300
Simulation	161.4	108.5	yes	no	no	126'000
Simulation	154.6	105.0	yes	yes	yes	208'732

Table 9.57: Ti6Al4V: Experimental and simulated process forces for experiment V0060.

9.8.2 Ck45

The material parameters determined from the parameter identifications for Ck45:

- without friction coefficient, set 1 in table 9.44
- with friction coefficient and without SSL, set 1 in table 9.48
- with friction coefficient and SSL, set 1 in table 9.50

are used here to recompute a few cutting experiments at other process conditions and compare the experimental versus the computed process forces and chip thicknesses. The selection of experiments is compiled in table 9.58 The process forces and chip shapes are compared to the numerical results and are shown in tables 9.60 (F_c), 9.61 (F_f) and 9.62 (chip thickness h). An example of the experimental and numerically simulated chip shapes is provided in figure 9.91 for the experiment V0300, which was used in all identifications of the JC-CLASSIC model coefficients for Ck45.

Feed [mm]	$v_c = 70m/min$	$v_c = 200m/min$	$v_c = 450m/min$
0.02	V0186 ($r_n = 36.4\mu m$)	V0278 ($r_n = 40.1\mu m$)	V0286 ($r_n = 40.0\mu m$)
0.06	V0189 ($r_n = 39.9\mu m$)	V0280 ($r_n = 38.8\mu m$)	V0289 ($r_n = 38.0\mu m$)

Table 9.58: Recomputation of cutting experiments with the identified material constitutive sets for Ck45.

A [MPa]	B [MPa]	C [-]	m [-]	n [-]	μ_{fric}	Comment	SSL	Reference
569.0	736.6	0.06	0.7147	0.0685	0.35		no	table 9.44
567.5	592.6	0.063	0.6742	0.0956	0.5107	μ_{fric} identified	no	table 9.48
331.0	762.2	0.045	0.9176	0.0215	0.6623	μ_{fric} identified	yes	table 9.50

Table 9.59: Best material constitutive sets for Ck45 from the inverse parameter identifications.

The cut forces match better with experimental results than the feed forces. At cut speeds of $v_c = 200m/min$ and $v_c = 450m/min$ the cut force deviation in the numerical simulation is between 5...20% and for $v_c = 70m/min$ up to 50%, see also table 9.60 and figure 9.89. The error in the feed force is up to almost 150% at the lowest simulated cut speed and for both higher v_c between 8...45%, see also table 9.61 and figure 9.89 Whether the friction coefficient was identified together with the material constitutive parameters or not, affects the process force only marginally. The chip thickness prediction is slightly better when the friction coefficient was identified with the constitutive parameters but the error in the prediction is generally high in the order of 34...75%, see table 9.62 and figure 9.90. An example of the experimental and numerically simulated chip shapes is provided in figure 9.91 for the experiment V0300, which was used for the identification of the JC-CLASSIC model coefficients for Ck45.

Experiment	F_c^{exp} [N]	$F_c^{\mu=0.35}$ [N]	Δ [%]	$F_c^{\mu_{noSSL}}$ [N]	Δ [%]	$F_c^{\mu_{SSL}}$ [N]	Δ [%]
V0300	260.3	260.2	-0.02	260.3	0.02	260.3	0.0
V0186	66.1	96.9	46.54	94.5	42.96	99.5	50.5
V0189	167.1	180.2	7.85	165.2	-1.15	167.8	0.4
V0278	81.1	100.6	24.03	97.3	19.99	100.5	23.9
V0280	213.6	177.2	-17.06	168.6	-21.07	171.1	-19.9
V0286	86.5	99.2	14.71	95.7	10.66	98.9	14.3
V0289	193.1	182.3	-5.57	172.9	-10.47	169.8	-12.1

Table 9.60: Ck45: Experimental and simulated cut forces F_c with inversely identified material constitutive parameters.

Experiment	F_f^{exp} [N]	$F_f^{\mu=0.35}$ [N]	Δ [%]	$F_f^{\mu_{noSSL}}$ [N]	Δ [%]	$F_f^{\mu_{SSL}}$ [N]	Δ [%]
V0300	174.6	174.5	-0.03	174.5	-0.04	174.6	0.0
V0186	40.6	98.8	143.23	89.3	119.85	100.7	148.1
V0189	109.4	124.1	13.47	102.2	-6.59	112.8	3.1
V0278	80.3	116.8	45.47	102.9	28.15	108.7	35.4
V0280	220.6	137.0	-37.89	131.7	-40.32	134.7	-38.9
V0286	91.1	131.6	44.46	106.4	16.83	119.1	30.7
V0289	167.8	153.5	-8.55	126.7	-24.52	141.1	-15.9

Table 9.61: Ck45: Experimental and simulated feed forces F_f with inversely identified material constitutive parameters.

Experiment	h^{exp} [μm]	$h^{\mu_{fric}=0.35}$ [μm]	Δ [%]	$h^{\mu_{noSSL}}$ [μm]	Δ [%]	$h^{\mu_{SSL}}$ [μm]	Δ [%]
V0186	65.8	39	-40.8	37.3	-43.3	40.3	-38.8
V0189	166.1	84.8	-48.9	100.2	-39.7	96.3	-42
V0278	58	36.8	-36.5	38	-34.4	38.2	-34.1
V0280	201	80.5	-59.9	85.1	-57.7	95.9	-52.3
V0286	69	30.8	-55.3	36.9	-46.5	35.9	-47.9
V0289	145.9	76.9	-47.3	79.3	-45.7	85.8	-41.2
V0300	216.6	116.4	-46.3	136.9	-36.8	141.9	-34.5

Table 9.62: Ck45: Experimental and numerical predicted chip thicknesses h with inversely identified material constitutive parameters.

In figure 9.91 the experimental chip shape is shown together with numerical results for experiment V0300.

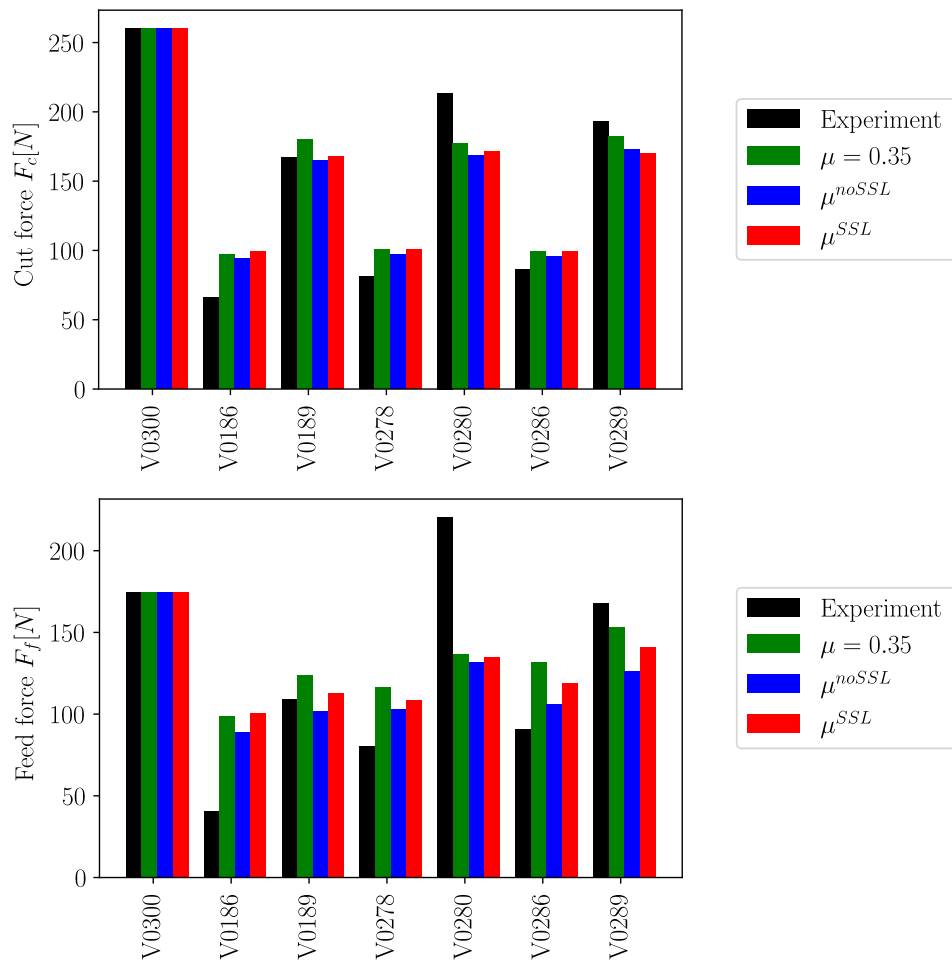


Figure 9.89: Ck45: Experimental and predicted cut (top) and feed force (bottom).

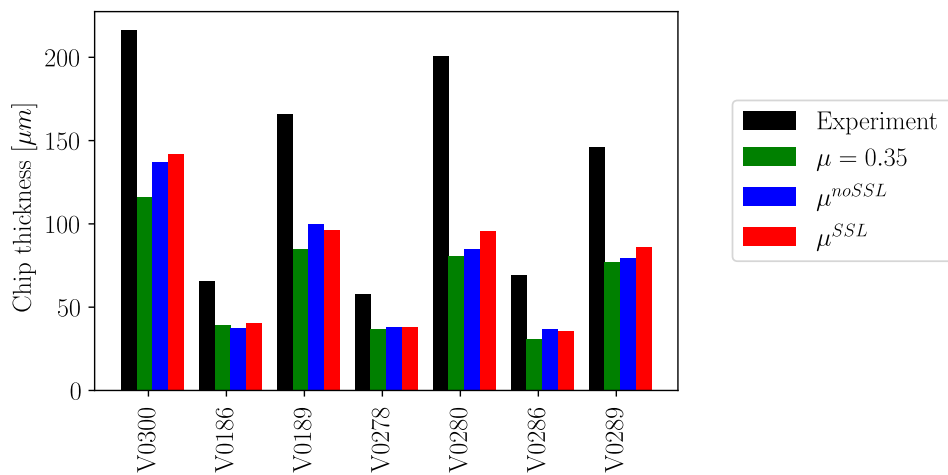


Figure 9.90: Ck45: Experimental and predicted chip thicknesses.

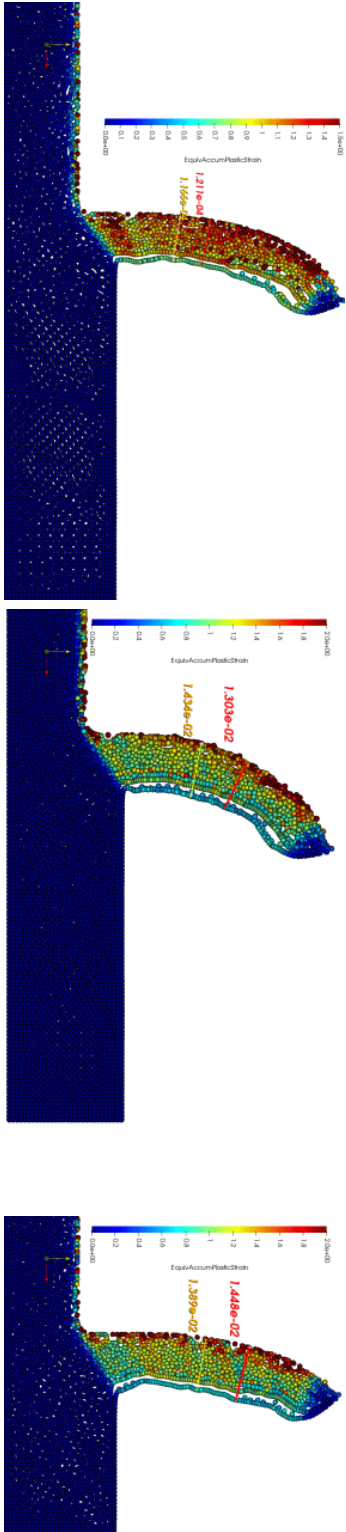
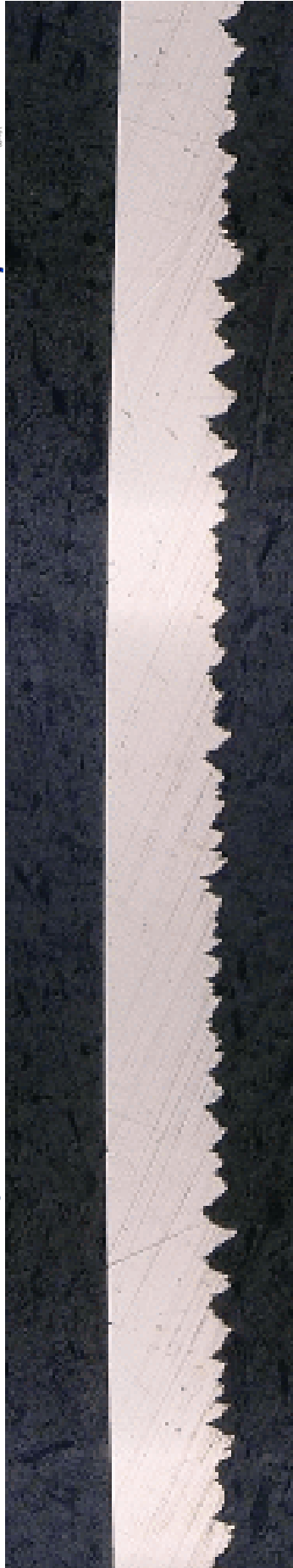


Figure 9.91: CK45: Experimental chip from V0300 $v_c = 500\text{m/min}$, $f = 0.1\text{mm}$ (top) with numerical chip thicknesses: parameter identification without friction coefficient (bottom left), identification with friction coefficient no SSL (bottom middle) and with friction coefficient and SSL (bottom right).

9.8.3 Comparison of Parameter Identification Results

9.8.3.1 Static Flow Curve

The Johnson-Cook model parameters A , B and n obtained from the parameter identifications are compared versus the JC model parameters extracted from the tensile tests in chapter 9.2.1 and versus literature values. In figure 9.92 the comparison is shown for Ti6Al4V and in figure 9.93 for Ck45. For Ti6Al4V the parameters identified from the tensile test give almost the same flow stress characteristics as the parameters from literature [62]. Parameter sets identified without friction coefficient and with friction coefficient and SSL are in the range of the flow stress curve from literature values, while the parameter set from the identification with friction coefficient without SSL differs largely with flow stresses roughly 20% lower over the whole plastic strain range.

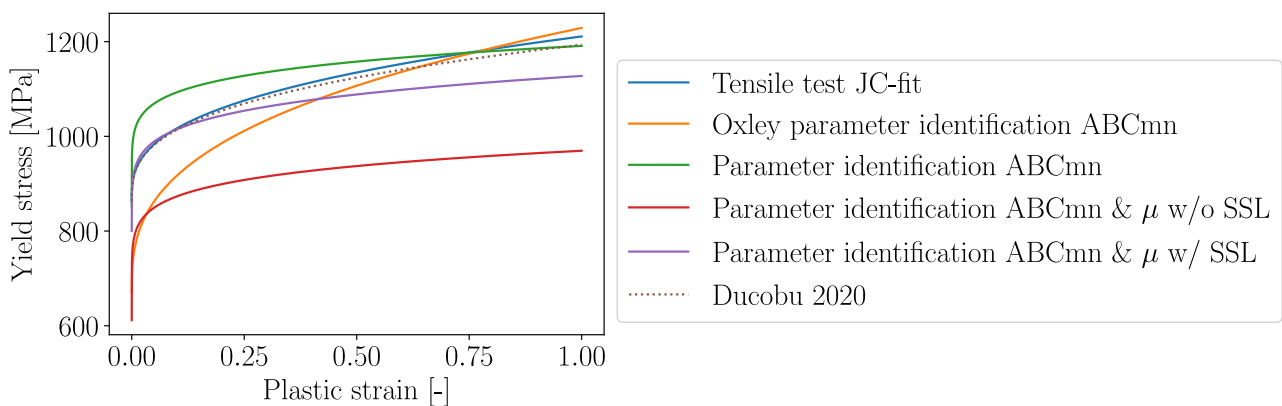


Figure 9.92: Ti6Al4V: Flow stress curve comparison of the identified JC-CLASSIC-parameter A , B and n versus parameters from tensile test and values from literature [62].

In the Ck45 parameter identification the parameter sets identified together with the friction coefficients and the set from the analytical process force model give very similar static flow curves. The parameter set from the literature [101] and from the tensile test give lower flow stresses for small plastic strains and for plastic strains around $\varepsilon_{pl} \approx 1$ the flow stresses are almost the same for all parameter sets except the one from the parameter identification without friction coefficient. The latter gives over the whole plastic strain range about 20% higher flow stresses.

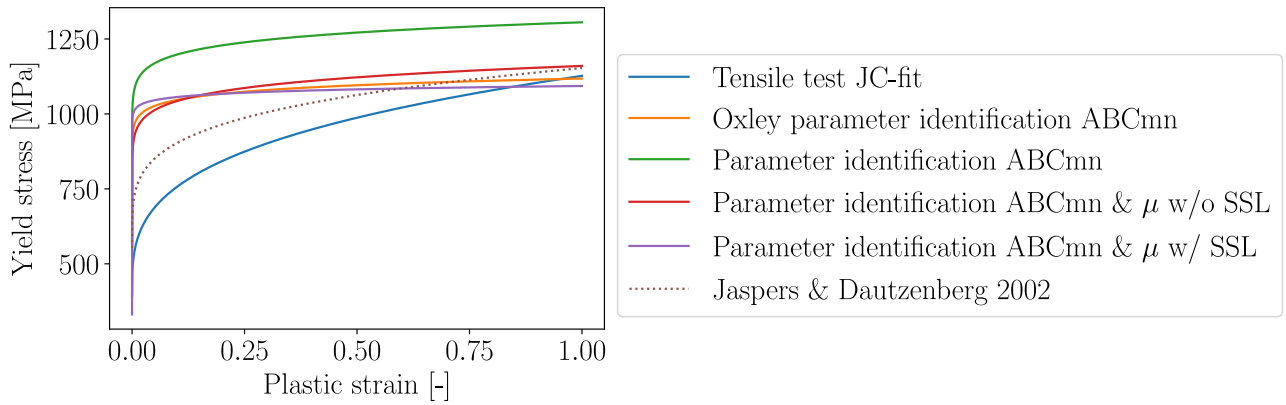


Figure 9.93: Ck45: Flow stress curve comparison of the identified JC-CLASSIC-parameter A, B and n versus parameters from tensile test and values from literature [101].

9.8.3.2 Strain Rate Sensitivity

Here the strain rate sensitivities are compared between those from experiments at low strain rates, the parameter identifications and literature values. The material parameters used in this comparison are provided in table 9.63.

Material	C [-]	$\dot{\epsilon}_{pl}^0$ [-]	Source
Ti6Al4V	0.0145	0.002	tensile test, chapter 9.2.3.1
Ti6Al4V	0.0377	1.0	Oxley model, table 9.30
Ti6Al4V	0.02754	1.0	SPH ABCmn, table 9.52
Ti6Al4V	0.01609	1.0	SPH ABCmn & μ w/o SSL, table 9.52
Ti6Al4V	0.01292	1.0	SPH ABCmn & μ w/ SSL, table 9.52
Ti6Al4V	0.012	1.0	Ducobu [62]
Ck45	0.0108	0.002	tensile test, chapter 9.2.3.2
Ck45	0.07	1.0	Oxley model, table 9.32
Ck45	0.06	1.0	SPH ABCmn, table 9.59
Ck45	0.063	1.0	SPH ABCmn & μ w/o SSL, table 9.59
Ck45	0.045	1.0	SPH ABCmn & μ w/ SSL, table 9.59
Ck45	0.0134	1.0	Jaspers & Dautzenberg [101]

Table 9.63: JC-Parameters used for the strain rate sensitivity comparison.

For each set the yield stress ratio σ_y^{ratio} is computed in the strain rate range $\dot{\epsilon}_{pl} = 1...10^6/s$ by using the strain rate sensitivity part from the Johnson-Cook flow stress model (3.95):

$$\sigma_y^{ratio} = 1 + C \cdot \ln \left(\frac{\dot{\epsilon}_{pl}}{\dot{\epsilon}_{pl}^0} \right) \tag{9.24}$$

and the resulting charts are displayed in figure 9.95 (Ck45) and 9.94 (Ti6Al4V). The strain rate sensitivity from the tensile tests are in general low and for Ck45 comparable to literature

values. For both materials, Ck45 and Ti6Al4V, the sensitivities obtained from the identification with the OXLEY-model are the highest in comparison to the other parameter sets. The sensitivities from literature values are in both cases the lowest which might be due to their determination from SHB-tests as well as a different delivery condition of the material. It has to be noted that the Johnson-Cook strain rate sensitivity increases only linearly in the semi-logarithmic display while it is known from literature [131, 245] that towards higher strain rates the yield stress is progressively increasing. This progressive increase cannot be modelled with the Johnson-Cook flow stress model which possibly means that the identified strain rate sensitivities have limited validity only at the process conditions used for the inverse identification of the material parameters.

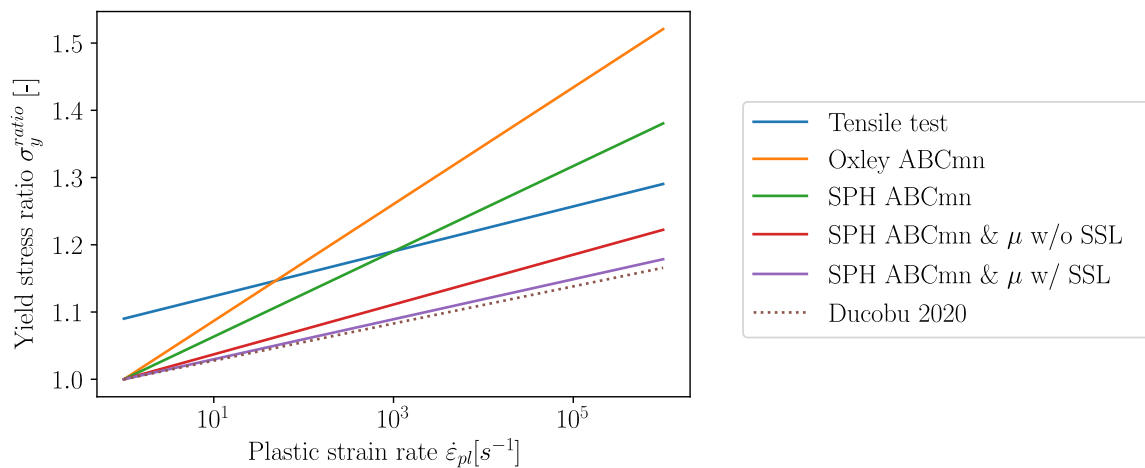


Figure 9.94: Ti6Al4V: Strain rate sensitivities in the range from $\dot{\epsilon}_{pl} = 1...10^6/s$ computed for results from tensile tests, parameter identifications and values from literature [62].

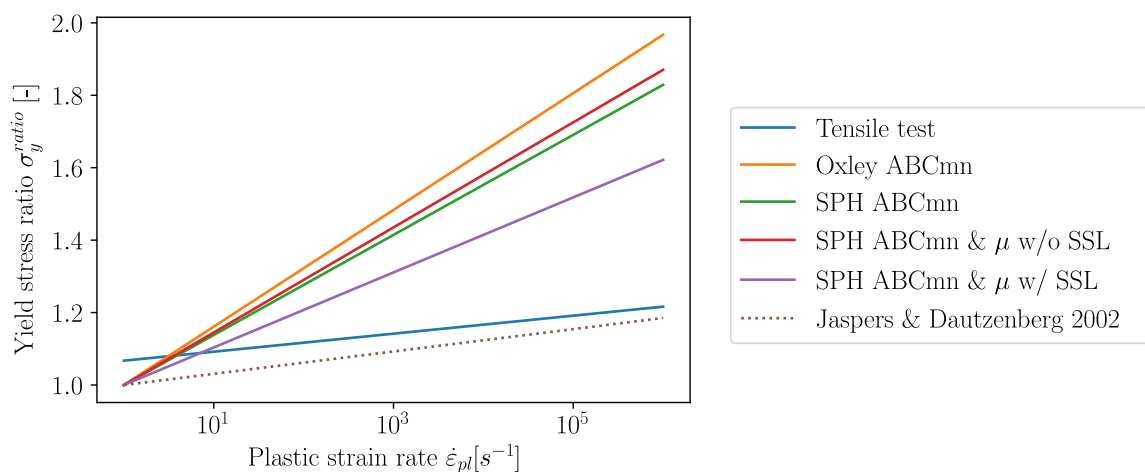


Figure 9.95: Ck45: Strain rate sensitivities in the range from $\dot{\epsilon}_{pl} = 1...10^6/s$ computed for results from tensile tests, parameter identifications and values from literature [101].

9.8.3.3 *Flow Stress Curves at Different Strain Rates and Temperatures*

The full JC-parameter sets are used to compute flow stress curves at three different temperatures ($T = 473, 1073, 1473\text{K}$) and three different strain rates ($\dot{\epsilon}_{pl} = 1, 1'000, 500'000/s$) for Ti6Al4V (figure 9.96) and Ck45 (figure 9.97). For Ti6Al4V the flow stress curve for parameters identified with the OXLEY-model give a similar characteristics as values from literature [62] at the lowest strain rate. All three parameter sets identified with the SPH give the lowest yield stresses at all temperatures and strain rates. Towards the highest strain rate the flow stresses predicted with the parameter set from the literature comes closer to the predicted yield stresses with parameter sets from the SPH parameter identification. For the Ck45 material the predicted flow stresses from the parameter sets identified with the OXLEY-model and the SPH simulations give similar characteristics while the flow stress curve created with the parameter set from the literature [101] predicts at the lowest strain rate higher flow stresses than the other sets. At $\dot{\epsilon}_{pl} = 1'000/s$ it gives similar yield stresses and at $\dot{\epsilon}_{pl} = 500'000/s$ it shows lower yield stresses than the other flow stress curves. The reason for this behaviour is the very low strain rate sensitivity parameter C of the parameter set from the literature. It increases in the range from $\dot{\epsilon}_{pl} = 1...10^6/s$ by less than 20%, while for the other parameter sets the increase is between 60...100%.

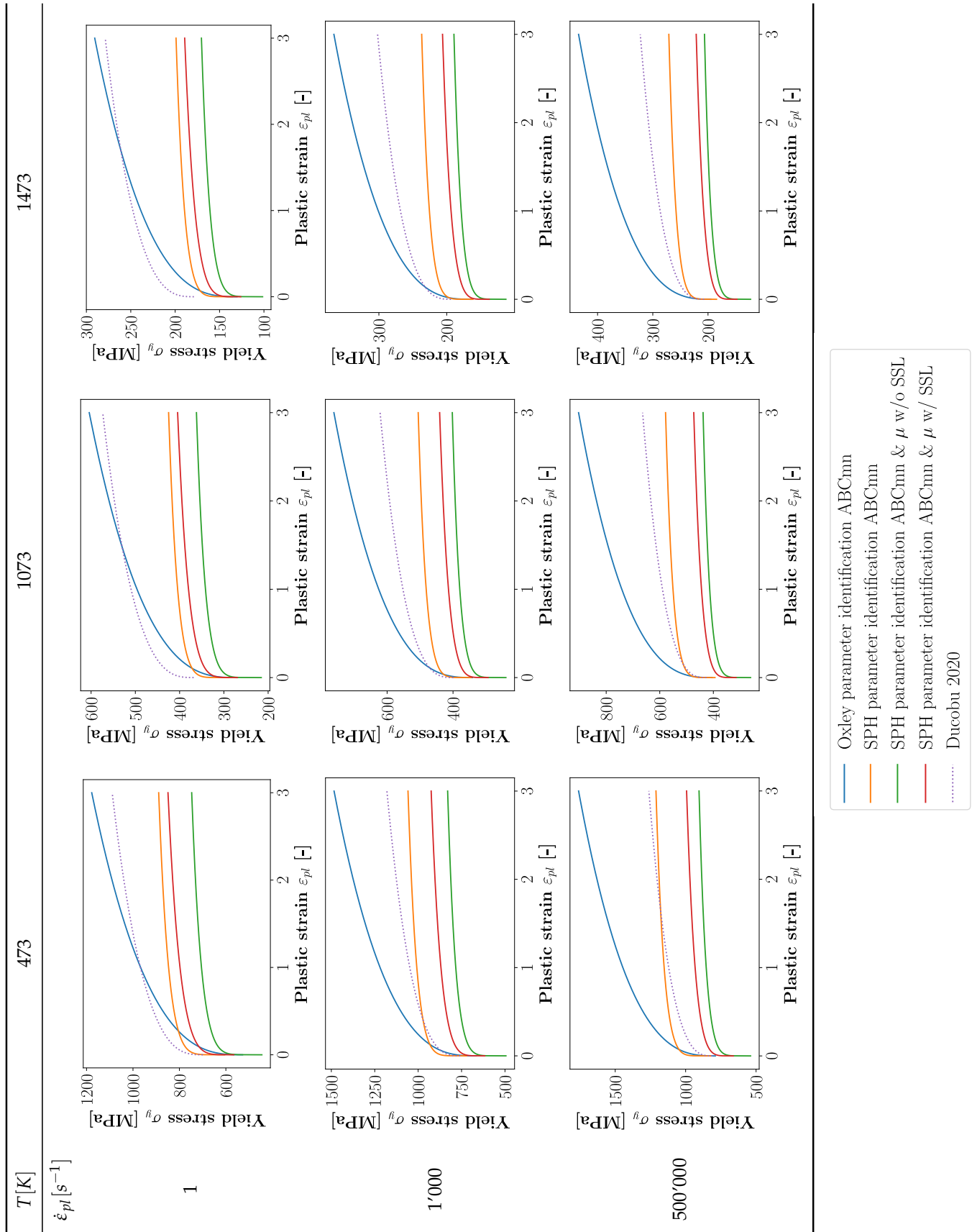


Figure 9.96: Ti6Al4V: flow stress curve comparison for different JC-parameter sets.

$\dot{\epsilon}_{pl} [s^{-1}]$

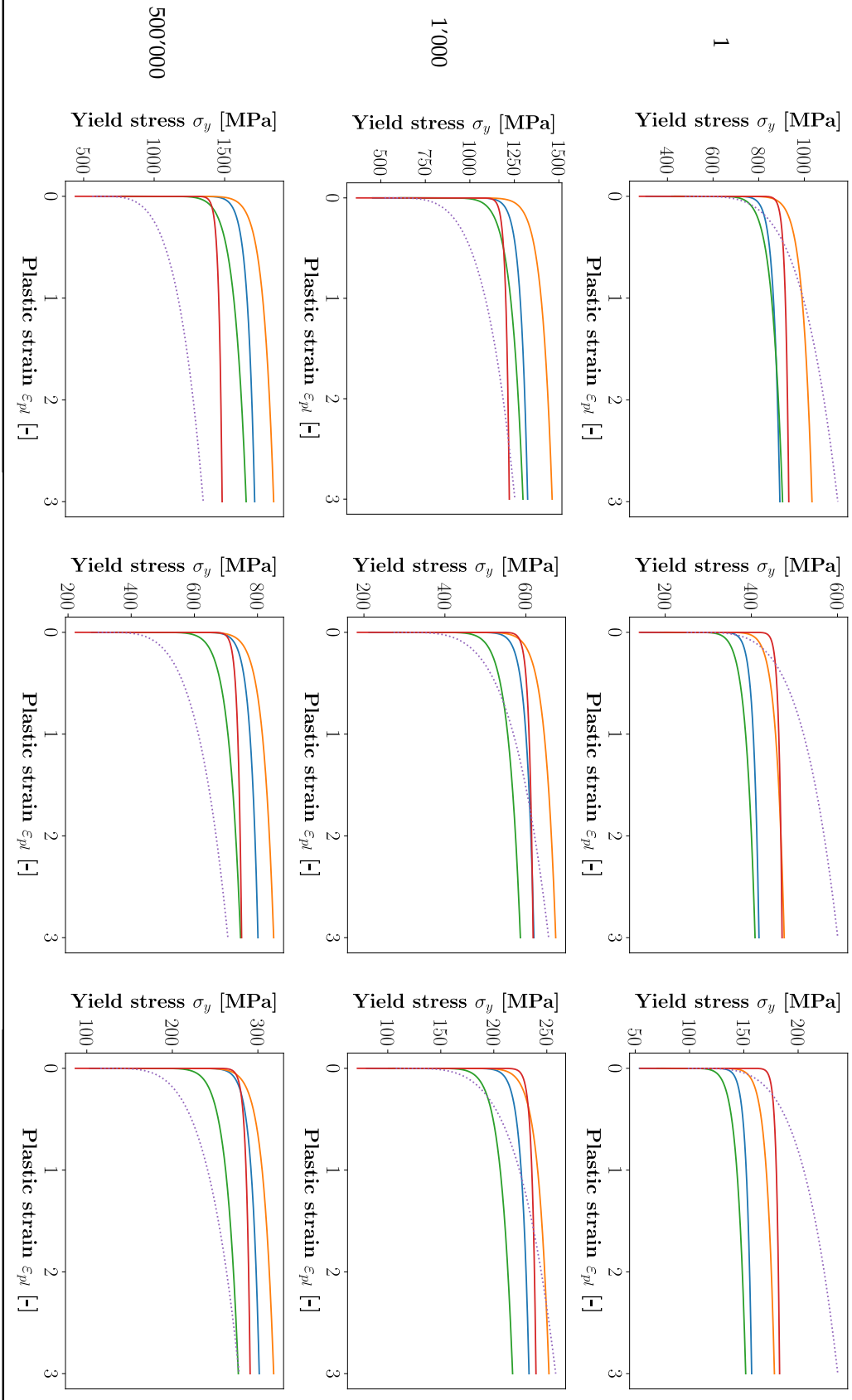


Figure 9.97: CK45: flow stress curve comparison for different J-C-parameter sets.

9.8.4 *Results Discussion*

Based on orthogonal cutting experiments material parameters were inversely identified within a numerical simulation model of the cutting process. Three different optimization methods were used of which the DE-method proved to be the most versatile but demanding in terms of computation time. The BAYES-method showed in the initial phase of the optimization good progress in minimizing the cost function but suffered from largely increasing overhead of the process model evaluation which made it not suitable to minimize the cost function. The SIMPLEX-method is efficient but tends to trap often in local minima leading to higher process force errors. The identified parameter sets for each of both materials provide similar predictions at other process conditions in terms of forces and chip thicknesses. The chip segmentation can not be reproduced for the Ti6Al4V even though the predicted average chip thicknesses are similar to the experimental values. If however the resolution is increased by a factor of about 40, chip segmentation can be predicted even with the classic Johnson-Cook flow stress model. This model resolution is however not suitable for the parameter identification since the runtimes increase from a few minutes to more than 2 hours. For the Ck45 material the chip thicknesses are under-predicted with errors in the order of 30..40%. The feed force error in the predictions for Ck45 at other process conditions is partially up to 60% for each of the three identified parameter sets. This is remarkable since the prediction at reference experiment conditions gives negligible errors in the process forces. Apparently, the identified Johnson-Cook flow stress model parameters have limited validity only at similar process conditions which are used for the inverse identification of the material parameters. As discussed in the strain rate sensitivity comparison in chapter 9.8.3.2, the likely reason for this is that the Johnson-Cook strain rate sensitivity term increases only linearly in the semi-logarithmic display while it is known from literature [131, 245] that towards higher strain rates the yield stress is usually progressively increasing. A possibility to improve here would be the use of the Cowper-Symonds model [46] for the strain rate sensitivity term at the expense of an additional material parameter to be identified.

The identified friction coefficients for Ck45 and Ti6Al4V are much higher than known from tests. These high friction coefficients indicate that obviously an adhesion condition of the chip on the rake face is required to force shearing (internal friction) inside the chip. Possibly a dependence of the friction coefficient on temperature, sliding velocity and contact pressure should be considered in future investigations. A further improvement is expected when other aspects, such as temperatures, chip thicknesses, or the chip segment geometry are considered in the optimization as well. The difficulty here is to automate the measurement of the numerically predicted chip shapes within every loop of the optimization. If this is solved, one can also use the extended JC flow stress models within the parameter identification to be able to predict the chip segmentation at lower model resolutions already. Alternatively other constitutive models, e.g. with anisotropic hardening, can be used as well in the parameter identification but here the problem is that the larger amount of parameters to be fitted may needs supportive experiments for a proper down-selection of possible parameter ranges within the inverse parameter identification procedure.

CONCLUSIONS AND OUTLOOK

The complicated physics of the metal cutting process is a challenging task for the numerical simulation of such processes since various severe conditions are overlaid. Large deformations, high temperatures, strains and strain rates occur in the process zone in conjunction with the forming of new surfaces due to material separation. Classic numerical approaches like the FEM are fast and reliable approaches for problems that are subject to small deformations but applied to the simulation of metal cutting they require remeshing upon increasing mesh distortion. This leads to an enormous drawback in the computation times for such simulations as the cost for remeshing is intense.

An alternative method are meshfree methods which dissolve the continuum into particles and do not require remeshing upon large deformations or material separations since field values and their derivatives are approximated from the current neighbourhood of each particle being updated in every compute increment. This makes them unappealing in situations where deformations stay small due to higher computational cost compared to the FEM. In the simulation of a SHTB-experiment in this work the runtime difference between FEM and SPH, each computed on a single core of a CPU, was shown to be in the order of a factor 100 in favour of the FEM. On the other hand, the SPH becomes attractive in situations where large deformations occur. Exploiting the capabilities of GPGPU-computing allows for extremely short compute times in the order of minutes for the simulation of orthogonal cutting experiments at high speeds. This is so far a unique feature and sets a new state of the art in metal cutting simulations. With this acceleration it became possible to use the simulation tool for the inverse identification of material constitutive constants by optimization methods which require a huge amount of evaluations, e.g. within genetic algorithms. So far, such optimizations were only possible with the application of an analytical force model (OXLEY). The direct use of the FEM is possible only, when the number of evaluations is limited, e.g. with the SIMPLEX-method, and higher errors in the process forces are accepted. OXLEY's model was used in this work to inversely identify from almost every cutting experiment (510 tests) JC-CLASSIC material parameters with the SIMPLEX-method by minimizing the error in the process force prediction. There are two main findings:

- The material parameters show large scatter which does not allow to reduce the range of each material parameter for a large scale inverse identification with a numerical model of the cutting experiment.
- SIMPLEX traps sometimes into local minima. Therefore it should be envisaged to include more experimental data into the objective function of the optimization, for example, in addition to the process forces the chip thicknesses or temperatures.

In this work the inverse identification of material constitutive constants was done for two materials, Ck45 and Ti6Al4V, by means of numerical simulation models of the cutting

experiments - the cutting experiment itself served as a material test. Due to the GPU-acceleration, the numerical simulation models had compute times in the order of 3...4 minutes for every parameter set. For Ck45 the process force error was far lower than 1% for the identified parameter set, while for Ti6Al4V the cut force error was in the order 3% and for the feed force in the order of 5%. Using these material parameter sets for recalculation of cutting experiments at other feeds and cut speeds showed surprisingly for the well fitted Ck45 constants larger deviations in the process forces which are smallest for experiments being close to the conditions of the experiment which was used for the inverse identification of the constitutive model constants. A slightly different picture is seen for the identified constitutive model constants of Ti6Al4V where the deviations for predictions at higher cutting speeds are less than 10%. When simulating experiments at one third of the cut speed from the identification, the force errors increase to about 20% and when using for recalculations of experiments at only 5% of the cut speed of the identification the deviations increase to about 20% in the cut force and about 30% for the feed force.

In an attempt to improve the process force predictions, the friction coefficients were determined together with the material parameters for Ck45 and Ti6Al4V. While the process force errors at the process conditions of the experiment used for the inverse identification stayed at similar low levels, the prediction at other process conditions changed only slightly. For this reason another inverse identification was performed where the friction coefficient and the material parameters were inversely determined, but here the frictional shear stress was limited to the current shear yield limit of the material. This again did not lead to improvements in the process force prediction at other process conditions. It seems that the identified material parameters have limited validity in the proximity of the process conditions which were used for the inverse parameter identifications. A potential reason for this is the inability of the Johnson-Cook flow stress model to describe progressively increasing flow stresses towards higher strain rates. To improve here, the strain rate term of the Cowper-Symonds model [46] could be used instead at the expense of an additional material parameter to be identified.

Independent of the friction coefficient determination within the parameter identification or not, the comparison of experimental and simulated chip thicknesses revealed differences in the order of 30...40% for Ck45. This is not the case for Ti6Al4V - the chip thickness prediction was in general closer to the experimentally observed ones but still not sufficient.

All simulations suffer to correctly predict the resulting chip thicknesses. The chip segmentation of Ti6Al4V could not be predicted with the low particle resolution used within the numerical model for the inverse parameter identification. This is because the length scale of the shear layer is much smaller than the used particle length scale. If however the model resolution is increased drastically, the chip segmentation can be predicted at the cost of roughly 30x times increased computational time. Interestingly, the predicted process forces vary only slightly upon changes of the model resolution. These results show that empirical extensions of the JC-CLASSIC-model like those of Calamaz [38, 39] or Sima [224] are not required to model the chip segmentation. In future research it should be investigated in how far the chip segment shape prediction can be improved when using the aforementioned extensions of the JC-CLASSIC-model even though they would add at least four more empirical material constants which complicate the parameter identification even more. Alternatively,

the consideration of damage initiation and evolution was shown to predict chip segmentation with the JC-CLASSIC flow stress model but again adds another six parameters which need to be determined - be it inversely or by separate tests. A completely different attempt to tackle the problems would be the use of physical models which are - at least partially - able to describe the physics of the complex behaviour of Ti6Al4V, for example the model from [17] which was already successfully applied to metal cutting in [203, 205]. Improvements can be expected also when using constitutive models which consider anisotropic yield since it was shown that the loading path is not uniform in orthogonal cutting and the material investigation showed some indications for anisotropy in the raw material and for the Ck45 the analysis of the chip microstructure revealed that along the chip thickness only one heavily distorted grain remains with a very large aspect ratio. The application of the JC-CLASSIC flow stress model in such situations is questionable.

How much results can differ when changing from the JC-CLASSIC-model to another constitutive model, in this case the SCGL-model, was demonstrated in a numerical simulation of micro milling of OFHC copper. While JC-CLASSIC predicts almost no burr formation, the SCGL-model was able to reproduce the burr formation but to a slightly higher extent than experimentally observed. In this simulation still some improvements are to expect as for example the tool heat transfer was not modelled.

Another aspect that needs to be scrutinized is why the process force predictions are lower with the SPH when compared to the same numerical simulation with the FEM. This is seen with SPH in commercial solvers like ABAQUS and LS-DYNA as well as with the solver `MFREE_IWF` used in the investigations here and also reported in literature [229, 248]. The issue is so far not understood and probably stems from the remeshing in FEM where due to remapping from the old to the new mesh internal variables are dispersed. Further, distorted elements appear to have higher stiffness than the continuum, which is the actual reason for remeshing.

APPENDIX

11.1 STRESS STATES IN ORTHOGONAL CUTTING

11.1.1 Load Path Visualization Particle A

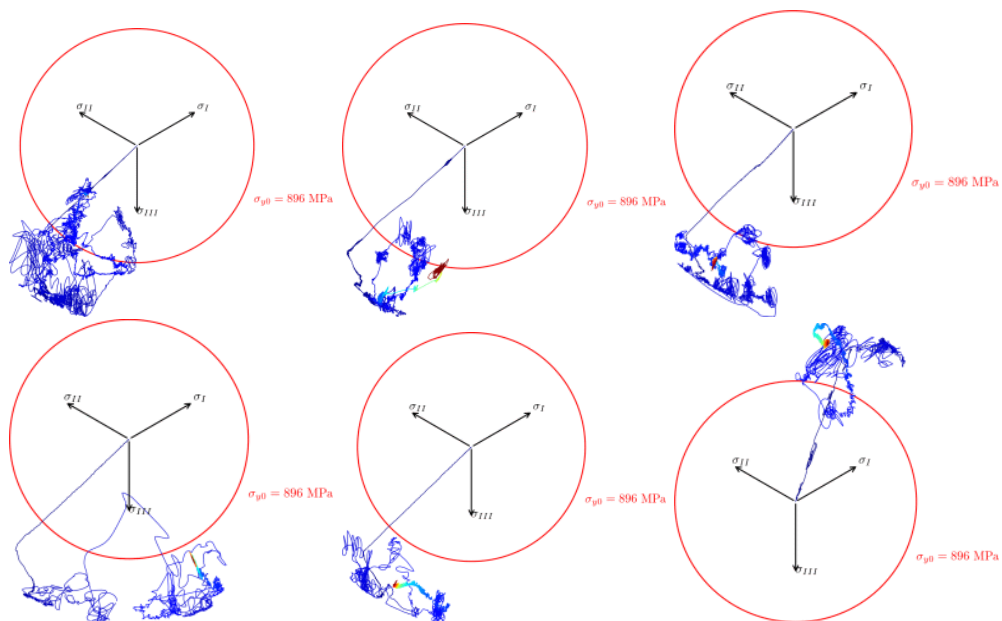


Figure 11.1: Load path visualization of particle A in the principal axis system. Top row case 1 (left), case 2 (middle) and case 3 (right), bottom row case 4 (left), case 5 (middle) and case 6 (right).

11.1.2 Load Path Visualization Particle D

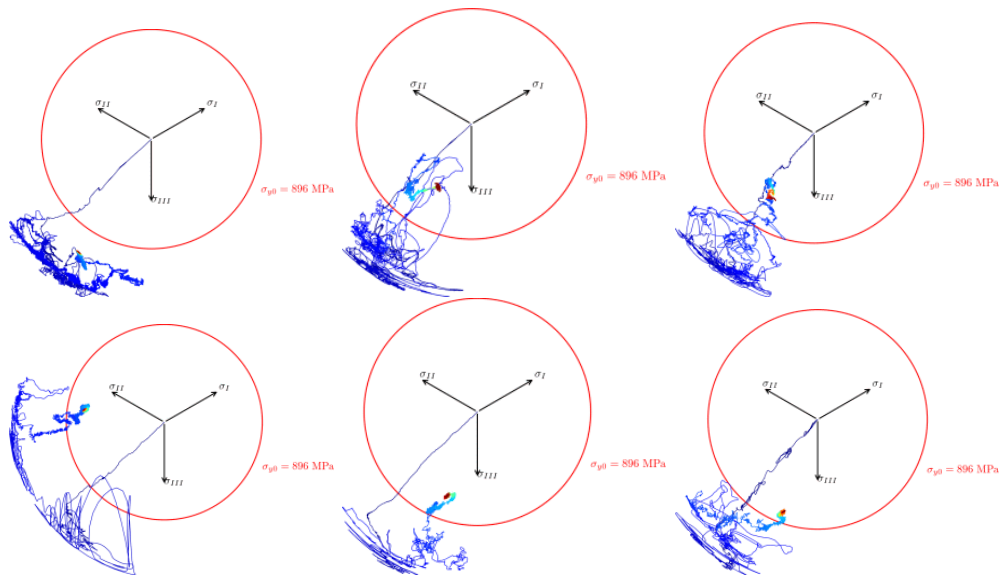


Figure 11.2: Load path visualization of particle D in the principal axis system. Top row case 1 (left), case 2 (middle) and case 3 (right), bottom row case 4 (left), case 5 (middle) and case 6 (right).

11.1.3 Load Path Visualization Particle E

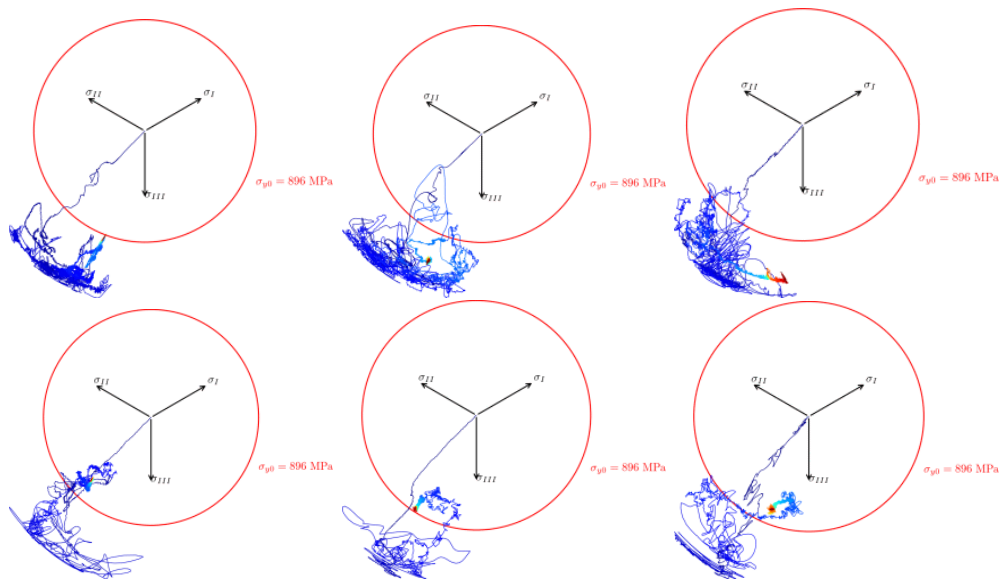


Figure 11.3: Load path visualization of particle E in the principal axis system. Top row case 1 (left), case 2 (middle) and case 3 (right), bottom row case 4 (left), case 5 (middle) and case 6 (right).

11.1.4 Load Path Visualization Particle K

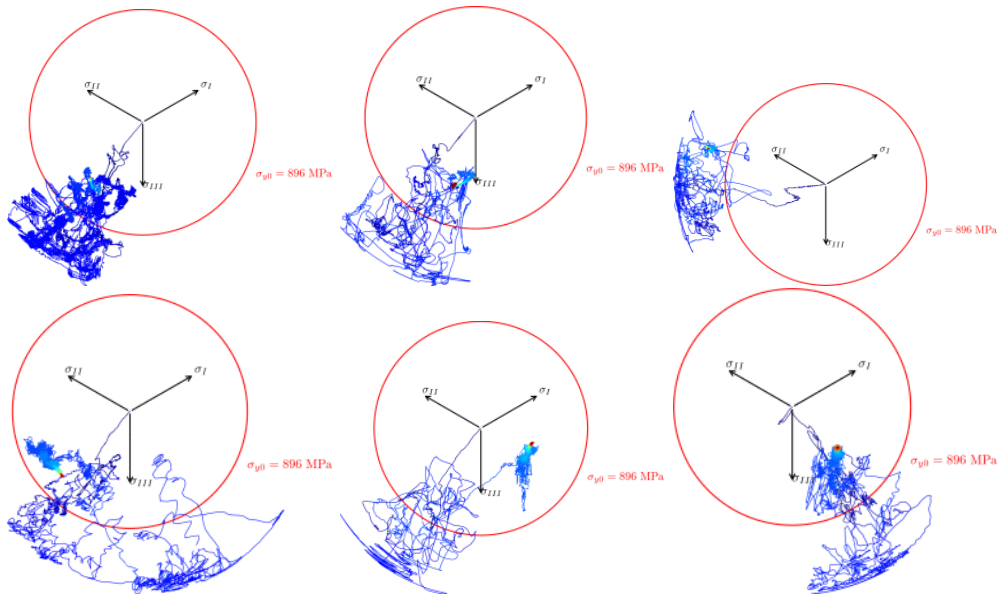


Figure 11.4: Load path visualization of particle K in the principal axis system. Top row case 1 (left), case 2 (middle) and case 3 (right), bottom row case 4 (left), case 5 (middle) and case 6 (right).

11.2 JC FLOW STRESS AND FRACTURE STRAIN MATERIAL USER SUBROUTINE VUMAT

11.2.1 Abaqus VUMAT User Subroutine

The following listing shows the VUMAT material user subroutine used for the FEM simulations of the 50SiB8 SHTB-test specimen with classic and modified JC fracture strain model from chapter 7.4.3.

```

C Subroutine für Abaqus/Explizit --> Werkstoff mit Johnson-Cook Fließ
  spannung; HK, So, 23.09.2018
C Basierend auf Matlabversion der radialen Rückprojektion für JC
C
C Elementlöschung über *DEPVAR, DELETE = Variablennummer: file:///home/
  hk/abqdoc/Documentation/docs/v6.14/books/usb/default.htm?startat=
  pt05ch26s07abm69.html#usb-mat-cusermat
C
C Adiabate Simulation mit plastischer Dissipation: muß auch hier
  implementiert werden mit eigener Statusvariable für die Temperatur,
  da Variablen TempOld / TempNew nicht beeinflußt werden können!
C
C ACHTUNG: Implizite Typvereinbarung: "The default implicit typing rule
  is that if the first letter of the name is I, J, K, L, M, or N,
  then the data type is integer, otherwise it is real."; implicit real
  (a-h,o-z)
C
C ACHTUNG2: Nur für 3D-Probleme zu verwenden!
C
C Modifikation (=universal) mit Werkstoffkennwertübergabe über die
  Abaqus-Input-Datei; HK, Fr, 26.04.2019
C
C
  *****
      SUBROUTINE VUMAT(NBLOCK, NDIR, NSHR, NSTATEV, NFIELDV, NPROPS, LANNEAL,
C Nur lesbar
      + StepTime, TotalTime, dt, CMName, CoordMP, CharLength,
      + Props, Density, StrainInc, RelSpinInc,
      + TempOld, StretchOld, DefGradOld, FieldOld,
      + StressOld, StateOld, EnerInternOld, EnerInelasOld,
      + TempNew, StretchNew, DefGradNew, FieldNew,
C Muß definiert werden
      + StressNew, StateNew,
C Kann definiert werden
      + EnerInternNew, EnerInelasNew)

      INCLUDE 'vaba_param.inc'

C Statusvariablen:
C STATE(*,1) = Plastische Vergleichsverzerrung
C STATE(*,2) = Plastische Vergleichsverzerrungsrate

```

APPENDIX

```

C STATE(*,3) = Temperatur (durch plastische Dissipation)
C STATE(*,4) = Schadenvariable (-> Element-/Partikellöschung über *
DEPVAR, DELETE=... siehe Kommentar oben)

      INTEGER NBLOCK, NDIR, NSHR, NPROPS, NSTATEV

      DIMENSION Props(NPROPS), Density(NBLOCK), COORDMP(NBLOCK,*),
+ CharLength(NBLOCK), StrainInc(NBLOCK, NDIR+NSHR),
+ RelSpinInc(NBLOCK, NSHR), TempOld(NBLOCK),
+ StretchOld(NBLOCK, NDIR+NSHR), DefGradOld(NBLOCK,NDIR+NSHR+NSHR)
+
+ FieldOld(NBLOCK,NFIELDV), StressOld(NBLOCK,NDIR+NSHR),
+ StateOld(NBLOCK, NSTATEV), EnerInternOld(NBLOCK),
+ EnerInelasOld(NBLOCK), TempNew(NBLOCK),
+ StretchNew(NBLOCK,NDIR+NSHR), DefGradNew(NBLOCK,NDIR+NSHR+NSHR),
+ FieldNew(NBLOCK, NFIELDV), StressNew(NBLOCK,NDIR+NSHR),
+ StateNew(NBLOCK, NSTATEV), EnerInternNew(NBLOCK),
+ EnerInelasNew(NBLOCK)

      CHARACTER*80 CMNAME

C NBLOCK      - Anzahl zu bearbeitender materieller Punkte in diesem
Schleifendurchlauf
C NDIR        - Anzahl direkter Komponenten eines symmetrischen Tensors
C NSHR        - Anzahl indirekter Komponenten eines symmetrischen Tensors
C NPROPS      - Anzahl übergebener Eigenschaften (Werkstoffkennwerte)
C NSTATEV     - Anzahl Statusvariablen

C      IMPLICIT NONE
C      IMPLICIT INTEGER (i-k)
C
C *****
C *** Erste Zeile einlesen (1-8) *****
C *****
      p_E = Props(1)
      p_nu = Props(2)
C *****
C      Johnson-Cook Fließspannungskennwerte
      p_A = Props(3)
      p_B = Props(4)
      p_C = Props(5)
      p_m = Props(6)
      p_n = Props(7)
C      Zulässiger Fehler für radiale Rückkehrprojektion
      p_maxFehlerRR = Props(8)
C *****
C *** Zweite Zeile einlesen (9-16) *****
C *****
C      Schmelztemperatur für JC-Fließspannung
      T_m = Props(9)
C      Raumtemperatur für JC-Fließspannung

```



```

      T_R = Props(10)
C   Referenz Dehnrage für JC-Fließspannung
      eps_pl_ref = Props(11)
C   ****
C   Taylor-Quinney Koeffizient
      p_TQ = Props(12)
      p_cp = Props(13)
C   ****
C   *** Dritte Zeile einlesen (17-24) ****
C   ****
C   JC- Schadenmodell (klassisch)
      p_D1 = Props(17)
      p_D2 = Props(18)
      p_D3 = Props(19)
      p_D4 = Props(20)
      p_D5 = Props(21)
      p_Damage_eps_pl_ref = Props(22)
C   ****
C   *** Vierte Zeile einlesen (25-32) ****
C   ****
C   *** Achtung, wenn M.GG Erweiterung für den ****
C   *** T-Term benutzt wird, wird D5 ****
C   *** überschrieben! ****
      IF (NPROPS .GT. 24) THEN
          p_D5 = Props(25)
          p_D6 = Props(26)
          p_D7 = Props(27)
          p_D8 = Props(28)
      ENDIF
C   ****
C
      p_G = p_E/(2.0*(1.0+p_nu))
      p_K = 2.0*p_G*(1.0+p_nu)/(3.0*(1.0-2.0*p_nu))
C
      p_LambdaLame = p_K - 2.0 * p_G / 3.0
C   ****
C
C   PRINT *, "E: ", p_E, ", G: ", p_G, ", K: ", p_K, ", nu: ", p_nu
      delta_t = dt

C   Schleife über aktuellen Block materieller Punkte
      DO km = 1, NBLOCK
C   Plastische Vergleichsverzerrung / -srate initialisieren, wenn
      Totalzeit = 0
          eps_Vgl = StateOld(km, 1)
          eps_Vgl_Rate = StateOld(km, 2)
C   Adiabate Temperatur (-> Taylor-Quinney)
          T_Adiabat = StateOld(km,3)
C   Schadenvariable
          Schaden = StateOld(km,4)
C   Variable für Lösungsstatus (1 - aktiv, 0 - inaktiv)

```

APPENDIX

```

        StatusLoeschung = StateOld(km,5)
C   Statusvariablen im ersten Schritt initialisieren
C   ACHTUNG: Scheinbar werden diese Werte später in den Feldern nicht
        gesichert! HK, Fr, 28.09.2018 --> TODO: kontrollieren
        IF (TotalTime .EQ. 0.0) THEN
            eps_Vgl = 0.0
            eps_Vgl_Rate = 0.0
            T_Adiabat = T_R
            Schaden = 0.0
            StatusLoeschung = 1.0

            IF (km .EQ. 1) THEN
                PRINT*, "JC_A:", p_A, "JC_B:", p_B, "JC_C:", p_C,
+                 "JC_m:", p_m, "JC_n:", p_n
                PRINT*, "JC_D1:", p_D1, "JC_D2:", p_D2, "JC_D3:", p_D3,
+                 "JC_D4:", p_D4, "JC_D5:", p_D5
C             PRINT*, "NBlock: ", NBLOCK
            ENDIF
        ENDIF
C *****
C Deformationsgradient sichern *****
C *****
        IF (NSTATEV.GT.5) THEN
            DO I = 1, 9
                StateNew(km, 5+I) = DefGradNew(km, I) !
                Deformationsgradienten vom Inkrementende sichern
            END DO
        ENDIF
C *****
        IF (T_Adiabat.LT.T_R) T_Adiabat = T_R ! Sicherheitshalber,
        falls Initialisierung nicht wie vorgesehen läuft!
C *****
C S - Cauchy Spannungstensor zum Inkrementbeginn
        Sxx = StressOld(km, 1)
        Syy = StressOld(km, 2)
        Szz = StressOld(km, 3)
        Sxy = StressOld(km, 4)
        Syz = StressOld(km, 5)
        Szx = StressOld(km, 6)
C     print *, "Cauchyspannungen ausgelesen"
C     print *, "S1: ", Sxx, ", S2: ", Syy, ", S3: ", Szz, ", S4: ",
C     +     Sxy, ", S5: ", Syz, ", S6: ", Szx
        SHydro = (Sxx + Syy + Szz)/3.0
C Sd - Spannungsdeviator zum Inkrementbeginn
        Sdxx = Sxx - SHydro
        Sdyy = Syy - SHydro
        Sdzz = Szz - SHydro
        Sdxy = Sxy
        Sdyz = Syz
        Sdzx = Szx

```

```

C ACHTUNG: Schubdehnungen hier mit Faktor 2! (Abaqus-Konvention); HK,
  Do, 27.09.2018
      Sdxx = Sdxx + 2.0*p_G * StrainInc(km,1)
      Sdyy = Sdyy + 2.0*p_G * StrainInc(km,2)
      Sdzz = Sdzz + 2.0*p_G * StrainInc(km,3)
      Sdxy = Sdxy + 2.0*p_G * StrainInc(km,4)
      Sdyz = Sdyz + 2.0*p_G * StrainInc(km,5)
      Sdzx = Sdzx + 2.0*p_G * StrainInc(km,6)

C
      EpsInkr_Spur = StrainInc(km,1)+StrainInc(km,2)+StrainInc(km,3)
      SHydroNeu = SHydro + p_LambdaLame * EpsInkr_Spur
C - Norm der Testspannung
      STrialNorm = sqrt(Sdxx**2.0+Sdyy**2.0+Sdzz**2.0+
+      2.0*(Sdxy**2.0+Sdyz**2.0+Sdzx**2.0))
C Misesspannung
      SvM = sqrt(3.0/2.0)*STrialNorm
C Fließgrenze
C      SigY_JC = SyJC(p_A,p_B,p_C,p_m,p_n,eps_pl_ref ,
C      +      eps_Vgl,eps_Vgl_Rate,TempOld(km),T_R,T_m)
      SigY_JC = SyJC(p_A,p_B,p_C,p_m,p_n,eps_pl_ref ,
+      eps_Vgl,0.0,T_Adiabat,T_R,T_m)
C Unterhalb der Fließgrenze rein elastischer Schritt
      IF (SvM .LE. SigY_JC) THEN
C Unterhalb der Fließgrenze rein elastischer Schritt, 3% Fließflä
chenfehler erlauben (bessere Konvergenz, da pl. Multiplikatoren größ
er werden)
C      IF (SvM .LE. (1.03 * SigY_JC)) THEN
          StateNew(km, 1) = eps_Vgl
C          StateNew(km, 2) = eps_Vgl_Rate
          StateNew(km, 2) = 0.0
          StateNew(km, 3) = T_Adiabat
          StateNew(km, 4) = Schaden
          StateNew(km, 5) = StatusLoeschung
C
          StressNew(km,1) = Sdxx + SHydroNeu
          StressNew(km,2) = Sdyy + SHydroNeu
          StressNew(km,3) = Sdzz + SHydroNeu
          StressNew(km,4) = Sdxy
          StressNew(km,5) = Sdyz
          StressNew(km,6) = Sdzx
C          Plastische Dehnungsraten, Spannungen und
Temperaturraten sichern *****
          IF (NSTATEV.GT.14) THEN
              StateNew(km, 15) = eps_Vgl_Rate      ! Plastische
              Dehnungsrate sichern
              StateNew(km, 16) = SvM              ! Spannung (Mises)
              sichern
              StateNew(km, 17) = 0.0              ! Temperaturrate [K/
              s] sichern
          ENDIF

```

APPENDIX

```

        CYCLE      ! nächsten Integrationspunkt bearbeiten, da
                   elastisches MV vorliegt
    ENDIF

C      PRINT *, "SvM: ", SvM, ", SigYJC: ",SigY_JC,", T: ",TempOld(
km)
C      PRINT *, "SvM: ", SvM, ", SigYJC: ",SigY_JC,", T: ",T_Adiabat

C Plastischer Multiplikator, Initialisierung
C      p_lambda1 = 1e-9 ! Macht bei Single Precision keinen Sinn!
      p_lambda1 = 1e-6
C      p_lambda = 1e-7
      g1 = 2*p_maxFehlerRR

C
      nSchleife = 0
      maxnS = 100
      DO WHILE ((g1 .GT. p_maxFehlerRR) .AND. (nSchleife .LT. maxnS)
)
C
      nSchleife=nSchleife+1
C      PRINT *, nSchleife, p_lambda1, g1
C
      eps_Vgl1 = eps_Vgl + p_lambda1 * sqrt(2.0/3.0)
      eps_Vgl_Rate1 = (eps_Vgl1-eps_Vgl) / delta_t

C
      SigY_JC1 = SyJC(p_A,p_B,p_C,p_m,p_n,eps_pl_ref,
+      eps_Vgl1,eps_Vgl_Rate1,T_Adiabat,T_R,T_m)
C
C Fließflächenfehler bei aktuellem lambda
      g1 = STrialNorm - 2.0 * p_G * p_lambda1 -
+      sqrt(2.0/3.0) * SigY_JC1
C Lambda1 für zweiten Stützpunkt für Sekantenverfahren
      p_lambda2 = p_lambda1 * 1.01;
C Vergleichsdehnung und -srate für zweiten Stützpunkt
      eps_Vgl2 = eps_Vgl + p_lambda2 * sqrt(2.0/3.0)
      eps_Vgl_Rate2 = (eps_Vgl2-eps_Vgl) / delta_t
C JC-Fließgrenze für zweiten Stützpunkt; Term_C (Temperatur) wird als
unveränderlich angenommen im Inkrement
      SigY_JC2 = SyJC(p_A,p_B,p_C,p_m,p_n,eps_pl_ref,
+      eps_Vgl2,eps_Vgl_Rate2,T_Adiabat,T_R,T_m)
C Fließflächenfehler bei aktuellem lambda1
      g2 = STrialNorm - 2.0 * p_G * p_lambda2 -
+      sqrt(2.0/3.0) * SigY_JC2
C Sekantenverfahren
      delta_l = p_lambda1 - p_lambda2;
      delta_g = g1 - g2;

C
C      PRINT *, "delta_lambda: ", delta_l, ", delta_g: ",
delta_g,
C      +      ",g1:",g1,", g2: ",g2,", l1: ",p_lambda1,",l2:",
p_lambda2,

```

```

C      +           ", SigY1: ", SigY_JC1, ", SigY2: ", SigY_JC2
C      Anstieg für Sekantenverfahren
          AnstiegSekante = delta_g / delta_l;
C      Neues lambda
          IF ((g1 / AnstiegSekante) .GT. p_lambda1) THEN
              p_lambda1 = p_lambda1 / 10.0;
          ELSE
              p_lambda1 = p_lambda1 - g1 / AnstiegSekante;
          ENDIF
C      Schleifenende über Fehler:maxFehlerRR implementieren! HK, Di,
25.09.2018
          END DO
C
          eps_Vgl1 = eps_Vgl + p_lambda1 * sqrt(2.0/3.0);
          eps_Vgl_Rate1 = (eps_Vgl1-eps_Vgl) / delta_t;
C
C      Temperaturerhöhung per TQ berechnen
          delta_Temp = 0.0      ! Initialisierung
          IF ((p_TQ.GT.0.0).AND.(eps_Vgl_Rate1.GT.0.0)) THEN      ! Nur
              Ausführung wenn TQ-Koeffz > 0,0
              SY = SyJC(p_A,p_B,p_C,p_m,p_n,eps_pl_ref ,
+                  eps_Vgl1,eps_Vgl_Rate1,T_Adiabat,T_R,T_m)
              delta_Temp=dt_TQ(eps_Vgl1-eps_Vgl,density(km),p_cp,p_TQ,SY)
          ENDIF
C      Schaden berechnen, Modell beliebig
C
          Delta_Schaden = 0.0
          IF (eps_Vgl_Rate1.GT.0.0) THEN      ! Schadeninkrement nur bei
              aktivem Fließen im Inkrement ausführen
              SY = SyJC(p_A,p_B,p_C,p_m,p_n,eps_pl_ref ,
+                  eps_Vgl1,eps_Vgl_Rate1,T_Adiabat,T_R,T_m)
              SigStar = SHydroNeu/SY
              TStar = (T_Adiabat + delta_Temp - T_R)/(T_m-T_R)
              d_eps_pl = eps_Vgl_Rate1 * delta_t
              IF (NPROPS .EQ. 24) THEN
                  Delta_Schaden = Damage_JC(p_D1, p_D2, p_D3, p_D4, p_D5,
+                  TStar, SigStar, eps_Vgl1, d_eps_pl,
+                  eps_Vgl_Rate1/p_Damage_eps_pl_ref)
              ELSE IF(NPROPS .EQ.32) THEN
                  Delta_Schaden = Damage_JC_GG(p_D1, p_D2, p_D3, p_D4,
+                  p_D5, p_D6, p_D7, p_D8, TStar, SigStar, eps_Vgl1,
+                  d_eps_pl, eps_Vgl_Rate1/p_Damage_eps_pl_ref)
              ELSE
                  Delta_Schaden = 0.0
              ENDIF
          ENDIF
C
C      Statusvariablen am Inkrementende sichern

```

```

StateNew(km, 1) = eps_Vgl1
StateNew(km, 2) = eps_Vgl_Rate1
T_Adiabat_neu = T_Adiabat + delta_Temp
IF (T_Adiabat_neu .GT. T_m) T_Adiabat_neu = T_m      ! Hö
    chsttemperatur auf die Schmelztemperatur limitieren
StateNew(km, 3) = T_Adiabat_neu ! Temperaturerhöhung durch
    plastische Dissipation
SchadenNeu = Schaden + Delta_Schaden
IF (SchadenNeu .GE. 1.0) THEN
    SchadenNeu = 1.0
    StatusLoeschung = 0.0
    PRINT *, "IntPunkt gelöscht, bei eps_pl: ", eps_Vgl1
    PRINT *, "eps_pl_alt: ", eps_Vgl
    PRINT *, " Spannung: ", SY
    PRINT *, " Aktuelle Bruchdehnung: ", d_eps_pl/Delta_Schaden
ENDIF
StateNew(km, 4) = SchadenNeu
StateNew(km, 5) = StatusLoeschung
C
Sxx = Sdxx+SHydroNeu-Sdxx/STrialNorm*p_lambda1*2.*p_G
Syy = Sdyy+SHydroNeu-Sdyy/STrialNorm*p_lambda1*2.*p_G
Szz = Sdzz+SHydroNeu-Sdzz/STrialNorm*p_lambda1*2.*p_G
Sxy = Sdxy - Sdxy/STrialNorm * p_lambda1 * 2.0 * p_G
Syz = Sdyz - Sdyz/STrialNorm * p_lambda1 * 2.0 * p_G
Szx = Sdzx - Sdzx/STrialNorm * p_lambda1 * 2.0 * p_G
C
StressNew(km,1)= Sxx
StressNew(km,2)= Syy
StressNew(km,3)= Szz
StressNew(km,4)= Sxy
StressNew(km,5)= Syz
StressNew(km,6)= Szx
C
C          Plastische Dehnungsraten, Temperaturrate und
Spannungen sichern *****
IF (NSTATEV.GT.14) THEN
    StateNew(km, 15) = eps_Vgl_Rate1 ! Plastische Dehnungsrate
        sichern
C          Misesspannung nach radialer Rückkehr
*****
    SvM = sqrt(0.5*((Sxx-Syy)**2 + (Syy-Szz)**2 + (Szz-Sxx)**2)
        +
        + 3.0*(Sxy**2+Syz**2+Szx**2))
C
    StateNew(km, 16) = SvM                ! Spannung
        (Mises) sichern
    StateNew(km, 17) = delta_Temp / delta_t !
        Temperaturrate [K/Zeit] sichern
ENDIF
C
END DO

```

```
RETURN
```

```
END
```

```
C
```

```
*****
```

```
C *** Fließspannung nach Johnson-Cook
```

```
C
```

```
FUNCTION SyJC(pA,pB,pC,pm,pn,eps0,eps,epsRate,T,TR,Tm)
```

```
C
```

```
C Dehnungsabhängiger Term
```

```
Term_A = pA+pB*eps**pn
```

```
C Dehnratenabhängiger Term; Weiche für epsRate<eps0 -> sonst Abstürze
```

```
Term_B = 1.0
```

```
IF (epsRate .GE. eps0) THEN
```

```
Term_B = 1.0+pC*log(epsRate/eps0)
```

```
END IF
```

```
C Temperaturabhängiger Term
```

```
theta = 0.0
```

```
IF (T.GE.TR) THEN
```

```
theta = (T - TR)/(Tm-TR)
```

```
END IF
```

```
Term_C = 1.0-theta**pm
```

```
SyJC = Term_A * Term_B * Term_C
```

```
C
```

```
C PRINT *, pA,",",pB,",",pC,",",pm,",",pn,",",eps0,",",eps,",",  
C + epsRate,",",T,",",TR,",",Tm,",Y:",SyJC
```

```
RETURN
```

```
END
```

```
C
```

```
*****
```

```
C *** Temperaturerhöhung durch plastische Dissipation (Taylor-Quinney)
```

```
C
```

```
FUNCTION dt_TQ(delta_eps_pl, rho, cp, TQ, sigmaY)
```

```
C
```

```
C delta_eps_pl - plastisches Vergleichsdehnungsinkrement
```

```
C rho - Dichte
```

```
C cp - spezifische Wärmekapazität
```

```
C TQ - Taylor-Quinney Koeffizient
```

```
C sigmaY - aktuelle Fließspannung
```

```
C
```

```
C dt_TQ = 0.0
```

```
dt_TQ = TQ/(cp*rho)*delta_eps_pl*sigmaY;
```

```
C
```

```
C PRINT *, dt_TQ
```

```
C
```

APPENDIX

```

RETURN
END
C
C
*****
C *** Bruchdehnung nach Johnson-Cook (1985)
C
FUNCTION Damage_JC(D1, D2, D3, D4, D5, TStar, SigStar,
+ eps_tot, delta_eps_pl, epsRate)
C
C D1-D5:      JC-Bruchdehnungskonstanten
C SigStar:    Verhältnis Misesspannung zu Fließspannung (
Mehrachsigkeit)
C TStar:      Dimensionslose Temperatur, analog zu "theta" in JC-Flie
ßspannung
C eps:        Plastisches Dehnungsinkrement
C epsRate:    Dehnrate
C
C Damage_JC:  gibt Verhältnis von aktuellem pl. Dehnungsinkrement zur
aktuellen Bruchdehnung zurück (Schadenzuwachs bei linearer
Akkumulation)
C
Damage_JC = 0.0
C
IF (epsRate .LT. 1.0) epsRate = 1.0
epsB = (D1+D2*EXP(D3*SigStar))*(1.0+D4*LOG(epsRate))*(1.0+D5*TStar
)
IF (epsB .LE. 0.0) epsB = 1e-09
Damage_JC = delta_eps_pl/epsB
C
RETURN
END
C
C
*****
C *** Modifizierte Bruchdehnung Gerstgrasser, nach Johnson-Cook (1985)
C *** nach Glg. 38 im Veröffentlichungsentwurf von 2018
C
FUNCTION Damage_JC_GG(D1, D2, D3, D4, D5, D6, D7, D8, TStar,
+ SigStar, eps_tot, delta_eps_pl, epsRate)
C
C D1-D4:      Klassische JC-Bruchdehnungskonstanten
C D5-D8:      JC-Erweiterungskonstanten für Temperatur (Gerstgrasser)

```



```

C   SigStar:    Verhältnis Misesspannung zu Fließspannung (
C   Mehrachsigkeit)
C   TStar:     Dimensionslose Temperatur, analog zu "theta" in JC-Flie
C   ßspannung
C   eps:       Plastisches Dehnungsinkrement
C   epsRate:   Dehnrage
C
C   Damage_JC: gibt Verhältnis von aktuellem pl. Dehnungsinkrement zur
C   aktuellen Bruchdehnung zurück (Schadenzuwachs bei linearer
C   Akkumulation)
C
C       Damage_JC = 0.0
C
C       IF (epsRate .LT. 1.0) epsRate = 1.0
C
C       TFak = 1.0 + D5*TStar + D6*TStar**2 + D7*TStar**3 + D8*TStar**4
C
C   ***** Modifikation HK, Di, 28.04.2020 *****
C       IF (TFak .GT. 2.5) THEN
C           TFak = 2.5
C       PRINT *, "Temperaturfaktor JC-modGG gekappt auf 2,5"
C       END IF
C   *****
C
C       epsB = (D1+D2*EXP(D3*SigStar))*(1.0+D4*LOG(epsRate))*(1.0+D5*
C   TStar)
C       epsB = (D1+D2*EXP(D3*SigStar)) * (1.0+D4*LOG(epsRate)) * TFak
C       IF (epsB .LE. 0.0) epsB = 1e-09
C
C       Damage_JC = delta_eps_pl/epsB
C
C       RETURN
C       END
C

```

11.2.2 Abaqus Input File Template

The subroutine requires the specification of the Abaqus *USER MATERIAL-card to specify the material parameters to be used in the VUMAT user subroutine. When the user material definition contains 3 lines, the classic JC fracture strain model (3.165) is used, when it contains 4 lines the modified JC fracture strain model (7.35) is used. An input file template is presented in the following where first the *PARAMETER-card is used to define all material constants in variables which are then replaced in the *USER MATERIAL-card for the classic JC fracture strain and modified JC fracture strain model.

```

*PARAMETER
** 24 -> JC-Schaden klassisch, 32-> JC-Schaden Erweiterung GG
JC_A = 430.9E6
JC_B = 908.7E6

```

APPENDIX

```

JC_C = 0.00447
JC_m = 0.7361
JC_n = 0.3854
maxRRFehler = 1E-6
JC_Tmelt = 2006.0
JC_Tref = 293.15
JC_epsplref = 1E-3
JC_TQ = 0.9
JC_cp = 466.0
** JC-Schadenmodell
JC_D1 = 0.0733
JC_D2 = 0.7204
JC_D3 = -1.5643
JC_D4 = 0.0371
JC_D5 = 1.5583
JC_Depsref = 1E-3
** JC-Schadenmodell, Erweiterung GG
JCGG_D5 = -3.5642
JCGG_D6 = 69.5723
JCGG_D7 = -318.5630
JCGG_D8 = 428.9243
*****
*MATERIAL, NAME=JC_50SiB8_HK_VUMAT_JCGG
*USER MATERIAL, TYPE=MECHANICAL, CONSTANTS=32
**E,          nu,          A,          B,
              C.          m,          n,
              max_RadialReturnFehler
2.14e+11,     0.334875,     <JC_A>,     <JC_B>, <JC_C>, <JC_m>,
              <JC_n>, <maxRRFehler>,
** Tmelt,     Tref,     eps_pl_ref,     TQ,          cp
<JC_Tmelt>, <JC_Tref>, <JC_epsplref>, <JC_TQ>, <JC_cp>
** Schadenmodell: D1, D2, D3, D4, D5, eps_pl_ref
<JC_D1>, <JC_D2>, <JC_D3>, <JC_D4>, <JC_D5>, <JC_Depsref>
** Schadenmodell: D5, D6, D7, D8 (Erweiterung M. GG)
<JCGG_D5>, <JCGG_D6>, <JCGG_D7>, <JCGG_D8>
*****
*MATERIAL, NAME=JC_50SiB8_HK_VUMAT_klassisch
*USER MATERIAL, TYPE=MECHANICAL, CONSTANTS=24
**E,          nu,          A,          B,
              C.          m,          n,
              max_RadialReturnFehler
2.14e+11,     0.334875,     <JC_A>,     <JC_B>, <JC_C>, <JC_m>,
              <JC_n>, <maxRRFehler>,
** Tmelt,     Tref,     eps_pl_ref,     TQ,          cp
<JC_Tmelt>, <JC_Tref>, <JC_epsplref>, <JC_TQ>, <JC_cp>
** Schadenmodell: D1, D2, D3, D4, D5, eps_pl_ref
<JC_D1>, <JC_D2>, <JC_D3>, <JC_D4>, <JC_D5>, <JC_Depsref>

```

For the display of results quantities from the user subroutine the Abaqus *DEPVAR-card for user dependent variables is used with the fifth variable defined as the damage status

variable DELETE=5 for element deletion. The string after the number defines the displayed variable identifier (output variable key) for postprocessing:

```
*DEPVAR, DELETE=5
5
1, PEEQ, "Plastic strain"
2, EPS_PL_Rate, "Plastic strain rate"
3, Temperatur, "Temperature"
4, Schaden, "Damage variable"
5, Status, "Activity status of the integration point"
```

11.3 ORTHOGONAL CUTTING EXPERIMENTS

The cutting test results are provided for Ti6Al4V (V0001-V0068, V0301-V0520) in table 11.1 and for Ck45 (V0069-V0300) in table 11.2. The process forces F_c and F_f were normalized to a cutting width of $w = 1\text{mm}$ and are given together with their respective standard deviations μ_{F_c} and μ_{F_f} . The second last two columns contain the averaged cutting edge radius r_n and its standard deviation μ_{r_n} . The last column STATUS gives a quality statement of the process forces. Tests labelled with **ok** are without any objections. Tests labelled **short** have to be treated with care as prolongations of such experiments is recommended. If however the standard deviations in the process forces of such tests are small, they still can be considered as valid. Results from tests labelled **questionable** or **initially stable** should not be used for parameter identifications while tests labelled with **saturation** ran into the amplifier limits and are therefore invalid for further use. Tests marked **instable** are most likely of insufficient quality and must not be used for parameter identifications.

Test	v_c [m/min]	f [mm]	F_c [N]	μ_{F_c} [N]	F_f [N]	μ_{F_f} [N]	r_n [μm]	μ_{r_n} [μm]	Status
V0001	10.5	0.01	55.7	2.1	83.8	4.9	37.1	2.0	ok
V0002	12.6	0.01	55.2	1.8	76.4	4.2	32.0	2.4	ok
V0003	10.5	0.01	57.4	1.8	80.7	4.6	30.8	4.0	ok
V0004	12.6	0.1	214.0	7.7	149.0	6.5	33.5	3.2	ok
V0005	10.5	0.1	209.1	7.0	130.7	5.2	27.4	5.0	ok
V0006	12.6	0.1	210.4	7.0	138.1	6.0	29.8	2.1	ok
V0010	10.5	0.2	361.3	15.3	189.1	7.1	31.4	2.4	ok
V0011	12.6	0.2	363.5	14.2	182.5	6.2	28.1	5.7	ok
V0012	10.5	0.2	366.1	14.5	199.1	7.4	31.7	2.9	ok
V0013	12.6	0.01	54.9	1.8	76.2	4.4	32.0	4.1	ok
V0014	10.5	0.01	53.3	1.6	70.2	3.8	25.4	3.3	ok
V0015	12.6	0.01	53.8	1.6	74.0	4.0	31.6	4.0	ok
V0016	10.5	0.1	207.0	6.6	132.8	5.0	28.9	3.9	ok
V0017	12.6	0.1	208.0	7.2	138.3	5.6	31.3	2.1	ok
V0018	10.5	0.1	211.4	7.2	141.6	6.2	31.9	2.0	ok
V0019	12.6	0.2	362.2	13.9	181.2	6.4	26.2	3.1	ok
V0020	10.5	0.2	360.2	12.0	179.2	5.6	25.2	3.8	ok
V0021	12.6	0.2	358.8	12.8	186.6	6.7	30.5	2.1	ok
V0022	74.3	0.01	40.3	1.2	61.0	2.7	27.2	3.3	ok
V0024	74.3	0.01	42.7	1.3	73.2	3.3	34.2	2.9	ok
V0025	88.9	0.1	194.8	5.4	133.6	3.8	31.3	2.8	short
V0026	74.3	0.1	195.9	5.3	137.5	4.6	33.6	5.3	short
V0027	88.9	0.1	196.3	4.2	139.4	3.3	30.8	2.5	short
V0028	74.3	0.2	316.1	9.1	170.5	3.8	32.0	1.9	short
V0029	88.9	0.2	308.8	4.5	147.6	2.3	27.1	4.0	short
V0030	74.3	0.2	319.2	6.7	172.1	3.3	33.3	1.8	short
V0031	190.5	0.01	35.1	0.7	53.2	1.1	23.8	1.9	ok
V0032	159.1	0.01	37.1	1.0	64.2	1.4	29.1	2.9	ok
V0033	190.5	0.01	41.3	0.7	79.2	1.3	34.2	1.7	ok

Test	v_c [m/min]	f [mm]	F_c [N]	μ_{F_c} [N]	F_f [N]	μ_{F_f} [N]	r_n [μ m]	μ_{r_n} [μ m]	Status
V0034	159.1	0.1	179.4	4.6	126.9	2.2	33.6	2.4	short
V0035	190.5	0.1	175.5	1.4	119.2	0.8	32.7	1.8	short
V0037	159.1	0.2	288.5	6.2	144.5	2.8	29.7	4.0	short
V0038	190.5	0.2	289.8	4.8	158.9	2.4	32.8	2.2	short
V0039	159.1	0.2	289.2	3.3	145.0	2.2	29.3	3.6	short
V0040	190.5	0.4	491.3	7.5	225.5	9.3	28.9	4.2	short
V0041	159.1	0.4	471.4	16.9	203.5	19.6	33.3	2.9	short
V0042	190.5	0.4	490.8	8.5	238.2	8.3	35.6	2.4	short
V0043	212.2	0.01	36.0	1.1	67.5	1.4	30.0	4.3	ok
V0044	254.1	0.01	42.3	0.8	84.2	1.5	37.5	1.7	ok
V0045	212.2	0.01	38.0	0.9	66.4	1.5	30.5	2.0	ok
V0046	254.1	0.01	39.5	0.8	72.5	1.2	32.1	3.6	ok
V0047	212.2	0.1	171.0	2.3	120.9	1.0	33.8	2.8	short
V0048	254.1	0.1	168.3	2.3	119.0	1.9	32.9	2.5	short
V0049	212.2	0.1	171.8	2.8	126.7	2.0	36.8	1.9	short
V0050	254.1	0.2	269.5	4.1	145.0	2.9	31.4	2.1	short
V0051	212.2	0.2	288.3	6.1	165.0	4.4	37.5	2.1	short
V0052	254.1	0.2	271.2	7.1	143.7	4.7	31.3	2.8	short
V0053	212.2	0.4	481.5	13.6	214.9	5.9	31.7	2.3	short
V0054	254.1	0.4	449.8	12.2	208.4	7.9	35.3	3.4	short
V0055	212.2	0.4	483.4	8.0	216.1	4.1	33.4	3.7	short
V0056	381.3	0.01	38.6	0.7	68.6	1.2	33.0	3.0	ok
V0057	318.5	0.01	38.0	0.8	69.0	1.2	34.2	2.2	ok
V0058	381.3	0.01	36.2	0.7	61.0	1.0	28.4	2.3	ok
V0059	318.5	0.1	162.0	3.5	112.1	2.6	32.2	2.2	short
V0060	381.3	0.1	157.5	3.3	115.5	2.8	33.0	2.4	short
V0061	318.5	0.1	159.1	3.8	104.9	3.0	28.7	4.6	short
V0062	381.3	0.2	262.1	5.7	162.7	11.8	34.1	2.1	short
V0063	318.5	0.2	270.3	4.9	158.3	6.0	32.5	2.1	short
V0064	381.3	0.2	260.0	4.3	165.6	9.5	35.2	2.7	short
V0065	318.5	0.4	455.6	10.5	272.1	32.2	36.8	2.2	short
V0066	381.3	0.4	468.5	9.4	412.3	59.6	34.8	2.1	short
V0067	318.5	0.4	453.9	12.1	253.6	28.6	35.8	4.2	short
V0068	254.1	0.2	299.5	12.7	305.9	103.5	29.8	5.0	instable
V0301	10.0	0.02	79.0	2.3	85.7	5.3	36.8	3.0	ok
V0302	10.0	0.02	83.5	2.4	97.2	5.9	41.2	2.2	ok
V0303	10.0	0.02	78.5	2.2	84.9	5.3	34.1	2.8	ok
V0304	10.0	0.06	155.4	4.8	121.7	6.5	40.6	2.4	ok
V0305	10.0	0.06	154.3	4.9	118.9	6.5	39.9	2.9	ok
V0306	10.0	0.06	156.4	5.0	125.0	6.9	41.3	2.5	ok
V0308	10.0	0.1	223.0	7.2	152.4	7.7	42.2	4.4	ok
V0309	10.0	0.1	223.5	7.8	154.6	8.4	42.4	3.6	ok
V0310	50.1	0.02	61.7	1.7	71.4	3.3	32.4	4.0	ok
V0311	50.1	0.02	68.2	1.9	95.1	4.7	42.5	1.9	ok

APPENDIX

Test	v_c [m/min]	f [mm]	F_c [N]	μ_{F_c} [N]	F_f [N]	μ_{F_f} [N]	r_n [μm]	μ_{r_n} [μm]	Status
V0312	50.1	0.02	67.1	1.8	89.8	4.4	40.7	2.4	ok
V0313	50.1	0.06	139.8	4.2	121.3	4.5	38.4	2.9	ok
V0314	50.1	0.06	141.5	4.4	126.7	4.7	40.2	3.6	ok
V0315	50.1	0.06	138.4	4.2	117.8	4.4	38.3	2.7	ok
V0316	50.1	0.1	211.4	6.2	143.2	3.7	38.7	2.5	ok
V0317	50.1	0.1	210.8	6.2	141.6	3.8	36.7	2.2	ok
V0318	50.1	0.1	210.9	5.9	140.6	3.4	36.3	2.2	ok
V0319	10.0	0.1	221.9	7.1	145.8	7.1	37.7	2.4	ok
V0320	19.9	0.01	55.9	3.1	84.5	5.2	40.5	2.8	ok
V0321	19.9	0.01	57.2	1.8	85.8	5.1	39.2	2.3	ok
V0322	19.9	0.01	56.2	2.2	84.3	5.0	39.5	2.2	ok
V0323	19.9	0.04	111.7	4.2	108.5	5.9	38.1	3.1	ok
V0324	19.9	0.04	104.3	3.1	87.8	4.4	31.2	3.6	ok
V0325	19.9	0.04	110.5	3.5	104.9	5.6	37.5	2.6	ok
V0326	19.9	0.1	211.1	6.5	146.8	6.4	37.3	2.0	ok
V0327	19.9	0.1	213.5	6.8	158.1	7.1	42.9	2.2	ok
V0328	19.9	0.1	205.8	6.4	133.0	5.5	33.5	3.5	ok
V0329	100.0	0.01	44.1	1.0	81.4	3.3	40.6	2.1	ok
V0330	100.0	0.01	43.5	1.1	77.7	3.1	40.0	2.7	ok
V0331	100.0	0.01	43.6	1.0	78.7	3.1	38.8	2.7	ok
V0332	100.0	0.04	99.0	2.1	96.0	2.4	33.8	3.3	ok
V0333	100.0	0.04	98.4	2.0	93.9	2.1	34.5	3.2	ok
V0334	100.0	0.04	102.8	2.4	111.5	3.0	41.0	2.7	ok
V0335	100.0	0.1	203.3	2.9	140.0	2.3	37.9	4.7	ok
V0336	100.0	0.1	200.0	2.3	122.0	1.5	32.5	3.6	ok
V0337	100.0	0.1	199.2	2.5	123.6	2.0	32.8	3.2	ok
V0338	39.9	0.01	48.5	1.3	77.5	3.9	42.4	2.2	ok
V0339	39.9	0.01	47.1	1.2	72.6	3.8	39.1	4.8	ok
V0340	39.9	0.01	45.9	1.2	68.2	3.6	35.2	2.4	ok
V0341	39.9	0.04	102.3	3.0	100.2	4.6	36.7	2.4	ok
V0342	39.9	0.04	103.1	3.0	103.7	4.9	38.0	2.4	ok
V0343	39.9	0.04	100.3	2.9	97.7	4.4	36.0	4.4	ok
V0344	39.9	0.1	211.9	6.8	152.2	5.1	40.1	3.2	ok
V0345	39.9	0.1	209.0	6.6	143.5	4.4	37.4	2.3	ok
V0346	39.9	0.1	209.3	6.8	143.8	4.9	36.7	2.1	ok
V0347	125.0	0.01	35.0	0.7	49.1	1.5	28.6	4.1	ok
V0348	125.0	0.01	42.7	0.9	77.5	2.6	38.3	2.4	ok
V0349	125.0	0.01	43.1	0.9	78.8	2.6	38.9	2.3	ok
V0350	125.0	0.04	102.3	2.3	110.9	3.2	37.9	2.4	ok
V0351	125.0	0.04	97.7	2.2	93.0	2.5	32.9	2.6	ok
V0352	125.0	0.04	101.5	2.3	107.1	3.0	39.5	4.2	ok
V0353	125.0	0.1	197.3	2.1	141.2	1.7	40.5	3.0	ok
V0354	125.0	0.1	197.7	2.0	141.2	1.8	40.1	3.1	ok
V0355	125.0	0.1	195.9	2.0	138.9	1.7	39.8	2.4	ok

Test	v_c [m/min]	f [mm]	F_c [N]	μ_{F_c} [N]	F_f [N]	μ_{F_f} [N]	r_n [μ m]	μ_{r_n} [μ m]	Status
V0356	19.9	0.02	69.9	1.9	77.8	4.2	36.1	2.8	ok
V0357	19.9	0.02	75.1	2.0	91.4	5.1	40.9	2.1	ok
V0358	19.9	0.02	71.8	1.9	82.0	4.5	35.4	2.0	ok
V0359	19.9	0.08	170.1	5.1	112.5	4.4	30.7	3.3	ok
V0360	19.9	0.08	174.4	5.4	127.9	6.0	38.8	2.8	ok
V0361	19.9	0.08	177.0	5.6	138.3	6.6	42.5	2.4	ok
V0362	19.9	0.15	291.4	9.5	171.8	5.9	38.5	2.7	ok
V0363	19.9	0.15	292.8	9.7	176.4	6.1	39.2	2.3	ok
V0364	19.9	0.15	293.2	9.4	172.8	5.5	38.4	3.2	ok
V0365	100.0	0.02	61.0	1.4	80.6	3.0	37.2	2.8	ok
V0366	100.0	0.02	62.9	1.5	89.9	3.2	37.5	3.0	ok
V0367	100.0	0.02	60.9	1.3	82.5	3.0	35.0	3.1	ok
V0368	100.0	0.08	173.8	3.3	129.3	2.8	39.2	3.4	ok
V0369	100.0	0.08	175.4	3.1	137.6	2.6	42.5	3.5	ok
V0370	100.0	0.08	174.7	3.2	135.9	2.7	44.6	7.2	ok
V0371	100.0	0.15	265.0	3.0	161.1	2.1	43.3	4.0	ok
V0372	100.0	0.15	265.7	3.0	161.8	2.2	42.6	3.2	ok
V0373	100.0	0.15	264.8	3.0	159.1	2.0	41.1	3.0	ok
V0374	19.9	0.06	148.2	4.4	122.5	5.6	34.5	2.6	ok
V0375	19.9	0.06	150.9	4.5	134.9	6.7	40.7	2.1	ok
V0376	19.9	0.06	143.6	4.3	115.4	5.1	32.4	3.1	ok
V0377	19.9	0.12	248.4	7.8	172.7	6.2	40.4	2.2	ok
V0378	19.9	0.12	240.7	7.3	149.2	4.5	33.0	4.2	ok
V0379	19.9	0.12	245.1	7.8	169.6	6.3	40.7	2.7	ok
V0380	19.9	0.2	366.6	14.0	198.7	9.1	40.9	2.8	ok
V0381	19.9	0.2	366.3	13.4	198.0	9.8	37.8	2.1	ok
V0382	19.9	0.2	367.6	13.6	190.7	9.5	36.5	3.0	ok
V0383	70.0	0.06	140.0	3.7	127.8	3.3	41.6	2.2	ok
V0385	70.0	0.06	139.1	3.2	122.6	2.9	39.4	3.3	ok
V0386	70.0	0.12	237.6	4.0	151.1	4.0	39.4	2.4	ok
V0387	70.0	0.12	236.2	4.3	149.3	4.4	38.2	2.8	ok
V0388	70.0	0.12	240.0	4.0	162.5	3.9	43.9	2.6	ok
V0389	70.0	0.2	330.7	4.2	167.6	3.3	37.9	3.4	ok
V0390	70.0	0.2	334.4	4.8	181.7	5.8	40.5	2.4	ok
V0391	70.0	0.2	335.3	4.1	188.1	3.7	41.9	2.0	ok
V0392	19.9	0.06	137.7	3.1	122.0	3.0	39.3	2.4	ok
V0393	50.1	0.04	99.0	2.4	95.8	3.5	34.6	3.5	ok
V0394	50.1	0.04	99.3	2.4	98.8	3.6	36.0	2.8	ok
V0395	50.1	0.04	101.3	2.4	107.4	4.0	40.8	3.2	ok
V0396	50.1	0.08	172.2	4.6	129.9	3.5	38.4	3.8	ok
V0397	50.1	0.08	174.5	4.5	141.3	3.8	42.2	2.5	ok
V0398	50.1	0.08	166.4	4.6	110.6	3.1	32.4	3.4	ok
V0399	50.1	0.15	281.3	2.7	166.9	2.7	41.7	2.3	ok
V0400	50.1	0.15	279.3	2.9	162.5	3.3	40.8	2.6	ok

APPENDIX

Test	v_c [m/min]	f [mm]	F_c [N]	μ_{F_c} [N]	F_f [N]	μ_{F_f} [N]	r_n [μ m]	μ_{r_n} [μ m]	Status
V0401	50.1	0.15	274.1	2.9	144.9	2.9	34.9	3.3	ok
V0402	70.0	0.04	100.6	2.5	108.0	3.6	40.5	2.5	ok
V0403	70.0	0.04	99.6	2.4	104.4	3.4	37.7	2.4	ok
V0404	70.0	0.04	98.4	2.2	99.3	3.0	36.2	2.8	ok
V0405	70.0	0.08	168.2	3.5	121.4	2.3	36.6	2.7	ok
V0406	70.0	0.08	165.7	3.3	113.2	1.8	33.9	3.0	ok
V0407	70.0	0.08	165.7	3.5	115.7	2.2	35.9	2.9	ok
V0408	70.0	0.15	271.8	2.9	149.0	2.2	33.7	4.3	ok
V0409	70.0	0.15	272.6	3.5	158.4	2.8	37.3	2.5	ok
V0410	70.0	0.15	274.1	3.3	160.4	2.6	37.6	2.4	ok
V0411	70.0	0.1	202.7	4.2	133.0	3.4	36.8	3.0	ok
V0412	70.0	0.1	202.7	4.3	133.7	3.4	38.1	3.1	ok
V0413	70.0	0.1	203.0	4.3	138.5	3.7	38.6	2.3	ok
V0414	50.1	0.2	337.4	5.8	174.0	6.1	38.5	2.8	ok
V0415	50.1	0.2	328.4	5.5	143.0	4.3	29.1	4.1	ok
V0416	50.1	0.2	336.8	6.3	174.0	5.5	37.6	2.5	ok
V0417	52.0	0.02	67.8	1.5	89.3	3.7	37.3	2.5	ok
V0418	52.0	0.02	64.6	1.5	79.1	3.2	36.1	2.9	ok
V0419	52.0	0.02	67.3	1.5	89.0	3.6	39.1	2.4	ok
V0420	52.0	0.08	183.0	4.5	143.0	3.7	39.5	2.3	ok
V0421	52.0	0.08	180.6	4.5	138.5	3.5	38.1	2.2	ok
V0422	52.0	0.08	180.7	4.3	138.1	3.4	37.8	1.9	ok
V0423	52.0	0.12	247.7	4.7	153.7	2.8	38.9	2.8	ok
V0424	52.0	0.12	247.9	4.6	152.1	2.7	38.8	4.0	ok
V0425	52.0	0.12	248.4	4.7	162.1	3.2	41.1	2.6	ok
V0426	162.4	0.02	65.9	0.9	98.2	1.7	41.9	2.2	ok
V0427	162.4	0.02	63.1	0.9	86.9	1.5	37.8	3.2	ok
V0428	162.4	0.02	58.1	0.7	68.4	1.1	30.5	4.3	ok
V0429	162.4	0.08	171.5	1.6	137.6	2.2	39.6	2.4	ok
V0430	162.4	0.08	169.4	1.3	128.1	1.5	37.7	3.0	ok
V0431	162.4	0.08	171.5	1.6	138.5	2.3	41.0	1.9	ok
V0432	162.4	0.12	222.3	1.9	146.5	2.3	38.1	2.8	ok
V0433	162.4	0.12	222.6	2.4	150.6	3.0	39.4	2.3	ok
V0434	162.4	0.12	221.7	2.0	150.3	2.6	42.0	2.2	ok
V0435	60.0	0.02	65.4	1.4	86.1	3.4	36.6	2.4	ok
V0436	60.0	0.02	63.8	1.3	81.7	3.1	36.6	3.1	ok
V0437	60.0	0.02	66.3	1.4	88.9	3.5	39.0	2.6	ok
V0438	60.0	0.1	211.8	3.6	136.2	2.3	37.3	3.1	ok
V0439	60.0	0.1	212.3	3.7	140.0	2.3	37.2	2.1	ok
V0440	60.0	0.1	214.3	3.7	145.3	2.7	39.8	2.9	ok
V0441	60.0	0.2	353.5	5.6	191.6	5.3	40.4	3.2	ok
V0442	60.0	0.2	354.2	5.6	192.5	3.9	39.9	3.0	ok
V0443	60.0	0.2	353.4	5.5	193.8	3.1	39.4	2.7	ok
V0444	60.0	0.02	65.0	1.3	86.3	3.4	39.9	6.3	ok

Test	v_c [m/min]	f [mm]	F_c [N]	μ_{F_c} [N]	F_f [N]	μ_{F_f} [N]	r_n [μ m]	μ_{r_n} [μ m]	Status
V0445	60.0	0.02	67.8	1.4	96.3	3.9	41.3	2.0	ok
V0446	79.9	0.02	66.5	1.4	95.8	3.5	41.2	2.4	ok
V0447	79.9	0.1	205.6	3.6	126.9	3.7	32.8	3.9	ok
V0448	79.9	0.1	213.0	3.4	148.4	3.6	39.5	3.0	ok
V0449	79.9	0.1	212.0	3.4	149.3	3.7	41.1	3.7	ok
V0450	79.9	0.2	337.1	4.0	171.6	2.1	37.7	3.4	ok
V0451	79.9	0.2	340.5	4.6	186.4	2.9	41.8	2.8	ok
V0452	79.9	0.2	339.0	4.0	179.4	2.4	38.9	2.1	ok
V0453	79.9	0.02	64.0	1.4	88.2	3.2	36.6	2.8	ok
V0454	79.9	0.02	66.4	1.4	96.5	3.5	40.8	2.6	ok
V0455	150.0	0.1	196.3	1.4	137.2	1.3	38.5	2.9	ok
V0456	150.0	0.1	195.9	1.8	134.3	1.5	36.4	2.3	ok
V0457	150.0	0.1	200.1	1.6	152.6	1.7	42.9	2.9	ok
V0458	199.9	0.1	192.7	1.6	137.2	2.8	38.2	2.8	short
V0459	199.9	0.1	190.5	1.1	142.5	1.8	40.6	2.7	short
V0460	199.9	0.1	188.3	1.5	121.4	2.2	32.7	3.7	short
V0461	400.1	0.01	41.2	0.2	74.3	0.4	35.5	4.5	ok
V0462	400.1	0.01	37.8	0.2	61.4	0.3	31.7	2.9	ok
V0463	400.1	0.01	40.6	0.2	72.6	0.5	35.9	4.4	ok
V0464	400.1	0.02	61.1	0.4	84.0	0.7	36.7	3.1	ok
V0465	400.1	0.02	63.8	0.4	94.0	0.8	40.9	2.4	ok
V0466	400.1	0.02	62.7	0.5	90.3	0.6	38.2	2.6	ok
V0467	400.1	0.03	80.5	0.8	96.6	0.8	37.0	2.7	ok
V0468	400.1	0.03	81.2	0.7	98.4	0.8	38.7	3.2	ok
V0469	400.1	0.03	82.9	0.6	108.1	0.7	42.5	2.4	ok
V0470	400.1	0.04	98.6	1.0	109.0	1.3	38.2	3.2	short
V0471	400.1	0.04	99.8	0.6	116.0	0.9	41.9	2.9	ok
V0472	400.1	0.04	97.2	1.0	101.6	1.7	38.4	3.4	short
V0473	500.0	0.01	42.2	0.6	76.6	0.6	37.7	3.2	ok
V0474	500.0	0.01	44.3	0.7	83.6	0.7	39.1	3.6	ok
V0475	500.0	0.01	43.2	0.6	81.2	0.7	37.6	2.4	ok
V0476	500.0	0.02	64.0	0.9	91.6	0.9	38.4	2.6	ok
V0477	500.0	0.02	66.0	0.6	101.1	0.8	42.3	2.5	ok
V0478	500.0	0.02	65.6	0.6	98.7	1.0	39.9	2.3	ok
V0479	500.0	0.1	234.1	14.0	603.5	23.7	39.9	2.3	short
V0480	40.0	0.06	139.5	3.6	115.9	4.1	34.7	2.8	ok
V0481	40.0	0.06	142.7	3.8	127.8	4.8	39.7	2.4	ok
V0482	40.0	0.06	140.4	3.7	121.2	4.4	36.9	2.5	ok
V0483	40.0	0.15	290.2	7.9	174.8	8.7	42.1	3.1	ok
V0484	40.0	0.15	286.8	7.5	173.3	10.3	40.0	3.4	ok
V0485	40.0	0.15	285.3	7.4	162.7	9.8	38.0	2.4	ok
V0486	40.0	0.2	349.7	6.5	178.7	9.7	33.2	4.4	ok
V0487	40.0	0.2	352.3	5.2	169.1	6.0	33.4	3.1	ok
V0488	40.0	0.2	353.1	6.2	180.6	8.8	37.2	3.3	ok

Test	v_c [m/min]	f [mm]	F_c [N]	μ_{F_c} [N]	F_f [N]	μ_{F_f} [N]	r_n [μ m]	μ_{r_n} [μ m]	Status
V0489	125.0	0.06	141.9	2.2	123.3	2.0	37.7	3.2	ok
V0490	125.0	0.06	141.7	2.3	122.8	2.3	37.9	3.3	ok
V0491	125.0	0.06	141.9	2.2	125.2	2.1	39.0	3.2	ok
V0492	125.0	0.15	258.3	2.6	150.5	1.8	37.1	4.0	ok
V0493	125.0	0.15	256.5	2.6	137.3	1.7	34.6	3.2	ok
V0494	125.0	0.15	259.2	2.6	154.2	1.9	39.3	2.7	ok
V0495	125.0	0.2	322.3	4.9	166.6	5.0	35.4	2.4	short
V0496	125.0	0.2	324.0	5.3	176.1	5.0	38.6	3.3	short
V0497	125.0	0.2	321.7	4.1	173.4	3.6	42.9	4.6	ok
V0498	100.0	0.06	143.9	3.1	136.8	3.7	46.8	2.8	ok
V0499	100.0	0.06	142.5	3.4	132.2	4.0	40.5	3.2	ok
V0500	100.0	0.06	140.9	3.1	128.7	3.6	39.3	3.0	ok
V0501	100.0	0.12	229.3	2.0	147.5	1.4	39.1	3.0	ok
V0502	100.0	0.12	227.1	1.9	142.5	1.6	37.7	2.9	ok
V0503	100.0	0.12	229.4	1.9	149.9	1.6	38.1	2.9	ok
V0504	100.0	0.2	325.2	4.1	172.5	2.3	39.4	4.0	ok
V0505	100.0	0.2	329.4	4.1	177.2	2.7	41.0	2.2	ok
V0506	100.0	0.2	323.9	3.8	164.0	2.4	35.9	2.7	ok
V0507	150.0	0.06	138.2	1.4	118.3	1.1	36.5	3.0	ok
V0508	150.0	0.06	139.8	1.4	130.6	1.5	41.0	2.8	ok
V0509	150.0	0.06	137.4	1.3	117.1	1.2	37.3	3.0	ok
V0510	150.0	0.12	218.6	1.7	144.3	1.7	39.0	2.4	ok
V0511	150.0	0.12	219.6	1.8	149.3	1.9	41.2	2.3	ok
V0512	150.0	0.12	216.9	1.7	137.5	1.5	35.4	2.2	ok
V0513	150.0	0.2	324.2	4.7	176.0	7.3	36.0	2.9	short
V0514	150.0	0.2	325.1	5.8	185.3	7.9	37.8	2.8	short
V0515	150.0	0.2	326.2	5.2	184.0	7.3	37.3	2.1	short
V0516	150.0	0.02	63.6	1.0	91.0	1.9	38.3	2.5	ok
V0517	150.0	0.02	61.6	0.8	83.2	1.5	34.8	3.6	ok
V0518	150.0	0.02	63.4	0.8	89.0	1.6	36.2	3.9	ok
V0519	150.0	0.03	85.4	1.2	105.7	1.8	40.0	2.8	ok
V0520	150.0	0.03	87.1	1.2	108.3	1.9	38.1	4.1	ok

Table 11.1: Experimental results Ti6Al4V orthogonal cutting tests

Test	v_c [m/min]	f [mm]	F_c [N]	μ_{F_c} [N]	F_f [N]	μ_{F_f} [N]	r_n [μ m]	μ_{r_n} [μ m]	Status
V0069	10.1	0.01	52.1	11.0	31.6	6.7	33.9	1.6	short
V0070	10.1	0.01	47.0	7.1	28.4	4.2	35.5	2.3	ok
V0071	10.1	0.01	47.7	9.5	28.4	5.7	39.5	4.9	ok
V0072	10.1	0.1	325.1	26.7	185.5	19.3	42.3	2.4	ok
V0073	10.1	0.1	312.1	38.8	175.8	20.0	39.2	3.0	ok
V0074	10.1	0.1	310.3	25.2	173.0	15.9	39.0	3.8	ok
V0075	10.1	0.2	509.0	9.2	303.2	27.0	42.4	2.0	saturation
V0076	10.1	0.2	543.9	39.7	306.9	30.7	39.2	4.0	ok
V0077	10.1	0.2	543.7	39.9	298.6	32.0	42.4	2.3	ok
V0078	10.1	0.2	542.9	32.6	297.3	28.2	33.2	4.7	ok
V0079	70.1	0.01	38.5	9.5	24.3	6.4	41.2	2.5	instable
V0080	70.1	0.01	38.0	9.0	23.7	5.6	36.3	4.6	instable
V0081	70.1	0.01	37.0	9.8	23.3	6.2	42.4	2.5	ok
V0082	70.1	0.1	283.7	14.6	233.6	25.6	40.6	2.6	instable
V0083	70.1	0.1	329.6	8.9	319.8	11.2	39.5	3.6	instable
V0084	70.1	0.1	379.7	4.0	401.0	5.7	38.2	4.1	ok
V0085	70.1	0.1	387.3	2.9	412.2	2.9	43.8	2.3	ok
V0086	70.1	0.2	612.8	9.9	511.3	2.7	38.1	3.5	saturation
V0087	70.1	0.2	617.0	8.1	511.5	0.7	41.4	2.5	saturation
V0088	70.1	0.2	614.7	8.5	511.5	0.7	41.4	2.5	saturation
V0089	70.1	0.2	614.3	8.3	544.9	14.6	36.0	2.6	instable
V0091	150.0	0.01	36.5	5.9	25.0	4.3	41.7	2.1	ok
V0092	150.0	0.01	36.3	6.4	24.9	4.6	39.5	2.5	ok
V0093	150.0	0.1	344.4	1.2	334.9	1.6	41.5	3.5	ok
V0094	150.0	0.1	346.8	2.3	340.2	3.8	43.4	2.0	ok
V0095	150.0	0.1	342.9	2.3	332.4	3.6	36.1	3.0	ok
V0096	150.0	0.2	549.0	3.0	410.3	4.1	40.6	2.5	ok
V0097	150.0	0.2	544.6	5.0	401.9	9.7	44.7	2.1	ok
V0098	150.0	0.2	544.8	3.7	402.0	6.1	41.3	2.2	ok
V0099	150.0	0.4	876.9	20.6	470.4	39.7	42.9	2.5	instable
V0100	150.0	0.4	920.4	5.9	515.7	4.5	40.0	2.5	ok
V0101	150.0	0.4	899.5	15.1	498.8	23.7	42.0	2.9	ok
V0102	30.0	0.02	72.6	27.8	45.2	16.3	40.5	2.9	ok
V0103	30.0	0.02	71.6	24.5	43.9	14.2	39.2	2.9	ok
V0104	30.0	0.02	70.2	24.1	43.2	14.3	40.2	2.7	ok
V0105	30.0	0.06	188.3	20.8	108.6	14.2	42.4	2.4	questionable
V0106	30.0	0.06	170.6	29.0	96.9	16.4	36.0	3.9	questionable
V0107	30.0	0.06	166.2	32.6	95.5	18.1	42.3	2.1	questionable
V0108	30.0	0.15	377.0	29.3	216.1	19.9	38.3	2.9	ok
V0109	30.0	0.15	370.1	27.3	209.4	20.3	42.9	2.3	ok
V0110	30.0	0.15	377.1	26.8	218.9	18.8	39.9	2.7	ok
V0111	100.0	0.02	64.0	18.6	41.2	12.1	40.5	2.4	questionable
V0112	100.0	0.02	64.1	19.9	41.9	12.9	38.2	4.9	questionable
V0113	100.0	0.02	63.2	12.6	41.2	8.3	42.4	3.0	ok

APPENDIX

Test	v_c [m/min]	f [mm]	F_c [N]	μ_{F_c} [N]	F_f [N]	μ_{F_f} [N]	r_n [μ m]	μ_{r_n} [μ m]	Status
V0114	100.0	0.06	198.4	2.9	177.9	4.6	41.6	2.3	ok
V0115	100.0	0.06	196.9	2.3	175.5	3.9	38.1	4.5	ok
V0116	100.0	0.06	195.8	2.7	172.6	4.8	37.3	3.7	ok
V0117	100.0	0.15	455.2	6.2	405.4	12.7	38.4	3.5	initially stable
V0118	100.0	0.15	461.8	6.5	420.1	11.5	37.2	4.0	short
V0119	100.0	0.15	476.3	8.1	443.7	14.2	39.5	3.0	short
V0120	30.0	0.04	126.3	25.2	72.6	15.5	38.2	2.6	questionable
V0121	30.0	0.04	127.7	23.3	75.3	13.3	40.5	3.1	ok
V0122	30.0	0.04	121.7	35.2	71.5	20.1	35.2	4.5	questionable
V0123	30.0	0.1	262.5	23.4	152.9	15.5	43.1	2.1	ok
V0124	30.0	0.1	253.2	26.7	144.5	16.8	39.0	2.9	ok
V0125	30.0	0.1	258.1	25.7	147.2	15.7	38.4	2.5	ok
V0126	30.0	0.2	488.6	26.6	289.1	23.2	39.6	3.2	ok
V0127	30.0	0.2	501.3	28.5	307.1	30.0	44.0	2.1	ok
V0128	30.0	0.2	493.3	25.7	296.3	25.5	40.6	3.5	ok
V0129	100.0	0.04	122.9	8.3	91.6	9.0	43.4	2.1	ok
V0130	100.0	0.04	120.1	10.7	85.4	8.7	31.6	3.3	ok
V0131	100.0	0.04	113.6	12.7	79.9	11.4	36.5	4.7	ok
V0132	100.0	0.1	350.9	3.1	360.2	5.4	39.2	3.5	short
V0133	100.0	0.1	350.0	2.4	355.7	5.5	37.6	2.3	short
V0134	100.0	0.1	353.6	1.8	364.8	2.8	38.3	2.7	short
V0135	100.0	0.2	565.3	10.5	459.0	19.1	38.5	6.2	initially stable
V0136	100.0	0.2	552.9	12.3	444.3	24.6	44.3	5.2	initially stable
V0137	100.0	0.2	565.9	9.2	461.8	16.3	40.4	3.2	initially stable
V0139	50.1	0.02	67.9	25.9	41.2	15.0	38.9	3.7	questionable
V0140	50.1	0.02	73.1	22.6	45.3	13.3	39.9	3.3	questionable
V0141	50.1	0.02	68.0	28.1	42.1	17.0	40.4	2.6	questionable
V0142	50.1	0.06	164.3	40.3	99.1	23.0	38.4	3.3	ok
V0143	50.1	0.06	167.2	29.7	100.9	16.6	35.2	5.2	ok
V0144	50.1	0.06	158.0	40.8	94.6	23.1	36.6	2.6	ok
V0145	50.1	0.15	506.7	10.7	487.4	16.5	42.8	2.6	short
V0146	50.1	0.15	511.1	6.1	493.2	9.5	43.3	2.5	ok
V0147	50.1	0.15	504.7	7.7	483.2	15.1	38.1	2.8	short
V0148	150.0	0.02	73.5	4.9	59.7	4.3	36.3	2.6	ok
V0149	150.0	0.02	68.2	7.9	51.6	6.2	39.3	2.9	ok
V0150	150.0	0.02	69.2	6.3	53.7	5.5	41.0	4.3	ok
V0151	150.0	0.06	224.4	1.8	239.6	3.0	37.2	2.1	ok
V0152	150.0	0.06	226.2	1.4	244.7	2.0	38.2	3.3	ok
V0153	150.0	0.06	224.5	1.4	239.9	3.0	40.8	1.9	initially stable
V0154	150.0	0.15	428.6	2.9	353.1	4.1	35.3	2.9	ok
V0155	150.0	0.15	425.4	2.3	345.2	3.0	35.4	7.9	ok
V0156	150.0	0.15	430.4	3.6	356.7	4.7	37.9	2.4	ok
V0157	50.1	0.04	113.1	28.8	65.8	16.2	38.2	2.6	questionable
V0158	50.1	0.04	122.7	23.1	73.0	13.4	37.8	4.4	questionable

Test	v_c [m/min]	f [mm]	F_c [N]	μ_{F_c} [N]	F_f [N]	μ_{F_f} [N]	r_n [μ m]	μ_{r_n} [μ m]	Status
V0159	50.1	0.04	114.3	40.4	68.6	23.4	43.5	4.8	questionable
V0160	50.1	0.1	262.1	19.9	168.6	18.4	42.2	3.0	ok
V0161	50.1	0.1	261.7	20.0	167.3	17.0	39.5	2.0	ok
V0162	50.1	0.1	257.4	18.4	160.1	14.1	33.6	3.0	ok
V0163	50.1	0.2	654.4	6.4	623.0	10.6	42.4	2.4	short
V0164	50.1	0.2	651.7	5.2	615.7	8.6	43.2	2.2	short
V0165	50.1	0.2	649.6	5.3	613.7	8.6	42.1	2.9	short
V0166	150.0	0.04	141.8	5.2	131.9	11.9	33.6	3.1	short
V0167	150.0	0.04	137.9	3.7	128.9	10.2	40.4	2.1	initially stable
V0168	150.0	0.04	139.7	5.7	133.5	14.6	40.5	1.8	initially stable
V0169	150.0	0.1	325.3	3.9	312.0	6.1	35.4	2.9	short
V0170	150.0	0.1	322.4	6.1	307.5	10.7	36.3	2.7	short
V0171	150.0	0.1	326.6	6.6	313.6	11.5	40.5	2.7	short
V0172	150.0	0.2	517.5	7.9	373.6	13.5	32.7	3.6	ok
V0173	150.0	0.2	519.2	4.3	377.3	5.5	40.3	4.5	ok
V0174	150.0	0.2	520.0	12.2	380.3	20.9	40.7	2.8	ok
V0175	150.0	0.02	77.3	3.7	77.2	1.7	36.0	3.0	ok
V0176	10.0	0.02	80.9	15.4	48.6	8.9	39.0	2.4	ok
V0177	10.0	0.02	81.9	16.3	49.3	9.5	40.6	2.8	ok
V0178	10.0	0.02	80.8	16.4	48.3	9.2	37.2	2.7	ok
V0179	10.0	0.06	195.0	29.5	111.5	15.5	43.5	1.8	ok
V0180	10.0	0.06	190.9	18.7	106.3	10.8	33.9	2.7	ok
V0181	10.0	0.06	189.1	28.3	104.9	15.4	35.1	3.4	ok
V0182	10.0	0.15	404.7	24.7	221.7	18.4	41.3	2.2	ok
V0183	10.0	0.15	409.8	22.6	225.3	18.9	35.8	2.4	ok
V0184	10.0	0.15	414.3	23.3	233.3	19.9	40.3	2.0	ok
V0185	69.9	0.02	62.9	7.8	36.8	5.1	30.0	3.5	ok
V0186	69.9	0.02	66.1	22.0	40.6	13.8	36.4	2.5	ok
V0187	69.9	0.02	66.7	12.3	40.9	7.6	40.9	2.3	ok
V0188	69.9	0.06	167.1	17.3	109.0	12.7	37.5	4.8	ok
V0189	69.9	0.06	167.0	16.7	109.4	11.7	39.9	2.8	ok
V0190	69.9	0.06	166.2	15.1	107.8	10.7	36.1	3.5	ok
V0191	69.9	0.15	501.5	5.3	491.3	7.8	39.3	2.8	short
V0192	69.9	0.15	497.3	3.7	485.0	6.1	32.9	4.6	short
V0193	69.9	0.15	501.2	3.6	490.2	6.3	39.5	3.2	short
V0194	199.9	0.01	36.9	3.3	26.0	2.5	33.5	3.2	ok
V0195	199.9	0.01	39.5	3.8	28.3	2.9	40.5	3.8	ok
V0196	199.9	0.01	39.5	3.2	28.4	2.8	39.5	3.1	ok
V0197	199.9	0.04	159.1	1.0	171.3	1.6	40.8	3.1	ok
V0198	199.9	0.04	158.0	1.2	170.2	1.8	33.0	4.1	ok
V0199	199.9	0.04	159.3	0.9	172.3	1.1	38.3	3.7	ok
V0200	199.9	0.08	269.7	2.8	261.2	4.1	41.6	4.0	short
V0201	199.9	0.08	268.2	2.5	257.7	3.5	36.3	3.6	short
V0202	199.9	0.08	273.3	2.6	267.9	4.2	40.9	2.8	short

APPENDIX

Test	v_c [m/min]	f [mm]	F_c [N]	μ_{F_c} [N]	F_f [N]	μ_{F_f} [N]	r_n [μ m]	μ_{r_n} [μ m]	Status
V0203	300.0	0.01	49.6	0.9	51.7	1.2	35.8	3.4	ok
V0204	300.0	0.01	51.5	1.2	55.9	1.8	38.6	2.7	ok
V0205	300.0	0.01	51.2	1.2	55.6	1.7	37.8	3.0	ok
V0206	300.0	0.04	146.9	3.3	150.4	3.4	43.5	2.0	short
V0207	300.0	0.04	149.2	3.2	152.9	5.3	41.7	2.5	short
V0208	300.0	0.04	149.9	2.4	152.9	3.5	36.6	2.9	short
V0209	300.0	0.08	260.1	2.7	233.5	1.9	42.4	3.0	short
V0210	300.0	0.08	259.7	1.4	233.0	1.0	43.3	2.5	short
V0211	300.0	0.08	257.5	1.8	227.2	2.1	40.4	2.3	short
V0212	10.0	0.01	45.2	14.2	28.6	8.3	36.9	2.9	ok
V0213	10.0	0.01	46.0	7.4	28.7	4.6	40.5	2.6	ok
V0214	10.0	0.01	44.9	7.8	27.6	4.6	35.4	2.8	ok
V0215	10.0	0.04	144.6	27.7	84.1	16.0	39.1	2.9	ok
V0216	10.0	0.04	145.4	27.6	85.1	15.2	41.6	3.4	ok
V0217	10.0	0.04	138.0	30.8	79.1	16.8	39.6	2.8	ok
V0218	10.0	0.08	249.5	20.2	142.7	12.1	36.3	3.4	ok
V0219	10.0	0.08	249.5	17.4	142.6	11.3	36.7	2.5	ok
V0220	10.0	0.08	244.7	18.2	138.7	12.0	36.7	2.5	ok
V0221	349.9	0.01	49.7	0.5	49.6	0.4	33.5	3.9	ok
V0222	349.9	0.01	56.3	0.5	61.1	0.4	42.6	2.0	ok
V0223	349.9	0.01	54.0	0.5	56.0	0.4	39.8	1.9	ok
V0224	349.9	0.04	152.1	1.1	156.1	1.6	36.2	2.5	short
V0225	349.9	0.04	152.1	0.8	154.1	1.5	34.9	2.2	short
V0226	349.9	0.04	153.4	2.0	158.2	2.7	38.7	3.1	short
V0227	349.9	0.08	250.3	2.3	213.0	2.1	40.6	2.6	short
V0228	349.9	0.08	245.8	2.0	203.6	2.3	36.5	2.2	short
V0229	349.9	0.08	242.0	3.0	198.0	2.8	34.6	3.2	short
V0230	250.1	0.02	83.6	0.5	82.3	0.4	43.0	1.8	ok
V0231	250.1	0.02	81.6	0.5	79.3	0.5	39.8	2.5	ok
V0232	250.1	0.02	82.5	0.7	80.6	0.5	41.6	3.0	ok
V0233	250.1	0.06	207.7	2.4	202.2	3.9	39.9	3.5	short
V0234	250.1	0.06	213.0	2.8	212.8	4.1	41.3	2.4	short
V0235	250.1	0.06	206.2	2.3	198.2	3.8	33.3	3.7	short
V0236	250.1	0.1	304.0	1.8	256.9	2.8	38.6	2.2	ok
V0237	250.1	0.1	304.5	2.8	258.5	4.0	39.5	2.3	short
V0238	250.1	0.1	304.6	2.6	258.2	3.2	39.2	2.8	short
V0239	349.9	0.02	87.8	0.7	93.5	0.9	36.2	2.5	short
V0240	349.9	0.02	88.7	0.9	94.4	1.0	33.6	2.9	short
V0241	349.9	0.02	89.3	1.3	97.2	1.6	35.2	3.0	short
V0242	349.9	0.06	207.1	2.1	194.6	2.5	38.2	3.4	short
V0243	349.9	0.06	208.6	2.4	199.6	3.0	39.7	2.4	short
V0244	349.9	0.06	204.3	2.2	187.9	3.0	34.7	3.0	short
V0245	349.9	0.1	285.0	2.6	216.7	1.8	40.1	2.5	ok
V0246	349.9	0.1	283.0	3.5	212.8	5.4	37.7	2.6	ok

Test	v_c [m/min]	f [mm]	F_c [N]	μ_{F_c} [N]	F_f [N]	μ_{F_f} [N]	r_n [μm]	μ_{r_n} [μm]	Status
V0247	349.9	0.1	283.3	3.1	215.1	3.8	39.5	2.7	ok
V0249	349.9	0.15	369.7	4.8	229.6	6.0	35.2	3.1	ok
V0250	349.9	0.15	375.2	3.3	236.9	4.2	38.4	3.0	ok
V0252	50.0	0.01	39.7	13.2	26.8	7.9	34.3	3.8	ok
V0253	50.0	0.01	38.0	9.0	24.2	5.6	40.0	2.4	ok
V0254	50.0	0.01	37.8	7.4	24.4	4.7	40.4	3.3	ok
V0255	50.0	0.08	211.2	24.2	128.1	15.2	36.0	2.8	ok
V0256	50.0	0.08	210.5	26.3	128.9	16.8	38.3	2.1	ok
V0257	50.0	0.08	209.5	29.4	128.9	18.0	38.1	2.3	ok
V0258	50.0	0.12	320.4	19.8	234.3	33.8	40.2	2.3	short
V0259	50.0	0.12	325.1	16.7	241.1	29.7	41.2	2.5	short
V0260	50.0	0.12	322.7	20.0	238.8	36.0	40.5	2.0	short
V0261	250.0	0.01	51.1	0.5	53.9	0.7	35.6	3.1	ok
V0262	250.0	0.01	52.6	1.1	57.3	1.3	41.6	2.1	short
V0263	250.0	0.01	49.3	0.9	51.4	1.3	35.5	2.9	short
V0264	250.0	0.08	250.4	1.8	223.6	2.6	32.0	3.1	short
V0265	250.0	0.08	255.7	2.7	234.4	3.4	37.0	2.1	short
V0266	250.0	0.08	259.8	2.9	241.9	3.9	40.6	2.4	short
V0267	250.0	0.12	335.9	2.9	265.3	3.3	41.7	2.2	ok
V0268	250.0	0.12	330.6	1.5	253.5	1.8	33.3	3.2	ok
V0269	250.0	0.12	334.6	1.8	262.0	2.2	38.3	2.8	ok
V0271	50.0	0.18	566.4	8.5	521.5	9.9	36.6	2.6	ok
V0272	50.0	0.18	569.1	8.6	527.6	12.9	38.7	2.7	ok
V0273	50.0	0.18	572.7	8.9	536.3	13.1	36.0	2.9	ok
V0274	50.0	0.22	678.0	7.3	614.7	12.0	38.5	2.4	ok
V0275	50.0	0.22	678.0	9.8	615.2	12.3	37.6	2.5	ok
V0276	50.0	0.22	679.5	13.3	612.1	24.7	40.1	1.9	short
V0277	200.0	0.02	84.4	1.8	83.5	2.3	38.2	2.3	questionable
V0278	200.0	0.02	81.1	1.1	80.3	1.1	40.1	2.6	ok
V0279	200.0	0.02	79.8	1.0	77.9	1.3	36.2	3.6	ok
V0280	200.0	0.06	213.6	1.9	220.6	3.3	38.8	2.6	short
V0281	200.0	0.06	213.1	1.4	218.9	2.4	38.9	2.3	short
V0282	200.0	0.06	215.6	1.4	224.1	2.6	38.8	3.0	short
V0283	200.0	0.1	307.6	2.5	275.4	4.3	35.9	2.8	short
V0284	200.0	0.1	308.3	2.3	272.1	3.6	37.1	3.6	short
V0285	200.0	0.1	310.3	3.0	279.7	4.3	37.9	2.3	short
V0286	450.0	0.02	86.5	1.2	91.1	0.6	40.0	2.7	short
V0287	450.0	0.02	86.5	1.2	92.9	0.9	41.1	2.3	short
V0288	450.0	0.02	86.2	1.5	92.9	1.6	40.6	2.3	short
V0289	450.0	0.06	193.1	2.6	167.8	1.9	38.0	2.4	short
V0290	450.0	0.06	196.0	3.6	173.7	2.1	40.3	2.2	short
V0291	450.0	0.06	190.1	2.1	162.1	1.8	34.4	3.6	short
V0292	450.0	0.1	265.1	3.2	183.9	2.9	41.8	2.1	ok
V0293	450.0	0.1	263.6	2.2	180.2	1.2	37.5	2.8	ok

APPENDIX

Test	v_c [m/min]	f [mm]	F_c [N]	μ_{F_c} [N]	F_f [N]	μ_{F_f} [N]	r_n [μ m]	μ_{r_n} [μ m]	Status
V0294	450.0	0.1	261.6	3.6	178.5	3.8	37.4	2.1	ok
V0295	50.0	0.2	644.5	4.6	611.4	6.9	34.3	3.5	ok
V0296	50.0	0.2	643.6	4.6	608.4	6.1	37.7	2.7	ok
V0297	50.0	0.2	642.6	14.5	596.9	23.9	38.3	2.5	ok
V0298	500.0	0.1	259.6	1.9	169.5	2.6	37.2	3.8	ok
V0299	500.0	0.1	259.4	2.5	173.2	3.6	40.2	3.4	ok
V0300	500.0	0.1	260.3	1.5	174.6	2.3	42.0	2.4	ok

Table 11.2: Experimental results Ck45 orthogonal cutting tests

BIBLIOGRAPHY

- [1] Adibi-Sedeh AH, Madhavan V, Bahr B (2003) Extension of Oxley's analysis of machining to use different material models. *J Manuf Sci Eng* 125(4):656–666
- [2] Administration I, Group EPGAM, Boothroyd G (1963) Temperatures in orthogonal metal cutting. *Proceedings of the Institution of Mechanical Engineers* 177(1):789–810
- [3] Afrasiabi M, Röthlin M, Wegener K (2019) Contemporary meshfree methods for three dimensional heat conduction problems. *Archives of Computational Methods in Engineering* pp 1–35
- [4] Afrasiabi M, Röthlin M, Klippel H, Wegener K (2019) Meshfree simulation of metal cutting: an updated Lagrangian approach with dynamic refinement. *International Journal of Mechanical Sciences* 160:451–466
- [5] Afrasiabi M, Meier L, Röthlin M, Klippel H, Wegener K (2020) GPU-accelerated mesh-free simulations for parameter identification of a friction model in metal machining. *International Journal of Mechanical Sciences* 176:105571
- [6] Akbari M, Buhl S, Leinenbach C, Wegener K (2016) A new value for Johnson Cook damage limit criterion in machining with large negative rake angle as basis for understanding of grinding. *Journal of Materials Processing Technology* 234:58–71
- [7] Akbari M, Smolenicki D, Roelofs H, Wegener K (2019) Inverse material modeling and optimization of free-cutting steel with graphite inclusions. *The International Journal of Advanced Manufacturing Technology* 101(5-8):1997–2014
- [8] Allahdadi FA, Carney TC, Hipp JR, Libersky LD, Petschek AG (1993) High strain Lagrangian hydrodynamics: a three dimensional SPH code for dynamic material response. Tech. rep., DTIC Document
- [9] Altenbach J, Altenbach H (1994) Einführung in die Kontinuumsmechanik. BG Teubner Stuttgart. Tech. rep., ISBN 978-3-519-03096-6
- [10] Amada T, Imura M, Yasumuro Y, Manabe Y, Chihara K (2004) Particle-based fluid simulation on GPU. In: *ACM workshop on general-purpose computing on graphics processors*, Citeseer, vol 41, p 42
- [11] Ambati R, Pan X, Yuan H, Zhang X (2012) Application of material point methods for cutting process simulations. *Computational Materials Science* 57:102–110
- [12] Arrazola P, Ozel T (2008) Numerical modelling of 3D hard turning using arbitrary Lagrangian Eulerian finite element method. *International Journal of Machining and Machinability of Materials* 4(1):14–25

Bibliography

- [13] Arrazola P, Özel T, Umbrello D, Davies M, Jawahir I (2013) Recent advances in modelling of metal machining processes. *CIRP Annals-Manufacturing Technology* 62(2):695–718
- [14] Arrazola PJ, Özel T (2010) Investigations on the effects of friction modeling in finite element simulation of machining. *International Journal of Mechanical Sciences* 52(1):31–42
- [15] Ayed Y, Robert C, Germain G, Ammar A (2017) Orthogonal micro-cutting modeling of the Ti17 titanium alloy using the crystal plasticity theory. *Finite Elements in Analysis and Design* 137:43–55
- [16] Babu B (2018) Mechanism-based flow stress model for Ti-6Al-4V: applicable for simulation of additive manufacturing and machining. PhD thesis, Luleå University of Technology
- [17] Babu B, Lindgren LE (2013) Dislocation density based model for plastic deformation and globularization of Ti-6Al-4V. *International Journal of Plasticity* 50:94–108
- [18] Bai Y, Wierzbicki T (2008) A new model of metal plasticity and fracture with pressure and Lode dependence. *International journal of plasticity* 24(6):1071–1096
- [19] Bailey R (1930) Creep of steel under simple and compound stress. *Engineering* 121:129–265
- [20] Bammann D, Chiesa M, Johnson G (1996) Modeling large deformation and failure in manufacturing processes. *Theoretical and Applied Mechanics* 9:359–376
- [21] Banerjee B (2005) An evaluation of plastic flow stress models for the simulation of high-temperature and high-strain-rate deformation of metals. arXiv preprint cond-mat/0512466
- [22] Bauschinger J (1886) Über die Veränderung der Elastizitätsgrenze und der Festigkeit des Eisens und Stahls durch Strecken und Quetschen, durch Erwärmen und Abkühlen und durch oftmals wiederholte Beanspruchung. *Mitt Mech-Techn Lab K Techn Hochsch München* 13:108–112
- [23] Belytschko T, Liu WK, Moran B, Elkhodary KI (2014) *Nonlinear Finite Elements for Continua and Structures*. Wiley
- [24] Benaarbia A, Chatzigeorgiou G, Kiefer B, Meraghni F (2019) A fully coupled thermo-viscoelastic-viscoplastic-damage framework to study the cyclic variability of the Taylor-Quinney coefficient for semi-crystalline polymers. *International Journal of Mechanical Sciences* 163:105128
- [25] Bergs T, Hardt M, Schraknepper D (2020) Determination of Johnson-Cook material model parameters for AISI 1045 from orthogonal cutting tests using the Downhill-Simplex algorithm. *Procedia Manufacturing* 48:541–552
- [26] Böhme W, Luke M, Blauel J, Rohr I, Harwick W, et al. (2007) FAT-Richtlinie Dynamische Werkstoffkennwerte für die Crashsimulation. *FAT-Schriftenreihe* 211(211)

- [27] Bolton J (2008) A “characteristic-strain” model for creep. *Materials at High Temperatures* 25(3):197–204
- [28] Borovkov A, Maslov L, Tarasenko F, Zhmaylo M, Maslova I, Solovev D (2021) Development of elastic–plastic model of additively produced titanium for personalised endoprosthetics. *The International Journal of Advanced Manufacturing Technology* pp 1–16
- [29] Boyce B, Chen X, Peters J, Hutchinson J, Ritchie R (2003) Mechanical relaxation of localized residual stresses associated with foreign object damage. *Materials Science and Engineering: A* 349(1-2):48–58
- [30] Brackbill JU, Ruppel HM (1986) FLIP: A method for adaptively zoned, particle-in-cell calculations of fluid flows in two dimensions. *Journal of Computational physics* 65(2):314–343
- [31] Bridgman P (1953) The effect of pressure on the tensile properties of several metals and other materials. *Journal of Applied Physics* 24(5):560–570
- [32] Bridgman PW (1964) *Studies in large plastic flow and fracture*. Harvard University Press
- [33] Bronstein I, Semendjajew K, Musiol G, Mühlig H (2005) *Taschenbuch der Mathematik* ((6. Auflage) ed.). Verlag Harri Deutsch, Frankfurt am Main
- [34] Brookshaw L (1985) A Method of Calculating Radiative Heat Diffusion in Particle Simulations. *Astronomical Society of Australia, Proceedings* (ISSN 0066-9997)
- [35] Buchkremer S, Klocke F, Veselovac D (2016) 3D FEM simulation of chip breakage in metal cutting. *The International Journal of Advanced Manufacturing Technology* 82(1-4):645–661
- [36] Büttner H, Vieira G, Hajri M, Vöggtlin M, Kuster F, Stirnimann J, Wegener K (2019) A comparison between micro milling pure copper and tungsten reinforced copper for electrodes in EDM applications. *Precision Engineering* 60:326–339
- [37] Büttner H, Vieira G, Wiessner M, Wegener K (2019) BURR FREE MICRO MILLING FOR ELECTRODES IN DIE-SINKING EDM. In: 25th ABCM International Congress of Mechanical Engineering (COBEM 2019)
- [38] Calamaz M, Coupard D, Girot F (2008) A new material model for 2D numerical simulation of serrated chip formation when machining titanium alloy Ti–6Al–4V. *International Journal of Machine Tools and Manufacture* 48(3-4):275–288
- [39] Calamaz M, Coupard D, Girot F (2010) Numerical simulation of titanium alloy dry machining with a strain softening constitutive law. *Machining Science and Technology* 14(2):244–257
- [40] Calamaz M, Coupard D, Nouari M, Girot F (2011) Numerical analysis of chip formation and shear localisation processes in machining the Ti–6Al–4V titanium alloy. *The International Journal of Advanced Manufacturing Technology* 52(9-12):887–895

- [41] Campbell RVJRRJ (2006) SPH in a Total Lagrangian Formalism. CMES
- [42] Chabbi L, Hasler S, Roelofs H, Haupt-Peter H (2017) Challenges and Innovation in Steel Wire Production. In: Materials Science Forum, Trans Tech Publications Ltd, vol 892, pp 3–9
- [43] Chaboche J (1977) Viscoplastic constitutive equations for description of cyclic and anisotropic behavior of metals. Bulletin De L Academie Polonaise Des Sciences-Serie Des Sciences Techniques 25(1):39–48
- [44] Chen Y, Li H, Wang J (2015) Further development of Oxley's predictive force model for orthogonal cutting. Machining Science and Technology 19(1):86–111
- [45] Cockcroft M, Latham D (1968) Ductility and the workability of metals. J Inst Metals 96(1):33–39
- [46] Cowper GR, Symonds PS (1957) Strain-hardening and strain-rate effects in the impact loading of cantilever beams. Tech. rep., Brown Univ Providence Ri
- [47] Crichigno Filho J (2017) Applying extended Oxley's machining theory and particle swarm optimization to model machining forces. The International Journal of Advanced Manufacturing Technology 89(1-4):1127–1136
- [48] CTDyka R (1995) An approach for tension instability in smoothed particle hydrodynamics (SPH). Computers & Structures
- [49] Degond P, Mas-Gallic S (1989) The weighted particle method for convection-diffusion equations. I. The case of an isotropic viscosity. Mathematics of computation 53(188):485–507
- [50] Denkena B, Tönshoff HK (2011) Spanen: Grundlagen. Springer-Verlag
- [51] Desmorat R, Desmorat B, Olive M, Kolev B (2018) Micromechanics based framework with second-order damage tensors. European Journal of Mechanics-A/Solids 69:88–98
- [52] DIN50125:2016-12 (2016) Prüfung metallischer Werkstoffe – Zugproben
- [53] Directive E (2011) Directive 2011/37/EC of the European Parliament and of the Council on End-of Life Vehicles. Official Journal of the European Communities, Article
- [54] DLHicks JSMF (1994) An Analysis of Smoothed Particle Hydrodynamics. •
- [55] Doege E, Meyer-Nolkemper H, Saeed I (1986) Fließkurvenatlas metallischer Werkstoffe: mit Fließkurven für 73 Werkstoffe und einer grundlegenden Einführung. Hanser
- [56] Doherty R, Hughes D, Humphreys F, Jonas J, Jensen DJ, Kassner M, King W, McNelley T, McQueen H, Rollett A (1997) Current issues in recrystallization: a review. Materials Science and Engineering: A 238(2):219–274
- [57] Ducobu F, Rivière-Lorphèvre E, Filippi E (2014) Numerical contribution to the comprehension of saw-toothed Ti6Al4V chip formation in orthogonal cutting. International Journal of Mechanical Sciences 81:77–87

- [58] Ducobu F, Arrazola PJ, Rivière-Lorphèvre E, Filippi E (2015) Comparison of several behaviour laws intended to produce a realistic Ti6Al4V chip by finite elements modelling. In: *Key Engineering Materials*, Trans Tech Publ, vol 651, pp 1197–1203
- [59] Ducobu F, Rivière-Lorphèvre E, Filippi E (2015) Experimental contribution to the study of the Ti6Al4V chip formation in orthogonal cutting on a milling machine. *International Journal of Material Forming* 8(3):455–468
- [60] Ducobu F, Rivière-Lorphèvre E, Filippi E (2016) Material constitutive model and chip separation criterion influence on the modeling of Ti6Al4V machining with experimental validation in strictly orthogonal cutting condition. *International journal of mechanical sciences* 107:136–149
- [61] Ducobu F, Rivière-Lorphèvre E, Filippi E (2017) On the importance of the choice of the parameters of the Johnson-Cook constitutive model and their influence on the results of a Ti6Al4V orthogonal cutting model. *International Journal of Mechanical Sciences* 122:143–155
- [62] Ducobu F, Arrazola PJ, Riviere-Lorphevre E, Filippi E (2020) On the selection of an empirical material constitutive model for the finite element modeling of Ti6Al4V orthogonal cutting, including the segmented chip formation. *International Journal of Material Forming* pp 1–14
- [63] Ehrhardt F (2014) Thermo-Mechanical Lifetime Assessment of Components for 700°C Steam Turbine Applications. PhD thesis, ETH Zürich
- [64] Ernst H (1939) *Physics of metal cutting*. Cincinnati Milling Machine and Cincinnati Grinders
- [65] Fishelov D (1990) A new vortex scheme for viscous flows. *Journal of computational physics* 86(1):211–224
- [66] Fogel LJ (1963) *Biotechnology: concepts and applications*. Prentice-Hall
- [67] Follansbee P, Kocks U (1988) A constitutive description of the deformation of copper based on the use of the mechanical threshold stress as an internal state variable. *Acta Metallurgica* 36(1):81–93
- [68] Garg S, Pant M (2018) Meshfree methods: A comprehensive review of applications. *International Journal of Computational Methods* 15(04):1830001
- [69] Gerstgrasser M, Smolenicki D, Akbari M, Klippel H, Roelofs H, Cadoni E, Wegener K (2021) Analysis of two parameter identification methods for original and modified Johnson-Cook fracture strains, including numerical comparison and validation of a new blue-brittle dependent fracture model for free-cutting Steel 50SiB8. *Theoretical and Applied Fracture Mechanics* p 102905
- [70] Göddeke D, Strzodka R, Turek S (2005) Accelerating double precision FEM simulations with GPUs. Univ.

Bibliography

- [71] Göddeke D, Strzodka R, Mohd-Yusof J, McCormick P, Buijssen SH, Grajewski M, Turek S (2007) Exploring weak scalability for FEM calculations on a GPU-enhanced cluster. *Parallel Computing* 33(10-11):685–699
- [72] Goldberg D (1991) What every computer scientist should know about floating-point arithmetic. *ACM computing surveys (CSUR)* 23(1):5–48
- [73] Gordon R Johnson WHC (1985) Fracture Characteristics of three Metals subjected to various Strains, Strain Rates, Temperatures and Pressures. *Engineering Fracture Mechanics*
- [74] Goto D, Bingert J, Reed W, Garrett Jr R (2000) Anisotropy-corrected MTS constitutive strength modeling in HY-100 steel. *Scripta materialia* 42(12):1125–1131
- [75] Green S (2010) Particle simulation using cuda. *NVIDIA whitepaper* 6:121–128
- [76] Gross D, Seelig T (2007) *Bruchmechanik—Mit einer Einführung in die Mikromechanik-4, bearbeitete Auflage*
- [77] Grüneisen E (1912) Theorie des festen Zustandes einatomiger Elemente. *Annalen der Physik* 344(12):257–306
- [78] Guilkey J, Harman T, Luitjens J, Schmidt J, Thornock J, de St Germain J, Shankar S, Peterson J, Brownlee C, Reid C, et al. (2009) Uintah user guide. Tech. rep., SCI Institute Technical Report
- [79] Guinan MW, Steinberg DJ (1974) Pressure and temperature derivatives of the isotropic polycrystalline shear modulus for 65 elements. *Journal of Physics and Chemistry of Solids* 35(11):1501–1512
- [80] Guo Y, Wen Q, et al. (2000) A hybrid modeling approach to investigate chip morphology transition with the stagnation effect by cutting edge geometry. *Society of Manufacturing Engineers*
- [81] Guo Y, Wen Q, Woodbury K (2006) Dynamic material behavior modeling using internal state variable plasticity and its application in hard machining simulations. *Journal of Manufacturing Science and Engineering* 128(3):749–759
- [82] Göldner H (1985) *Lehrbuch Höhere Festigkeitslehre, Band 2. Physik- Verlag Weinheim*
- [83] Hallquist JO, et al. (2006) *LS-DYNA theory manual. Livermore software Technology corporation* 3:25–31
- [84] Hardt M, Schraknepper D, Bergs T (2020) Investigations on the Application of the Downhill-Simplex-Algorithm to the Inverse Determination of Material Model Parameters for FE-Machining Simulations. *Simulation Modelling Practice and Theory* 107:102214
- [85] Harlow FH, Evans M (1955) A machine calculation method for hydrodynamic problems. *LAMS-1956*

- [86] Harris C, Millman K, van der Walt S, Gommers R, Virtanen P, Cournapeau D, Wieser E, Taylor J, Berg S, Smith N, Kern R, Picus M, Hoyer S, van Kerkwijk M, Brett M, Haldane A, del Río JF, Wiebe M, Peterson P, Gérard-Marchant P, Sheppard K, Reddy T, Weckesser W, Abbasi H, Gohlke C, Oliphant T (2020) Array programming with NumPy. *Nature* 585(7825):357–362, DOI 10.1038/s41586-020-2649-2, URL <https://doi.org/10.1038/s41586-020-2649-2>
- [87] Härtel S, Graf M, Awiszus B, Abstoss KG, Hild R (2018) Novel Approach for the Determination of the Taylor-Quinney Coefficient. In: *Materials Science Forum*, Trans Tech Publ, vol 918, pp 103–109
- [88] Heinstein M, Segalman D (1997) Simulation of orthogonal cutting with smooth particle hydrodynamics. Sandia National Laboratories, California
- [89] Hibbitt D, Karlsson B, Sorensen P (2014) ABAQUS user-manual release 6.14. Dassault Systèmes Simulia Corp, Providence, RI
- [90] Hibbitt K, Sorensen I (1998) ABAQUS theory manual. Hibbitt, Karlsson, and Sorensen, Inc Pawtucket, RI
- [91] Hiermaier S (2007) Structures under crash and impact: continuum mechanics, discretization and experimental characterization. Springer Science & Business Media
- [92] Hill R (1948) A theory of the yielding and plastic flow of anisotropic metals. *Proceedings of the Royal Society of London Series A Mathematical and Physical Sciences* 193(1033):281–297
- [93] Hillerborg A, Modéer M, Petersson PE (1976) Analysis of crack formation and crack growth in concrete by means of fracture mechanics and finite elements. *Cement and concrete research* 6(6):773–781
- [94] Hobart R (1965) Peierls stress dependence on dislocation width. *Journal of Applied Physics* 36(6):1944–1948
- [95] Hodowany J, Ravichandran G, Rosakis A, Rosakis P (2000) Partition of plastic work into heat and stored energy in metals. *Experimental mechanics* 40(2):113–123
- [96] Holland JH (1975) Adaptation in natural and artificial systems, University of Michigan press. Ann arbor, MI 1(97):5
- [97] Hopkinson B (1914) X. A method of measuring the pressure produced in the detonation of high explosives or by the impact of bullets. *Philosophical Transactions of the Royal Society of London Series A, Containing Papers of a Mathematical or Physical Character* 213(497-508):437–456
- [98] IEEE (2008) IEEE Standard for Floating-Point Arithmetic. IEEE Std 754-2008 pp 1–70, DOI 10.1109/IEEESTD.2008.4610935
- [99] Issa M, Labergère C, Saanouni K, Rassineux A (2012) Numerical prediction of thermomechanical field localization in orthogonal cutting. *CIRP Journal of Manufacturing Science and technology* 5(3):175–195

Bibliography

- [100] Jaiswal AP, Khanna N, Bajpai V (2020) Orthogonal machining of Heat Treated Ti-10-2-3: FE and Experimental. *Materials and Manufacturing Processes* 35(16):1822–1831
- [101] Jaspers S, Dautzenberg J (2002) Material behaviour in conditions similar to metal cutting: flow stress in the primary shear zone. *Journal of Materials Processing Technology* 122(2-3):322–330
- [102] Jawahir I, Brinksmeier E, M'saoubi R, Aspinwall D, Outeiro J, Meyer D, Umbrello D, Jayal A (2011) Surface integrity in material removal processes: Recent advances. *CIRP Annals-Manufacturing Technology* 60(2):603–626
- [103] JKChen C JE Beraun (1999) An improvement for tensile instability in smoothed particle hydrodynamics. *Computational Mechanics*
- [104] Johnson G (1985) Strength and fracture characteristics of a titanium alloy (. 06al,. 04v) subjected to various strains, strain rates, temperatures and pressures. Naval Surface Weapons Center NSWC TR pp 86–144
- [105] Johnson G, Cook W (1983) A Constitutive modeling and data for metals subjected to large strain rates and high temperatures. *Proceedings of 7th international symposium on ballistics* pp 541–577
- [106] Johnson GR, Beissel SR (1996) Normalized smoothing functions for SPH impact computations. *International Journal for Numerical Methods in Engineering* 39(16):2725–2741
- [107] JP Gray R JJ Monaghan (2001) SPH elastic dynamics. *Computer methods in applied mechanics and engineering*
- [108] Kachanov L (1958) On creep rupture time. *Izv Acad Nauk SSSR, Otd Techn Nauk* 8:26–31
- [109] Kawamura K, Hashimoto H, Matsuda A, Terada D (2016) SPH simulation of ship behaviour in severe water-shipping situations. *Ocean Engineering* 120:220–229
- [110] Kienzle O, Victor H (1957) Spezifische Schnittkräfte bei der Metallbearbeitung. *Werkstattstechnik und Maschinenbau* 47(5):224–225
- [111] Kleijnen JP, Sargent RG (2000) A methodology for fitting and validating metamodels in simulation. *European Journal of Operational Research* 120(1):14–29
- [112] Klippel H, Gerstgrasser M, Smolenicki D, Cadoni E, Roelofs H, Wegener P, et al. (2020) Johnson Cook Flow Stress Parameter for Free Cutting Steel 50SiB8. *arXiv preprint arXiv:200714087*
- [113] Klippel H, Röthlin M, Wegener K (2021) Load Path Visualization in the Principal Stress System. -
- [114] Kocks U (2001) Realistic constitutive relations for metal plasticity. *Materials Science and Engineering: A* 317(1):181–187

- [115] Kolsky H (1949) An investigation of the mechanical properties of materials at very high rates of loading. *Proceedings of the physical society Section B* 62(11):676
- [116] Kotyk M (2020) Analytic Model of Maximal Experimental Value of Stress Intensity Factor K_Q for AA2519–AA1050–Ti6Al4V Layered Material. *Materials* 13(19):4439
- [117] Koza JR, Koza JR (1992) Genetic programming: on the programming of computers by means of natural selection, vol 1. MIT press
- [118] Kress G, Keller D (2007) Structural optimization. Lecture notes Zentrum für Strukturtechnologien, ETH Zurich, Switzerland
- [119] Kröner E (1959) Allgemeine kontinuumstheorie der versetzungen und eigenspannungen. *Archive for Rational Mechanics and Analysis* 4(1):273
- [120] Lalwani D, Mehta N, Jain P (2009) Extension of Oxley's predictive machining theory for Johnson and Cook flow stress model. *Journal of materials processing technology* 209(12-13):5305–5312
- [121] Lee E (1951) The theory of plasticity applied to a problem of machining. *ASME J Appl Mech* 18:405
- [122] Lee E, Liu D (1967) Finite-strain elastic—plastic theory with application to plane-wave analysis. *Journal of Applied Physics* 38(1):19–27
- [123] Lee WS, Lin CF (1998) Plastic deformation and fracture behaviour of Ti–6Al–4V alloy loaded with high strain rate under various temperatures. *Materials Science and Engineering: A* 241(1-2):48–59
- [124] Leinonen J, von Lerber A (2018) Snowflake melting simulation using smoothed particle hydrodynamics. *Journal of Geophysical Research: Atmospheres* 123(3):1811–1825
- [125] Lemaitre J, Chaboche JL (1994) *Mechanics of solid materials*. Cambridge university press
- [126] Lemaitre J, Desmorat R (2005) *Engineering damage mechanics: ductile, creep, fatigue and brittle failures*. Springer Science & Business Media
- [127] Li J, Li Q, Jiang J, Dai J (2018) Particle swarm optimization procedure in determining parameters in Chaboche kinematic hardening model to assess ratcheting under uniaxial and biaxial loading cycles. *Fatigue & Fracture of Engineering Materials & Structures* 41(7):1637–1645
- [128] Li L, He N (2006) A FEA study on mechanisms of saw-tooth chip deformation in high speed cutting of Ti–6–Al–4V alloy. In: *Fifth international conference on high speed machining (HSM)*, Metz, France, vol 14, p 16
- [129] Libersky LD, Randles PW, Carney TC, Dickinson DL (1997) Recent improvements in SPH modeling of hypervelocity impact. *International Journal of Impact Engineering* 20(6-10):525–532

Bibliography

- [130] Libersky RVJCL (1998) A treatment of zero-energy modes in the smoothed particle hydrodynamics method. *Computer methods in applied mechanics and engineering*
- [131] Lim J (2007) High speed tensile test of automotive steel sheets at the intermediate strain rate. *Technical Rep 16*
- [132] Linjiang H, Honghua S, Jiuhua X, Zhang L (2018) Inverse identification of constitutive parameters of Ti₂AlNb intermetallic alloys based on cooperative particle swarm optimization. *Chinese Journal of Aeronautics* 31(8):1774–1785
- [133] Liu G, Huang C, Su R, Özel T, Liu Y, Xu L (2019) 3D FEM simulation of the turning process of stainless steel 17-4PH with differently texturized cutting tools. *International Journal of Mechanical Sciences* 155:417–429
- [134] Liu J, Bai Y, Xu C (2014) Evaluation of ductile fracture models in finite element simulation of metal cutting processes. *Journal of Manufacturing Science and Engineering* 136(1)
- [135] Liu M, Liu G, Zong Z, Lam K (2000) Numerical simulation of underwater explosion by SPH. *Advances in Computational Engineering & Science* 1:1475–1480
- [136] Liu M, Liu G, Zong Z, Lam K (2001) Numerical simulation of incompressible flows by SPH. In: *International Conference on Scientific & Engineering Computational*, Beijing
- [137] Lizotte DJ, Wang T, Bowling MH, Schuurmans D (2007) Automatic Gait Optimization with Gaussian Process Regression. In: *IJCAI*, vol 7, pp 944–949
- [138] Llanos I, Villar J, Urresti I, Arrazola P (2009) Finite element modeling of oblique machining using an arbitrary Lagrangian–Eulerian formulation. *Machining Science and Technology* 13(3):385–406
- [139] Lode W (1926) Versuche über den Einfluß der mittleren Hauptspannung auf das Fließen der Metalle Eisen, Kupfer und Nickel. *Zeitschrift für Physik* 36(11-12):913–939
- [140] Lucy LB (1977) A numerical approach to the testing of the fission hypothesis. *The astronomical journal* 82:1013–1024
- [141] Mabrouki T, Deshayes L, Ivester R, Rigal J, Jurens K (2004) Material modeling and experimental study of serrated chip morphology. In: *Proceedings of the 7th CIRP International Workshop on The Modeling of Machining Operations, ENSAM, Cluny, France*, pp 4–5
- [142] Mabrouki T, Girardin F, Asad M, Rigal JF (2008) Numerical and experimental study of dry cutting for an aeronautic aluminium alloy (A2024-T351). *International Journal of Machine Tools and Manufacture* 48(11):1187–1197
- [143] MacDonald RA, MacDonald WM (1981) Thermodynamic properties of fcc metals at high temperatures. *Physical review B* 24(4):1715
- [144] MacGregor C, Fisher J (1946) A velocity-modified temperature for the plastic flow of metals. *Journal of applied mechanics-transactions of the ASME* 13(1):A11–A16

- [145] Madaj M, Píška M (2013) On the SPH orthogonal cutting simulation of A2024-T351 alloy. *Procedia CIRP* 8:152–157
- [146] Maier M, Zwicker R, Akbari M, Rupenyan A, Wegener K (2019) Bayesian optimization for autonomous process set-up in turning. *CIRP Journal of Manufacturing Science and Technology* 26:81–87
- [147] Malakizadi A, Cedergren S, Sadik I, Nyborg L (2016) Inverse identification of flow stress in metal cutting process using Response Surface Methodology. *Simulation Modelling Practice and Theory* 60:40–53
- [148] Markus Becker MT Markus Ihmsen (2009) Corotated SPH for deformable solids. *Eurographics Workshop on Natural Phenomena*
- [149] Mazen Issa CLAR Khemais Saanouni (2011) Prediction of serrated chip formation in orthogonal metal cutting by advanced adaptive 2D numerical methodology. *Int J Machining and Machinability of Materials*
- [150] McClintock FA (1968) A criterion for ductile fracture by the growth of holes. *Journal of Applied Mechanics*
- [151] Meier L (2019) Methods to reduce variation in cutting tool life tests. *The International Journal of Advanced Manufacturing Technology* 103(1):355–365
- [152] Meier L, Schaal N, Wegener K (2017) In-process Measurement of the Coefficient of Friction on Titanium. *Procedia Cirp* 58:163–168
- [153] Merchant HEM, Ernst H (1941) Chip formation, friction and high quality machined surfaces. *Sur Treat Metal* pp 299–378
- [154] Merchant M (1998) An interpretive look at 20th century research on modeling of machining. *Machining Science and Technology* 2(2):157–163
- [155] Merchant ME (1945) Mechanics of the metal cutting process. I. Orthogonal cutting and a type 2 chip. *Journal of applied physics* 16(5):267–275
- [156] Merchant ME (1945) Mechanics of the metal cutting process. II. Plasticity conditions in orthogonal cutting. *Journal of applied physics* 16(6):318–324
- [157] Meyer Jr HW, Kleponis DS (2001) An analysis of parameters for the Johnson-Cook strength model for 2-in-thick Rolled Homogeneous Armor. Tech. rep., Army Research Lab Aberdeen Proving Ground MD
- [158] Meyer Jr HW, Kleponis DS (2001) Modeling the high strain rate behavior of titanium undergoing ballistic impact and penetration. *International Journal of Impact Engineering* 26(1-10):509–521
- [159] Mie G (1903) Zur kinetischen Theorie der einatomigen Körper. *Annalen der Physik* 316(8):657–697
- [160] Mockus J, Tiesis V, Zilinskas A (1978) The application of Bayesian methods for seeking the extremum. *Towards global optimization* 2(117-129):2

Bibliography

- [161] Mohammadnejad M, Dehkhoda S, Fukuda D, Liu H, Chan A (2020) GPGPU-parallelised hybrid finite-discrete element modelling of rock chipping and fragmentation process in mechanical cutting. *Journal of Rock Mechanics and Geotechnical Engineering* 12(2):310–325
- [162] Monaghan J (1989) On the problem of penetration in particle methods. *Journal of Computational physics* 82(1):1–15
- [163] Monaghan JJ (2000) SPH without a tensile instability. *Journal of Computational Physics* 159(2):290–311
- [164] Monaghan JJ (2005) Smoothed particle hydrodynamics. *Reports on progress in physics* 68(8):1703
- [165] Monaghan JJ, Gingold RA (1983) Shock simulation by the particle method SPH. *Journal of computational physics* 52(2):374–389
- [166] Mou ZY, Gao PF, Wang WF, Wen DH (2011) 3D Finite Element Simulation on the Orthogonal Cutting Processes with Different Commercial Codes. In: *Advanced Materials Research, Trans Tech Publ*, vol 188, pp 555–560
- [167] Moufki A, Molinari A, Dudzinski D (1998) Modelling of orthogonal cutting with a temperature dependent friction law. *Journal of the Mechanics and Physics of Solids* 46(10):2103–2138
- [168] Mroz Z (1967) On the description of anisotropic workhardening. *Journal of the Mechanics and Physics of Solids* 15(3):163–175
- [169] Müller M, Schirm S, Teschner M (2004) Interactive blood simulation for virtual surgery based on smoothed particle hydrodynamics. *Technology and Health Care* 12(1):25–31
- [170] Müller SD (2002) Bio-inspired optimization algorithms for engineering applications. PhD thesis, ETH Zurich
- [171] Murugesan M, Jung DW (2019) Two flow stress models for describing hot deformation behavior of AISI-1045 medium carbon steel at elevated temperatures. *Heliyon* 5(4):e01347
- [172] Nairn JA (2015) Numerical simulation of orthogonal cutting using the material point method. *Engineering Fracture Mechanics* 149:262–275
- [173] Nelder JA, Mead R (1965) A simplex method for function minimization. *The computer journal* 7(4):308–313
- [174] Nguyen HP, Derewońko A, Niezgodą T (2015) THERMAL-MECHANICAL COUPLED SIMULATION. *Journal of KONES Powertrain and Transport* 22(3)
- [175] Norton FH (1929) *The creep of steel at high temperatures*. 35, McGraw-Hill Book Company, Incorporated

- [176] Oliver J, Cante J, Weyler R, González C, Hernández J (2007) Particle finite element methods in solid mechanics problems. In: Computational plasticity, Springer, pp 87–103
- [177] Olleak AA, El-Hofy HA (2015) Prediction of Cutting Forces in High Speed Machining of Ti6Al4V Using SPH Method. In: ASME 2015 International Manufacturing Science and Engineering Conference, American Society of Mechanical Engineers, pp V001T02A018–V001T02A018
- [178] Oñate E, Idelsohn SR, Del Pin F, Aubry R (2004) The particle finite element method—an overview. *International Journal of Computational Methods* 1(02):267–307
- [179] Osorio-Pinzon JC, Abolghasem S, Maranon A, Casas-Rodriguez JP (2020) Cutting parameter optimization of Al-6063-O using numerical simulations and particle swarm optimization. *The International Journal of Advanced Manufacturing Technology* 111(9):2507–2532
- [180] Ottosen NS, Ristinmaa M (2005) *The mechanics of constitutive modeling*. Elsevier
- [181] Oxley P, Hastings W (1977) Predicting the strain rate in the zone of intense shear in which the chip is formed in machining from the dynamic flow stress properties of the work material and the cutting conditions. *Proceedings of the Royal Society of London A Mathematical and Physical Sciences* 356(1686):395–410
- [182] Oxley PLB (1989) *The mechanics of machining: an analytical approach to assessing machinability*. Ellis Horwood
- [183] Papenfuss C, Van P (2007) Scalar, vectorial and tensorial damage parameters from the mesoscopic background. arXiv preprint arXiv:07120087
- [184] Parisch H (2003) *Festkörper-Kontinuumsmechanik*. BG Teubner 144
- [185] Payten WM, Dean DW, Snowden KU (2010) A strain energy density method for the prediction of creep–fatigue damage in high temperature components. *Materials Science and Engineering: A* 527(7):1920–1925
- [186] Pedregosa F, Varoquaux G, Gramfort A, Michel V, Thirion B, Grisel O, Blondel M, Prettenhofer P, Weiss R, Dubourg V, Vanderplas J, Passos A, Cournapeau D, Brucher M, Perrot M, Duchesnay E (2011) Scikit-learn: Machine Learning in Python. *Journal of Machine Learning Research* 12:2825–2830
- [187] Perzyna P (1966) Fundamental problems in viscoplasticity. In: *Advances in applied mechanics*, vol 9, Elsevier, pp 243–377
- [188] Petschek LDLA (1991) *Smooth Particle Hydrodynamics With Strength of Materials*. Unklar; Center for Explosives Technology Research and Department of Physics
- [189] Pirozzi C, Franchitti S, Borrelli R, Chiariello A, Di Palma L (2020) The Effect of Post-Processing on the Mechanical Behavior of Ti6Al4V Manufactured by Electron Beam Powder Bed Fusion for General Aviation Primary Structural Applications. *Aerospace* 7(6):75

Bibliography

- [190] Prasad MD, kumar Namala K (2018) Process parameters optimization in friction stir welding by ANOVA. *Materials Today: Proceedings* 5(2):4824–4831
- [191] Preston DL, Tonks DL, Wallace DC (2003) Model of plastic deformation for extreme loading conditions. *Journal of Applied Physics* 93(1):211–220
- [192] Price DJ (2012) Smoothed particle hydrodynamics and magnetohydrodynamics. *Journal of Computational Physics* 231(3):759–794
- [193] Puls H, Klocke F, Lung D (2012) A new experimental methodology to analyse the friction behaviour at the tool-chip interface in metal cutting. *Production engineering* 6(4-5):349–354
- [194] PWRandles L (1996) Smoothed Particle Hydrodynamics: Some recent improvements and applications. *Computational Methods in applied mechanics and engineering*
- [195] PWRandles L (2000) Normalized SPH with stress points. *International Journal for Numerical Methods in Engineering*
- [196] R A Gingold JJM (1977) Smoothed Particle Hydrodynamics: theory and application to non-spherical stars. *Monthly Notices of the Royal Astronomical Society*
- [197] Rabotnov YN, Leckie F, Prager W (1970) Creep Problems in Structural Members. *Journal of Applied Mechanics* 37:249
- [198] Rechenberg I (1973) *Evolutionsstrategie—Optimierung technischer Systeme nach Prinzipien der biologischen Information*
- [199] Reckling KA (1967) *Plastizitätstheorie und ihre Anwendung auf Festigkeitsprobleme*. Springer
- [200] Reveles JR (2007) Development of a Total Lagrangian SPH Code for the Simulation of Solids Under Dynamic Loading. PhD thesis, Cranfield University
- [201] Rice JR, Tracey DM (1969) On the ductile enlargement of voids in triaxial stress fields. *Journal of the Mechanics and Physics of Solids* 17(3):201–217
- [202] Rodríguez J, Cante J, Oliver X (2015) On the numerical modelling of machining processes via the Particle finite Element method (PFEM). Monograph CIMNE
- [203] Rodríguez J, Jonsén P, Svoboda A (2017) Simulation of metal cutting using the particle finite-element method and a physically based plasticity model. *Computational Particle Mechanics* 4(1):35–51
- [204] Rodríguez JM, Carbonell JM, Cante J, Oliver J (2017) Continuous chip formation in metal cutting processes using the Particle Finite Element Method (PFEM). *International Journal of Solids and Structures* 120:81–102
- [205] Rodríguez JM, Larsson S, Carbonell JM, Jonsén P (2020) Dislocation density based flow stress model applied to the PFEM simulation of orthogonal cutting processes of Ti-6Al-4V. *Materials* 13(8):1979

- [206] Rodriguez Prieto JM, Jonsén P, Svoboda A (2016) A particle finite element method for machining simulations. In: VII European Congress on Computational Methods in Applied Sciences and Engineering, Crete Island, Greece, 5–10 June 05/06/2016–10/06/2016, National Technical University of Athens, vol 1, pp 539–553
- [207] Roelofs H, Renaudot N, Smolenicki D, Boos J, Kuster F (2017) The behaviour of graphitized steels in machining processes. In: Materials Science Forum, Trans Tech Publications Ltd, vol 879, pp 1600–1605
- [208] Röthlin M (2019) Meshless Software Tool to Simulate Metal Cutting Operations by Employing Contemporary Numerical Methods. ETH Zurich
- [209] Röthlin M, Klippel H, Wegener K (2018) Meshless methods for large deformation elastodynamics. arXiv preprint arXiv:180701117
- [210] Röthlin M, Klippel H, Afrasiabi M, Wegener K (2019) Meshless single grain cutting simulations on the GPU. *International Journal of Mechatronics and Manufacturing Systems* 12(3-4):272–297
- [211] Röthlin M, Klippel H, Afrasiabi M, Wegener K (2019) Metal cutting simulations using smoothed particle hydrodynamics on the GPU. *The International Journal of Advanced Manufacturing Technology* 102(9):3445–3457
- [212] Rumpf M, Strzodka R (2001) Using graphics cards for quantized FEM computations. Citeseer
- [213] Rüttimann N (2012) Simulation of Metal Cutting Processes Using Meshfree Methods. PhD thesis, ETH Zürich
- [214] Rüttimann N, Buhl S, Wegener K (2010) Simulation of single grain cutting using SPH method. *Journal of Machine Engineering* 10
- [215] Sabel M, Sator C, Müller R (2014) A particle finite element method for machining simulations. *Computational Mechanics* 54(1):123–131
- [216] Sandvik (2021) Sandvik Homepage. <https://www.sandvik.coromant.com/de-de/products/Pages/productdetails.aspx?c=CCMW%2009%20T3%2004%20%20%20%20%20%20%20%20H13A>, accessed: 23.02.2021
- [217] Sen S, Banerjee B, Shaw A (2020) Taylor impact test revisited: Determination of plasticity parameters for metals at high strain rate. *International Journal of Solids and Structures* 193:357–374
- [218] Shao G, Zhu S, Wang Y, Zhao Q (2017) An internal state variable thermodynamic model for determining the Taylor-Quinney coefficient of glassy polymers. *International Journal of Mechanical Sciences* 126:261–269
- [219] Shaofan Li WKL (2004) *Meshfree Particle Methods*. Springer
- [220] Shirakashi T, Usui E (1976) Simulation analysis of orthogonal metal cutting process. *J Japan Soc Prec Eng* 42(5):340–345

Bibliography

- [221] Shrot A, Bäker M (2010) Is it possible to identify Johnson-Cook law parameters from machining simulations? *International Journal of Material Forming* 3(1):443–446
- [222] Shrot A, Bäker M (2012) A study of non-uniqueness during the inverse identification of material parameters. *Procedia CIRP* 1:72–77
- [223] Sievert R, Noack H, Hamann A, Löwe P, Singh K, Künecke G, Clos R, Schreppe U, Veit P, Uhlmann E, et al. (2003) Simulation der Spansegmentierung beim Hochgeschwindigkeits-zerspanen unter Berücksichtigung duktiler Schädigung. *Technische Mechanik* 23(2-4):216–233
- [224] Sima M, Özel T (2010) Modified material constitutive models for serrated chip formation simulations and experimental validation in machining of titanium alloy Ti-6Al-4V. *International Journal of Machine Tools and Manufacture* 50(11):943–960
- [225] Smolenicki D (2017) Chip formation analysis of innovative graphitic steel in drilling processes. PhD thesis, ETH Zurich
- [226] Snoek J, Larochelle H, Adams RP (2012) Practical bayesian optimization of machine learning algorithms. arXiv preprint arXiv:12062944
- [227] de Souza Neto EA, Peric D, Owen DR (2011) *Computational methods for plasticity: theory and applications*. John Wiley & Sons
- [228] Spendley W, Hext GR, Himsworth FR (1962) Sequential application of simplex designs in optimisation and evolutionary operation. *Technometrics* 4(4):441–461
- [229] Sridhar P, Prieto JMR, de Payrebrune KM (2020) Discretization approaches to model orthogonal cutting with Lagrangian, Arbitrary Lagrangian Eulerian, Particle Finite Element method and Smooth Particle Hydrodynamics formulations. *Procedia CIRP* 93:1496–1501
- [230] Steinberg D, Lund C (1989) A constitutive model for strain rates from 10^{-4} to 10^6 s⁻¹. *Journal of Applied Physics* 65(4):1528–1533
- [231] Steinberg D, Cochran S, Guinan M (1980) A constitutive model for metals applicable at high-strain rate. *Journal of Applied Physics* 51(3):1498–1504
- [232] Stöcker DMM (2007) *Untersuchung von Optimierungsverfahren für rechenzeitaufwändige technische Anwendungen in der Motorenentwicklung*
- [233] Storn R, Price K (1997) Differential evolution—a simple and efficient heuristic for global optimization over continuous spaces. *Journal of global optimization* 11(4):341–359
- [234] Strenkowski J, Moon KJ (1990) Finite element prediction of chip geometry and tool/workpiece temperature distributions in orthogonal metal cutting. *Journal of Engineering for Industry* 112(4):313–318
- [235] Sulsky D, Chen Z, Schreyer H (1992) The application of a material-spatial numerical method to penetration. Tech. rep., Sandia National Labs., Albuquerque, NM (United States)

- [236] Sulsky D, Chen Z, Schreyer HL (1994) A particle method for history-dependent materials. *Computer methods in applied mechanics and engineering* 118(1-2):179–196
- [237] Takahashi Y, Dogan B, Gandy D (2009) Systematic evaluation of creep-fatigue life prediction methods for various alloys. In: *ASME 2009 Pressure Vessels and Piping Conference*, American Society of Mechanical Engineers, pp 1461–1470
- [238] Taylor FW (1907) The art of cutting metals. *Scientific American* 63:25942–25944
- [239] Taylor GI (1948) The use of flat-ended projectiles for determining dynamic yield stress I. Theoretical considerations. *Proceedings of the Royal Society of London Series A Mathematical and Physical Sciences* 194(1038):289–299
- [240] Taylor GI, Quinney H (1934) The latent energy remaining in a metal after cold working. *Proceedings of the Royal Society of London Series A, Containing Papers of a Mathematical and Physical Character* 143(849):307–326
- [241] Taylor ZA, Cheng M, Ourselin S (2008) High-speed nonlinear finite element analysis for surgical simulation using graphics processing units. *IEEE transactions on medical imaging* 27(5):650–663
- [242] for Testing AS, Materials (2008) Standard test method for measurement of fatigue crack growth rates: designation: E 647-08. ASTM International
- [243] Thimm B (2018) *Werkstoffmodellierung und Kennwertermittlung für die Simulation spanabhebender Fertigungsprozesse*. PhD thesis, Universität Siegen
- [244] Trent E (1977) *Metal Cutting*. Butterworths & Ltd. Butterworth & Co
- [245] Uenishi A, Teodosiu C (2004) Constitutive modelling of the high strain rate behaviour of interstitial-free steel. *International Journal of Plasticity* 20(4-5):915–936
- [246] Uhlmann E, Gerstenberger R, Schäfer M, Kuhnert J (2011) Entwicklung der netzfreien Finite-Pointset-Methode für die Zerspannsimulation. *Zeitschrift für wirtschaftlichen Fabrikbetrieb* 106(7-8):510–514
- [247] Uhlmann E, Gerstenberger R, Kuhnert J (2013) Cutting simulation with the meshfree finite pointset method. *Procedia CIRP* 8:391–396
- [248] Umer U, Qudeiri JA, Ashfaq M, Abdulrahman AA (2016) Chip morphology predictions while machining hardened tool steel using finite element and smoothed particles hydrodynamics methods. *Journal of Zhejiang University-SCIENCE A* 17(11):873–885
- [249] de Vaucorbeil A, Hutchinson CR (2020) A new total-Lagrangian smooth particle hydrodynamics approximation for the simulation of damage and fracture of ductile materials. *International Journal for Numerical Methods in Engineering* 121(10):2227–2245
- [250] Verleysen P, Peirs J (2017) Quasi-static and high strain rate fracture behaviour of Ti6Al4V. *International Journal of Impact Engineering* 108:370–388

Bibliography

- [251] Von Bednarczyk H (1968) Eine einfache Herleitung der Jaumannschen Spannungsgeschwindigkeit. *Zeitschrift für Angewandte Mathematik und Physik (ZAMP)* 19(1):140–141
- [252] VonNeumann J, Richtmyer RD (1950) A method for the numerical calculation of hydrodynamic shocks. *Journal of applied physics* 21(3):232–237
- [253] Wang Y, Tran HT, Nguyen GD, Ranjith PG, Bui HH (2020) Simulation of mixed-mode fracture using SPH particles with an embedded fracture process zone. *International Journal for Numerical and Analytical Methods in Geomechanics* 44(10):1417–1445
- [254] Wang Z, Zhang J, Xu Z, Zhang J, ul Hassan H, Li G, Zhang H, Hartmaier A, Fang F, Yan Y, et al. (2019) Crystal plasticity finite element modeling and simulation of diamond cutting of polycrystalline copper. *Journal of Manufacturing Processes* 38:187–195
- [255] Weber G, Anand L (1990) Finite deformation constitutive equations and a time integration procedure for isotropic, hyperelastic-viscoplastic solids. *Computer Methods in Applied Mechanics and Engineering* 79(2):173–202
- [256] Wendland H (1995) Piecewise polynomial, positive definite and compactly supported radial functions of minimal degree. *Advances in computational Mathematics* 4(1):389–396
- [257] Wieland, Kupral (2021) Wieland-Kupral Homepage. https://www.wieland-kupral.hu/files/shared_com/data_sheets/ex/K30_EN.pdf, accessed: 25.02.2021
- [258] Wilkins ML (1963) Calculation of elastic-plastic flow. Tech. rep., California Univ Livermore Radiation Lab
- [259] Wing Kam Liu YFZ Sukky Jun (1995) Reproducing Kernel Particle Methods. *International Journal for Numerical Methods in Fluids*
- [260] Wyen CF (2011) Rounded cutting edges and their influence in machining titanium. PhD thesis, ETH Zürich
- [261] Wyen CF, Wegener K (2010) Influence of cutting edge radius on cutting forces in machining titanium. *CIRP annals* 59(1):93–96
- [262] Wyen CF, Knapp W, Wegener K (2012) A new method for the characterisation of rounded cutting edges. *The International Journal of Advanced Manufacturing Technology* 59(9-12):899–914
- [263] Xiao G, Ren M, Hong H (2018) 50 million atoms scale molecular dynamics modelling on a single consumer graphics card. *Advances in Engineering Software* 124:66–72
- [264] Zaera R, Rodríguez-Martínez JA, Rittel D (2013) On the Taylor–Quinney coefficient in dynamically phase transforming materials. Application to 304 stainless steel. *International Journal of Plasticity* 40:185–201
- [265] Zemzemi F, Rech J, Salem WB, Dogui A, Kapsa P (2009) Identification of a friction model at tool/chip/workpiece interfaces in dry machining of AISI4142 treated steels. *Journal of materials processing technology* 209(8):3978–3990

- [266] Zerilli FJ (2004) Dislocation mechanics-based constitutive equations. *Metallurgical and Materials Transactions A* 35(9):2547–2555
- [267] Zerilli FJ, Armstrong RW (1987) Dislocation-mechanics-based constitutive relations for material dynamics calculations. *Journal of Applied Physics* 61(5):1816–1825
- [268] Zerilli FJ, Armstrong RW (1994) Constitutive relations for the plastic deformation of metals. In: *High-pressure science and technology—1993*, AIP Publishing, vol 309, pp 989–992
- [269] Zhang B, Bagchi A (1994) Finite element simulation of chip formation and comparison with machining experiment. *Journal of engineering for industry* 116(3):289–297
- [270] Zhang D, Zhang XM, Nie GC, Yang ZY, Ding H (2021) In situ imaging based thermo-mechanical analysis of built-up edge in cutting process. *Journal of Manufacturing Processes* 71:450–460
- [271] Zhang Y, Mabrouki T, Nelias D, Gong Y (2011) Chip formation in orthogonal cutting considering interface limiting shear stress and damage evolution based on fracture energy approach. *Finite Elements in Analysis and Design* 47(7):850–863
- [272] Zhang Y, Mabrouki T, Nelias D, Gong Y (2011) FE-model for titanium alloy (Ti-6Al-4V) cutting based on the identification of limiting shear stress at tool-chip interface. *International journal of material forming* 4(1):11–23
- [273] Zienkiewicz O, Cormeau I (1974) Visco-plasticity—plasticity and creep in elastic solids—a unified numerical solution approach. *International Journal for Numerical Methods in Engineering* 8(4):821–845
- [274] Zimmermann M, Schindler S, Aurich J, Steinmann P (2018) Improvement of the Machining Accuracy in Dry Turning of Aluminum Metal Matrix Composites via Experiments and Finite Element Simulations. In: *Thermal Effects in Complex Machining Processes*, Springer, pp 35–62
- [275] Zocher MA, Maudlin PJ (2000) An evaluation of several hardening models using Taylor cylinder impact data. Tech. rep., Los Alamos National Lab., NM (US)
- [276] Zorev N (1963) Inter-relationship between shear processes occurring along tool face and shear plane in metal cutting. *International research in production engineering* 49:143–152
- [277] Zou Z, Liu L, Li B, Deng W (2016) Research on burr formation mechanism in metal cutting with a backup material. *The International Journal of Advanced Manufacturing Technology* pp 1–13

CURRICULUM VITAE

- Born 26.09.1980 in Neubrandenburg (Mecklenburg, Germany), citizen of Germany
- 1987-1999 School
- 1999-2000 Civilian Service
- 2000-2008 Mechanical Engineering (Applied Mechanics) at TU Dresden, Diplom-Ingenieur
- 2003/2004 Internship at Alstom (SCHWEIZ) AG, "Probabilistische Lebensdaueranalyse von Gasturbinenrotoren und Einflußuntersuchung des Fahrkonzepts auf den Kriechlebensdauerverbrauch von Gasturbinenrotoren" (Probabilistic Creep Lifetime Assessment of Gas Turbine Rotors and Investigation of Creep Lifetime Consumption with regards to the Engine Operation Concept)
- 2004/2005 "Großer Beleg": Institute for Fluid Dynamics and Turbomachinery at TU-Dresden, "Programmierung und Validierung einer Oberfläche für das Probabilistikprogramm ProSi" (GUI Development for the in-house probabilistic software ProSi)
- 2005 Internship at Siemens Power Generation, Mülheim "Probabilistische Betrachtung von Fremdkörperschäden an der Wärmedämmschicht der ersten Turbinenlaufschaufel" (Probabilistic Lifetime Optimisation of 1st row turbine blades)
- 2007 Diploma Thesis at Alstom (SCHWEIZ) AG, "Rissfortschrittsuntersuchung an einem Fixierungselement eines Gasturbinengehäuses" (Crack Propagation Assessment of the Backholder GT24/GT26)
- 2007-2013 R&D Engineer Alstom (SCHWEIZ) AG, Gas Turbine Combustor Development (Mechanical Integrity)
- 2013-2015 R&D Engineer Alstom (SCHWEIZ) AG, Steam Turbines Valves Development (Mechanical Integrity)
- 2015-2021 Research Assistant at ETH Zürich

PUBLICATIONS

The following publications are partially included in this thesis:

- M Röthlin, H Klippel, K Wegener. (2018) "Meshless Methods for Large Deformation Elastodynamics", arXiv preprint arXiv:1807.01117
- M Röthlin, H Klippel, M Afrasiabi, K Wegener. (2019) "Metal cutting simulations using smoothed particle hydrodynamics on the GPU", in: The International Journal of Advanced Manufacturing Technology 102(9):3445–3457
- M Röthlin, H Klippel, M Afrasiabi, K Wegener. (2019) "Meshless single grain cutting simulations on the GPU", International Journal of Mechatronics and Manufacturing Systems 12(3-4):272–297
- H Klippel, M Gerstgrasser, D Smolenicki, E Cadoni, H Roelofs, K Wegener. (2020) "Johnson Cook Flow Stress Parameter for Free Cutting Steel 50SiB8", in: arXiv preprint arXiv:2007.14087
- M Gerstgrasser, D Smolenicki, M Akbari, H Klippel, H Roelofs, E Cadoni and K Wegener. (2021) "Analysis of two parameter identification methods for original and modified Johnson-Cook fracture strains, including numerical comparison and validation of a new blue-brittle dependent fracture model for free-cutting Steel 50SiB8", in: Theoretical and Applied Fracture Mechanics p 102905
- H Klippel, S Süssmaier, K Wegener, "Dry Cutting Experiments Database Ti6Al4V and Ck45" (in preparation)
- H Klippel, M Röthlin, M Afrasiabi, K Wegener, "Inverse Identification of Flow Stress Parameters for Ti6Al4V and Ck45 from cutting experiments with SPH cutting model" (in preparation)
- H Klippel, S Buettner, M Röthlin, M Afrasiabi, K Wegener, "Micro Milling Simulation of OFHC copper with SPH" (in preparation)
- H Klippel, M Röthlin, M Afrasiabi, K Wegener, "SPH Simulation of Metal Cutting with modified Johnson-Cook flow stress models with and without damage modelling" (in preparation)
- H Klippel, M Röthlin, K Wegener, "Load Path Visualization in the Principal Stress System" (in preparation)
- H Klippel, M Röthlin, K Wegener, "Investigation of Stress States in Numerical Cutting Simulations" (in preparation)

Publications which topics are not covered in this PhD-thesis:

- M Afrasiabi, M Röthlin, H Klippel, K Wegener,(2019) "Meshfree simulation of metal cutting: an updated Lagrangian approach with dynamic refinement", International Journal of Mechanical Sciences 160:451–466
- M Afrasiabi, L Meier, M Röthlin, H Klippel, K Wegener, (2020) "GPU-accelerated mesh-free simulations for parameter identification of a friction model in metal machining", International Journal of Mechanical Sciences 176:105571
- M Afrasiabi, H Klippel, M Röthlin, K Wegener, (2020) "Parameter Identification of a Friction Model in Metal Cutting Simulations with GPU-Accelerated Meshfree Methods", Proceedings of the 14th World Congress on Computational Mechanics, Paris, France (pp. 19-24)
- H Klippel, S Süssmaier, M Röthlin, M Afrasiabi, U Pala, K Wegener, (2021) "Simulation of the ductile machining mode of silicon", in: The International Journal of Advanced Manufacturing Technology: 1-14
- M Afrasiabi, H Klippel, M Röthlin, K Wegener, (2021) "Smoothed Particle Hydrodynamics Simulation of Orthogonal Cutting with Enhanced Thermal Modeling", Applied Sciences, 11(3), 1020
- M Afrasiabi, H Klippel, M Röthlin, K Wegener (2021) "An improved thermal model for SPH metal cutting simulations on GPU", Applied Mathematical Modelling, 100, 728–750
- M Afrasiabi, J Saelzer, S Berger, I Iovkov, H Klippel, M Röthlin, K Wegener, (2021). "A Numerical-Experimental Study on Orthogonal Cutting of AISI 1045 Steel and Ti6Al4V Alloy: SPH and FEM Modeling with Newly Identified Friction Coefficients", Metals, 11(11), 1683

COLOPHON

This document was typeset in \LaTeX using the typographical look-and-feel `classicthesis`.
The bibliography is typeset using `biblatex`.